

Université du Québec
Institut National de la Recherche Scientifique
Centre Eau Terre Environnement

**THE RAINY RIVER GOLD DEPOSIT, WABIGOON SUBPROVINCE,
WESTERN ONTARIO: STYLE, GEOMETRY, TIMING AND
STRUCTURAL CONTROLS ON ORE DISTRIBUTION AND GRADES**

Par

Mireille Pelletier

Mémoire présenté pour l'obtention du grade de
Maître ès sciences (M.Sc.)
en sciences de la Terre

12 mai 2016

Jury d'évaluation

Président du jury et examineur interne	Pierre-Simon Ross INRS Centre Eau Terre Environnement
Examineur externe	George J. Hudak Natural Resources Research Institute University of Minnesota Duluth
Directeur de recherche	Patrick Mercier-Langevin Commission géologique du Canada
Codirecteur de recherche	Marc Richer-Laflèche INRS Centre Eau Terre Environnement
Codirecteur de recherche	Benoît Dubé Commission géologique du Canada

RÉSUMÉ

Le dépôt aurifère Rainy River, situé dans la partie ouest de la Sous-province du Wabigoon (Province du Supérieur), contient des ressources minérales estimées à 6,7 millions d'onces d'or. Ce gîte est encaissé dans un complexe volcanique sous-marin calco-alcalin de compositions dacitique à rhyodacitique entouré de basaltes tholéitiques. La minéralisation en or est en grande partie associée à des disséminations et stockwerks de pyrite, sphalérite et chalcopryrite, regroupés en quatre zones aurifères empilées dans la succession hôte et de façon perpendiculaire à la foliation principale (S_2 : 102N/61°SO). Ces zones aurifères ont une géométrie tabulaire, parallèle à S_2 et contiennent des zones à plus forte teneur situées le long de la linéation d'étirement associée (L_2 : 225N/51°SO). De l'or visible est occasionnellement présent dans des veines de quartz-carbonate-pyrite±électrum plissées lors de la phase de déformation D_2 et transposées dans S_2 . Dans le cadre de cette étude, la documentation des faciès volcaniques, de la déformation ainsi que de la minéralogie et de la géochimie associées à l'altération hydrothermale métamorphisée, combinée aux travaux de géochronologie U-Pb, d'analyses isotopiques de l'oxygène ainsi que de cartographie ICP-MS de grains de pyrite ont permis d'exposer une zonation spatiale des assemblages d'altération ainsi que des associations métalliques générées par un système hydrothermal fertile pré déformation principale (D_2). De plus, les unités volcaniques à porosité primaire élevée (p.ex. : niveaux volcanoclastiques) contrôlent en grande partie la distribution de l'or, suggérant également une chronologie relative de déposition de l'or pré-déformation principale. La déformation subséquente des roches hôtes est associée au raccourcissement N-S à NE-SO et est responsable de la géométrie actuelle des zones aurifères maintenant parallèles à S_2 , ainsi que la remobilisation locale de l'or le long de L_2 .

L'information détaillée présentée dans ce mémoire quant aux différents contrôles sur la présence et la concentration de l'or à Rainy River permet de comparer ce dépôt avec d'autres gisements aurifères synvolcaniques connus de la Province du Supérieur, notamment ceux du camp Doyon-Bousquet-LaRonde dans la Sous-province de l'Abitibi. Toutefois, la minéralisation aurifère de type disséminée ainsi que la grande taille des zones aurifères à Rainy River en font un dépôt « atypique » qui se démarque des gisements d'or « plus communs » (p.ex. : or orogénique et sulfures massifs volcanogènes) des ceintures de roches vertes archéennes.

Mots-clés: Rainy River; or; Archéen; synvolcanique; Wabigoon

ABSTRACT

The 6.7 Moz Rainy River auriferous system, located in the western Wabigoon Subprovince of the Superior Province, is hosted in a subaqueous, calc-alkaline dacitic to rhyodacitic complex bounded by tholeiitic basalts. The bulk of the gold is associated with pyrite, chalcopyrite and sphalerite disseminations and stockworks that form isolated, stacked mineralized zones with a present geometry now parallel to the main foliation (S_2 : $102^\circ/61^\circ\text{SW}$). Higher grade mineralized subzones are collinear with a stretching lineation (L_2 : $225^\circ/51^\circ\text{SW}$). Visible gold occasionally occurs in D_2 -folded, quartz-carbonate-pyrite±electrum veins that are now transposed into S_2 . The study of volcanic facies, deformation, alteration mineralogy and geochemistry as part of this study, along with U-Pb geochronology, oxygen isotopes and LA-ICP-MS pyrite mapping allow illustration of the spatial zonation of alteration assemblages and metal associations generated by a fertile, pre- D_2 hydrothermal system. Volcanic products of high primary porosity (e.g., volcanoclastic strata) represent favourable traps for gold. Subsequent deformation, mostly associated with a N-S to NE-SW shortening, is responsible for the present geometry of the mineralized zones that are now parallel to S_2 , with local remobilization along L_2 .

Detailed information on the primary and secondary geological controls on mineralization grade and distribution presented in this thesis allows comparison between the Rainy River system and other known Archean synvolcanic gold systems of the Superior Province such as the ones from the Doyon-Bousquet-LaRonde camp in the Abitibi Subprovince. However, the disseminated nature of mineralization and the large size of the mineralized bodies make it an "unusual" style of system that contrasts with "more common" greenstone-hosted gold deposits such as orogenic gold or volcanogenic massive sulphide deposits.

Keywords: Rainy River; gold; Archean; synvolcanic; Wabigoon

ACKNOWLEDGMENTS

I would first like to thank my thesis director, Patrick Mercier-Langevin, for being such a generous mentor and for sharing his passion and knowledge of geology. You have helped me become a better geologist and I couldn't say thank you enough. Thank you Benoît Dubé and Marc Richer-Lafèche, my co-directors, for your support throughout the project. You and Patrick made a strong mentoring group and this project has greatly benefited from it.

This project was made possible by funding from New Gold Inc., the National Sciences and Engineering Research Council (NSERC) and the Fonds de Recherche Nature et Technologies Québec (FRQNT) through a BMP Innovation scholarship awarded to the author. The Geological Survey of Canada, through the Targeted Geoscience Initiative 4 (TGI-4) lode gold project, also provided funding for analyses and research equipment usage time.

Many thanks to New Gold Inc. for funding, granting access to the property and data; giving me all the necessary resources to complete this thesis. Special thanks to Dean Crick and Justin Tolman, who supervised me while on site and always made time to answer my questions, and to Mark Petersen who made the project possible. Thank you to Rainy River Resources Ltd., notably Kerry Sparkes and Andrew Tims, who initiated the project. Thank you as well to the geology team of the Rainy River project, notably Harvey Buck, Floyd House, Darrell Hyde, Sarah Miller, Jason Pattison, Marilyn Rousseau, Cameron Shaw and Amy Shute for their interest and collaboration. Students Martin Desormiers, Rosina Hiebert, Genvieve Laidlaw and Katie Turner are also thanked for their assistance in the field.

Through this project, I also had the opportunity to exchange with Jim Franklin and Howard Poulsen who kindly provided additional data, ideas and references on northwestern Ontario geology. Thanks to Pierre-Simon Ross and Lyal Harris at INRS with whom I had the opportunity to discuss the project and who provided valuable input. Kathleen Lauzière and Valérie Bécu from the GSC are thanked for their help with data management and field logistics. GIS specialist Marco Boutin from INRS is thanked for his help in generating maps included in this thesis.

Maintenant en français, j'aimerais remercier mes parents Marie Gaudreault, Claude Pelletier et Anne-Marie Cournoyer pour m'avoir fait croire en mes rêves et m'avoir donné les outils pour les réaliser.

Je salut mes compagnons (potes!) de bureau Alex, Anne-Marie, Antoine, Arnaud, Nathalie, Sarane, Vincent, Vivien et William pour votre bonne compagnie. Vous avez rendu mon séjour dans la capitale nationale mémorable.

Now one last word in English: I thank you Ian for being there for me every single step of the way. It has been a great adventure and hopefully one of many to come!

TABLE OF CONTENTS

1	INTRODUCTION.....	1
1.1	PURPOSE OF STUDY	1
1.2	OBJECTIVES.....	2
1.3	METHODOLOGY	3
1.3.1	Determining the immediate geological setting of the deposit.....	3
1.3.2	Hydrothermal alteration assemblages.....	6
1.3.3	Characterizing auriferous zones.....	7
1.3.4	Determining the timing of events in the area.....	8
2	REGIONAL GEOLOGY	9
2.1	SUPERIOR PROVINCE	9
2.2	WABIGOON SUBPROVINCE.....	11
2.2.1	Western Wabigoon lithostratigraphic assemblages	11
2.2.1	Regional structural context.....	12
2.2.2	Rainy River greenstone belt.....	13
2.2.3	Geology of the Rainy River property	14
2.2.4	Deformation in the Wabigoon Subprovince.....	17
2.3	GOLD DEPOSITS AND ADVANCED PROJECTS WITHIN THE WABIGOON SUBPROVINCE	18
2.3.1	Other syngenetic base metal deposits hosted in felsic to intermediate volcanics	19
3	GEOLOGY OF THE RAINY RIVER DEPOSIT.....	21
3.1	INTRODUCTION	21
3.2	VOLCANIC LITHOLOGIES	21
3.2.1	Initial sample classification	22
3.2.2	Felsic coherent facies lavas and shallow intrusions volcanic facies	24
3.2.3	Felsic volcanoclastic facies	34
3.2.4	Mafic tholeiitic units	40
3.2.5	Sedimentary units: mafic and felsic volcanic-dominated	46
3.2.6	Post-volcanic intrusive units.....	49
3.2.7	Summary of the different lithologies present at Rainy River	50
3.3	REPRESENTATION IN SPACE OF THE DIFFERENT VOLCANIC LITHOLOGIES.....	52
3.3.1	Oblique plane	52
3.3.2	Cross section.....	54
3.4	DETAILED MAPS.....	56
3.4.1	Introduction.....	56

3.4.2	McClain outcrop.....	57
3.4.3	Scott outcrop	70
3.5	GEOCHRONOLOGY.....	78
3.6	TECTONIC SETTING AND PETROGENESIS	79
3.6.1	Dacites.....	81
3.6.2	Basalts.....	83
3.6.3	Intrusive bodies	85
4	DEFORMATION AND METAMORPHISM IN THE RAINY RIVER DEPOSIT AREA	87
4.1	INTRODUCTION	87
4.2	METAMORPHISM.....	87
4.2.1	Regional context and previous work	87
4.2.2	Metamorphic mineral assemblages of the Rainy River project.....	88
4.3	DEFORMATION.....	92
4.3.1	Relation to the Quetico Fault.....	92
4.3.2	Early fabrics and pre-D ₂ structures	94
4.3.3	Structural elements: main deformation (D ₂)	95
4.3.4	Late structures.....	105
4.3.5	Structural data from Scott and McClain outcrops.....	106
4.3.6	Timeline of structural events and associated structures in the Rainy River deposit area...	109
4.3.7	Previous structural setting interpretations of the Rainy River deposit.....	110
4.3.8	Structural setting interpretation for the Rainy River deposit area	111
4.3.9	Deformation and mineralization.....	113
5	HYDROTHERMAL ALTERATION	119
5.1	INTRODUCTION	119
5.2	DEPOSIT SCALE: PROTOLITHS AND INTENSITY OF ALTERATION.....	120
5.3	ALTERATION MINERALOGY: NATURE, DISTRIBUTION AND COMPOSITION	125
5.3.1	Sericite- and chlorite-dominated alteration zones: composition, intensity, and distribution	126
5.3.2	Epidote	137
5.3.3	Carbonates	140
5.3.4	Aluminosilicates (kyanite and chloritoid)	147
5.3.5	Garnets.....	149
5.3.6	Rutile	152
5.3.7	Implicit modelling of the distribution of secondary alteration minerals	154
5.3.8	Summary on the distribution and nature of secondary alteration minerals at Rainy River .	161
5.4	MASS BALANCE CALCULATIONS	162
5.3.9	Determining element immobility and predecessors	163

5.3.10	Mass variations: geometry and zonation.....	169
5.3.11	Mass variation with relationship to alteration mineralogy.....	179
5.3.12	Mass variation with relationship to primary volcanic facies.....	179
5.5	OXYGEN ISOTOPES.....	180
5.3.13	Results.....	182
5.3.14	Interpretation of $\delta^{18}\text{O}$ values	186
5.6	SUMMARY ON THE HYDROTHERMAL ALTERATION	189
6	MINERALOGY, GEOCHEMISTRY, AND DISTRIBUTION OF THE MINERALIZED ZONES	193
6.1	INTRODUCTION	193
6.1.1	Mineral resource estimates and grades	193
6.2	MINERALIZED ZONES.....	194
6.2.1	Overview.....	194
6.2.2	ODM zone	196
6.2.3	HS zones	205
6.2.4	433 zone.....	208
6.2.5	Cap zone	212
6.2.6	Summary of style and mineralogy of all mineralized zones	217
6.3	METAL ASSOCIATIONS AND ZONATION.....	218
6.3.1	Metals correlated to gold: deposit scale	218
6.3.2	Metal associations and zonation: section 425475E	221
6.3.3	Metal associations and metal zonation at deposit scale	222
6.4	SUMMARY	247
6.4.1	Summary of the main sulphide phases and accessory phases	247
6.4.2	Zonation in base and precious metals and implications for conditions of gold transport and deposition	248
6.4.3	Paragenetic sequence.....	249
7	SUMMARY, DISCUSSION AND CONCLUSION.....	251
7.1	SUMMARY	251
7.2	DISCUSSION.....	255
7.2.1	Timing of gold deposition and source of metals.....	255
7.2.2	Potential geodynamic context and influence on gold endowment	256
7.2.3	Potential evolution of the volcanic environment and role in trapping/precipitation of metals....	257
7.2.4	Potential nature of fluids and discussion on gold transport and metal zonation	258
7.2.5	Deformation of the Rainy River deposit and impact on mineralization	260

7.2.6	Potential analogues and comparison with other known synvolcanic gold deposits of the Superior Province and other localities.....	261
7.3	CONCLUSION AND IMPLICATIONS FOR EXPLORATION	262
8	REFERENCES.....	269
	APPENDIX I : DETAILED MAPS AND CROSS SECTION	283
	APPENDIX II : MICROPROBE ANALYSES RESULTS	284
	II.I ALUMINOSILICATES.....	284
	II.II BIOTITE	287
	II.III CARBONATE.....	290
	II.III CHLORITE	292
	II.IV EPIDOTE	302
	II.V FELDSPAR.....	307
	II.VI GARNET	309
	II.VII MUSCOVITE.....	311
	APPENDIX III : SEM AND EDS SPECTROMETRY ANALYSES.....	325
	III.I SAMPLE RRR435502	331
	III.II SAMPLE RRR435506	333
	III.III SAMPLE RRR435572	337
	III.IV SAMPLE RRR435732.....	337
	III.V SAMPLE RRR435737	341
	III.VI SAMPLE RRR435749.....	343
	III.VII SAMPLE RRR435795.....	344
	III.VIII SAMPLE RRR435806.....	347
	III.IX SAMPLE RRR435830.....	349
	III.X SAMPLE RRR435875.....	354
	III.XI SAMPLE RRR435883.....	358
	APPENDIX IV: SELECTED MICROPROBE RESULTS FROM KJARSGAARD (2013) STUDY	358

LIST OF TABLES

TABLE 3.1 : Summary of the different lithologies present at the Rainy River deposit	50
TABLE 4.1 : Mean foliation orientation measured at mapped outcrops and above the deposit itself	108
TABLE 5.1 : r^2 values of the regression lines for each bivariate plots of figure 5.36.....	166
TABLE 5.2 : Precursor composition (major oxides and Zr only) based on the average composition of samples RRR435870 and RRR435900 for mass variation calculation.....	166
TABLE 5.3 : Major oxide and Zr mass concentration for sample RRR435562 chosen as the precursor composition for mass variation calculation.....	168
TABLE 5.4 : Mass variation (in wt. %) of major oxides for a kyanite-chloritoid bearing sample	179
TABLE 6.1 : Resource and reserve estimates for the planned open pit and underground mining activities at the Rainy River Gold project	193
TABLE 6.2 : Open pit mineral resources at a 0.3 ppm Au cut-off, assuming a gold metallurgical recovery of 90%	195
TABLE 6.3 : Mineralization styles of the different mineralized zones of the Rainy River deposit	217
TABLE 6.4 : Mineralogy of the metal-bearing phases for the Rainy River deposit with respect to the different mineralized zones	218
TABLE 6.5 : Correlation matrix of metals.....	218

LIST OF FIGURES

Figure 1.1: Location of the Rainy River gold project in Ontario.	1
Figure 1.2 : Screen shot from Leapfrog [®] Mining software of the different diamond drill core intercepts (in yellow and red) that compose the oblique plane (in gray, oriented 323N/43°)	4
Figure 1.3 : The oblique plane (in reduced opacity) with the 425475E north-south cross section.	5
Figure 2.1 : Superior Province geological map	10
Figure 2.2 : Simplified geological map of the western Wabigoon Subprovince.	12
Figure 2.3 : Rainy River project simplified geologic map, with final pit outline.	16
Figure 2.4 : Regional faults in the Rainy River area (see Chapter 4 for raw mag data).	17
Figure 2.5 : Simplified geological map with location of significant Au deposits and prospects around the Rainy River gold deposit.	20
Figure 3.1 Volcanic rock classification diagram (Winchester and Floyd, 1977) with samples from the Rainy River project previously sorted according to their magmatic affinity.	22
Figure 3.2 : Rock classification diagram from Winchester and Floyd (1977), with samples from the Rainy River project previously sorted according to their magmatic affinity.	23
Figure 3.3 : Th/Yb vs. Zr/Y logarithmic diagram for discrimination of magmatic affinities from Ross and Bédard (2009).	23
Figure 3.4 : AFM diagram (Irvine and Baragar, 1971) using major oxydes and total iron, plotting the previously classified tholeiitic and calc-alkaline samples.	24
Figure 3.5 : Coherent facies: dacite	26
Figure 3.6 : Felsic flows and shallow sub-volcanic intrusions.....	28
Figure 3.7 : Felsic flows and shallow intrusions : QFP dacite.....	30
Figure 3.8 : Felsic flows and shallow intrusions : QFP dacite.....	31
Figure 3.9 : Ternary feldspar classification diagram, with plotted microprobe data of the different feldspar grains analyzed	32
Figure 3.10 : Dacitic muscovite schists	34
Figure 3.11 : Felsic volcanoclastic facies : monomict clast-supported dacitic breccia	36
Figure 3.12 : Felsic volcanoclastic facies : polymict, clast-supported dacitic lapilli tuff breccia.....	38
Figure 3.13 : Chondrite-normalized multi-element plots for the calc-alkaline dacitic volcanoclastic and coherent felsic rocks of the Rainy River deposit.	39
Figure 3.14 : Felsic volcanoclastics : quartz crystal tuff.....	40
Figure 3.15 : Mafic tholeiitic units : drill core and thin section observations.	42
Figure 3.16 : REE profiles normalized to the primitive mantle composition from Sun and McDonough (1989) along with multi-element chondrite-normalized profiles after McDonough and Sun (1995) for tholeiitic basalt samples without HFSE decoupling.	43

Figure 3.17 : Multi-element profiles of all tholeiitic basalts, normalized after the C1 chondrite values from McDonough and Sun (1995)	44
Figure 3.18 : Mafic tholeiitic units : outcrop exposures	46
Figure 3.19 : Potential sedimentary units: felsic and mafic, volcanic-dominated	48
Figure 3.20 : Mean multi-element profiles comparing the mafic and felsic lavas with the sedimentary units of the samples from the Rainy River deposit.	49
Figure 3.21 : Post volcanic intrusive units.....	50
Figure 3.22 : Representation of the volcanic lithologies on the oblique plane (323N/43°) with respect to the different mineralized zones	53
Figure 3.23 : 425475E cross section with volcanic lithologies documented with respect to the different mineralized zones.....	55
Figure 3.24 : Projected mining site plan of the Rainy River project with the location of the Scott and McClain outcrops.....	56
Figure 3.25 : McClain outcrop detailed map (1:100).....	57
Figure 3.26 : McClain outcrop dacitic tuffs and coherent dacite.....	60
Figure 3.27 : Coherent and feldspar-phyric dacites, McClain outcrop.....	62
Figure 3.28 : Dacitic breccia and pyrite-rich mafic tuff, McClain outcrop.....	65
Figure 3.29 : Veins and structures, McClain outcrop.....	68
Figure 3.30 : Veins and structures, McClain outcrop.....	69
Figure 3.31 : Detailed map (1:100) of Scott outcrop.....	72
Figure 3.32 : Scott outcrop, southern portion.....	74
Figure 3.33 : Northern portion of Scott outcrop.	77
Figure 3.34 : Ta vs. Y discrimination diagram of Pearce et al. (1984).....	80
Figure 3.35 : Th/Ta vs. Yb tectonic discrimination diagram from Gorton and Schandl (2000) with all felsic volcanic rock samples with a Th/Ta ratio below 30 (n=160).	80
Figure 3.36 : A) Diagram from Hart et al. (2004) with data from Archean felsic rocks.	81
Figure 3.37 : Mafic tholeiitic and felsic calc-alkaline samples plotted on assimilation and fractional crystallization (AFC) diagram leading to idealized tonalite-trondhjemite-granodiorite (TTG) pole.....	82
Figure 3.38 : Spider plot of tholeiitic samples normalized to N-MORB values from Sun and McDonough (1989). LREE enrichment is on average 3 times above the idealized N-MORB composition.	84
Figure 3.39 : Th-Nb proxy diagram for oceanic basalt classification adapted from Pearce (2008).....	84
Figure 3.40 : Median and mean values for multi-element C1-normalized profiles of the different calc-alkaline volcanic facies along with the granitic to gabbroic dykes that cross-cut the deposit.	86
Figure 3.41 : Individual multi-element C1-normalized profiles of the dyke samples in comparison with the coherent dacites within the deposit	86
Figure 4.1 : Metamorphic mineral assemblages.....	90
Figure 4.2 : Metamorphic mineral assemblages	91

Figure 4.3 : Raw aeromagnetic data (total magnetic field) clipped to the present Rainy River property (as of September 2015).....	93
Figure 4.4 : Regional faults in the Rainy River area.	94
Figure 4.5 : Structural fabrics : S_0 , D_1 and D_2 -related structures.	97
Figure 4.6 : Structural fabrics and trends.....	99
Figure 4.7 : Kinematic indicators : drill core and outcrop.....	102
Figure 4.8 : Kinematic indicators on un-oriented thin section and vein arrays	104
Figure 4.9 : Post- D_2 brittle-ductile and brittle structural features.. ..	106
Figure 4.10 : Foliation measurements on McClain outcrop. Equal area projection, lower hemisphere. ...	107
Figure 4.11 : Joint set in coherent dacite on McClain outcrop. Wulf projection.....	107
Figure 4.12 : Foliations and bedding measurements on Scott outcrop.	108
Figure 4.13 : Three dimensional diagram of the different structural elements associated with the D_2 deformation episode observed at the Rainy River deposit within an inclined transpression model.	113
Figure 4.14 : Deformation intensity visual index with associated reference sample photomicrographs ..	115
Figure 4.15 : Oblique plane oriented perpendicular to L_2 ($323N/43^\circ$) illustrating the distribution of deformation intensity with respect to the main mineralized zones of the deposit.	117
Figure 5.1: Pie chart of all samples from this study (n=327)	121
Figure 5.2 : Titanium-vanadium bivariate plot.....	121
Figure 5.3 : REE profiles of tholeiitic rocks.	122
Figure 5.4 : Modified Alteration box plot from Large et al. (2001a) with least-altered fields from Trépanier (2011) and Bigot (2014).	123
Figure 5.5 : Hashimoto index (AI; Ishikawa, 1976) versus advanced argillic alteration index (AAAI; Williams and Davidson, 2004) in a modified box plot.....	124
Figure 5.6 : Alkali-alumina molar ratio diagram (Davies and Whitehead, 2006) with all dacitic samples (excluding intrusives; n=256).....	127
Figure 5.7 : K_2O (%) versus Rb (ppm) plot of all dacitic samples (excluding intrusives, n=256).....	128
Figure 5.8 : Sericite photos.	129
Figure 5.9 : Oblique plane ($323N/43^\circ$) representing the distribution of sericite alteration intensity based on detailed core logging.	130
Figure 5.10 : Bubble plot of fluorine versus $Fe/(Fe+Mg)$ ratio for muscovites.....	131
Figure 5.11 : Implicit modelling of the zones of ≥ 7 vol. % chlorite based on detailed core logging.....	133
Figure 5.12 : Chlorite photos.....	134
Figure 5.13 : Chlorite classification diagram.....	135
Figure 5.14 : Abundance of MnO in chlorites.....	135
Figure 5.15 : Histogram of $Fe/(Fe+Mg)$ ratios in chlorites	136
Figure 5.16 : Bubble plot with size proportional to Au content of sample for chlorite grains.	137
Figure 5.17 : Epidote photos.	138

Figure 5.18 : Epidote photos	139
Figure 5.19 : Microprobe data of the epidote analyses.....	140
Figure 5.20 : Carbonate photos.	142
Figure 5.21 : Carbonate photos.	143
Figure 5.22 : Carbonate alteration diagram.	145
Figure 5.23 : Composition of carbonate grains from this study (n=77) plotted on a carbonate classification diagram.....	146
Figure 5.24 : Bivariate plot of the CaCO ₃ and MnCO ₃ content of carbonates.....	147
Figure 5.25 : Aluminosilicates photos.	149
Figure 5.26 : Aluminosilicates and garnet photos.....	151
Figure 5.27 : Classification of garnets based on their composition evaluated via microprobe.....	152
Figure 5.28 : Garnet and rutile photos.	153
Figure 5.29 : Implicit modelling of the zones of intense carbonate alteration (8 to 15 vol.% carbonates) based on data from detailed core logging.	155
Figure 5.30 : Implicit modelling of intense carbonate alteration (8 to 15 vol.% carbonates) on oblique plane.....	156
Figure 5.31 : 425475E cross section, looking west. Implicit modelling of the zones with presence of aluminosilicates (kyanite ± chloritoid) based on data from detailed core logging.....	157
Figure 5.32 : 425475E cross section, looking west. Implicit modelling of the zones with presence of garnets based on data from detailed core logging.....	158
Figure 5.33 : Oblique plane oriented 323N/43°, looking 43° towards 233N (perpendicular to plane). Implicit modelling of spessartine garnets based on detailed core logging data.....	159
Figure 5.34 : 425475E cross section, looking west. Implicit modelling of the zones with rutile dusting, based on data from detailed core logging.....	160
Figure 5.35 : Al ₂ O ₃ (wt. %) versus Zr (ppm) plot.....	163
Figure 5.36 : Bivariate plots with regression line of immobile compatible-incompatible as well as incompatible-incompatible element pairs.	165
Figure 5.37 : Volcanic rock classification TAS diagram.....	167
Figure 5.38 : XY plots with regression lines of Zr mass concentrations with respect to various immobile elements for the tholeiitic affinity samples.....	168
Figure 5.39 : Evolution of mass balance variations down hole through the different mineralized zones along composite drill hole NR060058 and NR060067E within the 425475E cross section (± 25m E-W metres).....	170
Figure 5.40 : Modelling of CaO mass addition over 1.7 wt.% for the calc-alkaline lithologies along the 425475E cross section.	172
Figure 5.41 : Modelling of CO ₂ mass addition (over 0 wt.%) for the calc-alkaline lithologies along the 425475E cross section.	173

Figure 5.42 : Modelling of Na ₂ O mass variation (between -2.7 and +4.8 wt.%) along the 425475E cross section for all lithologies.	174
Figure 5.43 : Modelling of MnO positive mass addition (over 0 wt.%) for the calc-alkaline lithologies along the 425475E cross section.	175
Figure 5.44 : Modelling of SiO ₂ mass addition over 5.0 wt.% for the calc-alkaline lithologies along the 425475E cross section.	176
Figure 5.45 : Modelling of K ₂ O mass addition over 1.5 wt.% for the calc-alkaline lithologies along the 425475E cross section.	177
Figure 5.46 : Combined modelling of SiO ₂ mass addition over 5.0 wt.% and K ₂ O mass addition over 1.5 wt.% for the calc-alkaline lithologies along the 425475E cross section.	178
Figure 5.47 : Comparative bar chart illustrating mean (n=257) mass variation values (wt.%) between dacitic samples of coherent and volcanoclastic facies.	180
Figure 5.48 : Rainy River project geologic map with sample location for oxygen isotope analyses.	181
Figure 5.49 : Histogram of all δ ¹⁸ O _{VSMOW} values for samples from this study.	182
Figure 5.50 : Whisker plot illustrating quartiles (25, 75), median, maximum and minimum δ ¹⁸ O _{VSMOW} values for all samples from this study.	183
Figure 5.51 : Variation of δ ¹⁸ O values within the Rainy River deposit area.	184
Figure 5.52 : Variation of δ ¹⁸ O values within the oblique plane.	185
Figure 5.53 : XY plot of Zr and TiO ₂ for all calc-alkalic samples.	186
Figure 5.54 : Plot of δ ¹⁸ O values from calc-alkalic samples with respect to mass variations of SiO ₂ and Na ₂ O.	188
Figure 5.55 : Plot of δ ¹⁸ O values from calc-alkalic samples (n=44) with respect of the advanced argillic alteration index.	188
Figure 5.56: Relative timing of the metamorphism and hydrothermalism-related minerals of the Rainy River deposit.	192
Figure 6.1 : Three-dimensional view of the mineralized zones that compose the Rainy River deposit ...	195
Figure 6.2 : ODM mineralized zone photos.	199
Figure 6.3 : ODM mineralized zone photos.	200
Figure 6.4 : ODM mineralized zone photos.	201
Figure 6.5 : ODM mineralized zone backscattered electron images (15 kV operating voltage).	202
Figure 6.6 : LA-ICP-MS element mapping of a pyrite grain from sample RRR435508 of the ODM zone. Element correlated to Au content.	204
Figure 6.7 : LA-ICP-MS element mapping of pyrite grain from sample RRR435508 from the ODM zone. Elements poorly correlated to Au content.	205
Figure 6.8 : HS mineralized zone photos.	207
Figure 6.9 : HS mineralized zone photos.	208
Figure 6.10 : 433 mineralized zone photos.	210

Figure 6.11 : 433 mineralized zone photos	211
Figure 6.12 : Cap mineralized zone photos.	214
Figure 6.13 : Cap mineralized zone photos.	215
Figure 6.14 : Cap mineralized zone photos.	216
Figure 6.15 : Whisker plots for a suite of metals correlated to gold values at Rainy River.	220
Figure 6.16 : Metal concentration values down composite drill hole going through all mineralized zones at 425475E	222
Figure 6.17 : Screen shot of Leapfrog [®] Mining showing histogram for Zn data to be modelled.	224
Figure 6.18 : NewGold inc. 0.3 g/t Au shells obtained from wireframing work of the Cap (in green), ODM (in yellow) and 433 (in blue) zones, onto which are superimposed the 0.3 g/t Au shells generated in this study using Leapfrog [®] Mining implicit modelling.	226
Figure 6.19 : Grade modelling of silver (≥ 2.2 ppm) using Leapfrog [®] Mining.	230
Figure 6.20 : Grade modelling of arsenic (≥ 31 ppm) using Leapfrog [®] Mining.	232
Figure 6.21 : Grade modelling of bismuth (≥ 2 ppm) using Leapfrog [®] Mining.	234
Figure 6.22 : Grade modelling of copper (≥ 150 ppm) using Leapfrog [®] Mining.	236
Figure 6.23 : Superimposed gold and copper grade modelling using Leapfrog [®] Mining.	237
Figure 6.24 : Grade modelling of lead (≥ 25.0 ppm) using Leapfrog [®] Mining.	239
Figure 6.25 : Grade modelling of zinc (≥ 500 ppm) using Leapfrog [®] Mining.	241
Figure 6.26 : Superimposed arsenic (≥ 31 ppm) and copper (≥ 150 ppm) grade shells constrained within proposed pit and underground mining area	243
Figure 6.27 : Superimposed lead (≥ 25 ppm) and copper (≥ 150 ppm threshold) grade shells constrained within proposed pit and underground mining area.	244
Figure 6.28 : Superimposed zinc (≥ 500 ppm) and copper (≥ 150 ppm) grade shells constrained within proposed pit and underground mining area.	245
Figure 6.29 : Superimposed silver (≥ 2.2 ppm) and copper (≥ 150 ppm) grade shells constrained within proposed pit and underground mining area.	246
Figure 6.30 : Graphic summary of the distribution of base and precious metals with respect to the different mineralized zones.	247
Figure 7.1 : Potential volcanic architecture and emplacement of the calc-alkaline dacitic body hosting the Rainy River deposit.	265
Figure 7.2 : A. Present zonation of alteration mineral assemblages and associated mass variations represented on the Rainy River deposit pre-deformation. B. Metal associations characterizing the Rainy River deposit with potential sources of metals and conditions of metal transport and precipitation at peak hydrothermalism (pre-deformation).....	266
Figure 7.3 : Sketches of potential deformation of the Rainy River deposit post hydrothermal activity and volcanism.....	267

LIST OF MAPS

Map 3.1 : Distribution of volcanic facies and lithologies on the oblique plane	appendix I (end of document)
Map 3.2 : Distribution of volcanic facies on 425475E cross section	appendix I (end of document)
Map 3.3 : McClain outcrop	appendix I (end of document)
Map 3.4 : Scott outcrop	appendix I (end of document)

SOMMAIRE RÉCAPITULATIF

Buts et objectifs de la recherche

Le gisement Rainy River est un projet aurifère présentement en phase de développement appartenant à la compagnie minière New Gold Inc. et situé dans le nord-ouest de l'Ontario (figure 1.1). La minéralisation aurifère est répartie en quatre zones minéralisées parallèles à la foliation principale, qui sont, du sud vers le nord, les zones Cap, ODM, HS et 433. Les ressources minérales mesurées et indiquées totalisent 185,6 millions de tonnes de minerai à une teneur de 1,13 g/t Au pour un total de 6,7 millions d'onces (208,4 tonnes) d'or (New Gold Inc., 2015a), faisant de ce gisement un des principaux projets aurifères en développement en Ontario. Ce gisement de taille et d'intérêt économique important est caractérisé par une basse teneur en or comparativement aux gisements d'or archéens traditionnellement exploités dans les ceintures de roches vertes. Cette caractéristique en fait un gisement a priori atypique. Dans une perspective d'exploration minérale pour la recherche de gisements similaires, la caractérisation d'un tel gisement est essentielle.

La présente étude a pour but de :

1. Décrire le contexte géologique immédiat ainsi que la nature de la minéralisation aurifère à Rainy River et;
2. Définir les contrôles primaires et secondaires sur la distribution ainsi que la concentration de l'or à travers le gisement, et ce dans le but de générer des vecteurs d'exploration pour des gisements similaires au Canada.

Ce travail de maîtrise s'inscrit à l'intérieur d'un projet de recherche pancanadien de la Commission Géologique du Canada (CGC) nommé Initiative Géoscientifique Ciblée 4 (IGC-4). Ce projet a pour but d'approfondir les connaissances géoscientifiques reliées à l'exploration minière en plus d'optimiser les techniques préexistantes d'exploration (Dubé *et al.*, 2011, 2015).

Les objectifs de ce projet de maîtrise sont :

1. Améliorer la caractérisation géochimique des unités volcaniques hôtes du gisement et établir une corrélation avec les unités stratigraphiques de la région identifiées dans des travaux publiés antérieurement.

2. Documenter les différents assemblages de minéraux d'altération associés à la minéralisation aurifère en termes de minéralogie, de signature géochimique ainsi que distribution dans l'espace.
3. Caractériser les zones minéralisées via l'identification des phases métalliques et sulfurées présentes ainsi que leurs textures, la reconnaissance d'associations métalliques et leur distribution dans l'espace. La distribution des zones minéralisées et des associations métalliques est également mise en relation avec la distribution des différents assemblages de minéraux d'altération.
4. Établir la nature ainsi que l'ordre chronologique des différents éléments structuraux recensés dans le gisement ainsi que leur influence sur la distribution et la présence de minéralisation aurifère.
5. Établir une chronologie relative et absolue des différents événements dans la région (minéralisation, altération, déformation, métamorphisme, remobilisation et apport additionnel potentiel de minéralisation) à l'aide de datation U-Pb.
6. Définir l'environnement géologique de mise en place des différentes zones minéralisées en termes volcanique, hydrothermal ainsi que de déformation structurale.
7. Déterminer l'origine, la température ainsi que le cheminement probable des fluides minéralisateurs dans le gisement à l'aide de l'étude des signatures isotopiques de l'oxygène.
8. Définir les indicateurs lithologiques, structuraux et lithogéochimiques de minéralisation dans le gisement.
9. À partir des informations recueillies sur le gisement Rainy River, comparer ce dernier avec d'autres gisements d'or et de métaux de base de la Sous-province du Wabigoon et, à plus grande échelle, de la Province du Supérieur.
10. Proposer un modèle de formation du gisement Rainy River révisé et amélioré.

Méthodologie de la recherche

Afin de répondre aux objectifs cités plus haut, une approche multidisciplinaire a été priorisée lors de l'étude du gisement. Les activités de recherche réalisées ainsi que la méthodologie de recherche sont résumées ici-bas.

Une compilation de la littérature existante concernant le gisement ainsi que de la géologie régionale a été réalisée. En plus des différents articles et rapports publiés, une série de rapports internes de New Gold Inc. et de Rainy River Resources Ltd. (compagnie propriétaire du projet de 2005 à 2013) ainsi que le mémoire de maîtrise de J. Wartman (2011) ont été consultés.

Les travaux de terrain réalisés par l'auteur se sont échelonnés sur les étés 2013 et 2014. Durant cette période, la description ainsi que l'échantillonnage de carottes de forages ont été réalisés afin d'acquérir des données permettant de préciser la volcanologie, la déformation, l'altération hydrothermale et la nature de la minéralisation caractéristique du gisement. À cela s'ajoute la cartographie de détail de deux affleurements situés dans l'environnement immédiat du gisement ainsi que des travaux de cartographie de reconnaissance afin de documenter les unités volcaniques hôtes du gisement ainsi que les différents éléments de déformation enregistrés à l'échelle de l'affleurement. Le logiciel de cartographie utilisé est Mapinfo Professional™ version 10.5.

Trois cent vingt-sept échantillons recueillis ont été analysés suite à une digestion de roche totale au laboratoire ActLabs situé à Ancaster en Ontario, en utilisant une trousse d'analyse spécifique aux échantillons de projets IGC-4. Le lecteur peut se référer à la publication Pelletier *et al.* (2016) pour de plus amples informations sur les techniques utilisées ainsi que sur les procédures de contrôle de qualité. Une lame mince de 30 μm d'épaisseur a également été fabriquée à partir de chaque échantillon envoyé pour analyse lithogéochimique. Ces lames minces ont été confectionnées par la compagnie Vancouver Petrographics à Langley en Colombie-Britannique. Les lames minces utilisées pour les analyses *in situ* par ablation laser ont une épaisseur de 200 μm .

En plus des données lithogéochimiques recueillies en laboratoire, des analyses à la microsonde de certains minéraux d'altération furent réalisés à l'Université Laval sous la supervision de Dr. M. Choquette à l'aide d'une microsonde CAMECA® SX-100. Un microscope électronique à balayage JEOL® 840-A, combiné à un spectromètre EDS (analyse dispersive en énergie) a également été utilisé pour caractériser les phases métalliques. Ces analyses furent réalisées à l'Université Laval sous la supervision de M. A. Ferland.

Les logiciels Leapfrog® Mining version 2.5.361, Leapfrog® Geo version 2.1.2 et REFLEX® ioGAS version 6.0.1 furent utilisés afin de traiter et interpréter les résultats d'analyses géochimiques pour ensuite les modéliser dans un environnement tridimensionnel.

En plus des activités de recherche réalisées à Rainy River dans le cadre de ce projet de maîtrise s'ajoutent des activités de recherche conduites par la CGC dans le cadre du projet IGC-4. Des rapports isotopiques de l'oxygène ont été mesurés sur 46 échantillons analysés (section 5.5). Ces analyses furent réalisées par K. Law de l'université Western Ontario à London en Ontario. Des cartographies LA-ICP-MS de pyrite ont été réalisées par les Drs. S.E. Jackson et Z. Yang à la CGC à Ottawa (figures 6.6 et 6.7). La publication Gao *et al.* (2015) offre de plus amples renseignements sur les procédés analytiques quant à la cartographie de la pyrite par ablation laser. Des travaux de géochronologie U-Pb sur zircon par la méthode ID-TIMS ont été réalisés sur deux échantillons par V. McNicoll à la CGC d'Ottawa. Les résultats sont présentés à la section 3.5 du mémoire et le lecteur est invité à consulter la publication McNicoll *et al.* (2014) pour plus d'information sur la méthodologie utilisée.

Contexte géologique et métallogénique

Le gisement Rainy River est situé dans la Sous-province du Wabigoon, dans la partie sud-ouest de la Province du Supérieur (Fig. 2.1). Cette province tectonique est interprétée comme étant le résultat de l'accrétion vers le Nord d'une succession de terranes durant la période de 2,72-2,68 Ga (Krogh et Davis, 1971; Ayer et Davis, 1997; Percival, 2007).

La Sous-province du Wabigoon est composée d'une série de ceintures de roches vertes entrecoupées par des batholithes de granitoïdes (figure 2.2). La majorité de l'activité volcanique de cette région est datée entre 2745 et 2711 Ma (Blackburn *et al.*, 1991) et le volcanisme enregistré dans chaque ceinture volcanique est généralement divisé en deux séquences : une séquence inférieure mafique et ultramafique constituée de komatiites, de tholéiites et de rares andésites suivi d'une séquence supérieure différenciée et d'affinité calco-alcaline.

L'accrétion de la Sous-province du Wabigoon à la Sous-province de la Rivière Winnipeg (située au nord) s'est produite lors de l'orogène Kénoréenne (2,71-2,70 Ga; Percival *et al.*, 2006a) et est responsable de la majorité de la déformation enregistrée dans le Wabigoon. Cette accrétion a généré un raccourcissement N-S important responsable de plis isoclinaux P_1 suivi d'un raccourcissement NE-SO auquel est associé une foliation pénétrative S_2 ainsi que des plis P_2 et des failles de chevauchement. Un métamorphisme et plutonisme associés à l'orogène est responsable de la crénulation de S_2 et de la formation de foliations secondaires (S_3) associées à la mise en place des batholithes (Sanborn-Barrie, 1991). Aux frontières nord et sud de la Sous-province une composante de cisaillement importante est observée et se reflète par la

présence de failles subverticales à déplacement horizontal important (par exemple 128 km pour la faille Quetico; Fernandez *et al.*, 2013). Suite à cette accréation, la Sous-province de Quetico, située au sud du Wabigoon et majoritairement composée de roches métaédimentaires, a été accrétée au Wabigoon et la frontière entre ces deux sous-provinces est soulignée par la faille Quetico.

Le gisement Rainy River est situé à l'intérieur de la «ceinture de roches vertes Rainy River». Cette nomenclature informelle a été introduite par la compagnie Rainy River Resources Ltd. et désigne une succession de roches volcaniques et sédimentaires s'étendant du batholithe de Sabaskong au nord à la faille Quetico au sud et bordée à l'est par le complexe de batholithes de Rainy Lake (figure 2.2). La faille de Quetico et ses structures secondaires associées ont été interprétées à partir de données géophysiques (Siddorn, 2008; figures 4.3, 4.4). Selon ces travaux, une structure secondaire de la faille serait située à moins de 5 km au sud du gisement.

La vaste majorité du gisement est encaissée dans des dacites calco-alcalines qui sont bordées au nord et au sud par des basaltes tholéiitiques (figure 2.3). À l'extrémité sud de la propriété se trouve un ensemble de roches métasédimentaires appelés sédiments Mather dans certains ouvrages (p.ex. : Fletcher et Irvine, 1954; Poulsen, 2005). Les travaux de Fletcher et Irvine (1954) indiquent une polarité vers le sud pour ces roches sédimentaires.

En terme de contexte métallogénique, le gisement Rainy River ne fait partie d'aucun camp ou district minier, par contre quelques gisements connus sont situés dans la partie ouest du Wabigoon (figure 2.5). La plupart de ces gisements sont de type orogénique, c'est-à-dire associés à la déformation régionale. Le projet d'exploration Goliath Gold ainsi que le complexe de Sturgeon Lake sont deux systèmes minéralisés de la région caractérisés par la présence de nombreuses minéralisations synvolcaniques polymétalliques (figure 2.5).

Volcanologie, classification géochimique et environnement tectonique de formation des roches hôtes du gisement

Une classification initiale des roches volcaniques à partir de données d'analyse géochimique a permis d'établir deux lithologies principales : des dacites calco-alcalines qui encaissent une très grande partie des zones minéralisées ainsi que des basaltes tholéiitiques généralement périphériques aux zones aurifères (figures 3.1, 3.2 et 3.3). Parmi ces deux lithologies, plusieurs faciès volcaniques ont été identifiés à partir des descriptions de forages, des travaux

de cartographie détaillées ainsi que des travaux de Wartman (2011) portant sur la volcanologie du secteur. L'altération hydrothermale des roches volcaniques à Rainy River a partiellement détruit ou encore introduit de fausses textures volcaniques (Allen, 1988). Seulement les textures clairement reconnaissables ont été prises en considération. La distribution des différentes lithologies et faciès volcaniques est illustrée en section et en plan oblique sur les cartes 3.1 et 3.2 présentées à la fin du document.

Un faciès de dacite cohérente associé à des coulées de lave ou encore des dômes, cryptodômes ou intrusions subvolcaniques a été identifié grâce à la présence de textures d'écoulement laminaire bien préservées (carte 3.3) et de texture microporphyrrique à quartz et/ou feldspaths en lame mince. Un échantillon de dacite cohérente provenant d'un affleurement minéralisé situé dans le mur structural du gisement a été daté par méthode U-Pb (ID-TIMS) et possède un âge approximatif de 2717 Ma (V. McNicoll, commun. pers., 2014). Des tufs dacitiques ainsi que des tufs à lapilli monogéniques ont également été identifiés en carottes de forage ainsi qu'en affleurement. Ces unités volcanoclastiques sont corrélées avec des zones minéralisées à l'échelle du gisement (cartes 3.1 et 3.2). Un contact de type pépéritique entre une séquence de tuf dacitique lité et une unité de dacite cohérente a été observé en affleurement (carte 3.4), indiquant un environnement de déposition sous-marin. Le régime volcanique inféré pour la mise en place des unités dacitiques est un environnement sous-marin de dômes et coulées associées. Cet environnement est en accord avec la présence de basaltes coussinés situés de part et d'autre du complexe dacitique.

Des unités sédimentaires à grains fins à composition dominante mafique ont également été identifiées en forages ainsi qu'en surface, ce qui est également compatible avec un environnement de déposition sous-marin.

Les faciès volcaniques identifiés pour les roches mafiques sont des basaltes coussinés ainsi que des coulées mafiques à amygdules (figures 3.19A, B). En forage, aucune texture diagnostique de faciès volcanique mafique n'a pu être identifiée.

Des dykes de gabbro et de diabase, tardifs et non déformés, recoupent le gisement et sont peu communs (cartes 3.1, 3.2). Des dykes granitiques (figures 3.21A, B) affectés par D_2 recoupent également les zones minéralisées et ne sont pas altérés. Un de ces dykes qui recoupe la zone Cap a été échantillonné pour datation U-Pb et possède un âge maximal approximatif de 2693 Ma (McNicoll, commun. pers., 2014).

Les dacites calco-alkalines sont caractérisées par une faible variation du rapport TiO_2/Zr ou encore Al_2O_3/Zr (figure 5.36), impliquant une faible différenciation magmatique à l'intérieur de la séquence volcanique hôte. Les dacites du gisement Rainy River possèdent des spectres de terres rares et éléments traces typiques du groupe de roches felsiques F1 (figure 3.37) de la classification de Leshner *et al.* (1986). Ceci indique un environnement de formation magmatique à l'intérieur du champ de stabilité du grenat, c'est-à-dire à haute pression, donc à une grande profondeur dans la croûte archéenne. Ces dacites montrent également une signature géochimique semblable à celles de volcanites d'arc insulaires modernes selon les diagrammes de Pearce *et al.* (1984; figure 3.35). Toutefois, ce type de signature géochimique peut également être obtenu par assimilation et cristallisation fractionnée à haute pression impliquant la base de la croûte archéenne.

Les basaltes tholéitiques échantillonnés à Rainy River montrent des spectres de terres rares et d'éléments traces similaires à ceux des basaltes modernes associés à des environnements d'arrière-arc. Les abondances en terres rares légères des basaltes de Rainy River sont trois fois supérieures à celles des MORB primitifs provenant de la compilation de Sun et McDonough (1989; figure 3.39). Les rapports Nb/Yb et Th/Yb des basaltes de Rainy River sont également similaires à ceux recensés dans les études portant sur les basaltes de 2,9 à 3,0 Ga du nord de la Province du Supérieur (figure 3.40; Pearce, 2008).

Déformation et métamorphisme du gisement

Des minéraux métamorphiques progrades et rétrogrades ont été identifiés à Rainy River et indiquent un pic métamorphique de niveau schiste vert supérieur à amphibolite inférieur. La cristallisation métamorphique atteint son apogée après le pic de l'épisode de déformation D_2 comme en témoigne la présence de grenats possédant une auréole non-déformée entourant un cœur riches en inclusions parallèles à S_2 (figure 4.1B).

Deux structures dominantes contrôlent la forme ainsi que la distribution des zones minéralisées à Rainy River. Celles-ci consistent en une foliation pénétrative (S_2) d'orientation moyenne $102N/61^\circ$ à laquelle les zones minéralisées ainsi que les contacts entre les différentes unités lithologiques sont maintenant parallèles. Cette foliation pénétrative s'exprime également par l'alignement des micas ainsi que l'étirement/aplatissement des phénocristaux de quartz et des clastes volcaniques. La linéation d'étirement L_2 , d'orientation moyenne $225N/55^\circ$, plonge vers l'ouest lorsque projetée sur le plan de la foliation S_2 et des zones de minéralisation aurifère à

plus fortes teneurs sont allongées parallèlement à L_2 . L'étude de la distribution de l'intensité de déformation à l'intérieur du gisement sur un plan oblique orienté perpendiculairement à L_2 (323N/43°; figure 4.12) met en évidence l'absence de corrélation directe entre une intensité de déformation quelconque et les différentes zones minéralisées. Sur ce même plan oblique, il est possible de constater l'existence d'un corridor de déformation intense à la base de la zone ODM (mur structural) où la fabrique S_2 est pénétrative et destructrice (figure 4.11). Cette zone est également caractérisée par une augmentation du pendage moyen de S_2 ainsi que par la présence de kink bands subhorizontaux affectant S_2 (figure 4.5D).

À l'intérieur du gisement Rainy River, plusieurs éléments structuraux ont été recensés et sont le résultat du raccourcissement NE-SO suivi d'un cisaillement dextre. Voici une séquence d'événements proposée et d'éléments structuraux résultants issue de la compilation de rapports préexistants (Poulsen, 2005, 2006; Siddorn, 2008; Hrabí et Vos, 2010; Rankin, 2013), et d'observations d'affleurements et de carottes de forages.

- D_1 est interprété comme l'évènement principal de raccourcissement NE-SO relié à l'accrétion du Wabigoon à la Sous-province de la rivière Winnipeg. Aucun élément structural associé à D_1 n'est observé avec certitude à Rainy River. Cependant, des veines aurifères à quartz-carbonate-pyrite de la partie ouest de la zone ODM, préalablement plissées et maintenant transposées dans le plan S_2 , pourraient avoir subi un plissement associé à D_1 ou encore précoce par rapport à D_2 . Selon Hrabí et Vos (2010), ces veines auraient également subies une rotation de leur axe de pli parallèle à la linéation d'étirement L_2 .
- À l'échelle régionale, l'épisode D_2 est interprété comme étant le résultant d'une contrainte de raccourcissement N-S soutenue avec une composante de cisaillement dextre initiée dans des structures d'orientation E-O. À Rainy River, l'épisode D_2 s'exprime par la foliation pénétrative S_2 ainsi que par la linéation d'étirement L_2 . Hrabí et Vos (2010) interprètent également la rotation de l'axe de pli P_1 des veines aurifères dans une position maintenant parallèle à L_2 . La formation d'une seconde génération de veines aurifères à quartz-ankérite pyrite, situées à l'intérieur de la zone Cap et encaissées dans des roches mafiques (figure 4.8E), est interprétée par Poulsen (2006) comme résultant de l'élongation responsable de la linéation d'étirement L_2 . Des indicateurs cinématiques affectant S_2 , observés en forage ainsi que sur les affleurements, soulignent un mouvement dextre en surface ainsi qu'un mouvement inverse le long de S_2 .

- Les données aéromagnétiques (figure 4.3) ainsi que l'étude de lames minces (figure 4.6B) soulignent une crénulation mineure de S_2 attribuée à l'évènement D_3 .
- Une série de failles cassantes à ductile-cassantes orientées approximativement N-S recouper la foliation S_2 ainsi que les zones minéralisées et sont de mouvement apparent senestre, avec des déplacements subhorizontaux à l'échelle du mètre. Certaines failles cassantes observées en forage ont remobilisés une partie de la minéralisation aurifère (figure 4.9C).

Altération hydrothermale des roches hôtes du gisement

L'altération hydrothermale à Rainy River est dominée par la séricite (terme descriptif regroupant tous les fins micas blancs). Les analyses à la microsonde indiquent qu'il s'agit de muscovite. Cette muscovite résulte de la destruction de l'albite (figure 5.6) et possède une composition magnésienne corrélée aux échantillons minéralisés en or (figure 5.9; annexe I). Une représentation de la distribution spatiale de l'intensité de la séricitisation (formation de muscovite) sur un plan oblique perpendiculaire à L_2 (figure 5.8) souligne une corrélation entre les échantillons fortement séricitisés et la zone ODM.

La chlorite est le second minéral d'altération le plus commun à Rainy River. Présent dans toutes les zones minéralisées (figure 5.10), elle possède également une composition plus magnésienne corrélée avec la présence d'or (figure 5.14; annexe I).

Les minéraux d'altération secondaires, identifiés dans cette étude ainsi que dans celle de Wartman (2011), sont notamment : l'épidote, les carbonates, le grenat manganifère (spessartite) et le rutile. La kyanite et le chloritoïde sont des équivalents métamorphiques de minéraux d'altération secondaires identifiés dans le cadre de cette étude.

L'épidote est de taille microscopique et peut être divisée en deux populations à partir de sa composition: une population primaire, affectée par D_2 et souvent remplacée par de la chlorite et des carbonates, et une seconde population syn- à tardi- D_2 associée au métamorphisme régional plutôt qu'à une activité hydrothermale.

Les résultats d'analyses à la microsonde des carbonates montrent la présence de calcite et d'ankérite - dolomite ferrifère (figure 5.19). Les carbonates sont présents en remplacement de feldspaths potentiellement primaires et d'épidote ainsi que dans des veines millimétriques à centimétriques transposées dans S_2 . L'analyse de la concentration en $MnCO_3$ des carbonates démontre que les échantillons minéralisés de la zone ODM possèdent de fortes concentrations

en MnCO_3 (>4 %; figure 5.20), ce qui peut être interprété comme un apport de l'eau de mer dans le système hydrothermal (Franklin, commun. pers., 2015) et correspondrait donc à une carbonatation hydrothermale antérieure à la déformation des roches. Même si, à l'échelle du gisement, les roches mafiques possèdent un plus grand pourcentage modal de carbonates que les roches felsiques, leur taux de saturation en carbonates est similaire (figure 5.18). À partir du même graphique, un gradient de saturation en carbonates vers l'ouest est souligné dans la zone ODM. Ceci est corroboré en forage par l'observation dans la partie ouest de la zone ODM d'une plus grande concentration de carbonates disséminés dans la matrice ainsi que par la présence de veines aurifères à quartz-carbonate-pyrite plissées et par la suite transposées dans S_2 .

Des lentilles discontinues de moins de 20 mètres d'épaisseur et composées de kyanite, chloritoïde et quartz (figure 5.26B) sont observées à l'intérieur de la zone ODM (figure 5.31). Ces dernières ne montrent aucune texture volcanique primaire préservée. Parmi l'ensemble des échantillons recueillis dans le cadre de cette étude, les échantillons provenant de ces zones possèdent les valeurs les plus élevées de l'indice d'altération argileuse acide (AAAI; Williams et Davidson, 2004). Ces lentilles d'aluminosilicates sont interprétées comme l'équivalent métamorphique post-altération d'une altération argileuse commune dans plusieurs environnements modernes.

Des porphyroblastes de grenats manganésifères (spessartite; figure 5.21) sont présents dans les dacites calco-alcalines de la zone ODM (figure 5.32, 5.33). Ces grenats sont fracturés et comportent de nombreuses inclusions riches en sulfures. Ces inclusions sont orientées par rapport à S_2 , impliquant une période de formation pré- à syn- D_2 . Des porphyroblastes de grenats à composition almandin dominante (figure 5.21) sont présents dans les roches mafiques tholéitiques de la zone minéralisée Cap.

Une altération à rutile est présente dans les roches mafiques de la base de la zone HS et de la zone 433. Cette concentration élevée en rutile (échantillon contenant jusqu'à 2,7 % poids TiO_2) est attribuée à la remobilisation locale de titane initialement présents dans des feldspaths, tel que proposé au gisement LaRonde Penna (Dubé *et al.*, 2007).

La représentation en section de la distribution des différents minéraux d'altération secondaires met en lumière une zonation par rapport aux zones minéralisées qui est également corrélée à une zonation observée des bilans de masse d'éléments majeurs (CaO , CO_2 , Na_2O , MnO , SiO_2 et K_2O). Ces calculs de bilans de masse sont présentés dans la section 5.4 et se basent sur les travaux de Barrett et MacLean (1991, 1993).

Le toit de la zone ODM est une zone caractérisée par l'addition de CO_2 , CaO et Na_2O , reflétant une destruction partielle de l'albite ainsi que la présence de carbonates et d'épidote. La zone minéralisée ODM est celle où les plus fortes variations de masse d'éléments majeurs sont développées (figures 5.40 à 5.46 inclusivement). Cette zone minéralisée correspond à une zone d'addition de K_2O et de lessivage de Na_2O , causées par la destruction de l'albite et la cristallisation de muscovite. Une zone d'enrichissement en MnO est également observée et corrélée à la présence de spessartite ainsi que de carbonates riches en Mn. Les échantillons provenant des zones à aluminosilicates sont caractérisés par une perte importante de tous les oxydes d'éléments majeurs (tableau 5.4). Dans le corridor de déformation situé dans le mur de la zone ODM, un gain en CO_2 est corrélé avec une augmentation de concentration de veinules de carbonates. Les zones HS et 433 sont associées à une perte en CaO , Na_2O et MnO combinée à un enrichissement en MgO et K_2O , ce qui est reflété par l'abondance de muscovite et chlorite ainsi que par l'absence de minéraux d'altération secondaires.

Le calcul de la variation de masse moyenne des échantillons de dacite par faciès volcanique (figure 5.47) démontre une variation de masse plus importante dans les volcanoclastites versus les faciès cohérents, ce qui suggère que la porosité primaire des volcanoclastites exerce une influence probable sur l'intensité de l'altération hydrothermale.

Les données d'isotopes d'oxygène recueillies à l'échelle de la propriété et corrélées avec la minéralisation sont isotopiquement lourdes ($>12,8 \text{ ‰}$; figures 5.50, 5.51) et il existe une faible corrélation positive entre les données $\delta^{18}\text{O}$ et l'indice d'altération AAAI (figure 5.54).

Minéralisation

La minéralisation à Rainy River est répartie en quatre zones principales, c'est à dire les zones Cap, ODM, HS et 433. Mis à part la zone Cap, à dominance mafique tholéiitique, toutes ces zones sont encaissées dans les dacites calco-alcalines décrites plus haut. Ces zones minéralisées sont orientées parallèles à S_2 et superposées les unes sur les autres dans la succession hôte, de façon perpendiculaire à S_2 (figure 6.1). À l'intérieur de ces zones minéralisées se trouvent des zones à plus fortes teneurs en or sub-parallèles à la linéation d'étirement L_2 (figure 6.1). La zone ODM représente la majorité du gisement et contient approximativement 70% de la ressource en or totale. L'or et l'argent sont les seuls métaux présents en concentration économique, même si la présence de pyrite, sphalérite, chalcopyrite et galène est généralement corrélée avec celle de l'or.

La minéralisation à basse teneur (<1,5 g/t Au équivalent) est caractérisée par la présence de pyrite disséminée et regroupée en veinules et veines transposées dans S_2 . La minéralisation à plus forte teneur (>1,5 g/t Au eq.) est associée à la présence de veinules de pyrite-sphalérite-chalcopryrite-galène transposées dans S_2 s'ajoutant aux disséminations de pyrite. Cette étude a révélé la présence de nombreuses phases accessoires d'électrum, or natif et de tellurures d'or et d'argent (annexe II et III). Ces phases sont présentes à l'intérieur de fractures de phases sulfurées ou encore comme inclusions dans des grains de pyrite ou sphalérite (figures 6.5, 6.9, 6.11A, E, F, 6.13).

Les travaux de cartographie par technique LA-ICP-MS sur un grain de pyrite de la zone ODM démontrent au moins deux phases distinctes de cristallisation. La première, qui correspond au cœur de la pyrite riche en inclusions, contient la majorité des métaux précieux (figure 6.6). La seconde génération correspondant au pourtour du grain ne possédant pas d'inclusions et interprétée comme correspondant à la recristallisation métamorphique de la pyrite lors de l'épisode de déformation principale D_2 , est plutôt enrichie en Co, Ni et Bi et appauvrie en métaux précieux par rapport au cœur du grain (figure 6.7). Cette cartographie suggère une cristallisation de la majorité de l'or synchrone avec la première phase de cristallisation de pyrite.

Une série de modélisations 3D de distribution des métaux (p.ex. : argent, arsenic, bismuth, cuivre, plomb, zinc) à travers le gisement utilisant la banque de données de la compagnie a fait ressortir deux associations métalliques principales : Au-Ag-As-Pb-Zn±Cu et Au-Cu±Bi±Zn (figure 6.30). L'association Au-Ag-As-Pb-Zn±Cu s'étend de la zone Cap jusqu'à la moitié supérieure de la zone HS interprété comme étant la partie supérieure du système minéralisé, alors que l'association Au-Cu±Bi±Zn couvre le reste du gisement, soit la seconde moitié de la zone HS ainsi que la zone 433, interprétée comme étant la partie inférieure du système.

Conclusion

La caractérisation du gisement Rainy River, d'un point de vue de la volcanologie des roches hôtes, de l'altération hydrothermale ainsi que de la déformation par rapport aux zones minéralisées, a permis de montrer que la porosité primaire des roches hôtes ainsi qu'une minéralogie d'altération spécifique, gouvernée par des conditions hydrothermales spécifiques, contrôlent la présence d'une majorité de la minéralisation aurifère. Subséquemment, l'épisode de déformation D_2 est responsable de la remobilisation et de la transposition parallèle à S_2 des

différentes zones minéralisées ainsi que de la création de zones à plus fortes teneurs en or le long de L₂.

La minéralisation aurifère de Rainy River, de façon similaire aux sulfures massifs volcanogènes (SMV) aurifères, peut être attribuée du moins en partie à un processus synvolcanique pour les raisons suivantes : 1) l'empilement des zones minéralisées à l'intérieur de la succession volcanique, 2) le développement et l'association préférentielle de l'altération et de la minéralisation dans les roches volcanoclastiques, 3) l'association de l'or avec les métaux de base, 4) une association directe entre un complexe dacitique restreint et plusieurs zones minéralisées. La zonation des métaux à Rainy River ressemble à la zonation de haute et basse température proposée par Ohmoto (1996) pour les systèmes SMV et discutée en détail par Huston et Large (1989) et Hannington *et al.* (1999). Cette zonation de métaux suggère une polarité vers le sud, ce qui est concordant avec les observations faites en affleurement dans le cadre de cette étude et avec les travaux antérieurs (Fletcher et Irvine, 1954; Wartman, 2011).

Une tentative de classification du gisement Rainy River selon les modèles de gîtes préexistants met en lumière l'absence de caractéristiques diagnostiques permettant d'assigner le gisement à un seul modèle génétique. Le gisement Rainy River diffère des systèmes épithermaux *sensu stricto* par son milieu de formation sous-marin ainsi que par l'absence de veines à textures colloformes-crustiformes, de zones de lessivages intenses laissant des zones siliceuses «vuggy», ou encore d'évidences claires d'ébullition comme processus de précipitation des métaux. D'autant plus, Rainy River ne peut être classé comme un gisement de type SMV parce qu'il ne possède pas de lentilles de sulfures massifs ou encore de source thermique reconnue ayant pu agir comme moteur de convection hydrothermale soutenue. Pour ces raisons, le gisement Rainy River pourrait, de façon hypothétique, représenter un SMV avorté, où la température était trop basse pour permettre aux fluides de transporter et précipiter des métaux de base en grande quantité, ou encore les fluides n'auraient pas pu atteindre le fond marin et former des lentilles de sulfures massives. Une seconde hypothèse consiste en la classification du gisement Rainy River comme dépôt aurifère de type hybride épithermal-SMV peu profond, où la minéralisation précipite en milieu sous-marin comme dans les SMV, mais où la circulation des fluides hydrothermaux est contrôlée par une porosité primaire de la roche hôte et les métaux précipitent sous le fond marin, à une pression-température précise et ce par refroidissement ou encore ébullition. Dans des systèmes hydrothermaux sous-marins contemporains, l'ébullition des fluides sous le fond marin provoque la précipitation à haute température et profondeur du cuivre, suivie de la précipitation de zinc et plomb à plus faible

température et profondeur, laissant un fluide comparativement enrichi en or et argent pouvant précipiter des métaux précieux soit sur le fond-marin ou encore à faible profondeur (Monecke *et al.*, 2014).

Le gisement Rainy River possède des roches hôtes, une minéralogie d'altération ainsi qu'une minéralisation synvolcanique aurifère semblables, à plusieurs égards, aux gisements Bousquet 1, Bousquet 2-Dumagami, LaRonde Penna et Westwood du camp Doyon-Bousquet-LaRonde (Tourigney *et al.*, 1989; Tourigny *et al.*, 1993; Teasdale *et al.*, 1996; Dubé *et al.*, 2007; 2014; Mercier-Langevin *et al.*, 2007a; Yergeau *et al.*, 2015). Même si le gisement Rainy River possède une minéralisation à fort tonnage et basse teneur, il diffère grandement des autres gisements à fort tonnage basse teneur du Supérieur (p.ex. : Côté Gold, Hammond Reef et Canadian Malartic : Katz *et al.*, 2014; Backeberg, 2015; de Souza *et al.*, 2015), en termes de contexte tectonique et style de minéralisation.

Un modèle d'exploration pour la découverte d'autres gisements de type «Rainy River» devrait donc se baser sur les caractéristiques de l'altération hydrothermale ainsi que sur la volcanologie des gisements de type SMV aurifères de la Sous-Province de l'Abitibi (p. ex. centre volcanique calco-alcalin felsique important, séricitisation et silicification étendue et présence d'équivalents métamorphiques de minéraux d'altérations argileuse à argileuse avancée) en les appliquant toutefois sur des cibles de la taille et teneurs moyennes caractérisant les gisements à fort tonnage et basse teneur.

1 INTRODUCTION

1.1 Purpose of study

The present study focuses on: 1) describing the immediate geological setting and nature of the gold mineralization and; 2) defining the large and small-scale controls on ore distribution and grades within the Rainy River gold deposit in order to define exploration vectors for the discovery of similar deposits throughout the Superior Province.

The Rainy River gold project is an advanced-stage Au-Ag project owned by New Gold Inc. It is located within the western Wabigoon Subprovince in northwestern Ontario, approximately 75 km northwest of the town of Fort Frances (Fig 1.1). Gold mineralization occurs in a series of four foliation-parallel, stacked mineralized zones of 200 m to over 1600 metres in length along strike with ranging widths of 125 to 200 metres. Gold occurs in association with disseminated pyrite and veinlets of sphalerite, chalcopyrite and locally galena. NI43-101 compliant gold reserves and measured and indicated resources total 185.6 Mt at 1.13 g/t Au for the reserves and 1.11 g/t Au for the resources for a total of 6.67 Moz Au (New Gold Inc., 2015a), making it a "low grade, large tonnage" type deposit of significant size. At time of writing, an open pit-type mine operation at 21, 000 tons per day producing 325, 000 ounces of gold annually is envisaged, with production scheduled to commence by mid-2017 (New Gold Inc. website, 2015b).



Figure 1.1: Location of the Rainy River gold project in Ontario.

The atypical, disseminated-stockwork style of gold mineralization at Rainy River, the important size of the deposit, combined with its location in an area historically regarded as having a limited mineralization potential are factors that make this project an interesting target for research in economic geology. Delineating, through this MSc project and other research activities, the different controls and mechanisms responsible for the generation and preservation of gold mineralization at Rainy River could contribute to the understanding and characterization of a type of mineralization that is not yet fully recognized in present exploration models and help future exploration for similar deposits.

Ongoing research activities on the Rainy River gold project include this MSc thesis, U-Pb ID-TIMS geochronology work, LA-ICP-MS analyses and pyrite mapping, LA-MC-CIP-MS analyses, and Pb and S isotope analyses. These projects are all part of the Targeted Geoscience Initiative program (TGI-4) of Natural Resources Canada, a collaborative effort led by the Geological Survey of Canada between national and provincial government surveys, academia and industry. It aims at optimizing exploration-related geoscience knowledge and exploration models (Dubé *et al.*, 2011, 2015). Known ore systems and mining camps were studied individually and divided into seven projects: Lode Gold, Nickel-copper-chrome-PGE, Intrusion-related, SEDEX, Volcanogenic massive sulphide, Uranium, and specialty metals. The Rainy River research activities are part of the Lode Gold project that was centered on major gold systems in ancient, deformed and metamorphosed terranes (Dubé *et al.*, 2015).

A holistic approach was utilized to characterize the studied deposits and districts through the Lode Gold project (Dubé *et al.*, 2011). In terms of research activities, this meant that projects were primarily field oriented, using mapping and core logging, structural geology, geochemistry, geochronology, isotopes, and three dimension modeling and reconstruction.

1.2 Objectives

The objectives of this master project are:

- Improve the geochemical characterization of the metavolcanic units that host the deposit and correlate them with stratigraphic units previously identified in the literature and by the company operating the project.
- Document in detail the hydrothermal alteration assemblages associated with the different mineralized zones in terms of mineralogy, geochemistry and spatial distribution.

- Characterize the mineralized zones in terms of mineral assemblages, textures, distribution and zonations with other sulphides and their relation with alteration assemblages.
- Establish the nature of the main structural fabrics in the study area and their influence on gold.
- Constrain the relative and absolute timing of geological events in the area (mineralization, alteration, deformation, metamorphism, potential remobilization) using U-Pb geochronology, field mapping and core logging.
- Define the geologic environment of formation for the different mineralized zones from a structural, volcanological and hydrothermal point of view.
- Determine the approximate temperature, origin and potential pathways of mineralizing fluids using oxygen isotope analyses.
- Define lithological/structural, lithogeochemical and mineralogical indicators to ore.
- Compare the Rainy River deposit with other gold and base metal systems of the Wabigoon Subprovince and Superior Province.
- Propose an improved or revised genetic model for the Rainy River deposit.

1.3 Methodology

1.3.1 Determining the immediate geological setting of the deposit

Available information about the geological setting of the Rainy River deposit, including numerous internal reports and a master thesis (Wartman, 2011), were compiled. Newly acquired data for this project comes from detailed core logging, generation of cross sections, and regional and detailed mapping of key outcrops on the property.

Cross sections were elaborated to represent the distribution in space of the different lithologies identified at Rainy River. Rainy River Resources Ltd. and subsequently New Gold Inc. defined shells delineating the different mineralized zones at Rainy River. A key feature underlined by this work is the strong structural control on the mineralized zones geometry, dictated by the main foliation (S_2 ; $102^\circ/61^\circ\text{SW}$) and a well-developed stretching lineation (L_2 ; $225^\circ/55^\circ\text{SW}$) contained within this foliation plane (see chapter 4 on deformation for additional information). In

order to properly illustrate the distribution of the various geological features of importance and minimizing the effects of deformation, an oblique plane oriented 323°/43°NNE, i.e. perpendicular to the main stretching lineation, was built using Leapfrog® Mining software version 2.5.361 to better represent the geometry of the deposit (Fig. 1.2). This inclined plane has a composite thickness of 25 metres and is based on diamond drill core intervals. It is located so as to intercept most ore zones at proposed mining depth.

For this study, sixty-seven diamond drill hole intervals totalling 5592 metres were more specifically logged in detail to create this plane, with an emphasis put on the ODM zone and its hanging wall and footwall (see section 3.3.1; appendix I). Abundant drill holes going through the deposit and its vicinity, combined with an excellent drill core archiving infrastructure and up-to-date database made the generation of this oblique plane possible.

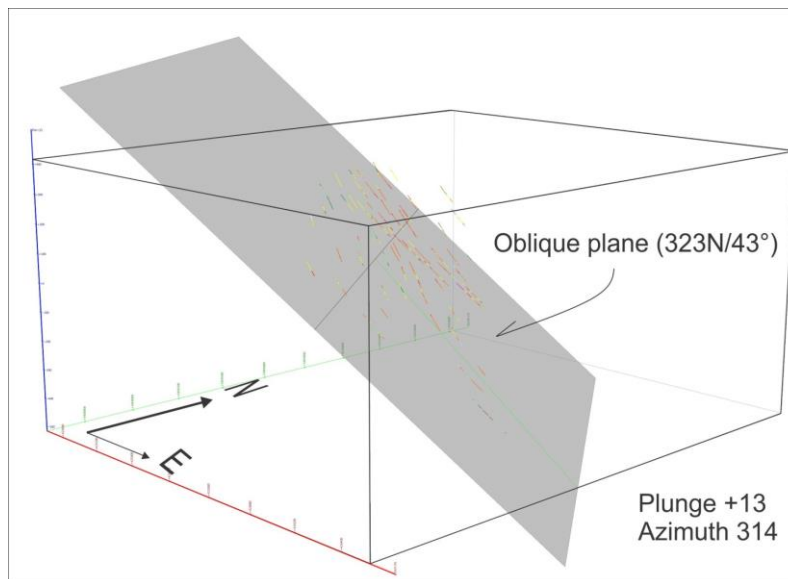


Figure 1.2 : Screen shot from Leapfrog® Mining software of the different diamond drill core intercepts (in yellow and red) that compose the oblique plane (in gray, oriented 323N/43°). Red axis points east, green axis north, and blue axis is elevation (looking 314°N with a +13 plunge).

A traditional, North-South oriented cross section was also constructed to represent the distribution of the different volcanic facies with respect to the different ore zones (Fig. 1.3; see section 3.3.2; appendix I). It is located approximately in the central part of the proposed pit (NAD83, Zone 15, 425475 mE; Fig. 1.3), where alteration and mineralization are better developed.

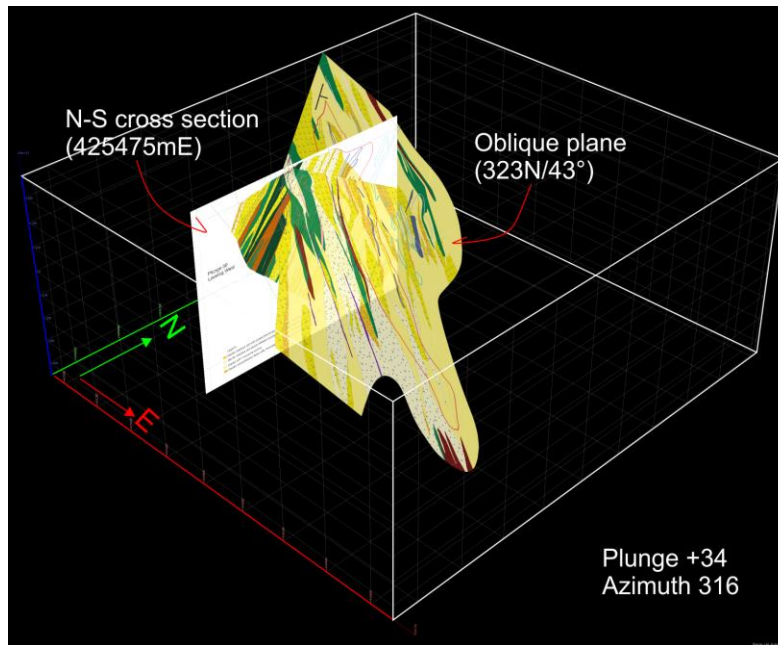


Figure 1.3 : The oblique plane (in reduced opacity) with the 425475E north-south cross section. Once again, green axis is north, red is east, and blue is elevation (z).

The software used to generate detailed outcrop maps is Mapinfo Professional™ version 10.5. Naming convention of the volcanic rocks, facies and textures were done based on accepted nomenclatures (McPhie *et al.*, 1993; White and Houghton, 2006; Harris and Rowland, 2015). The main goal of this 1:100 detailed mapping work was to assess with more precision the volcanic environment and regime responsible for the deposition of the volcanic sequence hosting the Rainy River deposit. The focus of this detailed mapping was on primary volcanic textures and structures, along with the spatial distribution of the different facies and the nature of their contacts. Additionally, detailed maps produced will provide records for future reference, as these outcrops will be hardly accessible once mining activities begin and overall outcrop density is poor in the deposit area. Interpretation of the Rainy River deposit area volcanic environment and facies architecture was also based on previous work done on Archean volcanic settings (e.g., Gibson *et al.*, 1999; Lafrance *et al.*, 2000; Mercier-Langevin, 2005, etc.).

Field trips in the Abitibi Subprovince and at the Sturgeon Lake camp further helped in the interpretation of the different structures and textures mapped in the Rainy River intermediate to felsic volcanic succession. Mineral deposits from these areas were used as a comparison basis for Rainy River. The additional knowledge and documentation acquired in these visits should translate in a more informed and in depth interpretation and discussion on the Rainy River immediate geological setting.

The geological setting of the deposit was also defined in terms of tectonic setting and from a petrogenetic point of view. Work in the literature (e.g., Leshner *et al.*, 1986; Richer-Laflièche *et al.*, 2000; Hart *et al.*, 2004; Pearce, 2008, etc.) provided an interpretation framework and classification nomenclature applied to trace and immobile elements analyses from Rainy River whole-rock samples. Sample analyses were conducted at ActLabs in Ancaster, Ontario, using a TGI-4 specific analytical package. For more information on analytical methods and instruments as well as quality assurance and quality control procedures, the reader is referred to Pelletier *et al.* (2016).

Structural fabrics were identified in drill core and measured on outcrop. The structural data acquired was then combined with previous structural studies done on the deposit (Siddorn, 2008; Hradi and Vos, 2010; Rankin, 2013). A good understanding of the different generations of structures within the deposit was crucial in order to evaluate the relative timing of hydrothermal alteration and ore-forming events with respect to deformation. Planar structures were recorded as strike/dip using the Canadian right-hand rule (strike direction is 90° counter clockwise from the dip direction). Linear structures were measured as pitch direction within the associated planar structure, and then converted to plunge direction using a stereonet.

1.3.2 Hydrothermal alteration assemblages

The different hydrothermal alteration assemblages at Rainy River were established using mineralogical and whole-rock geochemical data. These alteration assemblages were then represented on maps to document their spatial distribution, establish their geometry as well as their location with respect to mineralization, deduced primary volcanic facies and structures.

Primary hydrothermal alteration mineralogy and intensity were determined from detailed core logging. Over the field seasons of 2013 and 2014, 8187 metres of diamond drill core were logged for this purpose, looking at 75 different drill holes located within the deposit and its vicinity. Thin section study then helped refine the mineralogy and give an idea of hydrothermal activity-related minerals abundance. Rock thin sections, made by Vancouver Petrographics in Langley, British Columbia, are 30 µm thick and 26x46 mm in size. Thin sections used for LA-ICP-MS assays are 100-200 µm thick. Microprobe analyses were also conducted on selected thin sections for mineralogy and to try to establish a potential spatial zonation in alteration mineral composition. Microprobe analyses were done at Laval University in Quebec City, Quebec with a CAMECA® SX-100 instrument operated by Dr. M. Choquette. The 3D modelling

software used in this project to plot collected data is the Leapfrog[®] Mining software version 2.5.361 and the Leapfrog[®] Geo software version 2.1.2.

Whole-rock data analysis helped further describe the different hydrothermal assemblages generated by the ore-forming system. With this data, mass balance variations with respect to a least-altered protolith have been calculated using the method proposed in MacLean and Barrett (1993). Mass variations of individual samples were then plotted in the 3D environment, outlining the present geometry of alteration assemblages with specific element mobility caused by hydrothermal alteration reactions. In addition to mass balance calculations, multiple diagrams illustrating alteration trends and nature were used (e.g., Large *et al.*, 2001a; Davies and Whitehead, 2006, etc.) for the same purpose of describing the hydrothermal system at Rainy River. Three dimensional visualisation and implicit modelling of geochemical data was done using the combined Leapfrog[®] Geo version 2.1.2 and REFLEX[®] ioGAS version 6.0.1 softwares.

Oxygen isotopes data analyses have been performed on selected weakly to intensely altered host rocks to characterize the hydrothermal fluid that affected volcanic rocks of the deposit area. When combined with the results of the hydrothermal alteration study, this information helped further restrain the hydrothermal system formation conditions. Whole-rock oxygen isotopes were measured at the University of Western Ontario in London, Ontario by K. Law. The reader is referred to Mercier-Langevin *et al.* (2014) for analytical procedures and methodology.

1.3.3 Characterizing auriferous zones

Detailed logging of previously assayed drill core within the mineralized body provided a first general description of the different types of Au mineralization. Subsequent 3D implicit modelling of the Au distribution in space with respect to other metals and sulphides as well as several geochemical parameters allowed further description of the Au system. Thin section analysis, combined with scanning electron microscopy (SEM) and energy dispersive x-ray (EDS) spectroscopy allowed imaging of sulphide textures and identification of accessory phases in mineralized samples. SEM and coupled EDS work was conducted at Laval University using a JEOL[®] 840-A machine under the supervision of A. Ferland.

1.3.4 Determining the timing of events in the area

Determining the timing of Au mineralization with respect to volcanism, hydrothermal alteration, deformation and metamorphism is central in this project and a potential sequence of events for the Rainy River deposit is described in chapter 7. It is achieved by integrating the results of the previous chapters of this work into a single evolving system.

Careful examination of megascopic and microscopic cross-cutting relationships helped provide a sequence of events and relative timing. This relative chronology was then supported by pyrite LA-ICP-MS mapping and by U-Pb zircon geochronology data obtained from parallel research activities part of the TGI-4 lode gold project. LA-ICP-MS element mapping of pyrite was done by Dr. S.E. Jackson and Dr. Z. Yang at the Geological Survey of Canada in Ottawa. U-Pb ID-TIMS geochronology work was done by V. McNicoll of the Geological Survey of Canada, Ottawa. The reader is referred to Gao *et al.* (2015) and McNicoll *et al.* (2014) for information on analytical techniques.

2 REGIONAL GEOLOGY

The Rainy River gold project (RRGP) is located in the western Wabigoon Subprovince, located in the western part of the Archean Superior Province. The following section presents a brief geological summary of the main characteristics of the Superior Province and Wabigoon Subprovince, along with an overview of the different ore deposit types of the Wabigoon Subprovince.

Since all rocks documented in this work were metamorphosed to the greenschist to amphibolite facies, the prefix "meta" is omitted for clarity and conciseness.

2.1 Superior Province

The Archean Superior Province is the largest geological Province of the Canadian Shield and forms the core of the present day North American continent (Fig. 2.1). It is thought to be the result of a complex accretion of initial small continental blocks with parcels of oceanic crust, which took place between 2.72-2.68 Ga (Krogh and Davis, 1971, cited in Ayer and Davis, 1997; Percival, 2007). Boundaries between these subprovinces are expressed by faults and trend east-west in the southern part of the Superior, west-northwest in the northwest, and northwest in the northeastern Superior (Percival, 2007). Geochronology work (Percival *et al.*, 2006b) further outlined these previously recognized distinct lithological and structural subprovinces, with progressively younger depositional ages going southward. This observation, along with structural and stratigraphic relationships, suggests successive, northward oriented, terrane docking and associated collision tectonics within a north-dipping subduction tectonic regime. This Neoproterozoic-aged subduction generated both continental and oceanic arc volcanism, producing tracts of volcanic and sedimentary rocks (later deformed during terrane docking-induced collisional orogeny) surrounded or intruded by coeval to late granitoid rocks (Percival, 2006 a).

Revised Archean tectonic models were recently proposed (e.g., Kerrich and Polat, 2006; Bédard and Harris, 2014) to explain the evolution of the Superior Province. These models try to explain the extensive formation of Neoproterozoic greenstone belts, namely through vertical tectonics, mantle overturn events (Bédard and Harris, 2014), or thermochemical mantle convection events (Kerrich and Polat, 2006). Part of the rationale for these models is that, in the

Archean, the Earth was a lot hotter, therefore mantle convection was vigorous and rapid, preventing any slow plate movement and steep subduction such as observed in present day. Moreover, Archean greenstone belts lack typical rock assemblages observed in subduction environments, such as ophiolitic complexes and areas of blueschist metamorphism. Readers are referred to the contributions mentioned above for a detailed discussion.

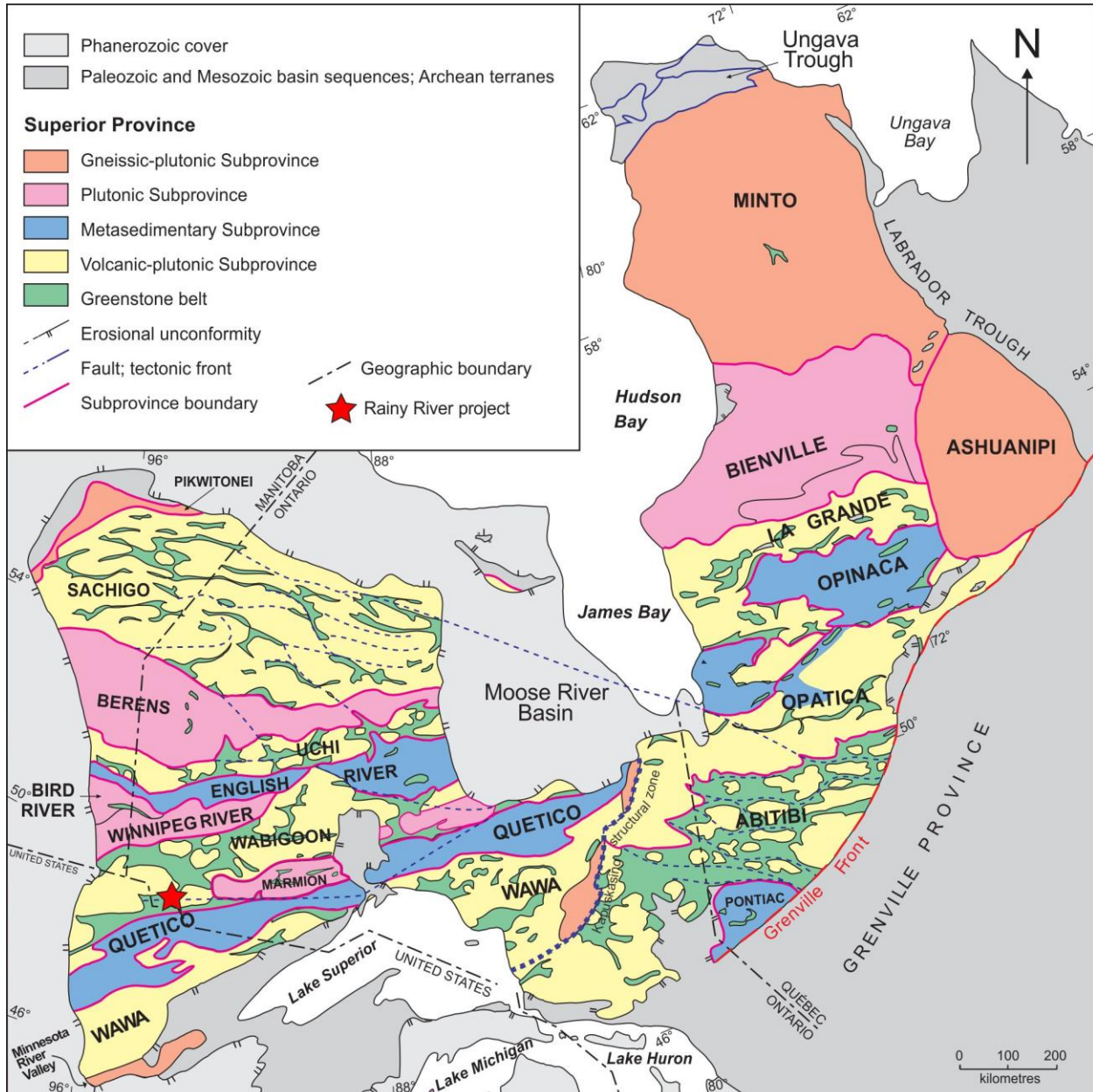


Figure 2.1 : Superior Province geological map (compiled from Card and Ciesielski 1986, Percival *et al.*, 2006a, Marquis, 2004).

2.2 Wabigoon subprovince

The Wabigoon Subprovince, located in the southwestern part of the Superior Province (Fig. 2.1), is composed mainly of volcanic rocks of tholeiitic to calc-alkaline affinity and sedimentary rocks, which are crosscut or intruded by large batholiths. It is over 900 km long and has been divided in three regions, namely the eastern, central, and western Wabigoon (Blackburn *et al.*, 1991). On a local scale, each segment of greenstone belts has been given a unique name, along with each distinct batholith.

The Wabigoon Subprovince is a mostly juvenile, oceanic arc-affinity terrane that has been accreted to the northern plutonic-dominated Winnipeg River terrane during the general Neoproterozoic Kenoran Orogeny, more precisely during the central Superior Orogeny (2.71-2.70 Ga) (Percival *et al.*, 2006a). To the south, it is bounded by the younger, metasedimentary-dominated Quetico Subprovince (Percival, 2007; Fig. 2.1).

2.2.1 Western Wabigoon lithostratigraphic assemblages

In the western Wabigoon region (WWR), volcanic sequences comprise ultramafic (tholeiitic) to felsic (mostly calc-alkaline) volcanics organised in a series of interconnected greenstone belts (Fig. 2.2). They surround large granitoid batholiths. Volcanism in the WWR occurred mostly within the 2745 to 2711 Ma interval (Percival, 2007).

Lithostratigraphic assemblages of the WWR have been regrouped in tectonically bounded assemblages. Four main sequences were identified within most of these assemblages (Blackburn *et al.*, 1991). They are, from oldest to youngest: 1) lower mafic sequences, composed of komatiites and tholeiites, with lesser amounts of andesitic flows and coeval intrusions, 2) diverse intermediate to felsic volcanic sequences of calc-alkaline affinity and lesser amounts of tholeiitic andesites to rhyolites, 3) upper ultramafic to mafic sequences, composed of komatiitic and tholeiitic flows and 4) sedimentary sequences of turbiditic, alluvial-fan or minor platform sequences. Contacts between these four sequences are faulted or conformable, depending on the location within the WWR (Blackburn *et al.*, 1991).

Mafic volcanic units are preferentially located at the base of the volcanic sequences, but geochronological constraints are lacking. As mentioned above, most felsic to intermediate volcanism in the WWR took place from 2745 to 2711 Ma, which is coeval to the early phases of

plutonism (Blackburn *et al.*, 1991) and in agreement with the typical late felsic portion of Archean volcanic cycles. These volcanic units are largely overlain by mostly synorogenic sedimentary sequences (Blackburn *et al.*, 1991). Granitoid batholiths cross-cut these volcano-sedimentary sequences, with their early, marginal phases being coeval to volcanism, although most of the plutonic activity is syn- to post-tectonic and occurred in the 2711 to 2685 Ma interval (Blackburn *et al.*, 1991).

Geochronology work is still sparse, but it seems that spatially dispersed stratigraphic sequences of similar characteristics can be correlated throughout the area in terms of depositional environment and stratigraphic position, although they are not coeval (Blackburn *et al.*, 1991).

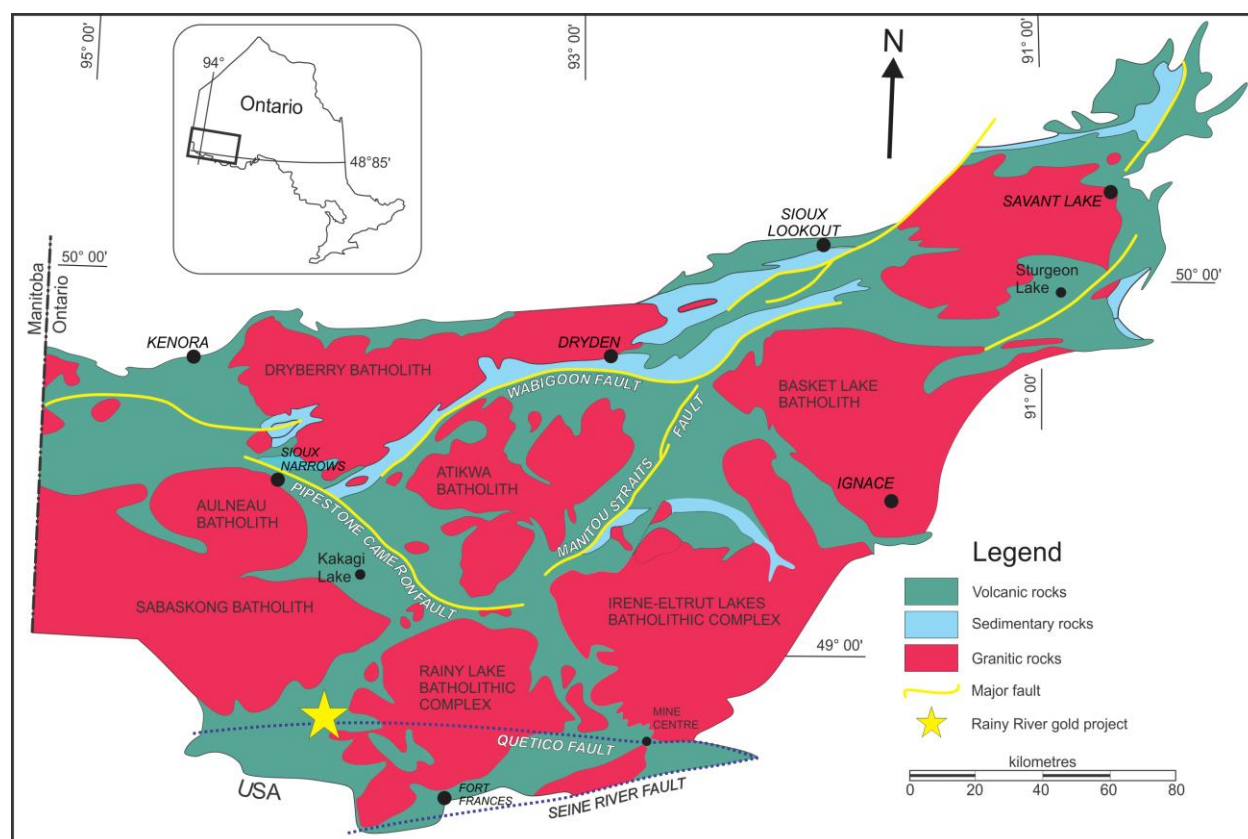


Figure 2.2 : Simplified geological map of the western Wabigoon Subprovince, modified after Blackburn *et al.* (1991).

2.2.1 Regional structural context

The Quetico Subprovince, to the South, is interpreted as a forearc setting to the Wabigoon, with depositional ages (2698 to 2690 Ma) overlapping the late arc magmatism in the Wabigoon

(Langford and Morin, 1976; Percival, 2007). Combined structural and geochronology studies by Melnyk *et al.* (2006) conclude that the Neoproterozoic western Wabigoon Subprovince terrane collided and overthrusts the Mesoproterozoic continental Winnipeg River terrane to the north over the 2717-2695 Ma time span. This northward overthrusting and combined accretion is responsible for the several generations of structures. D_1 generated north-trending upright F_1 folds within a north-south shortening regime. The subsequent ductile deformation event (D_2 , potentially representing an increase in N-S oriented shortening and transition to transpressional shearing: Poulsen, 2006) produced isoclinal F_2 folds (Siddorn, 2008) with potential north-directed thrusting according to Davis *et al.* (1988). D_2 , at the Quetico – Western Wabigoon boundary, is recorded as an east-striking S_2 foliation and an L_2 stretching mineral lineation plunging to the southwest, overprinting the F_1 folds (Sanborn-Barrie, 1991; Poulsen, 2006). This steeply dipping S_2 foliation is the main penetrative fabric present in the western Wabigoon Subprovince. D_3 structures are associated with the emplacement of relatively late intrusions and consist in swerving of foliation and crenulation of S_2 around the intrusive bodies (Sanborn-Barrie, 1991) as well as open folding of the lowermost mafic strata, which did not erase the S_2 fabric (Poulsen, 2005).

2.2.2 Rainy River greenstone belt

The informal term "Rainy River greenstone belt" has been introduced by the company (Rainy River Resources Ltd. at that time) and represents a succession of volcanic and sedimentary rocks bounded to the north by the Sabaskong batholith, to the east by the Rainy Lake batholithic complex and the Jackfish Lake pluton and by the Quetico fault to the south (Fig. 2.2). It is mainly composed of mafic volcanics, with interspersed, isolated felsic volcanic rocks. The sedimentary rocks are a minor component of the "belt" and their distribution is restrained to a sliver just to the north of the Quetico fault.

The Rainy River project is located within the "Rainy River greenstone belt" and, as will be further defined in subsequent sections of this work, is mainly hosted in a calc-alkaline intermediate to felsic volcanic assemblage.

The intermediate to felsic volcanic rocks in the "Rainy River greenstone belt" occur as spatially isolated blocks, but might be correlated to other felsic volcanic rocks within the WWR. Assuming that the intermediate to felsic volcanic rocks present in the "Rainy River greenstone belt" are located stratigraphically between the lower and upper mafic volcanics, they could be correlated

with other "intermediate-positioned" felsic volcanic centres from greenstone belts of the WWR who show similar relationships with adjacent units.

Stratigraphic compilation work within the WWR, undertaken by Blackburn *et al.* (1991) using preliminary results from U-Pb dating techniques (1 to 5 million years precision) outlined potential coeval intermediate to felsic volcanics successions to the ones found in the "Rainy River greenstone belt". They are: the Handy Lake Group in the Savant Lake area, the cycle 4 of the South Sturgeon assemblage in the Sturgeon Lake area, the Neepawa Group in the Sioux Lookout area, the Lower Wabigoon volcanics in the Dryden area, and, closest to the Rainy River greenstone belt, the Kakagi Lake Group in the Kakagi Lake area.

Paleoproterozoic diabase dykes of the Kenora-Fort Frances dyke swarm crosscut the area. Hundreds of dykes up to 100 km in length and with a NW trend cross-cut the Archean rocks in the area between Kenora and Fort Frances.

Several glaciations have affected northern Ontario, the last one being the Wisconsinan glaciation. At the Rainy River project, Labradorian till of northeastern provenance is overlain by glaciolacustrine silt and clay, which is in certain areas overlain by Keewatin till of western origin (BBA Inc., 2014). Average thickness of Quaternary deposits is between 20 to 40 metres and glacial striae measured on the Rainy River property outcrops all indicate a NE-SW trend.

2.2.3 Geology of the Rainy River property

The Ontario Geological Survey undertook regional-scale geological mapping in the Rainy River project area in 1953, 1971, 1975 and again in 1987-1988, this time equipped with a rotasonic drill (SRK, 2008). Even then, extensive overburden cover hindered precise local mapping, which largely relies on drill core logging and aeromagnetic geophysical survey interpretation.

Regional mapping work in the Rainy River district by Blackburn (1976, cited in Poulsen, 2005) proposes a subdivision of the volcanic rocks of the Rainy River deposit area into a lower mafic volcanic sequence and an upper diverse volcanic sequence. The lower mafic volcanic sequence extends from the Sabaskong batholith to the north to the intermediate to felsic volcanic package to the south, which consists in the upper diverse volcanic sequence (Fig. 2.3). Unpublished work by Poulsen (2006) recognizes southward facing indicators within the lower mafic volcanic sequence.

The Rainy River deposit is mainly hosted in intermediate to felsic, calc-alkaline volcanic rocks, bounded to the north and south by tholeiitic mafic units (Fig. 2.3). These strike almost east-west and dip to the south, subparallel to the main penetrative foliation measured on site (average of 109°N/46°SW). On the southern end of the property, metasedimentary rocks oriented parallel to the volcanic packages are commonly referred to as the Mather sediments (Fletcher and Irvine, 1954; Poulsen, 2005). Work by Fletcher and Irvine (1954) establish a southward facing of the Mather sedimentary rocks.

The trondhjemitic Sabaskong batholith occurs to the north of the property and intrudes the lower mafic volcanic sequence (Blackburn, 1976). Davis and Edwards (1986, cited in Poulsen, 2005) determined an age of 2720 Ma for the batholith, which is similar to the age of felsic volcanics of the Kakagi Lake area (Fig. 2.2). The ellipse-shaped Black Hawk stock is located to the east of the deposit and has a dominant monzonitic composition (Blackburn, 1976; Wartman, 2011; Fig. 2.3). The stock truncates the felsic volcanic package of the upper diverse volcanic sequence and is relatively unaltered, but recorded a weak foliation (Wartman, 2011). Earlier studies by Blackburn (1976) mention a distinct compositional zonation within the stock, with a 0.8 km wide rim of monzonite englobing a predominantly porphyritic granodioritic core.

Based on aeromagnetic geophysics, an interpreted splay of the Subprovince bounding Quetico Fault runs less than 5 km to the south of the deposit (Siddorn, 2008: Fig. 2.4).

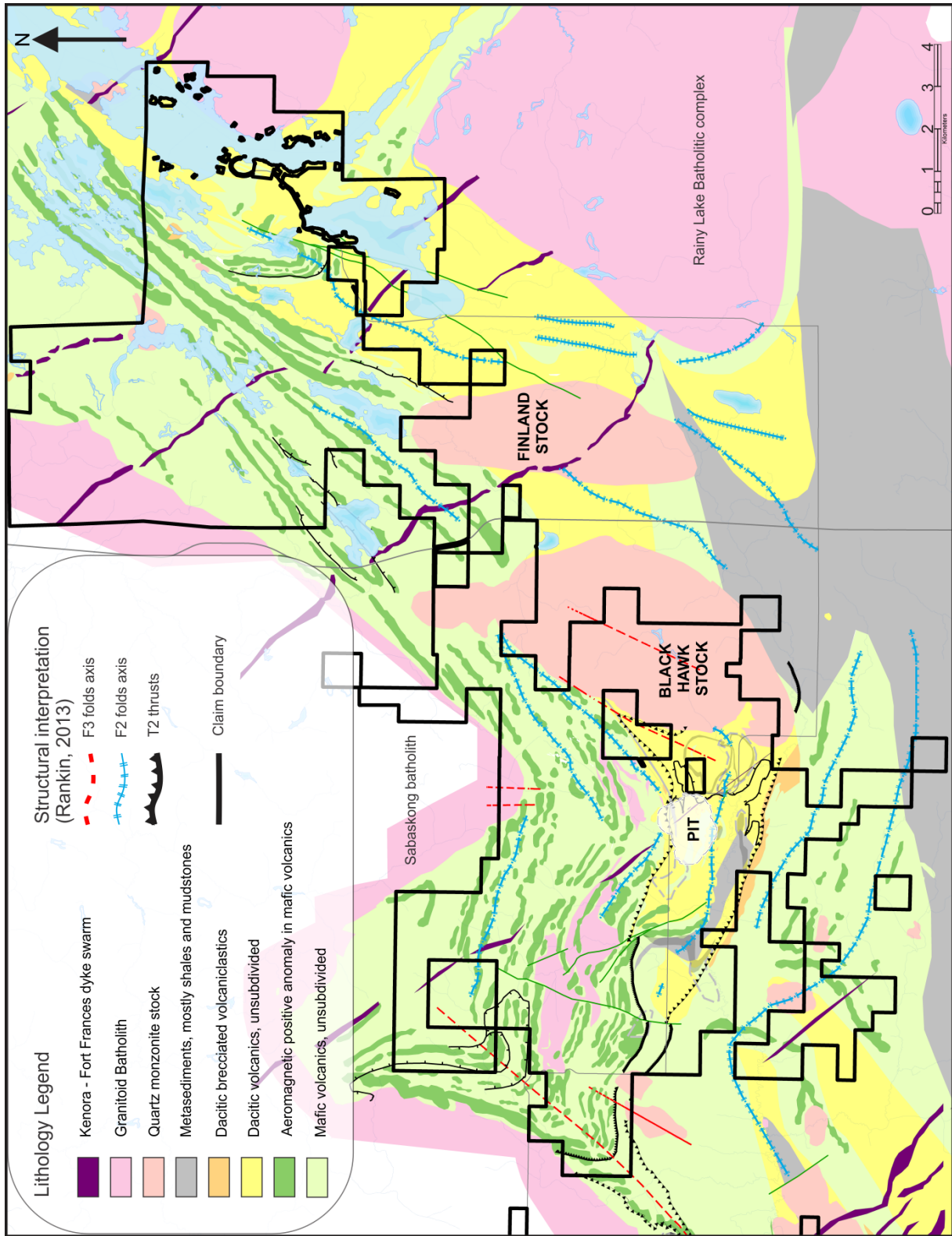


Figure 2.3 : Rainy River project simplified geologic map, with final pit outline. After Fletcher and Irvine, 1954, Rankin, 2013, and New Gold Inc., 2014. Adapted from a New Gold Inc. map.

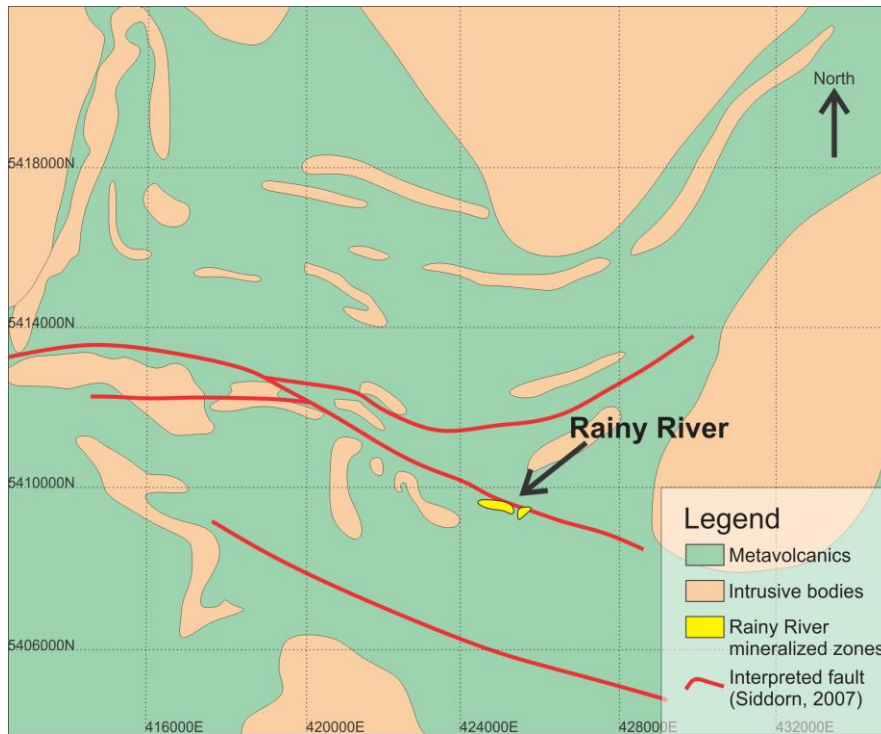


Figure 2.4 : Regional faults in the Rainy River area. Modified from Siddorn, 2008. Interpreted from aeromagnetics data (see Chapter 4 for raw mag data).

2.2.4 Deformation in the Wabigoon Subprovince

Most tectonic features and fabrics recorded in the Wabigoon Subprovince (polyphase deformation and metamorphism) are related to the central Superior Orogeny (Melnyk *et al.*, 2006; Percival *et al.*, 2006b). North-south oriented shortening during this orogeny generated folding and faulting, including thrusting, accompanied by metamorphism and plutonism. This orogen constitutes the culminating event in the progressive north-south accretionary regime that took place in the Superior between 2720 and 2660 Ma (Blackburn *et al.*, 1991).

Deformation in the central Superior Orogeny has been recorded differently depending on the location within the Wabigoon Subprovince. Near its boundaries, intense shearing and east-west fabrics are developed, whereas smaller and weaker curvilinear faults and deformation zones were produced in the inner parts of the Wabigoon Subprovince (Fig. 2.2). The rise of the granitoid domes and batholiths within the supracrustal belts in the core zone of the Wabigoon is probably responsible for the synformal-like geometry observed, where volcanic belts systematically face and dip away from the domes (Blackburn *et al.*, 1991).

Fold and shear zone development within the Rainy River greenstone belt hasn't been the subject of a structural study, although some correlations can be made with the Rainy Lake area, just to the east of the belt. In this area, work by Poulsen *et al.* (1980) and Davis *et al.* (1989) identified initial flat-lying imbrication and thrusting, layer-parallel shearing and small-scale folding (D_1). Later in the shortening history, deformation evolved into upright, east-west oriented folding (D_2). Final dextral shearing along the Quetico Fault (D_3) is recorded.

2.2.4.1 Metamorphism

Supracrustal rocks of the Wabigoon Subprovince record mostly low-grade metamorphic assemblages of the greenschist facies. Increasing intensity of metamorphism (up to middle amphibolite grade) is developed closer to batholiths and subprovince boundaries.

Timing of peak metamorphic conditions at the subprovince boundaries were reached following the major upright fold structures (D_2) (Poulsen *et al.*, 1980).

2.2.4.2 Quetico Fault

The Quetico Fault is over 200 km long and forms (in part) the southern boundary of the Wabigoon Subprovince (Fig. 2.2). Previous structural studies (Davis *et al.*, 1989; Blackburn *et al.*, 1991; Fernández *et al.*, 2013) characterize the fault as a subvertical shear zone with an overall dextral movement of up to 128 km within a northwest-shortening transpressive regime. This fault is a major crustal feature and was active into the Paleoproterozoic (Peterman and Day, 1989). Unlike other transcurrent faults of the Wabigoon, it is straight in orientation and cuts through lithologic boundaries, batholiths and greenstone belts.

2.3 Gold deposits and advanced projects within the Wabigoon Subprovince

Most of the known Au deposits and prospects of the Wabigoon are interpreted as epigenetic, shear-hosted Au-vein in nature. Notable examples are the Mine Centre areas (Poulsen, 1983), Shoal Lake (Duport mine: 1.8 Mt at 9.8 g/t Au) (Spooner and Barrie, 1993), and Cameron Lake mineralization (including the Cameron Gold project from Coventry Resources) hosted within the Pipestone-Cameron deformation zone (Melling, 1986).

The Hammond Reef project, located near the town of Atikokan and at the boundary with the Marmion terrane, has Au mineralization hosted in altered granitoid, occurring in a faults/shears-bounded stockwork of quartz vein and veinlets oriented parallel to the main NE-trending thrust zones that control the geometry of the deposit (source: Agnico Eagle Mines Ltd. website; Backeberg, 2015).

No syngenetic Au deposit associated with intermediate to felsic volcanics has been documented in the Wabigoon, with the potential exception of the Goliath gold project (G. Beakhouse, pers. commun. 2012). The Goliath deposit, located about 20 km northeast of the town of Dryden, is hosted in sericite-pyrite altered intermediate to felsic volcanic rocks and shows a good correlation between gold and lead-zinc sulphides (source: Treasury Metals website). Gold grades at Goliath are similar to those at Rainy River, with indicated resources of 9.14 Mt @ 2.6 g/t Au for 760,000 oz Au. The Maybrun copper-gold deposit (Setterfield *et al.*, 1983), which is hosted in mafic volcanics close to the Pipestone-Cameron deformation zone, is the only interpreted syngenetic gold deposit documented in the Wabigoon. Sulphides in inter-pillow space and fractures of mafic volcanics grade at 1.12 wt.% Cu and 1 g/t Au on average.

2.3.1 Other syngenetic base metal deposits hosted in felsic to intermediate volcanics

The Sturgeon Lake camp contains some of the most important ore deposits in the Wabigoon (Fig. 2.5). The camp comprises six, Mattabi-type, Zn-Cu volcanogenic massive sulphide deposits, all hosted in felsic pyroclastic breccias (using the classification of McPhie *et al.*, 1993). Deposits are all located within the Sturgeon Lake caldera structure (Morton and Franklin, 1987; Hudak, 2015).

The Headway-Coulee Zn-Cu-Pb-Ag prospect, located 60 km northwest of Geraldton, consists of disseminated-sulphide type syngenetic mineralization associated with altered mafic and felsic volcanics (Osterberg *et al.*, 1987).

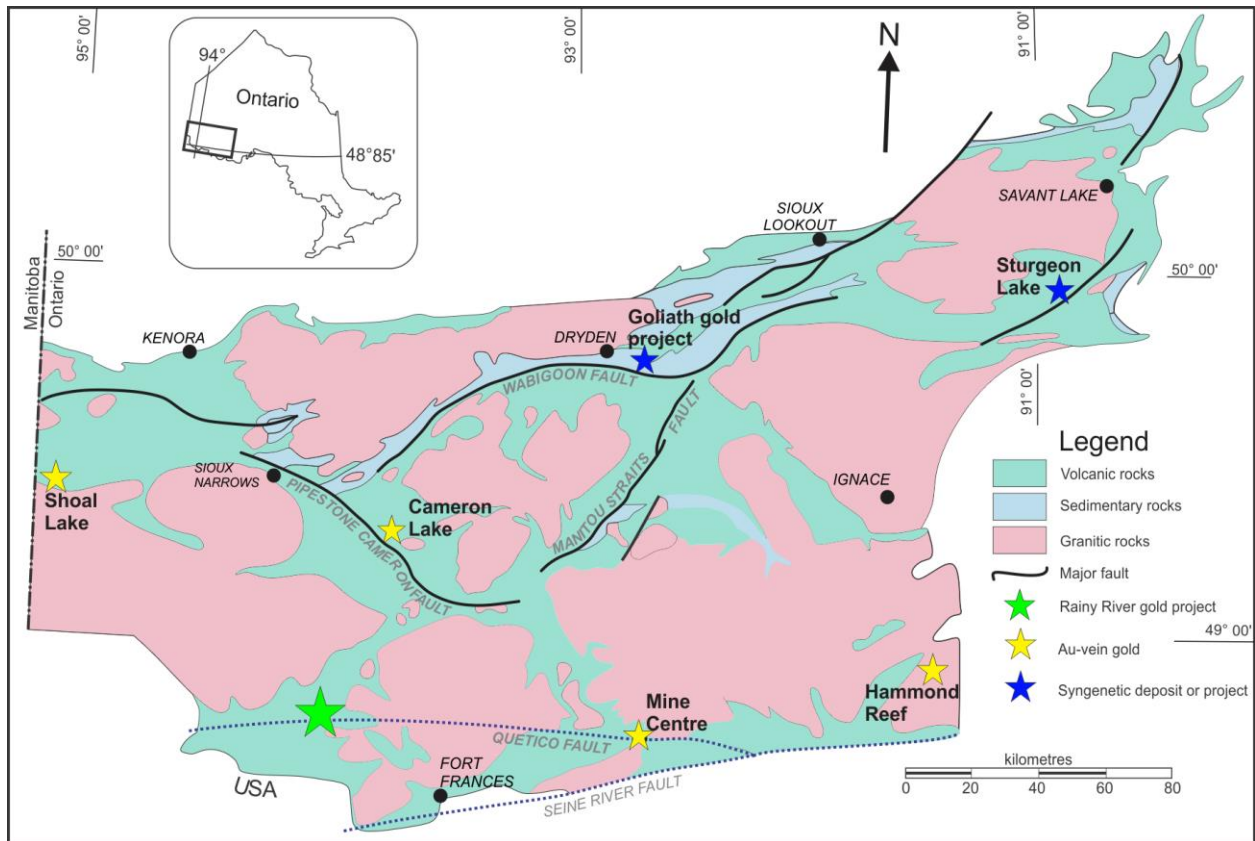


Figure 2.5 : Simplified geological map with location of significant Au deposits and prospects around the Rainy River gold deposit. Modified after Blackburn et al., 1991.

3 GEOLOGY OF THE RAINY RIVER DEPOSIT

3.1 Introduction

This chapter focuses on the description of the different lithological units and associated volcanic facies identified on outcrop and drill core. Petrographic observations on polished thin sections related to original volcanic textures and mineral abundances are also documented. The principal characteristics of the different units present at Rainy River are summarized in table 3.1. Cross sections and detailed maps (see section 3.3; appendix I) are shown to illustrate the spatial distribution of the different volcanic units and facies and can be found at the end of the document.

A discussion on the probable volcanic environment and tectonic regime in place at time of deposition is included. Post-volcanic intrusive units are also described.

Subsequently, a characterization and classification of the different lithological units in terms of rare earth and other trace elements is included, followed by a discussion on the tectonic setting and petrogenesis of the intermediate to felsic volcanic rocks hosting the Rainy River deposit.

3.2 Volcanic lithologies

The Rainy River deposit is predominantly hosted within dacitic to rhyodacitic volcanic rocks of calc-alkaline affinity. Although rocks have undergone hydrothermal alteration, metamorphism and polyphased deformation, some primary volcanic textures and structures are preserved and allow for a basic interpretation of the different emplacement processes and depositional environments characterizing the Rainy River deposit area. A previous study of the volcanology of the deposit area by Wartman (2011) identified seven dacitic units and two mafic units. Although partly preserved, primary volcanic textures in such complex environments can be difficult to differentiate from false pyroclastic textures in autoclastic lavas or intrusions caused by hydrothermal alteration, deformation and metamorphism (Allen, 1988). Only textures of certain primary origin are considered here.

3.2.1 Initial sample classification

Drill core and channel samples from the deposit area were initially classified into mafic and felsic groups based on visual observations. Subsequently, geochemical discrimination and classification diagrams helped further refine this classification, both in terms of composition (Figs. 3.1, 3.2) and magmatic affinity (s. 3.3, 3.4). The basaltic rocks are of tholeiitic to mildly transitional magmatic affinity, and dacitic to rhyodacitic samples all plot within the calc-alkaline affinity field. Mafic and felsic volcanic rocks in the Rainy River deposit vicinity are therefore associated with two distinct magmatic trends. The dacitic to rhyodacitic samples, which host most of the mineralized zones, possess a wide range of silica (SiO_2) content due to major element mobility in response to alteration (see chapter 5 for more details). In this study, the dacitic to rhyodacitic group will be referred to as dacitic in nature for conciseness purposes, although it does imply that some of these samples fall into the rhyodacite to rhyolite fields.

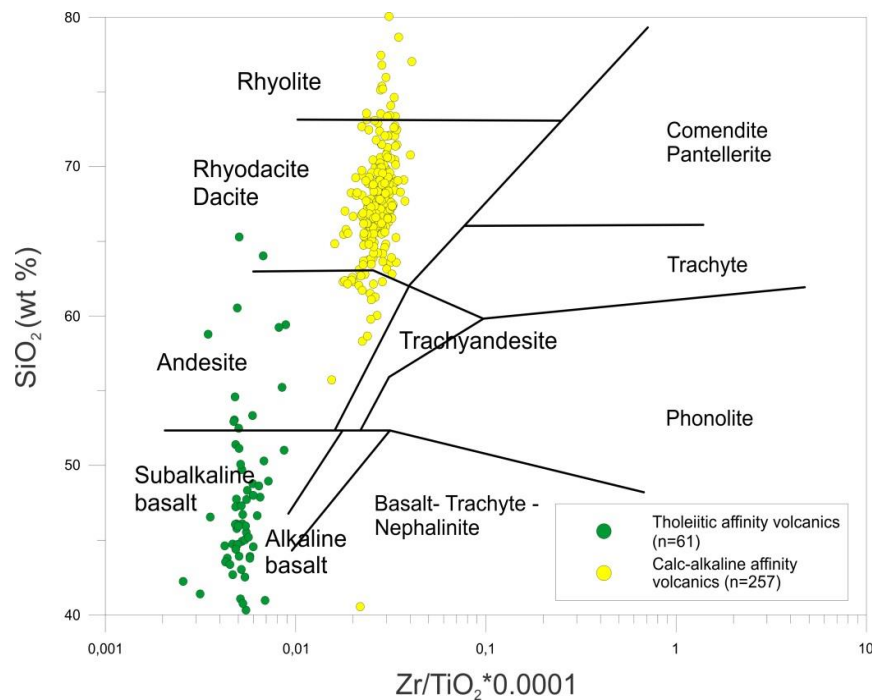


Figure 3.1 Volcanic rock classification diagram (Winchester and Floyd, 1977) with samples from the Rainy River project previously sorted according to their magmatic affinity. NOTE: three samples with high pyrite-pyrrhotite content and less than 40 wt.% SiO_2 , all of tholeiitic affinity, are not represented here.

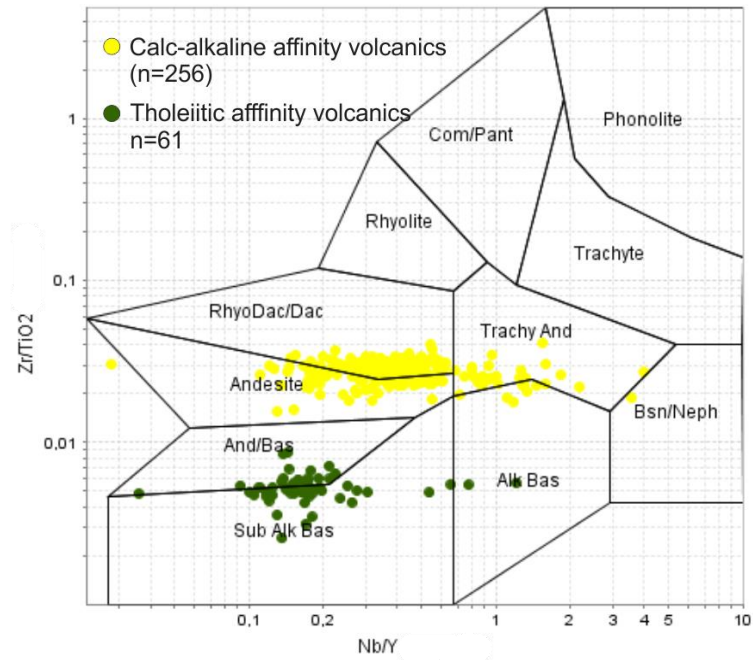


Figure 3.2 : Rock classification diagram from Winchester and Floyd (1977), with samples from the Rainy River project previously sorted according to their magmatic affinity.

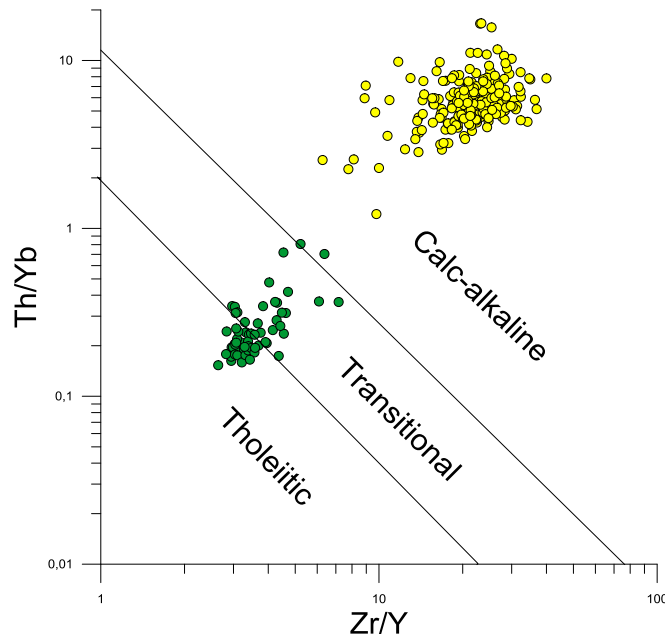


Figure 3.3 : Th/Yb vs. Zr/Y logarithmic diagram for discrimination of magmatic affinities from Ross and Bédard (2009) (n = 321). NOTE: three samples with less than 40 wt.% SiO₂, all of tholeiitic affinity, are not represented here.

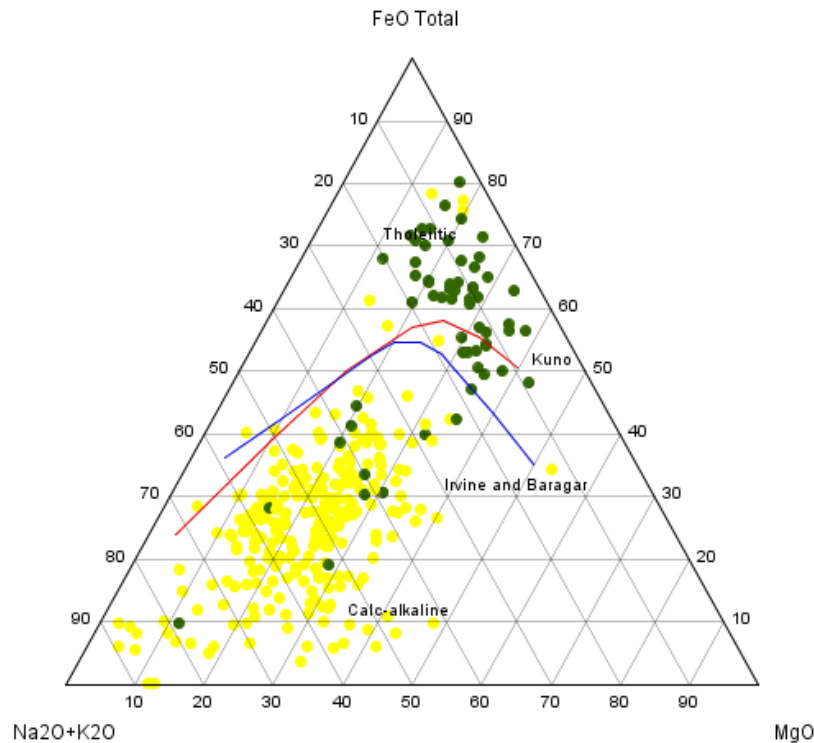


Figure 3.4 : AFM diagram (Irvine and Baragar, 1971) using major oxydes and total iron, plotting the previously classified tholeiitic and calc-alkaline samples. Samples that plot in the "opposite" field have undergone strong alteration affecting their Na_2O and K_2O content. This is further discussed in chapter 5.

3.2.2 Felsic coherent facies lavas and shallow intrusions volcanic facies

3.2.2.1 Coherent facies dacite: lava flows and/or shallow intrusions

Dacite of coherent facies, whether as lava flows and/or shallow intrusions, have been identified in drill core as well as outcrop on the property and constitute the main volcanic facies identified at Rainy River (appendix I, see section 3.3 for additional information: Wartman, 2011; Pelletier *et al.*, 2014). Coherent textures such as flow bands and flow folds are mapped on outcrop (Fig. 3.5A, B). Flow foliations and banding in these altered dacitic flows are defined by alternating siliceous and phyllosilicate (sericite or chlorite)-rich bands.

In volcanic rocks, alteration distribution and mineralogy is strongly influenced by devitrification patterns (McPhie *et al.*, 1993). With this in mind, alteration of flow bands, initially composed of alternating glassy and quartzo-feldspathic bands, generates alternating bands of respectively sericite-chlorite-quartz and quartz-albite products (McPhie *et al.*, 1993). Such alternating bands

of fine grained sericite-chlorite-quartz with coarser-grained quartz-albite products correspond to what is interpreted as flow bands at Rainy River.

Coherent dacites are characterized by subangular to rounded, blue-tainted quartz phenocrysts varying in size from 1-10 mm, and in abundance from <1 to 5 vol.%. Size and angularity of quartz phenocrysts are uniform within individual dacitic lava flow interval, but variations are noted between different diamond drill holes and likely represent distinct lava flows. Amygdules with sulphides and/or carbonates at their centre are also common within the blue quartz phenocrysts-bearing dacitic rocks (Fig. 3.5C, D). Amygdules are differentiated from phenocrysts by the presence of an additional mineral(s) phase(s) within the inclusion and an overall rounded appearance whereas phenocrysts are recognized as generally angular, without any inclusions. According to Barrett and MacLean (1999), the distinctive blue colour present in certain quartz eyes-bearing felsic lava flows is caused by elevated trace titanium contents within their structure. Groundmass is composed of a mosaic of microcrystalline quartz and feldspar grains (Fig. 3.6A, B, C, D) that can be interpreted as a granophyric texture generated during the devitrification of silicic glasses under prolonged heat and pressure (Lofgren, 1971). Coherent dacites also have microporphyritic to porphyritic feldspar grains that have been completely replaced by chlorite (Fig. 3.5D). Areas with chlorite-replacement of feldspars are diffuse and discontinuous at best and are intertwined with areas of different alteration styles (sericite-dominated, feldspar and phyllosilicate) and less altered patches.

Individual lava flow and/or subvolcanic intrusion boundaries are obscured by alteration and can be inferred where variations in quartz phenocryst abundance are documented (Wartman, 2011). On cross section (see section 3.3.2; appendix I), continuous sequences of coherent dacites in the deposit area are 10 to 80 metres in true thickness and followed along strike over 1 kilometre. These coherent dacitic bodies could potentially be thicker than 80 metres, but pervasive alteration in the deposit footwall makes it difficult to properly define such thick units that are in some cases crosscut by corridors of intense alteration and deformation.

On thin section, coherent dacites are composed, on average, of a matrix of microcrystalline quartz and feldspars accounting for 50-70 vol.% of the sample. Quartz phenocrysts are often broken and/or show undulose extinction (Fig. 3.6A, D), which indicates partial recrystallization during crystal-plastic deformation (Lagoeiro, 2003). Microporphyritic feldspar grains of albitic composition are also common, and altered by muscovite or carbonates at various degrees (Fig. 3.6B). Amygdules are composed of small grains of quartz, or a mix of several infill minerals,

including quartz, carbonate, and chlorite (Fig. 3.6C). Primary magmatic quartz grains with resorption bays are locally present (Fig. 3.6E), suggesting a rapid magma ascent to shallow depths and partial re-fusion of the recently crystallized quartz phenocrysts (Chang and Meinert, 2004). Alteration is also responsible for the introduction of false perlitic texture (Allen, 1988) observed on thin section in some intensely altered areas within the ODM zone (Fig. 3.6F).

When altered, the dacitic rocks contain various amounts of sericite, chlorite, carbonates, epidote, garnet, aluminosilicates, tourmaline, titanium oxydes, and sulphides. Mineralogy is strongly dependent on alteration and will be further discussed in chapter 5.

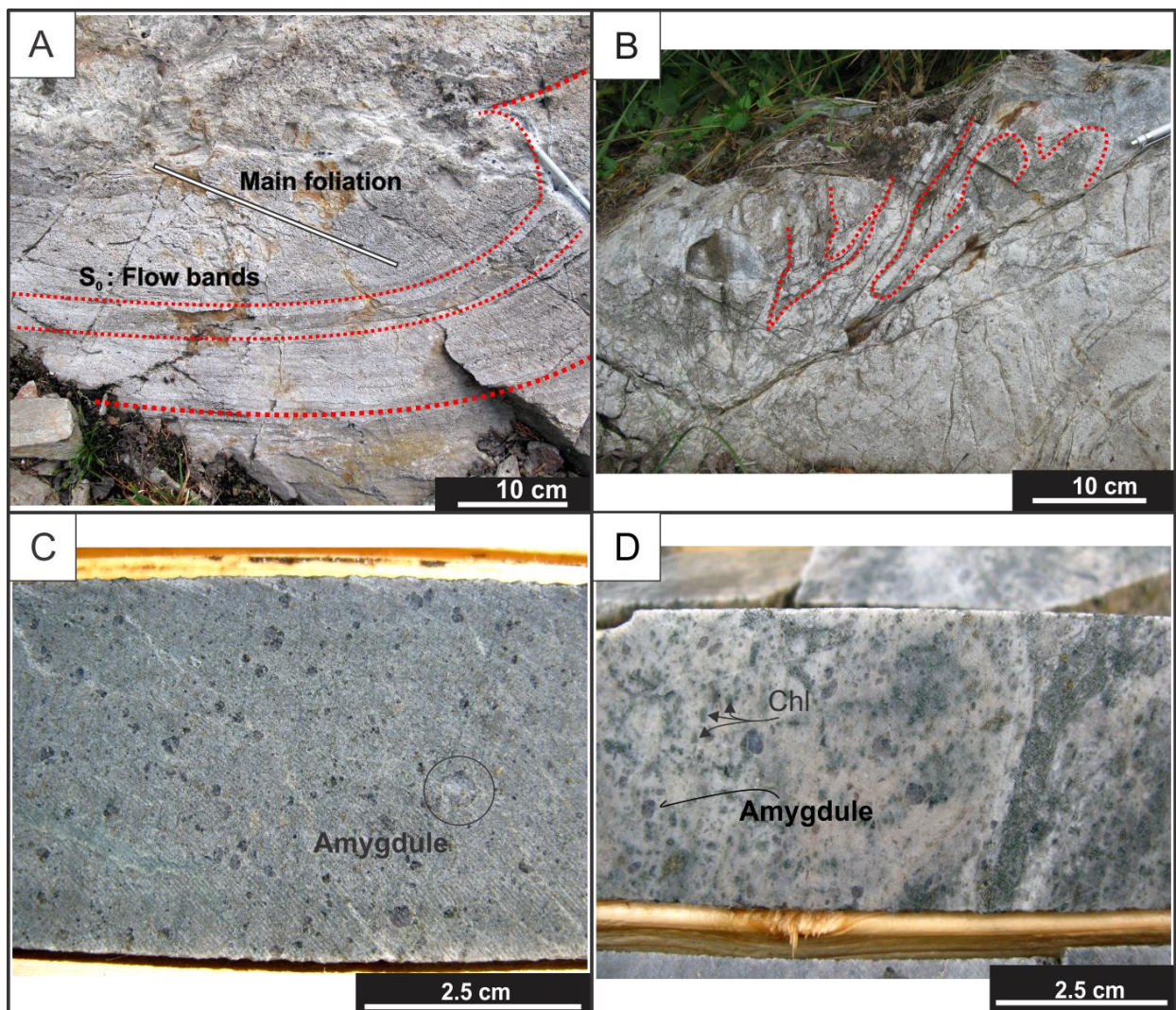


Figure 3.5 : Coherent facies: dacite. A) Flow banding in dacitic flow highlighted by alternating sericite-rich and quartz-feldspar-rich bands. McClain outcrop, deposit hanging wall (NAD83, Zone 15, 426130 mE, 5410328 mN). B) Flow folds and bands in dacite flow highlighted by alternating chlorite-rich and quartz-rich bands. McClain outcrop (NAD83, Zone 15, 426163 mE, 5410303 mN). C) Sericitized dacitic flow with subrounded blue quartz amygdules and fragmented blue quartz

phenocrysts. ODM zone hanging wall, DDH NR110771 at 158 m. D) Dacitic flow or intrusion where feldspars have been replaced by chlorite and now appear as dark spots. Both blue, rounded quartz eyes (amygdules?) and angular transparent quartz phenocrysts are present. Chlorite band subparallel to foliation might indicate poorly developed flow banding. North of deposit, DDH NR110797 at 205 m.

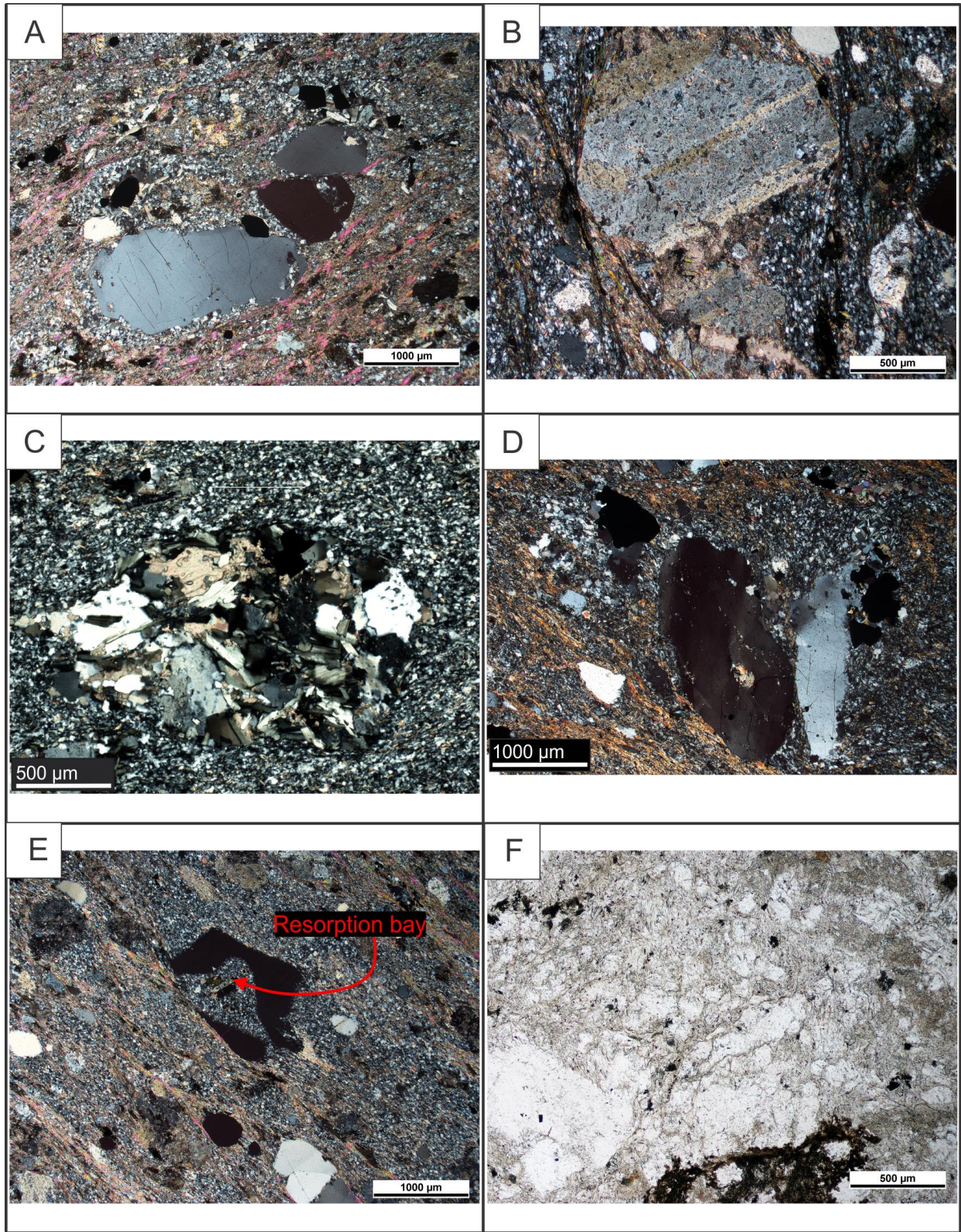


Figure 3.6 : Felsic flows and shallow sub-volcanic intrusions: Thin section observations. A) Photomicrograph (PL) of a felsic flow with fragmented quartz phenocryst, in formerly glassy groundmass (microcrystalline quartz-feldspar) with glomeroporphyritic chlorite clusters, that could potentially be

amygdule fillings. ODM zone, sample RRR435823, DDH NR080276 at 598 m. B) Photomicrograph (PL) of altered plagioclase with sericite and carbonate replacement in amygdular flow, weak to moderate sericite alteration. South of ODM zone, sample RRR435733, DDH NR060117 at 35 m. C) Photomicrograph (PL) of chlorite-quartz-carbonate replacement/filling of amygdale. HS zone, sample RRR435677, DDH NR110679 at 197 m. D) Photomicrograph (PL) of undulose extinction of recrystallized amygdule with muscovite and carbonate at its centre. Angular quartz phenocrysts are also present adjacent to the amygdule. 433 zone, sample RRR435884, DDH NR060067E at 745 m. E) Photomicrograph (PL) of resorption bay in primary magmatic quartz in amygdular flow. South of ODM zone sample RRR435733, DDH NR060117 at 35 m. F) Photomicrograph (TL) of false perlitic texture in strongly sericitized dacitic flow. Dendritic rutile dusting blebs also observed at bottom of photo. ODM high grade zone, sample RRR435845, DDH NR060058 at 364 m.

3.2.2.2 Quartz feldspar porphyritic-textured dacites

Observed both on outcrop and drill core, quartz feldspar porphyritic (QFP)-textured dacites occur mostly in less altered zones such as the deposit's hanging wall (section 3.3; appendix I) and within zones of extensive, low permeability-porosity dacite flows on outcrop (section 3.4.2; appendix I).

On drill core, QFP dacite is overprinted by foliation-parallel < 1 cm wide bands of sericite and chlorite (Fig. 3.7). Feldspar phenocrysts are angular to rounded, range in size from 1 to 6 mm and are evenly distributed within the matrix in abundance averaging 12 vol. %. Stretching/flattening parallel to the main foliation plane to a ratio of up to 3:1 has been documented on unoriented drill core (see chapter 4 on deformation). Alteration of feldspar grains mostly consists in replacement by muscovite and can easily be documented on thin section (Fig. 3.7B). On rare occasions, altered feldspars are partly replaced by carbonate (Fig. 3.7C). In general, destruction of feldspars and replacement by sericite increases in intensity towards the main ODM/17 zone. The QFP dacites also contain up to 3 vol.% bluish, rounded quartz phenocrysts that range in size from 1 to 8 mm. On average, this porphyritic dacite contains about 15 to 25 vol.% combined quartz and feldspar phenocrysts.

QFP-textured felsic rocks are common in greenstone belts, in both subvolcanic intrusions and effusive flows, making it difficult to characterize their origin and depositional environment. At Rainy River, QFP dacite has been mapped on outcrop in contact with dacitic amygdular flows (Fig. 3.8A). The contact is sharp, undulating and overprinted by foliation. Chlorite-rich bands (up to 5 cm-wide) are developed within the QFP bodies at the contact with the coherent dacitic flows, suggesting that these QFP bodies intruded dacitic amygdular flows. In drill core, the contact between the QFP dacites and the dacitic flows is diffuse or sometimes gradational, possibly due to the development of chilled margins in the QFP, making it hard to determine its nature.

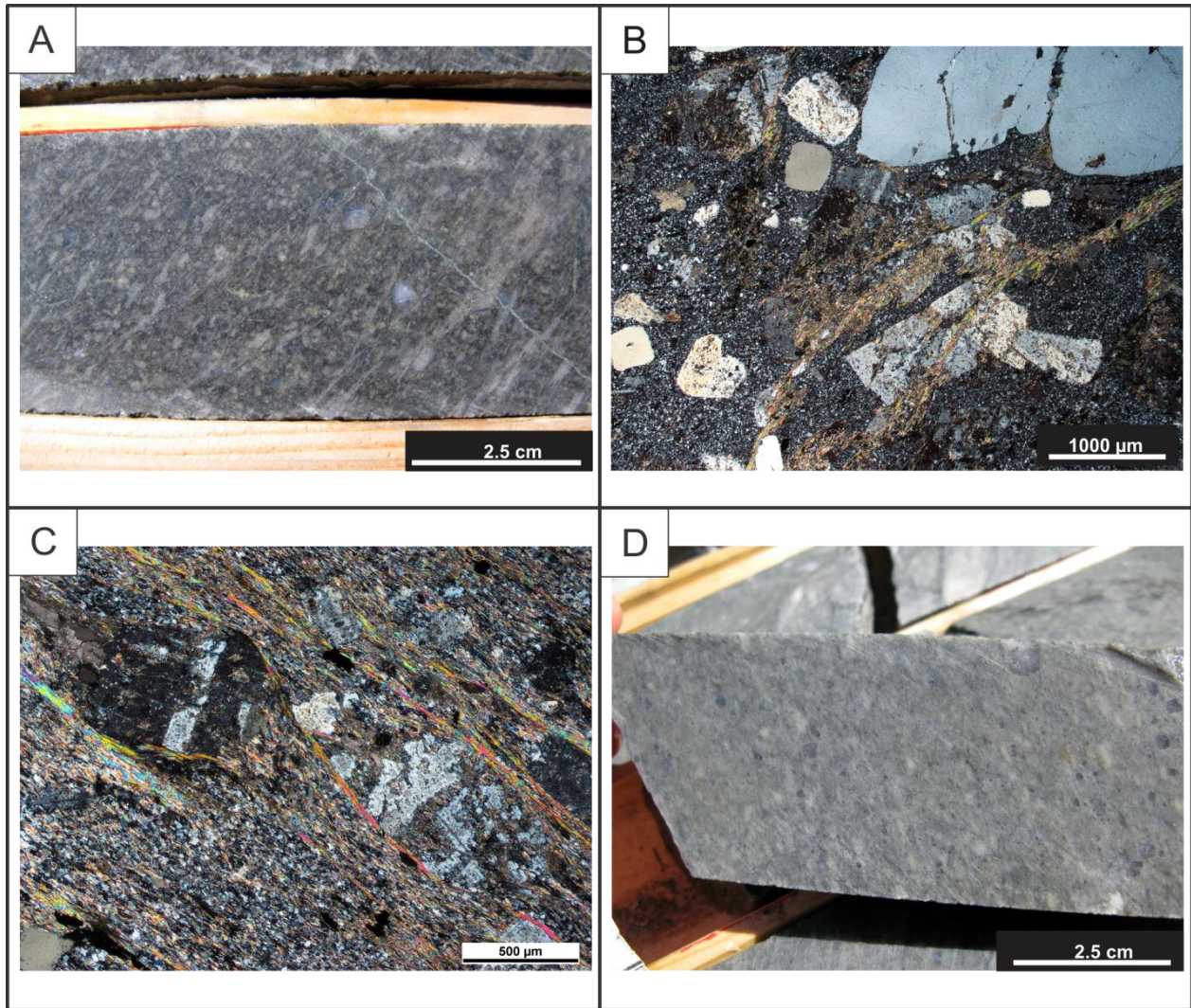


Figure 3.7 : Felsic flows and shallow intrusions : QFP dacite. A) Porphyritic quartz and feldspar grains, with moderate to strong sericite overprint affecting mostly the feldspars. Note flattening/elongation of relic feldspar grains parallel to main foliation plane. ODM zone hanging wall, DDH NR060058 at 91 m. B) Photomicrograph (PL) of QFP dacite with abundant (12 vol.%) euhedral feldspar crystals of albitic composition in a fine to very fine-grained microcrystalline matrix. Western ODM zone, sample RRR435515, DDH NR950025 at 116 m. C) Photomicrograph (PL) of altered and fractured plagioclase porphyroblasts with sericite and carbonate replacement in QFP dacite. Pervasive sericite alteration transposed into the main foliation in fine-grained quartzo-feldspathic matrix. ODM hanging wall, sample RRR435733, DDH NR060117 at 35 m. D) QFP dacite in the ODM zone hanging wall (compare with Fig. 3.7A photo), showing an increase in feldspar replacement by carbonates and sericite, along with an overall higher degree of sericitization and silica content, which gives it its lighter gray colour and diffuse QFP texture. ODM hanging wall, DDH NR060058 at 109 m.

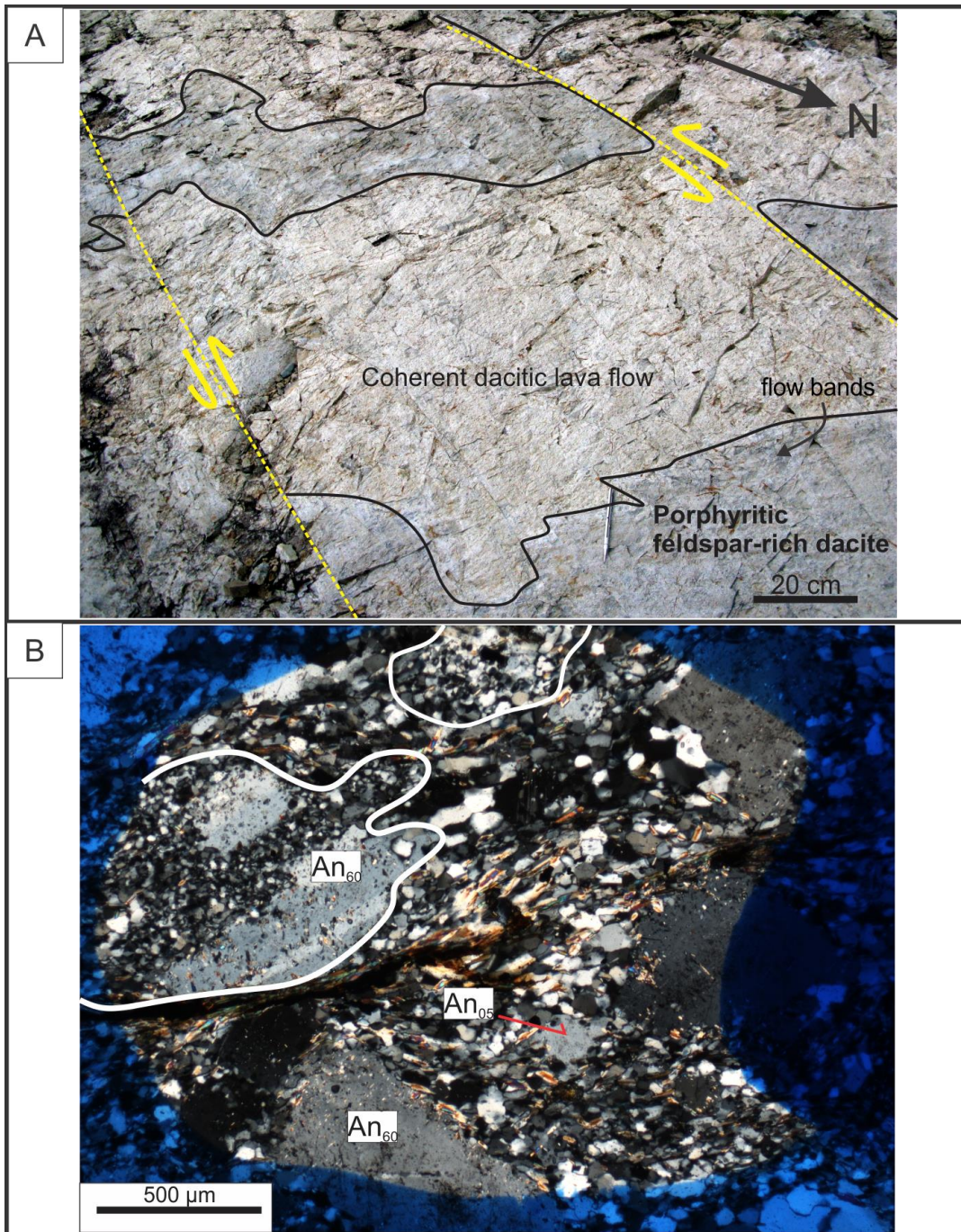


Figure 3.8 : Felsic flows and shallow intrusions : QFP dacite. A) Contact between the QFP dacite and the amygdaloidal dacitic lava flow on outcrop. Very fine laminations interpreted as flow bands are observed over less than 5 cm within the QFP body, at the contact with the coherent dacite flow. Contact is undulating, overprinted by the main foliation and affected by late senestral offset of less than 1 metre. Centre of proposed pit area, NAD83, Zone 15, 426263 mE, 5409530 mN. B) Photomicrograph (PL) of sample from Scott outcrop consisting in a coarse grained bed within a graded tuff sequence. Microprobe analyses demonstrate two populations of plagioclase feldspars with varying sodium content. Scott outcrop, sample RRR435867, NAD83, Zone 15, 427100 mE, 5408451 mN. NOTE : blue contour on photomicrograph corresponds to microprobe target delineation with a marker and is not part of the thin section.

3.2.2.3 Feldspar composition of dacites of the Rainy River deposit and vicinity

Microprobe analyses on feldspar phenocrysts (see Appendix II for complete data) returned compositions within the plagioclase group varying between An_0 and An_{75} (Fig. 3.9). Feldspars from the ODM zone and its hanging wall show no internal compositional zonation and have a fairly homogenous, sodium-rich composition (An_{0-30}). On the other hand, feldspars from the other mineralized zones within the deposit possess a more calcium-rich composition (An_{30-75}). Feldspars analyzed from graded dacitic tuff sequences at the Scott outcrop in the deposit's hanging wall (see section 3.4 for precise localization) are divided in two groups: a sodium-rich, albite (An_{05-25}) group similar to the one from the ODM zone, and an andesine to labradorite (An_{40-60}) group. Feldspars with a more calcium-rich composition are porphyritic, muscovite-altered and in clusters with very fine grained quartz and feldspar (Fig. 3.8B), whereas the sodium-rich albite grains are less altered and part of the coarser grained groundmass although based on a limited dataset. This suggests the presence of syngenetic calcium-rich plagioclase and alteration-related sodium-rich plagioclase (see chapter 5 for details).

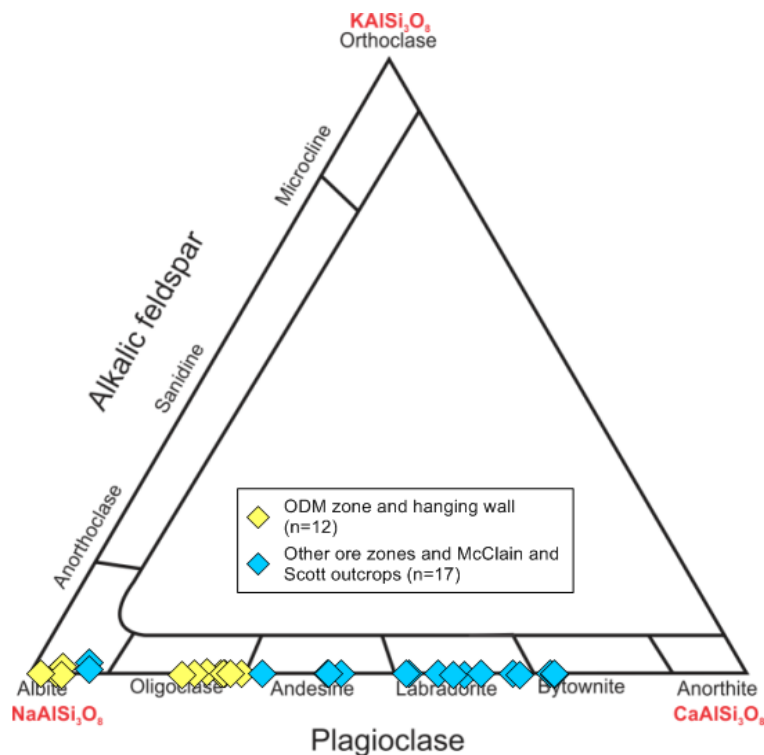


Figure 3.9 : Ternary feldspar classification diagram, with plotted microprobe data of the different feldspar grains analyzed. See appendix II for analytical data.

3.2.2.4 Dacitic muscovite schists

Dacitic muscovite schists are common in the footwall of the ODM/17 mineralized zone and in the 433 and HS zones. They form foliation-parallel corridors that are up to 100 m thick. The dacitic muscovite schists represent zones of intensely hydrothermally altered, deformed and metamorphosed dacites in which diagnostic original volcanic texture have been overprinted (Fig. 3.10A, B). These schists are mostly aphanitic, phyllosilicate- and microcrystalline quartz-rich. They are devoid of blue quartz phenocrysts or amygdules (Fig. 3.10C, D). Since quartz crystals are generally resistant to alteration, these muscovite schists units are thought to represent aphanitic coherent or volcanoclastic dacites similar to those mapped in less altered areas that are also devoid of blue quartz.

Petrographic studies of these schists can, locally, reveal textures and structures that may help identify volcanic facies. For example, remnant feldspars, almost completely replaced by sericite (Fig. 3.10C), indicate a potential coherent or autoclastic volcanic product. In other cases, jigsaw fit textures of microscopic quartz fragments suggest an autoclastic volcanic product.

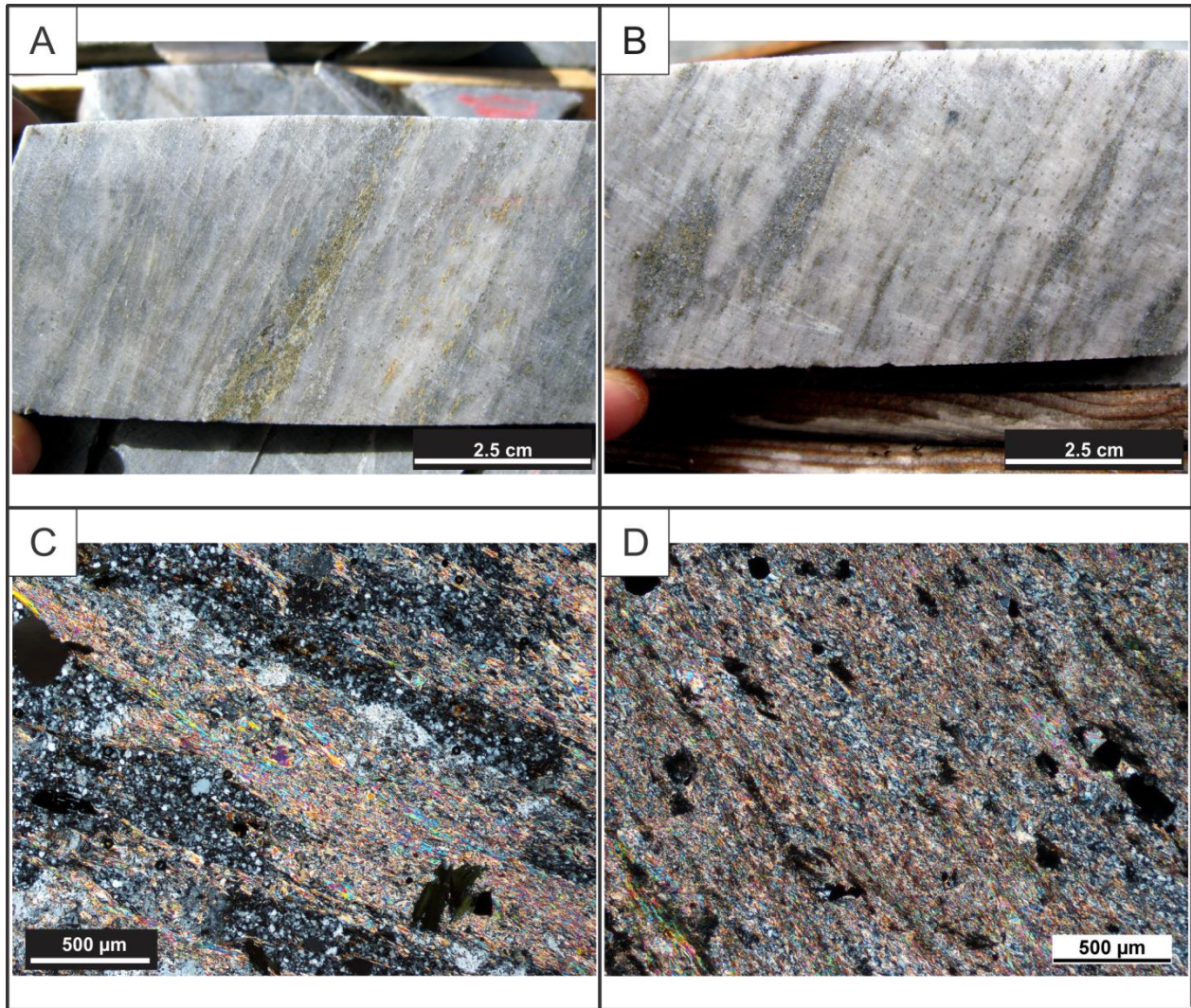


Figure 3.10 : Dacitic muscovite schists. A) Sericite-dominated schist with pyrite and sphalerite vein transposed into the main foliation plane. ODM high grade, DDH NR060058 at 368 m. B) Sericite and chlorite schist, where groundmass is pervasively altered by sericite, with folded and transposed chlorite-pyrite veins. Any primary volcanic texture has been overprinted and destroyed by alteration and deformation. ODM footwall, DDH NR060058 at 460 m. C) Photomicrograph (PL) of relict feldspar almost completely replaced by sericite in a microporphyritic lava, with a microcrystalline quartz-rich matrix. Coarse grain chlorite (bottom right) is late and related to metamorphism. ODM hanging wall, sample RRR435777, DDH NR060058 at 142 m. D) Photomicrograph (PL) of pervasive fine grained sericite alteration in sulphide-rich sample. ODM high grade, sample RRR435784, DDH NR060058 at 299 m.

3.2.3 Felsic volcanoclastic facies

Here, the term volcanoclastic is descriptive and has no genetic implications. It refers to volcanic facies composed predominantly of volcanic particles of any sizes, provenance, or lithology (Fisher, 1961; White and Houghton, 2006).

3.2.3.1 Monomict clast-supported tuff breccia

Monomict dacitic clast-supported tuff breccias, which are mainly present within the ODM/17 mineralized zone (appendix I; section 3.3), are recognized by their distinct, carbonate–chlorite–pyrite alteration stockwork (Fig. 3.11A, B, C, D) swerving around homogenous, fine-grained, light gray-coloured lapilli. The stockwork is now transposed parallel to the main foliation and the lapilli are closely packed and vary in size from <1 cm to ≤ 4.75 cm. They are moderately sorted and sometimes weakly graded parallel to core axis (perpendicular to the main S_2 $102N/61^\circ$ foliation). Fragments are flattened and stretched within S_2 and are subrounded to rounded. Their composition is very similar to the matrix, with a muscovite-dominated alteration disseminated in a microcrystalline quartz and feldspar groundmass (Fig. 3.11B). Rounded blue quartz phenocrysts are also present in low abundance (≤ 1 vol.%), and are evenly distributed within clasts.

This unit has been previously interpreted as a quench fragmented hyaloclastite deposit (Wartman, 2011) resulting from a non-explosive fracturing (autoclastic) of quenched lava or intrusion. Jigsaw fit texture has been recognized on certain thin sections (Fig. 3.11D), which is in agreement with Wartman (2011) interpretation. However, according to Allen (1988), massive coherent volcanic rocks can also possess an apparent massive breccia texture through two-phase phyllosilicate-rich and quartz-rich alteration. Although plausible, a coherent nature for this unit is unlikely, due to the weak grading of the lapilli parallel to core axis.

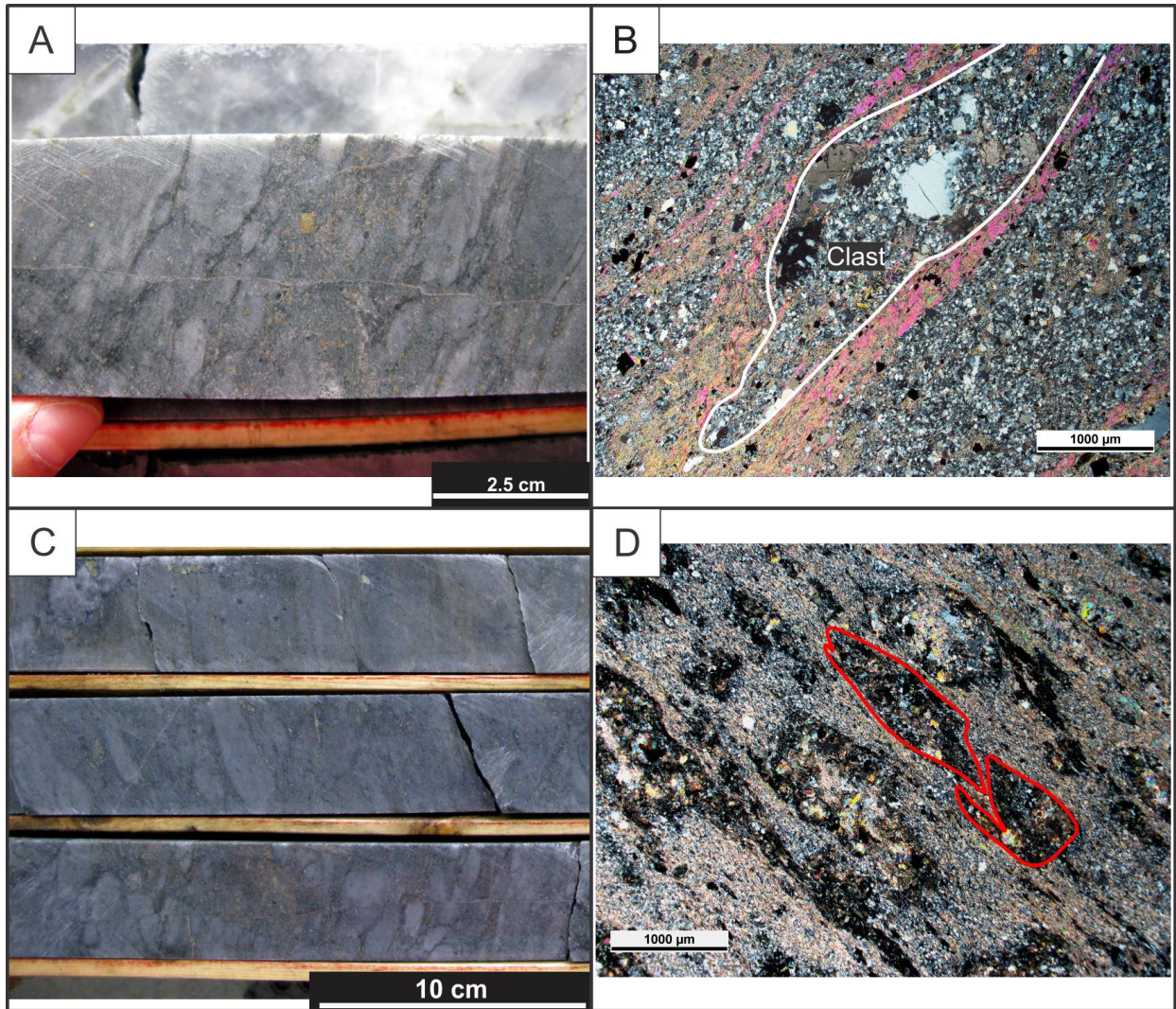


Figure 3.11 : Felsic volcanoclastic facies : monomict clast-supported dacitic breccia. A) Monomict lapilli breccia with sericitized clasts and matrix-controlled chlorite and carbonate alteration. Spessartine garnet-chlorite-pyrite stringers overprint this breccia. Note elongation/flattening of clasts parallel to the main foliation. ODM zone, DDH NR060058 at 335 m. B) Photomicrograph (PL) of monomict clast-supported tuff breccia, with matrix-controlled sericite alteration, and microporphyrific carbonate crystals restricted within the microcrystalline quartz-feldspar dominated lapilli. ODM zone, sample RRR435807, DDH NR070141 at 171m. C) Drill core interval of highly mineralized fragmental dacite. Lapilli margins are altered, which reduces their apparent size. ODM zone, DDH NR060058 at 325-335 m. D) Photomicrograph (PL) of a sample originally logged as sericite schist based on visual observation. Microcrystalline quartz-feldspar matrix with pervasive sericite alteration molding around hyaloclastite fragments showing a jigsaw fit texture later affected by the main foliation. Alteration of the clast margins and deformation partially obscured the original fine hyaloclastite clast shapes of what could be an autoclastic facies (see McPhie et al., 1993 for nomenclature of volcanoclastic deposits). South of deposit, sample RRR435653, DDH NR110702 at 187 m.

3.2.3.2 Polymict dacitic, clast-supported tuff breccia

The polymict dacitic clast-supported tuff breccia units are identified on drill core in intervals of less than 30 metres as well as on outcrop (Fig. 3.12A, B; see section 3.4 for maps). Lapilli are poorly sorted and graded, and in all cases are strongly flattened and stretched within the main 102N/61° foliation, with an elongation/flattening ratio of 3:1, measured along strike versus down dip (Fig. 3.12B). On outcrop, fragments are 0.5 to 20 cm in diameter, light-coloured and subangular. Also on outcrop, clasts with high silica content are easily recognized due to their positive relief (Fig. 3.12B).

The clasts composition varies from sericite-dominated to quartz-feldspar dominated. They have a dull gray to light peach colour, related to their high silica or sericite content for the former, and high rutile concentration for the later (Fig. 3.12B). Chlorite or sulphide-rich clasts are very rare and it is unclear as to whether or not they consist in a false texture related to hydrothermal alteration and deformation (Fig. 3.12C). Chlorite and sericite alteration as well as sulphide mineralization in this facies are matrix-controlled and fine grained (Fig. 3.12D), as further described in chapter 5.

Arguably, the polymict nature of the tuff breccias recognized on drill core can be attributed to alteration of an originally in-situ quench brecciated dacite rather than to reworked volcanoclastic deposits. This is similar to what is described in the hanging wall rhyolite of the Rosebery mine in Western Tasmania (McPhie *et al.*, 1993). As described in McPhie *et al.* (1993), heterogenous sericite-chlorite and feldspar alteration preferentially affects porous, volcanoclastic deposits and generates pseudoclasts, pseudo-pumice fiamme (not present at Rainy River) and pseudomatrix. The final product is a volcanic rock with fragments of heterogenous composition and/or aspect, although these fragments were most probably of similar initial composition, but with varying initial vesicularity, grain size, and porosity-permeability. At Rainy River, the variation in clast mineralogy could, like at the Rosebery mine, be due to preferential, heterogenous hydrothermal alteration of the lapilli and blocks with higher initial porosity rather than initial compositional variation. Indeed, rare earth element profiles of samples of polymict dacitic tuff breccia are almost identical to the patterns of the dacite flows (Fig. 3.13). This similarity indicates a common source for both volcanic facies and does not support the presence of lithological variations among clasts. Consequently, the polymict tuff breccias at Rainy River are interpreted as monolithic volcanoclastic rocks having undergone heterogenous alteration, in comparison to the

monomict dacitic tuffs facies, where fragments probably had a more homogeneous initial composition and porosity/ vesicularity.

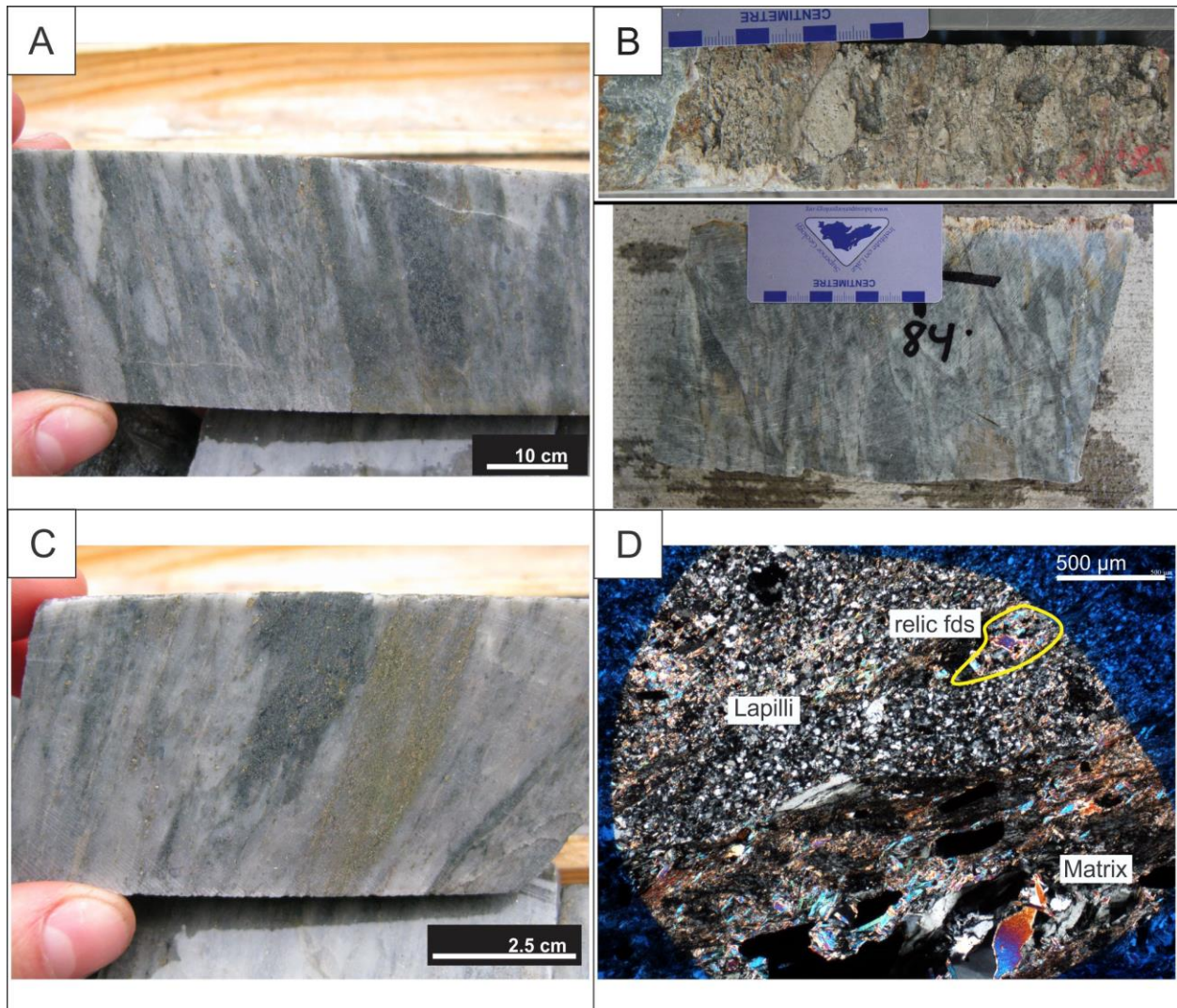


Figure 3.12 : Felsic volcanoclastic facies : polymict, clast-supported dacitic lapilli tuff breccia. A) Polymict clast-supported dacitic tuff, with lapilli ranging from aphanitic, sericite-rich to coarser grained, blue quartz phenocrysts-bearing. Chlorite and pyrite are mostly restricted to the matrix. Lapilli rims and contact with matrix are diffuse and offset by alteration. Strong transposition of primary fabric within the main foliation plane. HS zone, DDH NR070141 at 345 m. **B)** Channel sample from the McClain outcrop in the deposit's footwall, with view from surface and along the channel (oriented 322N, mostly perpendicular to main fabric on site). Notice stretching/flattening ratio of clasts between the surface and down the channel. Patches of pinkish hue correspond to clasts with rutile dusting alteration. Clasts are more angular and bigger in size when compared to previous photo from within the deposit, maybe due to weaker alteration in a more distal position with respect to mineralization. NAD83, Zone 15: 426158 mE, 54103412 mN. **C)** Diamond drill core located 3 metres down hole from rock shown in picture A, consisting in strongly altered and deformed polymict dacitic lapilli tuff. Clast boundaries are overprinted by post-depositional silica and sericite hydrothermal alteration and transposed into the main foliation plane. HS zone, DDH NR070141 at 348 m. **D)** Photomicrograph (PL) of a clast boundary in a mineralized, clast-supported polymict dacitic lapilli tuff. Sericite and chlorite are dominant within the matrix. The clasts are composed of microcrystalline quartz and feldspars, with microphorphyritic feldspar crystals

altered and replaced by sericite and chlorite. HS zone, sample RRR435718, DDH NR070142 at 302 m.

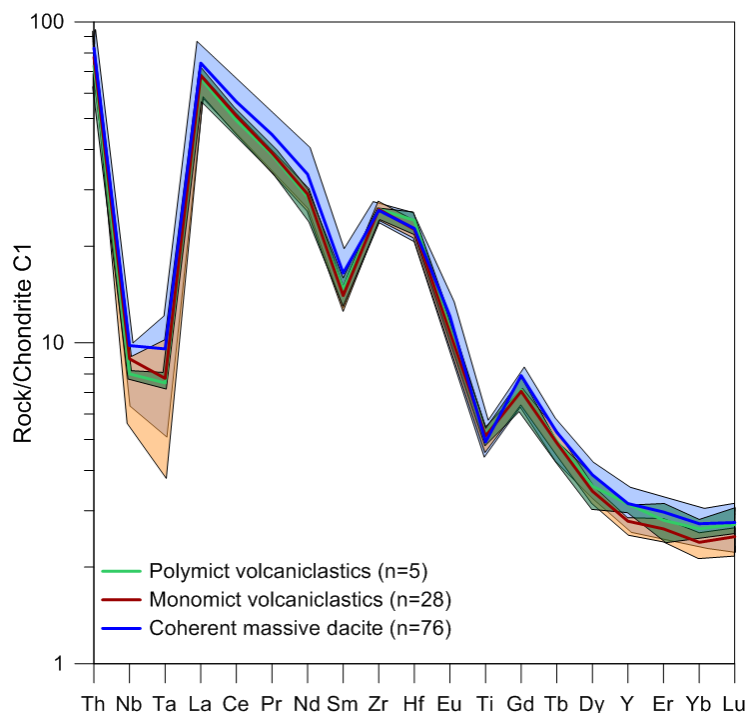


Figure 3.13 : Chondrite-normalized multi-element plots for the calc-alkaline dacitic volcanoclastic and coherent felsic rocks of the Rainy River deposit. C1 chondrite values from McDonough and Sun (1995).

3.2.3.3 Quartz crystal dacitic tuff

Quartz crystal dacitic tuffs are documented in a restricted, 20 to 60 m-wide assemblage located between the north of the ODM zone to the 433 zone. From visual observations, these tuffs greatly resemble the dacitic flow units previously described. Notable differences reside in the transparent colour of the quartz phenocrysts and their angularity. Quartz phenocrysts range in size from 3 to 7 mm, are commonly fragmented and abundant, accounting for 5-8 vol.% of the rock (Fig. 3.14A, B, C). The groundmass is microcrystalline and quartz and feldspar-dominated (Fig. 3.14D).

As with most other units within the deposit, this unit has undergone strong, texturally destructive hydrothermal alteration. As a consequence, diagnostic original volcanic textures have been erased and the term tuff is used here solely on a grain size basis and does not imply any genetic connotation.

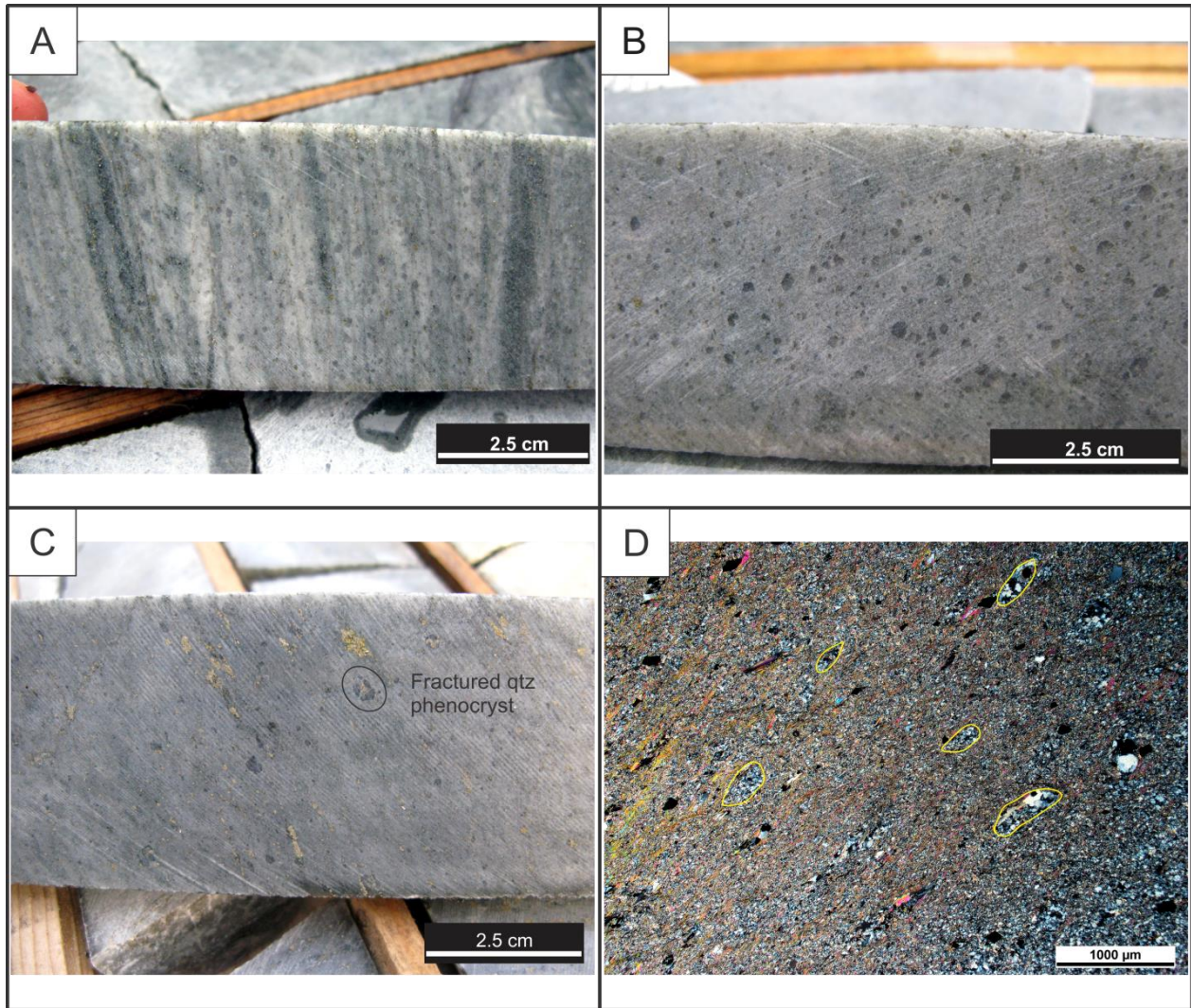


Figure 3.14 : Felsic volcanoclastics : quartz crystal tuff. A) Quartz crystal tuff with >8 area % angular transparent quartz phenocrysts and strongly deformed chlorite veins and veinlets parallel to main foliation plane. 433 zone, DDH NR070181 at 663 m. B) Quartz crystal tuff with abundant angular to subrounded transparent quartz phenocrysts in a homogenous, aphanitic silica and sericite-rich matrix. ODM zone, DDH NR060058 at 423 m. C) Quartz crystal tuff with disseminated, poorly-sorted angular quartz crystals, occasionally fractured with a jigsaw fit texture. Subtle very fine chlorite ± pyrite veinlets overprint the homogenous, pervasively silica and sericite-altered groundmass. HS zone, DDH NR060067E at 610 m. D) Photomicrograph (PL) of quartz crystal tuff with potential devitrified relict fiamme (recrystallized quartz blebs) or stretched vesicules (?) in microcrystalline homogenous sericite-dominated groundmass. Western ODM zone, sample RRR435732, DDH NR070146 at 222 m.

3.2.4 Mafic tholeiitic units

The Rainy River deposit is bounded to the north and south by mafic volcanic rocks of tholeiitic affinity (Fig. 2.3). Although most of the mineralized zones occur in dacitic rocks, some minor mineralized zones are hosted in the mafic rocks. At the scale of the "Rainy River greenstone

belt", mafic tholeiitic volcanic units largely dominate in volume and extent (Fig. 2.3), although the Rainy River mineralized zones are largely restricted to the dacitic volcanic package.

Tholeiitic basalts have been identified in drill core mostly within the Cap mineralized zone, but also in thin, 10-30 m wide, foliation-parallel bands in the ODM mineralized zone hanging wall and within the 433 mineralized zone (appendix I). Tholeiitic basalts are aphanitic to coarse grained, with iron-carbonate, magnetite, and pyrite alteration in the groundmass (Fig. 3.15A, B, C) at various intensity (see chapter 5 for details on alteration). Abundant, late, less than 5 cm-wide quartz-carbonate veinlets cross-cutting the foliation are present within most mafic rock intervals, whereas complexly folded iron carbonate+quartz+sulphide veins occur in mineralized mafic rock intervals.

Tholeiitic amygdaloidal basalts, which are chlorite-carbonate-magnetite-pyrite altered, are locally present and form discontinuous, tens of metres thick intervals (Fig. 3.15B, D). Amygdules are ≤ 1 cm wide and are blue-coloured, potentially due to their high trace titanium content (Barrett and MacLean, 1999). Whole-rock analyses of these rocks reveal low SiO_2 concentrations (48-55 wt.%), relatively flat REE patterns (Fig. 3.16), and high Ni and Cr values, typical of mafic volcanic rocks. For these reasons, the blue quartz eyes observed in these mafic rocks are interpreted as amygdules.

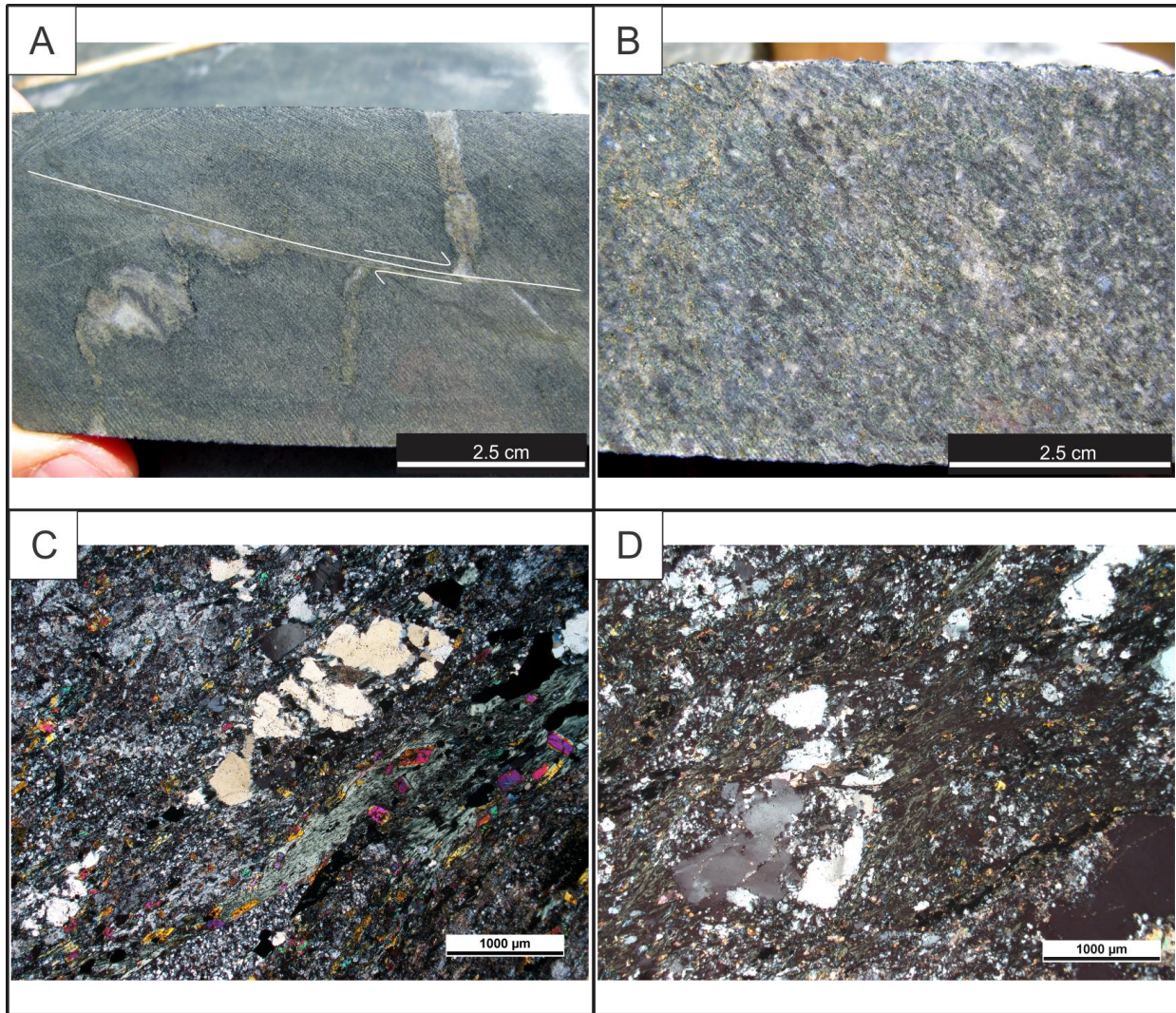


Figure 3.15 : Mafic tholeiitic units : drill core and thin section observations. A) Carbonate and chlorite-altered fine-grained mafic flow, with pyrite-bearing quartz carbonate vein that has undergone polyphase ductile deformation prior to brittle faulting (unoriented drill core). Cap zone footwall, DDH NR110771 at 295 m. B) Tholeiitic mafic coarse grained unit with strong magnetite and chlorite alteration in feldspar matrix. Rounded blue amygdule-bearing. Cap zone footwall, DDH NR110771 at 224 m. C) Photomicrograph (PL) of magnetic mafic flow with jigsaw fit textured fragmented feldspar in microcrystalline feldspar matrix. Strong chlorite-epidote veining parallel to main foliation. Cap zone footwall, sample RRR435837, DDH NR110771 at 247 m. D) Microphotograph (PL) of mafic tholeiitic unit showing blue amygdules with microcrystalline quartz-infill at centre in chlorite feldspar epidote and carbonate-dominated matrix. North of HS zone, sample RRR435748, DDH NR110687 at 382 m.

Mafic tuffs are also present at Rainy River (Wartman, 2011). These tuffs consist in a heterogenous group of fine grained samples of tholeiitic affinity. This subunit has not been incorporated in the present maps, since its distinction from the mafic flows is unclear texturally and both could represent the same unit. Furthermore, tuffs and flows have very similar geochemical signatures (table 3.1).

Rare earth element (REE) and multi-element profiles of the tholeiitic basalts (Fig. 3.17) reveal two subunits characterized by their flat REE profiles, in some cases coupled with anomalous Th-Nb-Ta values. On a cross section, these samples plot within the Cap zone and the hanging wall of the ODM/17 mineralized zone (appendix I). A distinction between these mafics and the rest of the mafic volcanics in the deposit cannot be made on a visual basis, perhaps due to the aphanitic nature of most mafic volcanic intervals.

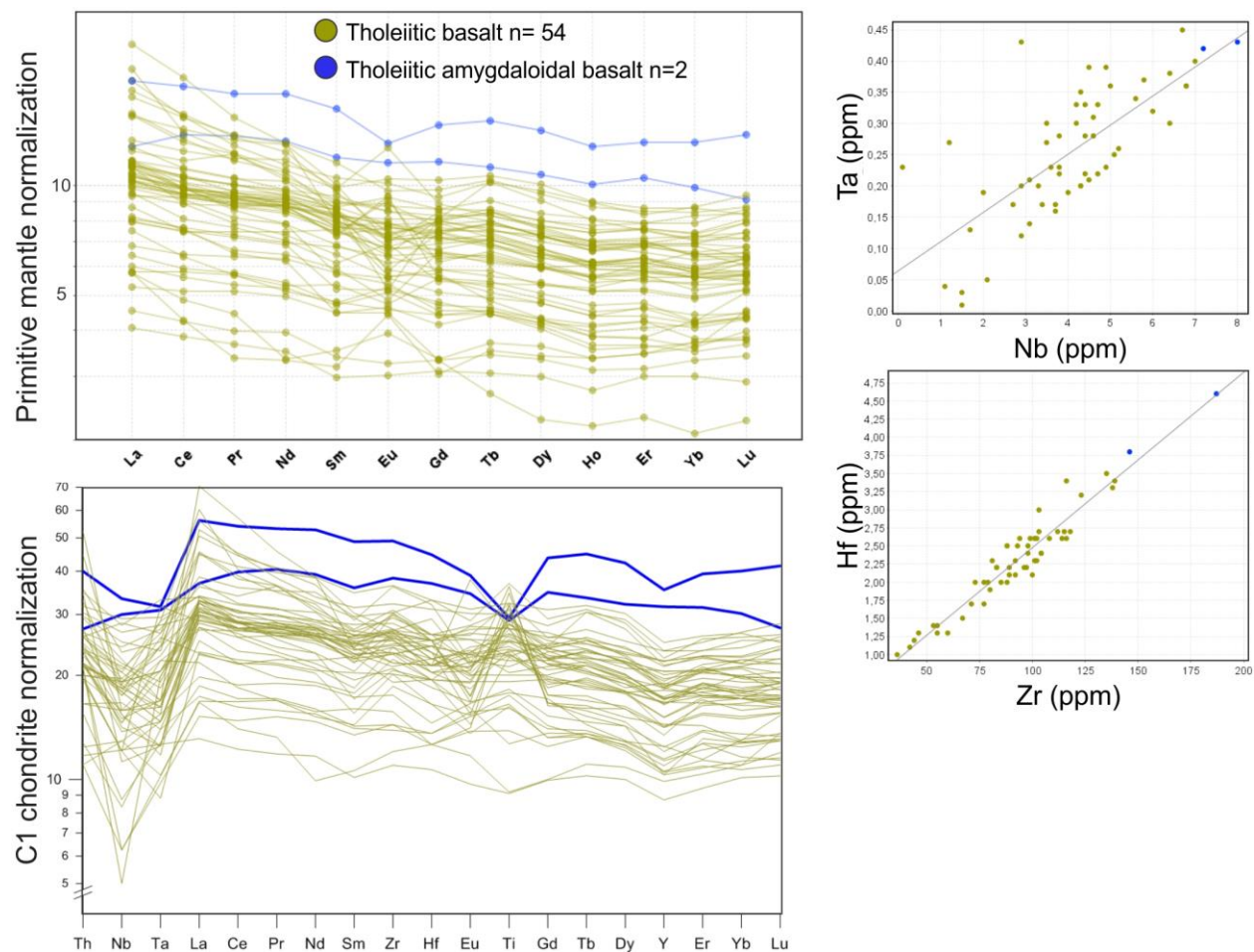


Figure 3.16 : REE profiles normalized to the primitive mantle composition from Sun and McDonough (1989) along with multi-element chondrite-normalized profiles after McDonough and Sun (1995) for tholeiitic basalt samples without HFSE decoupling.

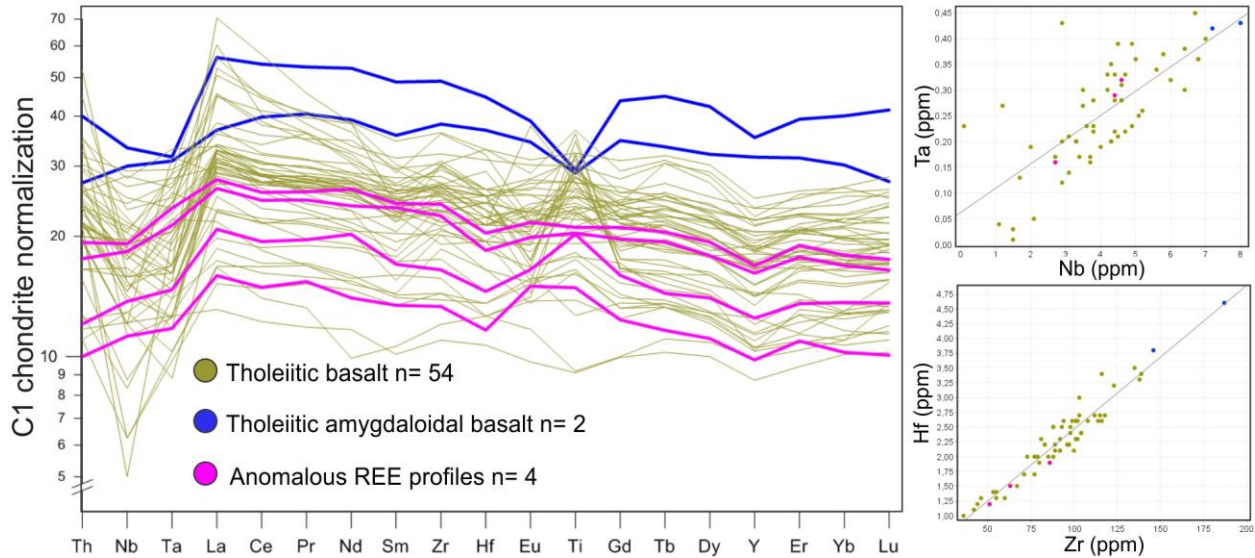


Figure 3.17 : Multi-element profiles of all tholeiitic basalts, normalized after the C1 chondrite values from McDonough and Sun (1995). Samples with HFSE decoupling have been removed from the dataset.

In the deposit area, the contact between the mafic and dacitic volcanic units is not exposed, but it has been documented numerous times on drill core. In the Cap zone, dacitic and mafic volcanics alternate with a sharp, foliation-parallel contact, every 20-70 metres (appendix I). Although it is probable that the contacts observed between mafic and dacitic units are conformable, these contacts have recorded the different deformation events and have most probably been transposed into the main foliation plane.

Mapping previously conducted in the deposit area identified volcanic facies of subaqueous basalt lava flows and mafic tuff (Wartman, 2011). Flows are massive to pillowed, whereas the tuffs are massive and contain very rare mafic lapilli clasts (Wartman, 2011).

Reconnaissance mapping by the author of outcrops exposing mafic rocks within the proposed pit area have also revealed identifiable original volcanic textures, providing clues to interpret their depositional environment. An outcrop located south-west of the Cap zone (the only mainly mafic-hosted mineralized zone of the deposit) displays centimetre to decimetre-scale, light grey-coloured, fine-grained nodular structures interpreted as spherulites in a chlorite and pyrite-altered basalt (Fig. 3.18A). These spherulites are composed of sericite-altered plagioclase, are sometimes coalesced, and occasionally possess a magnetite grain at their centre (Fig. 3.18B). Contact with the massive basalt present in the remaining part of the outcrop is sharp, conformable and oriented $258^{\circ}/72^{\circ}\text{NW}$. Spherulites have been documented in welded

ignimbrite deposits (Steven and Lipman, 1976; McPhie *et al.*, 1993) as well as formerly glassy lavas (McPhie *et al.*, 1993). At Rainy River, the absence of lithic fragments and/or broken crystals within the mafic rocks of this outcrop suggests an effusive (lava flows) rather than an explosive (ignimbrites) eruption regime for these mafic volcanic rocks. Abundant pillow basalts in the region along with the presence of argillites in the area also suggest an effusive regime for these rocks in an overall relatively deep subaqueous depositional environment.

Recent overburden stripping has been done on the property and exposed rocks at the projected surface location of the Cap zone. The exposed rock consists in a massive, pyrite, chlorite and magnetite-altered basaltic unit with a 30 to 70 cm wide, largely conformable, carbonate-altered volcanoclastic deposit between the coherent unit or, alternatively, an autobreccia or hyaloclastite breccia (Fig. 3.18C, D). Determination of a volcanoclastic or breccia nature for this semi-conformable layer is hindered by the alteration and deformation of the rock, which could have erased or deformed initial curvilinear surfaces distinctive of hyaloclastites. A subvertical exposure has also been stripped and washed, exposing laminated, Au-bearing quartz-ankerite-pyrite veins. Their nature and orientation will be further discussed in the chapter 4 on deformation in the study area.

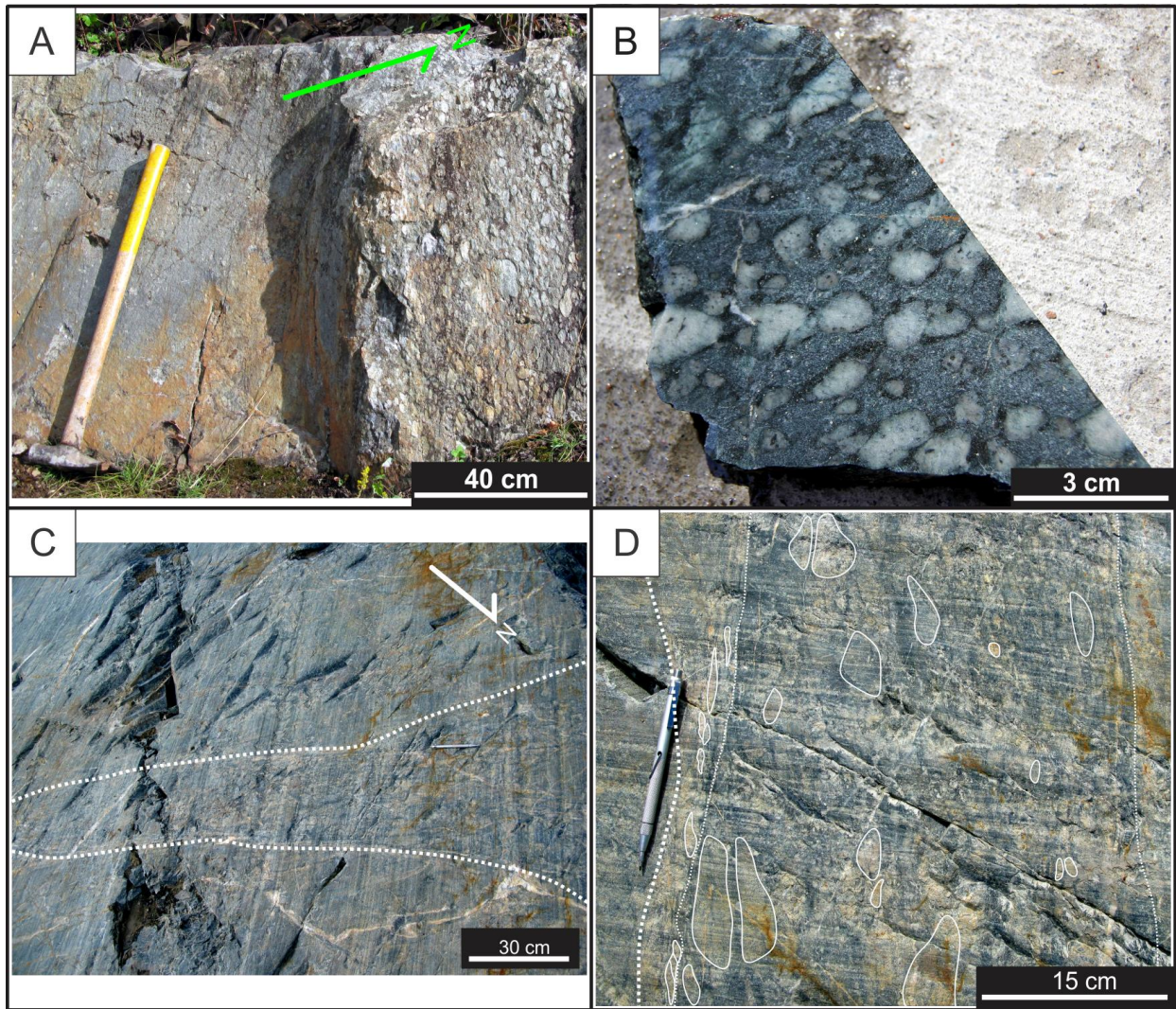


Figure 3.18 : Mafic tholeiitic units : outcrop exposures. A) Centimetre to decimetre-scale, light grey-coloured, fine-grained nodular structures interpreted as spherulites in a chlorite and pyrite-altered basalt. Contact with massive basalt at 258°/72°NW. NAD83, Zone 15, 426051mE, 5409408mN. B) Sample from unit described in A, with coalesced spherulites. Note concentration of chlorite and magnetite around the spherulites and the common magnetite grain at the centre. C) Recently trenched outcrop of the Cap zone, showing a semi-conformable, carbonate-altered, volcanoclastic or autobreccia or hyaloclastite breccia zone within massive pyrite+chlorite+magnetite-altered basalt. Patchy zones with traces of <1mm blue amygdules are present as well. NAD83, Zone 15, 425435mE, 5409396mN. D) Close-up view of the volcanoclastic or breccia band in the outcrop documented in C. Matrix-controlled chlorite alteration, and jigsaw fit texture of certain clasts. Their roundedness and size is probably affected by alteration. Fragments are smaller and more stretched at contact with the massive unit (to the left of the photo).

3.2.5 Sedimentary units: mafic and felsic volcanic-dominated

Sedimentary units have been reported on the Rainy River property (Ayres, 2005), mostly in the southernmost part of the host succession (Fig. 2.3). These sedimentary units consist mostly of

siltstones, mudstones and pyrite-rich (> 10 vol.%) siltstones. In this study, drill core intercepts with 0.5-3 cm wide, alternating bands of fine-grained chlorite and sericite have been studied and logged as mafic-dominated siltstones (appendix I). The absence of clear polarity indicators or of sedimentary facies textures and structures on drill core and thin section make it difficult to identify whether these rocks are actual sediments, or alternatively reworked volcanoclastic rocks, or simply volcanic units with sedimentary-like texture resulting from hydrothermal alteration, metamorphism and deformation (Fig. 3.19A, B, C, D). Furthermore, the geochemical signature and REE patterns of these potentially "sedimentary" units are very similar to the ones of the surrounding dacitic and basaltic volcanic rocks (Fig. 3.20). This suggests a unique, local volcanic-derived source for these fine-grained sedimentary rocks as suggested by Wartman (2011), or an expected volcanic signature for fine-grained volcanic units (dacitic or basaltic) that now possess false sedimentary-like textures.

A notable unit of possibly sedimentary origin consists in a 10-20 metre-thick sliver of granoblastic pyrite-rich sediments located in the immediate ODM mineralized zone hanging wall (appendix I; Fig. 3.19E). This unit is mafic-volcanic dominated, very fine grained and reddish brown and green coloured, with moderate to strong chlorite and epidote alteration (see chapter 5 for more information). Granoblastic pyrite and pyrrhotite compose up to 8 vol.% of this unit, and are regrouped in cm-scale bands parallel to foliation.

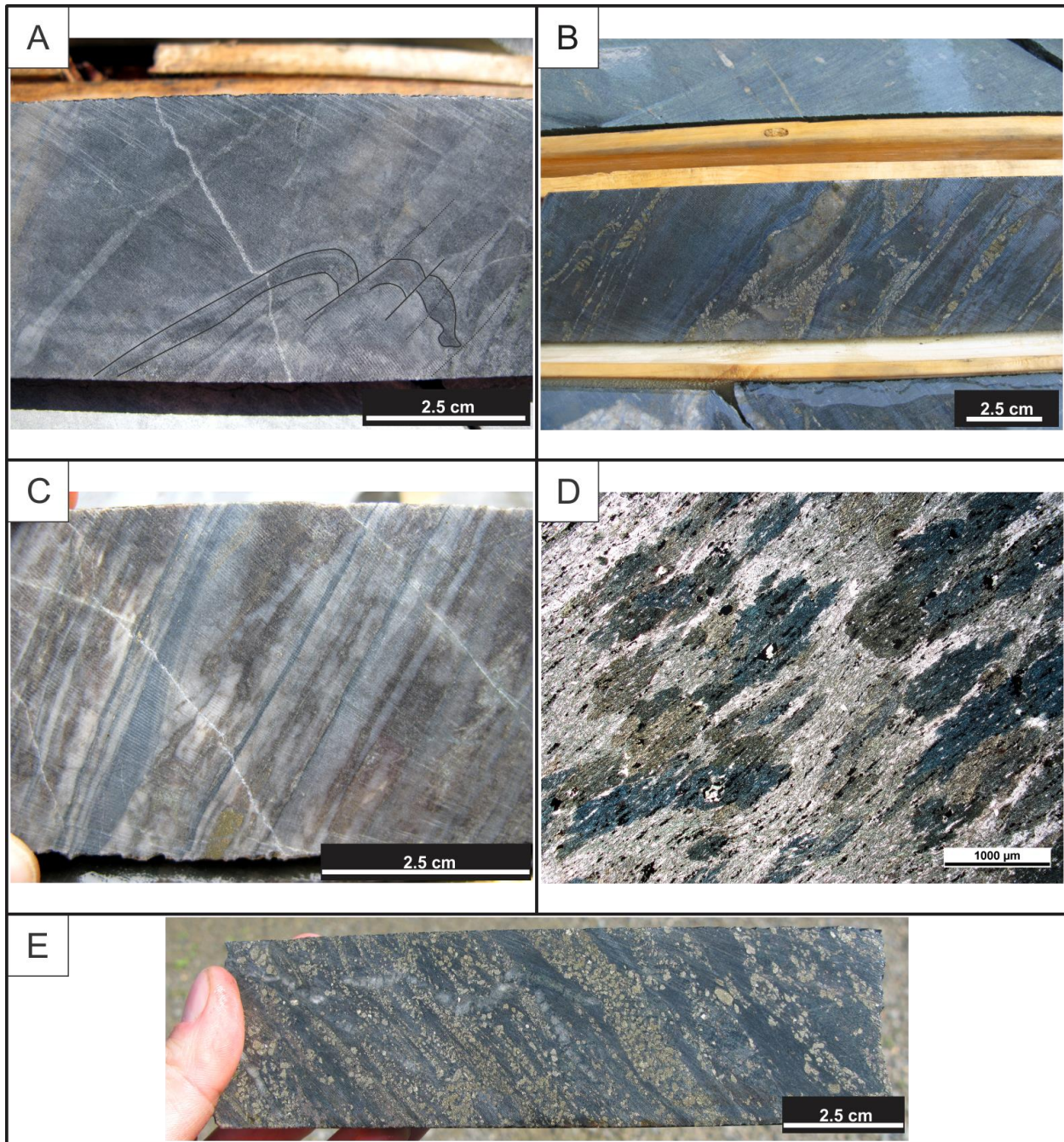


Figure 3.19 : Potential sedimentary units: felsic and mafic, volcanic-dominated. A) Mafic-dominated unit, with sericite alteration controlled by folded bedding and axial planar schistosity. Cap zone footwall, DDH NR110771 at 280m. B) Mafic-dominated pyritic rock with granoblastic pyrite and intensely folded and transposed sulphide veins, which can make a false bedding-like texture. Cap zone, DDH NR090358 at 62m. C) Felsic-dominated fine-grained unit at the eastern end of the E-W oriented ODM mineralized body. Alternating bands of chlorite and sericite such as observed here can also be the result of differential hydrothermal alteration of flow banding structures in felsic effusive volcanic packages. ODM zone, DDH NR110762 at 703m. D) Photomicrograph (TL) of fine-grained, strongly deformed actinolite-bearing unit, with chlorite-dominated matrix alteration. Groundmass of feldspars. Abundant foliation parallel ilmenite co-existing with actinolite and chlorite. Cap zone footwall, sample RRR435840, DDH NR110771 at

316m. E) Fine-grained unit with granoblastic pyrite and deformed quartz-carbonate veins. ODM hanging wall, DDH NR100583 at 243 m.

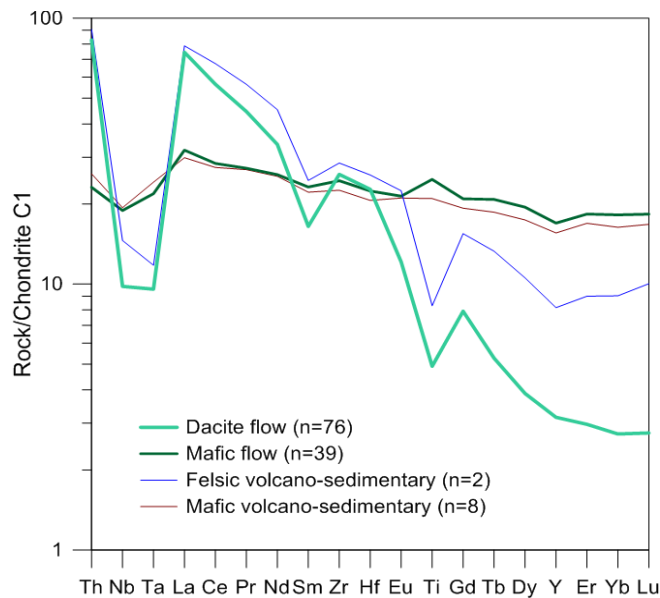


Figure 3.20 : Mean multi-element profiles comparing the mafic and felsic lavas with the sedimentary units of the samples from the Rainy River deposit. C1 chondrite values after McDonough and Sun (1995).

3.2.6 Post-volcanic intrusive units

Volcanic and sedimentary rocks of the Rainy River project area are cross-cut by two main types of intrusive bodies: deformed granitic (Fig. 3.21A, B) to gabbroic (Fig. 3.21C) dykes and late, post-metamorphism and deformation diabase dykes and gabbroic bodies (Fig. 3.21D). Neither of these intrusive bodies are mineralized. The deformed but unaltered quartz monzonitic to gabbroic dykes cross cut the deposit within the Cap and 433 mineralized zones. Geochronological work has been done in order to constrain the minimum age of the mineralization and the maximum age of the main deformation. This work is briefly presented in section 3.5. A coarse grained pyroxenite body within the Rainy River deposit (not sampled in this project) contains massive to semimassive sulphide Ni-Cu-PGE mineralization (zone 34). It is interpreted to be related to the mid continental rift system (Wartman, 2011).

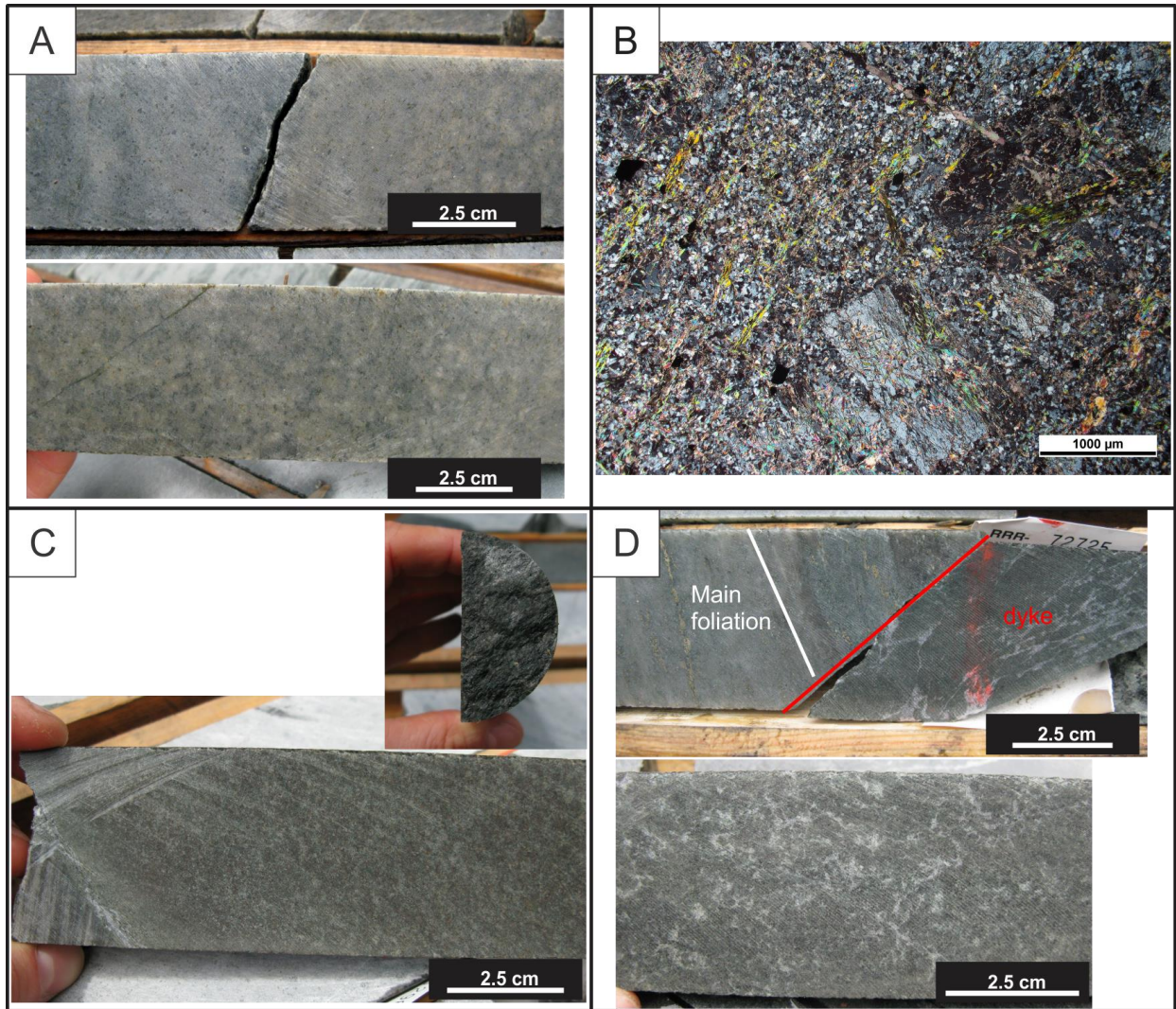


Figure 3.21 : Post volcanic intrusive units. A) Lightly foliated felsic dyke, with foliation parallel, alteration-free contact with dacitic flow host. 433 zone, DDH NR070181 at 658 m. B) Photomicrograph (PL) of rainbow dyke with glomeroporphyritic feldspar grains. Weak foliation underlined by preferential NE-SW alignment of sericite bands. HS zone footwall, DDH NR110664 at 225 m. C) Mafic-looking dyke that crosscuts the deposit. Deformed (see foliation on drill section), but unaltered nor mineralized. ODM zone immediate hanging wall, DDH NR100583 at 243 m. D) Late mafic dyke. Contact with host dacitic unit is not parallel to main, earlier foliation fabric. 433 zone footwall, DDH NR070181 at 825 m.

3.2.7 Summary of the different lithologies present at Rainy River

The following table summarizes the different characteristics defining each unit outlined within the Rainy River deposit. It is the result of a compilation of data acquired within this study, building on what was previously done by Wartman (2011).

Table 3.1 : Summary of the different lithologies present at the Rainy River deposit. Compiled from Wartman (2011) and this study.

Unit	SiO ₂	TiO ₂	Zr	Zr/Y	Petrographic texture	Volcanic interpretation
Coherent dacite	68.3	0.36	99	21.3	Microporphyrritic with qtz-fds.amygdules from 1 to 9 mm, from trace to 5% in abundance.	Effusive flow or subvolcanic intrusion in a dacitic flows and domes complex.
Dacitic tuffs and quartz crystal tuff	68.0	0.37	100	22.9	Very fine grained matrix, with 10 to 35% muscovite, sometimes crenulation cleavage developed and observed in thin section. Angular and transparent quartz phenocrysts (tr-8%) observed in quartz crystal tuff subunit.	Unit most affected by deformation and alteration, could represent autoclastic or pyroclastic deposits initially fine grained in nature.
Polymict dacitic breccia, matrix to clast-supported	67.9	0.38	100	20.5	Sub rounded and deformed clasts with varying alteration intensity and nature, from sericite alteration to pervasive rutile dusting. Moderate to strong matrix-controlled sericite and chlorite alteration.	Previous interpretation as debris-flow deposits (Wartman, 2011), revised as quench brecciated dacite or monomict pyroclastic unit. (see text for details).
Monomict dacitic breccia matrix to clast-supported	66.4	0.38	100	23.2	Microcrystalline matrix with deformed clasts containing microporphyrritic feldspars and carbonates. Matrix-controlled chl-carb alteration.	Quench fragmentation and autoclastic breccia deposits, or pyroclastic tuff breccia deposit.
QFP-textured dacite	65.6	0.36	95	18.9	Very fine grained microcrystalline quartz-feldspar matrix with abundant euhedral feldspar microphenocrysts up to 5mm in size. Blue quartz phenocrysts also abundant (0-3%)	Synvolcanic sills and dykes.
Felsic sediments	66.1	0.47	95	9.2	Layered fine grained pyrite with alternating bands of strongly chlorite and sericite-altered microcrystalline matrix.	Altered flow bands within coherent dacite.
Mafic flow	47.3	1.82	96	3.6	Medi. to coarse grained, with rare blue-quartz filled vesicles (0-4%). Very rare pillow selvages observed.	Subaqueous to subaerial lava flows or welded ignimbrite deposits (not observed on drill core).
Mafic tuff	49.0	1.64	84	3.8	Aphanitic, homogenous, with very rare stretched <4cm clasts blurred by alteration. Cross-cut by abundant deformed quartz-carbonate veins.	Fine to coarse tuff, syn or post-eruptive in nature
Mafic sediments	45.8	1.64	93	3.7	Banded siltstones with alternating chlorite-rich and carbonate-rich bands.	Discontinuous interflow sedimentary rocks.

3.3 Representation in space of the different volcanic lithologies

In order to assess the potential role of the volcanic products and architecture on the nature, distribution and evolution of the ore-forming hydrothermal system at Rainy River, various geological sections were constructed from detailed study of drill cores to better illustrate the distribution of the different lithologies present at Rainy River.

3.3.1 Oblique plane

A first representation of an oblique plane (see section 1.3.1 and Fig. 1.2 for further details on methods) was generated for this project, representing the distribution of the different volcanic facies identified with respect to the ore zones (Fig. 3.22, appendix I).

On this oblique plane, oriented perpendicular to the L_2 stretching lineation ($225^\circ/55^\circ\text{SW}$; see chapter 4 for additional information), the QFP dacite is almost exclusively restricted to the ODM zone hanging wall, and transitions into dacite flows along strike, moving towards the present-day surface (to the right of the map). Additionally, QFP dacites are also more abundant away from the centre of the mineralized system, towards the east, i.e. east of the area encompassing the ODM high grade zones, HS zone and 433 zones.

Intervals of dacitic tuff breccia, in orange on the map, are distributed in elongated, discontinuous bodies, mostly in contact with dacitic tuffs and occasionally with dacite flows. Dacitic tuff breccias, with high initial porosity-permeability, are correlated with the high grade ODM ore shells as well as part of the HS zone, which consists in pockets of higher grade mineralization when compared to the deposit's average grade (see chapter 6).

Dacitic tuffs (which comprise the quartz crystal tuff subunit) are volumetrically dominant in the ore deposit area. Although significant, this may be slightly overestimated, in part due to the strong, volcanic texture-destructive hydrothermal alteration and deformation that affects the host dacites, mostly within the deposit and its footwall, making it difficult to distinguish homogeneous fine-grained volcanoclastics from intensely altered coherent dacite.

Tholeiitic mafic units form small, isolated lenses throughout the map, from the Cap zone to the ODM zone hanging wall and below the deposit. Overall, the part of the host succession that was mapped in detail indicates that dacitic rocks are intercalated with mafic units, which appear every 200-600 metres (measured from the oblique plane). Mafic-dominated siltstones are

present in contact with tholeiitic basalts and a 10-30 m-wide sliver is documented at the immediate upper boundary of the ODM mineralized zone.

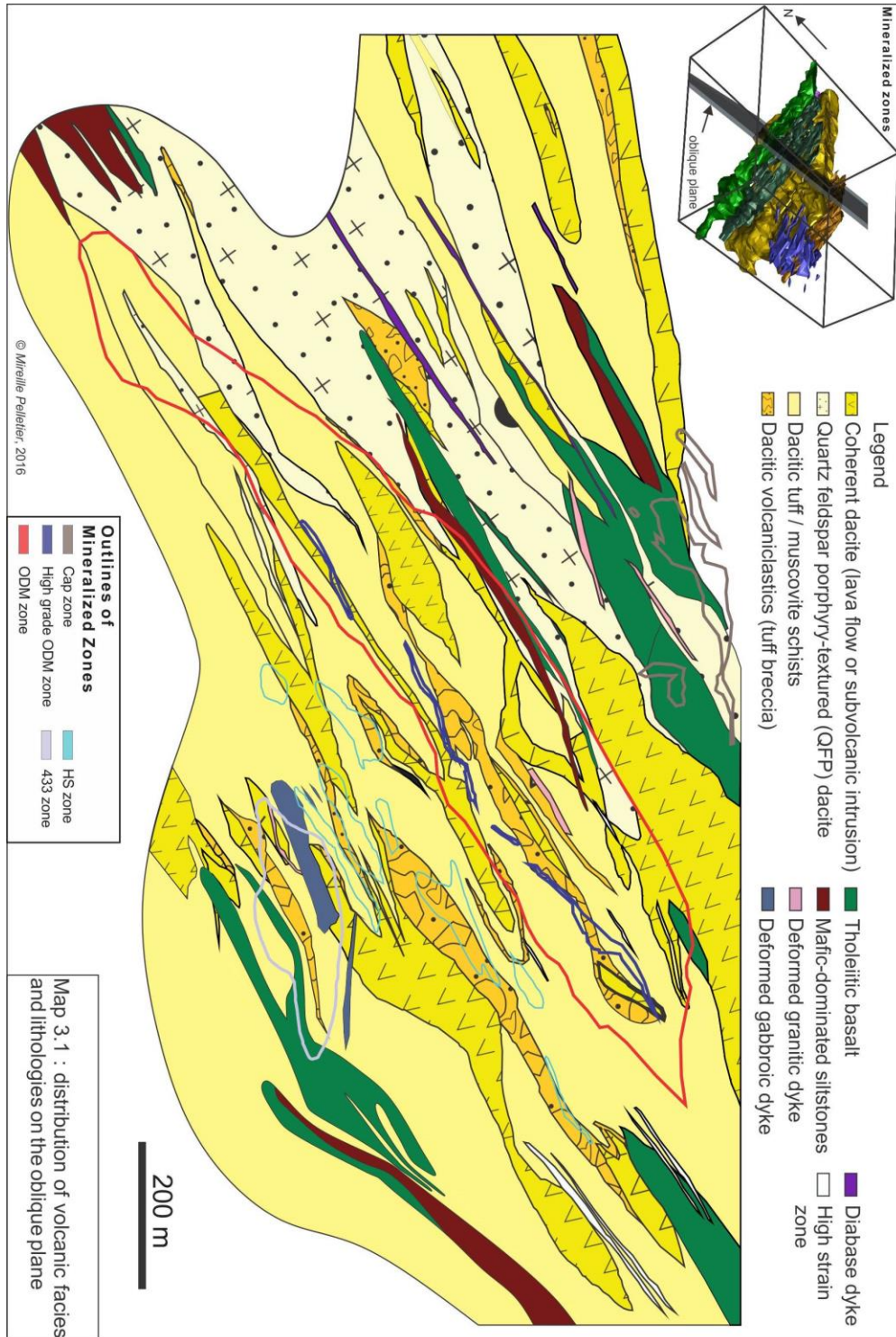


Figure 3.22 : Representation of the volcanic lithologies on the oblique plane (323N/43°) with respect to the different mineralized zones. See appendix I for higher quality image.

3.3.2 Cross section

Similar to the oblique plane, a correlation between higher grade zones of the ODM mineralized body and dacitic volcanoclastics is present on the 425475E section (Fig. 3.23, appendix I; see section 1.3.1 and Fig. 1.3 for information on methods).

Once again, QFP dacites are mostly restricted to the hanging wall of the main ODM zone, and dacitic tuffs and muscovite schist units are most abundant within and below the ODM zone. The sliver of pyrite-rich mafic siltstones, discontinuous along strike and located immediately above the ODM zone, is also present in section.

A notable difference between the cross section and the oblique plane is the existence of a mappable mafic subunit on the cross section. Coloured in darker green on the section, this unit was identified through lithochemistry and corresponds to a group of samples with anomalous Th-Nb-Ta values (refer to Fig. 3.17). The absence of the mafic subunit on the oblique plane (Fig. 3.22; appendix I) can be explained by a discontinuity along strike of the unit or by poor quality assay results, where Th, Nb and Ta would have been miscalculated.

In summary, the Rainy River deposit is hosted in a continuous, predominantly dacitic volcanic pile of calc-alkaline affinity that is almost 800 metres thick, as measured perpendicular to foliation. The pre-deformation thickness of this dacitic center is difficult to estimate with certainty because of heterogeneous alteration and deformation (e.g. shortening) in the deposit area.

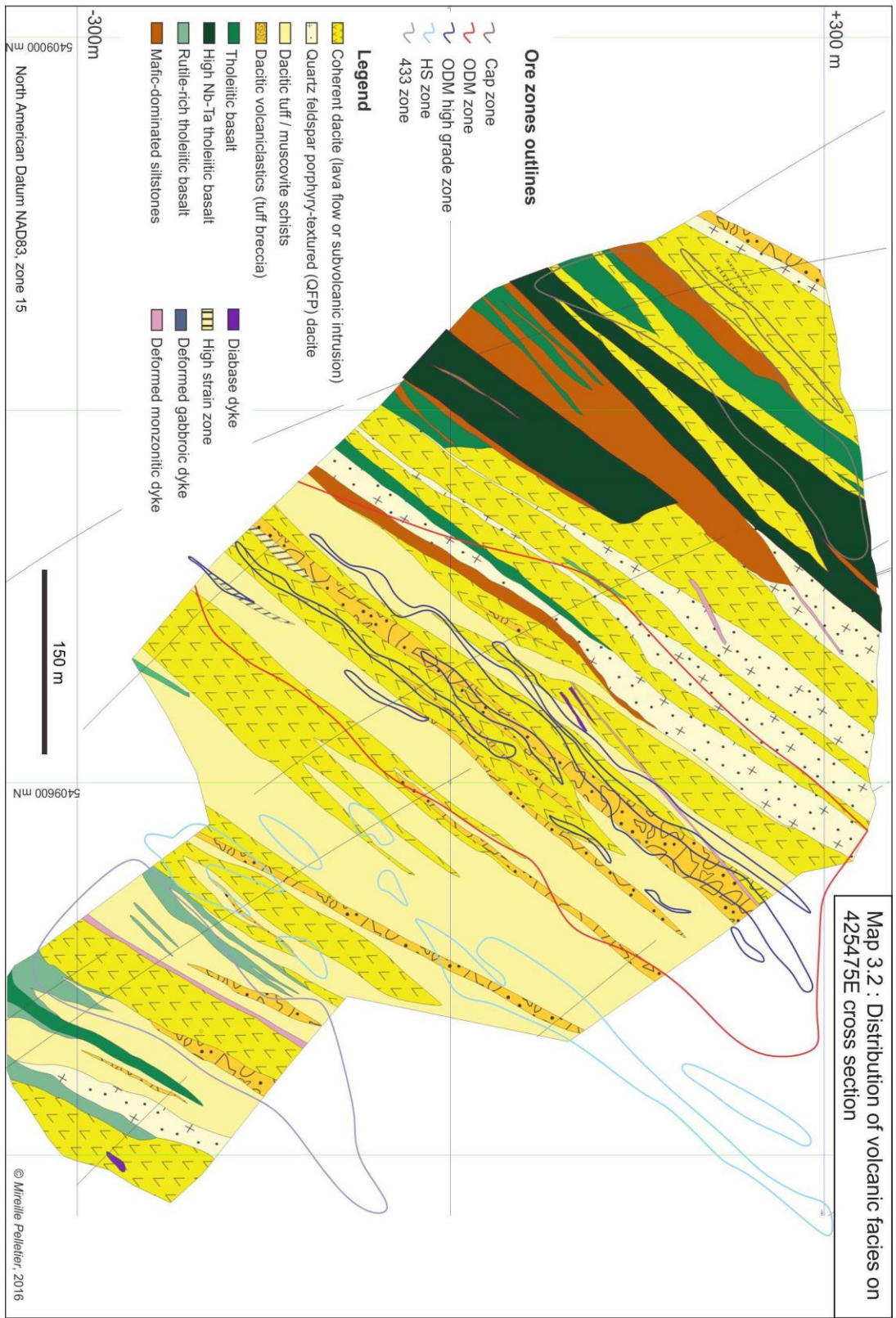


Figure 3.23 : 425475E cross section with volcanic lithologies documented with respect to the different mineralized zones. See appendix I for higher quality image.

3.4 Detailed maps

3.4.1 Introduction

The two outcrops chosen are named the McClain and Scott outcrops and are located respectively within the immediate footwall and 600 metres to the ESE of the deposit structural hanging wall (Fig. 3.24). Rocks exposed on these two outcrops mainly consist of calc-alkaline dacites with REE patterns that identify them as part of the main dacitic group that host the deposit. Prior to mapping, bleaching or power washing had been done, rendering the surface exposure optimal for mapping discrete textures and structures.

In the following section, each outcrop will be described separately; starting with a description of the different lithologies mapped, followed by a description and genetic interpretation for the different volcanic structures and textures.

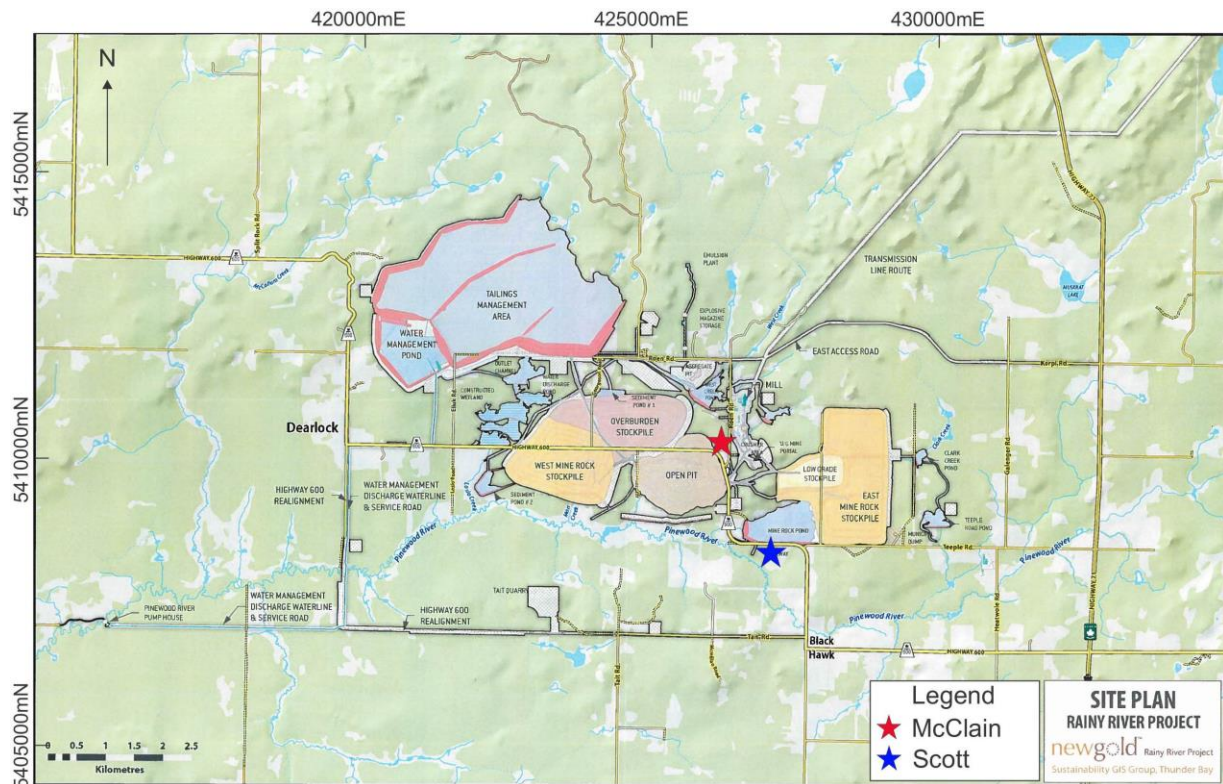


Figure 3.24 : Projected mining site plan of the Rainy River project with the location of the Scott and McClain outcrops. Modified from New Gold Inc. material (2015). North American Datum NAD83, zone 15.

3.4.2 McClain outcrop

The McClain outcrop is located just north of the present highway 600, behind the McClain house (NAD83, zone 15: 426156 mE 5410329 mN). It sits directly to the north of the ODM mineralized body and will be part of the northernmost part of the final pit (according to present site development plan; Fig. 3.24). It consists in a group of isolated zones totalling approximately 1026 m² in a 52 m (east-west) by 67 m (north-south) area (Fig. 3.25; appendix I).

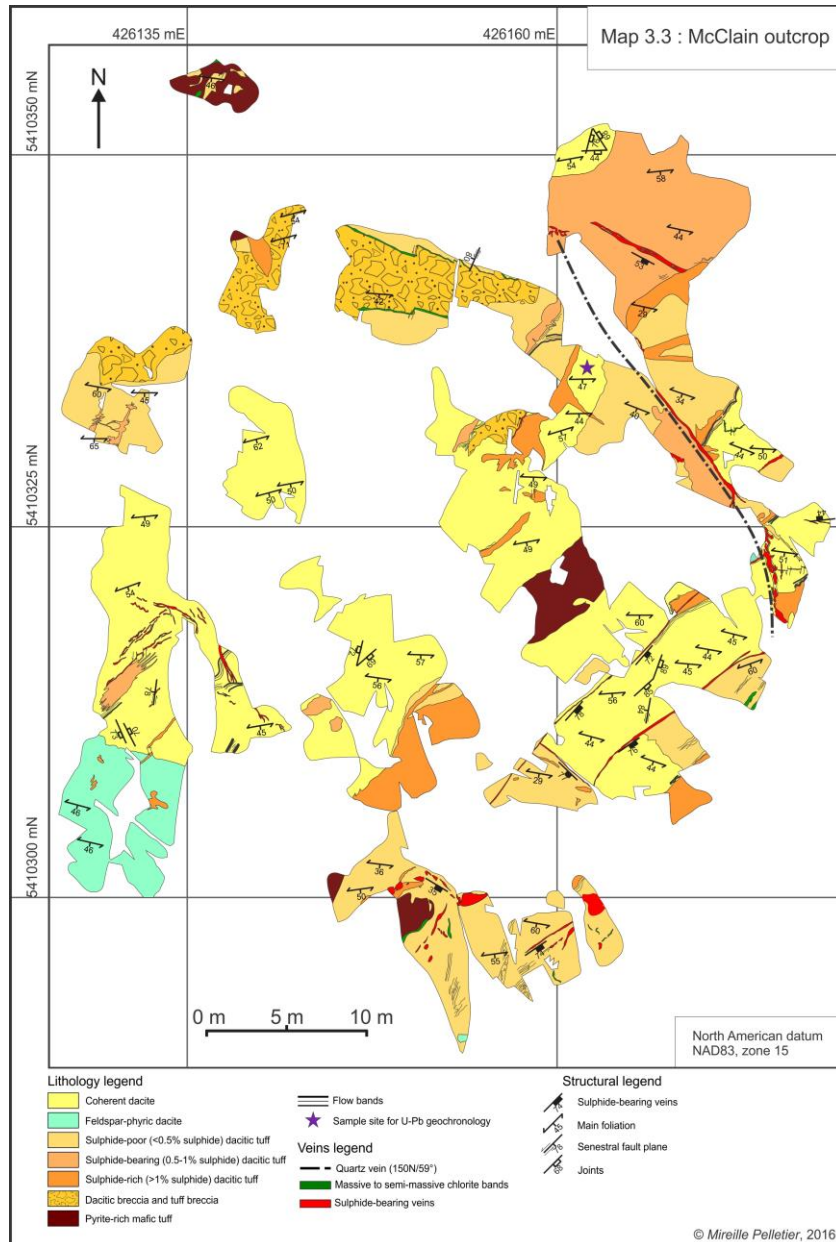


Figure 3.25 : McClain outcrop detailed map (1:100) showing the different volcanic units identified as well as structural measurements taken. See appendix I for higher quality image.

3.4.2.1 Dacitic tuffs

The dacitic tuff unit on McClain outcrop accounts for approximately 41 % of the surface area and is recognized by its homogenous, very fine-grained texture and light grey colour (Fig. 3.26A). The absence of quartz phenocrysts is the main attribute that distinguishes it from the coherent dacite unit (see below). It must be noted that the term tuff used here is based on grain size and does not have a genetic connotation.

The contact between the tuffs and the coherent dacite is often gradational and subject to interpretation. On rare occasions, flow bands within the coherent dacites are present at this contact (Fig. 3.25; appendix I). In contrast, contacts with other mapped units (sedimentary rocks and feldspar-phyric dacite, see below) are sharp and at angle with the main foliation plane.

A variation in sulphide content within the tuff unit is illustrated on the map using three subcategories, namely sulphide-poor (<0.5 vol. % sulphide), sulphide-bearing (0.5-1 vol. % sulphide) and sulphide-rich (>1 vol. % sulphide). Precise evaluation of sulphide content was attained through combined observations of freshly bleached outcrop surface, channel samples and thin section. The sulphide-bearing areas occur mostly on either side of a fault-fill vein oriented 150N/59° located in the eastern half of the outcrop (see structural elements of McClain outcrop section 3.4.2.6 and 3.4.2.7). Transition from sulphide-poor to sulphide-bearing is diffuse and associated with a diffuse stockwork (Fig. 3.26B). The sulphide-rich dacitic tuffs are in sharp contact with the less mineralized tuffs and massive dacites. In the latter case, flow bands within the coherent dacites underline the contact (Fig. 3.25; appendix I).

These sulphide-rich dacitic tuffs have a sulphide distribution restricted to deformed and dismembered bands of chlorite and sulphide (Fig. 3.26C, D), which can be observed on less weathered surfaces of the outcrop. It is unclear as to whether these chlorite bands represent folded veins resulting from polyphase deformation or are rather sulphide and chlorite-rich clasts.

3.4.2.2 Coherent dacite

Massive, quartz phenocrysts-bearing, calc-alkaline dacites represent 43 % of McClain's outcrop surface. These dacites are occasionally flow banded, with a homogenous porphyritic texture. Carbonate- and sericite-altered feldspar phenocrysts account for less than 20 vol. % of the rock. The phenocryst sizes are usually less than 3 mm and, on weathered surfaces, they can be inferred by the presence of dissolution holes (Fig. 3.26E, F). Angular quartz phenocrysts <3 mm

in size occur in these dacites, varying in abundance from 0.5 to 7 vol.% (Fig. 3.27A). Rare sub-angular to rounded 1-6 mm wide blue-quartz phenocrysts are also present in the coherent dacites (Fig. 3.27A). These coherent dacites are sericitized, with sericite concentrated in foliation-parallel, 1 to 3 mm wide veinlets and bands. Coherent dacites have a singularly low sulphide percentage; with only traces of disseminated pyrite (Fig. 3.27D).

Flow bands are present within the coherent dacites as well as at the contact with dacitic tuffs, pyritic sedimentary rocks and brecciated volcanoclastic facies. Internal flow bands are characterized by alternating 1-10 cm bands of sericite-rich (dark-coloured) and silica-rich (light-coloured) dacite (Fig. 3.27B) and have various orientations relative to the structural fabrics present on the outcrop (Fig. 3.25; appendix I). Experiments by Lofgren (1971) demonstrate that pale siliceous bands represent devitrified glass and dark bands represent obsidian (non-devitrified glass) that was subsequently altered to a phyllosilicate assemblage.

Flow bands located at the contact with pyrite-rich mafic tuffs are expressed as bands of chlorite-rich to purely chloritic composition alternating with silica-rich, pale-coloured dacites (Fig. 3.27C). Later alteration to chlorite of a quench-cooled contact layer can explain the formation of massive chlorite (McPhie *et al.*, 1993).

3.4.2.3 Feldspar-phyric dacites

Feldspar-phyric dacites represent 5 % of the outcrop and are located in the southern half of the mapped area (Fig. 3.25; appendix I). On outcrop, they can be differentiated from the coherent dacites by their darker grey colour and the absence of angular quartz phenocrysts (Fig. 3.27E). Additionally, feldspar phenocrysts abundance is between 20 and 40 vol. %, which is higher than for the coherent dacite unit. These phenocrysts are replaced by microcrystalline quartz and unoriented chlorite grains, with well-preserved angular boundaries (Fig. 3.27F). Very rare transparent subrounded quartz amygdules up to 5 mm in diameter are present in this unit.

The contact between the feldspar-phyric dacites and the coherent dacite unit is poorly exposed on McClain outcrop. A similar feldspar-phyric dacite unit is present in the outcrop located at the proposed pit main entrance, with a flow banded contact (Fig. 3.8A).

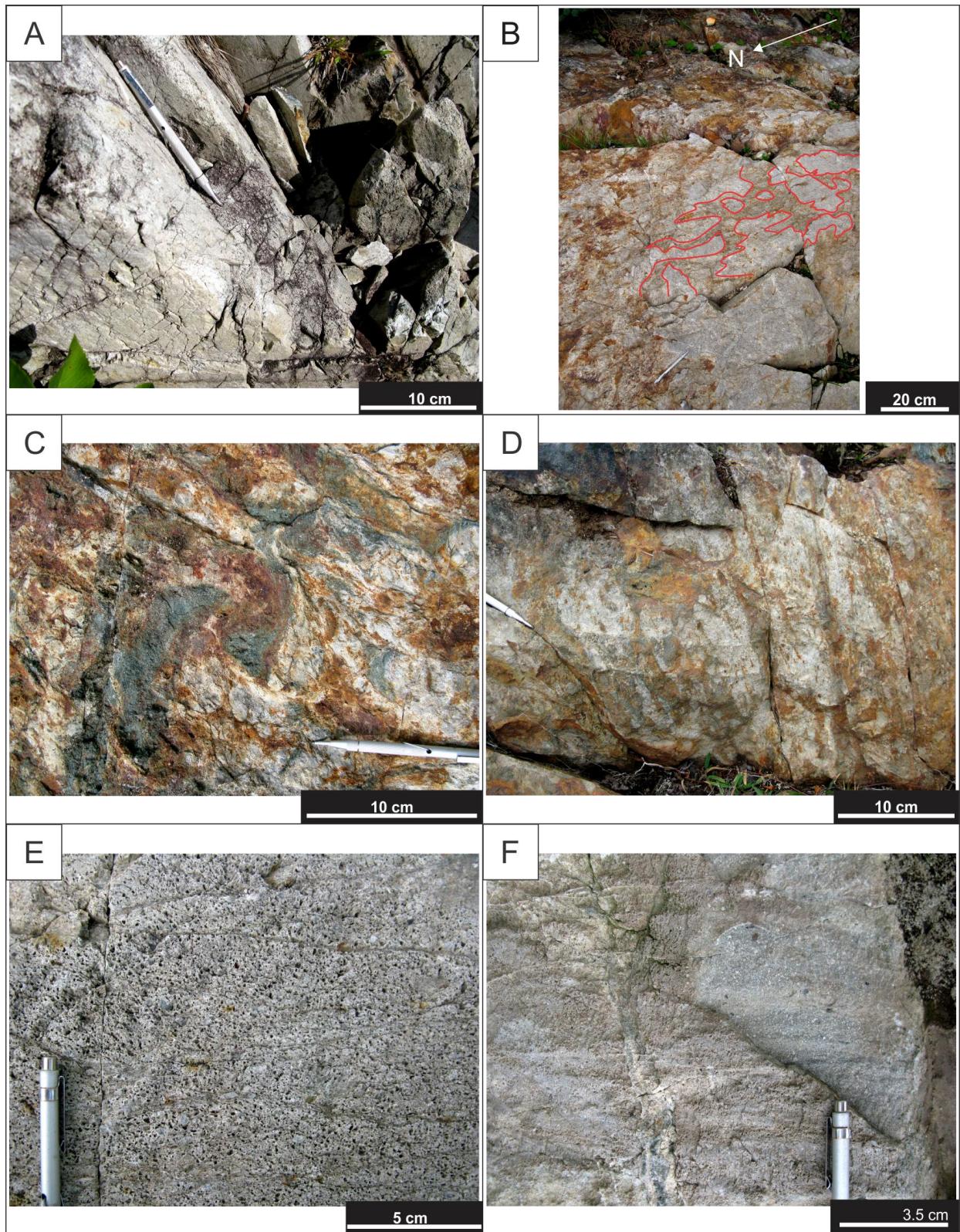


Figure 3.26 : McClain outcrop dacitic tuffs and coherent dacite. A) Aphanitic texture of massive dacitic tuff. NAD83, zone 15, 426160 mE, 5410339 mN. B) Sulphide-bearing tuffs in a stockwork texture (enhanced in red). NAD83, zone 15, 426169 mE, 5410335 mN. C) Sulphide-rich dacitic tuff

unit with dismembered chlorite bands (flow bands? Differential matrix alteration?). NAD83, zone 15, 426175 mE, 5410326 mN. D) Sulphide-rich dacitic unit with abundant chlorite bands. Note sulphide distribution is restricted to the chlorite bands. NAD83, zone 15, 426151 mE, 5410309 mN. E) Coherent massive dacite with abundant dissolution holes and rounded blue quartz phenocrysts. NAD83, zone 15, 426148 mE, 5410338 mN. F) Porphyritic texture observed on fresh surface in coherent dacite with relict, carbonate- and sericite-altered feldspar phenocrysts. Note weak flow banding underlined by silica-rich, light-coloured bands. NAD83, zone 15, 426172 mE, 5410333 mN.

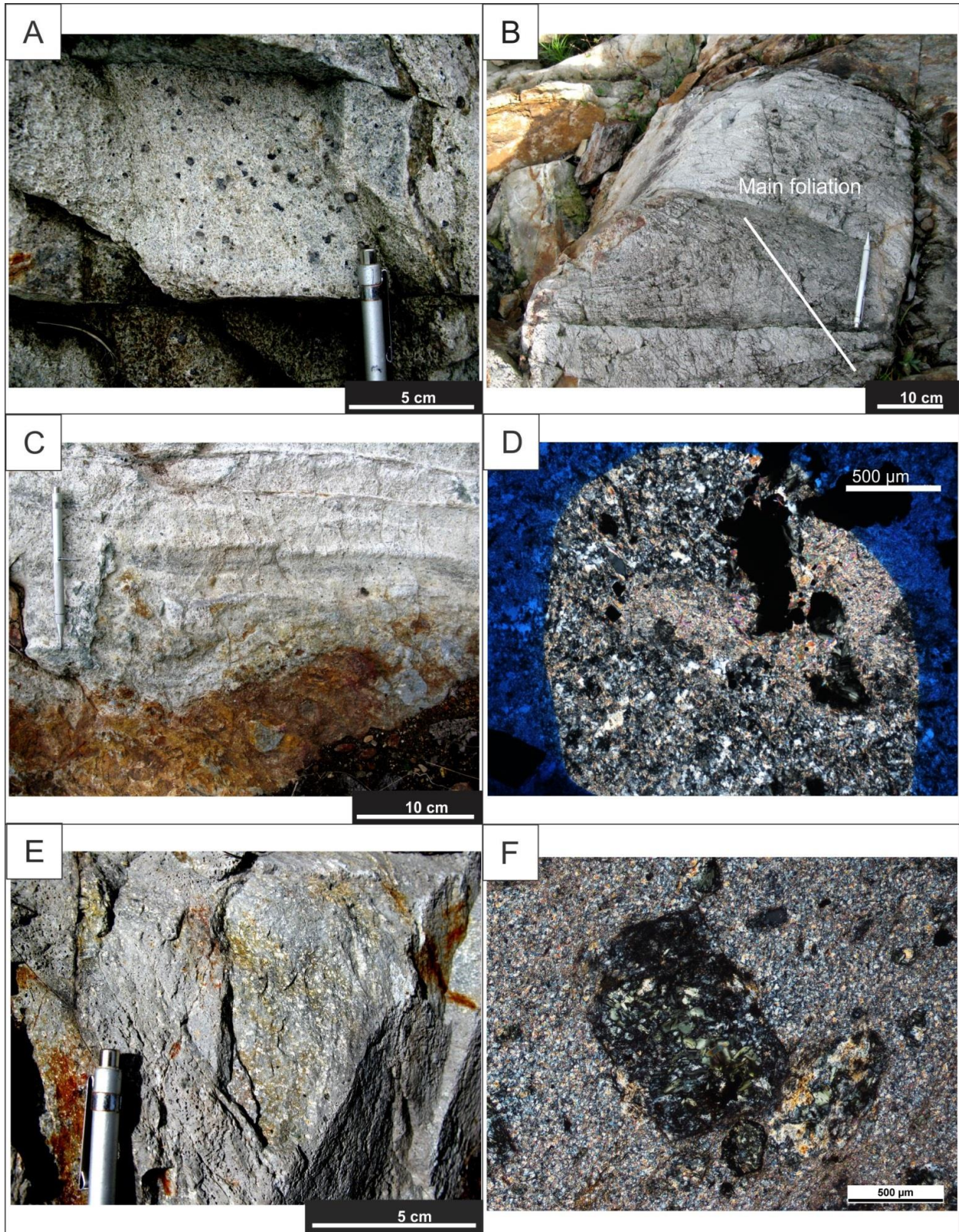


Figure 3.27 : Coherent and feldspar-phyric dacites, McClain outcrop. A) Abundant rounded blue quartz in coherent dacite unit. NAD83, zone 15, 426162 mE, 5410350 mN. B) Flow fold in coherent

dacite. NAD83, zone 15, 426153 mE, 5410333 mN. C) Flow bands composed of semi-massive chlorite in coherent dacite at contact with sulphide-rich dacite tuff. NAD83, zone 15, 427177 mE, 5410321mN. D) Photomicrograph (polarized light) of disseminated pyrite associated with deformed sericite veinlet in coherent dacite. NAD83, zone 15, 4216171 mE, 5410334 mN. E) Feldspar-phyric dacite unit on outcrop. Note characteristic dark grey colour and abundance of angular relic feldspar phenocrysts lightly stretched/flattened parallel to main foliation plane. NAD83, zone 15, 426134 mE, 5410303 mN. F) Photomicrograph (PL) of remnant feldspar phenocryst replaced by chlorite and microcrystalline quartz in QFP dacite. NAD83, zone 15, 426126 mE, 5410312 mN.

3.4.2.4 Dacitic breccia and tuff breccia

Dacitic breccia and tuff breccia represent ~7.5 % of McClain outcrop's surface and are located in its northern half. They are clast-dominated, poorly sorted, with subangular clasts varying in size from 2 to 15 cm. The breccia matrix contains disseminated pyrite and is mostly composed of quartz and sericite. Clasts vary in colour from beige to light pink and are all aphanitic (Fig. 3.28A). The polymictic appearance of this breccia unit can be the result of differential alteration of an initial product that has an identical initial composition but varies in grain size, similar to what is observed in the deposit. Rounding of the clasts can also be attributed to subsequent matrix-controlled alteration.

Contact of the breccia unit with the coherent dacite and tuff facies is sharp and characterized by a thin (<5 cm) chlorite-rich band (Fig. 3.28 B), with the exception of the easternmost, north-south oriented contact, which is gradational between the coherent dacite and breccia (Fig. 3.28C).

3.4.2.5 Pyrite-rich mafic tuff

Pyrite-rich mafic tuffs represent 3 % of McClain outcrop and are mapped on both its southern and northern ends (Fig. 3.25; appendix I). These rocks were easily identified on outcrop due to their homogenous rusty colour and a strong negative relief compared to the dacitic units (Fig. 3.28D). Within the pyrite-rich mafic tuffs, very rare (less than 5) pods of very altered and fine-grained dacite occur (Fig. 3.28D). These blocks are <25 cm across and do not possess an alteration rim.

Geochemical analyses of a channel sample from this volcanoclastic unit indicates a tholeiitic affinity and high sulphur content (6 wt.% S), corroborated by abundant granoblastic pyrite visible on freshly cut surface. This unit is non-magnetic, very fine-grained and green to purple in colour on a fresh surface. Petrographic work reveals a composition of alternating hornblende-rich and

biotite-chlorite-rich bands less than 1 cm in width. Unoriented epidote grains also occur within this unit, along with close to 1 vol. % disseminated fine-grained ilmenite (Fig. 3.28E).

The contact between the pyrite-rich mafic tuffs and the surrounding dacite is sharp, has various orientations and is characterized by a fine (<1 to 5 cm) chlorite-rich band (Fig. 3.28F). Once again, this chlorite-rich band is interpreted as a result of the alteration of a quenched rim during rapid cooling of hot dacite in contact with the cooler pyrite-rich mafic tuff.

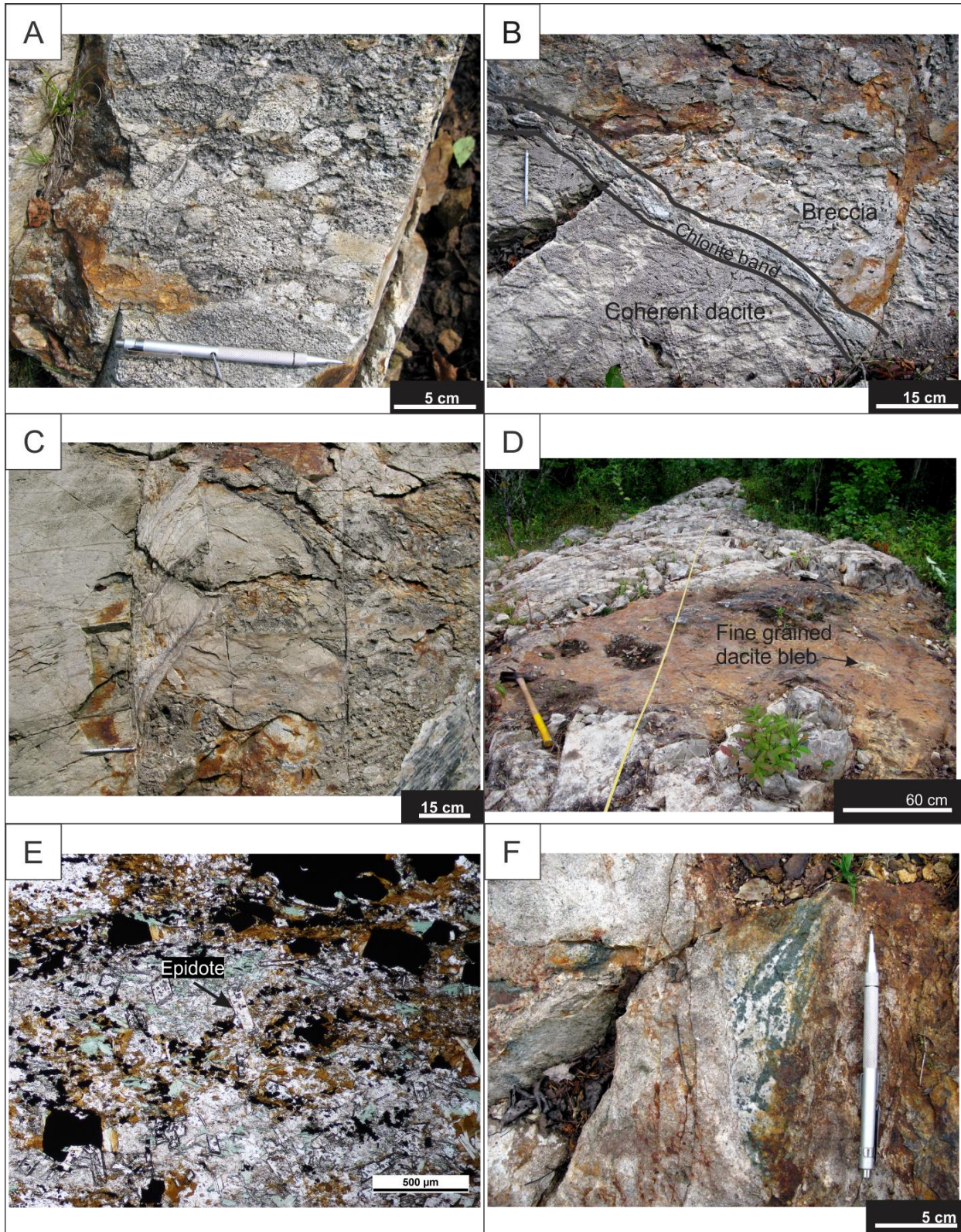


Figure 3.28 : Dacitic breccia and pyrite-rich mafic tuff, McClain outcrop. A) Poorly sorted dacitic breccia, with subangular clasts of varying colour from light pink to beige-grey. Interpreted as a monomict autobreccia (see text for discussion). NAD83, zone 15, 426147 mE, 5410344 mN. B)

Sharp contact between dacite brecciated and coherent facies, underlined by bands of semi-massive chlorite. NAD83, zone 15, 426154 mE, 5410343 mN. C) Gradational transition from the coherent to the autobrecciated in main dacite body. NAD83, zone 15, 426159 mE, 5410340 mN. D) Negative relief of pyrite-rich mafic tuff in comparison with dacitic tuff on McClain outcrop. NAD83, zone 15, 426150 mE, 5410300 mN. E) Photomicrograph (NL) of pyrite-rich mafic tuff showing weakly oriented biotite and chlorite grains with unoriented coarse epidote grains. NAD83, zone 15, 426153 mE, 5410300 mN. F) Massive chlorite at contact between pyritic sediments and dacite tuff. NAD83, zone 15, 426137 mE, 5410355 mN.

3.4.2.6 Veins

Veins mapped on the McClain outcrop, although very minor in terms of relative abundance, are categorized here according to their composition and relation to mineralized dacites.

The most abundant veins on the McClain outcrop consist of folded, quartz-chlorite-carbonate±tourmaline±pyrite veins (mapped in red). They are hosted in the coherent dacite unit and dacite tuffs, have undergone complex folding and vary in width from 1 to 50 cm (Fig. 3.29A). Rare sericite alteration halos are developed at the vein selvages over widths of less than 5 cm, and are proportional to the vein's width.

A vein swarm, oriented NE-SW (045-225N) occurs within the dacite flows on the western end of the outcrop (mapped in red). Its composition is chlorite and quartz-dominated, with traces of sulphides. An alteration halo is developed over 5-25 cm and consists in higher concentrations of sulphides and sericite within the dacite flow (Fig. 3.29B).

Discontinuous chlorite-rich patches (mapped in green) occur within the dacite flows and tuffs. These patches are generally less than 10 cm wide and do not possess an alteration halo. Their origin, i.e. whether or not these are veins or altered glass fragments, is uncertain. Late <5 cm-wide barren quartz-tourmaline veinlets crosscut these earlier chlorite-rich patches (Fig. 3.29C).

A quartz vein, located on the eastern half of the outcrop, is continuous throughout its length and has an average orientation of 150N/59° (mapped in red, along dotted line on Fig. 3.25; appendix I). It is folded and varies from 5 to 60 cm in width, and lithological units on either side are discontinuous (Fig. 3.29D), implying a vertical and/or horizontal fault movement. Dacites located on the eastern side of this structure possess a higher sulphide content compared to the dacites west of the structure. The vein is composed of quartz with traces of tourmaline, chlorite, carbonates and sulphides and no significant Au (<5 ppb Au; Fig. 3.29E). Sulphide-rich, <5 cm-wide quartz veinlets extend from this structure at an orientation of 043N/77°. These veinlets

possess alteration selvages (Fig. 3.29A). They are continuous over more than 20 metres, are not folded and are hosted within a continuous body of coherent dacites (Fig. 3.29B).

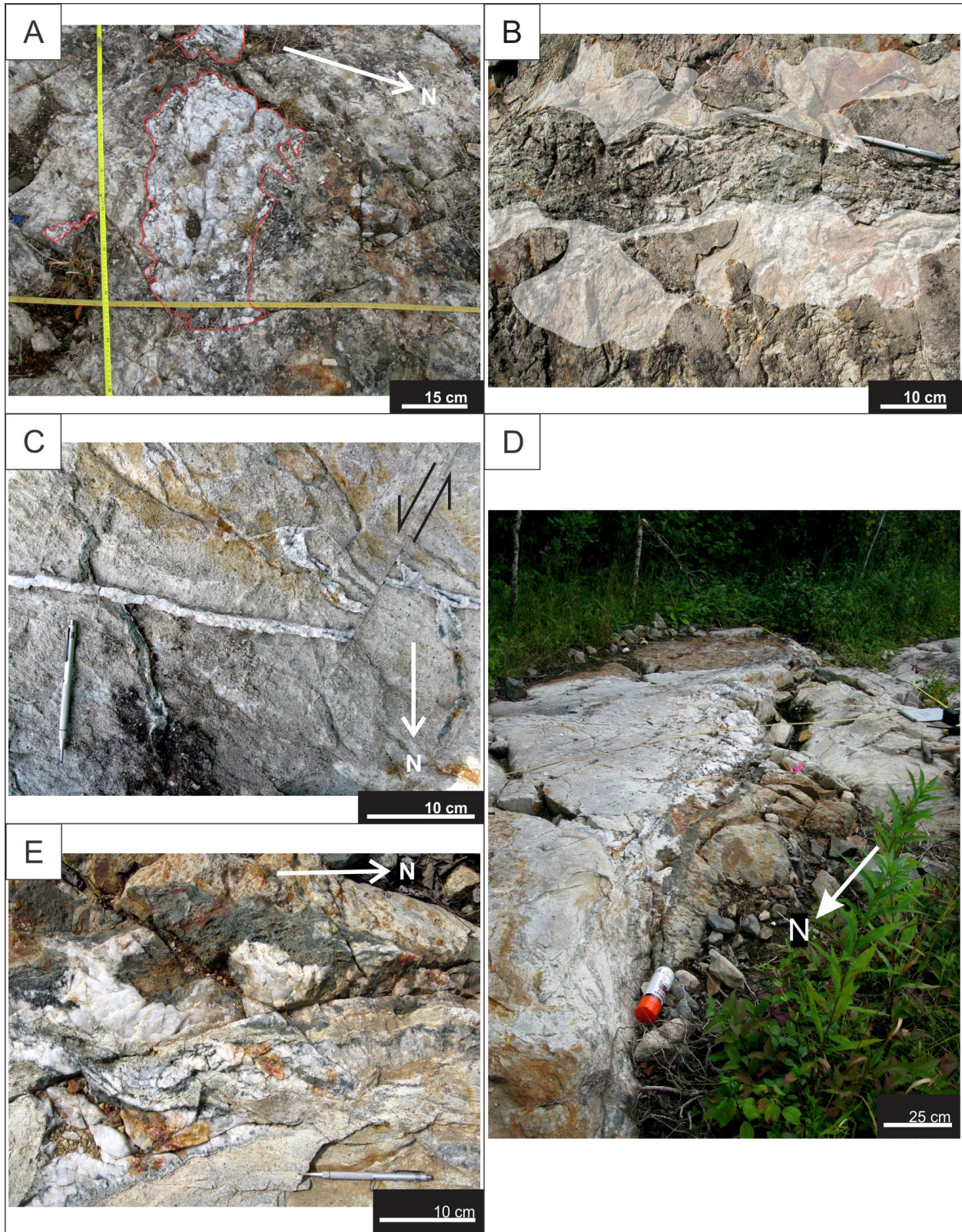


Figure 3.29 : Veins and structures, McClain outcrop. A) Folded $qtz\text{-}chl\text{-}cb\pm tl\pm py$ veins in sulphide-bearing dacitic tuff (highlighted in red). NAD83, zone 15, 426149 mE, 5410300 mN. B) $chl\text{-}qtz$ -sulphide vein swarm at middle of photo with associated alteration highlighted in white (see text).

NAD83, zone 15, 426132 mE, 5410319 mN. C) First generation chlorite and chlorite+sulphide veinlets crosscut by second generation qtz-tl+chl veins, later affected by brittle senestral offset. NAD83, zone 15, 426176 mE, 5410325 mN. D) Main vein visible along the entire length of outcrop, with discontinuous units on either side of the structure oriented 150N/59°. NAD83, zone 15, 426175 mE, 5410322 mN. E) Close up photo of the main vein potentially filling a fault (see text). NAD83, zone 15, 426175 mE, 5410320 mN.

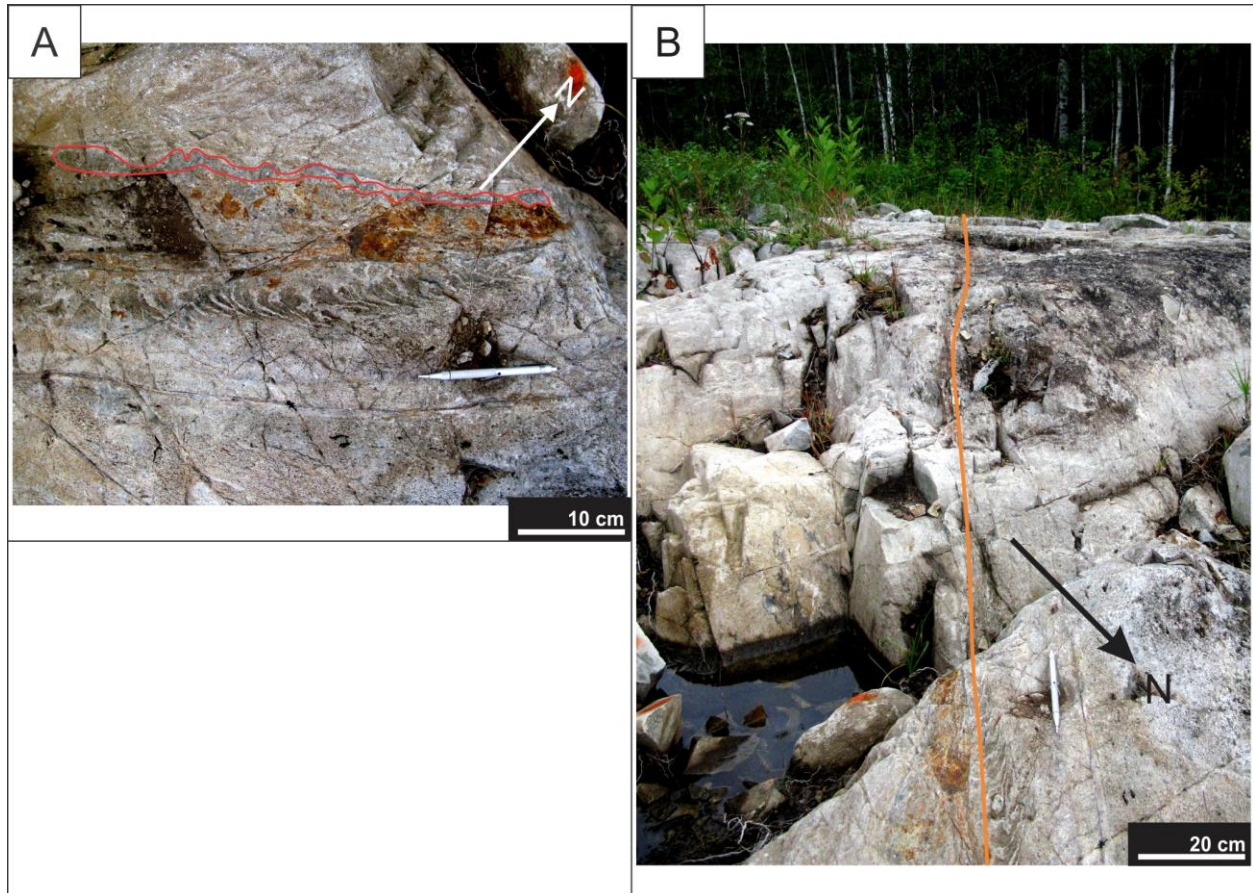


Figure 3.30 : Veins and structures, McClain outcrop. A) Sulphide-rich minor vein extending from the main 150N/59° oriented structure. Flow bands parallel to it indicate an early onset. Alteration halo highlighted in red on photo. NAD83, zone 15, 426170 mE, 5410320 mN. B) Photo illustrating the extent and linearity of the minor vein (in orange) photographed in A. Note well developed joint set in the coherent dacite to the left of the minor vein on photo. NAD83, zone 15, 426169 mE, 5410320 mN.

3.4.2.7 Genetic interpretation of the volcanic facies and potential associated volcanic environment

The presence of flow bands within the dacites is indicative of a coherent facies, intrusive or extrusive. Additionally, the presence of pyrite-rich mafic tuffs of potential sedimentary origin in flow banded contact with the coherent dacite points towards a sub-seafloor to seafloor depositional environment (Doyle and Allen, 2003). A transitional contact between the breccias

and the coherent dacite illustrates their cogenetic nature. An environment of silicic domes and stubby flows and associated breccias is in agreement with the observations made on McClain outcrop. This volcanic regime can also explain the asymmetry in spatial distribution of the coherent dacite unit and the absence of layering.

The deformed quartz-chlorite-tourmaline-sulphides vein, oriented 150N/59° and crossing the entire length of the outcrop in its eastern half, is interpreted as a syn- to late-main deformation (D_2) vein due to the discontinuity of contacts and lithologies observed on either side of it. Additionally, alteration minerals within the host dacites at the vein selvages are affected by the main path of deformation (D_2).

3.4.3 Scott outcrop

The Scott outcrop (Fig. 3.31; appendix I) was originally a small (less than 15 metres wide) exposure located one kilometre SSE of the proposed pit. Excavation work combined with pumping in 2013 augmented the outcrop's size considerably. Its present surface area now totals approximately 1500 m² within a 56 m x 75 m rectangle. It consists in two portions (north and south sections) isolated from one another due to a drop in topography (Fig. 3.32A).

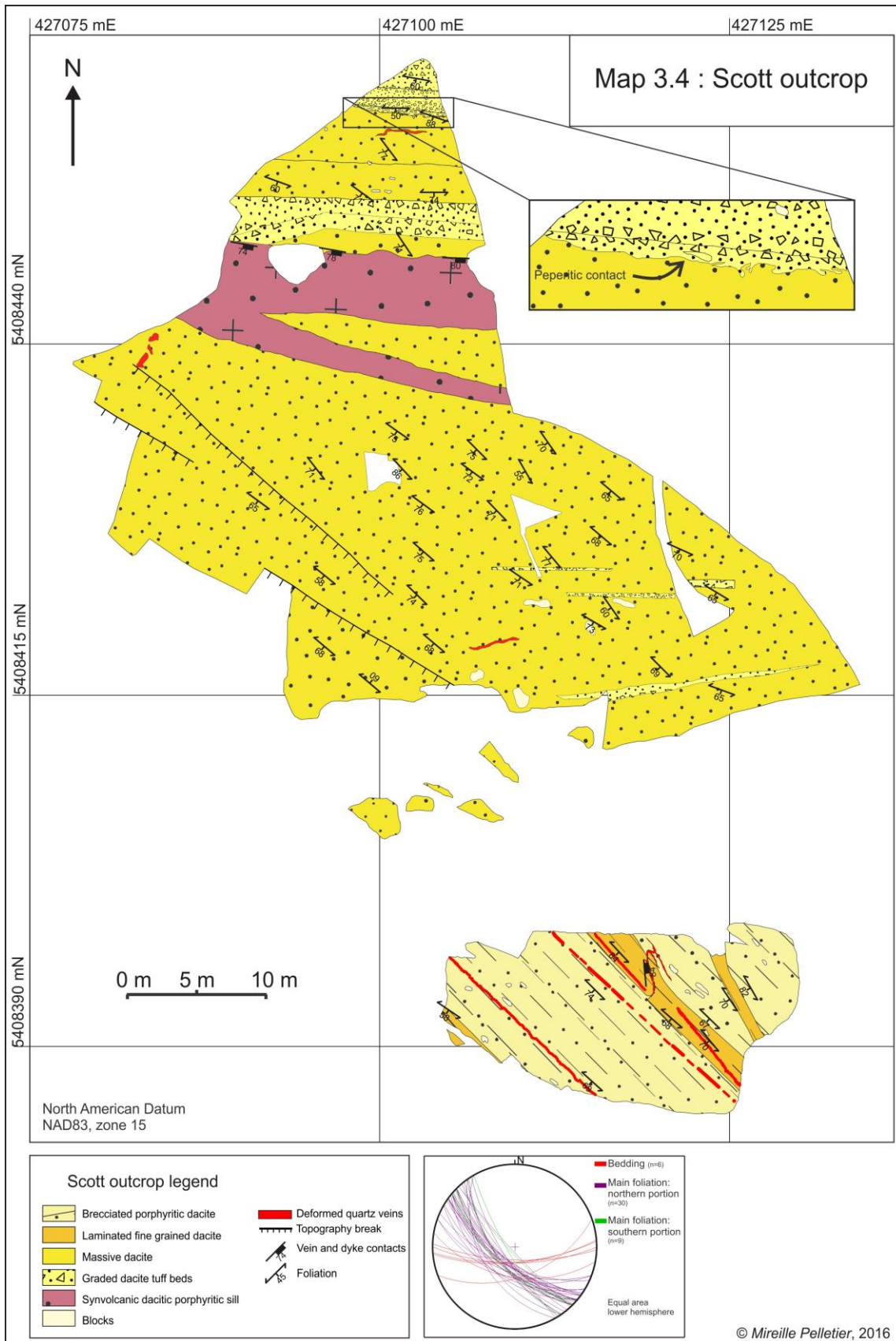


Figure 3.31 : (Previous page) Detailed map of Scott outcrop, showing volcanic units identified as well as the location of structural measurements. See appendix I for higher quality image.

3.4.3.1 South portion

The southern portion of Scott outcrop is characterized by alternating segments of laminated, fine-grained dacite and more brecciated, porphyritic dacite segments. Contacts between the two subunits are parallel to the main foliation averaging 130N/60°.

The laminated, fine-grained dacite unit (Fig. 3.32B) is characterized by alternating, foliation parallel, 2-5 cm-thick sericite-rich and sericite-poor bands. Matrix is aphanitic within both sericite-rich and sericite-poor bands and also along strike within individual bands. Phenocrysts of 1-3 mm in across represent 8 to 12 vol. % of the unit and consist in angular to subrounded feldspars and rare (<1 vol. %) angular blue quartz. Laminations are continuous along strike at the outcrop scale. Sericite-rich bands possess a cleavage oriented at 089N/61° (Fig. 3.32C), differing from the main fabric (130N/60°). This could be due to refraction of cleavage within a less competent host rock or superposition of a secondary fabric not recorded in less-altered dacites. Further sampling and petrography work is required to assess the chronology of this cleavage relative to the main phase of deformation (D₂).

The second volcanic facies present in the southern portion of the Scott outcrop consists in brecciated porphyritic dacite. Unlike the laminated facies described above, sericite alteration is concentrated in discontinuous and anastomosing bands less than 5 cm wide in a net-like texture (Fig. 3.32D). On surface view, this network is lightly flattened/stretched parallel to main foliation and contact (130N/60°).

In both subunits, subangular, decimetric to metric blocks are dispersed within the units, with a 1.2-3:1 length-width ratio on surface. Some blocks possess a 5 cm-wide pink-coloured alteration rim indicating potential remnant heat of the surroundings or, alternatively, interaction with water syn- to post-deposition of block within the lava flow (Fig. 3.32E). Another type of block is observed on the outcrop and possesses the same mineralogy as the host dacites, although with a coarser-grained porphyritic texture (Fig. 3.32D). Feldspar porphyroblasts are up to 2 cm in size. These blocks are in sharp contact with the host rock, enhanced by a higher degree of sericite alteration at their rim. Arguably, these blocks could represent coarser-grained zones that have not been subject to selective alteration, which would have only affected the more porous segments.

Contact between the laminated and brecciated facies within the southern portion of Scott outcrop are mostly gradational, underlined by an increase in linearity and extent along strike of sericite-rich bands, sometimes over distances of up to 1.5 metres (Fig. 3.32F).

Sulphide-bearing quartz veins devoid of alteration halos are present on the outcrop, with widths less than 20 cm and an attitude parallel to the main foliation. On one of these veins, back-rotated boudins indicating a synthetic rotation have been documented (see chapter 4).

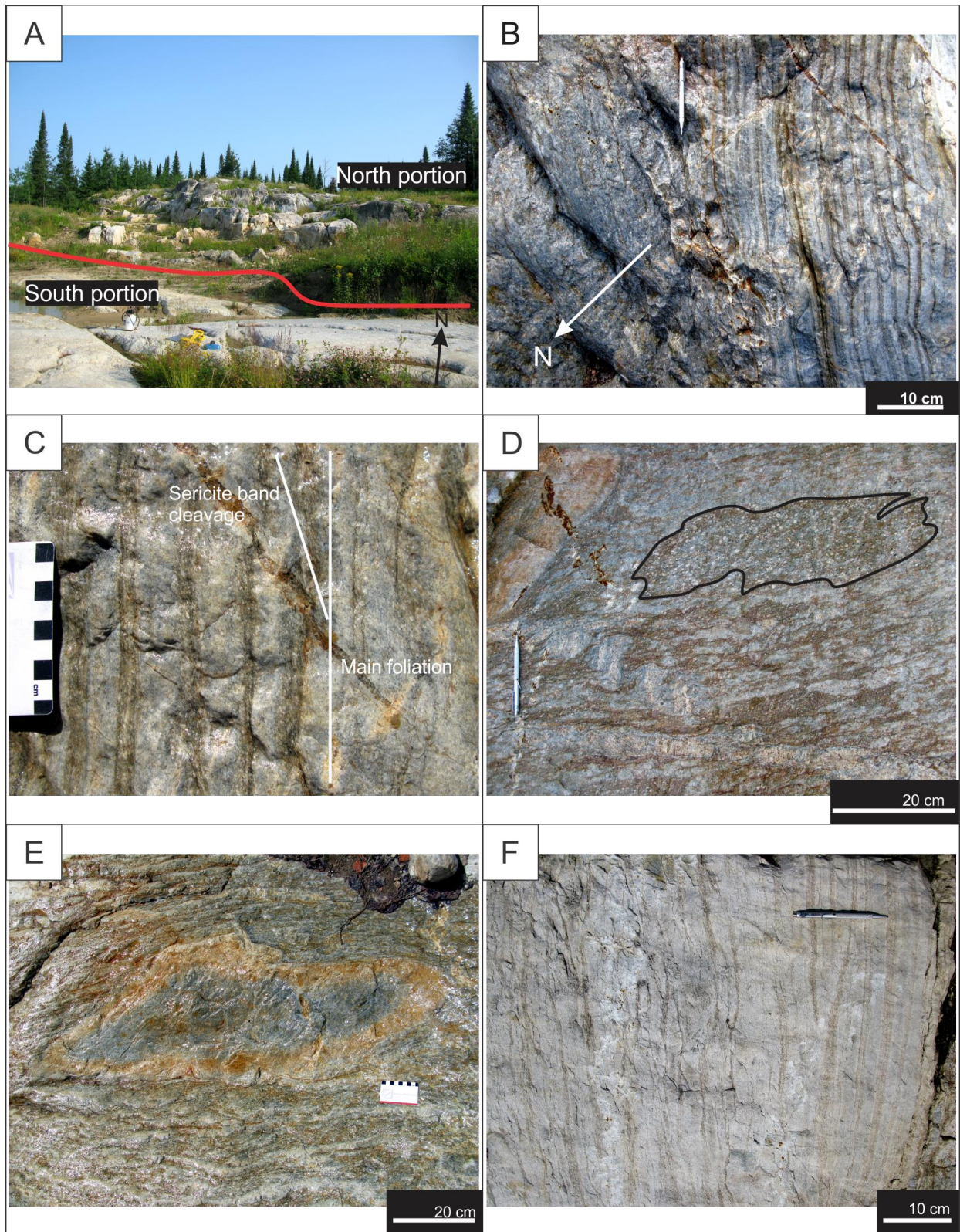


Figure 3.32 : Scott outcrop, southern portion. A) Photo taken on southern portion of the outcrop, looking at the north portion. Break between the two sections is shown in red. NAD83, zone 15, 427121 mE, 5408396 mN. B) Laminated fine grained dacite, potentially flow bands, in the southern

portion of Scott outcrop. NAD83, zone 15, 427105 mE, 5408392 mN. C) Secondary cleavage in sericite-rich bands oriented at 089N/61. Main foliation at this location is 130N/60°. NAD83, zone 15, 427105 mE 5408392 mN. D) Coarse-grained brecciated porphyritic dacite of the southern portion of Scott outcrop. Sericite-rich bands (in dark orange) are anastomosing in a net-like texture. Pseudo-block in top half of photo has the same composition as its host, but is coarser grained. NAD83, zone 15, 427110 mE, 5408394 mN. E) Alteration rim on fine grained block in brecciated porphyritic dacite. NAD83, zone 15, 427110 mE, 5408394 mN. F) Gradational transition between the laminated fine grained dacite to the brecciated porphyritic dacite. NAD83, zone 15, 427120 mE, 5408392 mN.

3.4.3.2 Interpretation of the genesis and depositional environment

Alternating sericite-rich and sericite-poor bands within the fine-grained dacite can be the result of flow banding within a dacitic lava flow. The second, porphyritic dacite facies with anastomosing discontinuous sericite bands represents a brecciated lava flow. Together, these two facies could be part of a flow, dome or cryptodome environment, where we would find laminated flows at the base and brecciated flows at the top of the dome (White *et al.*, 2015). In such a scenario, blocks represent wall fragments entrained within the flow.

3.4.3.3 North portion

The North portion of Scott outcrop is composed mostly of massive dacite (Fig. 3.33A). These dacites contain traces to 1 vol. % sub rounded to rounded, blue quartz phenocrysts of 1-2 mm size. Sub-angular plagioclase feldspar phenocrysts account for 6 to 8 vol. % of the rock, and vary in size from <1 to 5 mm. Groundmass is fine-grained and sericite-altered in 1-4mm bands, although alteration is, from visual observation, much weaker in this portion of the outcrop.

Within these massive dacite bodies are segments of graded tuff beds. Volcaniclastic sequences are developed over thicknesses of 10 cm to 6 metres and are very well-sorted and normal graded, from very coarse (≤ 1 cm) to very fine (≤ 1 mm) grained going southwards. A peperitic contact occurs between the massive porphyritic dacite and one of the graded tuff sequences (Fig. 3.33B). The graded tuff sequences are composed of progressively finer tuff beds towards the south, and a sharp southern contact between the very fine-grained tuff ending the sequence and the coarse-grained tuff at the base of the next sequence (Fig. 3.33C). Assuming that the beds fine upwards, this indicates a younging direction to the South. Blocks of coarser-grained porphyritic dacite are also present within volcaniclastic rocks in the north portion of the outcrop, although they are a lot less abundant and smaller in size than in the southern part of Scott outcrop (see Fig. 3.31; appendix I).

Attitude of bedding varies from 090°N to 105°N in strike and has an average dip of 60° (Fig. 3.31; appendix I). These values are similar to the main foliation recorded within the Rainy River deposit (102N/61°) and diverge from the ones measured in the southern portion of the outcrop (130N/60°). A second foliation is also recorded in the massive dacites (Fig. 3.33D), with an average orientation of 335N/77°, which is sub-parallel to minor, centimetre-scale brittle-ductile to brittle shear zones documented within the deposit (see chapter 4 for more information).

A porphyritic dyke cross-cuts graded tuff sequences (Fig. 3.33E) and massive dacites in the northern portion of Scott outcrop. It is foliated and its REE profile shows a parallel pattern to the dacites hosting the Rainy River deposit, although systematically enriched. This indicates a more evolved, late product derived from the same magma source. This dyke is weakly magnetic (mean magnetic susceptibility of 0.603×10^{-3} SI) and composed of 7 to 10 vol. % subangular, 1 to 4 mm feldspar grains with 3-4 vol.% chlorite sticks aligned parallel to the main foliation (Fig. 3.33F). Unoriented epidote grains (up to 6 vol. %) are also present. This dyke is interpreted as late in the intrusive activity and probably post volcanic activity, although pre main deformation (D_2) in timing.

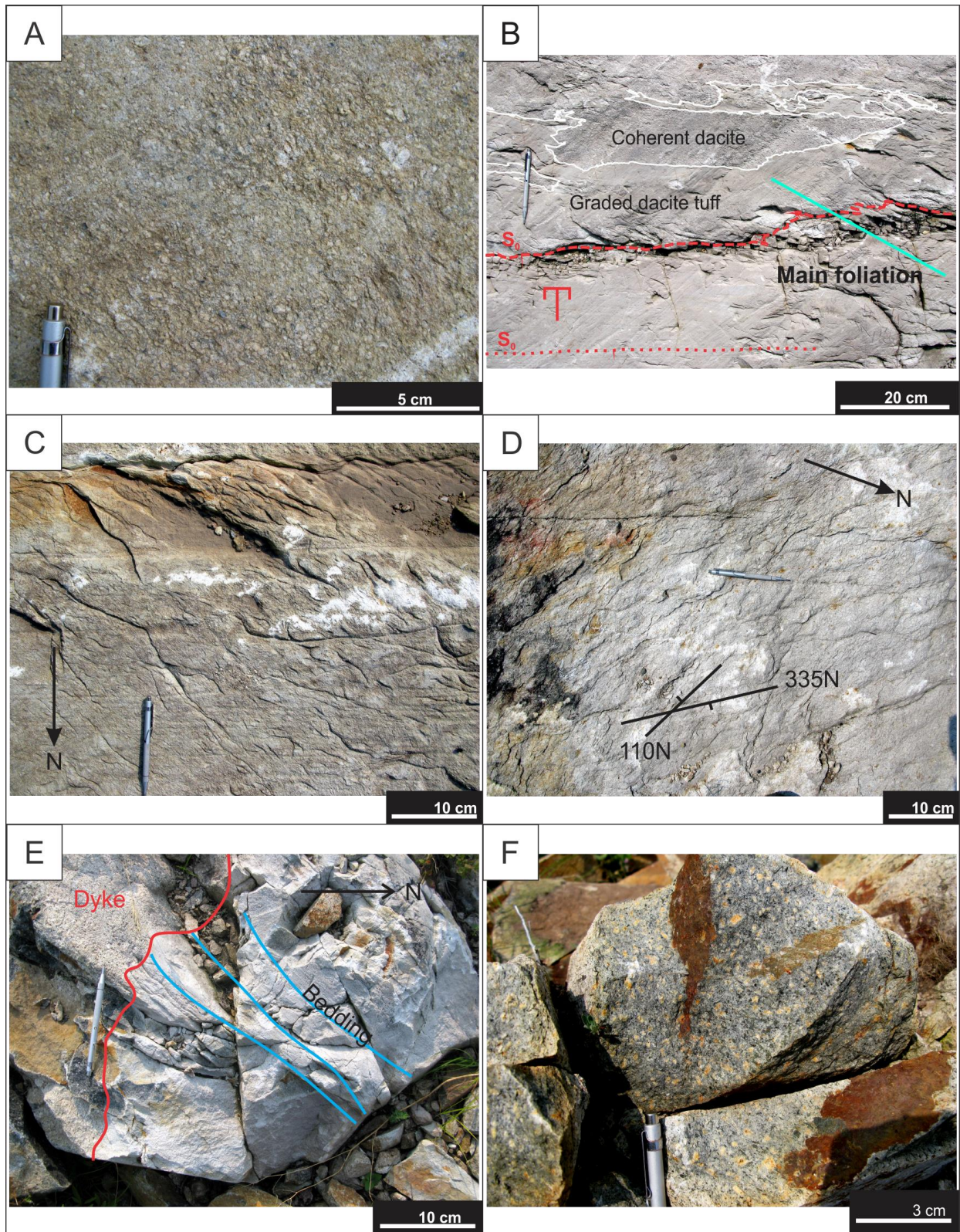


Figure 3.33 : Northern portion of Scott outcrop. A) Massive, blue quartz phenocrysts-bearing dacite. NAD83, zone 15, 427096 mE, 5408452 mN. B) Peperitic contact between graded tuff succession and coherent dacite. Also note the fragments of coherent dacite mixed in the graded

dacite tuff. NAD83, zone 15, 427105 mE, 5408392 mN. C) E-W oriented beds in a graded tuff successions, fining towards the South. NAD83, zone 15, 427104 mE, 5408448 mN. D) Two foliations recorded in massive porphyritic dacite. NAD83, zone 15, 427119 mE, 5408418 mN. E) Foliated porphyritic dyke crosscutting tuff beds. NAD83, zone 15, 427091 mE, 5408447 mN. F) Foliated porphyritic dyke, composed of quartz, feldspars, chlorite, sericite and around 6 vol. % epidote (from petrographic observations). NAD83, zone 15, 427098 mE, 5408443 mN.

3.4.3.4 Interpretation of the genesis and depositional environment

The peperitic contact with the massive dacites indicates water saturation in the volcanoclastic deposits at time of emplacement of the massive dacite, which is compatible with a subaqueous depositional environment, but gives no indication regarding water depth. Graded tuff sequences might indicate an explosive eruption deposit of flow, fall or surge nature, whether in an aerial or submarine environment. The high degree of grading, combined with the extensive thickness of the fine-grained tuffs within the sequence could indicate a distal position with respect to the eruptive centre. In proximity to the eruptive centre, we would expect coarser volcanoclastics such as blocks and weaker sorting of fragments. The massive dacite of the northern portion, because of its overall similar phenocrysts grain size as the brecciated porphyritic dacite of the south portion of the outcrop (section 3.4.3.1), is also interpreted as a brecciated dacite lava flow.

When put into relation with the McClain outcrop, where a volcanic environment of silicic domes and stubby flows and associated breccias was suggested, an interpretation of a depositional environment involving explosive eruption and associated pyroclastic deposit for the Scott outcrop seems unlikely. Alternatively, these graded tuff sequences could be generated through collapse of a lava dome and do not necessarily imply an explosive eruption. This latter interpretation of the depositional environment of the volcanic products on Scott outcrop is favoured over pyroclastic deposits from an explosive eruption, since it is more in line with the one proposed for the McClain outcrop located nearby.

3.5 Geochronology

U-Pb geochronology work was done by V. McNicoll at the Geological Survey of Canada, Ottawa, on two samples from the Rainy River deposit. These consist in samples RRR435526 and RRR435529 which are, respectively, coherent dacite from the McClain outcrop (Fig. 3.25 for location) and a monzonitic dyke from the Cap zone. The monzonitic dyke is non-mineralized or altered, but records the S_2 fabric and cross-cuts altered rocks associated with the Cap zone mineralization. The coherent dacite from the McClain outcrop is located within the deposit

footwall, is affected by S_2 and has traces of mineralization (32 ppb Au). Preliminary ages obtained through U-Pb isotope dilution thermal ionization mass spectrometry (ID-TIMS) techniques are 2717 Ma for the coherent dacite and 2693 for the monzonitic dyke. These ages imply an absolute mineralization age >2693 Ma, and D_2 between 2717 and 2693 Ma.

3.6 Tectonic setting and petrogenesis

The following section presents relevant geochemical data used to discuss the potential tectonic environment and petrogenesis of the deposit's host rocks. Part of the discussion is presented here and is continued in chapter 7, where the implications for Au endowment of this potential deposit's tectonic setting and petrogenesis are discussed.

As shown above, volcanic rocks from the Rainy River deposit define a bimodal succession with two distinct magmatic trends: a calc-alkaline trend represented by felsic volcanic and volcanoclastic rocks, and a tholeiitic trend defined by mafic to intermediate volcanic and volcanoclastic rocks. Within the basalts, a subgroup of samples, characterized by positive Nb and Ta anomalies, has been defined.

When plotted on a tectonic setting discrimination diagram for Phanerozoic volcanic rocks (Fig. 3.34), all samples from Rainy River plot into the volcanic arc group due to their low combined concentrations of yttrium (Y) and tantalum (Ta). Indeed, over 100 samples of calc-alkaline affinity have Ta values below 0.1 ppm, which could alternatively be attributed to crustal contamination (Tomlinson *et al.*, 2002). Another diagnostic characteristic of volcanic arc environments documented in both calc-alkaline and tholeiitic volcanic rock samples at Rainy River is a Nb-Ta trough in primitive mantle normalized trace and rare earth element profiles (Winter, 2001: Figs. 3.13 and 3.16 respectively), suggesting a volcanic, subduction-related tectonic setting for the volcanic rocks hosting the Rainy River deposit. It must also be noted that these diagrams were calibrated for Phanerozoic tectonic systems and may not perfectly apply to Archean rocks.

Due to their high Th and low Ta content, the felsic calc-alkaline rocks from this study mostly plot within the active continental margin field in a Yb vs. Th/Ta diagram (Fig. 3.35), although 97 samples with anomalous (above 30) Th/Ta ratio are not shown in this diagram. The abundance of anomalous samples could result from a combined low Ta values and high Th values. Once

again, low Ta and high Th values could result from crustal contamination rather than from a volcanic arc environment.

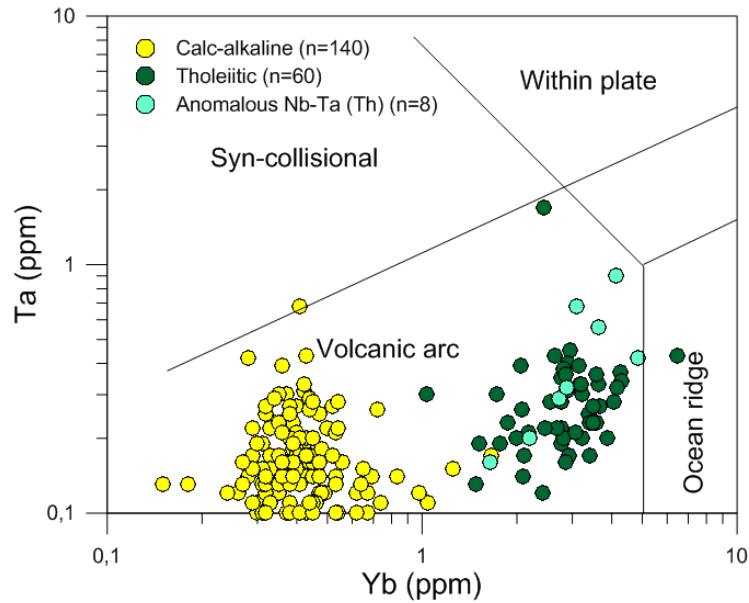


Figure 3.34 : Ta vs. Yb discrimination diagram of Pearce et al. (1984) showing the distribution of tholeiitic basalts (green), high Nb-Ta tholeiitic basalt subunit (light blue) and calc-alkaline dacites (yellow).

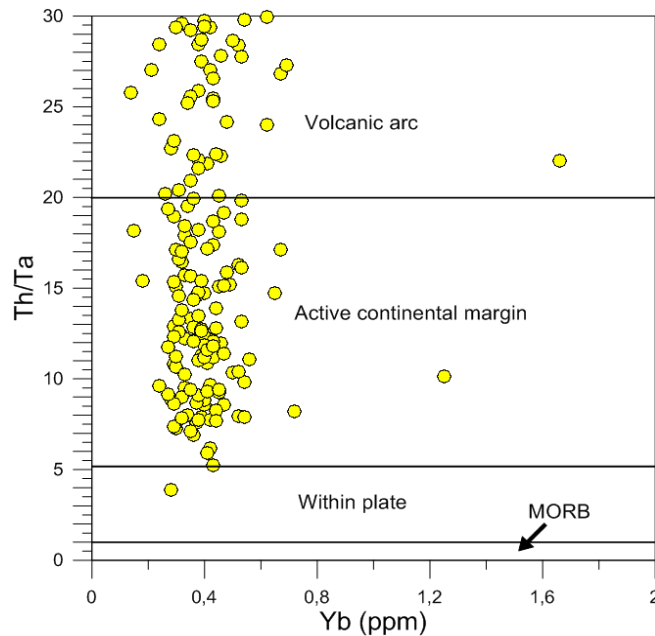


Figure 3.35 : Th/Ta vs. Yb tectonic discrimination diagram from Gorton and Schandl (2000) with all felsic volcanic rock samples with a Th/Ta ratio below 30 (n=160). Anomalous Th/Ta ratios (above 30) could be due to Ta depletion caused by crustal contamination combined with high Th values, which can also be caused by Archean crustal contamination.

3.6.1 Dacites

The dacites at Rainy River plot as FI-type rhyolites in Lesher *et al.* (1986) and Hart *et al.* (2004) classification diagrams for Archean rhyolites (Fig. 3.36) due to their high chondrite-normalized concentrations of light rare earth elements (LREE) combined with low concentrations in heavy rare earth elements (HREE).

HREEs, along with yttrium (Y) and scandium (Sc), are preferentially incorporated in garnets (and amphiboles, but to a lesser degree) and the presence of this mineral within the melt zone may explain the FI rhyolite depleted HREE signature. In mafic rocks, garnets are stable at high pressures, characteristic of great crustal depths, implying that FI felsic rocks are derived from melts produced at great depths. In contrast, FII and FIII rhyolites, which possess a flatter REE pattern, are derived from melts generated at shallower depths, i.e. outside the garnet stability field (Hart *et al.*, 2004). According to this classification, the tectonic environment for the formation of FI rhyolites is arc-related, with variable levels crustal contamination. FI-type, calc-alkaline rhyolites are common within the Superior Province in opposition to tholeiitic rhyolites that are present in isolated locations.

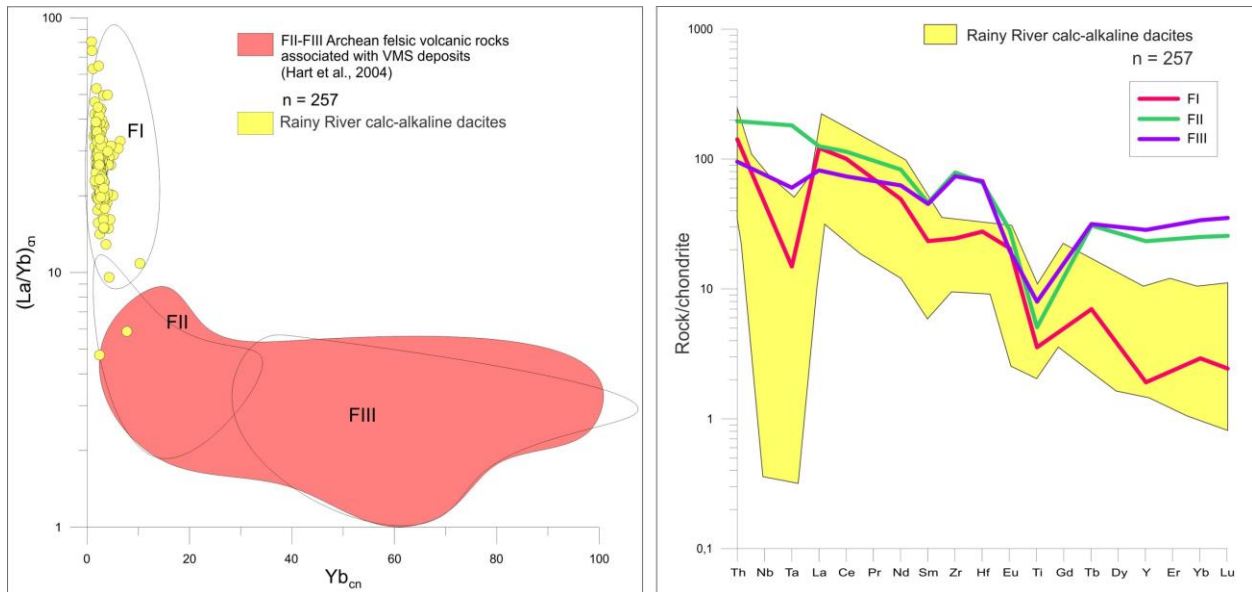


Figure 3.36 : A) Diagram from Hart et al. (2004) with data from Archean felsic rocks. Rainy River samples are in yellow. B) Rainy River calc-alkaline dacites chondrite-normalized multi-element profiles compared with FI rhyolite from Rope Island, FII rhyolite from Strugeon Lake complex, and FIII rhyolite from the Amulet formation (Blake River Group) in Rouyn-Noranda. Rhyolites data from Lesher et al. (1986).

Alternatively, an FI signature in dacites can also be obtained without subduction. FI-type dacites can be formed via assimilation and fractional crystallization (AFC) processes involving the base of the Archean crust. The diagram below (Fig. 3.37) illustrates the dacitic samples of this study regrouped along the AFC line starting at the primitive mantle composition towards an average tonalite-trondhjemite-granodiorite (TTG) composition. Present models interpret TTG suites as being the result of "low to moderate degree partial melting of hydrated basaltic crust at pressures high enough to stabilize garnet ± amphibole" (Martin *et al.*, 2005). TTG magma can originate from a high degree of melting of the subducting slab which would not be totally consumed by the interaction with mantle peridotite (Rapp *et al.*, 1999; Martin *et al.*, 2005), therefore allowing the emplacement of TTG rocks within the crust. Dacites from the Rainy River deposit, by their extrusive nature, differ from intrusive TTG suite rocks. On the other hand, they could hypothetically result from melting of a basaltic slab undergoing subsequent high levels of interaction with the crust (mantle wedge?) in a similar way to TTG-suite rocks, although the heat of the crust would have been sufficient to keep the melts from crystallizing before reaching surface.

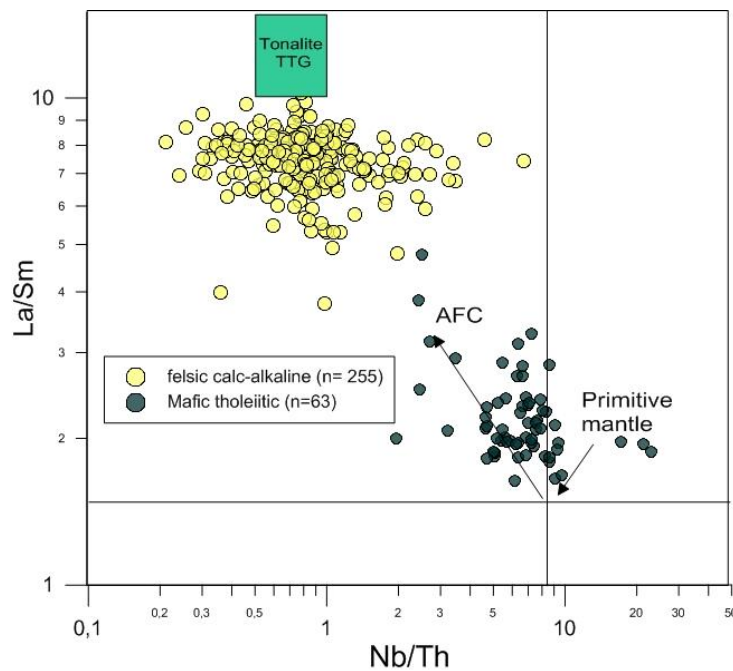


Figure 3.37 : Mafic tholeiitic and felsic calc-alkaline samples plotted on assimilation and fractional crystallization (AFC) diagram leading to idealized tonalite-trondhjemite-granodiorite (TTG) pole. Modified from Richer-Lafleche *et al.* (2000).

3.6.2 Basalts

Tholeiitic basalts sampled on the Rainy River project have an LREE-enriched profile when normalized to the idealized N-MORB composition of Sun and McDonough (1989; Fig. 3.38). Combined with a Nb-Ta trough (Figs. 3.16, 3,17), this signature is similar to those of basalts generated in modern back-arc basin tectonic environments. A back-arc basin represents an anomalous area of extensional tectonics in an overall compressive subduction regime. Within this environment, MORB-like melts are generated from a depleted mantle source, with an additional inherited signature from the limited interaction with the subducting slab and mantle wedge within the global compressional subduction zone (Winter, 2001).

It has been argued in the previous chapter that subduction and overall island arc environments were probably different during the early to mid Archean. For one thing, the higher mantle temperature at that time would imply that MORB-type basalts would have been generated in the garnet stability field. Also, Archean crust is very thick, and what is called trench lock could have occurred, i.e. when the crust is too thick and buoyant to subduct (J. Pearce, pers. commun., 2015). For these reasons, it is likely that basalts from Archean greenstone belts are not the typical oceanic crust generated by tectono-magmatic processes active today, but rather a hybrid product with continental interaction and crustal input.

All the tholeiitic basalt samples from this study plot above the modern MORB-OIB array in Pearce (2008) Th-Nb proxy diagram (Fig. 3.39), indicating that these basalts are not purely oceanic crust-type, but likely result from partial melting with some crustal input and continental interaction (Pearce, 2008). Most samples plot within the Northern Superior (3.0-2.9 Ga) basalts field, with a few exceptions plotting in both the Northern Superior and Abitibi-Wawa (2.7Ga) fields from Pearce (2008).

The high Nb-Ta basaltic subunit plots within the MORB field, due to the absence of a negative Nb anomaly. This pattern could be explained by processes and sources other than back-arc volcanism. This basaltic subunit is restricted in space and could be the result of partial melting of a basaltic source, or arguably issued from melts generated in a deeper, more primitive environment. In young arcs for example, a higher heat regime allows for a higher magma production, also increasing the chance of more primitive melts reaching the surface. In modern young arcs, the thin crust has been known to provide conduits for these primitive melts (Kay and Kay, 1994, cited in Winter, 2000).

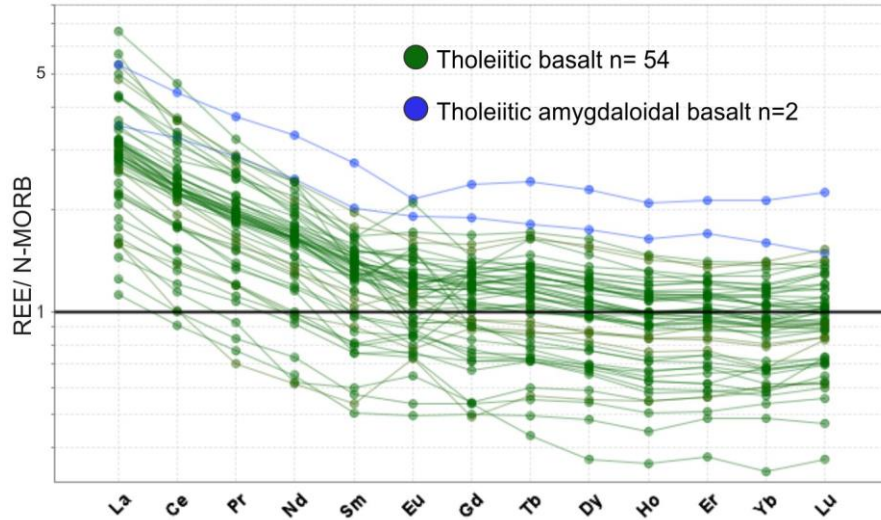


Figure 3.38 : Spider plot of tholeiitic samples normalized to N-MORB values from Sun and McDonough (1989). LREE enrichment is on average 3 times above the idealized N-MORB composition.

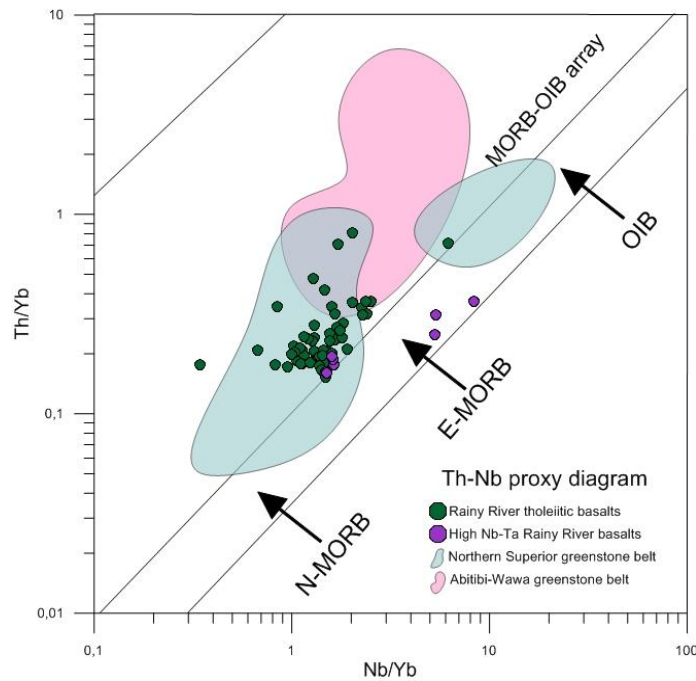


Figure 3.39 : Th-Nb proxy diagram for oceanic basalt classification adapted from Pearce (2008). Rainy River tholeiitic basalts plotted in green, and high Nb-Ta subunit plotted in blue. Fields correspond to compiled data from Pearce (2008) from the Abitibi-Wawa and Northern Superior greenstone belts.

In summary, the Rainy River deposit is hosted in a bimodal, dominantly calc-alkaline dacitic volcanic succession. The felsic succession is of FI type, implying a production of melts within

the garnet stability field. Mafic rocks are all tholeiitic basalts, with an LREE enrichment and Nb-Ta depletion, having undergone crustal interaction and/or subduction-related input, probably within a tectonic environment similar to modern-day back-arc environments.

The samples used in this study are all located within the Rainy River gold project and its immediate vicinity. Lithological variation within each magmatic trend is absent and each lithology probably represents a single stage within the tholeiitic or calc-alkaline magmatic trends. The absence of any other volcanic products within either magmatic differentiation trends impedes our ability to assess the magmatic differentiation processes that generated these two magmatic suites. Sampling at belt scale would be necessary to complete a thorough interpretation of the large-scale tectonic environment in which the Rainy River deposit host succession was generated, which goes beyond the scope of this study.

3.6.3 Intrusive bodies

The multi-element profiles of the early, foliated granitic intrusives are parallel to those of the main felsic calc-alkaline volcanic group (Fig. 3.40), although highly enriched. This suggests a single magma source for both units. In this scenario, the intrusive dykes and bodies are a later, more evolved and enriched product of the source that generated the felsic volcanic products. Alternatively, the highly enriched signature of these foliated granitic intrusives can be the crystallized product of crustal melts created by hot mafic magmas underplating the base of the crust, which would not involve co-magmatism with the felsic calc-alkaline volcanic rocks at Rainy River.

When comparing the different REE profiles for each intrusive sample (Fig. 3.41), there seems to be an evolution from an earlier, more primitive composition towards a more enriched one. The more "primitive" samples are located north of the deposit, whereas the more enriched profiles are from samples located within the deposit and south of it. This may indicate an intrusive activity progressively advancing southward in time. A severe Ti depletion of the intrusive rock samples in comparison to the coherent dacite samples on figure 3.41 could be attributed to the crystallization of a titanium oxide in the source magma.

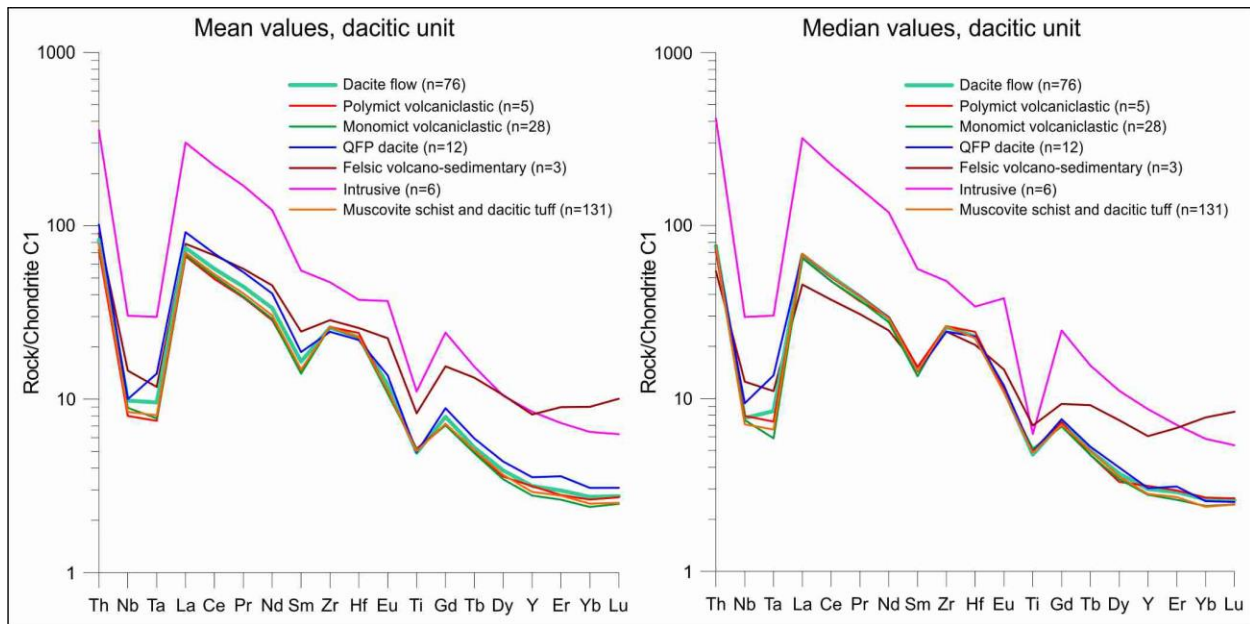


Figure 3.40 : Median and mean values for multi-element C1-normalized profiles of the different calc-alkaline volcanic facies along with the granitic to gabbroic dykes that cross-cut the deposit. Normalization values from McDonough and Sun (1995).

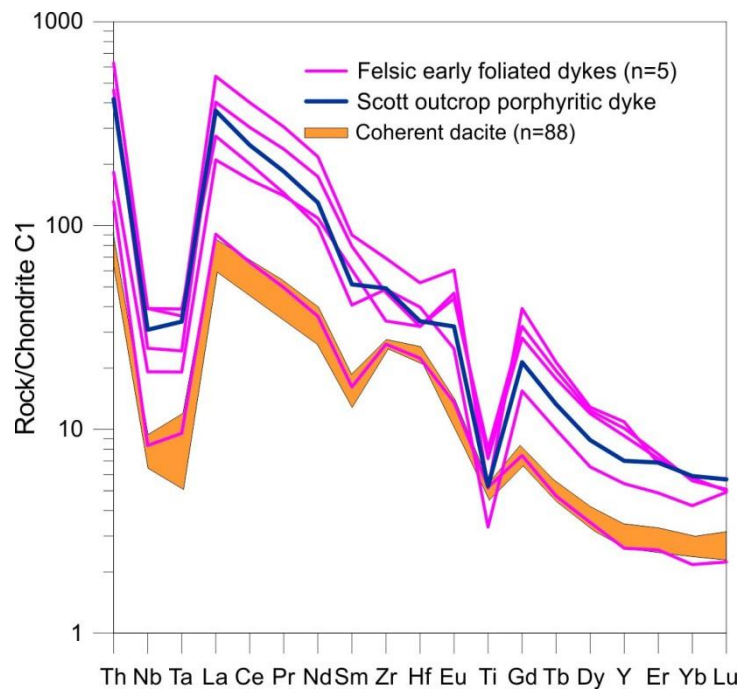


Figure 3.41 : Individual multi-element C1-normalized profiles of the dyke samples, showing higher normalized element concentrations for intrusive rocks in comparison with the coherent dacites within the deposit, represented by the field in orange. Normalization values from McDonough and Sun (1995).

4 DEFORMATION AND METAMORPHISM IN THE RAINY RIVER DEPOSIT AREA

4.1 Introduction

Deformation events, along with regional metamorphism within the Rainy River deposit area, modified the geometry and mineralogy of the deposit and enclosing rocks. Recognition of the different episodes of deformation and their relative chronology is crucial to further understand and quantify the extent to which deformation and metamorphism, at both the local and regional scales, affected the deposit. Likewise, constraining the pressure and temperature conditions as well as the evolution of regional metamorphism provides additional information on the evolution of the Rainy River deposit.

This chapter presents a description of metamorphic mineral assemblages that result from the evolution of pressure-temperature conditions due to regional metamorphism. Hydrothermal processes are documented in chapter 5. This is followed by a description of the different structures and fabrics documented on drill core and outcrop. A subsequent analysis and relative chronology of these structures is presented as well as their relation with deformation episodes and structures documented at regional scale.

4.2 Metamorphism

Mineral assemblages present at Rainy River result from the combined initial composition of the protolith, hydrothermal alteration, and overprinting regional metamorphism. In this section, the focus will be on mineral assemblages that allow us to deduce approximate pressure-temperature conditions at time of formation. The origin of these assemblages, whether attributed to initial rock composition, hydrothermal alteration or metamorphism will be discussed in the following chapter on alteration.

4.2.1 Regional context and previous work

The Wabigoon Subprovince is known to have a uniform greenschist metamorphic grade, with the exception of rocks in contact with large intrusive bodies as well as the North and South boundary zones, where the metamorphic grade gradually increases to the amphibolite-granulite

facies that characterizes both Subprovinces bounding the Western Wabigoon (i.e. the Quetico and Winnipeg River; Blackburn *et al.*, 1991). At Rainy River, regional metamorphism to the mid to upper greenschist facies has been previously documented (Mackie *et al.*, 2003; Wartman, 2011). The presence of typical greenschist facies minerals such as chlorite, epidote, muscovite and carbonates is in agreement with metamorphic temperatures and pressure within the greenschist facies range (300-500°C).

4.2.2 Metamorphic mineral assemblages of the Rainy River project

Regional metamorphism is defined here as a change in mineralogy due to a loss in volatiles triggered by an increase in temperature and/or pressure conditions that affects a large body of rock (Winter, 2001). Metamorphic rocks can preserve mineral assemblages that are stable at peak pressure and temperature levels (prograde path) as well as form mineral assemblages during decreasing pressure and temperature conditions (retrograde path). In the scenario where volatiles are present during the lowering of temperatures and/or pressures, the prograde mineral assemblages formed at peak P-T conditions can be gradually replaced by lower-temperature, retrograde metamorphic minerals. At Rainy River, both prograde and retrograde metamorphic minerals are present.

In the dacitic calc-alkaline package, thin section observations, along with microprobe analyses, delineated a prograde metamorphic mineral assemblage of spessartine-almandine garnet porphyroblasts, biotite, quartz and muscovite. A similar assemblage has also been documented in synvolcanic Archean gold deposits of the Doyon-Bousquet-LaRonde mining camp in the Abitibi greenstone belt, such as LaRonde Penna (Dubé *et al.*, 2004, 2007), Bousquet (Valliant and Barnett, 1982), Bousquet 2-Dumagami (Dubé *et al.*, 2014), and Westwood (Yergeau, 2015, Yergeau *et al.*, 2015). This assemblage has been associated with temperatures between 400 and 500°C and pressures from a maximum depth of 14 km (Mercier-Langevin, 2005). In comparison with other species of the garnet group, the high manganese concentration in spessartine garnets favours a lower crystallisation temperature (Paulick and Franz, 2001), which is compatible with the temperature interval proposed here. Garnets documented at Rainy River are fractured and inclusion-rich. Fractures in garnets are not oriented with respect to the main foliation trend (Fig. 4.1A), although inclusions are oriented parallel to the main fabric (S_2 , see below; Fig. 4.1B). All garnets possess inclusion-free and un-deformed rims (Fig. 4.1A, B). Similar observations were made at the LaRonde Penna deposit, where this feature has been interpreted as an indicator of metamorphic conditions within the garnet stability field lasting post-

main deformation (Mercier-Langevin, 2005). In some cases, remnant garnets are replaced by sulphides and chlorite, indicating retrograde metamorphic conditions (Fig. 4.1C; Kjarsgaard, 2013). Additionally, chloritization of biotite is present in numerous samples (Fig. 4.1D, E). Un-oriented chlorite is also overprinting deformed muscovite bands (Fig. 4.1F). This absence of orientation in chlorite grains indicates post-main deformation (D_2 ; see below) crystallization and implies retrograde metamorphism conditions late- to post- D_2 .

In tholeiitic basaltic rocks, almandine-spessartine garnets associated with hornblende, chlorite and biotite are present (Fig. 4.2A), suggesting a transitional metamorphic environment between greenschist and amphibolite facies. Depending on the pressure, this assemblage indicates metamorphic temperatures anywhere between 475 to 575°C (Liou *et al.*, 1974). Un-oriented, post-main deformation retrograde epidote is also present in deformed amphibole bands (Fig. 4.2B), suggesting a retrograde metamorphic event that took place after peak main deformation.

A quartz-kyanite-chloritoid assemblage is also present within the Rainy River deposit, concentrated in ≤ 20 m-thick isolated lenses parallel to the main fabric, which is interpreted as the metamorphic equivalent to previously hydrothermally altered volcanics (Pelletier *et al.*, 2014; see Chapter 5 for further description). The presence of kyanite is also documented within the Sturgeon Lake camp (Franklin *et al.*, 1975; Hudak, 2015), the Doyon Bousquet LaRonde camp (Marquis *et al.*, 1990; Dubé *et al.*, 2004, Wright-Holfeld *et al.*, 2010) as well as other deformed and metamorphosed VMS deposits in Sweden (Hannington *et al.*, 2003). Presence of this typically high-pressure metamorphic mineral (>2.5 kbar and $>400^\circ\text{C}$), in these seemingly lower-pressure environments can be explained by a hydrothermal, alteration-induced, singular mineralogy of the host volcanic rocks prior to regional metamorphism. In other words, kyanite in the alteration pipe is not necessarily indicative of high pressure metamorphic conditions. Hannington *et al.* (2003) put forward the idea that the presence of iron or variation in aluminium activity could expand the stability field of kyanite to lower P-T conditions. Alternatively, $P_{\text{H}_2\text{O}}$ variations could move the Al_2SiO_5 triple point to lower values (Hemley *et al.*, 1980; Hannington *et al.*, 2003) in the alumina stability diagram. At Rainy River, kyanite has recorded the D_2 deformation episode (Fig. 4.2C) and no other aluminosilicates (andalusite, sillimanite) are present, suggesting that the presence of this mineral is indicative of the aluminous nature of the altered volcanic rock prior to metamorphism rather than a high pressure-temperature environment. Kyanite formation occurred during prograde metamorphism and is syn- D_2 .

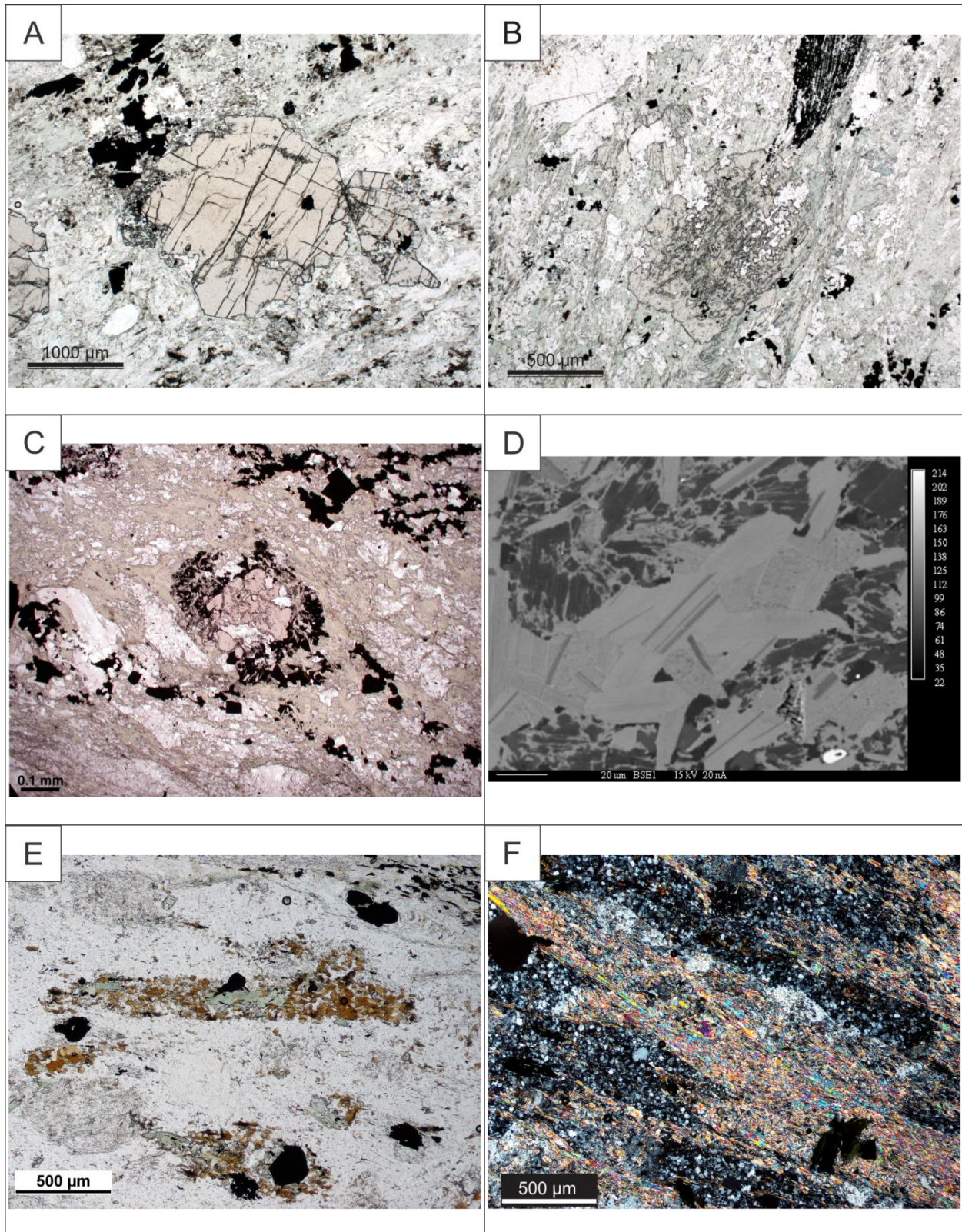


Figure 4.1 : Metamorphic mineral assemblages. A) Photomicrograph (natural light) of spessartine garnet porphyroblast with brittle fractures discordant with S_2 foliation. Inclusion-rich growth rim denotes multiple growth events. Sample RRR435593, DDH NR060050 at 314 m (centre of ODM body). B) Photomicrograph (NL) of almandine garnet with inclusion-poor, un-deformed rim in

chlorite-dominated matrix. Sample RRR435752, DDH NR090358 at 72 m (Cap zone). C) Photomicrograph (NL) of garnet porphyroblast retrograded to chlorite-chalcocopyrite in a chlorite-quartz-sericite matrix. Sample RRR128509 (photo by I. Kjarsgaard, 2013). D) Backscattered electron image of biotite (black sticks) being replaced in individual sheets by chlorite (lighter gray). Sample RRR435680, DDH NR110742 at 340 m (SE of deposit). E) Photomicrograph (NL) of chloritization of biotite. Chlorite is discordant to S_2 . Sample RRR435777, DDH NR060058 at 142 m (ODM hanging wall). F) Photomicrograph (polarized light) of un-oriented retrograde chlorite grain overprinting foliated sericite bands parallel to S_2 . Sample RRR435777, DDH NR060058 at 142 m (ODM hanging wall).

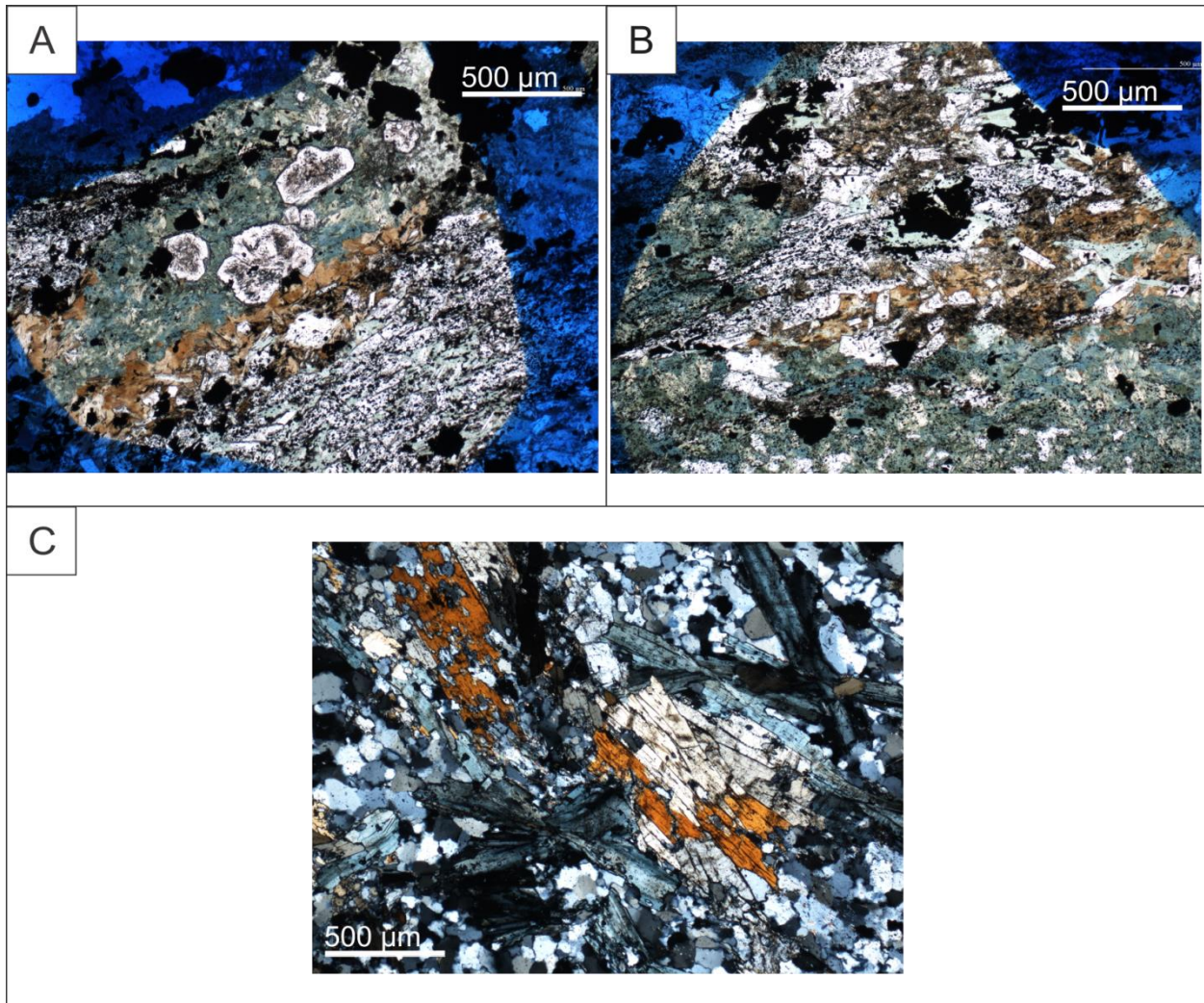


Figure 4.2 : Metamorphic mineral assemblages. A) Photomicrograph (NL) of S_2 -parallel amphibole- and garnet-rich band in contact with a chlorite-epidote-rich band. Note recrystallized, inclusion-free garnet rims. Sample RRR435680, DDHNR110742 at 340 m (SE of deposit). B) Photomicrograph (NL) of same sample as in A, with retrograde, un-oriented epidote crystals in hornblende-dominated matrix. C) Photomicrograph (NL) of kyanite and chloritoid grains parallel to S_2 in quartz matrix (rare sericite). Sample RRR435660, DDH NR060053 at 357 m (ODM high grade zone).

4.3 Deformation

The different deformation events that took place in the Rainy River deposit area were recorded by the host rocks of the deposit at various degrees and, more importantly, have modified the geometry of the different mineralized zones. In this section, deformation at Rainy River will be presented first through a description of the different structures documented on drill core, outcrop, thin section, and in a 3D model. Subsequently, a model illustrating the structural setting of the deposit area is presented, based on the three-dimensional distribution of the previously identified structural elements as well as existing structural studies (Blackburn, 1976; Poulsen, 2006; Melnyk *et al.*, 2006; Siddorn, 2008; Rankin, 2013). Lastly, a brief discussion on the impact of structural deformation on the distribution and concentration of mineralization is proposed.

4.3.1 Relation to the Quetico Fault

The Rainy River project is located 4.2 km north of the east-striking, subprovince-bounding Quetico fault. This fault is interpreted as a dextral shear zone caused by NW-SE oriented shortening (Fernandez, 2013). Previous aeromagnetic data interpretation of the area (Figs. 4.3, 4.4; Poulsen, 2005; Siddorn, 2008) identified WNW-striking splays of the Quetico fault that extend immediately North of the Rainy River project, within the Richardson Township (Fig. 4.4). The Quetico Fault, according to early works by Fletcher and Irvine (1954), truncates the Mather sediments south of the Rainy River deposit, although Johns (1987) traces the Quetico Fault through the Mather sediments. Timing of this fault with respect to stratigraphy is therefore uncertain and would require further regional mapping work. In a context of typical dextral strike-slip shear system, these WNW structures could correspond to second order, dextral Riedel – type structures (Fig. 4.4) within the main east-west dextral shear structure represented by the Quetico Fault.

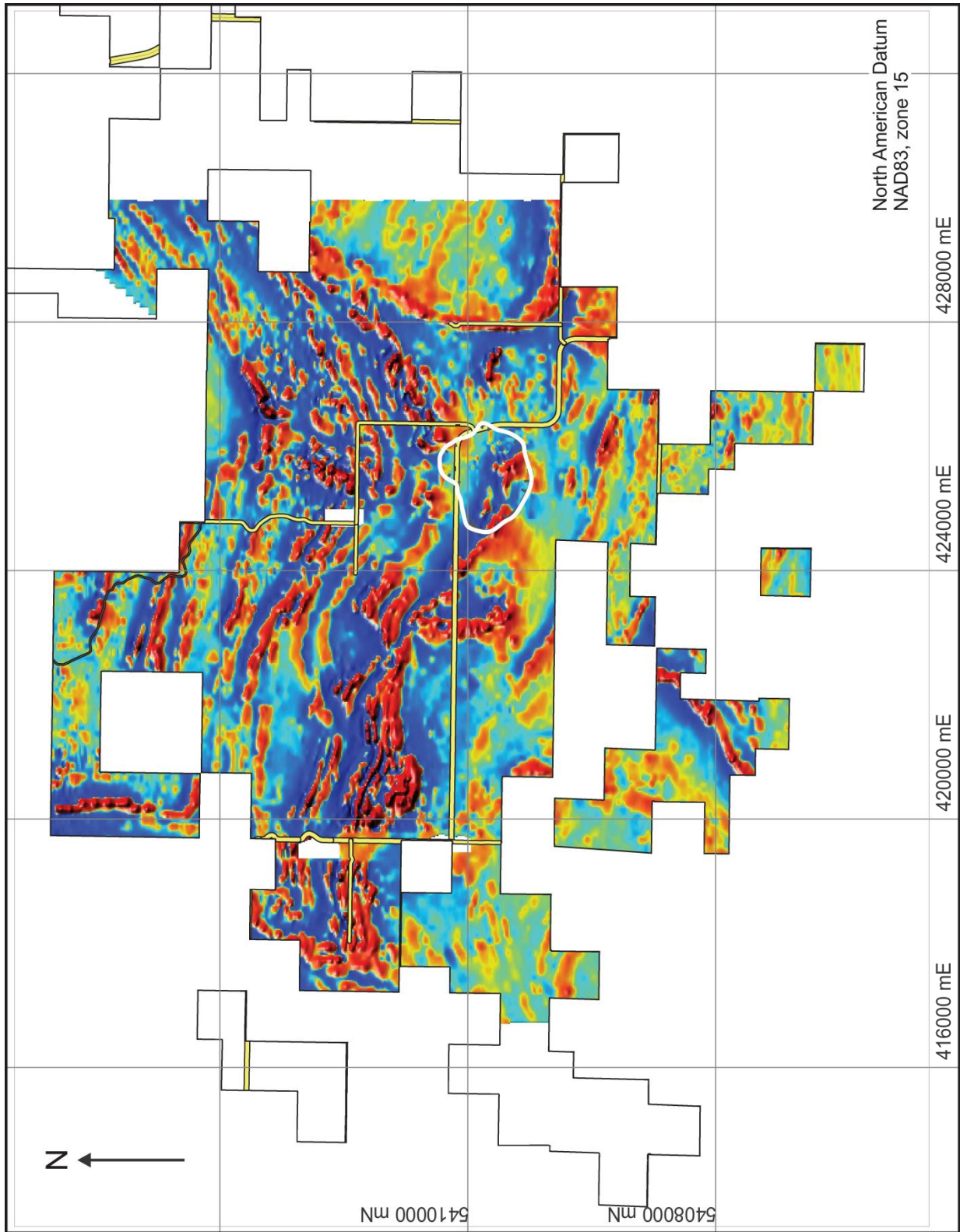


Figure 4.3 : Raw aeromagnetic data (total magnetic field) clipped to the present Rainy River property (as of September 2015). Proposed open pit extent highlighted in white. Image courtesy of New Gold Inc.

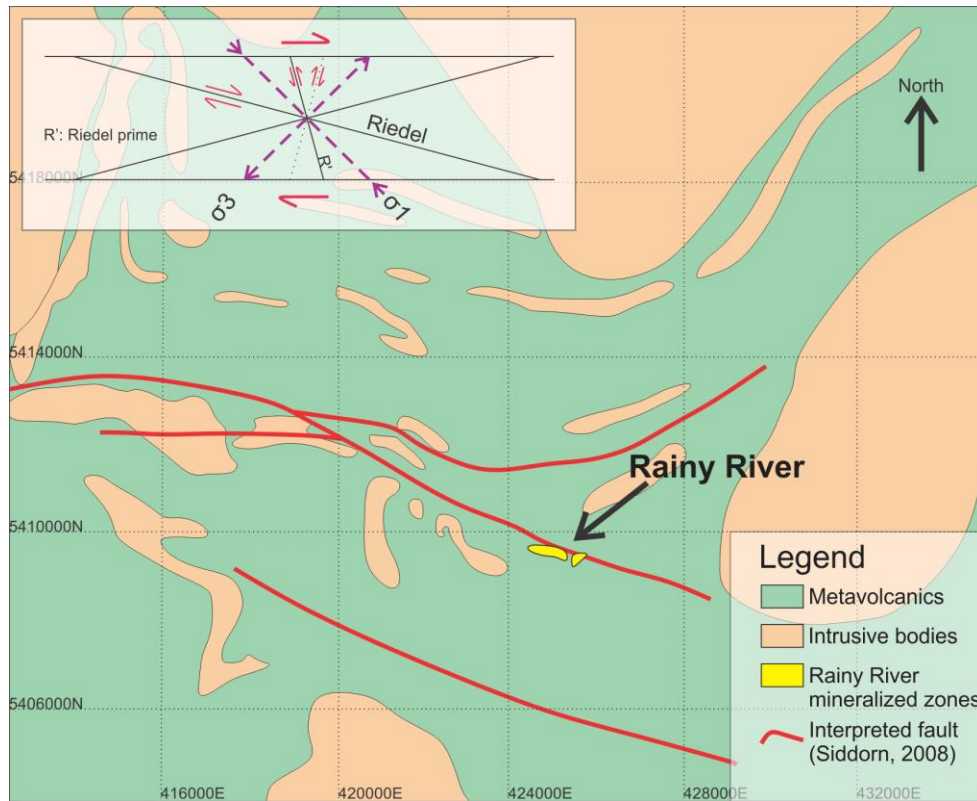


Figure 4.4 : Regional faults in the Rainy River area. Modified from Siddorn, 2008. Interpreted from Aeromagnetics data. North American Datum NAD83, zone 15.

4.3.2 Early fabrics and pre-D₂ structures

In the Rainy River deposit area, bedding-parallel foliation (S_0 - S_2) is present in the mafic-dominated sedimentary units and within graded tuff sequences in the dacites of Scott outcrop (Fig. 3.31; appendix I) and. Graded tuff sequences are not folded at Scott outcrop (see chapter 3 for location and description), whereas the bedding in mafic-dominated sediments is folded locally (Fig. 4.5A), with an axial planar S_2 foliation. Strain partitioning between competent felsic volcanics versus weaker mafic-dominated sedimentary rocks could explain this discrepancy. Within the Rainy River deposit, no D_1 structures have been recognized in this study, potentially due to strong overprinting by younger structures. Therefore, the intensity of the D_1 episode is difficult to comment.

Folds developed in sulphides and auriferous quartz-carbonate-pyrite veins, later transposed into the S_2 foliation (Fig. 4.5A,B) have been interpreted by Hrabí and Voss (2010) as having an early (pre- to early- D_2) onset and would have undergone rotation parallel to the plunge of gold mineralization and L_2 stretching lineation in a high strain environment. These folds are tight to

isoclinal and documented in un-oriented drill core, although they are developed in a plane perpendicular to S_2 . Barren quartz-carbonate±tourmaline folded veinlets are also present (Fig. 4.5C), mostly recording complex polyphase deformation, typical of gold deposits found within Archean greenstone belts having undergone several overprinting increments of deformation (Robert and Poulsen, 2001). As will be discussed in chapter 5 on alteration, a higher density (and associated carbonate alteration) of early- to syn- to late- D_2 auriferous ≤ 5 cm thick quartz-carbonate-pyrite veins and veinlets is present in the western end of the ODM body. It is also the area where the S_2 fabric swerves from an ESE-WNW orientation to a N-S strike. These auriferous veins represent a minor volume of the total Au content at Rainy River (see chapter 6).

4.3.3 Structural elements: main deformation (D_2)

4.3.3.1 Foliations and lineation

Host rocks of the Rainy River deposit all possess a prevailing south-dipping, east-west oriented penetrative foliation (S_2). To the west of the ODM zone, the S_2 foliation changes from an ESE-WNW to a NE-SW strike, as suggested by the raw aeromagnetics data (Fig. 4.3). The attitude of the S_2 foliation within the deposit has been compiled from hundreds of oriented drill core measurements and averages $102N/61^\circ$ (BBA Inc., 2012). This attitude is in agreement with measurements taken by the author on outcrops located within the deposit area. The average dip of the main foliation increases to approximately 75° within the structural footwall of the ODM zone in what is interpreted to be an east-west striking high strain corridor. Sub-horizontal kinking of S_2 (post- S_2 development: Fig. 4.5D) is also present within this corridor of high deformation intensity.

The S_2 foliation is predominantly expressed through the preferential alignment of micas (Fig. 4.5E), stretching/flattening of clasts parallel to this plane (Fig. 4.5F), and also through the transposition of previously folded veins (Fig. 4.5B,C). On a larger scale, the main lithological contacts between volcanic subunits as well as all mineralized zones are also parallel to this foliation trend (refer to Fig. 3.23), underlining its importance in the distribution of the mineralized zones.

A moderately southwest plunging stretching lineation (L_2) is present in the S_2 plane (Fig. 4.6A). It has an average plunge direction and plunge of $225N/55^\circ$ (BBA Inc., 2012) and is better developed in phyllosilicate-rich volcanics. L_2 lineations measured by the author on outcrops

located in the deposit area have a similar average orientation. Higher grade ore shoots zones within the S_2 -parallel mineralized bodies are parallel to L_2 . Boudins and potential F_1 fold hinges are commonly collinear with L_2 (Hrabi and Vos, 2010). This geometry is interpreted as resulting from rotation of features within a high strain environment, in agreement with Robert and Poulsen (2001) model.

A secondary foliation (S_s), crenulating the S_2 foliation, is locally developed (Fig. 4.6B) and was measured on outcrop at an orientation of 081N/53°.

Leapfrog[®] implicit modelling done as part of the preliminary economic assessment update (BBA, 2012) outlined a trend (S_{s2}) through preferential alignment of Au mineralized bodies (Fig. 4.6C). This trend has a NW-SE strike and unknown dip. Since secondary foliations observed on drill core and thin sections for this study originate from un-oriented drill core, it is not possible to determine the angular relationship between these foliations and the S_{s2} Au mineralization trend outlined by SRK (2011).

Relative timing of S_{s2} with regards to S_2 is unclear, since there is no evident cross-cutting or overprinting relationship and this trend has not been reproduced by the author as part of the Leapfrog[®] implicit modelling for this study. Being in close proximity to a splay of the Quetico Fault, these structures are perhaps all part of a weakly developed C-S-C' fabric system from a ductile shear system developed during a protracted D_2 event (Fig. 4.6E). The presence of kinematic indicators (see below) also supports the existence of a simple shear component during D_2 .

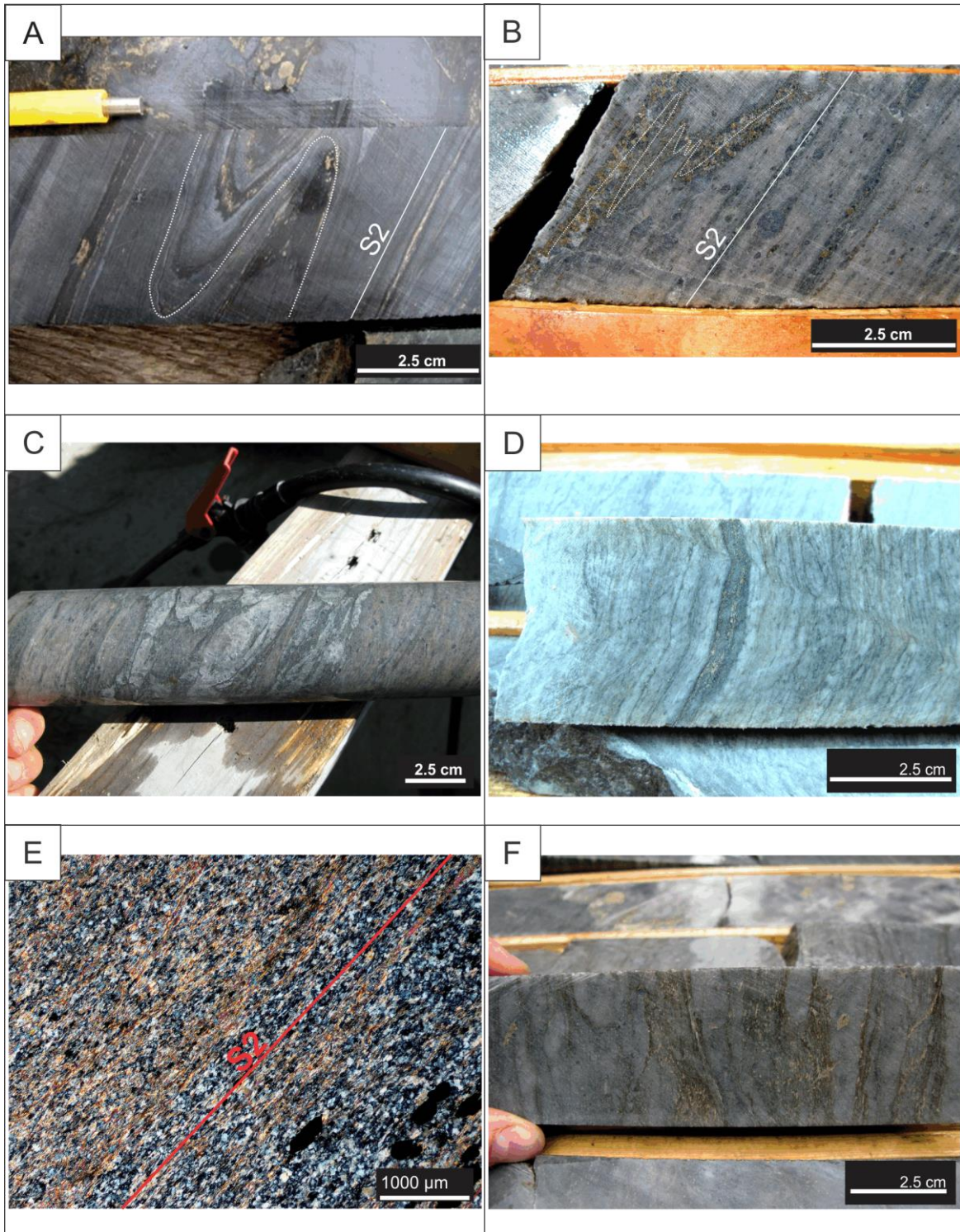


Figure 4.5 : Structural fabrics : S_0 , D_1 and D_2 -related structures. A) S_0 bedding having undergone isoclinal F_2 folding. Note concentration of sulphides at fold hinge. Mafic-volcanic dominated sediments. Unknown location. Photo from BBA Inc. preliminary economic assessment update (BBA Inc., 2012). B) Sulphide veins with asymmetrical folds transposed into the S_2 plane in dacitic flow. DDH NR100600 at 197 m. C) Polyphased folding in quartz-carbonate-chlorite vein subsequently transposed into the S_2 plane. DDH NR060117 at 44 m. D) Kink banding of S_2 foliation

developed in strongly chlorite and sericite-altered sericite schist from the ODM footwall shear zone. DDH NR060022 at 233 m. E) Photomicrograph (PL) of pervasive S_2 foliation defined by the preferential alignment of fine sericite grains. Sample RRR435830, DDH NR110771 at 121 m (Cap zone). F) S_2 foliation stretching and flattened clasts in monogenic dacitic tuff breccia. DDH NR060058 at 326 m.

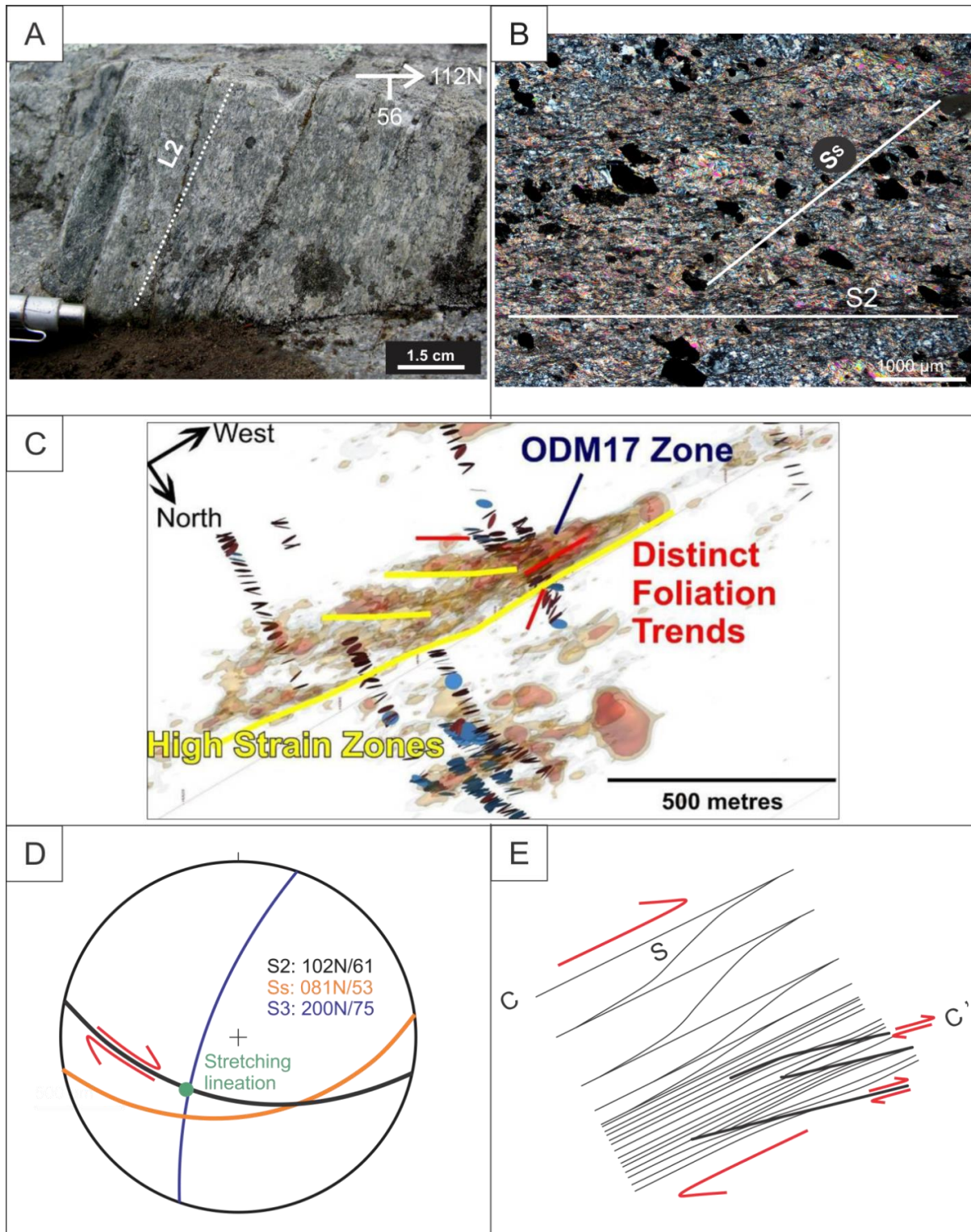


Figure 4.6 : Structural fabrics and trends. A) L_2 Mineral stretching lineation (55° - $214N$) observed on the S_2 plane ($112N/56^\circ$ at this location). Host rock are dacites located within the proposed pit area. NAD83, Zone 15, 425938 mE, 5409478 mN. B) Photomicrograph (PL) of secondary foliation trend (S_s) crenulating the S_2 foliation at approximately 45 degrees to principal S_2 foliation. Un-oriented thin section of sample RRR435789, DDH NR060058 at 374 m (ODM high grade zone). C)

NW-SE trending additional foliation trend (Ss_2) to the S_2 plane underlined in red and yellow on a Leapfrog® modelling project of 0.3, 0.5 and 1 g/t Au shells. Foliations were measured with an Optical Televiewer and are displayed as disks. Figure taken directly from the Rainy River preliminary economic assessment update (BBA, 2012). D) Equal angle (Wulff) Northern hemisphere plot of the average values for the S_2 , Ss and S_3 foliations and stretching lineation (L_2). See text for more information. E) Sketch of a C-S-C' shear fabric development within a dextral shear system. (Adapted from L. Harris, pers. commun., 2013).

4.3.3.2 Kinematic indicators

Kinematic indicators are used to determine shear sense within ductile shear zones. To assess the shear zone's dynamic and geometry through kinematic indicators, we need to observe them in a section that is mostly perpendicular to the vorticity vector (perpendicular to the foliation and relatively parallel to the lineation). Additionally, shear sense indicators should be observed in a section perpendicular to the foliation and lineation to check for lateral flow indicating deviation from a plane strain environment (L. Harris, pers. commun., 2013). In this study, kinematic indicators have been observed in both plane and section views, underlining a three dimensional shear zone combining dip-slip and strike-slip components. Shear sense indicators have been documented within the Rainy River project at the outcrop, drill core, and thin section scales. However, as Hanmer and Passchier (1991) put it: "intuitive or empirical deduction of the kinematic significance of a structure from its geometry alone is a hazardous undertaking". For example, elements with varying initial aspect ratios and angle with respect to flow orientation can have inverted apparent finite rotation directions (Hanmer and Passchier, 1991). In light of this, the kinematic indicators presented here and their interpretation can only be speculative and a more rigorous structural study of the kinematic indicators, along with a rigorous analysis of the strain ellipsoid within the deposit is recommended to better describe and characterize this shear system.

Most kinematic indicators observed on a plane perpendicular to S_2 and subparallel to the stretching lineation (subvertical) show a South over North reverse movement component. They consist in fold dragging (Fig. 4.7A), rotation in porphyroblasts (Fig. 4.7B), winged pressure shadows (Fig. 4.7C), and weak sigmoidal veining (Fig. 4.7D). A similar interpretation was previously made by Hrabí and Vos (2010) based on asymmetric pyrite grains.

Shear sense indicators are also identified on outcrop, more or less on a plane sub-perpendicular to S_2 and oblique to L_2 . From this study, back-rotated structures and σ -type porphyroblasts both indicate a clockwise (dextral) shear sense (Fig. 4.7E and Fig. 4.7F,

respectively). This is in agreement with the overall horizontal dextral movement of the Quetico Fault and its splay bounding the deposit to the North.

Other kinematic indicators, such as C-S structures, rotated porphyroblasts and preferential orientation of recrystallized quartz fibres are documented on thin section. Unfortunately, their orientation with respect to the S_2 plane is poorly constrained (Fig. 4.8A, B and C). Nonetheless, they do confirm the presence strike-slip and dip-slip shearing components during the D_2 episode.

4.3.3.3 Vein arrays

Deformed, laminated quartz-ankerite-pyrite veins hosted in mafic volcanic rocks occur on an outcrop located in the surface extension of the Cap zone. Mineralization within the host rocks occurs as disseminated pyrite within the mafic volcanic rocks (Fig. 4.8D). The quartz-ankerite-pyrite veins (Fig. 4.8E) contain traces of sulphides but assays results revealed Au contents between 4 and 7 g/t. These veins are cross-cut by later barren quartz-ankerite veins (Fig. 4.8E), which have undergone asymmetrical folding. Asymmetrical folds in the barren quartz-ankerite veins indicate a North over South, shallow (thrust?), synthetic rotation, which is in opposition to the kinematic indicators described earlier. However, the kinematic indicator observed in these barren veins is not sufficient to assess kinematics with certainty, and further investigation is necessary to clearly determine the deformation parameters recorded by these barren veins. According to Poulsen (2006), the shallow dip of some of the auriferous quartz-ankerite-pyrite veins suggests that they may have formed in response to the elongation of the rock that generated the L_2 stretching lineation, therefore attributing them a late D_2 timing. Comparing this auriferous quartz-ankerite-pyrite vein array with a typical shear zone model, it is possible that the early quartz-ankerite-pyrite veins were developed in Riedel structure, T structures (parallel to σ_1), and in normal-faulting Riedel prime (R') structures within a reverse dip-slip motion along S_2 (Fig. 4.8E). The presence of an array of laminated veins implies the presence of fluids during a late D_2 deformation event under brittle-ductile conditions.

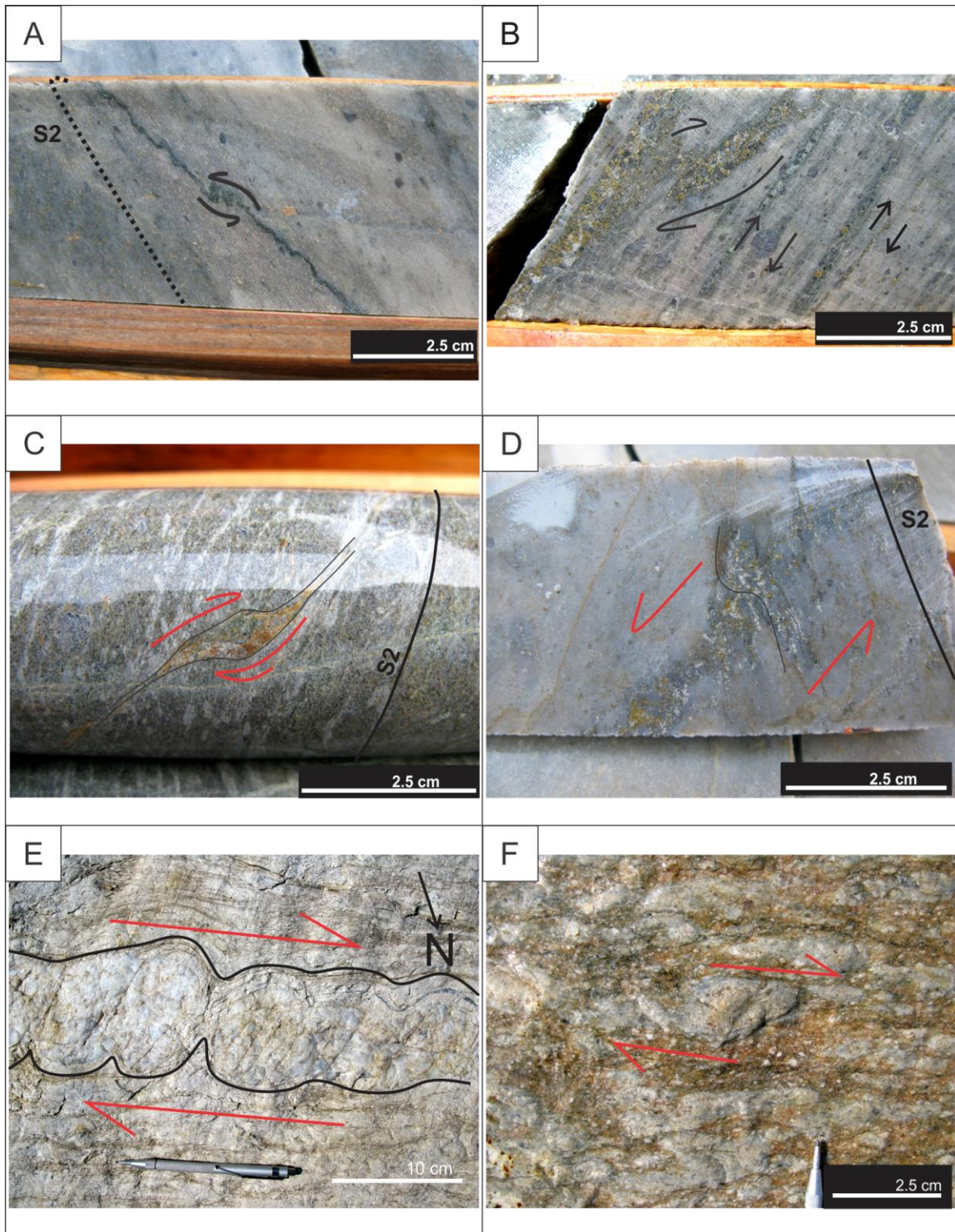


Figure 4.7 : Kinematic indicators : drill core and outcrop. A) Asymmetrical folds within a chlorite veinlet subparallel to S_2 indicating a clockwise rotation. DDH NR060073 at 385 m. B) Asymmetrical folds in a pyrite vein transposed into the S_2 plane. Additional kinematic indicator observed on this sample consist in a strain shadow asymmetry on a blue quartz phenocryst and asymmetrical fold in chlorite-pyrite veinlet. All three kinematic indicators record a clockwise shear sense. DDH

NR060058 at 126 m. C) Sphalerite-carbonate-chlorite vein recording a clockwise rotation towards a parallel alignment with respect to direction of maximum extension of the finite strain ellipsoid. DDH NR060051 at 168 m. D) Weak sigmoidal fabric development in a sphalerite-pyrite-chlorite vein in transparent quartz phenocryst-bearing sericite schist. DDH NR070146 at 221 m. E) Back-rotated boudins on a quartz vein indicating dextral shear. Scott outcrop, subhorizontal surface. NAD83, Zone 15, 427125 mE, 5408395 mN. F) Sigma-type porphyroblast indicating dextral shear-sense on sub horizontal surface. Scott outcrop. NAD83, zone 15, 427112 mE, 5408390 mN.

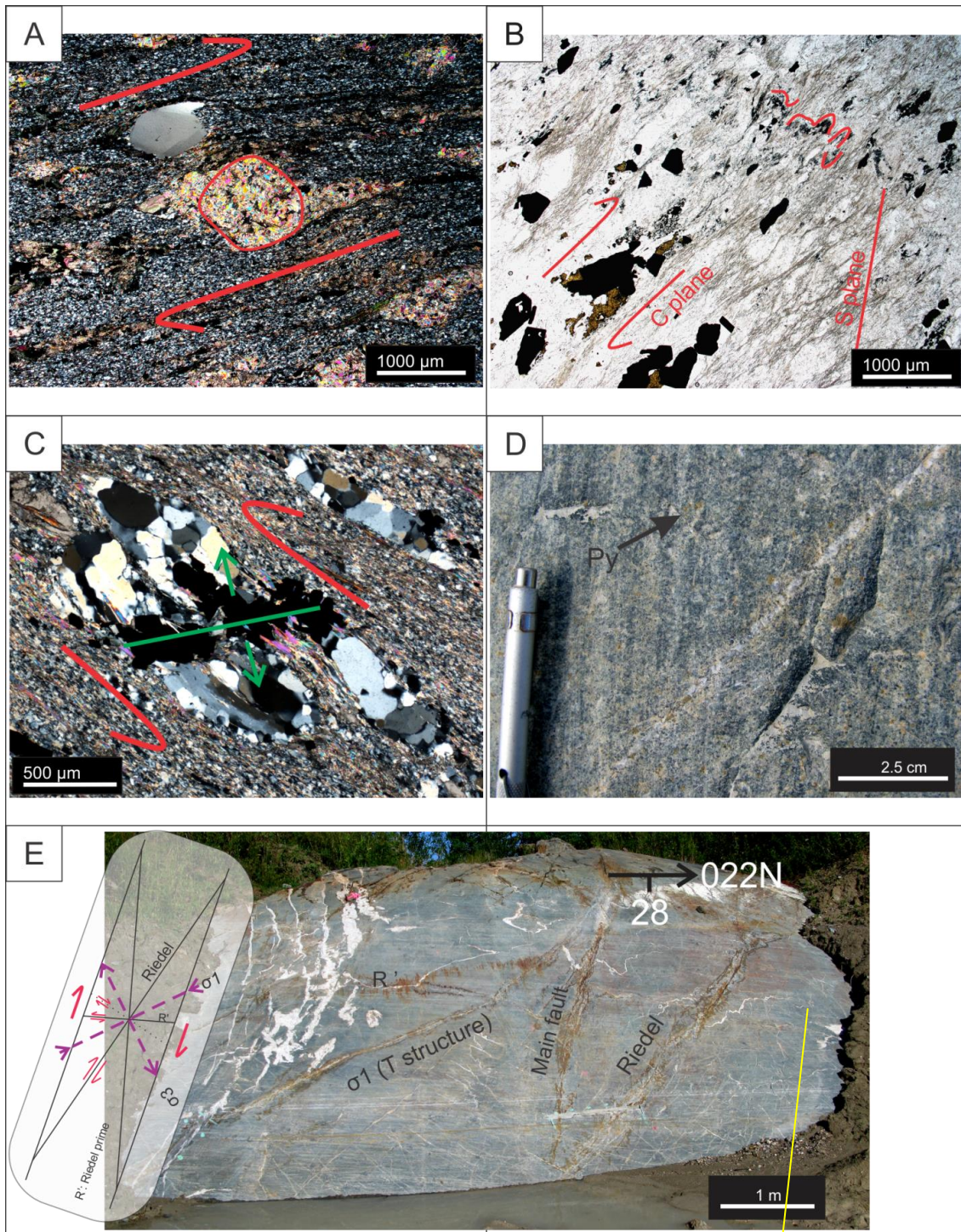


Figure 4.8 : Kinematic indicators on un-oriented thin section and vein arrays. A) Photomicrograph (PL) of retort-shaped deformed quartz phenocryst indicating clockwise rotation. Also on this photo, remnant feldspar porphyroblast replaced by sericite, with a δ -type asymmetry indicating clockwise rotation. Sample RRR435506, DDH NR110850 at 208.7m (Cap zone). B) Photomicrograph (NL) of weakly developed C-S fabric in dacitic tuff. Folded and transposed rutile-rich veinlet in NE quadrant of photomicrograph. Sample RRR435795, DDH NR060058 at 480.5m (HS zone). C) Photomicrograph (PL) of deformed recrystallized quartz fibres indicating an antithetic rotation. Tension gash parallel to σ_1 (in green) is a preferred site for pyrite precipitation. Sample RRR435604, DDH NR060073 at 352m (ODM zone). D) Close-up photo of the disseminated pyrite mineralization occurring on the Cap zone surface extension outcrop. NAD83, Zone 15,

425435 mE, 5409396 mN. E) Laminated quartz-carbonate-pyrite laminated vein array on the Cap zone surface extension outcrop face. The face is oriented at 022N/28°, which is at 64° from S2 and 56° from L2. Trace of S2 on this plane is underlined in yellow. These veins show a sinistral movement along a steeply South-dipping shear boundary parallel to the S2 trace. A later generation of barren quartz-calcite veins crosscuts the previous sulphide-bearing veins. Asymmetry in fold limbs point towards a North over South rotation. Reliability of this shear sense indicator is weak. NAD83, Zone 15, 425435 mE, 5409396 mN.

4.3.4 Late structures

Hrabi and Vos (2010) describe brittle-ductile shear zones at the western end of the ODM mineralized body. These shear zones are anastomosing and are expressed through rotation and crenulation of S₂. An average orientation of these structures was evaluated at 200N/75° (Fig. 4.6D). These late brittle ductile shear zones have also been documented with a 185-005N orientation on an outcrop (Fig. 4.9A) located above the centre of the ODM body. At the property-scale, these NNE-SSW discontinuities can also be deduced from the raw aeromagnetics data (Fig. 4.3), where they cut previously folded marker horizons.

Brittle structures with a sinistral offset, oriented at 195/75° on average, crosscut the D₂-related fabrics and are present on drill core and outcrop (Fig. 4.9B). This late event displaced mineralization at the metre scale at most and did not involve any remobilization (Pelletier *et al.*, 2014). Additional brittle fractures on un-oriented core have remobilized precious metals on a local scale (Fig. 4.9C).

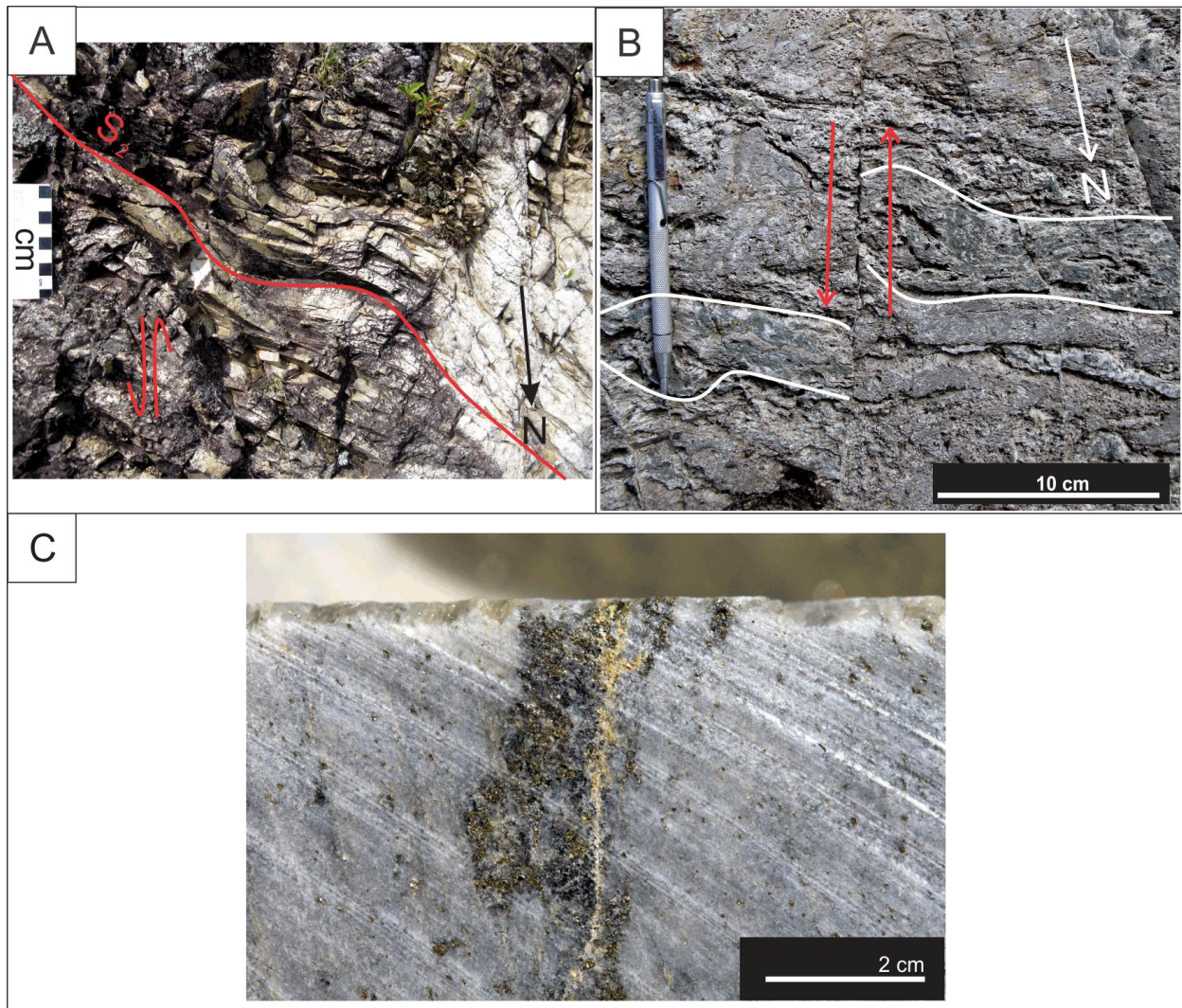


Figure 4.9 : Post-D₂ brittle-ductile and brittle structural features. A) Minor brittle-ductile shear zone striking 185-005N and expressed through rotation of S₂ foliation with senestral movement. Dacitic flow with trace to 2% rounded blue quartz phenocrysts. Main pit entrance outcrop, NAD83, Zone 15, 426263 mE, 5409530 mN. B) Brittle senestral offset of chlorite band on McClain outcrop. Brittle fault at 204N/80. McClain outcrop, NAD83, Zone 15, 426157 mE, 5410343 mN. C) Visible gold locally remobilized within a late brittle fracture. Photo by P. Mercier-Langevin (2012).

4.3.5 Structural data from Scott and McClain outcrops

4.3.5.1 McClain outcrop

Compilation of S₂ foliation measurements on the McClain outcrop reveal an average orientation of 091N/49° (Fig. 4.10). This orientation differs from the average orientation of the main foliation present within the immediate deposit area (102N/61°), which is notably steeper than on McClain outcrop, and within range with respect to the strike.

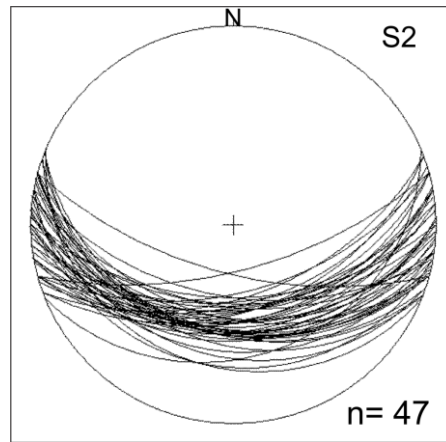


Figure 4.10 : Foliation measurements on McClain outcrop (n=47). S₂ foliations measured on McClain outcrop in all lithologies plotted to a stereonet. Equal area projection, lower hemisphere.

A joint set developed within the coherent dacites (Figs. 3.25, 4.11; appendix I) has also been measured. Joints are evenly spaced and best developed in the more competent intervals of coherent dacite. Average orientations for the main conjugate set are 329N/70° and 199N/74° (Fig. 4.11).

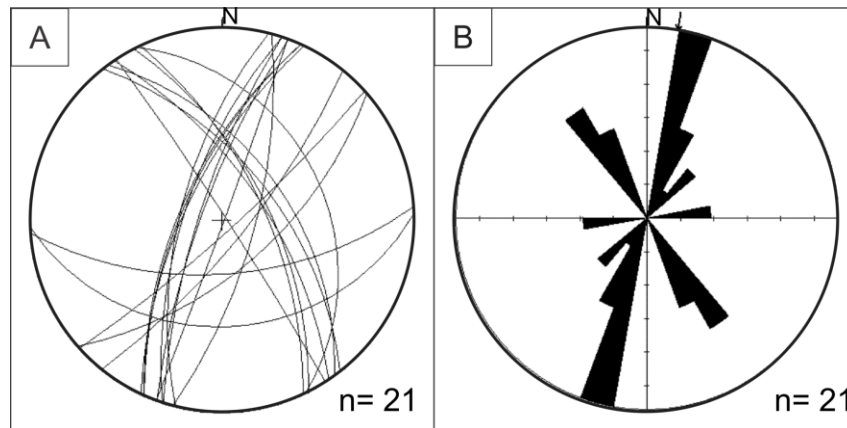


Figure 4.11 : Joint set in coherent dacite on McClain outcrop. A) All measurements (n=21) plotted to a stereonet. B) Azimuth data frequency plot of measurements in A, showing a main orientation set at 199N/74° and 329N/70°. Wulf projection.

4.3.5.2 Scott outcrop: comparison of North and South portions of Scott outcrop

Main foliations present within both portions of the outcrop have similar values, with an average orientation of 131N/69° and a mean standard deviation of 8° in strike and 5° in dip (Fig. 4.12). In the southern part of the outcrop, contacts between the more laminated dacite and brecciated dacite are sub-parallel to the main D₂ foliation. In the northern part of the outcrop, bedding

orientation in graded tuff sequences is set at 087N/70° (Fig. 4.12), which differs from the mean foliation measurements at McClain and Scott outcrop.

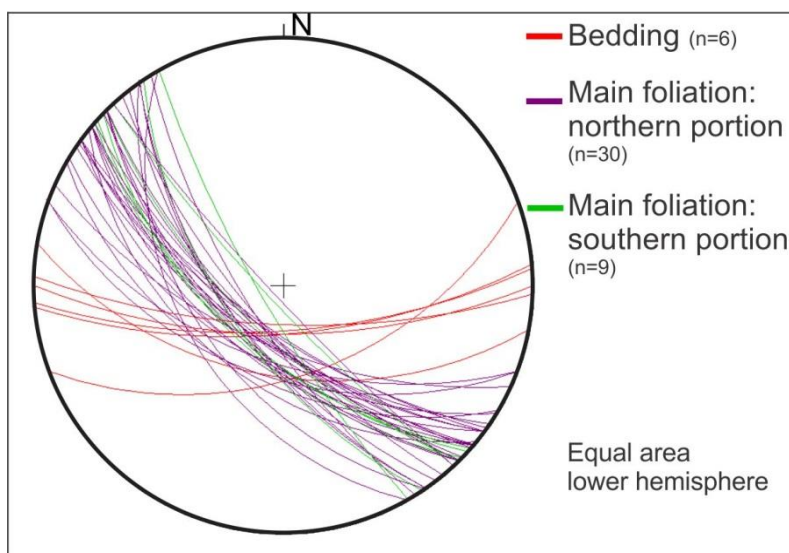


Figure 4.12 : Foliations and bedding measurements on Scott outcrop. Structural data is further discussed in chapter 4 on deformation.

4.3.5.3 Comparison of structural elements from the McClain and Scott outcrops

When comparing the mean orientation of main foliations measured at McClain, the deposit itself and Scott outcrop, we notice a progressive synthetic rotation of strike accompanied by a steepening of the dip when moving southwards on the Rainy River property. This general rotation of strike is highlighted by highly magnetic markers on the raw aeromagnetics map of the Rainy River property (see Chapter 4). This evolution of foliation orientation could, on speculative basis, result from a dextral shear movement of the shear system underlined by the main Quetico Fault located just 4.2 km south of the Rainy River deposit (see section 4.3.1, Figs. 4.3, 4.4). Late folding could also explain the change in the main foliation orientation.

Table 4.1 : Mean foliation orientation measured at mapped outcrops and above the deposit itself

Area	Mean foliation orientation
McClain outcrop (North of deposit)	091N/49°
Rainy River deposit	102N/61°
Scott outcrop (South of deposit)	131N/69°

4.3.6 Timeline of structural events and associated structures in the Rainy River deposit area

A timeline of the structural events and associated structures recorded in the Rainy River deposit area can be outlined by integrating the different structural elements described in this study and in previous structural studies mentioned earlier in this chapter. In chronological order, these structural elements are:

S_0 is pre-deformation and consists in graded tuff units within the dacitic calc-alkaline volcanics, and S_2 -parallel bedding within the mafic-dominated sedimentary units.

D_1 is interpreted at the regional scale as the main compressional event associated with the horizontal north-south shortening during the collision and overthrusting of the Western Wabigoon terrane on the Winnipeg River terrane located to the north (Melnyk *et al.*, 2006). D_1 -related structures at Rainy River are unclear, although certain structural elements could be interpreted as a result of D_2 superimposed on D_1 . These consist in tight, isoclinal folds present in mafic volcanics-dominated sedimentary rocks, and interference patterns in auriferous quartz-carbonate-pyrite veins of the western ODM area. According to Hrabi and Vos (2010), these veins are D_1 in timing and their F_1 fold axes were subsequently rotated parallel to L_2 . Arguably, these auriferous veins of the western ODM area could have had an early- D_2 onset within a protracted D_2 event. Most pre- D_2 structures have probably been overprinted by the strong and pervasive S_2 foliation.

On a regional-scale, the D_2 episode of deformation is associated with continued north-south shortening with an added NW-SE component, which initiated east-west fault zones such as the Quetico Fault, located 4.2 km south of Rainy River. An interpreted splay (second-order structure) of the Quetico Fault is located immediately north of the deposit. This fault could have been initiated earlier in the deformation history and reactivated during D_2 similar to what is interpreted for other crustal faults of the Superior Province, although the determination of the history and timing of the Quetico Fault is beyond the scope of this study.

A strong and pervasive, south-dipping S_2 foliation oriented $102N/61^\circ$ on average is present at Rainy River. Contacts between volcanic units and facies, along with the different ore zones of the Rainy River deposit, have been transposed parallel to S_2 .

An L_2 stretching lineation, oriented $225N/55^\circ$ (108° pitch east to west on the S_2 plane), is interpreted as F_1 fold hinges (Hrabi and Vos, 2010). Ore shoots are collinear with this lineation.

The formation of the auriferous quartz-ankerite-pyrite veins on the surface extension of the Cap zone show shallow dips and have been interpreted by Poulsen (2006) as having a syn- to late- D_2 onset, in response to the elongation responsible for the L_2 stretching lineation.

Drill core and petrographic analyses reveal a high strain corridor at the base (north) of the ODM body and parallel to S_2 . It is a zone of intense, steepened and sometimes kinked S_2 foliation and strong sericite-chlorite alteration.

Kinematic indicators indicate that D_2 and earlier structures are rotated following a steep South over North reversal movement along S_2 , and a dextral shear component is present on surface with a reverse-oblique motion.

Three dimensional modelling of the different ore zones (e.g., El-Rassi and Cole, 2014), detailed outcrop mapping in the deposit footwall and petrographic studies through this study underline secondary, weaker foliation and mineralization trends (S_s and S_{s2} respectively) with respect to S_2 . S_s crenulates S_2 and is therefore late- to post- S_2 in timing.

Brittle-ductile shear zones and brittle faults, approximately north-south-oriented, crosscut S_2 within the deposit area and can also be observed on aeromagnetics map (Fig. 4.3). Brittle faults offset mineralization on the metre scale and record a sinistral movement. Rare brittle faults on un-oriented drill core have remobilized, on a local scale, precious and base metal mineralization (Pelletier *et al.*, 2015).

4.3.7 Previous structural setting interpretations of the Rainy River deposit

Previous studies undertaken on the structural setting of the Rainy River deposit propose diverging structural interpretations. Early work (Blackburn *et al.*, 1976) interpret the immediate vicinity of the Rainy River deposit as being part of a large S-SW plunging antiform, with the S_2 foliation being axial planar. Siddorn (2008) and Hrabi and Vos (2010) indicate that fold axes of deformed quartz veins, boudin necks and ore shoots are all parallel to the L_2 stretching lineation. According to these reports, the current orientation of the ore shoots would result from a rotation of the ore plunge parallel to the L_2 stretching direction in a north-south oriented high strain compressional environment. Later brittle-ductile shear zones oriented at $200N/75^\circ$ offset the Beaver Pond domain with respect to the ODM mineralized body. Brief site visits by Poulsen (2005, 2006) allowed him to determine that the Rainy River project probably sits on an F_2 fold limb of similar orientation than what has been interpreted by Blackburn (1976), and that the F_2

folds in the study area were probably open and in any case not tight enough to see any major stratigraphic repetition, due to an overall southward facing of units in the area.

Another model, proposed by Rankin (2013) and largely based on aeromagnetic patterns, includes five main deformation episodes in the area, although only D_1 and D_2 have great influence on the overall geometry of the deposit. In summary, D_1 , through east verging thrusting and recumbent folding, is responsible for a pervasive S_1 foliation and mineral stretching lineation collinear to the L_1 fold axis. Subsequently, D_2 , which is, according to this model, characterized by ESE-trending upright to overturned folding, refolds S_1 and L_1 . The Rainy River deposit would lie in an F_2 limb, and the ore shoots are confined to F_1 fold hinges present on an F_2 limb. The deposit is later affected by D_3 -related kinking and D_4 brittle senestral offset. D_5 is Proterozoic in age and related to the emplacement of mafic dyke swarms.

4.3.8 Structural setting interpretation for the Rainy River deposit area

The model proposed here consists in a compilation of the observations made through this study and also integrates previous work done in the Rainy River deposit area (e.g., Poulsen, 2005, 2006; Siddorn, 2008; Hrabi and Vos, 2010; Fernandez *et al.*, 2013; Rankin, 2013).

At the regional scale, the N-S to NE-SW oriented shortening is the main tectonic event of the area and is associated with the accretion of the Wabigoon Subprovince onto the Winnipeg River Subprovince to the north. Associated regional metamorphism to the upper greenschist to lower amphibolite peaked after peak D_2 , as shown by the crystallization of late- to post- D_2 , undeformed rim around inclusion-rich garnets recording the S_2 fabric. Within the Rainy River deposit area, the dominant structures observed can be linked to the regional structural events outlined in previous studies (Blackburn *et al.*, 1976; Blackburn, 1991; Melnyk *et al.*, 2006). All polarity indicators, identified in the deposit area by Poulsen (2005) and within this study as well as within the Mather sediments by Fletcher and Irvine (1954), face South. Therefore, it can be suggested that the antiform structure identified by Blackburn *et al.* (1976), if it exists at all, is, in the Rainy River deposit area, open and we do not observe the other limb of the fold. Pre or early- to syn- D_2 auriferous quartz-carbonate-pyrite veins identified within the western ODM zone as well as syn- to late- D_2 auriferous quartz-ankerite-pyrite veins within the surface extension of the Cap zone indicate the presence of fluids early and late during D_2 , whether remobilizing pre-existing Au or introducing auriferous fluids to the system. Nonetheless, the total amount of Au in these veins remains very low in comparison with the total contained Au of the deposit. High

strain zones such as the one recorded at the base of the ODM zone could potentially represent reactivated thrust plane(s), although this remains highly speculative. The latest increment of deformation along these high strain zones is late relative to S_2 , and these high strain zones are thought to be responsible for the swerving of S_2 as well as its sub-horizontal kinking. Post D_2 deflection of mainly E-W oriented structural trends highlighted by aeromagnetism is, according to Poulsen (2005), attributed to several smaller synforms and antiforms. These minor structures are also recorded at the micro scale through the weak crenulation of S_2 by the S_s foliation.

The Rainy River deposit area is located just south of an interpreted splay of the dextral Quetico Fault (Siddorn, 2008) and it has been impacted by this structure that is interpreted to have formed within a NW-SE-oriented transpressive regime (Fernandez *et al.*, 2013). The term transpression used here can be defined as a deformation path combining pure shear and simple shear components (Sanderson and Marchini, 1984). This strain geometry occurs when the deformation zone boundaries are oblique with respect to the converging crustal blocks. Recent models of oblique transpression, where the displacement vector is not restricted to the horizontal plane (Jones *et al.*, 2004; Fernandez and Diaz-Azpiroz, 2009), have generated triclinic flow symmetry with oblique stretching lineation with respect to the shear zone strike and dip.

At Rainy River, the inclined or oblique nature of the stretching lineation with respect to S_2 dip is clear; indicating that a model of triclinic flow within a transpression regime can be considered to explain this geometry (Jones *et al.*, 2004; Fernandez and Diaz-Azpiroz, 2009). Indeed, a transpressive D_2 episode implies a mix of dip-slip and strike-slip movement, which results in a rotation in space during deformation. The observation of rotating structures in both planes parallel and perpendicular to the S_2 foliation at Rainy River supports the oblique transpressive nature of the deformation event in a non-planar (three dimensional) strain deformation environment. This would explain the parallel geometry between the stretching lineation and the F_1 fold hinges that would have undergone rotation during D_2 . It is also in agreement with the interpretation made from the structural study of Hrabí and Vos (2010). Additionally, vertical shear zone boundaries with orthogonal simple and pure-shear components strictly in the horizontal and vertical plane are unlikely to be observed in actual tectonic zones (Fernandez *et al.*, 2013).

When compiling the different structural elements in a three dimensional diagram (Fig. 4.13), one can notice that the present orientation of the L_2 stretching lineation cannot result from the reverse movement as shown on figure 4.13, although kinematic indicators on surface indicate

otherwise. This conflict in shear sense interpretation can tentatively be explained by the existence of an earlier reverse-senestral motion movement generating L_2 followed by dextral shear within an overall complex shear zone history (protracted D_2 event). Alternatively, tilting of the host sequence to the east following dextral shear can orient L_2 (which would still be generated during a dextral transpressive shear event) to the west. Lastly, shear sense indicators on surface might have been misinterpreted. Neither of these interpretations can be proved or disproved at the moment, lacking sufficient data, although the difficulty to combine all the structural elements observed within one single transpressive event underlines the complex structural history of the area.

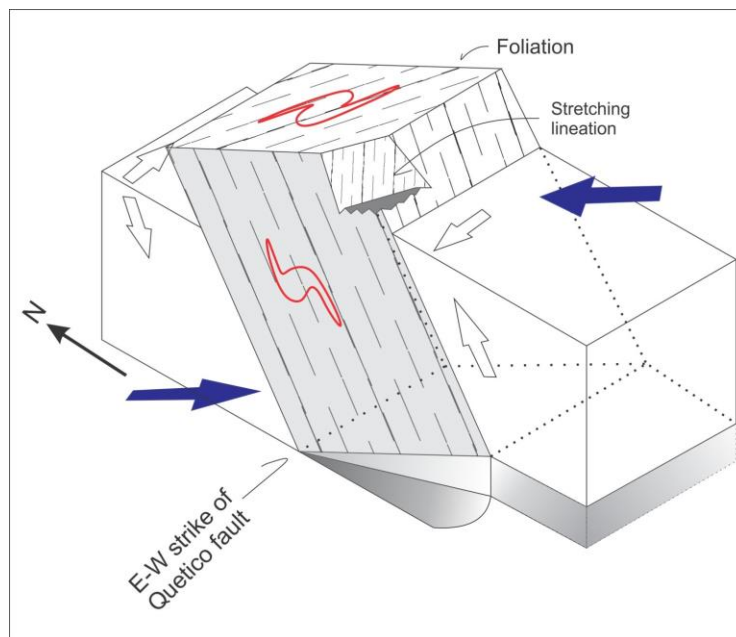


Figure 4.13 : Three dimensional diagram of the different structural elements associated with the D_2 deformation episode observed at the Rainy River deposit within an inclined transpression model. Modified after Jones *et al.* (2004). Blue arrows illustrate the main NW-SE transpressive forces identified by Fernandez *et al.* (2013) for the Queitico Fault. The white arrows are the vertical and horizontal components of the main transpressive vectors. Note the conflict between the dextral shear sense interpretation and the orientation of the L_2 stretching lineation (see text).

4.3.9 Deformation and mineralization

The different mineralized bodies that compose the Rainy River deposit are all parallel to the S_2 foliation, with higher grade ore shoots parallel with the L_2 stretching lineation (Hrabi and Vos, 2010; Pelletier *et al.*, 2014). This strong correlation between the distribution of mineralization in space and structural fabrics associated with D_2 illustrates the importance of structural deformation on the geometry of the deposit. But the role of deformation in the generation,

transport and deposition of mineralization and its post-deposition modifications needs to be taken into consideration in establishing the genesis and evolution of the deposit.

To better understand the relationship between structural deformation and the geometry of the mineralized zones at Rainy River, a composite map plotting the intensity of structural deformation with respect to the different mineralized zones has been constructed. Similar to the oblique composite map presented in the previous chapter, this map represents an oblique plane in space (oriented at 323N/43°) that is perpendicular to L_2 . It was produced from 66 drill holes intercept that have been logged systematically to assess their level of deformation intensity (see Fig. 1.2 for distribution for drill hole intercept on plane). While logging, a number from 1 to 5 was assigned to quantify the deformation intensity related to the D_2 fabrics. Megascopic observations were then verified on thin sections. Criteria used are defined in figure 4.11. Variations on deformation intensity are mostly based on the attitude of the deformed, weakly competent phyllosilicates, as they are present throughout the deposit and in every studied sample. Levels two and three of deformation intensity are characterized by anastomosing veinlets of phyllosilicates generally parallel to the main foliation (S_2), with an increased level of transposition within S_2 for level three. Level four is characterized by intense, planar, S_2 -parallel bands of phyllosilicates, whereas level 5 intervals are characterized by the dominant S_2 planar fabric in phyllosilicate-dominated samples. The classification of deformation intensity was done without taking into consideration minerals that were formed post- D_2 and therefore do not record S_2 .

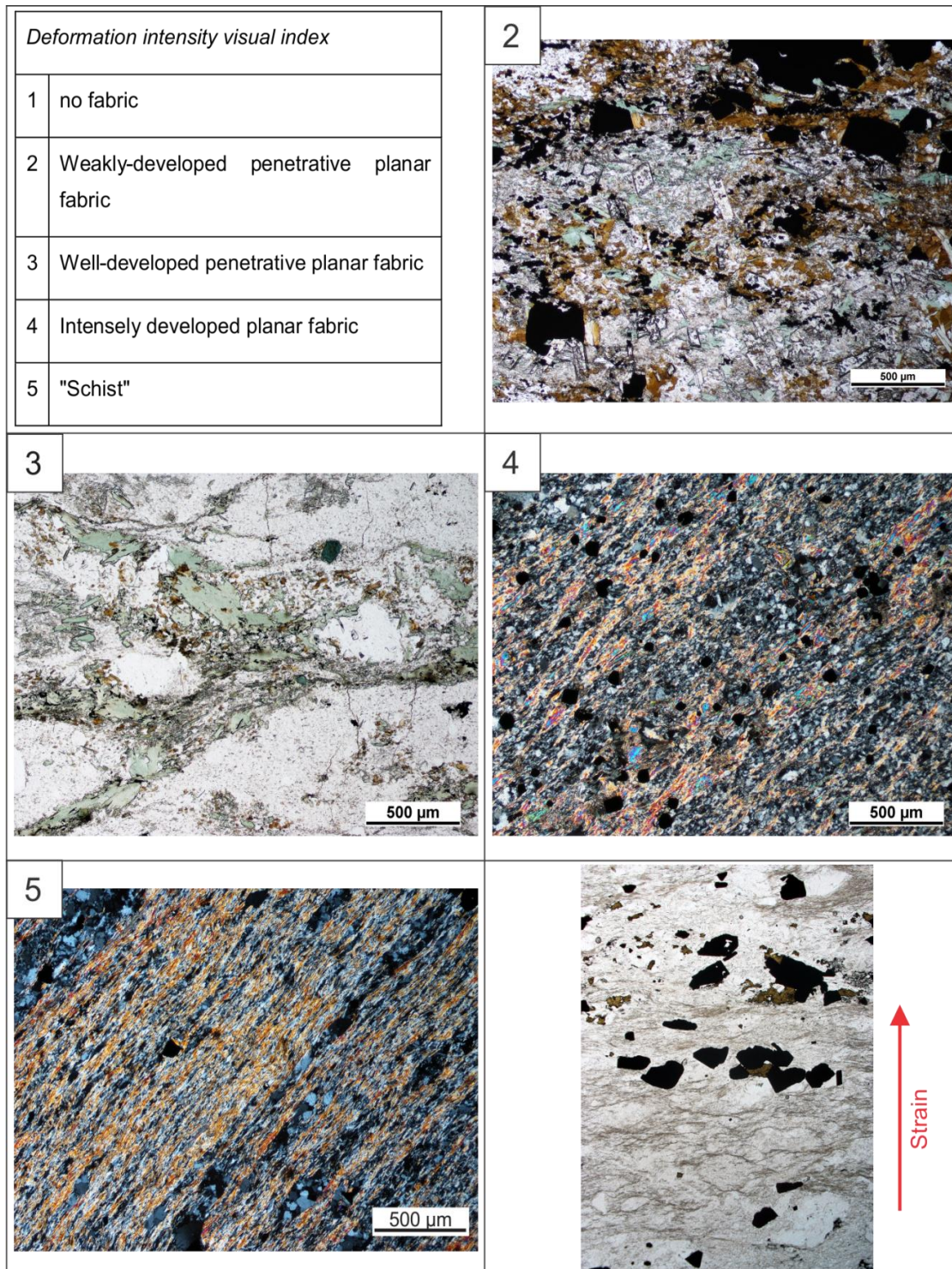
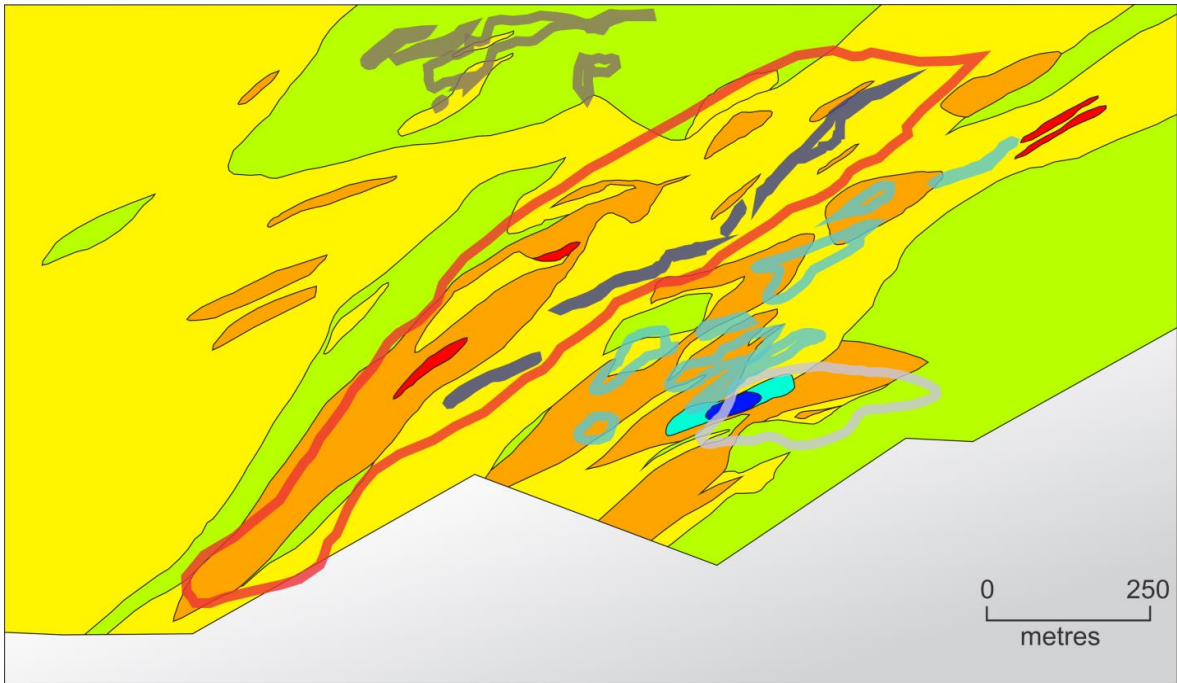


Figure 4.14: Deformation intensity visual index with associated reference sample photomicrographs. 2: Sample RRR435912, McClain outcrop, NAD83, zone 15, 426152 mE, 5410300 mN. 3: Sample RRR435780, DDHNR060058 at 191 m (ODM HW). 4: Sample RRR435786, DDH NR060058 at 326 m (ODM zone). 5: Sample RRR435787, DDH NR060058 at 353 m (ODM zone). Last photo shows strain partitioning at the microscopic scale, exposing the heterogeneity in the distribution of stain expressed by S_2 . Sample RRR435795, DDH NR060058 at 480 m (HS zone).

Error in the determination of deformation intensity through the process explained above may be induced through the varying initial content of weakly competent phyllosilicates within the host rock prior to deformation, as phyllosilicates are more susceptible of recording higher deformation intensity than more competent minerals. Even so, when comparing together the oblique planes illustrating the distribution of sericite alteration intensity (presented in chapter 5; Fig. 5.8) and deformation intensity (Fig. 4.12), zones of high sericite content are not directly correlated with zones of intense deformation as would be expected if deformation intensity was strictly controlled by initial mineralogical composition. Distribution of deformation intensity is therefore not solely controlled by the pre-deformation mineralogy of the host rock but rather has additional controls on its partition.

Based on information recorded on the oblique plane map (Fig. 4.12) and drill core logging, there is no direct correlation between the spatial distribution of mineralized bodies and the intensity of D_2 deformation. Indeed, the shape and distribution of the different mineralized zones do not correlate with the size, shape and distribution of zones of higher or weaker deformation intensity. The stacking of mineralized zones also cannot be explained by deformation partitioning. The distribution of deformation intensity on the oblique plane (Fig. 4.12) also highlights the high strain zone located within the ODM body hanging wall.

In light of this, we can propose that D_2 -related structural deformation cannot be the main control for the stacking geometry of the mineralized zones, although the intensity of the D_2 strain, expressed by S_2 and L_2 fabrics, controls the distribution of the high grade ore shoots and shape within the mineralized bodies. Based on this, timing of mineralization at Rainy River is most likely pre- to early- D_2 , although structural elements associated to D_2 (S_2 and L_2) have greatly affected the geometry, distribution and grade of the mineralization, which is now concentrated along the L_2 lineation in bodies parallel to S_2 .



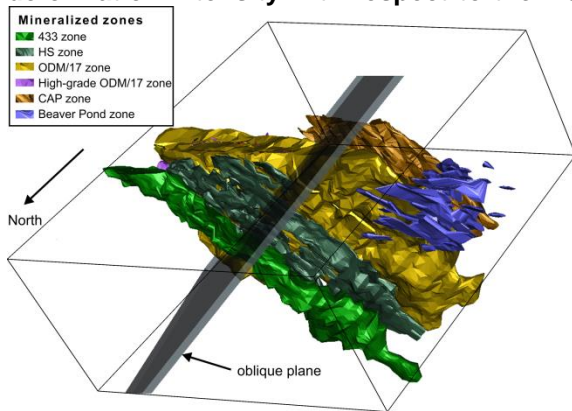
Legend

■ 0 None
 ■ 1 Very weak
 ■ 2 Weak
 ■ 3 Moderate
 ■ 4 Strong
 ■ 5 Very strong

Outlines of mineralized zones:

— Cap zone
 — High-grade ODM/17
 — ODM/17
 — HS zone
 — 433 zone

Figure 4.15 : Oblique plane oriented perpendicular to L_2 ($323N/43^\circ$) illustrating the distribution of deformation intensity with respect to the main mineralized zones of the deposit. Note the higher deformation intensity in the ODM body footwall and HS zones.



5 HYDROTHERMAL ALTERATION

5.1 Introduction

Mineral assemblages formed through hydrothermal activity are products of chemical reactions as elements are transferred and exchanged between the hydrothermal fluid and the host rock. In most mineralized systems, characteristic hydrothermal mineral assemblages spatially associated to mineralized structures or bodies are developed over an area greater than the mineralization itself (e.g., Spooner and Fyfe, 1973; Galley, 1993) forming a hydrothermal footprint commonly used by explorationists to outline potentially fertile areas and vector towards mineralization (e.g., Ishikawa et al., 1976; Franklin, 2005; Piercey, 2009).

Hydrothermal alteration at the Rainy River deposit has been characterized in order to assess its nature, distribution, and intensity as well as to establish its timing relative to volcanism, tectonic events, metamorphism, and mineralization.

This chapter first reviews the different protoliths within the deposit area, followed by an assessment of alteration intensity using common alteration indices. This evaluation is followed by a description of the different alteration minerals present and their distribution relative to the mineralized zones. This is presented using the oblique plane (323N/43°), a cross section, and composite down hole profiles. The distribution of the alteration assemblages and their spatial variation in intensity with respect to structural elements and volcanic facies is discussed. Microprobe data on phyllosilicates and other alteration minerals and their metamorphosed equivalents is presented as part of the description of the different alteration minerals. Microprobe analytical results are provided in Appendix II.

Subsequently, mass variation calculations (MacLean and Barrett, 1993) with reference to a least-altered protolith are presented in order to quantify alteration intensity and illustrate potential zonation of hydrothermal assemblages with respect to mineralization.

In addition to that, oxygen isotopic ratios were measured in selected sample pulps from the deposit area and its vicinity to outline a potential characteristic isotopic signature and potential hydrothermal fluid pathways.

Work presented in this study builds on previous interpretation and description made by Wartman (2011) as part of his thesis along with personal communications and internal documentation provided by the geology staff at the Rainy River project. Assay database used

for describing hydrothermal alteration of the Rainy River deposit consists of whole-rock lithogeochemistry from a large suite of samples (327) collected by the author. The data and analytical procedures are presented in Pelletier *et al.*, (2016).

5.2 Deposit scale: protoliths and intensity of alteration

The whole rock and immobile trace element geochemical signatures of the altered rocks are strongly dependent on their initial geochemical composition. Definition and characterization of alteration nature and intensity is therefore strongly dependent on a good identification of the different protoliths from which the altered rocks are issued.

At Rainy River, five different lithological groups have been previously outlined in this study (section 3.2) based on their REE profiles; a calc-alkaline dacite, a tholeiitic basalt, mafic volcanic-dominated siltstones, a tholeiitic amygdaloidal basalt, and tholeiitic basalts with an anomalous positive Nb-Ta composition (Fig. 5.1). In this chapter, they are the five lithogeochemical groups that will be used for selection of the least-altered protoliths. These representative protoliths will be used when discussing alteration assemblages and mobility of the major and trace elements.

When looking at a Ti-V bivariate plot (Fig. 5.2), an additional lithological group, represented by samples in pink located outside the main Ti-V trend, is outlined. This group consists in tholeiitic basalt samples with characteristic rutile-dusting and granoblastic pyrite. Although, when comparing their REE profiles with the ones from the main tholeiitic basalt lithological group (Fig. 5.3), their almost identical mean values indicate a common protolith. Therefore, these rutile-rich samples are part of tholeiitic basalt lithological group, but have undergone alteration and/or remobilization involving a titanium-vanadium decoupling. In light of this, the rutile-rich tholeiitic basalts will be considered as an alteration assemblage part of the main tholeiitic basalt group rather than an additional lithological group.

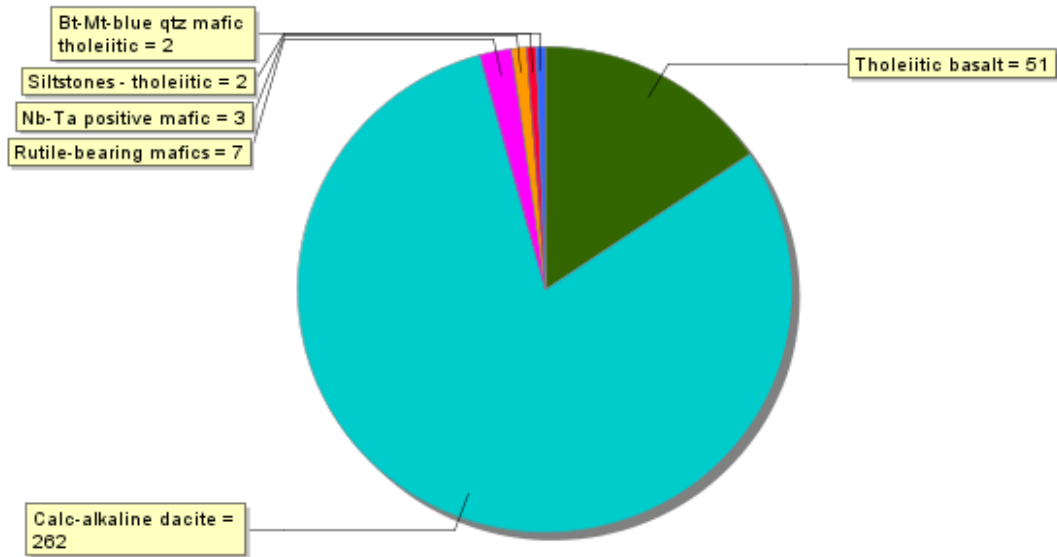


Figure 5.1: Pie chart of all samples from this study (n=327) and their lithological units outlined from the Ti-V bivariate plot.

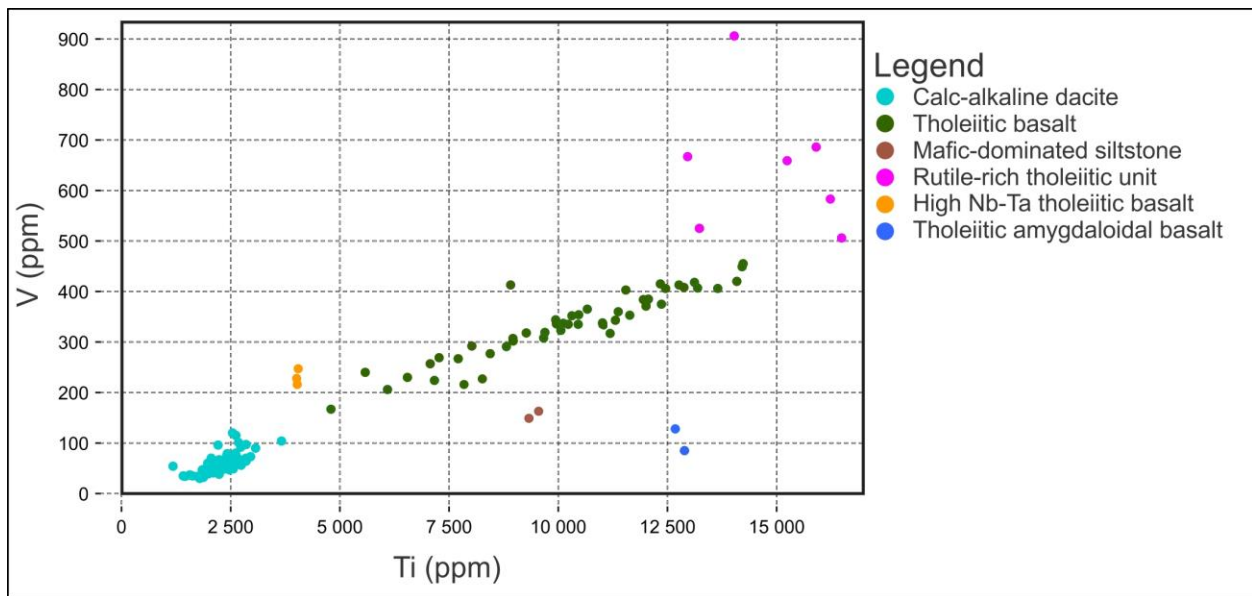


Figure 5.2 : Titanium-vanadium bivariate plot showing the different lithological groups at Rainy River.

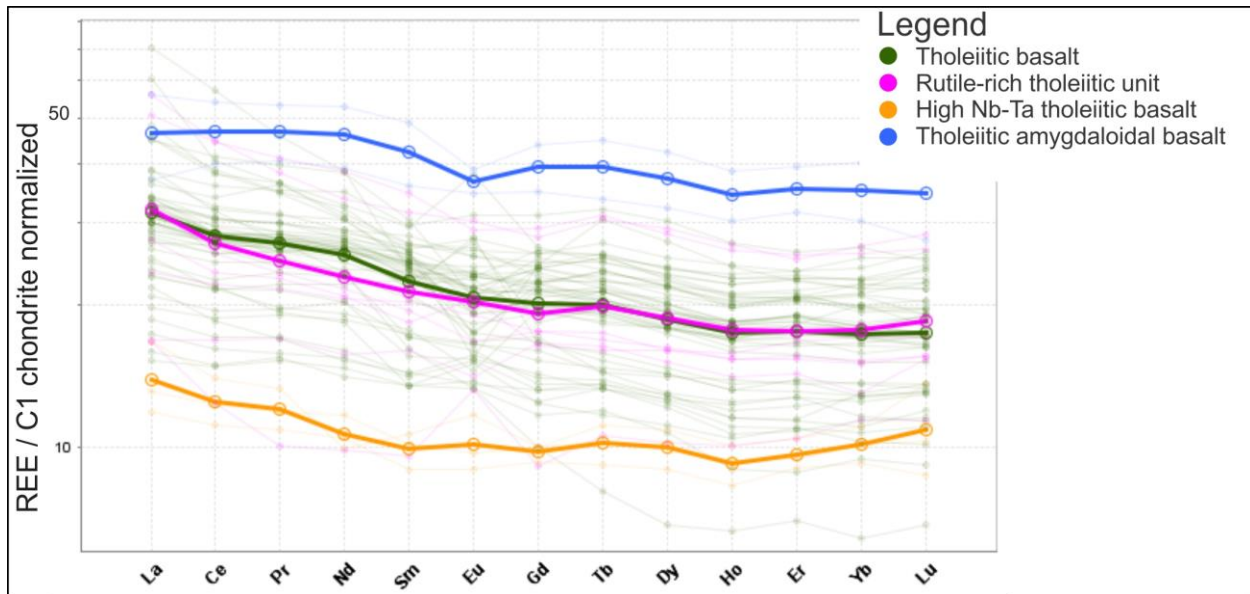


Figure 5.3 : REE profiles of tholeiitic rocks, using the same legend as in 5.1 and 5.2. Mean profiles for each group are represented in bold. The rutile-rich group (in pink) has an average profile almost identical to the average profile of the tholeiitic basalts (green), indicating a common protolith, although samples in pink, through alteration, have undergone a Ti-V decoupling (see fig. 5.2). Chondrite normalization values from McDonough and Sun (1995).

Prior to presenting the various alteration assemblages and minerals present at Rainy River, an overview of the alteration intensity using known alteration indices and diagrams allows for a recognition of the level of alteration of volcanic rocks from this study in comparison to other known hydrothermally-altered deposits. Common alteration indices (e.g., Ishikawa *et al.*, 1976; Large *et al.*, 2001a) were developed from the documentation of recurring element gains and losses of some mobile major elements involved during alteration processes in volcanogenic massive sulphide deposit environments. Although these alteration indices were not developed for gold deposits, the intermediate to felsic volcanic environment and probable submarine setting is to some extent similar to that of volcanogenic massive sulphide systems, and more particularly their deeper, sub-seafloor reaction zones, allowing for some comparisons (see chapter 7 for a discussion about the interpreted environment of formation for the deposit). In those indices, elements gained are normalized against elements lost during alteration, resulting in an increasing index value correlated to increased alteration intensity. Combining two alteration indexes as an XY plot (Large *et al.*, 2001a; Williams and Davidson, 2004) delineates linear alteration trends, starting from the least-altered box and ending at alteration mineral nodes along the perimeter of the box plot.

The alteration box plot (Fig 5.4; Large *et al.*, 2001a; Trépanier, 2011; Bigot, 2014) using the Hashimoto index (AI; Ishikawa *et al.*, 1976) and the chlorite-carbonate-pyrite index (CCPI; Large *et al.*, 2001a) shows that approximately a third of the calc-alkaline dacite samples plot within the least-altered box, determined by Trépanier (2011) through statistical analyses of an extensive dataset of un-altered rocks throughout the Superior Province. The remainder of the dacite samples are positioned along the pure muscovite, combined sericite+chlorite+pyrite generation trend. Since the alteration box plot highlights alteration trends (blue arrows on Fig. 5.4), a sample positioned within the least-altered field might be the result of superimposed alterations “cancelling” each other in terms of geochemical ratios. In light of this, this diagram has to be used with caution and, by itself, cannot be considered a reliable indicator of alteration intensity at Rainy River. As for the tholeiitic basalts, they show clustering below the ankerite and chlorite poles. They all have a high CCP index due to their high initial iron and magnesium content.

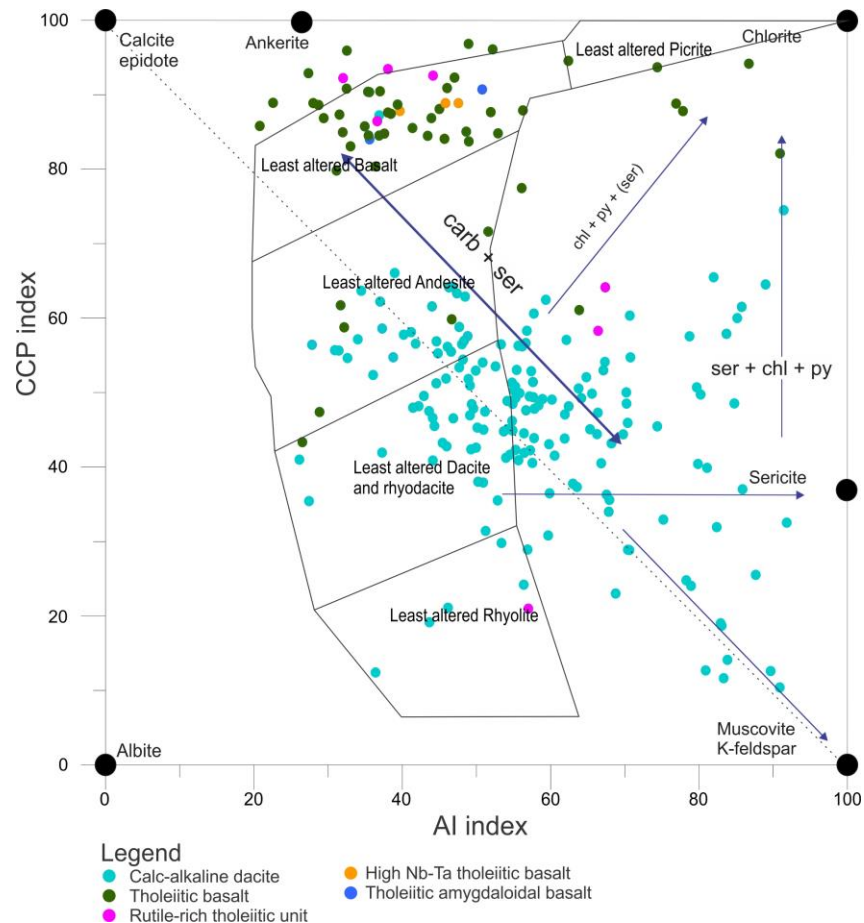


Figure 5.4 : Modified Alteration box plot from Large *et al.* (2001a) with least-altered fields from Trépanier (2011) and Bigot (2014) using the Hashimoto index (AI; Ishikawa *et al.*, 1976) and chlorite-carbonate-pyrite index (CCPI; Large *et al.*, 2001a). This diagram contains samples from this study (n=321), using the same colour code as figs 5.1-5.3. $AI = 100 \times ((K_2O+MgO)/(K_2O+MgO+CaO+Na_2O))$, $CCPI = 100 \times ((Fe_2O_{3T}+MgO)/(Fe_2O_{3T}+MgO+K_2O+Na_2O))$.

Similarly, a plot of the Hashimoto index (AI; Ishikawa *et al.*, 1976) versus the advanced argillic alteration index (AAAI; Williams and Davidson, 2004) illustrates a majority of samples within or just above the range of un-altered or least-altered rocks, with a dominant trend towards the muscovite pole (Fig. 5.5). In this box plot, the least-altered box was defined in the AAAI by the spread in propylitically altered samples in the Williams and Davidson (2004) study and in the AI by the study from Large *et al.* (2001a). Despite this seemingly weak alteration intensity, few samples from the deposit plotted close to the pyrophyllite and kaolinite poles, underlining areas of argillic-style alteration within the deposit. These samples with combined weak AI and strong AAAI are all kyanite and chloritoid bearing. This alteration mineralogy is further discussed in section 5.3.4.

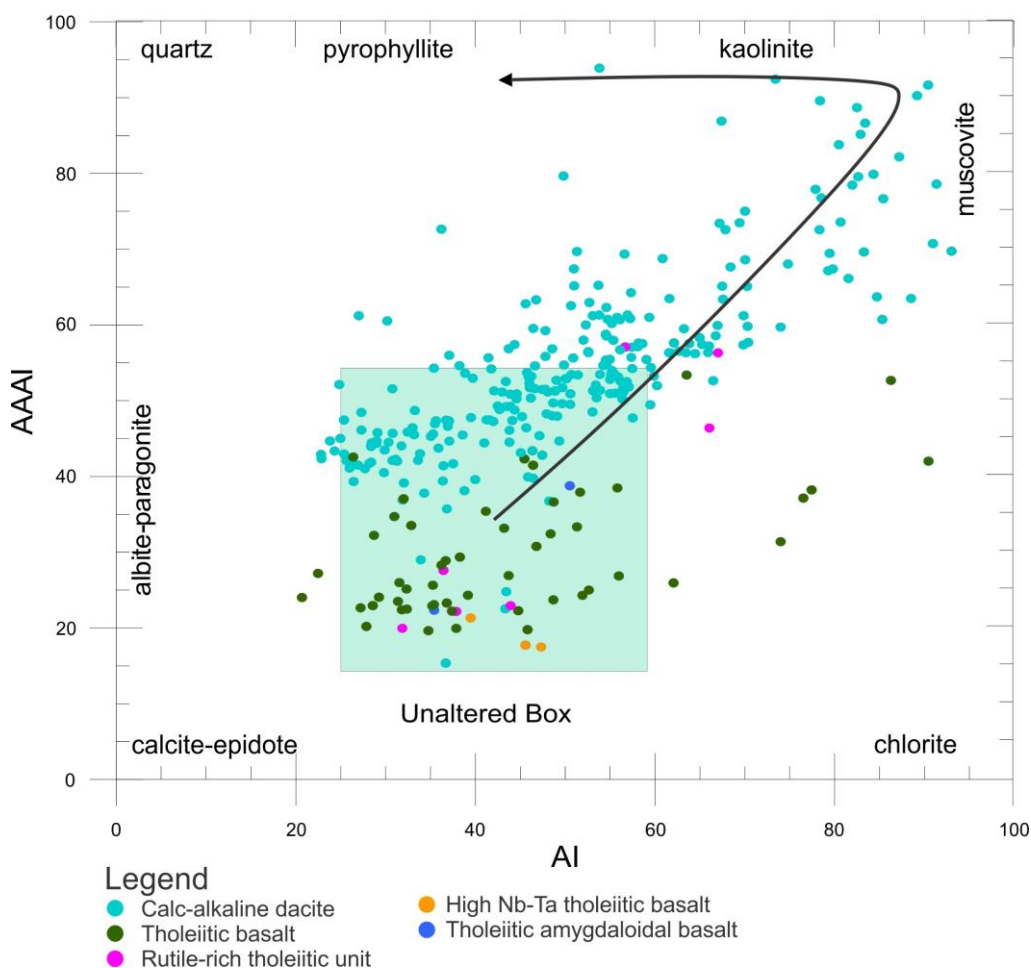


Figure 5.5 : Hashimoto index (AI; Ishikawa, 1976) versus advanced argillic alteration index (AAAI; Williams and Davidson, 2004) in a modified box plot. Samples from this study (n=321) are shown using the same colour code as previous figs. 5.1 to 5.4. $AAAI = 100 \cdot \frac{SiO_2}{(SiO_2 + 10 \cdot MgO + 10 \cdot CaO + 10 \cdot Na_2O)}$, (Williams and Davidson, 2004).

An overall weak alteration intensity, according to those indices, within the immediate deposit area at Rainy River distinguishes it from known mineral deposits associated to zoned hydrothermal systems with major fluid flow, for example VMS deposits (Franklin *et al.*, 2005) or porphyry deposits (Seedorff *et al.*, 2005), where samples present in proximity to the ore zones are generally systematically characterized by high alteration index values.

5.3 Alteration mineralogy: nature, distribution and composition

Previous work at Rainy River (Wartman, 2011) recognizes the ubiquitous distribution of chlorite and sericite¹, making it difficult to map spatially-distinct alteration assemblages. Indeed, in addition to being the products of hydrothermal alteration, chlorite and sericite are also formed during regional greenschist metamorphism at Rainy River (Wartman, 2011). The alteration was thus characterized using secondary alteration minerals observed at the macro and micro scales. Wartman (2011) divided his samples into five categories (least-altered, moderately sericite-altered, strongly sericite-altered, epidote-bearing, and chlorite-carbonate-altered).

In this study, the initial sample classification resembles the one proposed by Wartman (2011) as it is also based on the presence of secondary alteration minerals, also documented at the macro and micro scales. In addition to the previously identified epidote, garnets and carbonates, albite, aluminosilicates and rutile phases have been identified in this study.

This following section includes a description of the different alteration assemblages documented by the author at Rainy River. Each mineral is described using data gathered from detailed logging and petrographic work, as well as microprobe analyses when applicable. Distribution in space of these minerals is based on drill core data and illustrated on both the geological vertical cross section and oblique plane (see section 5.3.7). Information is presented here starting with the most abundant minerals (sericite and chlorite), followed by the secondary alteration minerals, presented in order from the structural and interpreted stratigraphic hanging wall (south) working towards the footwall (north) of the deposit.

¹ The term sericite used here refers to white micas observed at both the macro and micro scales. Further information on the nature and composition of white micas from Rainy River can be found in section 5.3.1 and Appendix II.

5.3.1 Sericite- and chlorite-dominated alteration zones: composition, intensity, and distribution

Sericite and chlorite, the dominant alteration minerals at Rainy River, can account for up to 40 area % of the rock and are present throughout the deposit area (Wartman, 2011). Core logging, detailed petrographic work, and microprobe analyses on both chlorite and sericite are presented below with an emphasis on the alteration assemblages developed in the calc-alkaline dacitic rocks.

5.3.1.1 Sericite

As highlighted in previous work (e.g., Franklin, 2001; Wartman, 2011; Pelletier *et al.*, 2014, 2015), the Rainy River deposit is characterized by sericite-dominated alteration assemblages. This observation is supported by the strong aluminous alteration trend of samples underlined by the alkali-alumina molar ratio in the Davies and Whitehead (2006) diagram (Fig. 5.6). On this diagram, “fresh” or least-altered samples cluster along the albite-muscovite line, about two thirds of the way to the muscovite pole. From there, the main alteration follows this albite-muscovite line, although it describes two different chemical reactions. The first reaction along the albite-muscovite line consists in albitization of the fresh samples (samples in yellow on diagram) followed by later plagioclase destruction- muscovite generation (samples in blue on diagram), generating a “back-and-forth movement” along the albite-muscovite line. A hydrothermal alteration-related provenance of albite is reinforced by the presence of albite (An_{0-10}) in mineralized samples of the ODM zone (see Fig. 3.9). This sequence in alteration is determined by the documentation of a systematic replacement of albite microphenocrysts by S_2 -parallel sericite and other alteration minerals. An additional trend towards aluminous but non-alkali minerals (for example chlorite, epidote and topaz) is also underlined (in purple on diagram).

The two alteration processes along the albite-muscovite line of the alkali-alumina molar ratio diagram (Davies and Whitehead, 2006; Fig. 5.6) are also verified through a Rb-K₂O plot (Fig. 5.7). This bivariate plot is based on the fact that Rb is incorporated into micas, but not into feldspars (Franklin, 2005), resulting in combined high K₂O and low Rb concentrations in albite-bearing samples, high Rb versus K₂O concentrations in muscovite-rich samples, and combined depleted K₂O and Rb concentrations in aluminous, non-alkali altered samples.

The fact that a majority of samples are located along the albite-muscovite trend on the molar ratio diagram of Davies and Whitehead (2006) underlines the importance of these minerals in the metamorphosed hydrothermal alteration at Rainy River. This reaction will be further discussed in the section on mass balance calculation and oxygen isotopes (sections 5.4 and 5.5 respectively).

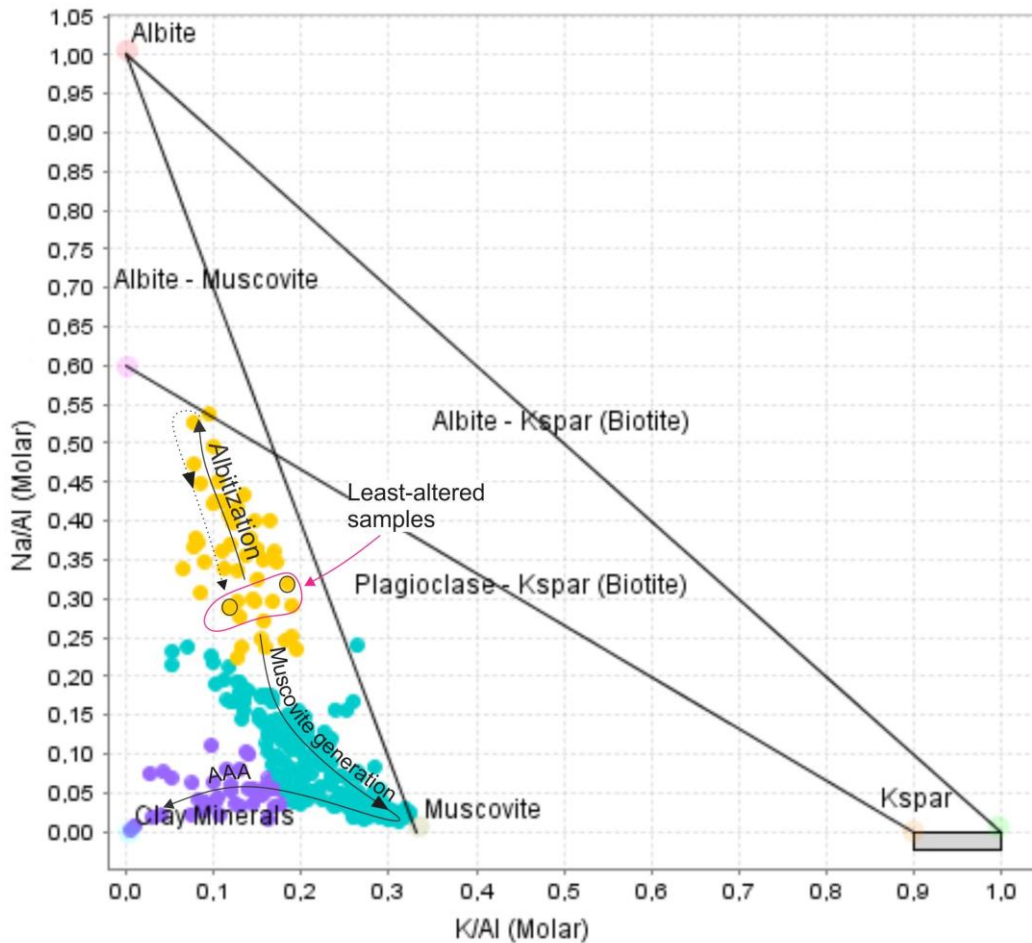


Figure 5.6 : Alkali-alumina molar ratio diagram (Davies and Whitehead, 2006) with all dacitic samples (excluding intrusives; n=256), illustrating a fresh population along the albite-muscovite line (circled in pink). Altered samples plot along the albitization trend (in yellow: n=47), the albite destruction-muscovite crystallization trend (blue, n=165), and finally towards the clay minerals (and/or epidote), chlorites and topaz pole (purple, n=42).

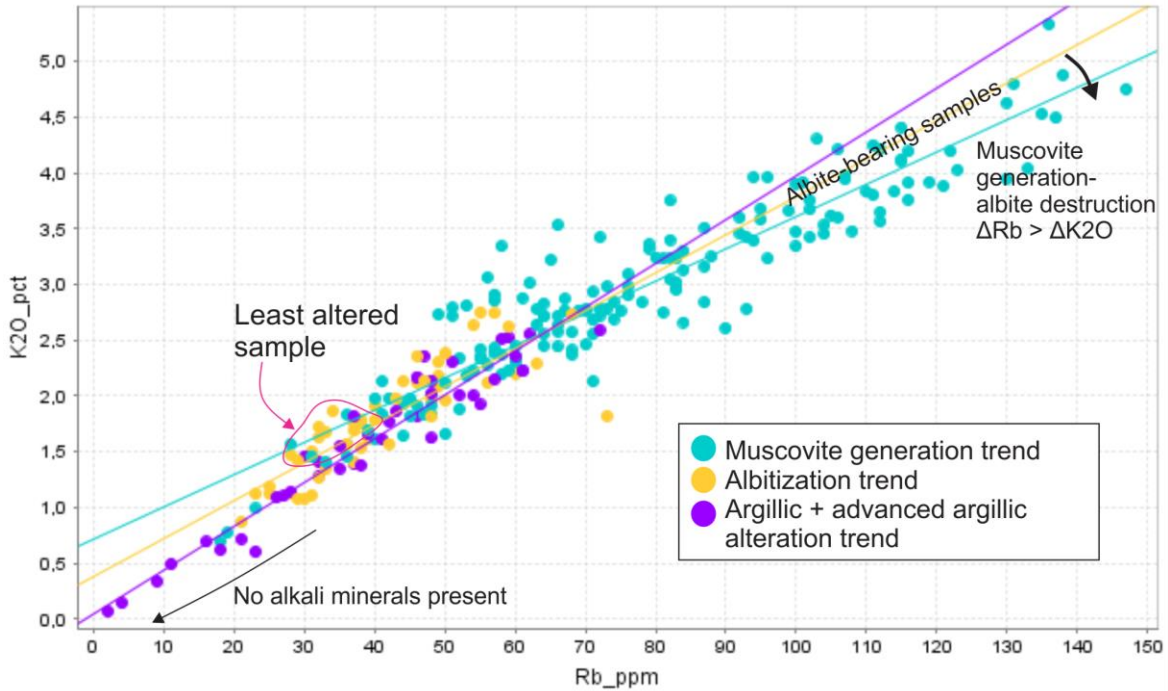


Figure 5.7 : K₂O (%) versus Rb (ppm) plot of all dacitic samples (excluding intrusives, n=256) with same legend as Fig. 5.6, demonstrating high Rb content of muscovite-rich samples (blue), and Rb and K₂O leaching of samples along the non-alkali mineral formation trend (purple). See text for more information.

Sericite within the deposit occurs as sparse to abundant bands and veinlets parallel to the S₂ plane (Fig. 5.8A) as well as replacing, partially to completely, relict hydrothermal-related albite grains within the coherent dacite (Pelletier *et al.*, 2015) (Fig. 5.8B). High strain zones are also characterized by abundant sericite content (up to 35 vol. %), occurring in S₂-parallel veinlets overprinted by kink bands (Fig. 5.8C). Within volcanoclastic facies, sericitization affects both matrix and clasts (Fig. 5.8D).

Sericite occurs in association with all secondary alteration minerals, with the exception of the intense kyanite-chloritoid-quartz alteration zones (see section 5.3.4). Sericite is also part of the regional background (*i.e.* in least-altered samples) in abundances of up to 5 area % (Wartman, 2011). Regional background sericite is un-oriented, and overprints the S₂-foliation, indicating a post peak deformation timing (Wartman, 2011). In this study, sericite grains overprinting the S₂ foliation were only observed in traces (<1 vol. %) in less than a dozen samples.

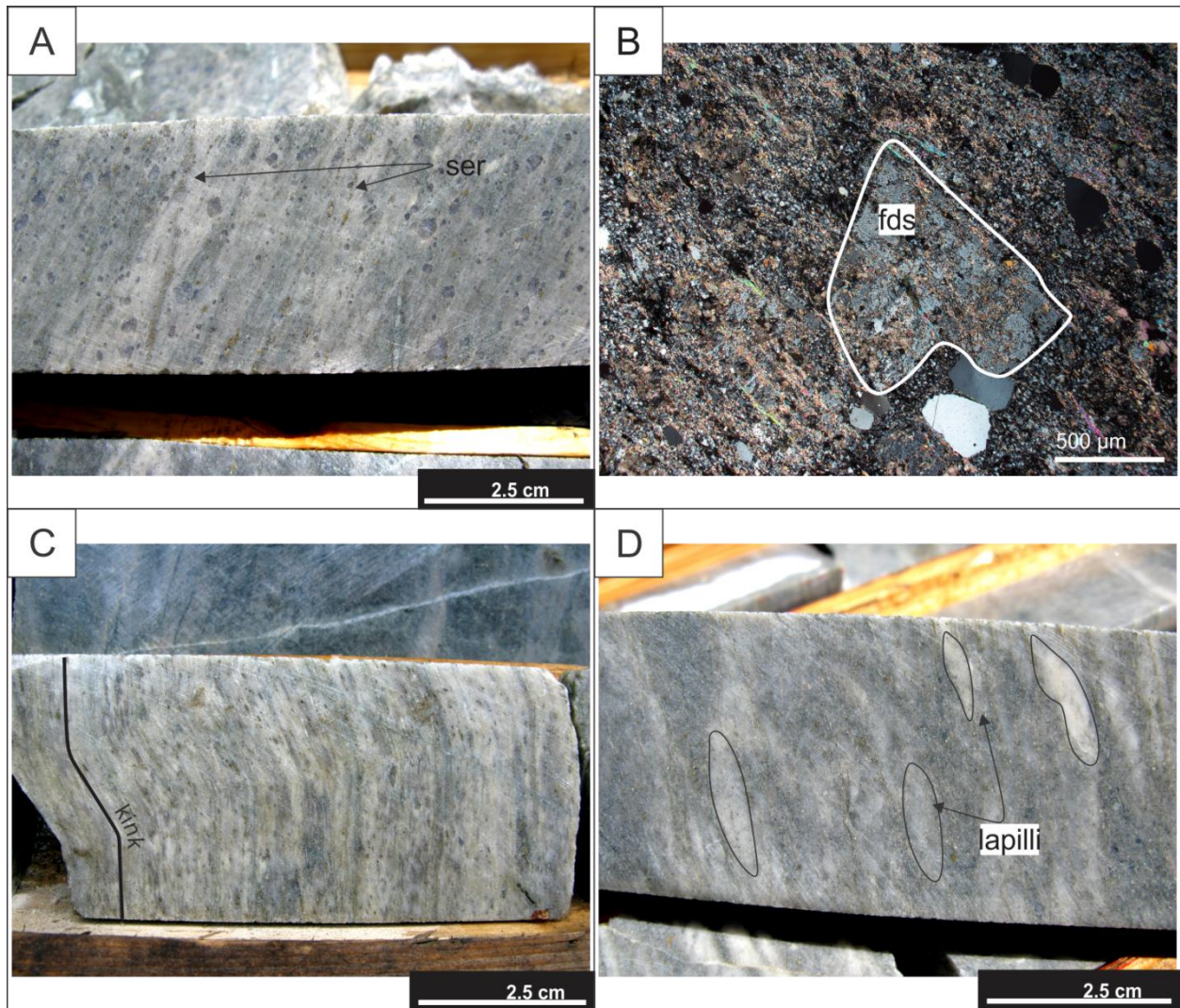


Figure 5.8 : Sericite. A. Sericite in veinlets and bands parallel to S_2 in dacite flow of the ODM zone. DDH NR100600 at 240m. B. Photomicrograph (PL) of sericite grains replacing earlier feldspar microphenocryst in quartz and feldspar-phyric dacites from the ODM structural hanging wall. Sample RRR435775, DDH NR060058 at 71m. C. Kink bands in sericite-dominated schist part of a high strain zone within the HS mineralized body. DDH NR060043E at 460m. D. Sericite-altered lapilli and matrix in dacitic volcaniclastic facies of the ODM high grade zone. DDH NR070141 at 205m.

Representation of sericitization intensity on the 323N/43° oblique plane via detailed core logging (Fig. 5.9; see section 1.3.1 for methods) illustrates a good correlation, in both shape and size, between the dacite-hosted mineralized zones and areas of strong sericitization. This would support a link between gold mineralization and the aluminous and potassic, sericite-dominated alteration.

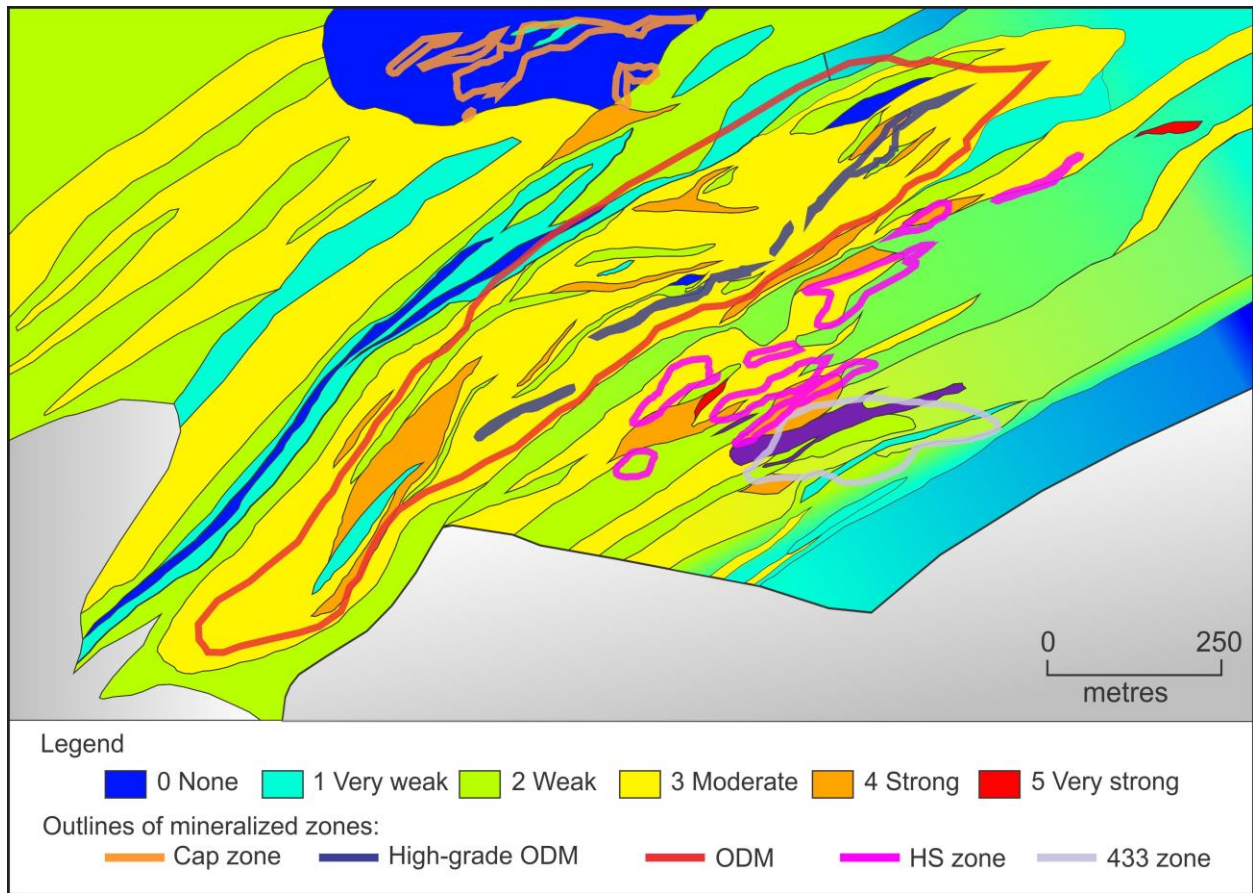


Figure 5.9 : Oblique plane (323N/43°) representing the distribution of sericite alteration intensity based on detailed core logging. Note the good correlation between the zone of moderate to strong sericite alteration and the ODM mineralized body (in red). Zones of absent sericite alteration are correlated to mafic bodies. Body in purple at bottom of map corresponds to un-deformed and un-altered gabbroic body.

At the McClain outcrop (Fig. 3.25; appendix I), sericite represents the main alteration mineral. Coherent dacite and dacitic tuffs have been sericitized to various degrees, and from visual observations, the intensity of sericitization directly correlates with the percentage of sulphides present. Estimated abundance of sericite varies from trace in least-altered samples to 15 vol.% in most altered and mineralized areas. Thin section study of a mineralized coherent dacite sample reveal that sericite is fine grained and occurs as disseminations within the matrix or as rare folded veinlets weakly transposed into the main foliation plane (Fig. 3.27D).

5.3.1.2 Microprobe analyses

Microprobe analyses (see Appendix II for data and analytical procedures) were conducted on sericite grains at Rainy River to test a potential compositional zonation of the white micas within

the volcanic rocks. In other Archean hydrothermal-related deposits, a clear compositional zonation of the white micas can be established between different alteration assemblages but also with respect to mineralization (e.g., LaRonde Penna: Mercier-Langevin, 2005; Bousquet 2-Dumagami: Dubé *et al.*, 2014; Lemoine: Mercier-Langevin *et al.*, 2014; Westwood: Yergeau, 2015).

One hundred and twenty-seven sericite grains from 36 samples across the deposit returned valid compositional data (i.e., total quantitative composition between 98 wt. % and 102 wt. %, see Appendix II). All sericite grains are of muscovite composition, with the Mg-rich ones approaching the phengitic composition. There is no clear association between sericitization intensity and specific muscovite composition. Gold mineralization is associated, in dacitic samples, with Mg-rich (low Fe/(Fe+Mg) ratio) muscovite (Fig. 5.10). Fluorine and chloride contents of muscovite are low, and do not correlate with Au values ($r^2 < 0.05$).

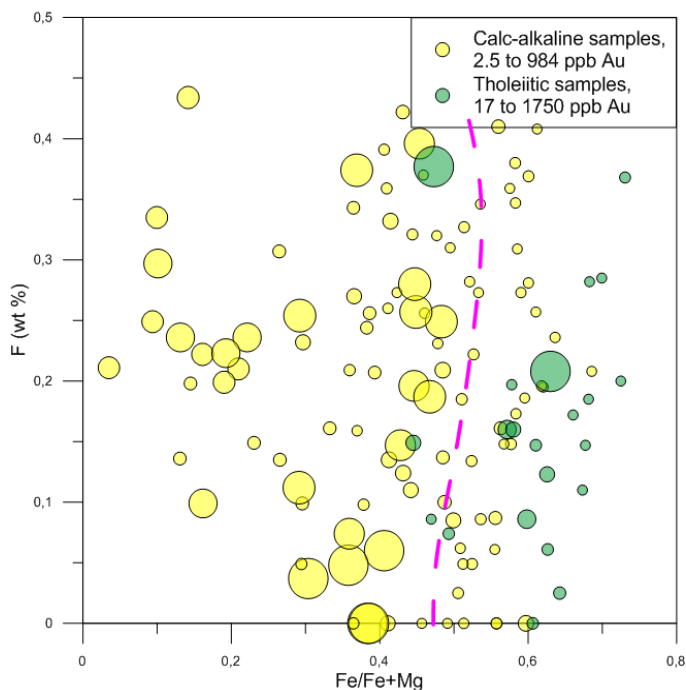


Figure 5.10 : Bubble plot of fluorine versus Fe/(Fe+Mg) ratio for muscovites within the Rainy River deposit. Bubble size is proportional to Au content of sample. In green are muscovites from tholeiitic-affinity samples (n=22) and in yellow from calc-alkaline samples (n=105). The dotted pink line represent the threshold Fe/(Fe+Mg) value in muscovite for Au mineralization in dacites.

5.3.1.3 Chlorite

Chlorite represents the second most abundant alteration mineral at Rainy River, after muscovite. Chlorite is common in all mineralized zones, at varying abundance (estimated from

core logging and petrographic work) with up to 10 vol. % in dacite, and up to 30 vol. % in mafic volcanics. In mafic volcanics, chlorite distribution is difficult to establish, due to the fine-grained nature of the mineral and the overall groundmass colour of the basalts that is very similar to the one of chlorite. Modelled distribution of chlorite (Fig. 5.11) highlights zones of high abundance in the ODM zone structural footwall as well as at the centre of the ODM zone, in both cases primarily as S_2 -transposed veinlets. Mafic rocks systematically possess higher chlorite concentration due to their initial high iron and magnesium content.

In dacite, chlorite occurs in narrow veins and veinlets that are boudinaged along S_2 (Fig. 5.12A) or folded and transposed into the S_2 fabric (Fig. 5.12B), as veinlets (≤ 1 mm) and rare ≤ 2 cm veins (Fig. 5.12C), blebs, clots, as well as rimming disseminated pyrite grains (Fig. 5.12D) (Pelletier *et al.*, 2015).

Chlorite is also present within the dacitic flows of the McClain outcrop (Fig. 3.25; appendix I). It is present in folded veins varying in width from <1 to 10 cm and affected by the later brittle senestral offset structures (Fig. 3.29C). On thin section, chlorite grains are un-oriented and coarse when compared to the sericite grains. They occur within the matrix as well as in replacement structures of remnant feldspars (Fig. 3.27F).

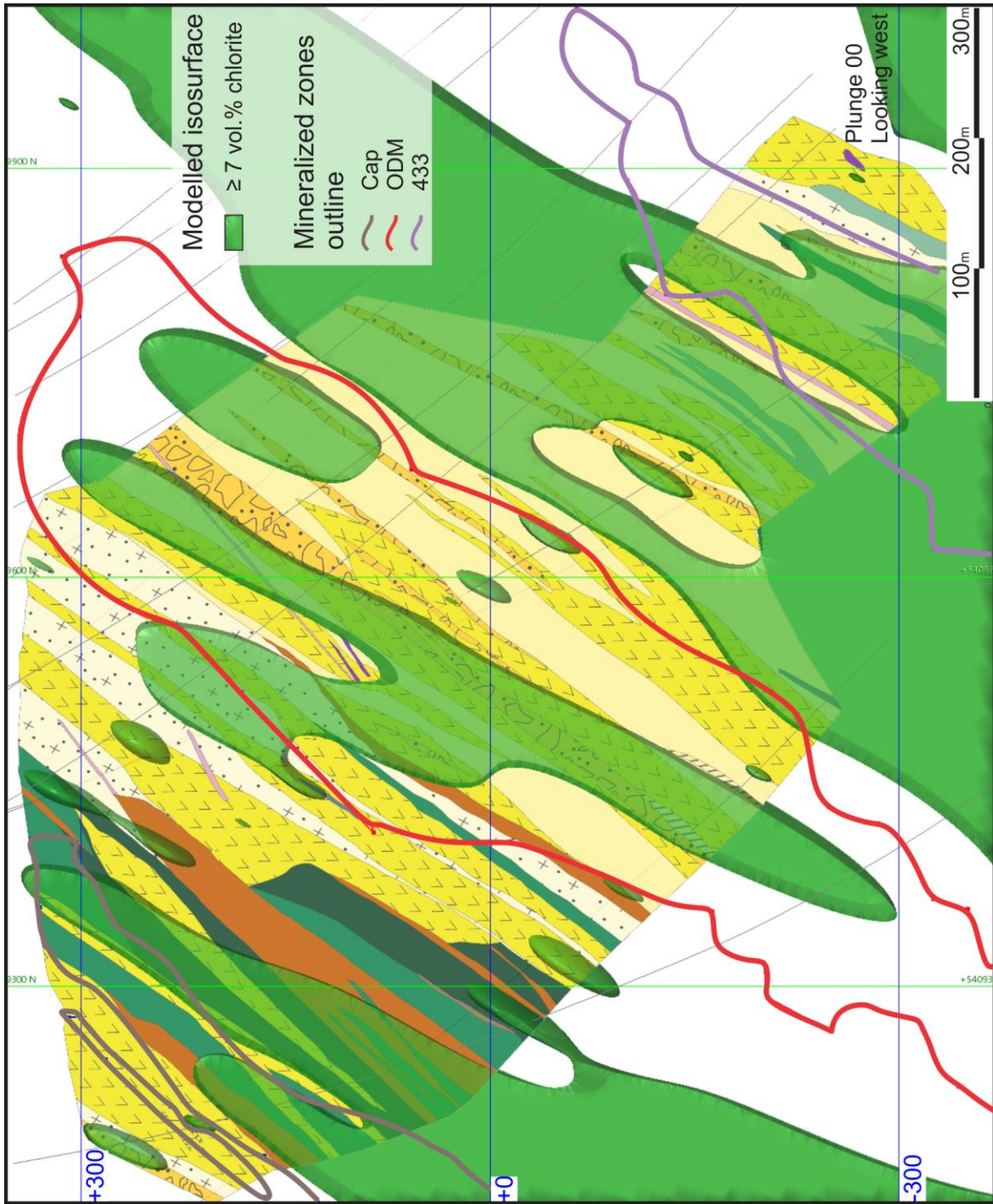


Figure 5.11 : 425475E cross section (NAD83 zone 15 datum), looking west. Implicit modelling of the zones of ≥ 7 vol. % chlorite based on detailed core logging. See Fig. 3.23 (appendix I) for volcanic facies legend. Further information on the implicit modelling parameters are presented in section 5.3.7

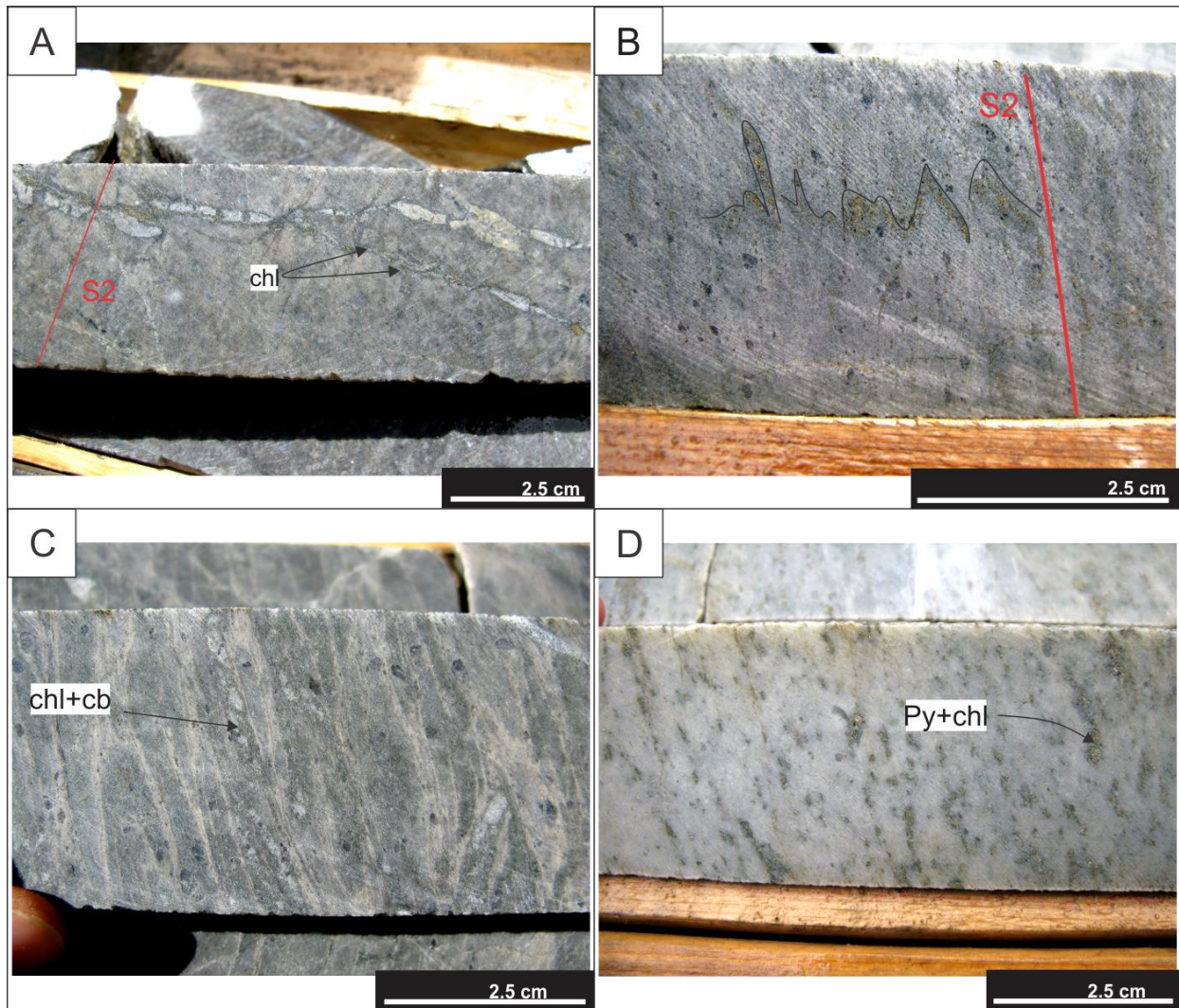


Figure 5.12 : Chlorite. A. Chlorite-carbonate veins deformed by S_2 in a dacite from the ODM zone structural hanging wall. DDH NR100600 at 225m. B. Chlorite-pyrite veinlet folded and transposed into the S_2 plane in dacite flow of the HS zone. DDH NR070181 at 610m. C. Chlorite-carbonate vein now transposed within the S_2 plane. Photo located below photo of Fig. 5.12A, illustrating an increase in S_2 intensity. Dacite flow of the ODM zone, DDH NR100600 at 327m. D. Chlorite associated with disseminated pyrite in muscovite-rich rocks structurally below the 433 zone. DDH NR070181 at 800m.

5.3.1.4 Microprobe analyses

One hundred and nineteen chlorite grains from 34 samples located in all ore zones and their vicinity were analysed by microprobe (see Appendix II for results). Chlorites from tholeiitic mafic volcanics are, on average, richer in Fe and poorer in Mn and Mg than the chlorites developed in dacite. According to the Hey (1954) chlorite classification diagram (Fig. 5.13), over 80% of the analysed chlorite grains from all mineralized zones plot within the ripidolite field. Sheridanite

specimens are from the ODM and HS zones, clinochlore from one sample located in the Intrepid zone, and pycnochlorite is from the ODM and 433 zones.

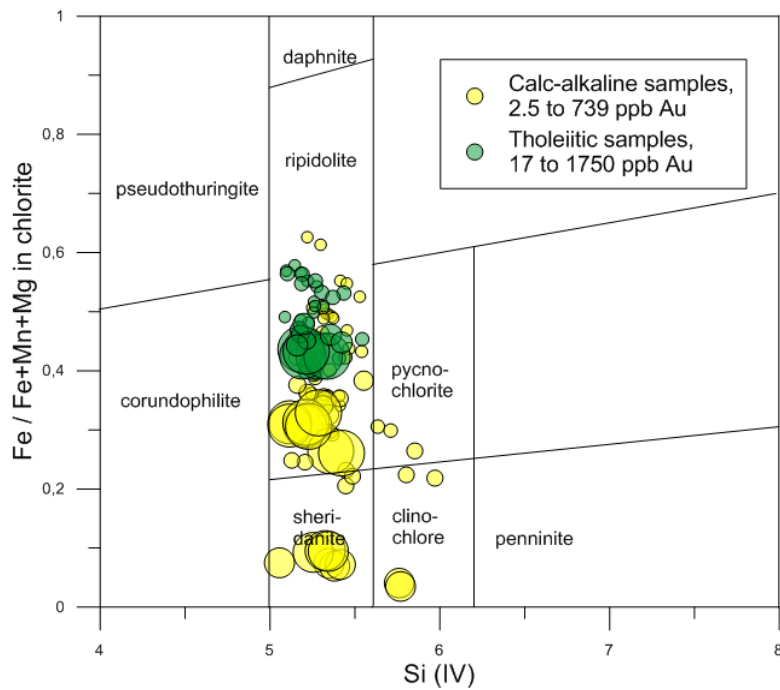


Figure 5.13 : Chlorite classification diagram after Hey (1954), with chlorites from tholeiitic samples in green (n= 40) and chlorites from calc-alkaline samples in yellow (n=79).

Histogram of MnO (wt. %) content of chlorites from calc-alkaline versus tholeiitic samples (Fig. 5.14) reveals a slightly higher modal MnO content for chlorites from calc-alkaline samples versus tholeiitic ones.

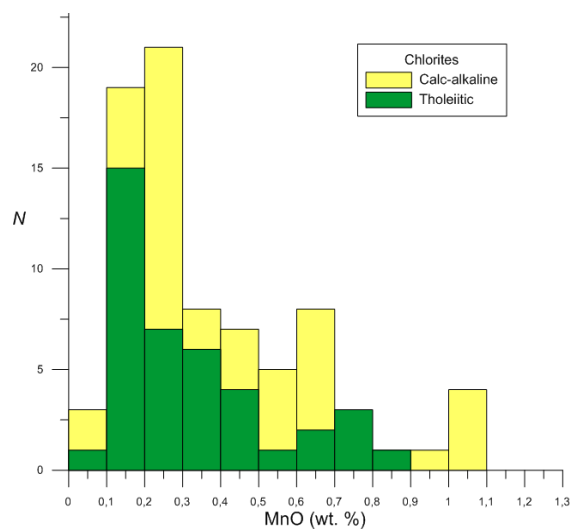


Figure 5.14 : Abundance of MnO in chlorites from the Rainy River deposit. N=119

Comparing the frequency distribution of Fe/(Fe+Mg) ratios of chlorites from calc-alkaline and tholeiitic-affinity samples (Fig. 5.15), we note that chlorites from calc-alkaline samples have a combined higher Mg content and lower Fe content. Unfortunately, fluorine (F) content of chlorites has not been measured, and it is therefore impossible to know if a lower Fe content in chlorites is due to the iron avoidance phenomenon in the chlorite structure due to the presence of fluorine (cf. Hannington *et al.*, 2003) or simply because the primary composition of the host rocks has higher concentration of Fe.

When solely taking into account the chlorites from the calc-alkaline dacitic samples, the majority of samples have a Fe/(Fe+Mg) ratio below 0.4, which is considered to be low (cf. Hannington *et al.*, 2003) and has been interpreted in that same study as the result of saturation of the volcanic pile with seawater and generally low temperatures of alteration. Additionally, the high magnesium content of chlorites from calc-alkaline samples may indicate preferential fixation of iron via pyrite crystallization triggered by the presence of seawater within the hydrothermal system (Hannington *et al.*, 2003).

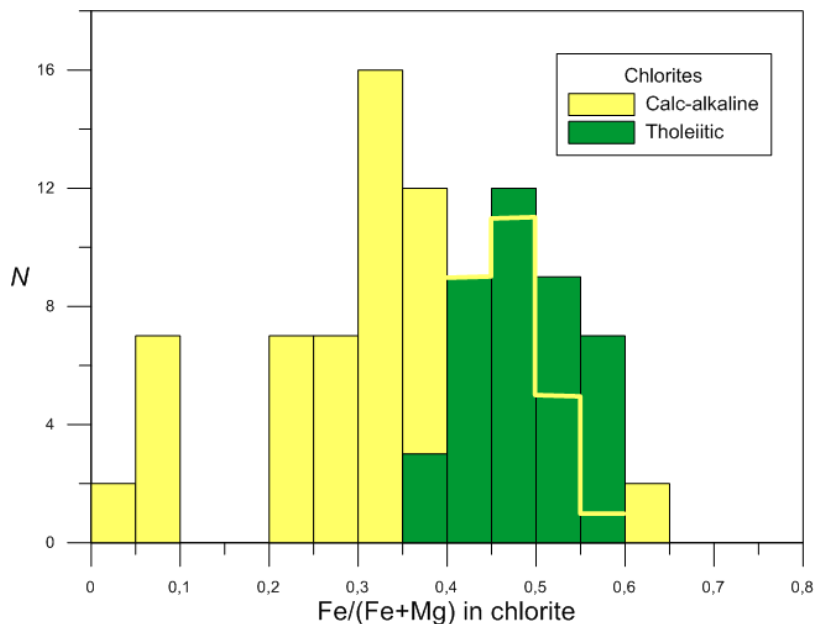


Figure 5.15 : Histogram of Fe/(Fe+Mg) ratios in chlorites from the Rainy River deposit. N = 119

There is a direct correlation between a high MgO and Al₂O₃ wt. % in the chlorites and a higher gold content in sample, for both calc-alkaline and tholeiitic samples (Fig. 5.16).

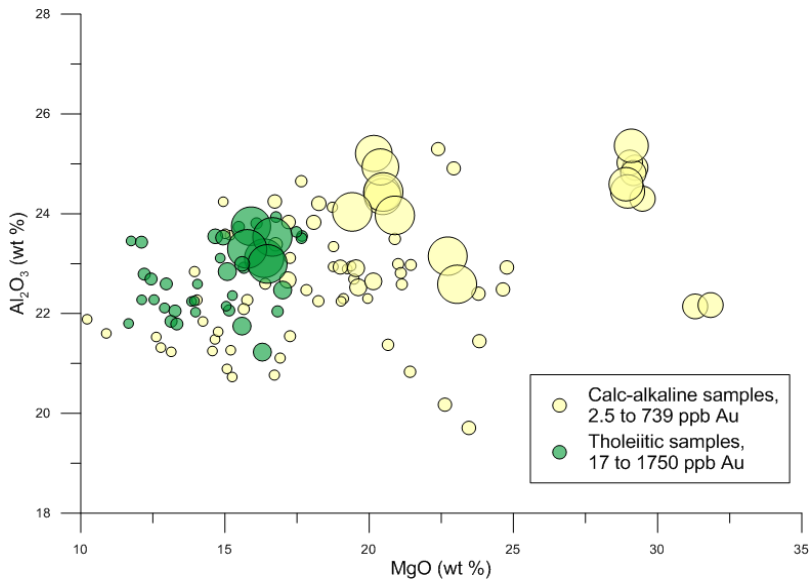


Figure 5.16 : Bubble plot with size proportional to Au content of sample for chlorite grains from tholeiitic (green, n=40) and calc-alkaline (yellow, n=79) samples.

5.3.2 Epidote

Epidote is present in dacites as well as in basalts in the Rainy River deposit area in two different generations: an early generation affected by S_2 and a second, later generation of underformed epidote overprinting the S_2 -oriented minerals. Epidote has been identified in this study in all mineralized zones, as well as outside the immediate deposit area. Grain size is on the tens of micron scale.

Abundance of early-generation epidote varies from trace to 3 vol. %. In the ODM, HS and 433 zones, it occurs in association with pyrite and chlorite and rare carbonates (Fig. 5.17A). Additionally, epidote commonly replaces feldspars (Fig. 5.17B). Early-generation epidotes of the HS and 433 zones are also found in epidote-pyrite-sericite-chlorite veinlets that are folded and transposed into S_2 (Fig. 5.17C). In the 433 zone, rare samples possess early phases of allanite (in trace abundance) rimmed by epidote, which are later overprinted by chlorite, carbonates and rare kyanite (Fig. 5.17D).

Late-generation epidote is generally more abundant in the mafic units and can account for up to 6 vol. % of the rock. It generally occurs as late, un-deformed, inclusion-free grains within a chlorite-carbonate-dominated matrix (Fig. 5.18A). Such late, un-deformed epidote grains are also present within the porphyritic sill at the Scott outcrop (Fig. 5.18B), within the broad structural hanging wall of the deposit.

Early generation epidotes formed later than albite in the paragenetic sequence as it replaces albite, which is also associated with the alteration of the host succession (see section 5.3.1.1). Furthermore, in carbonate-bearing samples, chlorite and carbonates seem to be formed at the expense of epidote (Fig. 5.18C), although no definitive crosscutting relationship can be confidently interpreted in this case. Since chlorite has a greater stability than epidote in a CO₂-rich environment (Poulsen, pers. commun., 2014), an early generation of epidote later destabilized and replaced by carbonates in chlorite-bearing zones is plausible. This early epidote crystallization event is also in agreement with the paragenetic sequence proposed by Wartman (2011). Un-deformed epidotes are not associated with carbonates.

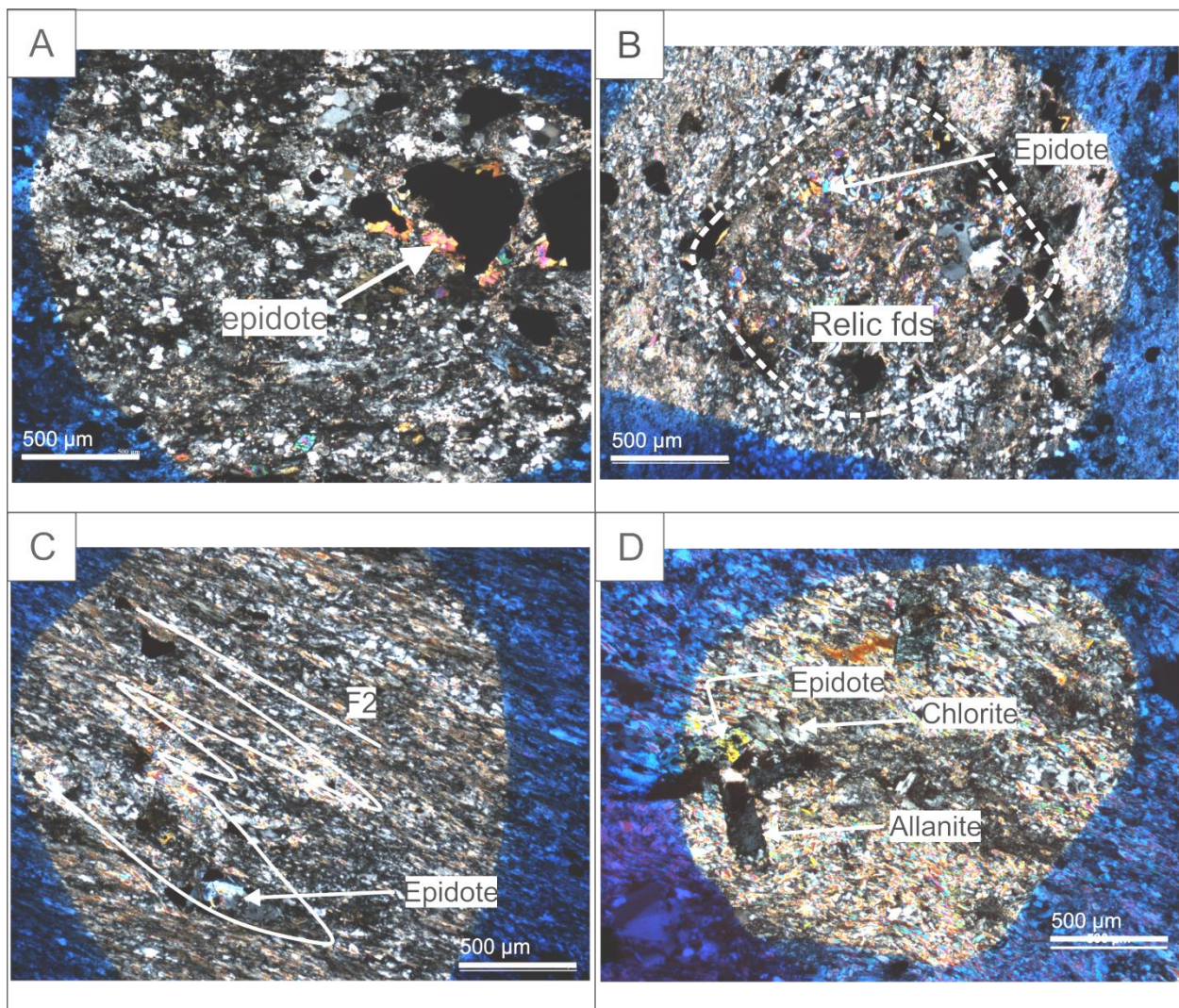


Figure 5.17 : Epidote. A. Photomicrograph (PL) of epidote associated with pyrite and chlorite in tholeiitic basalt in the immediate hanging wall of the ODM zone. Sample RRR435782, DDH NR060058 at 255 m. B. Photomicrograph (PL) of epidote replacing a feldspar microphenocryst in a dacitic flow from the ODM zone. Sample RRR435739, DDH NR110703 at 622 m. C. Photomicrograph (PL) of epidote in deformed quartz-sericite veinlet in a muscovite schist from

the HS zone. Sample RRR435798, DDH NR060067E at 732 m. D. Photomicrograph (PL) of epidote with allanite, carbonate and chlorite in a massive dacitic rock from the 433 zone. Sample RRR435883, DDH NR060067E at 732 m. NOTE : blue circle on photomicrographs correspond to targets for microprobe analyses and consist in marker film on the thin section glass.

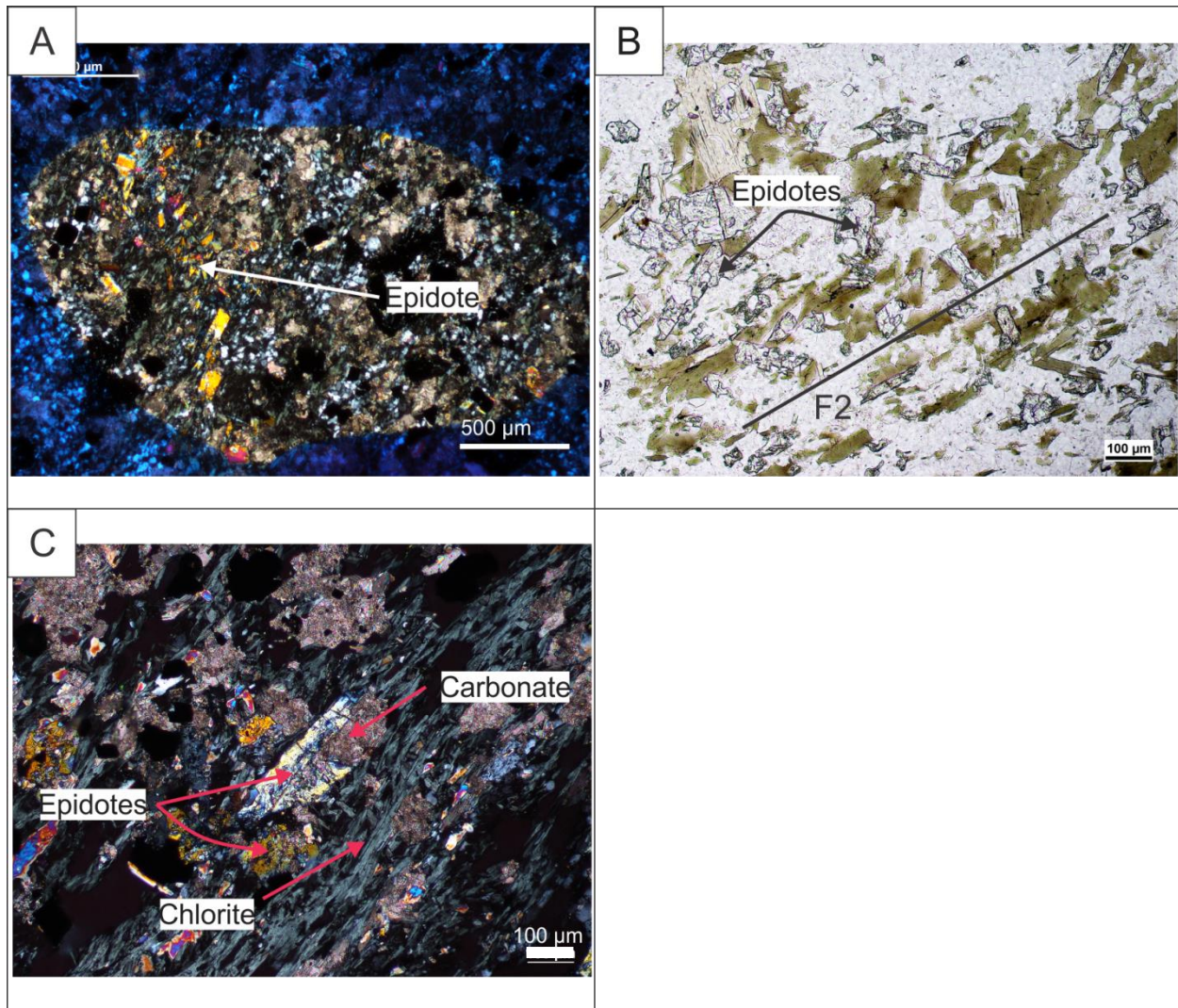


Figure 5.18 : Epidote. A. Photomicrograph (PL) of late, un-oriented (with respect to S2) epidote grains in basalt from the Cap zone structural footwall. Sample RRR435836, DDH NR110771 at 216 m. B. Photomicrograph (TL) of un-oriented epidote grains from a porphyritic sill at Scott outcrop. Sample RRR435866. C. Photomicrograph (PL) of carbonate and chlorite replacing earlier epidote grain in tholeiitic basalt in the Cap zone footwall. Sample RRR435837, DDH NR110771 at 247 m.

5.3.2.1 Microprobe analyses

Microprobe analyses were done on 46 epidote grains from 12 samples within the deposit area and from the Scott outcrop (results in Appendix II). According to the classification of Armbruster *et al.* (2006), almost all epidotes analysed have a composition approaching the typical epidote

composition, with a low clinozoisite component. Fifteen epidote grains from four different samples possess a dominant clinozoisite composition. These clinozoisite-bearing samples are located within the Cap, ODM, HS and 433 zones. Two epidote grains analysed belong to the allanite group of the epidote supergroup. They are affected by S_2 and are located within the 433 and ODM zones.

A classification of epidote grains based on their iron content reveals two groups of epidotes (Fig. 5.19). Iron-poor epidote grains (<8 wt.% FeO) are from the 433, ODM and HS zones. The iron-rich epidotes (>8 wt.% FeO) correspond to the late, un-deformed epidote grains located outside the deposit area as well as within the mafic volcanic rocks from the 433, ODM and HS mineralized zones.

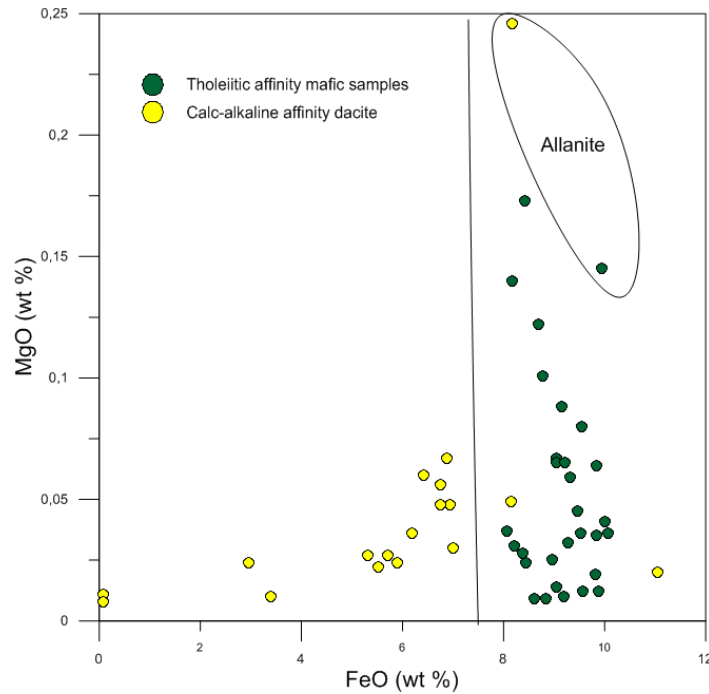


Figure 5.19 : Microprobe data of the epidote analyses (n=46), showing a bimodal distribution (left and right of curved line) of epidotes with respect to the FeO (wt. %) content. Epidotes of the allanite family are circled.

5.3.3 Carbonates

Carbonates have been recognized as alteration minerals associated with the mineralization (Wartman, 2011) and are present throughout the deposit area. Their abundance, composition and distribution vary at deposit scale.

Carbonate alteration has historically been underestimated in the sericite-dominated zones due to a lack of contrast between the minerals and a very fine-grained texture. However, exposure of drill core to weathering over time enhanced the contrast between Fe-Mg-bearing carbonates (now orange-brown coloured) and the very pale quartz-sericite-feldspar matrix. Because of this, evaluation of the percentage of Fe-Mg carbonates in the host rock from relogging is now much easier.

Spatial distribution of carbonate minerals at Rainy River consists in two zones of higher carbonate concentration (see section 5.3.7); one encompassing the structural hanging wall and the upper half of the ODM zone, the other corresponding to the Cap zone and other mafic, Fe and Mg-rich volcanic rocks in the vicinity.

Carbonates occur mostly as disseminated <1 cm grains within the dacitic rocks located in the carbonate-rich zone of the ODM hanging wall and upper ODM zone (Fig. 5.20A,B). Most of the carbonates are closely associated with chlorite, quartz and lesser amounts of sericite. They occur as replacement of earlier albite phenocrysts within the dacites (Fig. 5.20C, D). Carbonates are also common in pressure shadows of pyrite grains (Fig. 5.21A) and in microscopic carbonate-rich veinlets folded and transposed parallel to S_2 (Fig. 5.21B). On rare occasions, carbonates are present with kyanite (Fig. 5.20B).

The western part of the ODM zone is characterized by a slightly higher relative abundance of carbonates, corroborated by higher CO_2 contents (average of 3.65 wt.% CO_2 versus 3 wt.% CO_2 for the rest of the carbonate altered zone of the deposit; see section 5.3.7 for distribution of intense carbonate alteration zone). Dacites from the western part of the ODM zone, in addition to having abundant carbonates replacing earlier albite phenocrysts, also have early, folded quartz-carbonate-pyrite veins of <1 to 3 cm in width, which occasionally contain electrum and gold (Fig. 5.21C; see chapter 4 for discussion on formation and timing).

Within tholeiitic basalts of the Cap zone and surroundings, carbonate alteration is pervasive and very fine-grained. This translates into an orange hue colouring the weathered basalts (Fig. 5.21D). At the microscopic scale, carbonates are abundant, have a grain size of less than 100 μm and are associated with S_2 -parallel chlorite (see Fig. 5.12C). Common folded quartz-carbonate veins (<1 to 5 cm thick) are also present.

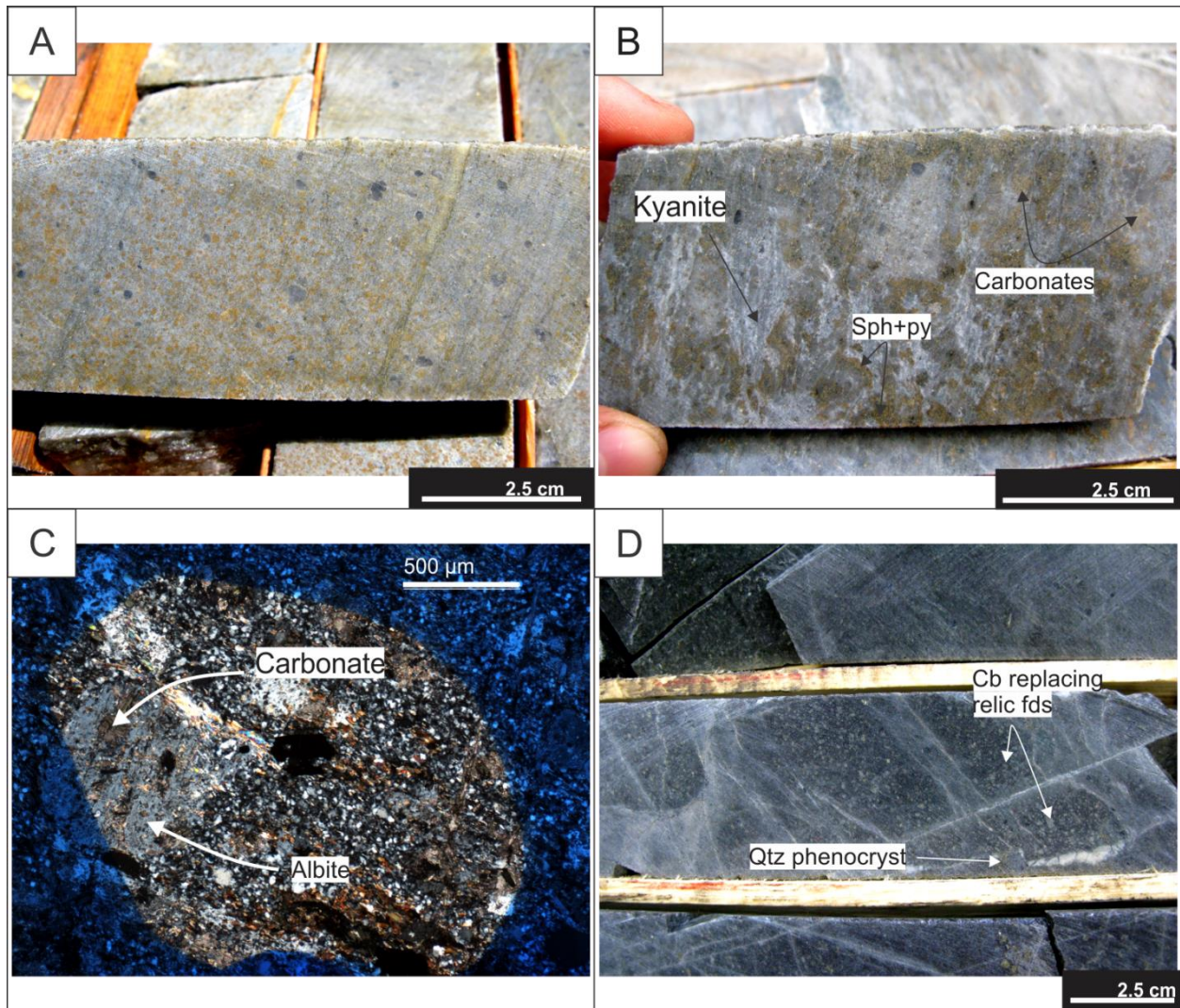


Figure 5.20 : Carbonate. A. Disseminated ankerite in dacite coherent facies from the ODM zone. DDH NR060092 at 326 m. B. Carbonates and kyanite in sphalerite and pyrite-bearing dacitic flow of the ODM zone. DDH NR070141 at 146 m. C. Photomicrograph (PL) of carbonates replacing earlier albite phenocrysts in QFP-textured dacite from the ODM hanging wall. DDH NR060058 at 141 m. D. Carbonates replacing feldspar, also in quartz and feldspar-phyric dacite from the ODM zone structural hanging wall. DDH NR060058 at 141 m.

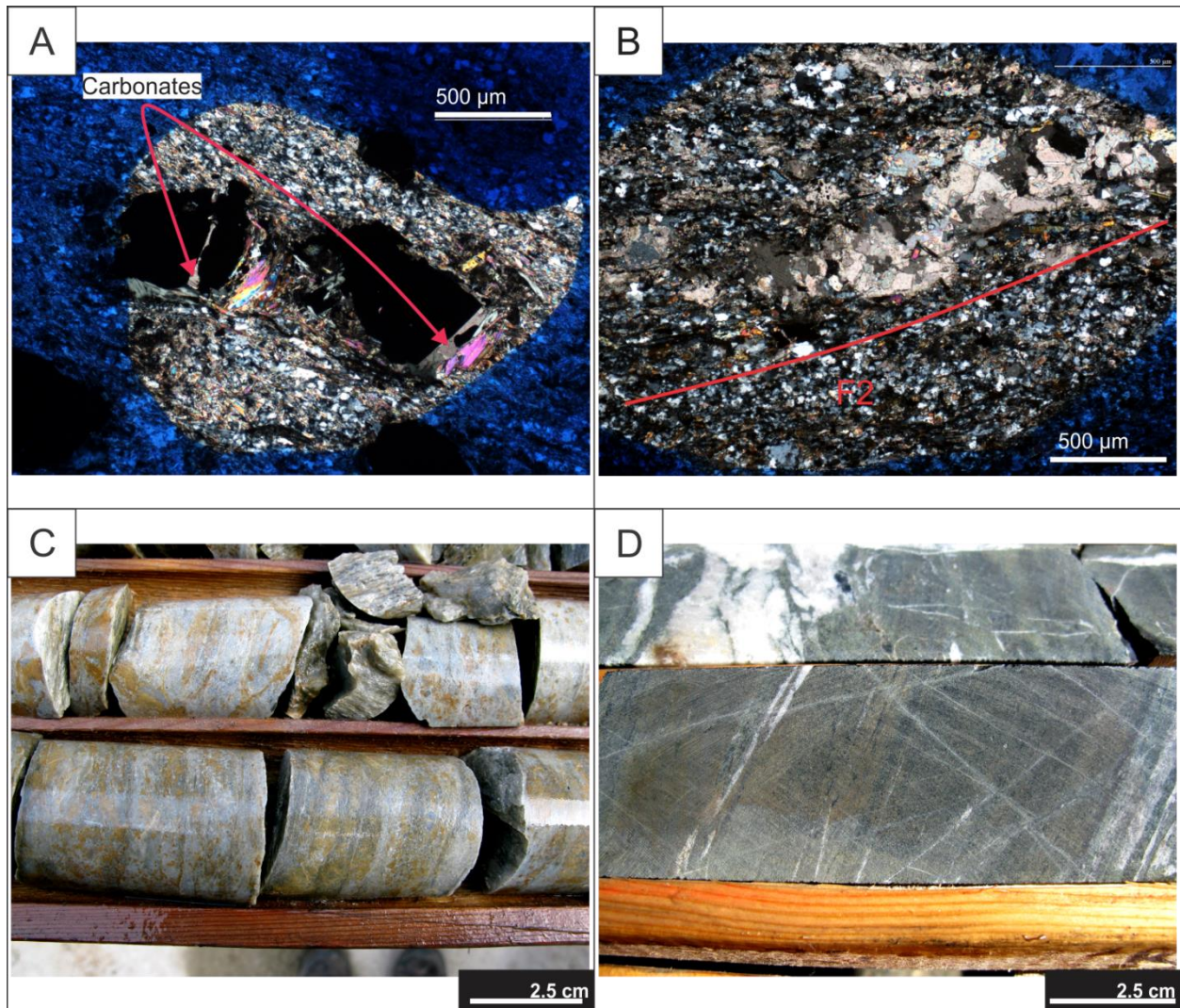


Figure 5.21 : Carbonate. A. Photomicrograph (PL) of carbonate and sericite in pressure shadows of pyrite grain in muscovite schist from the ODM zone. Sample RRR435612, DDH NR070195 at 397 m. B. Photomicrograph (PL) of extensional carbonate veinlet folded and transposed parallel to S_2 in tholeiitic basalt below the Cap zone. Sample RRR435773, DDH NR060058 at 30 m. C. Centimetre-scale, S_2 -parallel carbonate veins in muscovite schists from the western part of the ODM zone. DDH NR950027 at 165 m. D. Pervasive, very fine grained carbonate alteration in tholeiitic basalts, giving it its orange hue. From the ODM zone structural hanging wall (DDH NR100600 at 125 m).

5.3.3.1 Carbonate discrimination diagram and saturation index

Intense and extensive carbonate alteration is common in Archean greenstone belts that host orogenic gold deposits (Robert *et al.*, 2005) as well as for some types of VMS deposits (Franklin *et al.*, 2005). For this reason, many lithogeochemical tools using mobile elements were developed to assess the nature of the carbonates (e.g., Whitehead and Davies, 1988; Couture

and Pilote, 1993) as well as to determine the intensity of CO₂-related alterations (Kishida and Kerrich, 1987).

Nabil and Lafrance (2009) designed a diagram that combines both the saturation index of Kishida and Kerrich (1987) and the carbonate discrimination index of Whitehead and Davies (1988) to help discriminate carbonates associated with VMS-type systems from those associated with orogenic deposits. According to Nabil and Lafrance (2009), this diagram can also discriminate between proximal and distal carbonate alteration in a VMS context.

For the Nabil-Lafrance diagram, all volcanic rocks from this study were plotted according to their tholeiitic or calc-alkaline affinity, which in our case is equivalent to segregating the mafics from the felsics. When plotting the samples from this study (Fig. 5.22), this diagram clearly indicates that even though mafic rocks have higher CO₂ contents, they have a similar carbonate saturation level than the dacites. In this case, the higher natural concentration of Ca, Fe and Mg in the mafic rocks enabled the precipitation of higher volumes of carbonates for a similar saturation level than the Fe- and Mg-poor dacites. The only samples with a saturation index higher than 0.7 are located in the western part of the ODM mineralized body and farther west of the deposit. The samples from the Rainy River deposit all plot into the orogenic and/or volcanogenic field, leaving both hypotheses viable.

An important note to make regarding these results is that, since all rocks have undergone post-volcanism regional metamorphism to the upper greenschist to lower amphibolite facies, part of the CO₂ generated by combined volcanic activity and hydrothermalism might have been lost through metamorphism-related volatile loss. Conversely, additional CO₂ to the system could have been brought in during deformation of the previously carbonate-altered volcanic rocks, which is discussed in section 5.6 as well as in chapter 7.

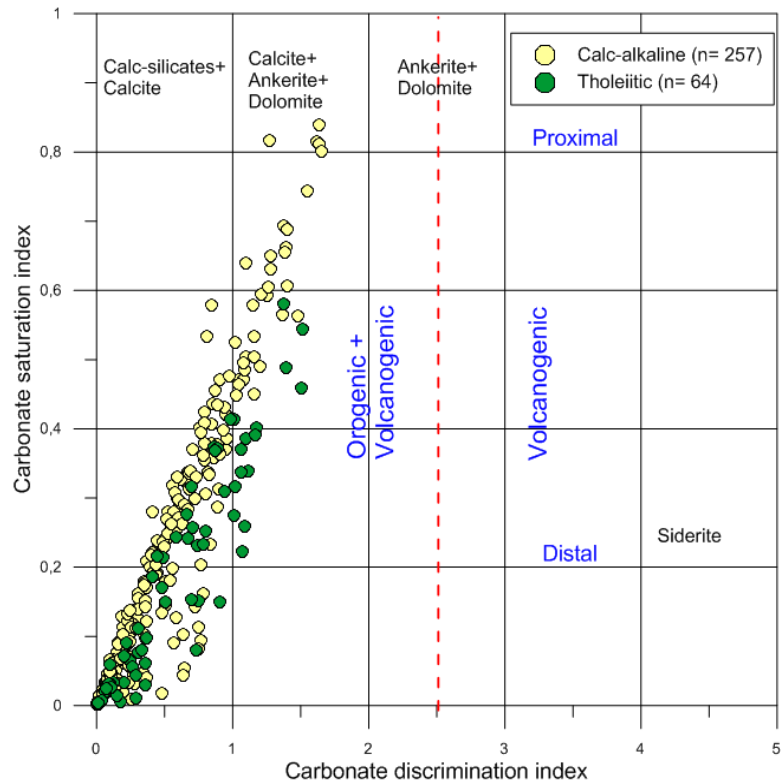


Figure 5.22 : Carbonate alteration diagram from Nabil and Lafrance (2009), using the carbonate discrimination index (CO_2/CaO molar) from Whitehead and Davies (1988) and the carbonate saturation index ($\text{CO}_2/(\text{CaO} + \text{FeO} + \text{MgO} + \text{MnO})$ molar) from Kishida and Kerrich (1987). In blue are fields corresponding to orogenic gold and volcanogenic massive sulphide deposit types, separated by the red dotted line. Rainy River samples in green are tholeiitic basalts and samples in yellow are calc-alkaline dacites. $N = 321$.

5.3.3.2 Microprobe analyses

Carbonate alteration diagrams are useful because they allow for a good approximation of the nature of the carbonate when only lithogeochemical data from loosely constrained, very large datasets is available. For this study, microprobe analyses on carefully selected samples were conducted to provide data on the exact composition of selected carbonates from the deposit. Seventy-seven carbonate grains from 28 samples from all mineralized zones within the deposit were analysed (see appendix II for analytical results).

Results indicate that 51 analysed grains plot within the calcite field (Fig. 5.23), while the remainder ($n=26$) mostly consist in ankerite, with compositions ranging within the Fe-rich ankerite to ferroan dolomite solid-solution.

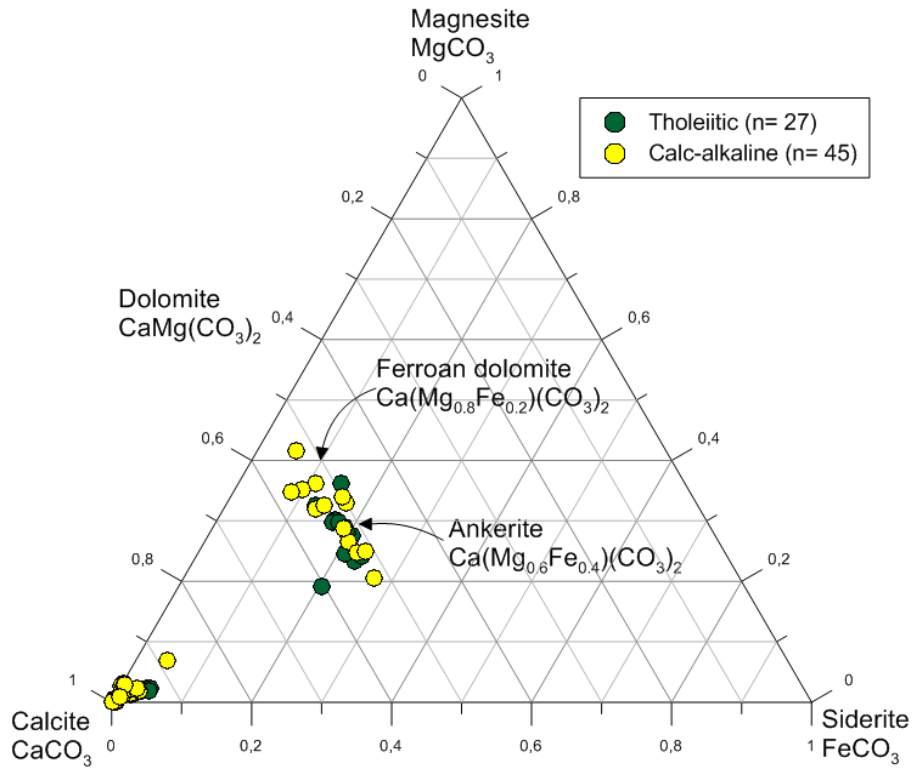


Figure 5.23 : Composition of carbonate grains from this study (n=77) plotted on a carbonate classification diagram. Carbonate nomenclature from Gittins and Harmer (1997).

The majority (n=23) of the ankerite grains come from tholeiitic basalts located within the Cap zone and the ODM hanging wall, and the remainder (n=3) are from mineralized, calc-alkaline dacites from the ODM body. When looking at the MnCO_3 content of carbonates (Fig. 5.24), ankerite grains show a gradational variation in MnCO_3 content, whilst the calcite grains show two distinct populations based on their MnCO_3 content. Six samples of both calcite and ankerite (circled on the diagram) from three different mineralized samples all located in the ODM zone show the highest manganese content of the analysed carbonates.

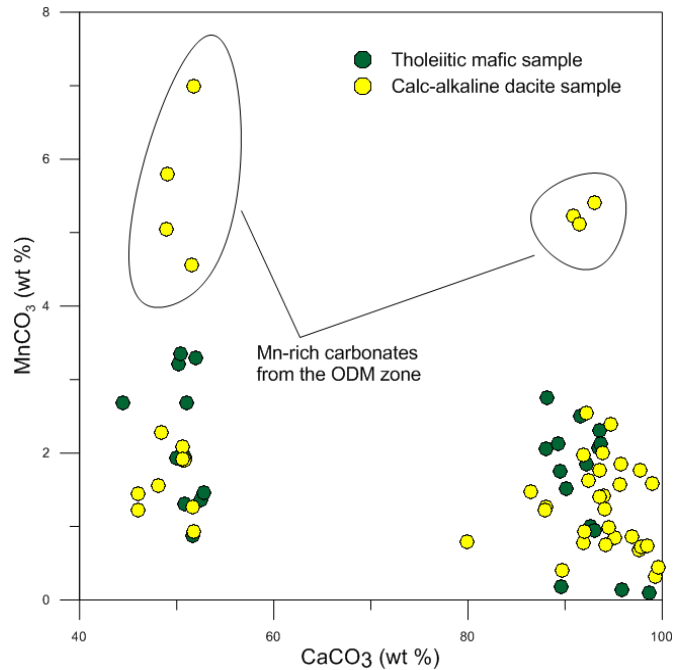


Figure 5.24 : Bivariate plot of the CaCO_3 and MnCO_3 content of carbonates ($n = 77$). Carbonates with high Mn content are all from the ODM mineralized body.

In Archean volcanogenic massive sulphides hydrothermal systems, manganese is considered to be an integral part of the ore-forming hydrothermal fluids, most probably sourced from the sea water, and scavenged from the fluid by previously formed carbonates in the upflow zone (Franklin, pers. comm., 2015), thus suggesting a potential interaction between the dacites within the ODM zone and hydrothermal fluids having a seawater component.

5.3.4 Aluminosilicates (kyanite and chloritoid)

Kyanite and chloritoid porphyroblasts locally occur in the deposit area (see section 5.3.7). In the Cap zone, chloritoid is the only aluminosilicate species present and only occurs in association with epidote and rare pyrite within the tholeiitic amygdaloidal basalt unit (Fig. 5.25A). Chloritoid in this unit in the Cap zone accounts for less than 1 vol.% of the rock and was identified on thin section only.

The highest concentration of aluminosilicates is found within the ODM zone. There, kyanite and chloritoid primarily occur in isolated, S_2 -parallel elongated siliceous lenses that are less than 20 metres thick. Samples from these lenses correspond to the ones with the highest AAI values plotted on figure 5.5. The relative abundance of combined kyanite and chloritoid in those lenses varies between 2 and 8 vol.%, with the remainder of the rock consisting of massive quartz (Fig.

5.25B). No primary textures are preserved in those lenses (Fig. 5.25C). Kyanite microporphyroblasts are disseminated within the matrix and are also concentrated along S_2 -parallel chloritoid veinlets that are <5 mm thick. In weaker aluminosilicate-bearing intervals (<2 vol.% aluminosilicates), kyanite and chloritoid occur as disseminated, abundant <0.5 cm patches (Fig. 5.25D), and in rare <3 mm S_2 -parallel veinlets. In the 433 zone, kyanite is the only aluminosilicate present and occurs within very fine (<3 mm) veinlets parallel to S_2 , representing less than 3 vol.% of the rock (Fig. 5.26A).

As previously mentioned (see section 4.2.2 on metamorphic mineral assemblages), these isolated, silica-rich, aluminosilicate-bearing lenses are interpreted as metamorphic analogues to modern-day argillic-style alteration assemblages found in hydrothermal activity zones affected by very low-pH fluids (Pelletier *et al.*, 2015). Similar alteration assemblages have been documented in other Archean hydrothermal deposits (e.g., Bousquet 2-Dumagami: Dubé *et al.*, 2014; Headway-Coulee prospect: Osterberg *et al.*, 1987; LaRonde Penna: Dubé *et al.*, 2004, 2007; Lemoine: Mercier-Langevin *et al.*, 2014; Mattabi: Franklin *et al.*, 1975).

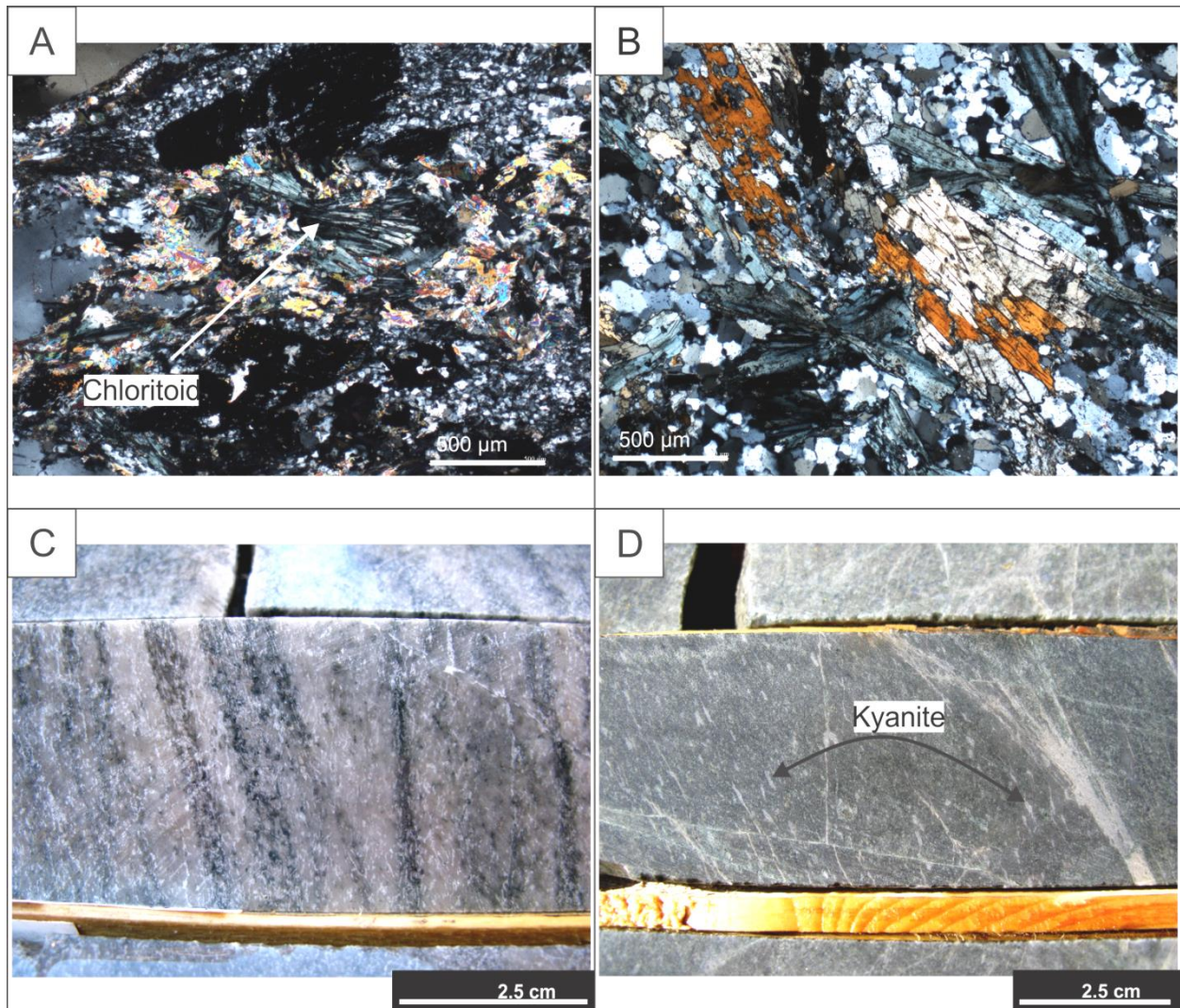


Figure 5.25 : Aluminosilicates. A. Photomicrograph (PL) of chloritoid in blue quartz phenocryst-bearing mafic tholeiitic unit of the Cap zone. Sample RRR435752, DDH NR090358 at 72 m. B. Photomicrograph (PL) of kyanite, chloritoid and quartz assemblage in lens of argillic alteration from the ODM zone. Sample RRR435660, DDH NR060053 at 357 m. C. Example of destruction of primary textures in the kyanite-chloritoid-quartz assemblage. Sample RRR435660, DDH NR060053 at 357 m. D. Small kyanite crystals parallel to S_2 in quartz and feldspar-phyric dacite of the ODM zone. DDH NR100600 at 318 m.

5.3.5 Garnets

Garnets are present in two distinct host rocks at Rainy River: in the tholeiitic basalts of the Cap zone and ODM hanging wall, and in the calc-alkaline dacites of the ODM zone and its structural footwall (partly the HS zone, see section 5.3.7).

The garnet porphyroblasts in the tholeiitic basalts are up to 1 mm in size and represent up to 3 vol.% of the rock. Zones with over 2 vol.% garnets are concentrated in the mafic units located in

the ODM structural hanging wall. Garnets are disseminated within the matrix (Fig. 5.26B), or in 2-5 cm-wide, S_2 -parallel bands. The garnet porphyroblasts are characterized by an inclusion-rich core affected by S_2 (Fig. 5.26C) and an inclusion-free rim (see section 4.2.2 for information on metamorphic significance of this feature). Occasionally, garnet inclusions contain sulphides (Fig. 5.26D).

The garnet porphyroblasts present in the calc-alkaline dacites are disseminated in the matrix, in abundance of <1 vol.%. They vary in size from microscopic to 3 mm and have a light red to pink colour (Fig. 5.28A). These garnets are all fractured and have irregular rims. The core of these porphyroblasts is commonly dominated by inclusions of various compositions (chlorite, quartz, carbonate, pyrite, pyrrhotite; Fig. 5.28B) which recorded the S_2 fabric, while the rims are undeformed and inclusion-free. Metamorphic and structural implications of these features were discussed in section 4.2.2.

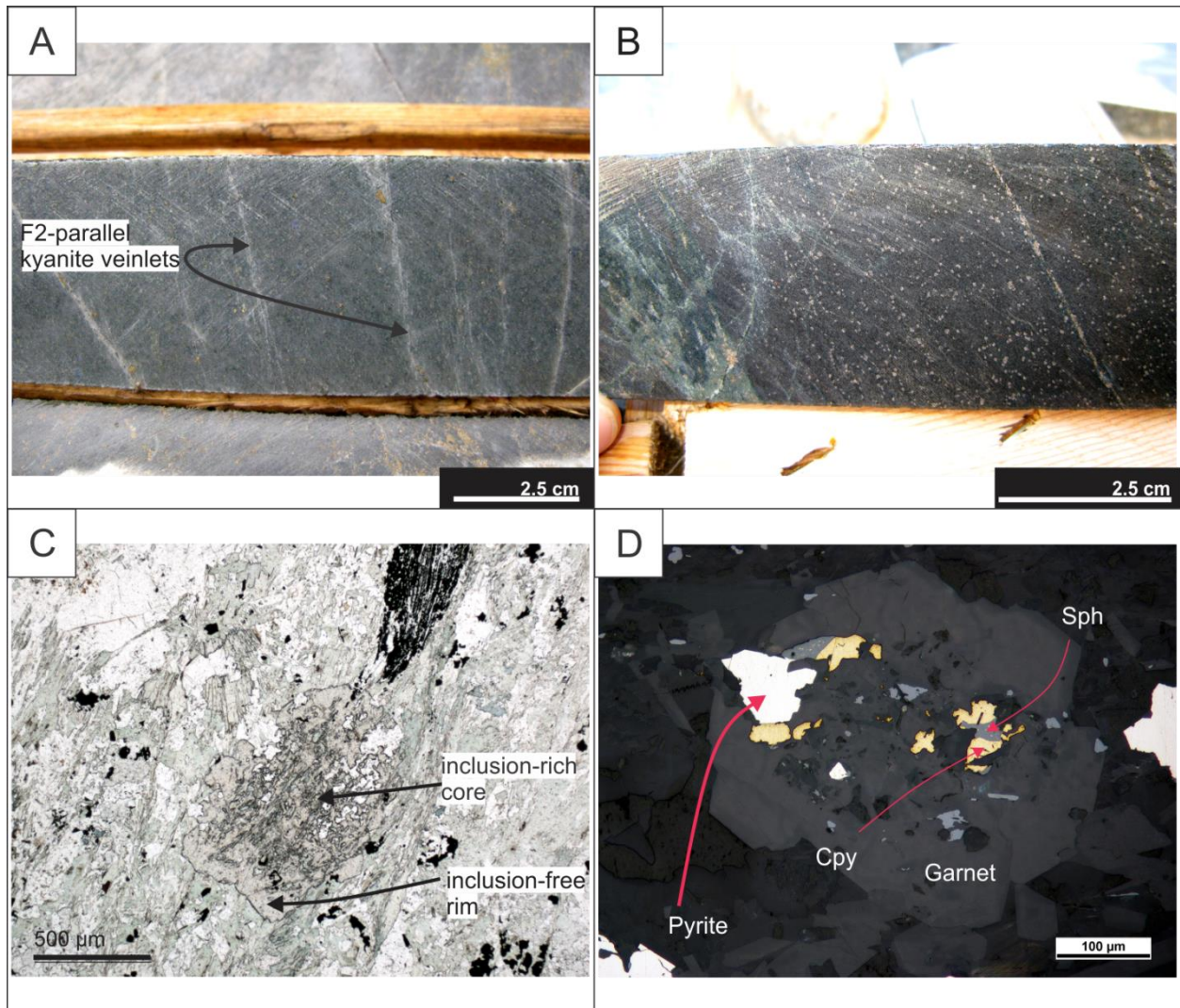


Figure 5.26 : Aluminosilicates and garnet. A. S_2 -parallel kyanite-rich veinlets in dacite from the 433 zone. DDH NR060067E at 782 m. B. Disseminated garnets in tholeiitic basalts of the ODM structural hanging wall. DDH NR100583 at 239 m. C. Photomicrograph (TL) of S_2 -parallel inclusions in garnet core with well-preserved, inclusion-poor rim in blue quartz-bearing mafic tholeiitic unit from the Cap zone. Sample RRR435752, DDH NR090358 at 72 m. D. Photomicrograph (RL) of sulphides (chalcopyrite, sphalerite and pyrite) within garnet inclusions in mafic volcanic dominated siltstones from the McClain outcrop. Sample RRR435912.

5.3.5.1 Microprobe analyses

Microprobe analyses of three garnet porphyroblasts from two mafic samples reveal an Fe-rich Mn-Ca almandine composition averaging $(Fe_{3.63}, Mn_{1.2}, Ca_{1.11}, Mg_{0.3})_6Al_4Si_6O_{24}$ (Fig. 5.27), with up to 26.3% $FeO+Fe_2O_3$. Analyses of 12 garnet porphyroblasts from five samples of calc-alkaline dacites indicate a Mn-rich Fe-Ca spessartine composition averaging $(Mn_{3.4}, Fe_{1.4}, Ca_{0.7}, Mg_{0.4})_6Al_4Si_6O_{24}$ (Fig. 5.27), with up to 29.3% MnO. content. A spessartine-dominated

composition for garnets has also been documented in other synvolcanic gold systems (e.g., LaRonde Penna Au-rich VMS: Dubé *et al.*, 2004, 2007; Westwood: Yergeau, 2015; Lemoine: Mercier-Langevin *et al.*, 2014).

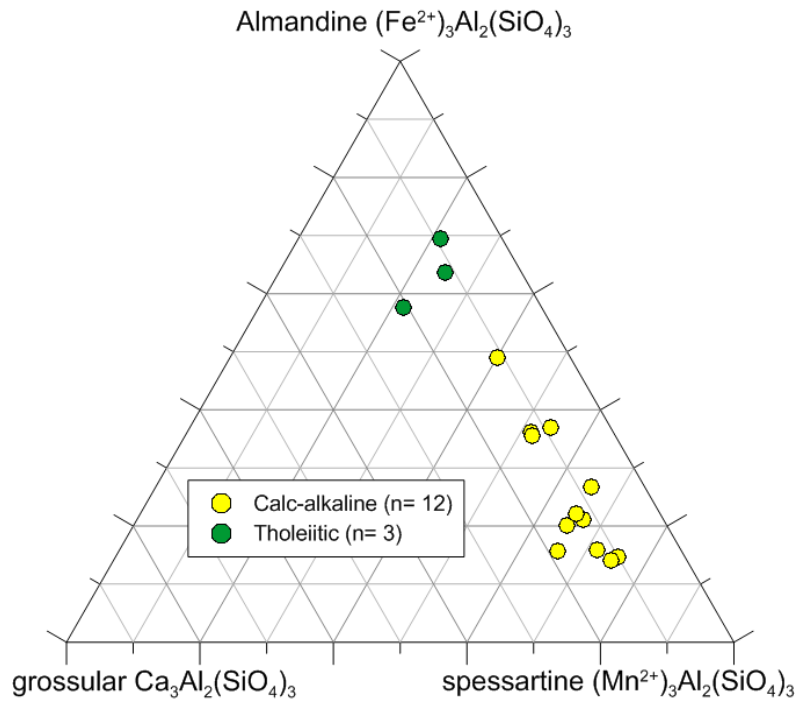


Figure 5.27 : Classification of garnets based on their composition evaluated via microprobe analyses (n = 15). Nomenclature and evaluation of garnet composition and formula is based on Grew *et al.*, 2013.

5.3.6 Rutile

Rutile is present in high concentrations (2 to 2.7 wt.% TiO₂) in mafic rocks in the deeper parts of the Rainy River deposit, namely structurally below the HS zone (see section 5.3.7). It occurs within S₂-parallel, <40 m-wide zones, as very fine and pervasive ‘rutile-dusting’, which gives the mafic rocks a distinct pinkish hue easily recognizable when logging (Fig. 5.28C). Mafic rocks with rutile-dusting are also characterized by granoblastic, boudinaged, S₂-parallel pyrite-chlorite veinlets. Rutile is very fine grained (<80 µm) and disseminated within the matrix (Fig. 5.28D).

Rutile is also documented in the calc-alkaline dacites of the ODM, HS and 433 zones at the microscopic scale only. Once again, it is very fine grained (<100 µm) and it is present in S₂-parallel sulphide veinlets, rimming relic feldspar grains and as inclusions within fractured garnets. Rare replacement textures from ilmenite (FeTiO₃) to rutile (TiO₂) are present (Fig. 5.28E).

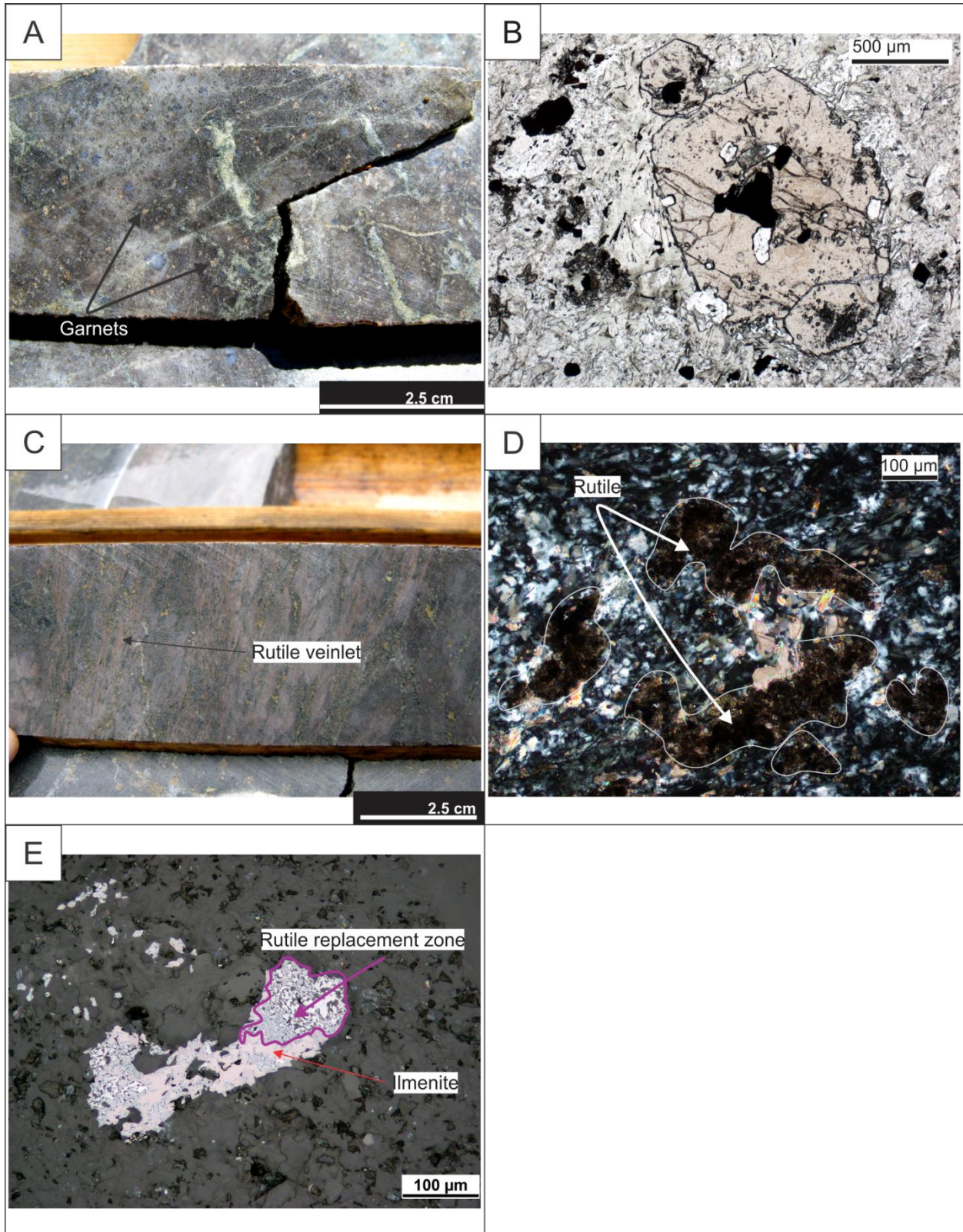


Figure 5.28 : Garnet and rutile. A. Spessartine garnets in dacite within the HS zone. DDH NR070170 at 515 m. B. Photomicrograph (TL) of spessartine garnet in dacitic volcanoclastic facies within the HS zone. Sample RRR435543, DDH NR060104 at 473 m. C. Rutile-bearing alteration on

mafic tholeiitic rocks within the 433 zone. DDH NR060067E at 795 m. D. Photomicrograph (PL) of patchy rutile in tholeiitic basalts of the 433 zone. Sample RRR435888, DDH NR060067E at 800 m. E. Photomicrograph (RL) of early ilmenite partially replaced by rutile in a coherent dacitic rock within the ODM structural hanging wall. Sample RRR435776, DDH NR060058 at 110 m.

5.3.7 Implicit modelling of the distribution of secondary alteration minerals

Drill logs for this study were compiled and imported into the Leapfrog[®] Mining software (version 2.5.3.61) in order to represent the distribution in space of the different alteration minerals that were systematically mapped. The following maps consist in a series of isosurfaces interpolated from the drill core logging data, plotted over the handmade maps of the different volcanic facies.

These isosurfaces were obtained by interpolation of logging data using a linear variogram incorporated within the Leapfrog[®] Mining with a global trend corresponding to the S_2 plane combined with the L_2 stretching lineation (dip, dip azimuth and pitch of respectively 61° , 192° and 108°), creating an ellipsoid ratio of 3:3:1. Nugget and slope values were set at 1. A linear variogram was used here because the dataset corresponds to a two dimensional vertical section, versus a three dimension environment where a spheroidal variogram is necessary.

The different isosurfaces modelled are solely based on visual observations data and, combined with the level of error induced through the mathematical transformations involved in implicit modelling; they can only represent an approximation of the actual distribution of secondary minerals.

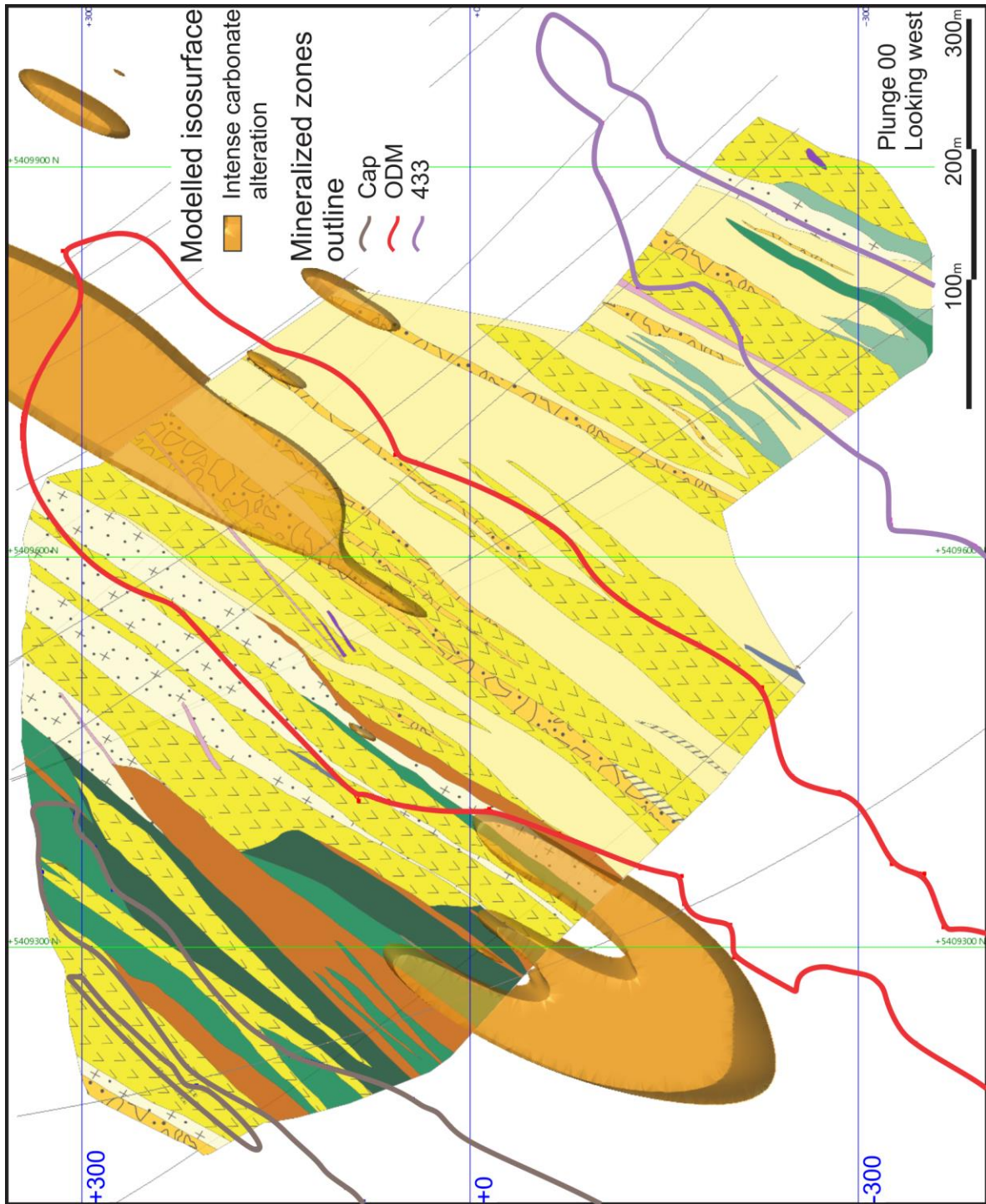


Figure 5.29 : 425475E cross section, looking west. Implicit modelling of the zones of intense carbonate alteration (8 to 15 vol.% carbonates) based on data from detailed core logging. See figure 3.23 (appendix I) for volcanic facies legend. NOTE: the apparent fold pattern observed in the southern carbonate modelled body is due to an artefact from the modelling constraints and does not imply the presence of a folded horizon.

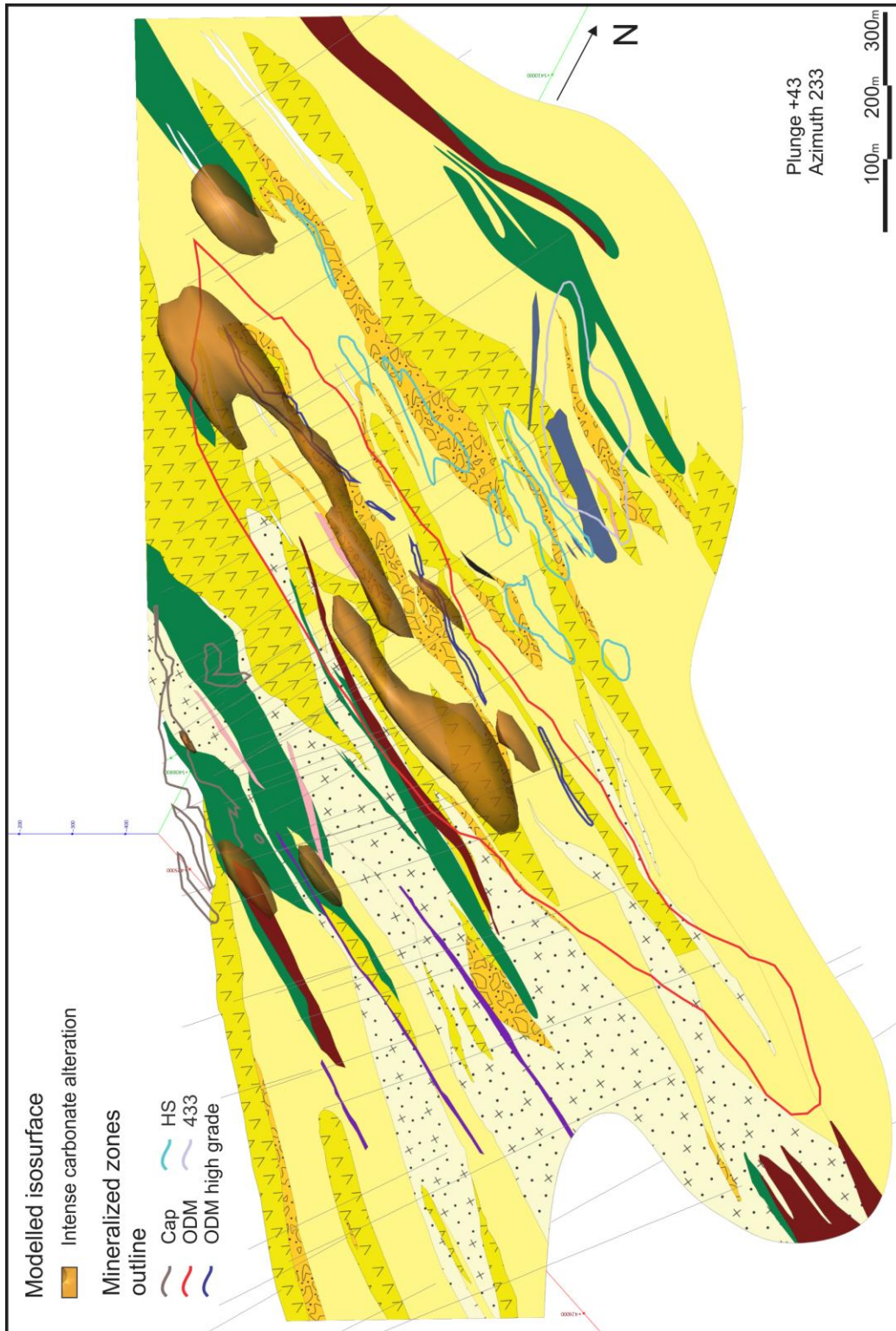


Figure 5.30 : Oblique plane oriented 323N/43°, looking down 43° towards 233N (perpendicular to plane). Implicit modelling of intense carbonate alteration (8 to 15 vol.% carbonates) based on detailed core logging data. Traces of the different ore zones are shown; same legend as figure 3.22 (appendix I) for the volcanic facies.

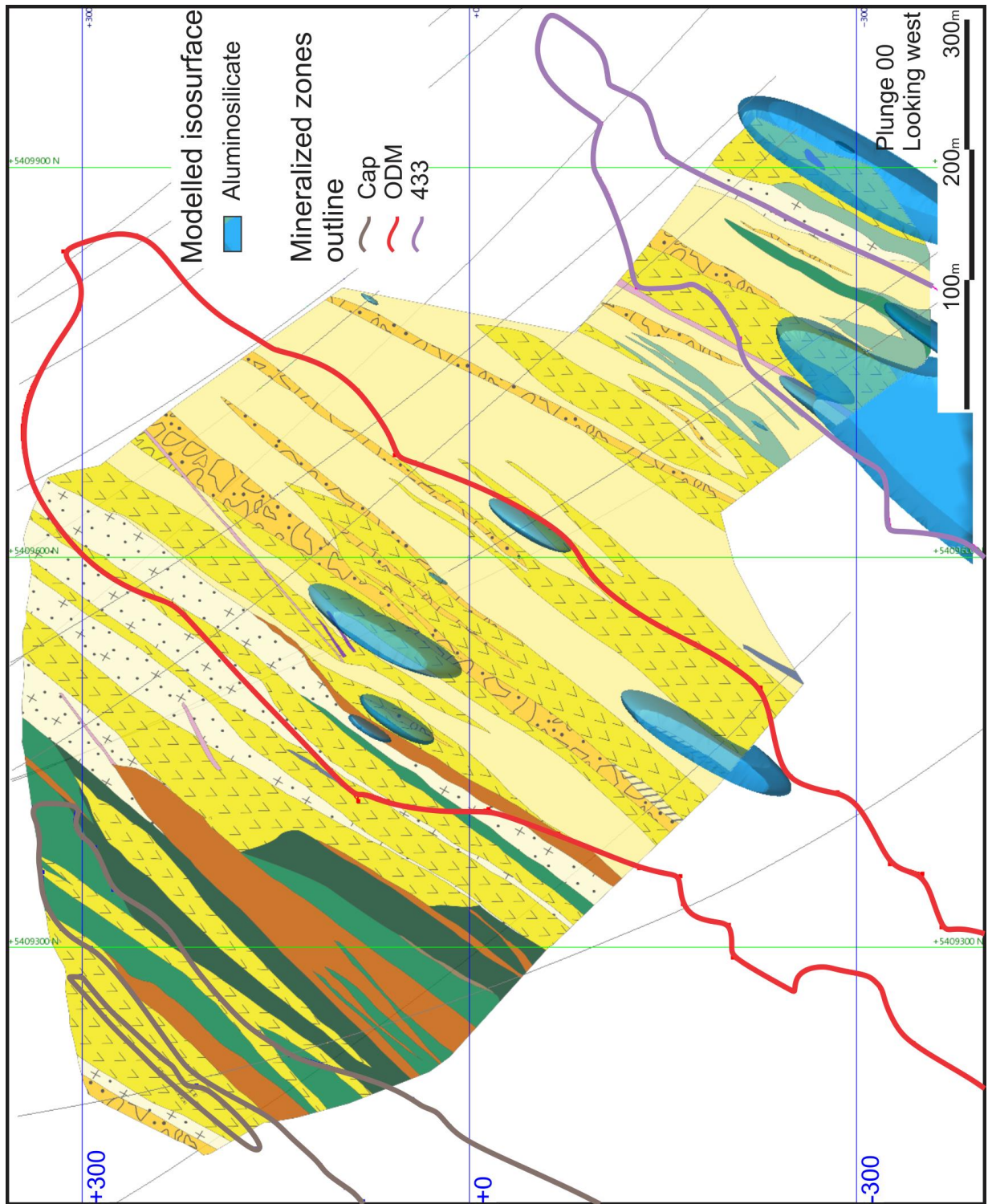


Figure 5.31 : 425475E cross section, looking west. Implicit modelling of the zones with presence of aluminosilicates (kyanite ± chloritoid) based on data from detailed core logging. See figure 3.23 (appendix I) for volcanic facies legend.

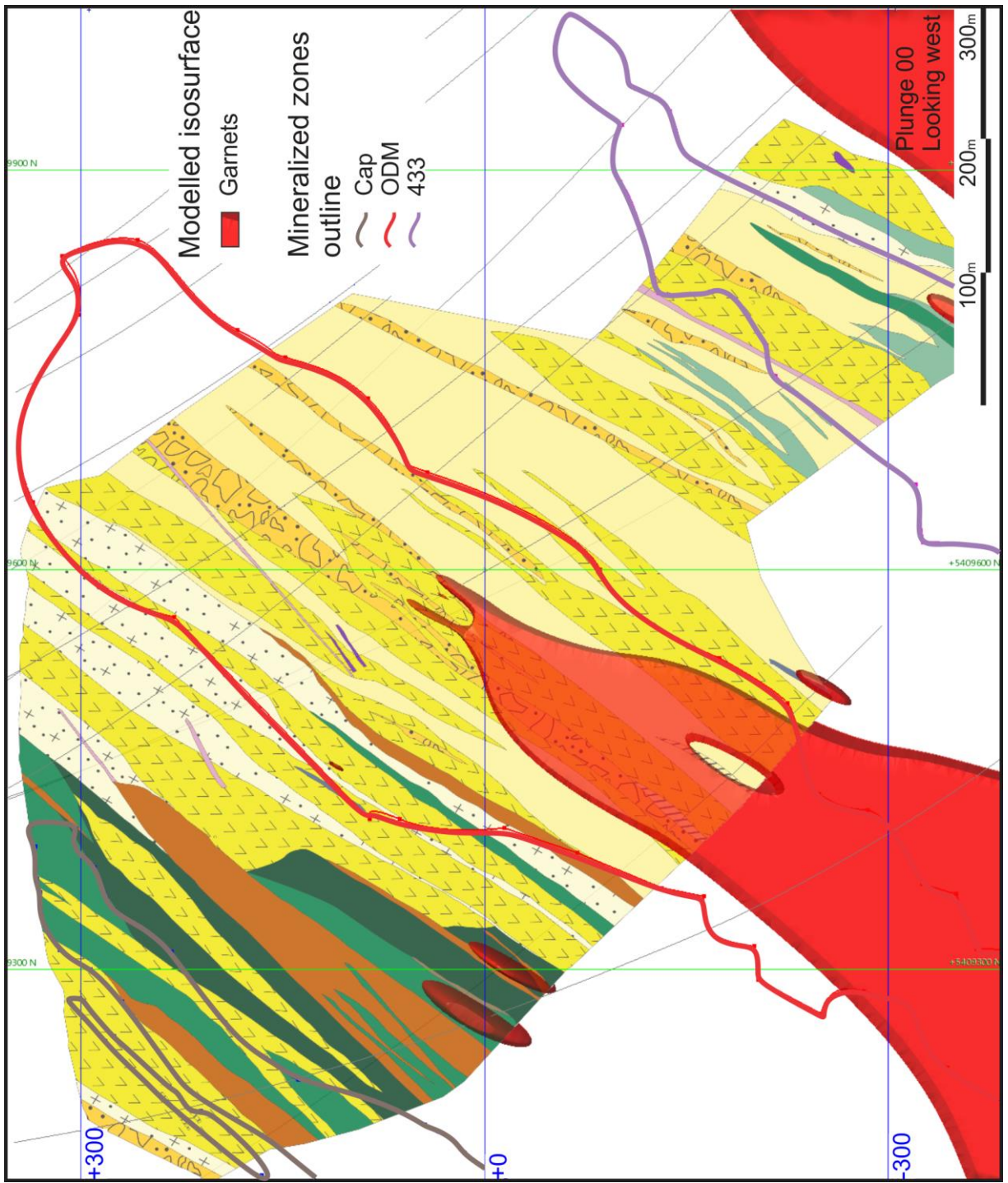


Figure 5.32 : 425475E cross section, looking west. Implicit modelling of the zones with presence of garnets based on data from detailed core logging. See figure 3.23 (appendix I) for volcanic facies legend.

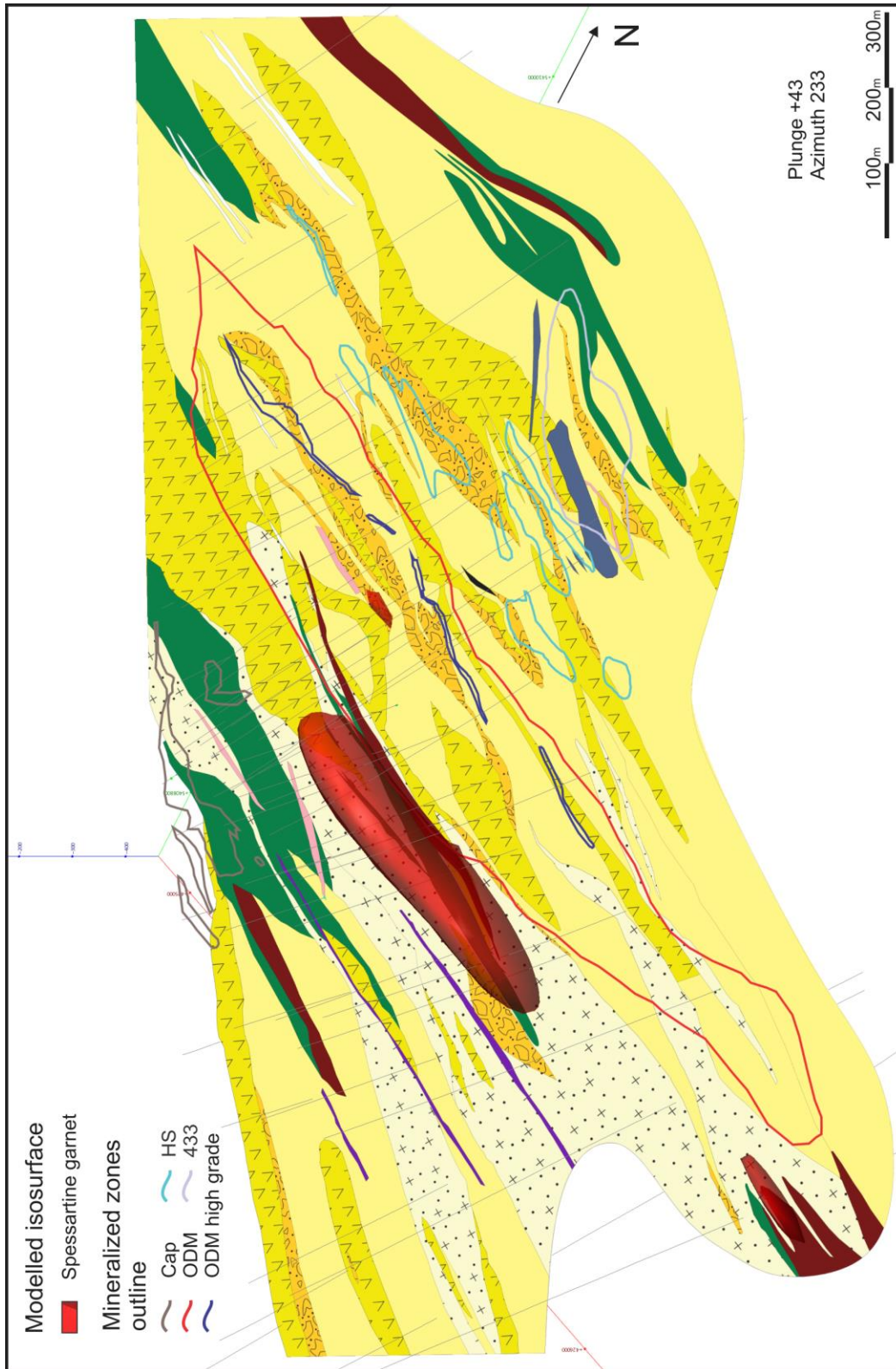


Figure 5.33 : Oblique plane oriented 323N/43°, looking 43° towards 233N (perpendicular to plane). Implicit modelling of spessartine garnets based on detailed core logging data. Traces of the different ore zones are shown; same legend as figure 3.22 (appendix I) for the volcanic facies.

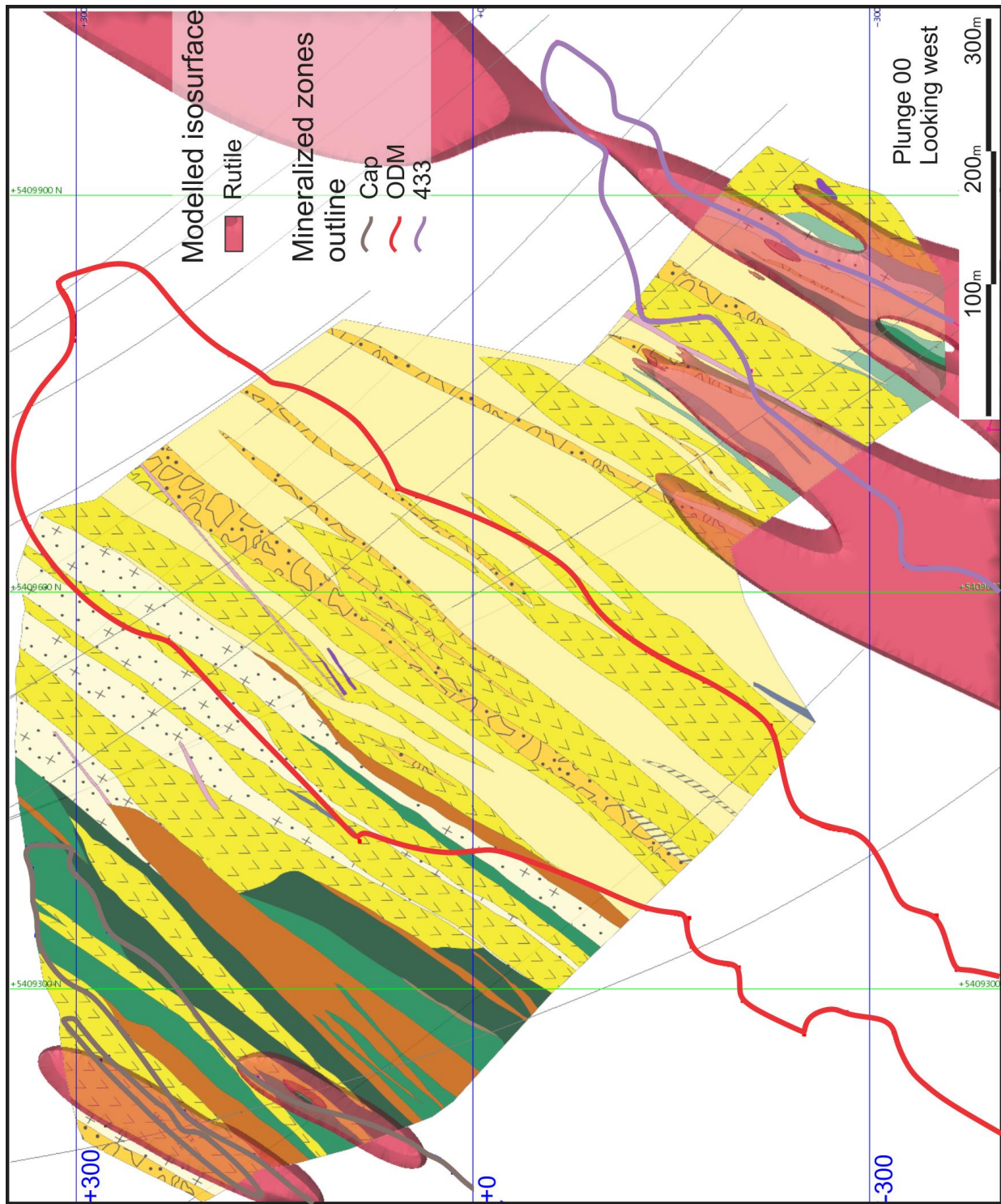


Figure 5.34 : 425475E cross section, looking west. Implicit modelling of the zones with rutile dusting, based on data from detailed core logging. See figure 3.23 (appendix I) for volcanic facies legend.

5.3.8 Summary on the distribution and nature of secondary alteration minerals at Rainy River

Mafic volcanics versus felsic volcanics have different alteration mineralogy due to their different initial composition; therefore the nature and distribution of secondary alteration minerals is controlled by both the hydrothermal systems and the initial protolith composition. Moreover, many of the characteristic minerals described above result from the metamorphism of the altered protoliths, therefore do not represent the initial alteration assemblage.

Using the information on the various secondary alteration minerals presented above, a schematic zonation in the distribution of these minerals with respect to the different mineralized zones can be established. The spatial zonation of secondary alteration minerals within the Rainy River deposit is described in the following paragraph starting from the structural hanging wall (south) moving towards the footwall (north).

The mafic volcanic rocks hosting the Cap zone, and those located above are characterized by an elevated ankerite abundance (up to 15 vol%), although their carbonate saturation index remains relatively low (i.e. below 70%). Moving downwards perpendicularly to S_2 , the carbonate-dominated domain gives way to an almandine garnet and chloritoid zone (both in minor amounts) developed in the blue quartz-bearing mafic volcanic rocks of the Cap zone and its immediate footwall. The ODM mineralized body, slightly lower in the stratigraphy, hosts various secondary alteration minerals, with Mn-rich ankerite closer to the present surface and spessartine garnets in the deeper parts of the mineralized body as shown in section (Figs. 5.29, 5.30, 5.32, 5.33). Once again, the carbonate saturation index is low, but an increase is recorded westward along strike (Fig. 5.30). Spessartine garnets are also rarely present in the dacite of the ODM zone footwall or the HS zone. Kyanite-chloritoid lenses are dispersed in the ODM body in lenses parallel to S_2 (Fig. 5.31). The lowermost parts (moving perpendicular to S_2 and lower in the stratigraphy) of the Rainy River deposit are characterized by the presence of rutile-dusting alteration within the mafic volcanics of the 433 zone and below (Fig. 5.34). Rare lenses of kyanite-bearing dacite are also present locally. Epidote, because it is generally very fine-grained and intermixed with sericite, chlorite and carbonates, is difficult to distinguish and, therefore, has not been constrained as well as other minerals in terms of its distribution. It is present in all mineralized zones of the deposit, apparently resulting from two distinct generations: one that is pre- D_2 and one that is late- to post- D_2 . Pre- D_2 epidote seems to be replaced by later, S_2 -foliated chlorite and carbonates, whereas the second generation of epidote is inclusion-free and not oriented along the S_2 plane. The presence of carbonates affects the

abundance of epidote, with carbonate-rich zones containing much less epidote, suggesting that carbonates developed at the expense of epidote, in agreement with the poor stability of epidote in CO₂-rich environments. Mg-rich epidote is developed exclusively within the dacite of the ODM, HS and 433 zones.

5.4 Mass balance calculations

Hydrothermal alteration, at various fluid-to-rock ratios, triggers major elements mobility, which in turn is responsible for mineralogical changes and mass (and volume) variations throughout the affected area. By calculating mass changes for each element using lithogeochemical data, it is possible to map zones of similar major element mass transfers, and, if applicable, define vectors in the alteration zones with respect to mineralization.

Lithogeochemical techniques using mobile and immobile, and compatible and incompatible elements allow us to assess mass variation of a hydrothermally altered sample by comparing its composition to a least-altered precursor of the same unit. For this study, the techniques used to calculate mass transfers attributed to hydrothermal chemical reactions are the ones presented by Barrett and MacLean (1991, 1993). Here, mass change is quantified based on the dilution or concentration of a determined immobile (or less mobile) component (MacLean and Barrett, 1993). Mass change is calculated for each mobile element by estimating the reconstructed composition (R.C.) of the altered sample based on the concentration ratio of the immobile element (acting as a monitor) between the precursor and the altered sample (Barrett and MacLean, 1991). A simple mathematical equation is used to determine the mass change. Below is an example using Zr as the immobile element used to monitor mass changes:

$$\text{R.C.} = w(\text{Zr}_{\text{precursor}}) / w(\text{Zr}_{\text{altered}}) * w(\text{mobile component}_{\text{altered in wt\%}})$$

$$\text{Mass change} = \text{R.C.} - \text{Precursor composition}$$

Where:

$w(i)$ = mass fraction of element i determined by whole-rock chemical analyses.

Similar techniques (Gresens, 1967; Grant, 1986) have also been elaborated to determine mass changes caused by hydrothermal alteration. These techniques use various elements as well as physical properties (specific gravity) to estimate volume change, rather than just one for the calculations of Barrett and MacLean. In all cases, these techniques avoid data closure by using element ratios rather than bivariate plots (e.g., Harker, 1909 diagrams).

5.3.9 Determining element immobility and predecessors

Prior to calculating mass variations for each sample, we need to determine how many units and predecessors are present in the Rainy River deposit area. This was outlined in chapter 3 and section 5.2, but further verifications must be done here. To do this, a plot of immobile compatible-incompatible element pair was generated (MacLean and Barrett, 1993). In this context, samples from a single precursor should plot along the same alteration line going through the origin, and various alteration lines indicate as many predecessors. At Rainy River, all samples of calc-alkaline affinity form one cluster on an Al_2O_3 - Zr plot (Fig. 5.35), in agreement with a single precursor.

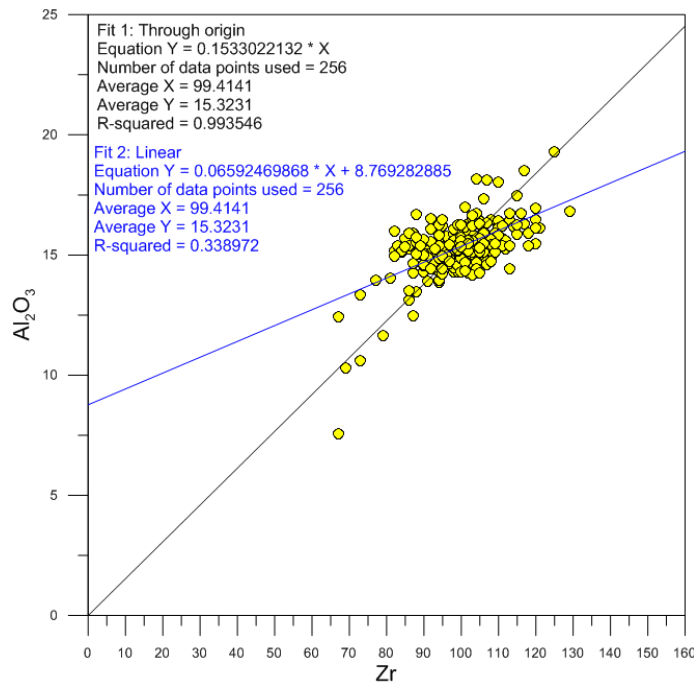


Figure 5.35 : Al_2O_3 (wt. %) versus Zr (ppm) plot demonstrating a single precursor for all calc-alkaline affinity samples at Rainy River (n=256).

The next step after determining the number of precursors is to choose the least mobile component from which the reconstructed composition of the altered sample will be evaluated. Elements such as high field strength elements (HFSE) can be used to calculate the mobility of major elements since they are highly incompatible and tend to be less mobile during hydrothermal alteration. The immobility test used in this study consists in generating a series of bivariate plots between incompatible elements, along with the calculated regression curve (Fig. 5.36). Comparison of the different coefficients of determination (r^2) for each regression lines

(table 5.1) allows us to determine the least mobile element of all the incompatible ones. From these results, it was decided to take Zr as the least mobile element from which mass variations between samples can be evaluated, since it has the highest r^2 value and because it is present in concentrations well above the detection limit in all samples.

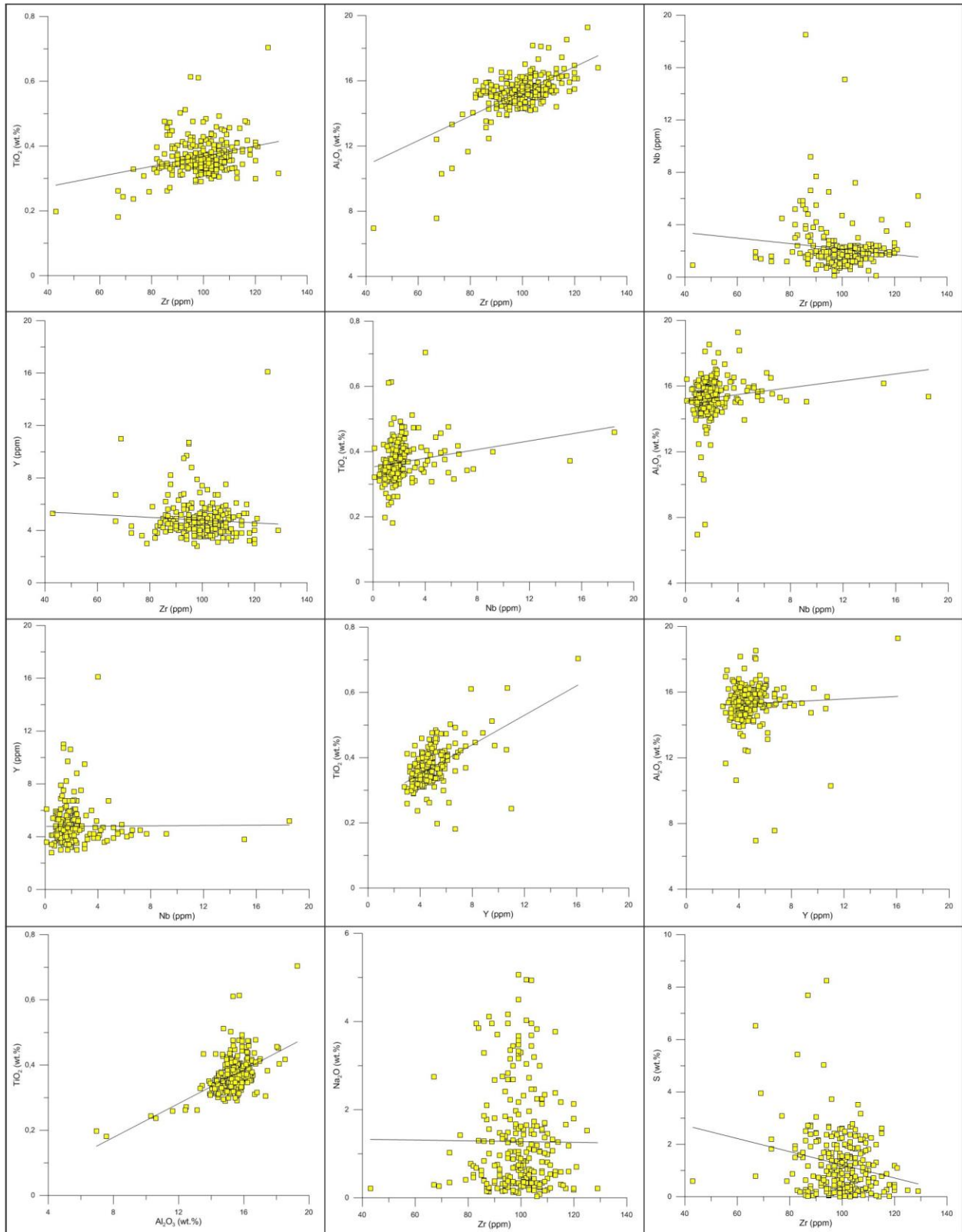


Figure 5.36 : Bivariate plots with regression line of immobile compatible-incompatible as well as incompatible-incompatible element pairs to determine least-mobile elements. Samples are all of calc-alkaline affinity (n=256).

Table 5.1 : Table of the different calculated r^2 values of the regression lines calculated for each bivariate plots of figure 5.36

	Zr	TiO ₂	Al ₂ O ₃	Nb	Y
Zr	-	0.0773	0.411	0.0144	0.00583
TiO ₂	0.0773	-	0.294	0.0426	0.304
Al ₂ O ₃	0.411	0.294	-	0.0242	0.002
Nb	0.0144	0.0426	0.0242	-	5.05x10 ⁻⁵
Y	0.0058	0.304	0.002	5.05x10 ⁻⁵	-

Once the least mobile element has been determined for the mass variation calculation, a precursor, or “least-altered” sample has to be determined from which element mobility can be assessed. At Rainy River, the least-altered precursor composition for the calc-alkaline affinity samples was chosen based on specific criterias. These consist in: 1) a LOI "loss-on-ignition" value lower than 2 wt.%, 2) a sulfur content of <0.5 wt.%, 3) a CO₂ content <1 wt.%, 4) no significant mineralization (<20 ppb Au), 5) a dacitic composition using a volcanic rock classification for un-altered modern rocks (Le Bas *et al.*, 1986; Fig. 5.37), and 6) a distal location with respect to the main mineralized bodies. The precursor composition was determined by calculating the average composition of the combined samples RRR435870 and RRR435900, which both filled all the above mentioned criterias (table 5.2).

Table 5.2 : Precursor composition (major oxides and Zr only) based on the average composition of samples RRR435870 and RRR435900. *The total (in wt. %) consists in the sum of mass concentrations for all elements assayed, most of which are not shown here (see Pelletier *et al.*, 2016 for full assay data).

Sample	RRR435870	RRR435900	Average
SiO ₂	69.62	68.8	69.21
TiO ₂	0.381	0.379	0.38
Al ₂ O ₃	15.58	15.43	15.51
Fe ₂ O ₃	1.12	0.65	0.89
FeO	1.7	2.3	2
MnO	0.058	0.059	0.059
MgO	1.69	2.1	1.90
CaO	3.99	3.01	3.5
Na ₂ O	2.72	3	2.86
K ₂ O	1.67	2.62	2.15

LOI	2.07	2.21	2.14
CO₂	0.62	0.68	0.65
S	0.01	0.15	0.08
Zr (ppm)	103	97	100
Total*	100.9	100.9	100.9

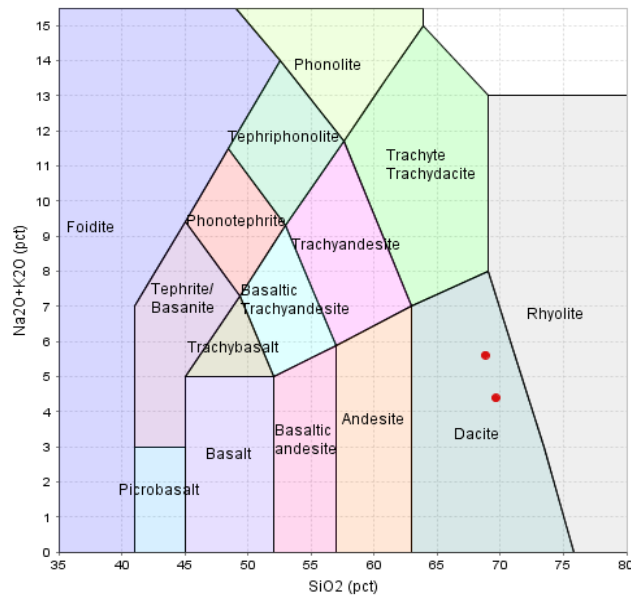


Figure 5.37 : Volcanic rock classification TAS diagram (Le Bas et al., 1986) using mobile major elements, showing the position within the dacite field of the two samples (in red) used to determine a precursor composition.

As for the mafic samples of tholeiitic affinity, the same methodology was used to determine the number of precursors, which element to be used to monitor mass variations (Fig. 5.38) as well as the composition of the least-altered precursor. Referring to figures 5.2 and 5.3, it was established that the tholeiitic basalts (in green) and rutile-altered tholeiitic basalts (in pink) are both part of the same unit, due to their close to identical REE profiles. Mass variations were estimated for these samples only, as we could not find suitable precursors for the other lithologies.

In the case of tholeiitic rocks, only one sample (RRR435562) was chosen to represent the precursor composition, as the tholeiitic basalt dataset was found to vary greatly in terms of Na₂O and K₂O contents, and sample RRR435562 has an average composition (table 5.3).

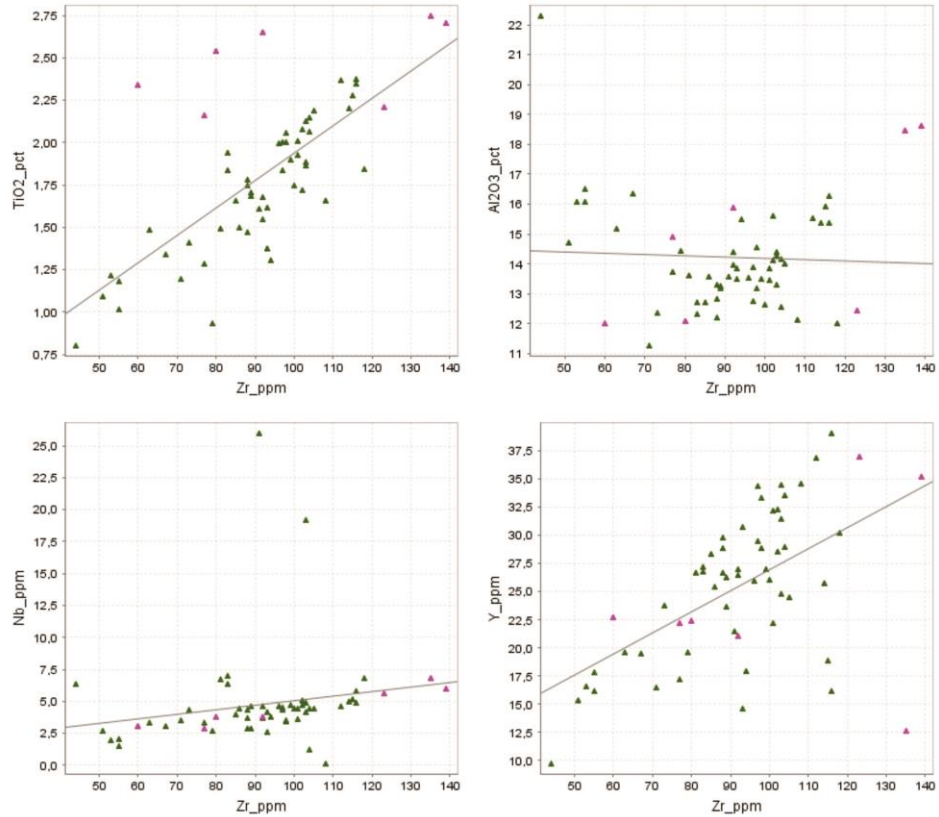


Figure 5.38 : XY plots with regression lines of Zr mass concentrations with respect to various immobile elements for the tholeiitic affinity samples part of the same precursor system (see fig 5.3). In green are tholeiitic basalts (n= 51), and in pink the rutile-altered tholeiitic basalts (n=7).

Table 5.3 : Major oxide and Zr mass concentration for sample RRR435562 chosen as the precursor composition for mass variation calculation. Mass concentrations are expressed in wt. %, except for Zr, which is in ppm.

Sample	RRR435562
SiO ₂	53.05
TiO ₂	2.058
Al ₂ O ₃	14.54
Fe ₂ O ₃	4.9
FeO	10
MnO	0.473
MgO	2.72
CaO	6.5
Na ₂ O	1.4
K ₂ O	1.18
LOI	2.38
Zr (ppm)	98
Total*	100.5

5.3.10 Mass variations: geometry and zonation

5.3.10.1 Mass variation down a composite drill hole

A composite drill core interval part of the 425475E cross section, using drill holes NR060058 and NR060067E, was chosen to represent the mass variation down hole through all mineralized zones. Both drill holes are oriented generally due North, except for some minor clockwise deviation, at a dip starting at around 70 degrees and progressively shallowing with depth. At first glance, there is a very good correlation between the mineralized zones and specific mass variation (Fig. 5.39).

Moving down hole, or from structural hanging wall to footwall, the first zone intersected consists in the Cap zone, combined with the structural hanging wall segment of the ODM zone. In this area, a consistent mass addition of Na_2O (around +2 wt.%), CaO (from +1 to +8 wt.%), CO_2 (0 to +5 wt.%), and SiO_2 (+5 to +20 wt.%) is recorded. A notable MnO mass addition starts at the base of the ODM hanging wall and continues down hole throughout the ODM mineralized zone. Moving down hole to the ODM zone, there is a notable switch from steady sodium addition to constant depletion between 0 and -3 wt.%. This sodium depletion is combined with a potassium (K_2O) addition from 0 to +3 wt.%. CO_2 and CaO , which have positive mass variations above the ODM zone, are now reduced to weak mass addition and local depletion in the case of CaO . This small interval of CaO depletion within the ODM zone is correlated to the interval of strongest K_2O addition and Na_2O loss. As for silica, it has an overall mass addition (+5 to +25 wt.%) similar to the one present in samples from the Cap zone and ODM hanging wall. Manganese (MnO) is added throughout the ODM zone and an increase in manganese addition from an average of + 0.1 to +0.2 wt.% is present at the base of the ODM zone. Moving further down hole towards the stratigraphically lowermost parts of the system, i.e. the HS and 433 zones, we observe constant sodium (Na_2O) depletion from -1 to -3 wt.%. Potassium (K_2O) is added, although in lesser amounts (+0.5 to +1.5 wt.%) compared to the ODM zone slightly higher in the stratigraphy. Manganese and calcium (MnO and CaO) vary from a weak, constant addition to a steady depletion moving downhole. Spikes of combined strong CO_2 addition and moderate SiO_2 depletion within the HS and 433 zones are correlated to spikes in metals.

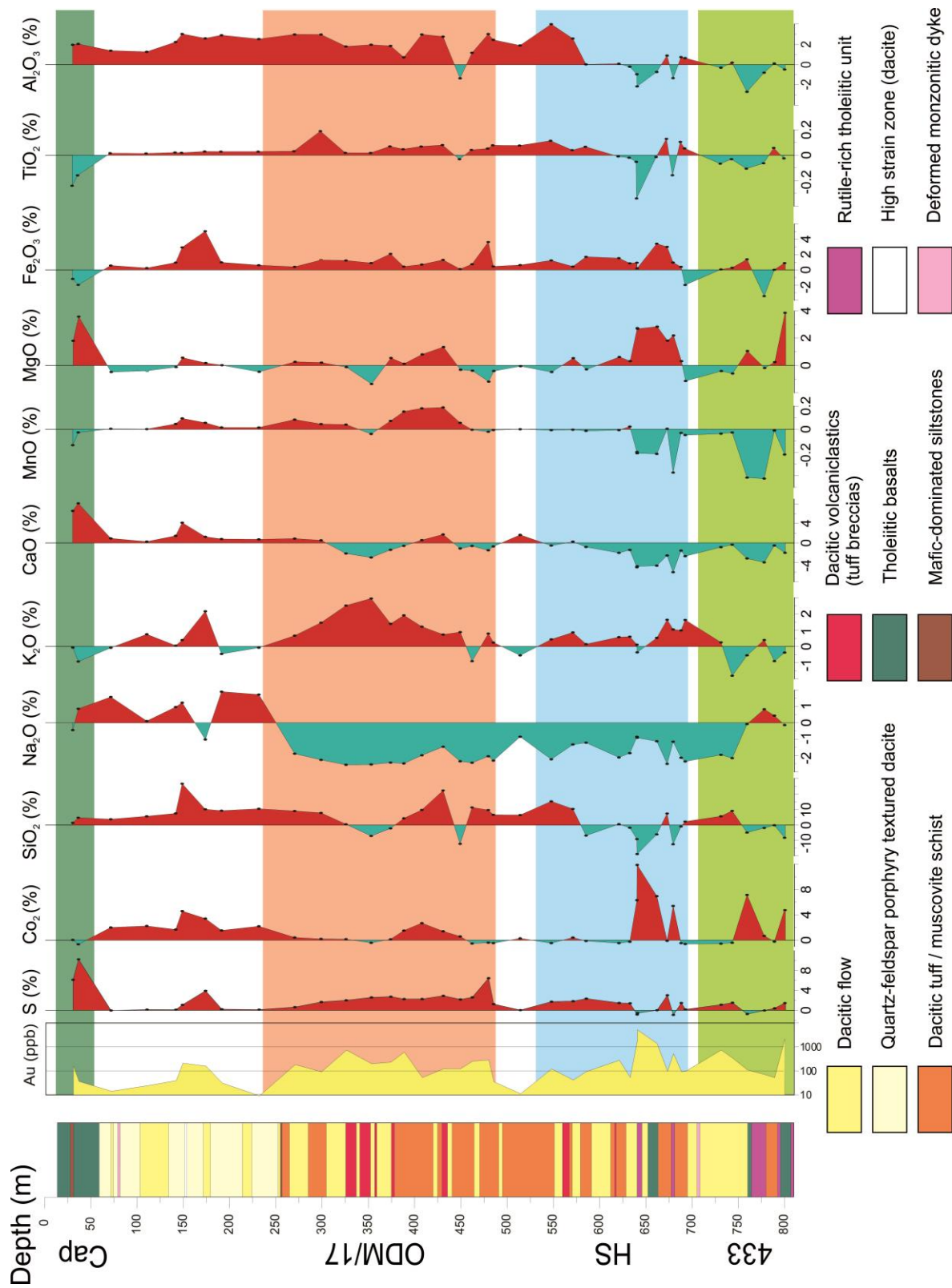


Figure 5.39 : Evolution of mass balance variations down hole through the different mineralized zones along composite drill hole NR060058 and NR060067E within the 425475E cross section (\pm 25m E-W metres).

5.3.10.2 Mass variation within the 425475E cross section

When plotting calculated mass variations in space, the zonation in element mass variation previously highlighted on the composite drill hole (Fig. 5.39) can be verified at a larger scale using additional drill holes located on the 425475E cross section (Fig. 3.23; appendix I). For this study, a series of volumes corresponding to specific mass variation threshold values were modelled using the Leapfrog[®] Mining software. Implicit modelling was done using the provided linear variogram model, with a global trend setting the ellipsoid ratios (3:3:1) along with the data range for interpolation (1.442, 1.442, 0.4807). The global modelling trend was oriented parallel to S_2 and included the L_2 stretching lineation, which corresponds to a dip, dip azimuth and pitch of 61°, 192° and 108° respectively. Linear modelling was favoured over spheroidal, to restrain the generated shells within the YZ plane of the North-South oriented cross section, rather than having noise generated through modelling along the X axis in a spheroidal variogram model. Colour maps draped on the modelled shells are graded according to the input mass variation value, with lower data values associated to cooler shades. Tholeiitic affinity samples had to be removed from the modelling, since shells are based on threshold values and mass variations of major oxides are influenced by protolith nature and chemistry.

Modelling of CaO mass addition over 1.7 wt.% (Fig. 5.40) reveals a calcium addition focused within the Cap zone and the ODM hanging wall. Positive mass variation of CO₂ (Fig. 5.41) is widespread and most intense within the Cap zone and the hanging wall and upper half of the ODM zone. A zone of sodium gain (Fig. 5.42) is localized in the ODM hanging wall, with greater enrichment closer to surface. The sodium addition shell located below the 433 zone may not be as important as depicted on the model as it is based on sparse data. The ODM zone is centered on an area of intense sodium loss (≤ 2.0 wt.% Na₂O). Manganese (MnO) addition (Fig. 5.43) is also widespread within the deposit, although a clear zone of increased intensity is centered on the ODM body. Silica addition (Fig. 5.44) with a threshold value of +5 wt.% was modelled, defining a tight distribution along both footwall and hanging wall of the ODM zone. In comparison, strong potassium (K₂O) addition (threshold value of +1.5 wt.%; Fig. 5.45) is centered on the core of the ODM zone, i.e. its higher grade part. When superimposing both modelled shells of silica (+5 wt.%) and K₂O (+1.5 wt.%) enrichment (Fig. 5.46), and taking into consideration zones of sodium depletion, we obtain a zone of potassic alteration centered on the main mineralized body, with a semi-conformable area of silicification bounding the potassic zone. This last figure illustrates the link between mass variation induced by pre-main deformation hydrothermal alteration and gold mineralization within the main ODM body.

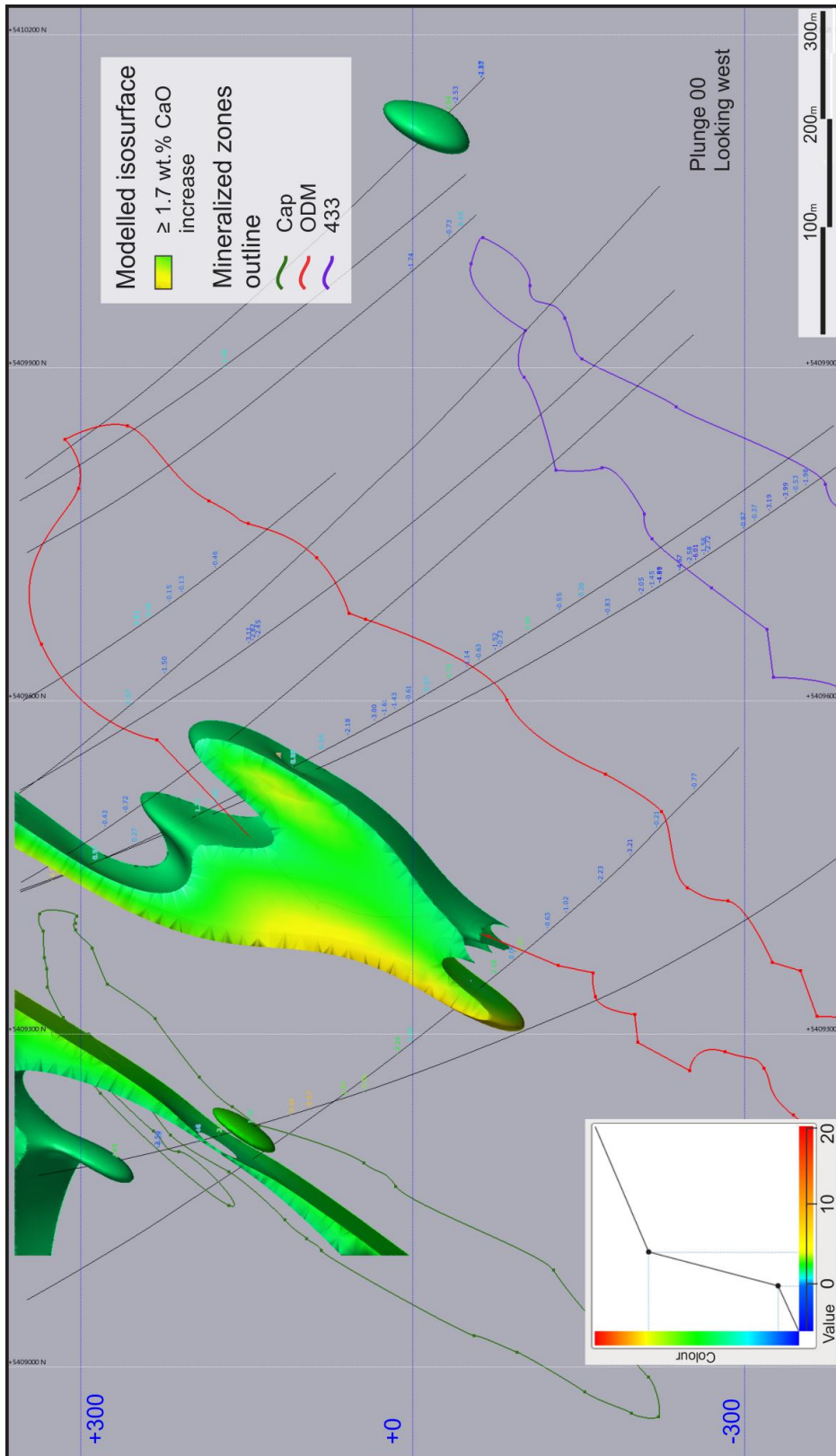


Figure 5.40 : Modelling of CaO mass addition over 1.7 wt.% for the calc-alkaline lithologies along the 425475E cross section.

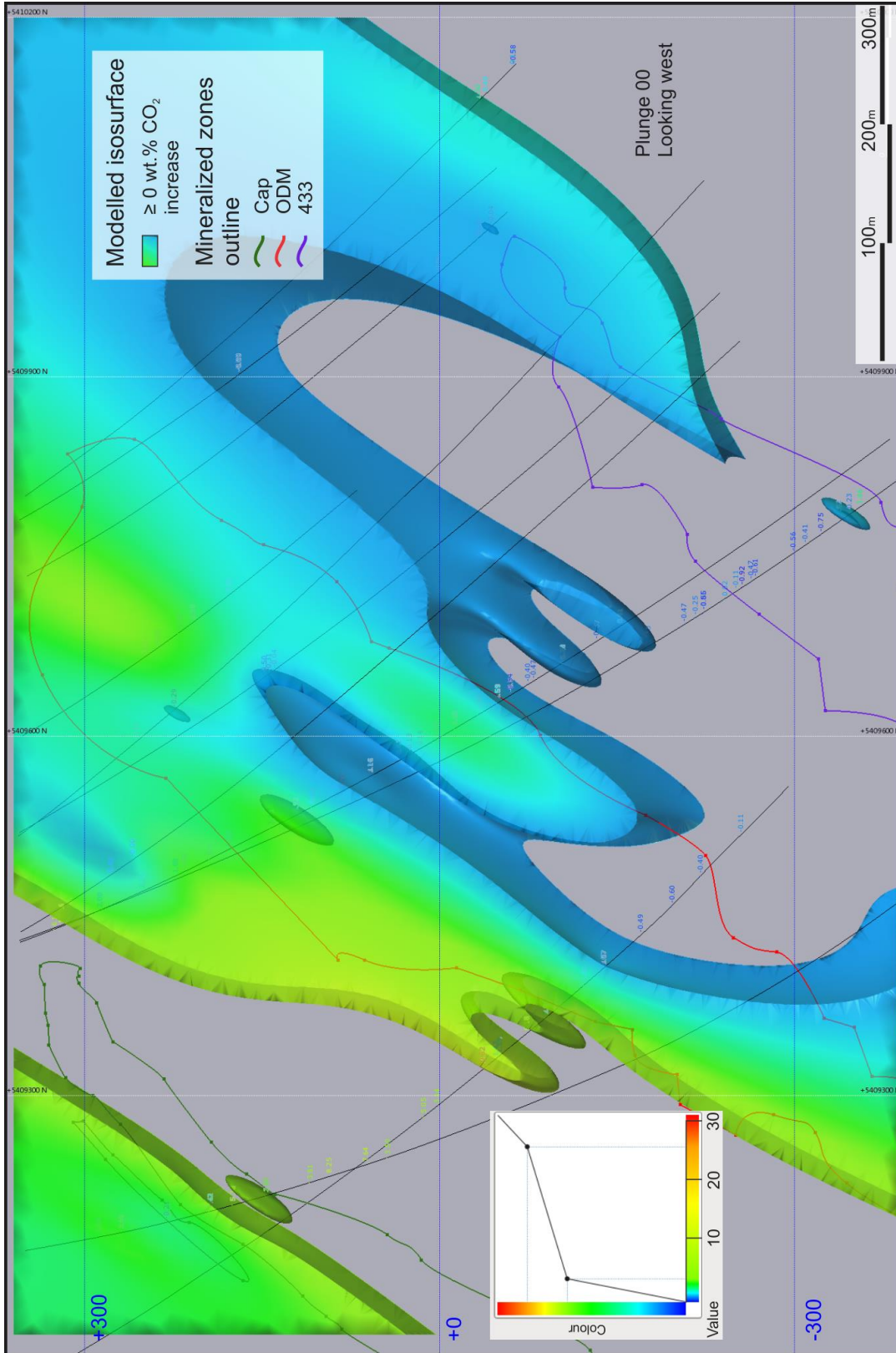


Figure 5.41 : Modelling of CO_2 mass addition (over 0 wt.%) for the calc-alkaline lithologies along the 425475E cross section.

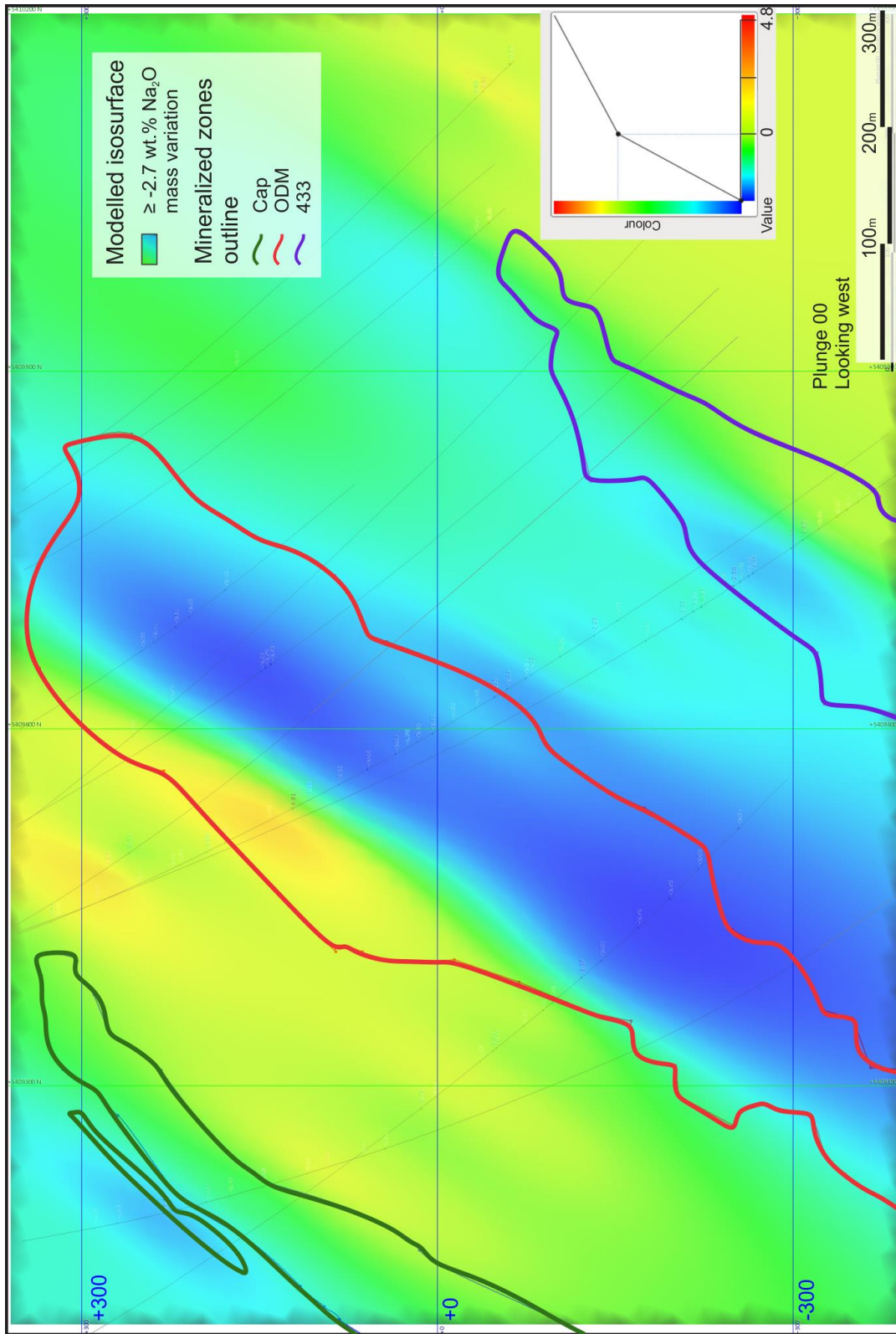


Figure 5.42 : Modelling of Na₂O mass variation (between -2.7 and +4.8 wt.%) along the 425475E cross section for all lithologies. Warm colours correspond to mass addition, cold colours to mass subtraction.

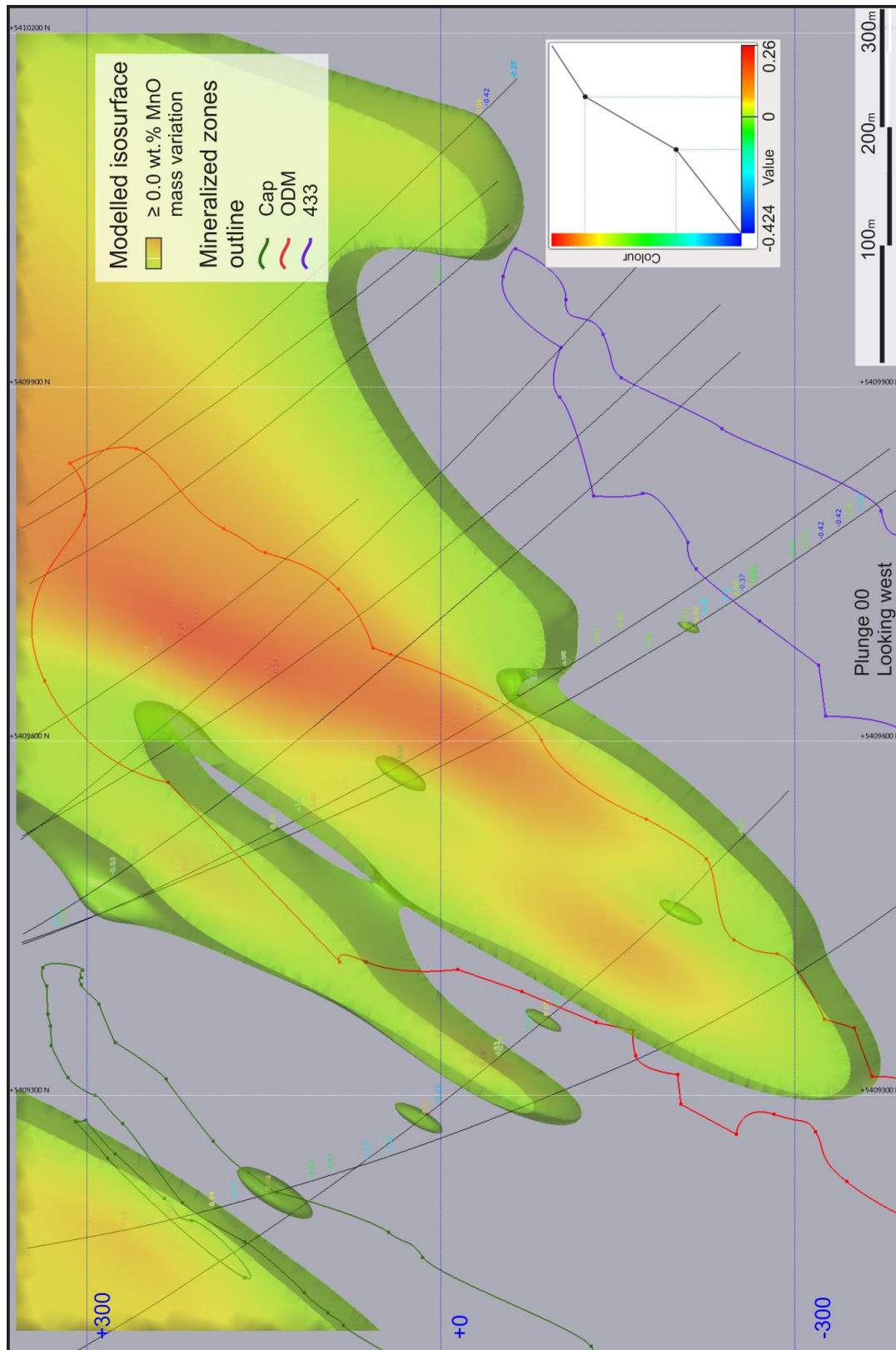


Figure 5.43 : Modelling of MnO positive mass addition (over 0 wt.%) for the calc-alkaline lithologies along the 425475E cross section.

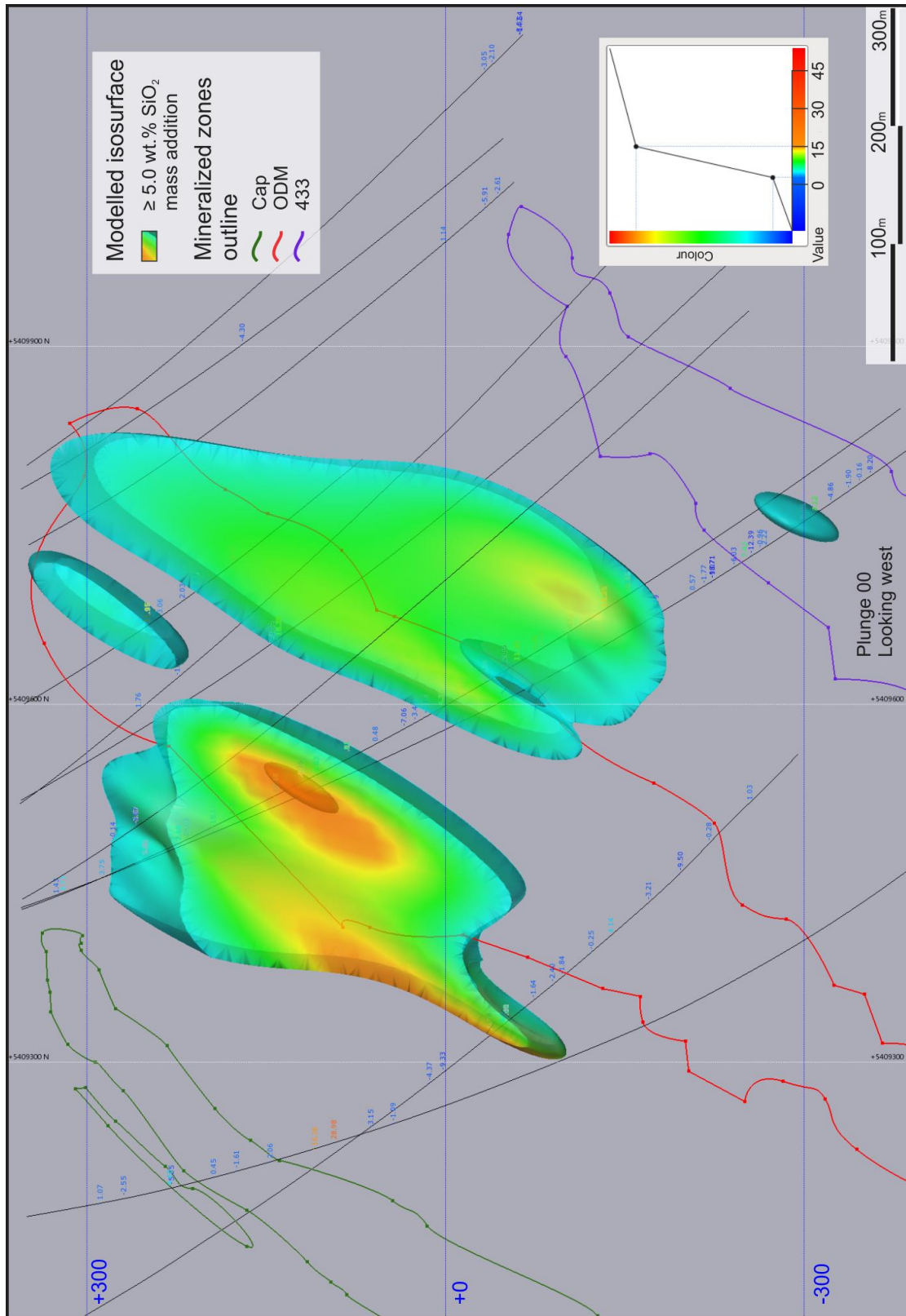


Figure 5.44 : Modelling of SiO₂ mass addition over 5.0 wt.% for the calc-alkaline lithologies along the 425475E cross section.

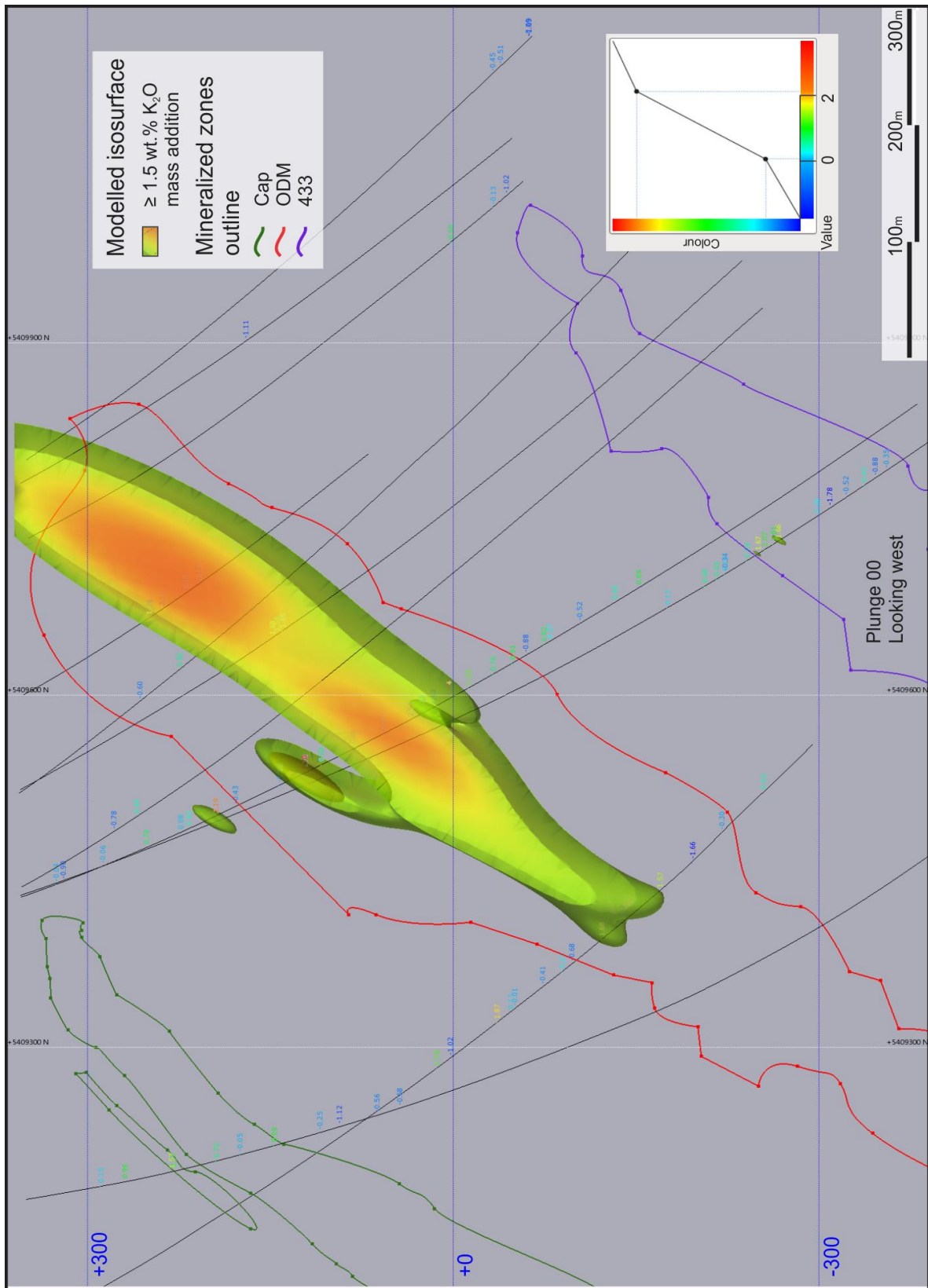


Figure 5.45 : Modelling of K₂O mass addition over 1.5 wt.% for the calc-alkaline lithologies along the 425475E cross section.

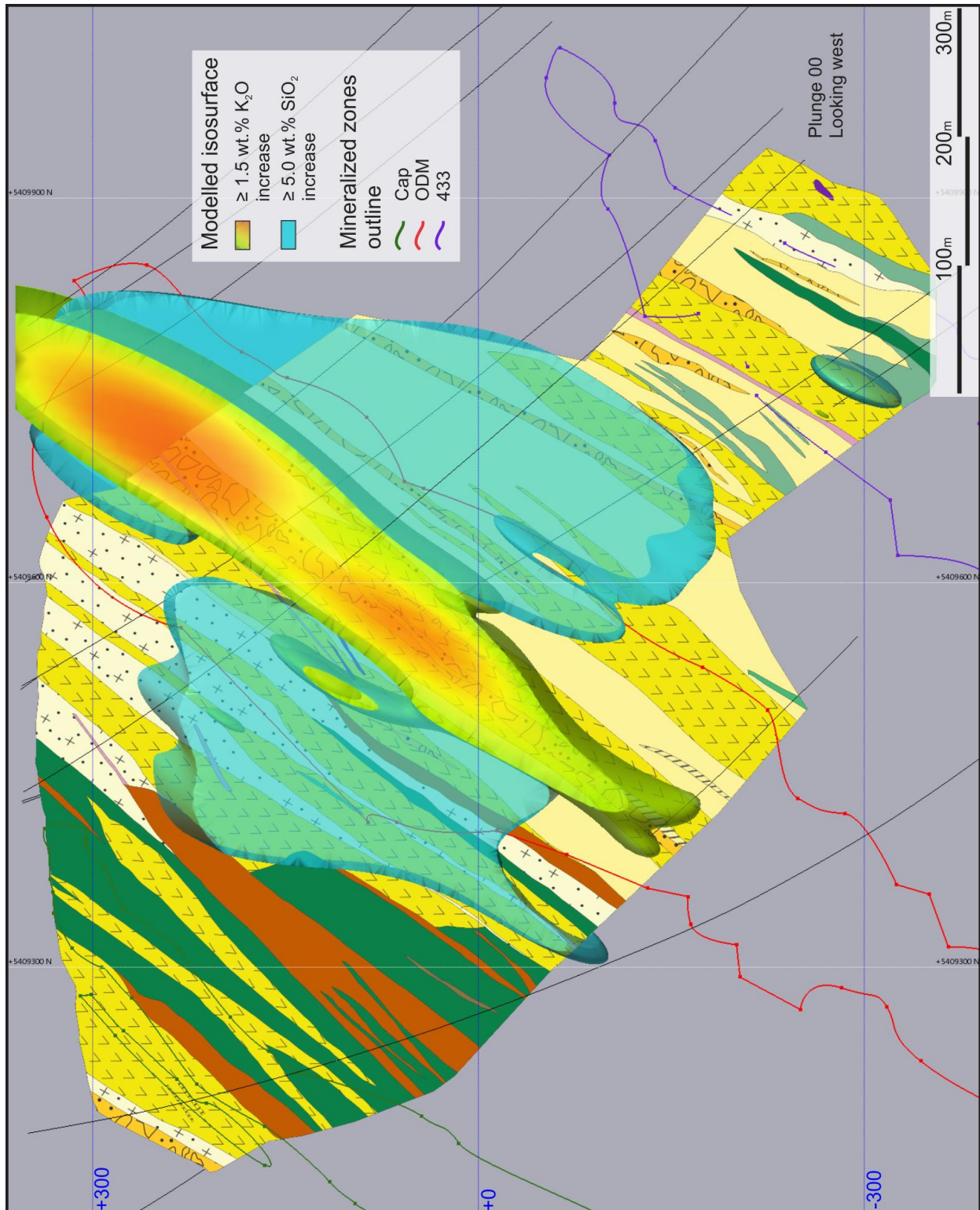


Figure 5.46 : Combined modelling of SiO₂ mass addition over 5.0 wt.% and K₂O mass addition over 1.5 wt.% for the calc-alkaline lithologies along the 425475E cross section. Cap zone trace is in green, ODM zone in red, and 433 zone in purple. See figure 3.23 (appendix I) for a legend of the different volcanic facies.

5.3.11 Mass variation with relationship to alteration mineralogy

The distribution in space of the various minerals associated with hydrothermal alteration (or their metamorphosed equivalents) can be correlated with discrete zones of specific mass gains or losses of certain elements.

The ODM hanging wall is an area of diagnostic CO₂, CaO and Na₂O addition, which is correlated with weaker albite destruction and the common presence of epidote and carbonates. Slightly lower in the succession, a zone of conformable potassium (K₂O) addition and Na₂O loss, which spatially corresponds to the ODM zone, correlates with a zone of strong albite destruction and muscovite (sericite) development. Strongest gain in MnO is located within the ODM zone close to surface and is correlated to the presence Mn-rich carbonates. The deeper parts of the ODM zone are characterized by a minor gain in MnO, which is concordant with the presence of spessartine (Mn-rich) garnet porphyroblasts. Lenses of aluminosilicates are very thin and discontinuous along strike, therefore they cannot be correlated to any zones of mass variation. If they did, one would expect to see a zone of intense combined leaching of all major oxides (table 5.4).

Table 5.4 : Mass variation (in wt. %) of major oxides for kyanite-chloritoid bearing sample RRR435660 showing strong leaching in most elements except SiO₂, Al₂O₃ and S.

SiO ₂	TiO ₂	Al ₂ O ₃	Fe ₂ O ₃	MnO	MgO	CaO	Na ₂ O	K ₂ O	S	CO ₂
+5.00	-0.09	+0.83	-0.76	-0.01	-1.46	-3.35	-2.83	-2.08	+0.12	-0.57

The HS and 433 zones are spatially associated with areas of significant CO₂ addition, which correlates with corridors of carbonate veining occurring in S₂-parallel high strain zones. In these mineralized zones, CaO, Na₂O and strong MnO leaching combined with MgO and K₂O addition is reflected in the ubiquity of sericite, quartz and chlorite and the overall poor occurrence of secondary alteration minerals.

5.3.12 Mass variation with relationship to primary volcanic facies

In order to establish the potential effect of primary volcanic facies (i.e. initial porosity and permeability) on the style, distribution and intensity of the hydrothermal alteration, mass

changes were calculated for each facies present in the dacitic rocks that host the bulk of the deposit.

Both coherent and volcanoclastic dacites have been previously identified as having the same protolith (section 3.2.3) and have therefore a common initial composition, allowing for comparison of the alteration products. Figure 5.47 illustrates systematic (with the exception of MgO), greater mass gains or losses in volcanoclastic rocks than in dacitic samples from coherent facies. This indicates the preferential alteration (and fluid flow) of the initially more permeable (volcanoclastic) units, which is in agreement with observations made by Wartman (2011).

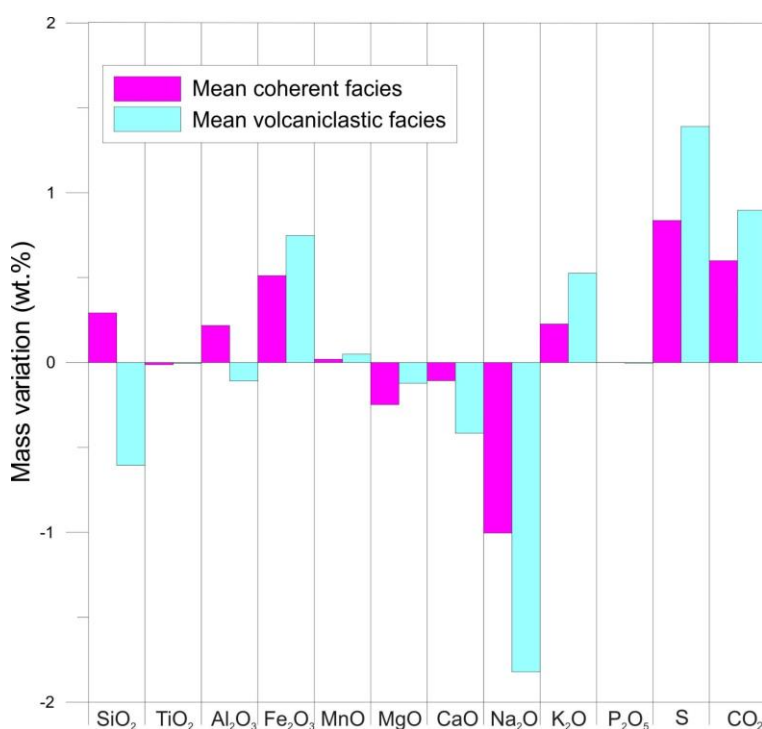


Figure 5.47 : Comparative bar chart illustrating mean (n=257) mass variation values (wt.%) between dacitic samples of coherent and volcanoclastic facies.

5.5 Oxygen isotopes

Whole-rock stable oxygen isotope ($\delta^{18}\text{O}$) ratios have been measured on a total of 46 samples in the deposit area and its surroundings (Fig. 5.48; see section 1.3.2 for information on techniques used). Measurements were conducted on powders from unassayed pulps. Samples from within the deposit were taken at various depths and are all part of the oblique plane (see Fig. 3.22;

appendix I), while the samples outside the deposit are from 25 metres or less from surface. All samples are calc-alkaline dacites (various facies), except for one tholeiitic basalt sample.

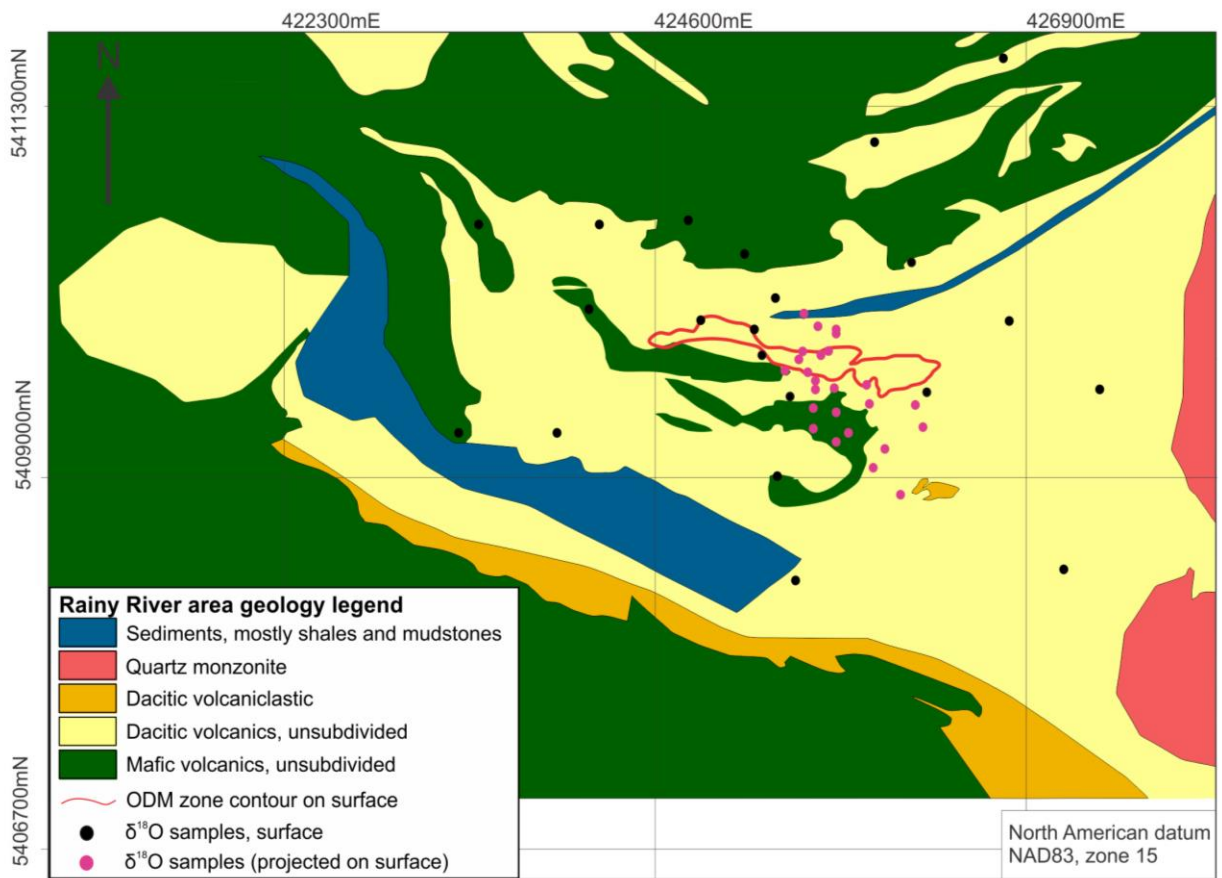


Figure 5.48 : Rainy River project geologic map with sample location for oxygen isotope analyses. Note that samples from the immediate deposit area were taken at various depths and projected at surface. Map compiled from Fletcher and Irvine (1954) and New Gold Inc. (2014).

Traditionally, isotopic values are reported as ratios between the number of atoms from the heavy isotope to that of the light isotope (Huston, 1999). However, absolute ratios on their own are less precise than isotopic values reported as differences in absolute ratios. In the case of oxygen isotopes, the standard from which the samples isotopic ratio is compared to is the Vienna Standard Mean Oceanic Water (V-SMOW). Isotopic ratio values are reported using the nomenclature $\delta^{18}\text{O}$, in per mil (‰).

Oxygen isotopes can help determine the approximate temperature of alteration, and also give an idea of the fluid source (Huston, 1999). For the Rainy River project, oxygen isotopes were measured to test a potential zonation in $\delta^{18}\text{O}$ values and its relationship to alteration zones and mineralized bodies. In addition to that, data collected for this study can be compared with data

from other known Archean, hydrothermal-related metamorphosed deposits of the Superior Province.

5.3.13 Results

Results obtained for all Rainy River samples show a strong clustering around an average value of 12.4‰ (Fig. 5.49). Considering an average value of 8-10‰ for an un-altered Archean rhyolite (Huston, 1999), $\delta^{18}\text{O}$ values for dacites from the Rainy River deposit and surroundings are systematically enriched (isotopically heavy).

$\delta^{18}\text{O}$ values from samples located within the deposit versus its surroundings have a slightly higher median value (12.87‰ vs. 12.1‰; Fig. 5.50) and a tighter distribution. One sample is considered as an outlier in this distribution and corresponds to the only mafic sample of the data set.

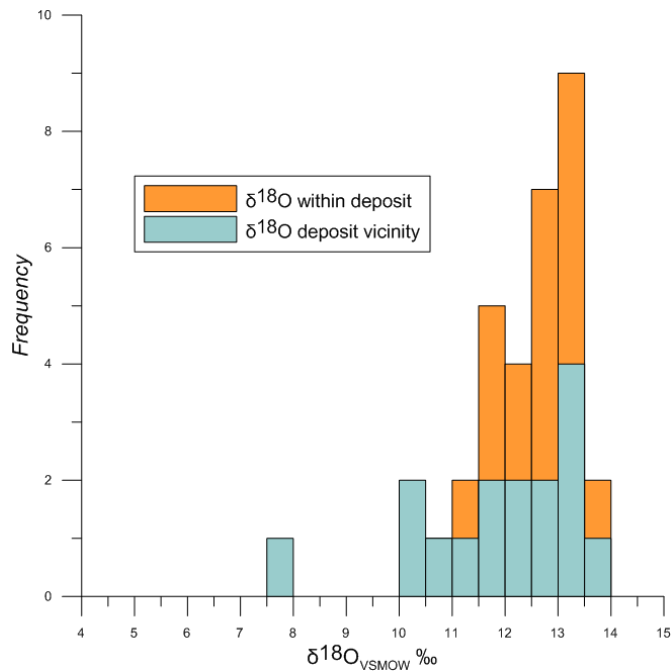


Figure 5.49 : Histogram of all $\delta^{18}\text{O}_{\text{VSMOW}}$ values for samples from this study (n=46).

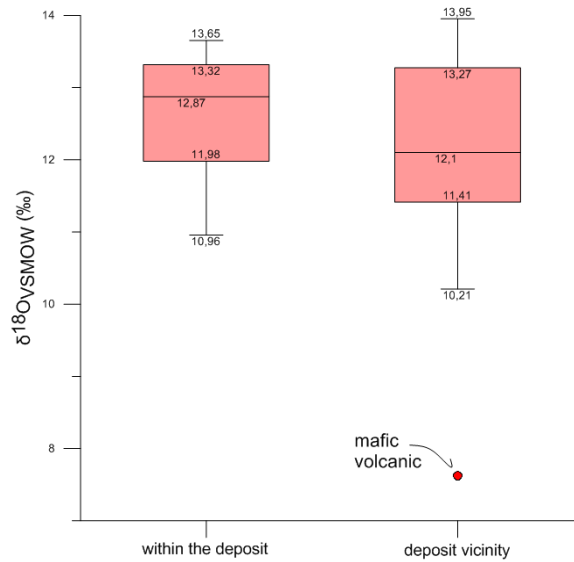


Figure 5.50 : Whisker plot illustrating quartiles (25, 75), median, maximum and minimum $\delta^{18}\text{O}_{\text{VSMOW}}$ values for all samples from this study (n=46).

When plotted in space (Fig. 5.51), isocontours of $\delta^{18}\text{O}$ values above 13‰ show a clear zonation with respect to the ODM zone. $\delta^{18}\text{O}$ values also seem to increase towards the Black Hawk stock to the west of the deposit, although samples in that area are very sparse which does not allow to verify this potential correlation. Alternatively, these high $\delta^{18}\text{O}$ values could also underline the Intrepid zone. In both cases, tighter sampling is required to test these hypotheses.

Focusing on the samples within the oblique plane (Fig. 5.52), we notice systematic high $\delta^{18}\text{O}$ values for samples located within all mineralized zones, with the highest values restricted to the lower half of the ODM zone and its hanging wall. Lower values (between 11.5 and 11.9‰) are systematically found within the ODM zone hanging wall.

In summary, all mineralized zones at Rainy River are characterized by $\delta^{18}\text{O}$ values above 12.8‰. $\delta^{18}\text{O}$ values above 13.3‰ clearly outline the ODM zone, at surface and at depth. Three additional samples with $\delta^{18}\text{O}$ values above 13‰ are located close to both the Intrepid mineralized zone and the Black Hawk stock.

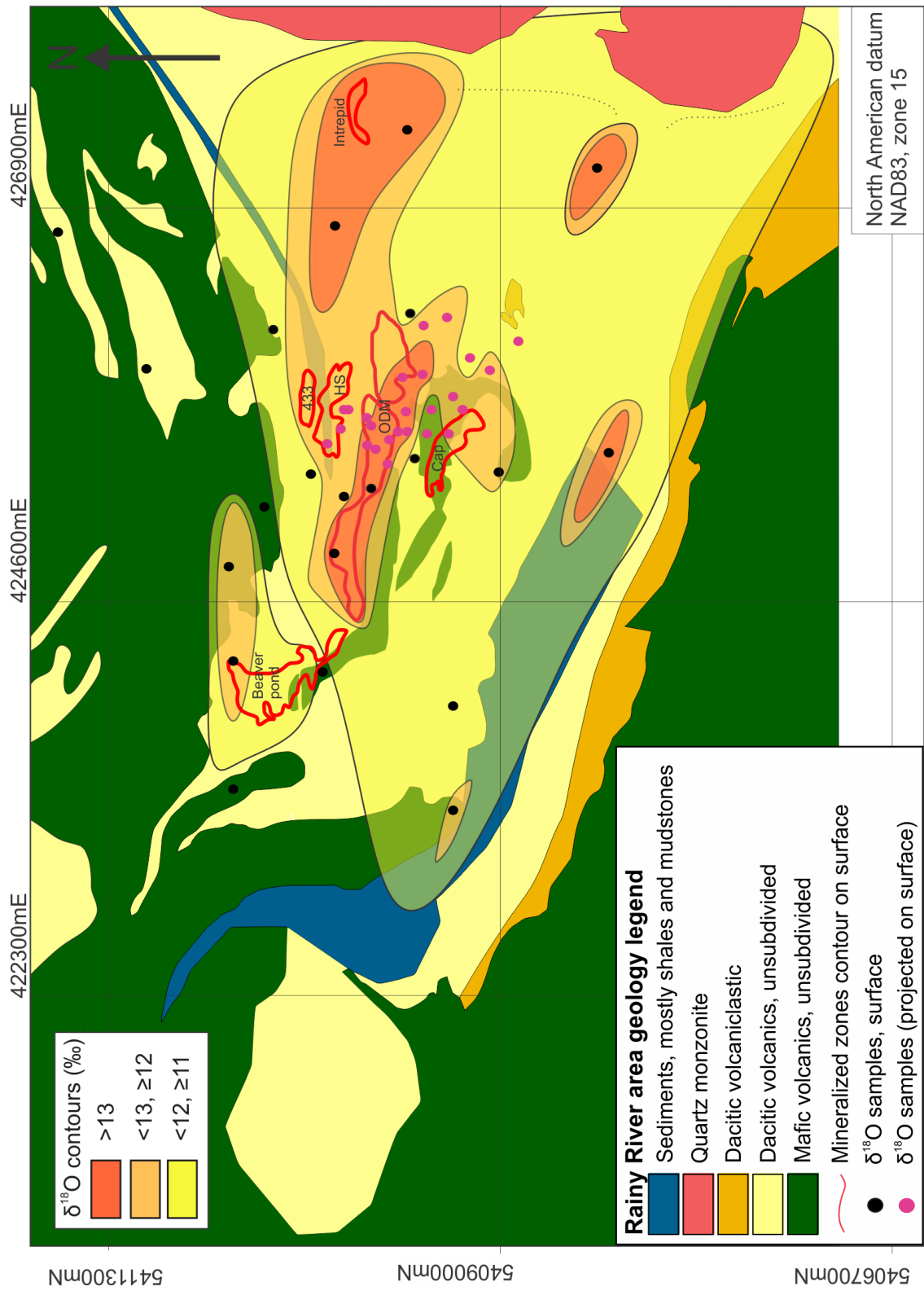


Figure 5.51 : Variation of $\delta^{18}\text{O}$ values within the Rainy River deposit area. NOTE: $\delta^{18}\text{O}$ values from within the deposit (in pink) are projected on surface. Map compiled after Fletcher and Irvine (1954) and New Gold Inc. (2014).

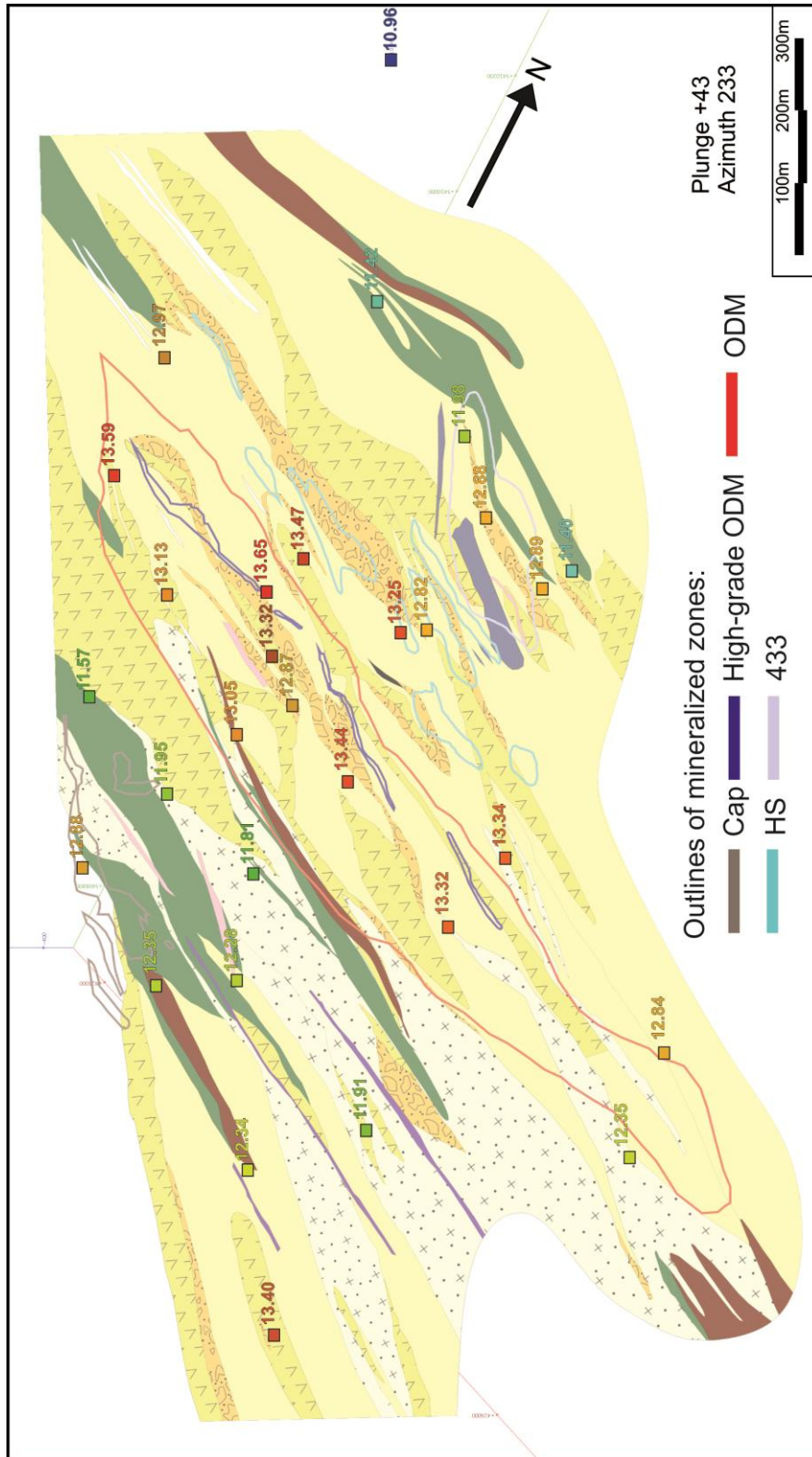


Figure 5.52 : Variation of $\delta^{18}\text{O}$ values within the oblique plane in space (oriented 323N/43°). Note good correlation between high grade ODM zone and enriched samples. See figure 3.22 (appendix I) for volcanic facies legend.

5.3.14 Interpretation of $\delta^{18}\text{O}$ values

As previously indicated, calc-alkaline dacites from this study are characterized by relatively tight Zr/TiO₂ ratio values (Fig. 5.53), which is interpreted as being caused by a homogenous protolith having undergone little to no fractional crystallization (MacLean and Barrett, 1993). Taking this into account, the variation in $\delta^{18}\text{O}$ values measured cannot be explained by fractional crystallization of an evolving source, but rather through processes taking place after partial melting and emplacement in the crust or at seafloor.

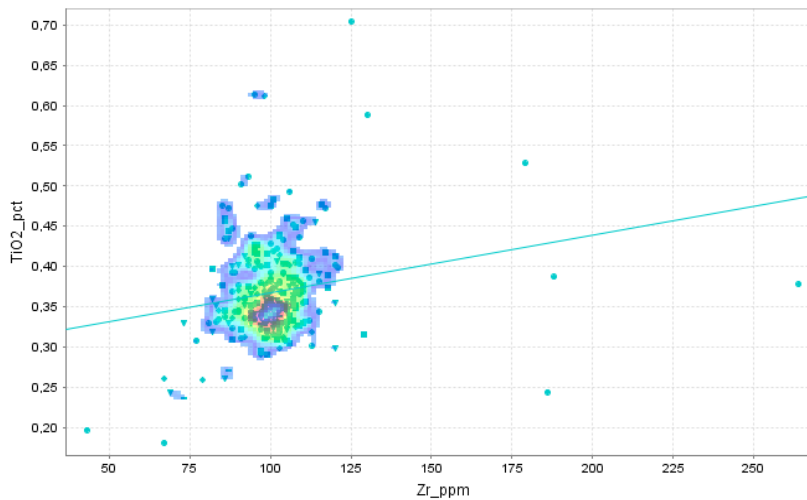


Figure 5.53 : XY plot of Zr and TiO₂ for all calc-alkalic samples, including intrusives (n = 262). Clustering around a single point along the fractionation curve indicates a homogenous protolith having undergone very little fractional crystallization (MacLean and Barrett, 1993).

In an Archean setting, high $\delta^{18}\text{O}$ values can be obtained through several processes, which lead to multiple plausible interpretations for the values obtained in this study. According to Galley (1993), the most common mechanism responsible for $\delta^{18}\text{O}$ values enrichment is the circulation of large volumes of low temperature seawater within a cooling volcanic pile. Alternatively, in a context of fertile hydrothermal system, zones of high $\delta^{18}\text{O}$ values can be generated through massive silica dumping (Galley, 1993; Huston, 1999). High values associated with large silica addition are present in silicified rhyolites from the Kidd Creek Cu-Zn VMS deposit in the Abitibi greenstone belt (Taylor and Huston, 1999; Huston, 1999). Such high $\delta^{18}\text{O}$ values as the one at Rainy River are characteristic of Au-rich hydrothermal systems from the Blake River Group in the Abitibi greenstone belt (Bousquet 2-Dumagami: Marquis *et al.*, 1992, LaRonde Penna: Beaudoin *et al.*, 2014). In the study by Beaudoin *et al.* (2014), the high $\delta^{18}\text{O}$ values from the LaRonde Penna deposit are interpreted as the result of low temperature ($\approx 150^\circ\text{C}$) hydrothermal

alteration at high water to rock ratio, although this interpretation is still debated (Mercier-Langevin, pers. commun., 2014). Marquis *et al.* (1992) propose a mixed interpretation for similar $\delta^{18}\text{O}$ values. High $\delta^{18}\text{O}$ values of the less altered country rocks containing both albite and quartz would indicate a strong seawater ($\delta^{18}\text{O} \approx 0\text{‰}$) interaction at low temperatures (125-150°C), whilst similar $\delta^{18}\text{O}$ values, this time from albite-bearing volcanics within the deposit's footwall, would result from interaction with a hydrothermal fluid of higher $\delta^{18}\text{O}$ value (7 to 12.5‰) in equilibrium with peak metamorphic conditions (400-500°C). Compilations of $\delta^{18}\text{O}$ values for various VMS systems (Beaty and Taylor, 1982; Huston, 1999) highlight a recurring zonation of values with respect to mineralized lenses. Typically, zones of intense, high temperature alteration in the footwall of the lens have very low $\delta^{18}\text{O}$ values, with the surrounding area characterized by higher values of up to 5‰ higher than the least-altered values (Huston, 1999). Still in VMS context, such zones of high $\delta^{18}\text{O}$ values are interpreted as recharge zones within the hydrothermal convection system (Huston, 1999).

At Rainy River, the high $\delta^{18}\text{O}$ values associated with all mineralized zones are not correlated to a large silica addition (Fig. 5.54), rejecting the hypothesis of silica dumping as being responsible for the isotopically heavy signature obtained. Conversely, $\delta^{18}\text{O}$ values show a fair negative correlation with mass variation in Na_2O (Fig. 5.54), with the exception of the samples located around the Intrepid zone and the Black Hawk stock. $\delta^{18}\text{O}$ values are also weakly positively correlated with an increase of the advanced argillic alteration index (Fig. 5.55), but not with the CCP and AI indexes (Ishikawa *et al.*, 1976; Large *et al.*, 2001a). These correlations suggest that the fluids responsible for the $\delta^{18}\text{O}$ signature measured in samples are the ones involved in hydrothermal reactions causing sodium loss and argillic alteration within the deposit.

The enriched $\delta^{18}\text{O}$ signature obtained at Rainy River is therefore the result of dissimilar processes than the ones invoked at the Kidd Creek and LaRonde Penna deposits (*i.e.* low temperature silica dumping from the hydrothermal system related to Au mineralization), although the $\delta^{18}\text{O}$ signature at the LaRonde Penna deposit is still debated. The existing literature available documenting $\delta^{18}\text{O}$ values in Archean Au-rich systems does not offer any viable explanation on the cause of the $\delta^{18}\text{O}$ signature observed at Rainy River. The high $\delta^{18}\text{O}$ values located around the Black Hawk stock and related to sodium addition (Fig. 5.54) could be the overprinted record of a later, low temperature interaction between seawater and the dacitic volcanic pile, with heat provided by the nearby Black Hawk stock, as suggested by Galley (1993). Alternatively, these $\delta^{18}\text{O}$ values measured could be caused by fluid circulation within the recharge zone of the hydrothermal cell based on the "typical" model for VMS-type systems

(Galley, 1993; Huston, 1999). As mentioned earlier, additional data from within the Intrepid zone along with a tighter sampling grid around the Black Hawk stock would be necessary to determine if the high $\delta^{18}\text{O}$ values are attributed to a proximal location to a cooling intrusive body or to a VMS-style hydrothermal cell (associated with the Intrepid zone?).

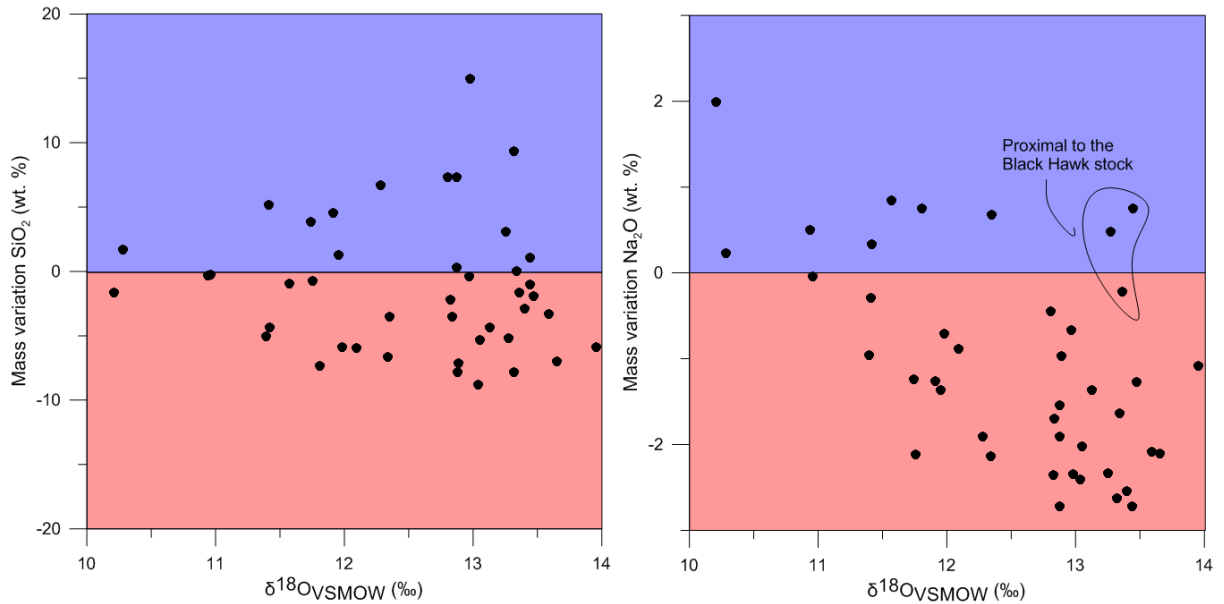


Figure 5.54 : Plot of $\delta^{18}\text{O}$ values from calc-alkalic samples with respect to mass variations of SiO_2 and Na_2O . $N=44$.

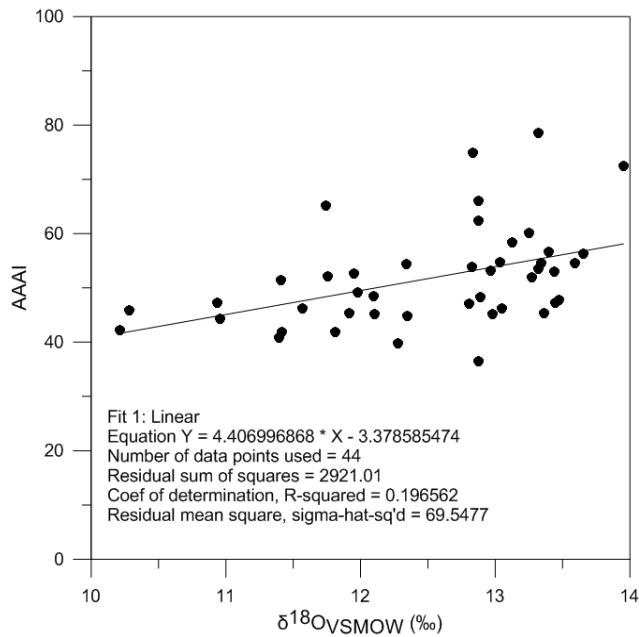


Figure 5.55 : Plot of $\delta^{18}\text{O}$ values from calc-alkalic samples ($n=44$) with respect of the advanced argillic alteration index (AAAI; Williams and Davidson, 2004), showing a weak positive correlation.

5.6 Summary on the hydrothermal alteration

The following is a summary of the information gathered on the hydrothermal alteration at the Rainy River deposit area that integrates data obtained from drill core logging, petrographic work, microprobe analyses, litho-geochemistry, mass balance calculations, and whole-rock oxygen isotopes.

Alteration mineralogy at Rainy River is pre-D2 and dominated by muscovite and chlorite, with accessory alteration phases of albite, biotite (almost completely retrograded to chlorite), chloritoid, epidote, Fe-Mg carbonates, kyanite, rutile, and spessartine garnets. Samples from the Rainy River deposit are characterized by seemingly "fresh" compositions when plotted on the Alteration Box Plot (Large *et al.*, 2001; Trépanier, 2009) as well as on an AI versus AAI plot (Figs. 5.4, 5.5), although the latter diagram reveals a strong muscovite alteration trend as well as samples characteristic of argillic alteration zones. Furthermore, the alkali-alumina molar ratio diagram by Davies and Whitehead (2006; Fig 5.6) illustrates the existence of both albitization and sericitization alteration processes. Visual and petrographic documentation of the replacement of albite phenocrysts and microphenocrysts by sericite (amongst others) confirms a sequence of events evolving from an early albitization followed by a marked sericitization. These two alteration processes have opposite effects on the sodium concentrations (i.e. albitization adds sodium whereas sericitization leads to sodium loss) and might explain why most samples possess a moderate alteration index value, leading to a misleading "poorly altered" classification on the Alteration Box Plot (Large *et al.*, 2001a), where in fact the samples AI values are the result of two alteration processes that cancel themselves out in terms of sodium concentrations. Additionally, the addition of CaO due to carbonate alteration lowers the AI value of samples, therefore also contributing to under valuating any potential sodium loss on the diagram. Knowing that carbonate alteration is present at Rainy River, it provides an additional explanation as to why many samples plot in a relatively fresh position on the Alteration Box Plot.

Distribution of the different primary (section 5.3.1) and secondary alteration minerals (section 5.3.8), along with zones of specific mass changes and mineral chemistry of the chlorite and muscovite (sericite) both show a zonation perpendicular to the stacking of the different mineralized zones, *i.e.* discordant to stratigraphy. Perpendicular to the mineralized zones, stacking alteration evolves from potassic restricted to the main ODM mineralized body, silicification and carbonate alteration in the proximal hanging wall and upper parts of the ODM

mineralized body, followed by a marked albitization and epidotization in the uppermost part of the system. Dispersed and discontinuous minor lenses of kyanite and chloritoid are also found within the ODM body and are interpreted as metamorphic equivalents of argillic alteration zones. This is supported by the position of aluminosilicates-bearing samples on the Al-AAAI diagram (Fig. 5.5).

Carbonate alteration is dominated by ankerite to ferroan-dolomitic compositions and affects both mafic and felsic rocks. Manganese-rich carbonates are associated to high grade mineralization within the ODM zone, hinting towards an interaction with seawater during alteration and a hydrothermal nature of the carbonate alteration. Additionally, samples with high carbonate saturation indexes located at the western end of the ODM zone have a more "orogenic" signature and could result from CO₂ addition early- to syn-D₂ in timing (see section 4.3.4). This will be further discussed in chapter 7.

The aerial extent of albitization and epidotization of the host rocks at Rainy River is interpreted to have covered a wider area than the one at which it is observed today, mostly due to the deformation recorded by the deposit and because the ODM zone below has undergone massive potassium addition (Figs 5.39, 5.45, 5.46), translating into muscovite crystallization at the expense of albite according to the following formula:



The area of most intense sericitization (muscovite alteration) through albite destruction (involving potassium addition and sodium removal) is centered on the main ODM mineralized body, underlining the association between gold mineralization and sericitization. The map of the oblique plane representing the modal distribution of sericite (Fig. 5.9) also illustrates this association. Furthermore, the highest δ¹⁸O values obtained within the deposit are centered on the ODM zone and its footwall (Figs. 5.51, 5.52), indicating that the fluids responsible for sericitization are also potentially responsible for the distinct enriched δ¹⁸O signature of the dacites hosting mineralization. Plot of δ¹⁸O values from calc-alkalic samples (n=44) also show a fair positive correlation with the advanced argillic alteration index (AAAI; Williams and Davidson, 2004), thus hinting at a common process responsible for higher AAI and δ¹⁸O values and muscovite content. Microprobe analyses of muscovite and chlorite indicate an Mg-rich composition associated with gold mineralization in the dacites from the ODM, HS and 433 zones.

Stratigraphically below the ODM body, intense and destructive chloritization and sericitization occur, with the rare presence of kyanite and garnets as secondary alteration minerals. Tholeiitic basalts of the 433 zone are in some cases rutile-altered, seemingly resulting from local remobilization of titanium initially present in titanomagnetite for basalts and/or as inclusions in feldspars as proposed elsewhere (e.g., LaRonde Penna deposit: Dubé et al., 2007).

In summary, all mineralized zones that compose the Rainy River deposit can be outlined by zones of specific mass variations as well as by $\delta^{18}\text{O}$ values of the host rock above 12.8 ‰. A series of alteration-related minerals of specific chemistry also outline the different mineralized zones. Furthermore, mass balance calculations demonstrate that volcanism-induced porosity of the host rock influences the intensity of alteration (Fig. 5.47).

Compiling the different observations made on thin section as well as from drill core observation, figure 5.56 offers a paragenetic sequence of alteration with relationship to: 1) the main sericitization event (linked to Au mineralization in the ODM), 2) the D_2 deformation event, and 3) regional upper greenschist metamorphism (syn- D_2).

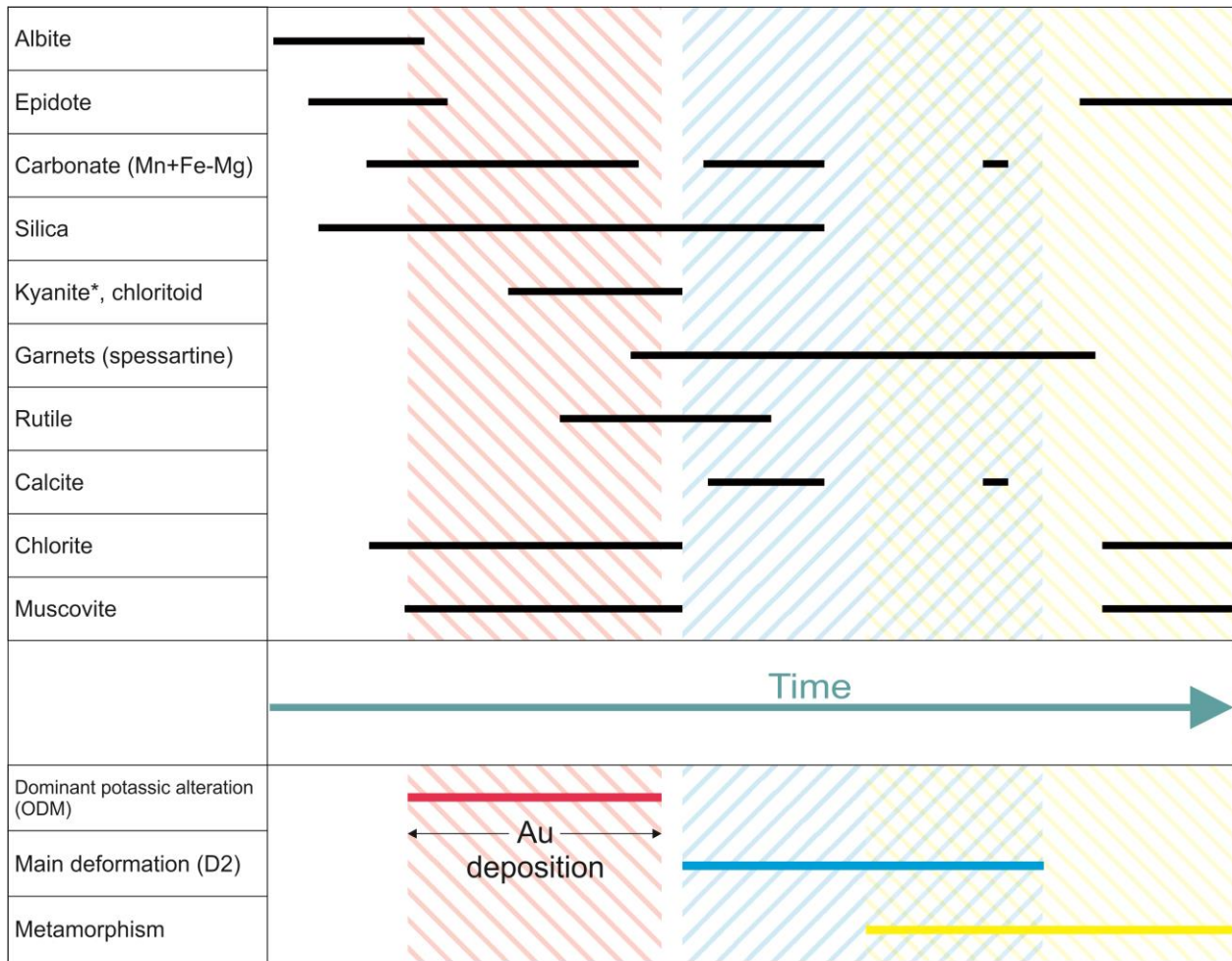


Figure 5.56: Relative timing of the metamorphism and hydrothermalism-related minerals of the Rainy River deposit. As demonstrated above, Au content for the ODM zone is correlated to localized potassic alteration, hence the labelled Au deposition event associated with sericitization on this diagram. *The timing of kyanite includes its pre-metamorphic equivalent.

6 MINERALOGY, GEOCHEMISTRY, AND DISTRIBUTION OF THE MINERALIZED ZONES

6.1 Introduction

This chapter focuses on the mineralized zones, starting with an overview of the deposit's total contained metal and the composition of the different mineralized zones. A description of the different metal-bearing phases documented at Rainy River through drill core logging, petrographic and scanning electron microscope (SEM) work and both energy-dispersive and wavelength dispersive x-ray spectrometry (EDS and WDS) analyses follows. SEM photos and coupled EDS results from this study are presented in appendix III, while some WDS (microprobe) analyses on sulphide phases from an unpublished report by Kjarsgaard (2013) can be found in appendix IV. The reader is referred to sections 1.3.2 and 1.3.3 for further information on equipment used and laboratories. Emphasis is on style, texture and distribution of the sulphide phases and their relationship to gold. Simple statistics about metal correlations are also presented. The distribution in space of these metals is then modelled at deposit scale to highlight potential zonation in the system.

6.1.1 Mineral resource estimates and grades

Mining plans of the Rainy River deposit, at time of writing, recognize gold and silver as the only metals economically viable for recovery. Proven and probable reserves (table 6.1) are based on cut-off grades of 0.3 g/t Au equivalent (combined gold and silver grades, where silver is reported as gold equivalent using current metal prices) for the open pit and 3.5 g/t Au equivalent for the underground operation. Measured and indicated resources (table 6.1), which exclude the reserve numbers, are estimated using a 0.3 g/t Au cut-off for the open pit operation and a 2.5 g/t Au cut-off for the underground operation (New Gold Inc. website, December 2015).

Table 6.1 : Resource and reserve estimates for the planned open pit and underground mining activities at the Rainy River Gold project. Adapted from the New Gold Inc. website. See text for cut-off grades.

	Contained metal Au (000 oz)	Contained metal Ag (000 oz)
Proven and probable reserves (total)	3,772	9,410
Measured and indicated resource (total)	2,896	9,999

Total	6,668	19,409
--------------	-------	--------

6.2 Mineralized zones

6.2.1 Overview

The mineralized zones at Rainy River were outlined through 3D wireframing work guided by predetermined threshold gold assay values, while considering: "structure, lithology, alteration, geochemical indices, as well as grade trends" (El-Rassi and Cole, 2014). These volumes were drawn for resource estimation purposes (El-Rassi and Cole: 2008, 2011, 2014).

The mineralized zones that compose the Rainy River deposit are, from north to south, the 433, HS, ODM/17, and Cap zones (Fig. 6.1). These zones, which are stacked in the host succession, are all parallel to the main ESE-WNW trending, south-dipping S_2 foliation. Higher grade bodies within all mineralized zones consist in cigar-shaped bodies parallel to the L_2 lineation ($225^\circ/55^\circ$), as shown on figure 6.1. In addition to the four main ore zones, the Beaver Pond zone (in blue on Fig. 6.1) and the Intrepid zone (to the east of the ODM/17 zone, not shown) consist in additional mineralized zones which are not included in this study, due to their peripheral position with respect to the proposed pit as well as a lack of data. Each mineralized zone is characterized by various mineralization styles as described below in sections 6.2.2 through 6.2.5 and summarized in table 6.3 in section 6.2.6.

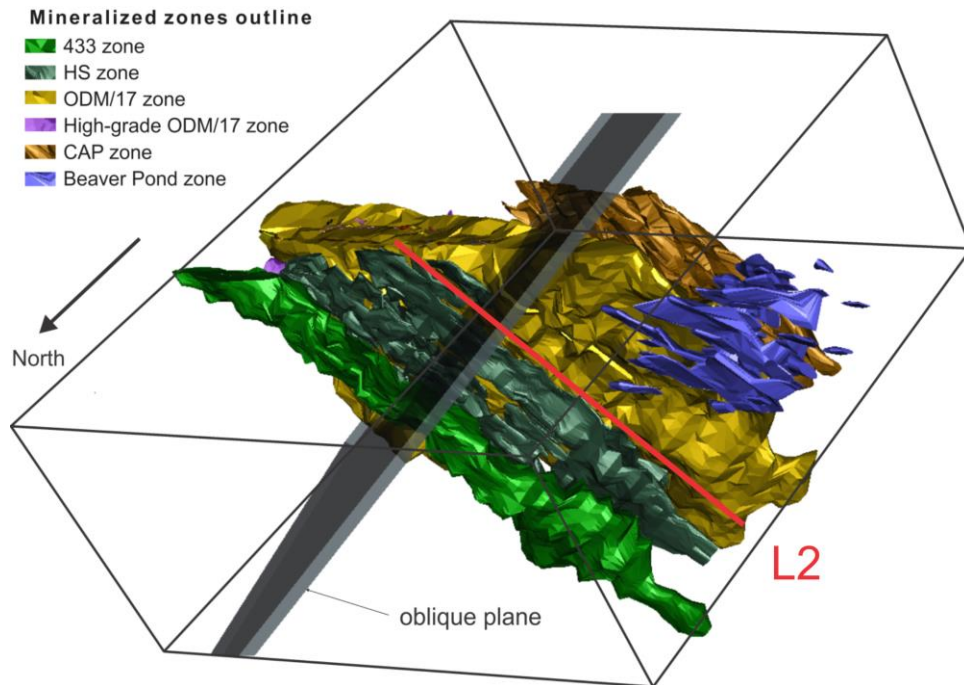


Figure 6.1 : Three-dimensional view of the mineralized zones that compose the Rainy River deposit. Image modified from New Gold Inc. material and from Pelletier et al. (2014).

Table 6.2 shows a breakdown of the total contained gold within the proposed open pit divided into the different mineralized zones. It illustrates the importance of the ODM/17 zone in terms of contained gold and its economic significance with respect to the other mineralized bodies. Mineral resources outlined in table 6.2 do not correspond to the main mineral resource statement of table 6.1, since they were obtained through block modelling using the conceptual pit shells from Cole and El-Rassi (2014).

Table 6.2 : Open pit mineral resources at a 0.3 ppm Au cut-off, assuming a gold metallurgical recovery of 90%. From the February 14, 2014 NI 43-101 feasibility study report.

Domain	Measured		Indicated		Inferred		Total
	Au (ppm)	Au metal (koz)	Au (ppm)	Au metal (koz)	Au (ppm)	Au metal (koz)	Au metal (koz)
ODM/17	1.20	860	1.06	3,228	0.56	1	4,089
433	1.16	161	1.06	451	0.66	5	617
HS			0.66	292	0.63	100	392
Cap			0.57	435	0.54	4	439

Bulk of the gold and silver at Rainy River is not visible, but gold values usually correlate with the abundance/presence of pyrite, chalcopyrite, sphalerite and galena, which are the most common sulphides in the deposit, although globally present in minor amounts (≤ 10 vol.%; < 8 wt.% sulphide gain).

6.2.2 ODM zone

6.2.2.1 Size and shape

The ODM zone (in yellow on Fig. 6.1) is modelled over a strike length of approximately 1600 m, over a vertical distance of approximately 975 m and a true width of up to 200 m (El-Rassi and Cole, 2014). In previous work (Wartman, 2011; BBA Inc., 2012, 2014), the ODM zone is referred to as the ODM/17 zone, although infill drilling between the ODM and 17 zones demonstrated that they represent the same body. In light of this and for conciseness purposes, the ODM/17 zone is referred to as the ODM zone in this text.

This zone hosts the bulk of the total contained gold and silver, with the proposed open pit centered on it. The ODM body has a lenticular shape that is parallel to the main S_2 fabric, with higher grade ore shoots parallel with the L2 stretching lineation. The ODM mineralized zone is hosted in calc-alkaline dacites of various facies, with higher grade zones preferentially associated with dacitic tuff breccias as discussed in Chapter 3 (see Figs. 3.22, 3.23; appendix I).

6.2.2.2 Base and precious metals: mineralogy and style

Pyrite is the most common sulphide within the ODM zone, with concentrations varying between 0.5 to 10 vol.%. Low grade gold and silver mineralization (≤ 1.5 g/t Au equivalent) within the ODM zone is characterized by disseminated pyrite and pyrrhotite hosted in dacitic volcanic rocks from coherent facies. This lower grade envelope is characterized by fine-grained pyrite mostly in disseminations (Fig. 6.2A). Pyrite is also present as veinlets parallel to S_2 and sometimes previously folded and subsequently transposed into S_2 . Pyrrhotite is present in small pitted grains associated with pyrite, whether disseminated within the matrix (Fig. 6.2B) or as inclusions in spessartine garnet porphyroblasts along with pyrite and chalcopyrite (Fig. 6.2C). Pyrrhotite is observed only at the microscopic scale, making it difficult to properly characterize its distribution within the ODM zone and at deposit scale.

Pyrites of the ODM zone show complex zoning, usually displaying an inclusion-rich core rimmed by a later, inclusion-free corona (Fig. 6.2D; Pelletier *et al.*, 2015). Inclusions are filled with pyrrhotite, chalcopyrite, sphalerite, galena and silicates in various abundances. Kjarsgaard (2013) identified electrum (0.3-0.45 atomic % Au) as well as troilite (instead of or in addition to pyrrhotite) in pyrite inclusions from samples within the ODM zone (appendix IV).

Sphalerite, chalcopyrite, and to a lesser extent galena are, after pyrite, the major sulphide phases within the ODM zone. Of these sulphides, sphalerite is the most abundant phase, followed by chalcopyrite and sometimes galena, which is only present in traces. Together, they are present in variable concentrations, accounting for ≤ 8 vol.% of the rock. Sphalerite and chalcopyrite commonly present a "chalcopyrite disease" texture. The presence of sphalerite, chalcopyrite and galena is correlated to higher grade Au (above 1.5 g/t Au equivalent) within the ODM zone. Such grades are mostly found in dacitic tuffs and tuff breccias (Figs. 3.22, 3.23; appendix I). Within the tuff breccia facies, mineralization consists in S_2 -parallel, ≤ 2 cm-thick pyrite-sphalerite±chalcopyrite veinlets swerving around the lapilli (matrix-controlled; Fig. 6.3A). Most common gangue minerals within these veins are Mn-rich carbonates, quartz and chlorite. Gangue accounts for less than 50 vol.% of the total veinlet. In the dacitic tuffs, pyrite-sphalerite-chalcopyrite-galena veinlets are present in addition to disseminated pyrite and pyrrhotite in the wallrocks. These veinlets are commonly parallel to S_2 due to folding and transposition into S_2 (Fig. 6.3B). The veins are usually less than 0.5 cm thick and have a mean composition (excluding minor phases) of 55 vol.% pyrite, 30 vol.% sphalerite, 13 vol.% chalcopyrite and 2 vol.% galena. Sphalerite is Fe-poor as indicated by its yellowish to beige colour. Microprobe analyses of sphalerite by Kjarsgaard (2013; appendix IV) returned values between 0.9 to 9.7 mole % FeS, with the Fe-rich sphalerite samples clustered in the eastern half of the ODM body. Very rare veins (≤ 10 cm thick) of massive to semimassive granoblastic pyrite are also present (Fig. 6.3C).

Polymetallic veinlets, in all mineralized zones, display a sulphide zonation based on their ductility, with the least ductile sulphides at the centre, and softer phases surrounding these least ductile phases (Fig. 6.3D). Pyrite is commonly heavily fractured, with galena, chalcopyrite and sphalerite filling those fractures (Fig. 6.4A).

Visible electrum is present in D_2 folded and transposed quartz-carbonate-pyrite veins (Fig. 6.4B), particularly in the western part of the ODM zone that is characterized by a slightly higher density of deformed carbonate veins and veinlets (Fig. 6.4C). Visible electrum is rare.

SEM coupled with EDS analyses allowed identification of accessory phases within the ODM zone (table 6.4; section 6.2.6; appendix III). Dacitic tuff breccias within the higher grade ODM bodies very locally contain arsenopyrite as inclusions within pyrite cores, coexisting with sphalerite (Fig. 6.4D). There are also automorph arsenopyrite grains growing outwards from pyrite grains within sulphide veinlets hosted in dacitic tuffs (Fig. 6.5A). Electrum is present in sulphide-free pyrite fractures (Fig. 6.5B) as well as in chalcopyrite-filled pyrite fractures or as part of a sulphide veinlet (Fig. 6.5C). The electrum composition varies between 18 and 35 atomic % Au (appendix III). Kjarsgaard (2013) identified gold (0.76 atomic % Au) intergrown with sphalerite in veins parallel to S_2 as well as in a late brittle vein crosscutting S_2 (appendix IV).

Minor phases identified in this study consist in gold-silver tellurides (Fig. 6.5; stützite: Ag_5Te_3 , hessite: Ag_2Te and petzite: $AuAg_3Te_2$) (appendix III). The tellurides are present as tiny grains associated with chalcopyrite and/or sphalerite along fractures in pyrite within sulphide veins (Fig. 6.5D, E). Tellurides are also present as isolated micro-inclusions in pyrite (Fig. 6.5F). Kjarsgaard (2013) also identified weak signals of silver±lead±bismuth telluride, ullmanite and Ag-pentlandite (table 6.4; appendix IV).

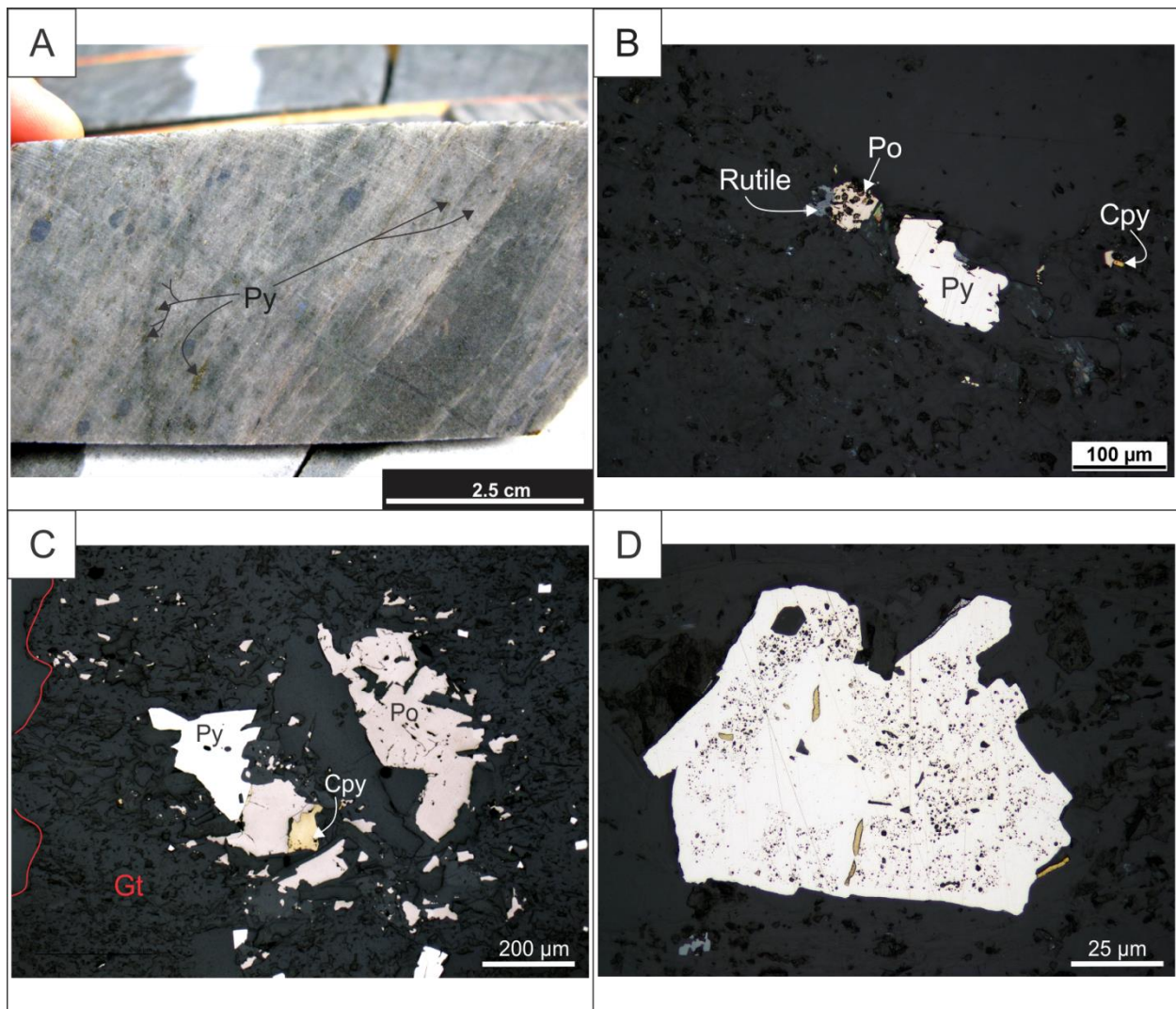


Figure 6.2 : ODM mineralized zone. A. Disseminated pyrite±chlorite in a coherent dacitic rock. DDH NR060058 at 258 m. B. Photomicrograph (RL) of pitted pyrrhotite grain rimmed by rutile along with pyrite, all rimming a quartz grain. Sample RRR435776, DDH NR060058 at 110 m. C. Photomicrograph (RL) of pyrrhotite, pyrite and chalcopyrite as inclusions in a spessartine garnet porphyroblast. Sample RRR435593, DDH NR060050 at 314 m. D. Photomicrograph (RL) of zoned pyrite grain with alternating inclusion-rich and inclusion-poor concentric zones. Inclusions include chalcopyrite, pyrrhotite, sphalerite, rutile and silicates. Sample RRR435806, DDH NR070141 at 157 m.

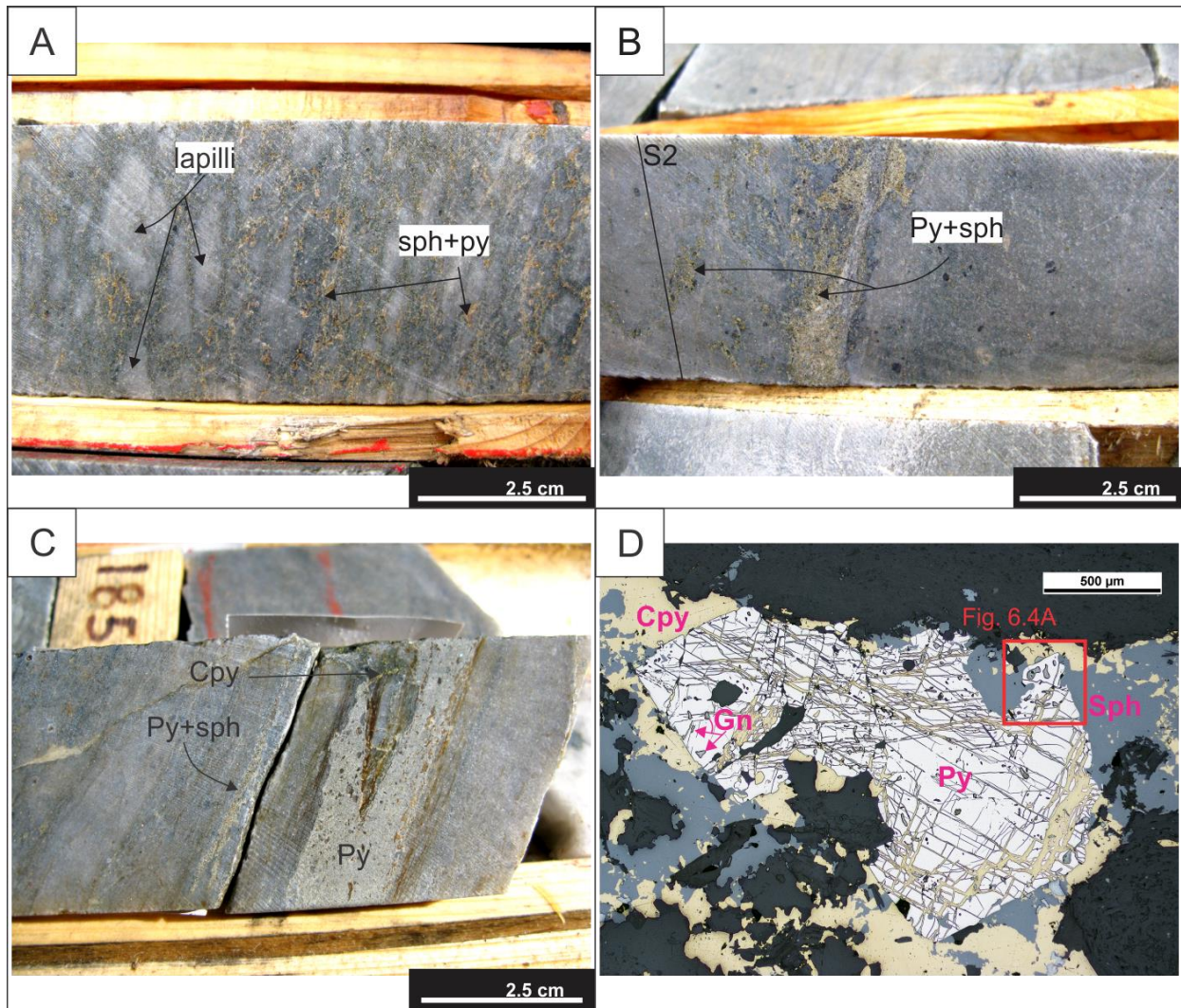


Figure 6.3 : ODM mineralized zone. A. Sphalerite and pyrite veinlets preferentially developed in the matrix of a dacitic tuff breccia. DDH NR060058 at 302 m. B. Pyrite and light yellow-coloured sphalerite in deformed veins partly transposed within S₂, hosted in a coherent dacite. DDH NR070141 at 136 m. C. Band of massive pyrite with very fine chalcopyrite veinlet, all parallel to S₂ and hosted in a muscovite schist. DDH NR070141 at 183 m. D. Photomicrograph (RL) of abundant conjugate brittle fractures in a granoblastic pyrite grain in much softer sulphides (sphalerite and chalcopyrite). Veinlet hosted in muscovite schist. Sample RRR435732, DDH NR070146 at 222 m.

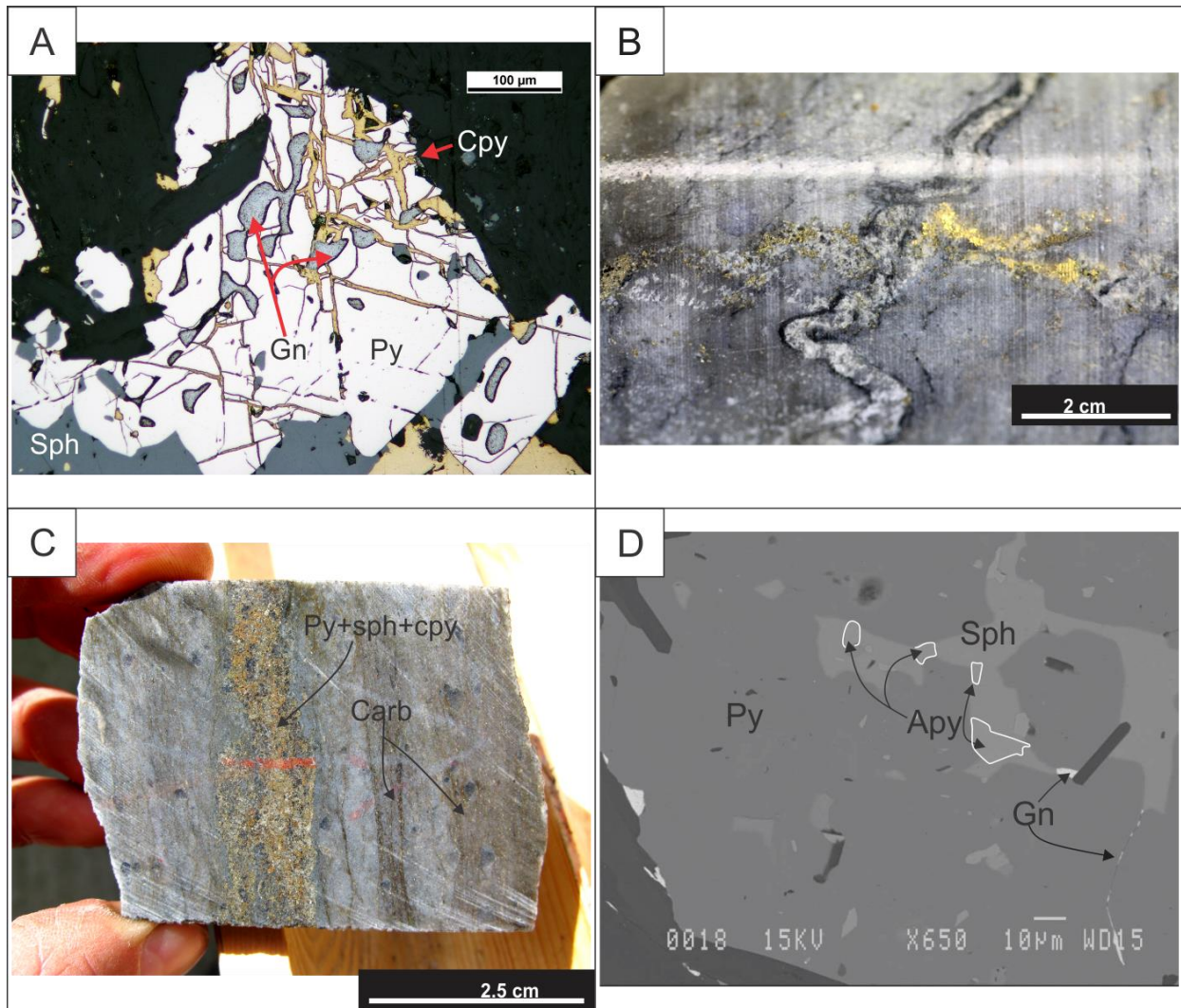


Figure 6.4 : ODM mineralized zone. A. Photomicrograph (RL) of galena and chalcopyrite remobilization in pyrite brittle fractures. Sample RRR435732, DDH NR070146 at 222 m. B. Deformed Au-rich (electrum) veinlet crosscut by latter qtz-cb-tl vein deformed by the S₂ foliation. DDH NR110783, western ODM area, photo P. Mercier-Langevin. C. Polymetallic vein parallel to S₂ and associated with Fe-Mg carbonate veining, also oriented parallel to S₂ in a dacitic flow of the western ODM zone. DDH NR060050 at 261 m. D. Backscattered electron image (15kV operating voltage) showing the presence of arsenopyrite with sphalerite as inclusions within a pyrite grain as well as galena remobilization within fractures. These sulphides are hosted in a dacitic tuff breccia. Sample RRR435806, DDH NR070141 at 157 m.

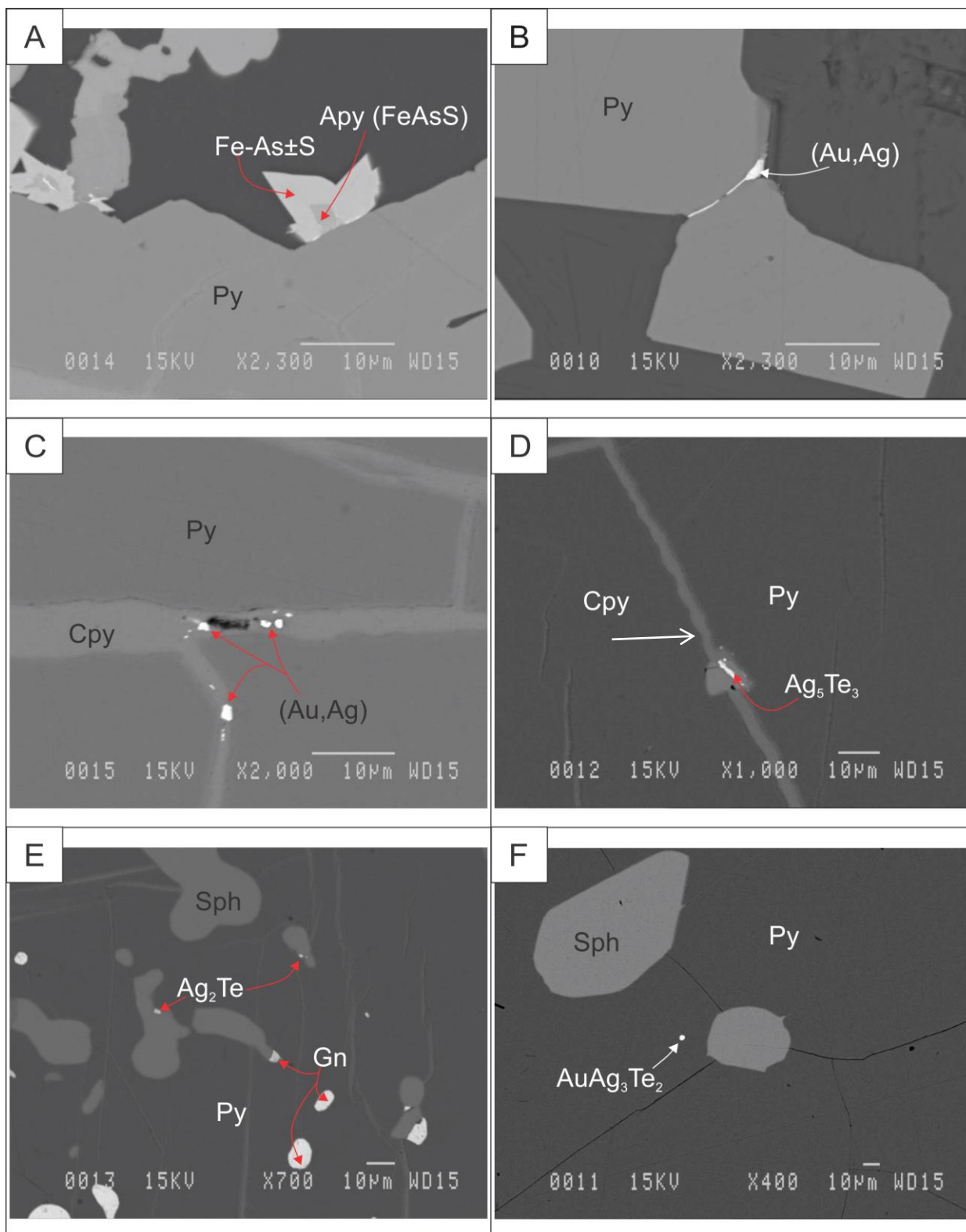


Figure 6.5 : ODM mineralized zone backscattered electron images (15 kV operating voltage). A. Very fine automorph arsenopyrite grain with a sulphur-rich core and sulphur-poor rim growing outwards from a pyrite grain within a polymetallic vein hosted in muscovite schist. Sample RRR435732, DDH NR070146 at 222 m. B. Electrum in pyrite grain fractures in a dacitic tuff breccia

of the ODM zone. Sample RRR435737, DDH NR950027 at 164 m. C. Electrum within a chalcopyrite-filled brittle fracture of a pyrite grain, part of a polymetallic vein hosted in muscovite schist. Sample RRR435732. D. Stützite within a chalcopyrite-filled pyrite grain fracture. Sample RRR435732, DDH NR070146 at 222 m. E. Zoom on inclusions from a pyrite grain which consist in hessite, galena and sphalerite. Sample RRR435732, DDH NR070146 at 222 m. F. Very fine petzite inclusion in pyrite, not related to fractures. Pyrite grain from dacitic tuff breccia of the ODM zone. Sample RRR435737, DDH NR950027 at 164 m.

6.2.2.3 LA-ICP-MS element concentration map of a pyrite grain

Pyrite element concentration maps were produced for a sample from the ODM zone. The element maps shown on figures 6.6 and 6.7 were done by laser ablation inductively-coupled plasma mass spectrometry (LA-ICP-MS) at the Geological Survey of Canada in Ottawa. Analytical and data analysis methods are given in Gao *et al.* (2015). For this study, a pyrite grain from sample RRR435508, which comes from the ODM zone, was selected for analysis and mapping. Sample RRR435508, which was taken in a 1 m-long, 10.5 g/t Au interval, gave a whole-rock value of 6.68 g/t Au, with 5.2 ppm Ag, 227 ppm Cu, and 403 ppm Zn. The laser ablation ICP-MS analyses and mapping shows the auriferous nature of the pyrite, with Au concentrations as high as 130 ppm in the core of the grain and concentrations of up to 22 ppm within two outer growth rims. In detail, the analysed grain is characterized by an inclusion-rich core, inclusion-free rim, and a brittle fracture running at its centre where chalcopyrite was remobilized (Fig. 6.6). A selection of elements represented on figures 6.6 and 6.7 shows at least two generations of pyrite crystallization, with much higher Au values within the early phase. Elements that are preferentially associated with Au in the core of the pyrite grain are Cu, Zn, As, Ag, In, Sn, Sb, and Pb (Pelletier *et al.*, 2015), while elements associated with Au in the outer growth rims are Cu, As, Ag, Sb, Pb and Te. The inclusion-free corona of the pyrite is interpreted as resulting from recrystallization during regional metamorphism and shows distinct Ni, Co and Bi and somewhat Te growth zones (Figs. 6.6, 6.7). This pyrite element map suggests an early Au-mineralizing phase in a system defined by at least two stages of pyrite crystallization.

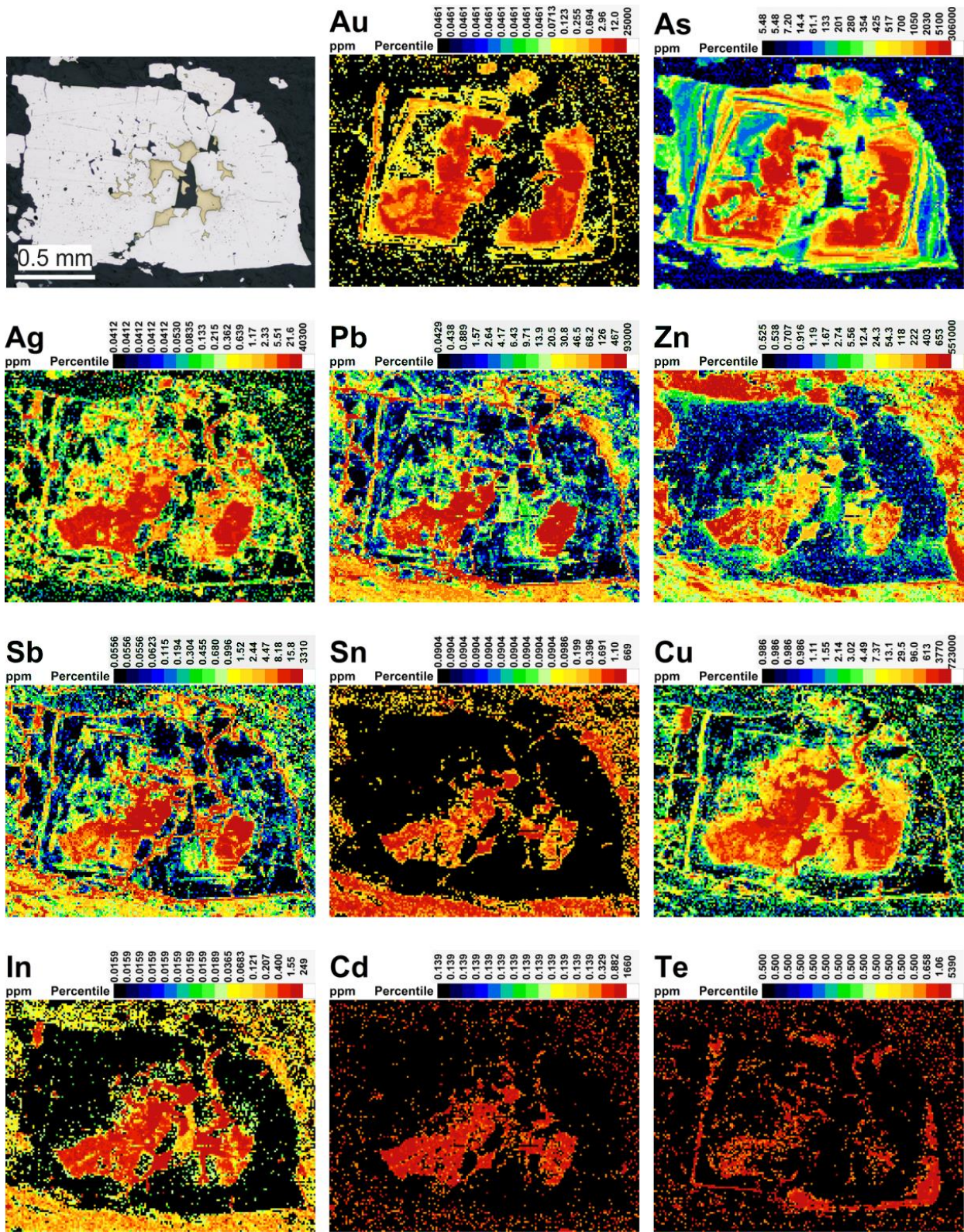


Figure 6.6 : LA-ICP-MS element mapping of a pyrite grain from sample RRR435508 of the ODM zone. Element correlated to Au content shown here. DDH NR080252 at 244 m.

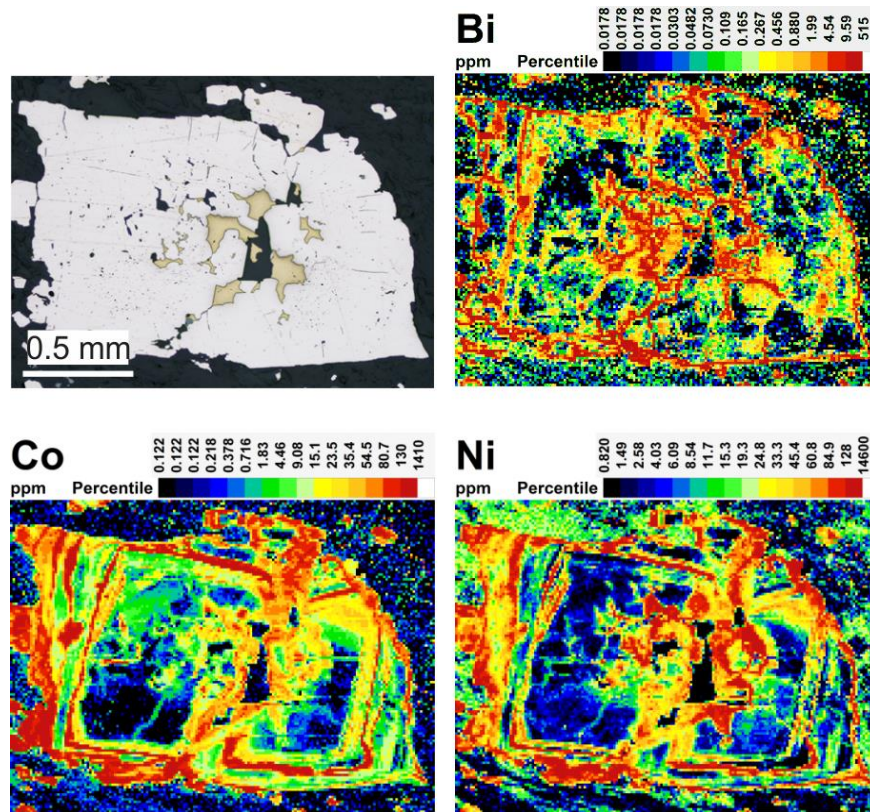


Figure 6.7 : LA-ICP-MS element mapping of pyrite grain from sample RRR435508 from the ODM zone. Elements poorly correlated to Au content shown here. DDH NR080252 at 244 m.

6.2.3 HS zones

6.2.3.1 Size and shape

The HS zone is located structurally below the ODM zone and above the 433 zone. It is composed of a series of small, discontinuous cigar-shaped low-grade bodies with their long axis parallel to L_2 (Fig. 6.1). Within the deposit area, the HS zone is centered on the zone having recorded the most intense, D_2 -deformation, hinting towards a greater impact on the distribution and concentration of mineralization.

The host rocks of the HS zone are dominantly calc-alkaline dacitic sericite (muscovite) schists, due to strong sericitization and overprinting deformation. Once again, mineralization hosted in these rocks is of similar grade to the one documented in the ODM zone, although mineralization style, mineralogy and metal association differ (see table 6.3).

6.2.3.2 Base and precious metals: mineralogy and style

Mineralization in the HS zone is characterized by disseminated pyrite in abundances varying between 0.5 and 3 vol.%. Pyrite is granoblastic (Fig. 6.8A), flattened along S_2 and amalgamated in ≤ 1 cm composite grains rimmed by chlorite. Pyrite grains possess inclusion-rich cores and inclusion-free rims, similar to the ODM zone.

Sulphide-rich veinlets less than 2 cm thick and parallel to S_2 are common within the HS zones (Fig. 6.8B) and are a good visual indicator of Au mineralization in this area of the deposit that has very discontinuous mineralization. Compared to the ODM zone, the HS zone possess a lower veining density (≤ 6 vol.%) and the veinlets are finer (≤ 1 cm). These veinlets are mostly composed of pyrite, with traces of chalcopyrite and Fe-poor sphalerite. As is the case in the ODM zone, sulphide veinlets are also distinguished by a “metal zonation” based on sulphide ductility (Fig. 6.8C). Veins of quartz-chlorite-carbonate-pyrite, intensely folded and transposed within S_2 , are also present (Fig. 6.8D), more so in the more competent dacitic coherent facies than in the muscovite schists. Close to the ODM zone, characteristic white sphalerite stringers parallel to S_2 are common (Fig. 6.9A).

Pyrrhotite grains have only been identified as inclusions (microscopic scale) within spessartine garnet (Fig. 6.9B). SEM and combined EDS work revealed accessory phases of pyrargyrite (Ag_3SbS_3) and one grain of electrum with 21 atomic % Au (appendix III). Both phases occur at grain boundaries (Fig. 6.9C, D) within a strongly folded and transposed chalcopyrite-pyrite-sphalerite veinlet. Sphalerite within this veinlet has a Fe concentration of 2.34 atomic %.

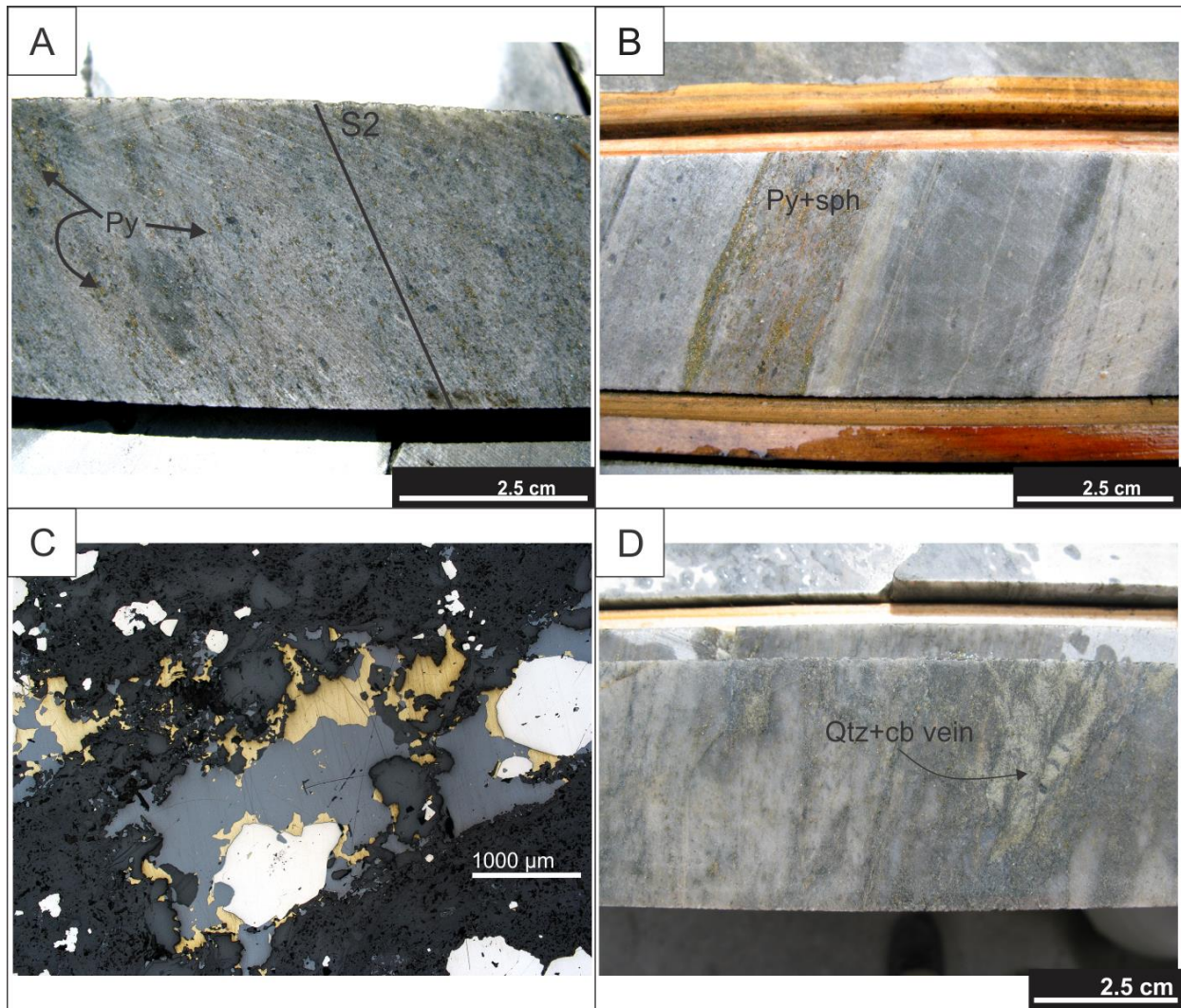


Figure 6.8 : HS mineralized zone. A. Granoblastic pyrite with chlorite flattened/stretched into S_2 in coherent dacite. DDH NR060058 at 492 m. B. Vein of pyrite and sphalerite parallel to S_2 at the contact between sericite (muscovite) schist (to the right) and coherent dacite (to the left). DDH NR060058 at 479 m. C. Photomicrograph (RL) of a polymetallic veinlet parallel to S_2 , with weak 'chalcopyrite disease' in sphalerite. Sample RRR435795, DDH NR060058 at 480 m. D. Folded and transposed quartz-carbonate-pyrite \pm chlorite vein within a dacitic flow unit. DDH NR070147 at 225m.

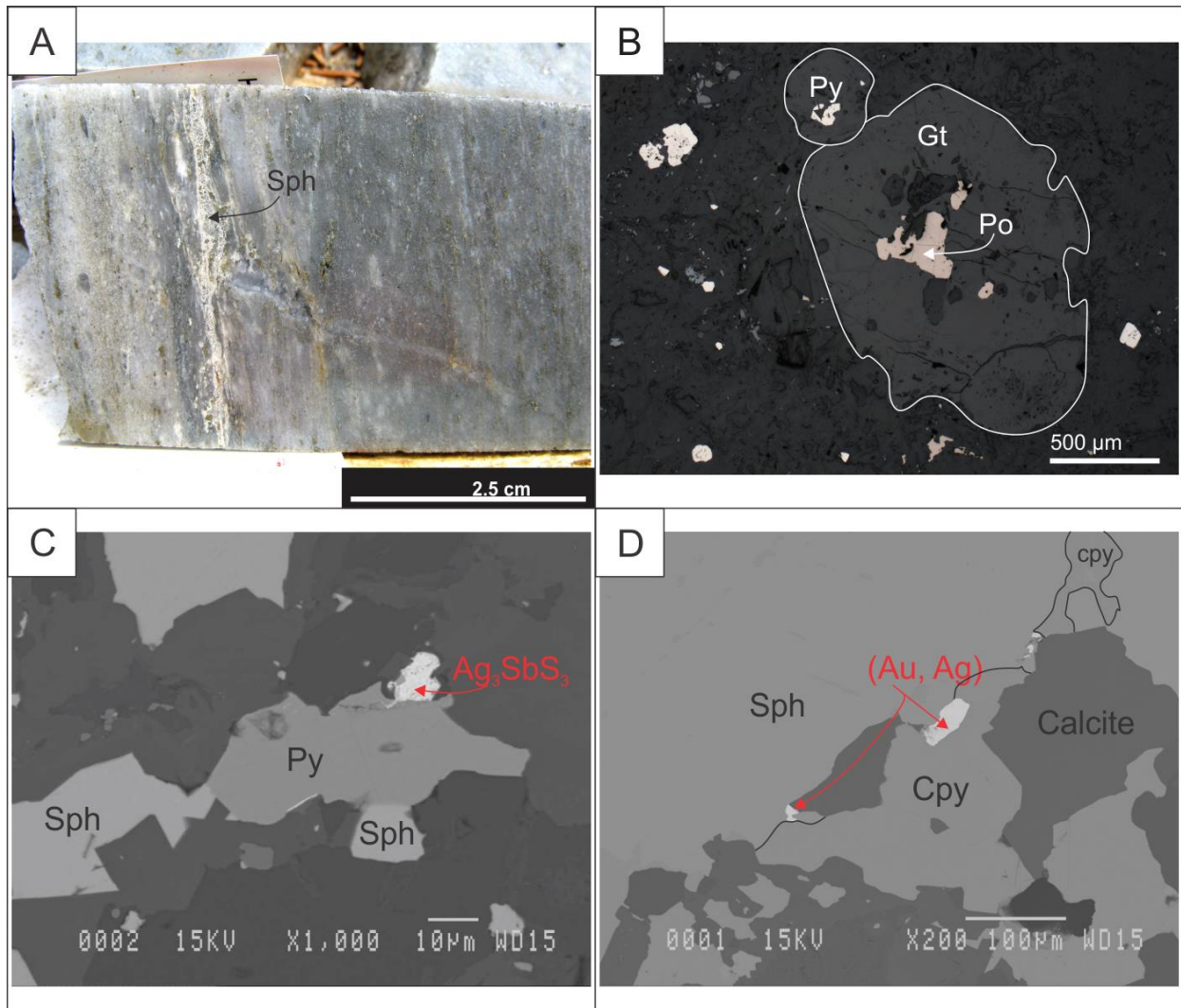


Figure 6.9 : HS mineralized zone. A. Characteristic white sphalerite veinlet parallel to S_2 in strongly sericitized and foliated muscovite schist from the upper parts of the HS zone. DDH NR070147 at 258 m. B. Photomicrograph (RL) of pyrrhotite and pyrite as inclusions in a fractured spessartine garnet porphyroblast. Sample RRR435543, DDH NR060104 at 474 m. C. Backscattered electron image (15kV operating voltage) of pyrrargyrite in association with pyrite and sphalerite in a muscovite schist. Sample RRR435795, DDH NR060058 at 480 m. D. Backscattered electron image (15kV operating voltage) of electrum at boundary between chalcopyrite and sphalerite in a veinlet hosted in a muscovite schist. Sample RRR435795, DDH NR060058 at 480 m.

6.2.4 433 zone

6.2.4.1 Size and shape

Located to the north (structurally below) of the Cap, ODM and HS mineralized zones, the 433 zone (in green on Fig. 6.1) is cigar-shaped with its long axis along L_2 and is followed along strike for approximately 325 metres, over a vertical distance of 820 metres and with a true width of up

to 125 metres (El-rassi and Cole, 2014). Compared to the ODM zone, the 433 zone is much more restrained along strike (325 m vs. 1,600 m), but has a similar extent down dip. Grades are very similar to the ones of the ODM zone, although mineralization style and metal association differ (see section 6.3).

The 433 zone host rocks are dominantly strongly sericitized calc-alkaline dacitic rocks that are strongly schistose due to overprinting deformation. Tholeiitic basalts with characteristic rutile-dusting host a minor part of mineralization within the 433 zone. Once again, mineralized zones hosted in mafic rocks are of similar grade to the one documented in the ODM zone, although mineralization style, mineralogy and metal association differ (table 3, section 6.2.6).

6.2.4.2 Base and precious metals: mineralogy and style

As mentioned above, the 433 zone is hosted in two different lithologies, and the mineralized zones possess respective sulphide mineralogy and style depending on the host unit (basalt versus dacite).

The dacitic package that hosts most of the 433 zone is characterized by abundant disseminated granoblastic pyrite rimmed by chlorite in a strongly deformed and sericitized host rock (Fig. 6.10A). Higher grade gold corresponds with the presence of deformed pyrite-chalcopyrite veins and veinlet (Fig. 6.10B). Pyrite show complex zoning, with inclusion-rich cores (Fig. 6.10C). Pyrite grains flattened into S_2 , with a series of brittle fractures developed perpendicular to S_2 subsequently filled by ductile chalcopyrite are also developed in the 433 zone (Fig. 6.10D). Native bismuth occurs locally in association with pyrite (Fig. 6.11A). Kjarsgaard (2013) also identified bismuthinite as very fine inclusions in gangue and tellurobismuthinite within pyrite fractures (appendix IV).

The mafic tholeiitic rocks with rutile dusting that host part of the 433 zone are characterized by granoblastic pyrite veins stretched parallel to S_2 (Fig. 6.11B) as well as disseminated pyrite. In areas of less intense S_2 overprint, textures of in-situ brecciation are present within the mineralized rutile-rich tholeiitic unit of part of the 433 zone (Fig. 6.11C). The disseminated pyrite grains are usually very small (<100 μm) and occur with abundant, very fine-grained rutile (<25 μm) (Fig. 6.11D). Silver telluride (stützite: Ag_5Te_3) and lead telluride (altaite: PbTe) were identified within a pyrite-sphalerite veinlet (Fig. 6.11E). Two sphalerite grains from a vein were analysed to estimate their composition (Fig. 6.11F). The first grain is part of the vein itself and gave back an iron-poor composition of 1.4 atomic % Fe while the second grain analysed, which

occurs as an inclusion within a pyrite grain that is also part of the vein, gave back an iron-rich composition (6.89 atomic % Fe).

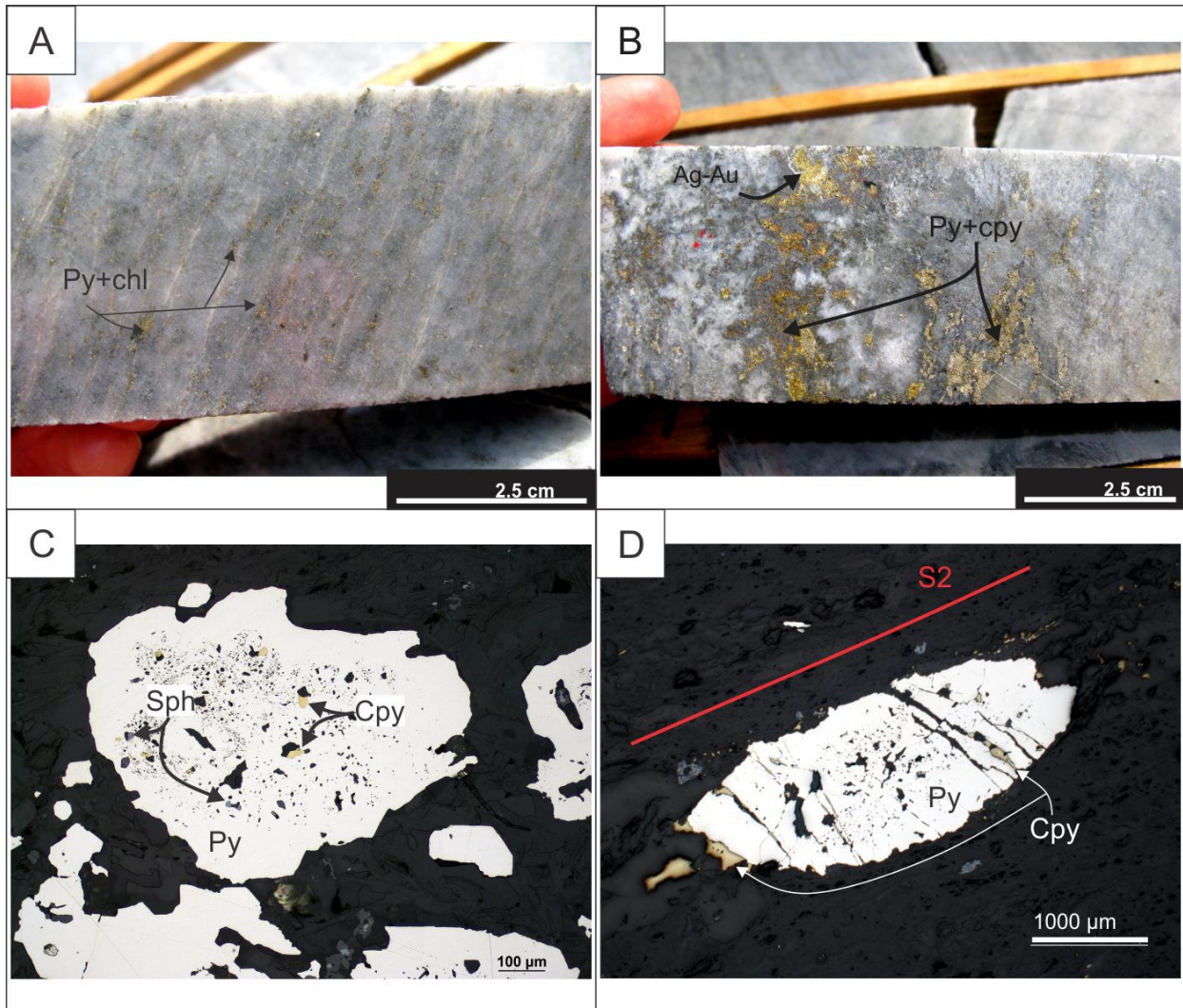


Figure 6.10 : 433 mineralized zone. A. Disseminated granoblastic pyrite grains with chlorite in a muscovite schist. DDH NR060067E at 758 m. B. Coarse chalcopyrite-pyrite veining. Very small electrum grain at top of photo. DDH NR060067E at 752 m. C. Photomicrograph (RL) of an inclusion-rich pyrite grain core with an inclusion-free rim. Part of an S_2 -parallel vein of pyrite-carbonate-chlorite-quartz± chalcopyrite hosted in tholeiitic basalt. Sample RRR435888, DDH NR060067E at 801 m. D. Photomicrograph (RL) of a pyrite grain with inclusion-rich core, inclusion-free rim, and later brittle fracturation ± perpendicular to S_2 , followed by chalcopyrite remobilization in fractures and strain shadows. Hosted in muscovite schist, sample RRR435645, DDH NR060044E at 558 m.

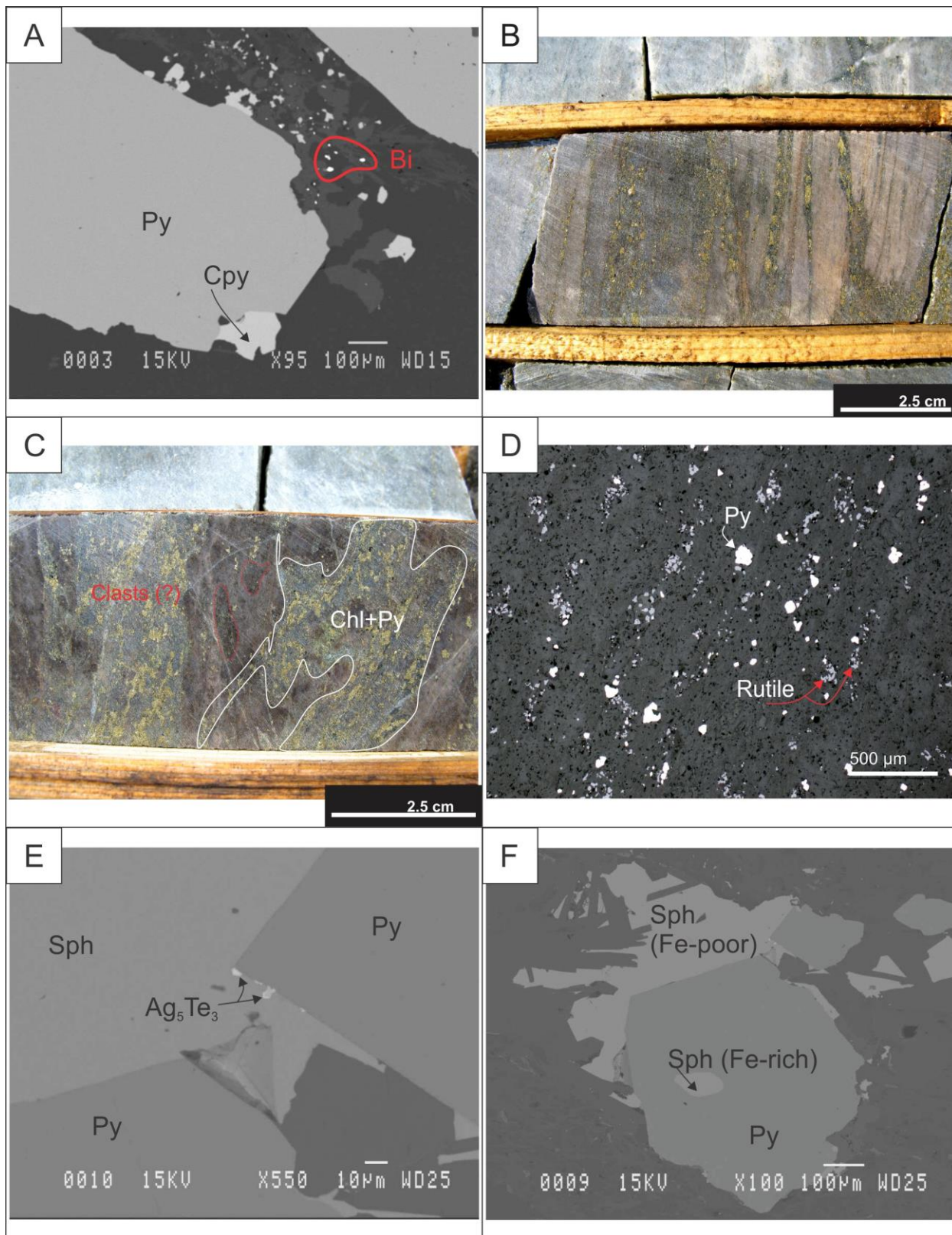


Figure 6.11 : 433 mineralized zone. A. Backscattered electron image (15kV operating voltage) of disseminated pyrite, chalcopyrite and native bismuth in a coherent dacitic rock. Sample

RRR435883, DDH NR060067E at 732 m. B. Granoblastic pyrite mineralization in the rutile-rich tholeiitic unit. DDH NR080251E at 640 m. C. Fracture-controlled texture (clasts highlighted in red) in rutile-rich tholeiitic unit with granoblastic pyrite + chlorite veining overprint (highlighted in white), later transposed within S_2 . DDH NR080246E at 559 m. D. Photomicrograph (RL) of disseminated pyrite and abundant fine-grained rutile oriented parallel to S_2 in rutile-rich tholeiitic unit. Sample RRR435625, DDH NR080244E at 704 m. E. Backscattered electron image (15kV operating voltage) of stützite at pyrite-sphalerite grain boundary in rutile-rich tholeiitic unit. Sample RRR435875, DDH NR060067E at 642 m. F. Backscattered electron image (15kV operating voltage) of pyrite grain with an iron-rich sphalerite inclusion and rimmed by iron-poor (less than 5 mol % FeS) sphalerite in rutile-rich tholeiitic unit. Sample RRR435875, DDH NR060067E at 642 m.

6.2.5 Cap zone

6.2.5.1 Size and shape

Located south (structural hanging wall) of the ODM zone, the Cap zone mineralization (in bronze on Fig. 6.1) is hosted in both tholeiitic basalts and calc-alkaline dacites. Like the ODM zone, it is lens-shaped and parallel to the S_2 foliation. It is significantly smaller in size compared with the other mineralized zones, with the lens modelled over a strike length of about 400 meters and followed from surface to a depth of approximately 400 meters (El-Rassi and Cole, 2014). Low grade mineralization is similar to that of the ODM low grade zone, although metal associations differ (see section 6.3). Higher grade mineralization is hosted in a tholeiitic basalt-hosted extensional quartz-carbonate-pyrite vein array described in Chapter 4.

6.2.5.2 Base and precious metals: mineralogy and style

The Cap zone crosscuts many lithologies and is hosted in mafic and felsic volcanic rocks as well as mafic-dominated siltstones, although only sulphide zones and veins hosted in volcanic rocks contain precious metals.

The mafic-dominated siltstones lenses that are intercalated with volcanic rocks in the Cap zone area (Figs 3.22, 3.23; appendix I) can contain over 10 vol.% combined pyrite-pyrrhotite (Fig. 6.12A), although samples assayed for this study returned only trace amounts of precious metals. In these rocks, pyrite and pyrrhotite coexist and have a coarse granoblastic texture. Sulphides are concentrated in ≤ 2 cm-thick veins oriented parallel to S_2 .

The tholeiitic basalts within the Cap zone host two main styles of mineralization. The first style consists in tight, fine-grained pyrite stockworks developed in amygdaloidal intervals of the tholeiitic basalts (Fig. 6.12B). The second mineralization style documented in tholeiitic basalts of the Cap zone consists in strongly foliated tholeiitic basalts having between 3 and 12 vol.% pyrite in diffuse, transposed ≤ 2 mm bands parallel to S_2 (Fig. 6.12C). These sulphide bands are

composed of zoned pyrite grains with recrystallized rims and inclusion-rich cores, with traces of very fine grained ($\leq 20 \mu\text{m}$) chalcopyrite and rutile-ilmenite grains of similar size (Fig. 6.12D, 6.13A) dispersed within the pyrite-rich bands. A complex growth history combined with diverse inclusion mineralogy is documented in pyrites of the Cap zone (Fig. 6.13A), similar to pyrites documented elsewhere in the deposit. SEM work on pyrite inclusions from grains within S_2 -parallel bands revealed the presence of accessory silver telluride phases (petzite: AuAg_3Te_2 ; and hessite: Ag_2Te), nickel telluride melonite (NiTe_2), as well as antimony sulphides stibnite (Sb_2S_3) and ullmanite (NiSbS) (Fig. 6.13B, C, D; appendix III).

Tholeiitic basalts within the Cap zone also host vein-style mineralization. Quartz-ankerite-pyrite auriferous extension veins crosscut tholeiitic mafic rocks and are documented in Chapter 4. These veins are between 1 and 20 cm thick with an average of 5-10 cm and consist in a minor source of gold due to their discontinuity.

Auriferous zones that are hosted in strongly deformed dacitic flow and dacitic tuff/muscovite schists contain, according to analyses from this study (Pelletier *et al.*, 2016), the highest gold and silver concentrations of the Cap zone (up to 8.65 g/t Au). On drill core, dacite-hosted Au mineralization of the Cap zone occurs as granoblastic pyrite concentrated in ≤ 3 cm-wide bands parallel to S_2 as well as in dismembered and transposed pyrite veinlets that can be up to 8 mm wide (Fig. 6.14A). Dark red (Fig. 6.14B) to light yellow (Fig. 6.14C) sphalerite is common in S_2 -parallel veins, in association with the pyrite. Common arsenopyrite (≤ 10 vol.% of the vein) is present along with granoblastic pyrite, sphalerite and rare chalcopyrite (Fig. 6.14D) as part of the sulphide veins. SEM analyses on this mineralization style revealed the presence gold-rich electrum (30 atomic % Au) between arsenopyrite grains, as well as the presence of ullmanite (NiSbS) in contact between pyrite and sphalerite (Fig. 6.14E, F; appendix III).

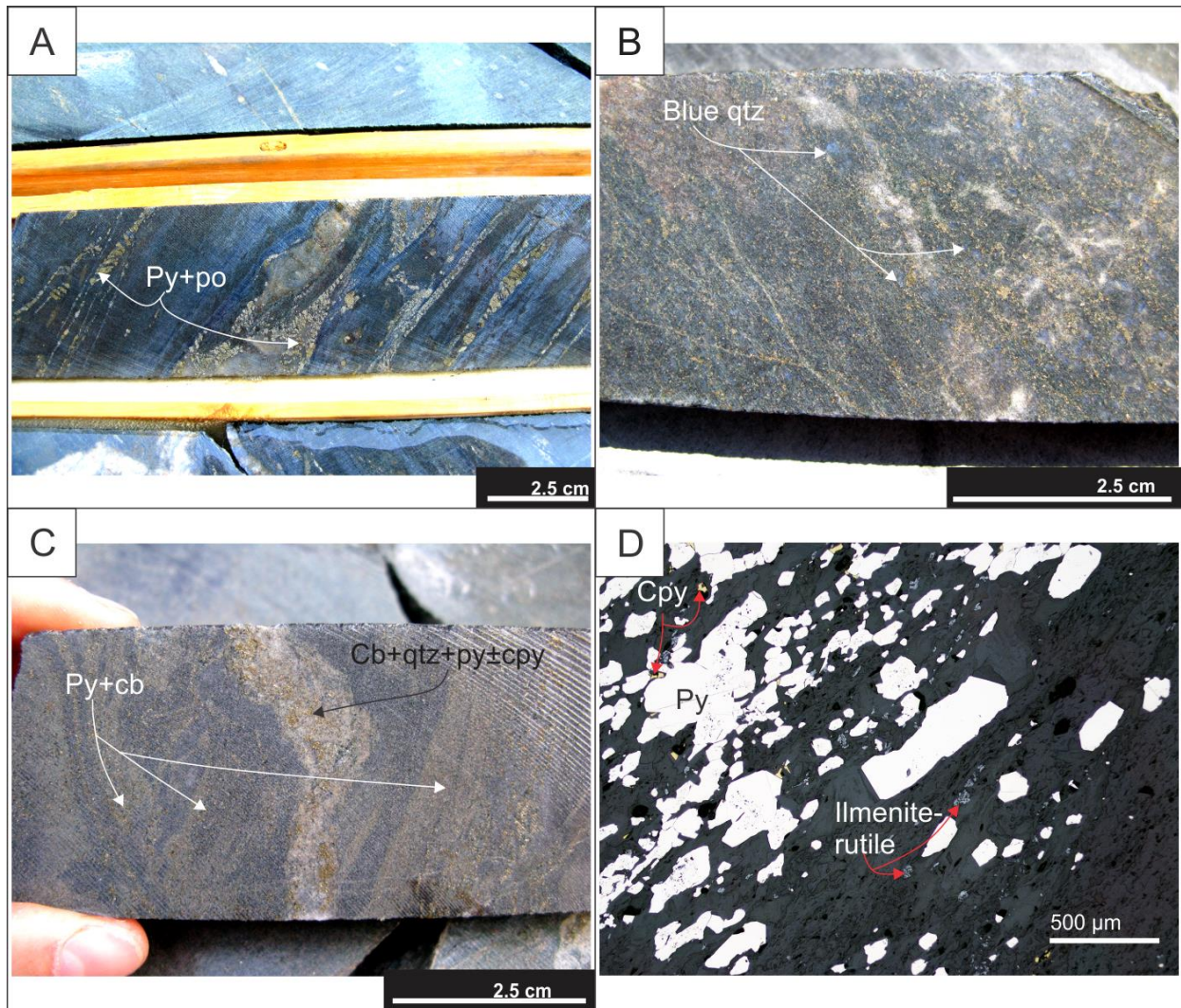


Figure 6.12 : Cap mineralized zone. A. Granoblastic pyrite and pyrrhotite in veins parallel to S_2 in barren mafic-dominated siltstones. DDH NR090358 at 63 m. B. Very fine pyrite stockwork in blue quartz amygdaloidal mafic tholeiitic unit. DDH NR110771 at 212 m. C. Disseminated fine-grained pyrite in bands parallel to S_2 as well as in carbonate-quartz-pyrite±chalcopyrite deformed vein in carbonate-altered mafic tholeiitic unit. DDH NR110771 at 180 m. D. Photomicrograph (RL) of pyrite and arsenopyrite-rich veinlet with very fine chalcopyrite and rutile-ilmenite grains. Pyrite grains show multiple crystallization events. Tholeiitic basalt sample RRR435506, DDH NR110850 at 209 m.

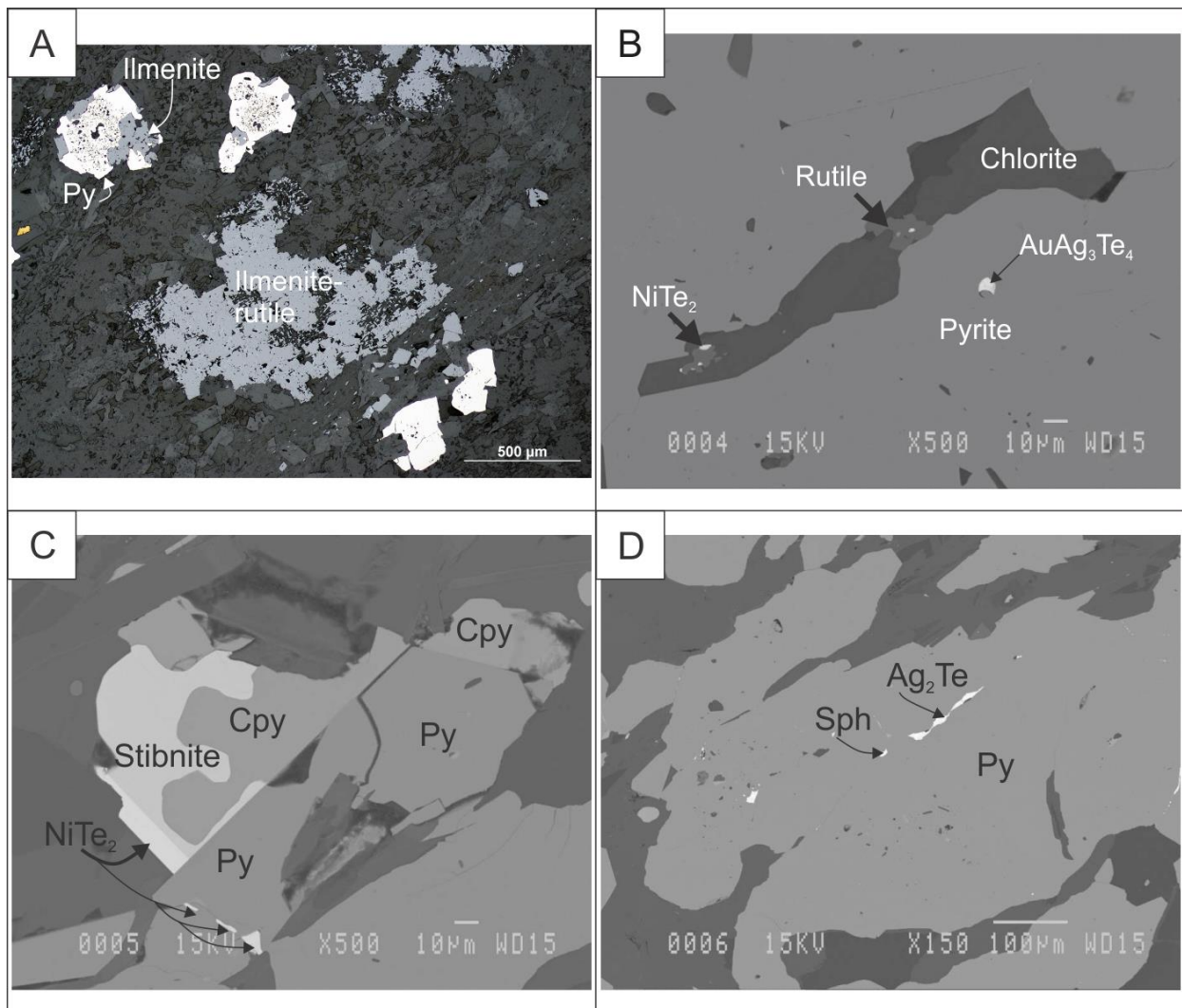


Figure 6.13 : Cap mineralized zone. A. Photomicrograph (RL) of zoned pyrite grains suggesting multiple growth events along with abundant ilmenite-rutile in tholeiitic basalt. Sample RRR435837, DDH NR110771 at 247 m. B. Backscattered electron image (15kV operating voltage) of petzite and melonite in pyrite, with melonite associated with rutile. Sample RRR435506, DDH NR110850 at 209 m. C. Backscattered electron image (15kV operating voltage) of melonite phase in pyrite grain fracture and at boundary with stibnite, both around a pyrite grain on sample RRR435506, DDH NR110850 at 209 m. D. Backscattered electron image (15kV operating voltage) of hessite as pyrite sample RRR435506, DDH NR110850 at 209 m.

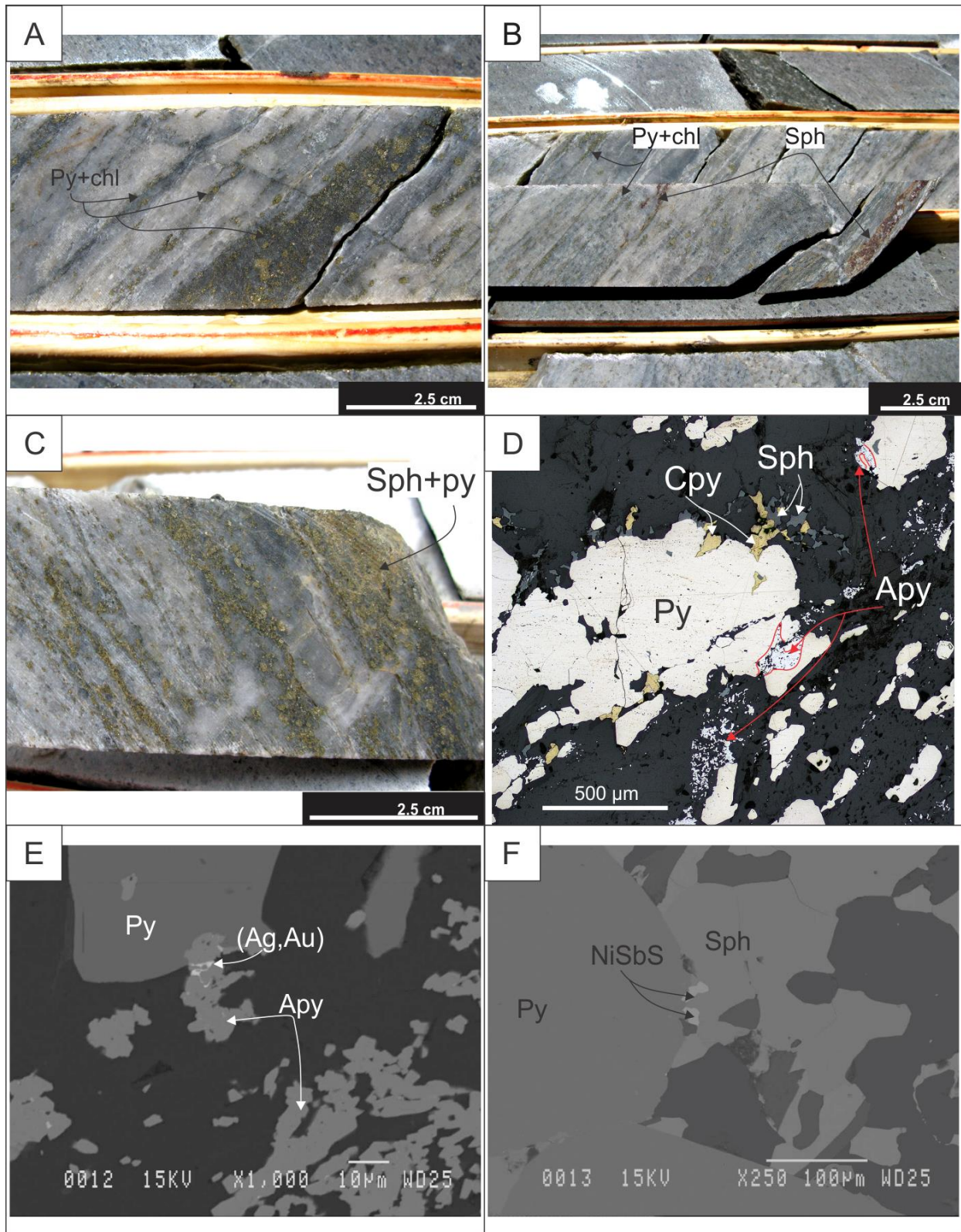


Figure 6.14 : Cap mineralized zone. A. Pyrite-chlorite vein and veinlets folded and transposed into S₂ in a muscovite schist. DDH NR110771 at 120 m. B. Iron-rich (dark coloured) sphalerite vein

parallel to S_2 in muscovite schist. DDH NR110771 at 121 m. C. Iron-poor (yellow coloured) sphalerite with pyrite and chlorite in vein and veinlets folded and transposed in S_2 . DDH NR110771 at 132 m. D. Photomicrograph (RL) of an S_2 -folded and transposed pyrite-arsenopyrite-sphalerite-chalcopryrite vein in muscovite schist. Sample RRR435830, DDH NR110771 at 121 m. E. Backscattered electron image (15kV operating voltage) of same veinlet as in fig 6.14D, showing electrum within arsenopyrite fracture. Sample RRR435830. F. Backscattered electron image of ullmanite at grain boundary between sphalerite and pyrite in same veinlet as fig. 6.14D, E. Sample RRR435830.

6.2.6 Summary of style and mineralogy of all mineralized zones

Tables 6.3 and 6.4 summarize the information of sections 6.2.2 through 6.2.5, using data from this study along with work from Wartman (2011) and Kjarsgaard (2013).

Table 6.3 : Mineralization styles of the different mineralized zones of the Rainy River deposit

Zone		Mineralization style (in order of importance) correlated with the presence of Au
Cap		<ul style="list-style-type: none"> Granoblastic pyrite \pm arsenopyrite concentrated in ≤ 3 cm-wide bands parallel to S_2 as well as in dismembered and transposed pyrite-sphalerite\pmchalcopryrite veinlets in dacites. Fine-grained pyrite stockwork and disseminations developed in tholeiitic basalts. ≤ 20 cm-wide quartz-ankerite-pyrite auriferous veins hosted in tholeiitic basalts.
ODM		<ul style="list-style-type: none"> Pyrite-sphalerite-chalcopryrite-galena veinlets transposed within S_2, within dacitic tuff breccias. Disseminated auriferous pyrite and pyrrhotite in coherent dacite. S_2-parallel pyrite-sphalerite-chalcopryrite-galena veinlets in higher grade intervals in coherent dacite. Electrum and Au-Ag tellurides in quartz-carbonate-pyrite veins folded and transposed in S_2 as well as at pyrite grain boundaries and associated with sphalerite. Present in all dacitic facies.
HS	Upper	<ul style="list-style-type: none"> Pyrite, Fe-poor sphalerite and chalcopryrite veinlets parallel to S_2 in strongly deformed dacitic tuff and tuff breccias.
	Lower	<ul style="list-style-type: none"> Disseminated granoblastic pyrite rimmed by chlorite, sometimes regrouped in veinlets folded and transposed within S_2, hosted in muscovite schists
433		<ul style="list-style-type: none"> Disseminated granoblastic pyrite rimmed by chlorite stretched and flattened parallel to S_2. Higher grade mineralization associated with pyrite-chalcopryrite-native bismuth stockwork. Hosted in dacite of all facies. S_2-parallel veins of granoblastic pyrite with abundant very fine-grained rutile disseminated in tholeiitic mafic rocks.

Table 6.4 : Mineralogy of the Rainy River deposit with respect to the different mineralized zones. Compiled from Kjarsgaard (2013), SRK (2014) and this study. *Indicates a mafic host rock, ° indicates a felsic host rock.

Zone	Sulphides, tellurides, oxides, and native metals	
	Major phases	Minor phases
Cap	Pyrite ^{°*} , pyrrhotite [*] , arsenopyrite [°] , chalcopyrite ^{°*} , sphalerite ^{°*} , rutile ^{°*} , ilmenite [*]	Electrum [°] , tetrahedrite [°] , melonite [*] , petzite [*] , stibnite [*] , ullmanite ^{**} , hessite [*]
ODM	Pyrite [°] , sphalerite [°] , chalcopyrite [°] , galena [°] , pyrrhotite [°] , rutile [°]	Arsenopyrite [°] , troilite [°] , electrum [°] , native gold [°] , native silver (lead-bismuth?) telluride [°] , petzite [°] , hessite [°] , stützite [°] , ullmanite [°] , Ag-pentlandite [°]
HS	Pyrite [°] , sphalerite [°] , chalcopyrite [°] , rutile [°]	Galena-altaite [*] , pyrargyrite [°] , stützite [*]
433	Pyrite ^{°*} , chalcopyrite ^{°*} , rutile ^{°*}	Pyrrhotite [°] , electrum [°] , native gold [°] , bismuthinite [°] , tellurobismuthinite [°] , native bismuth [°]

6.3 Metal associations and zonation

6.3.1 Metals correlated to gold: deposit scale

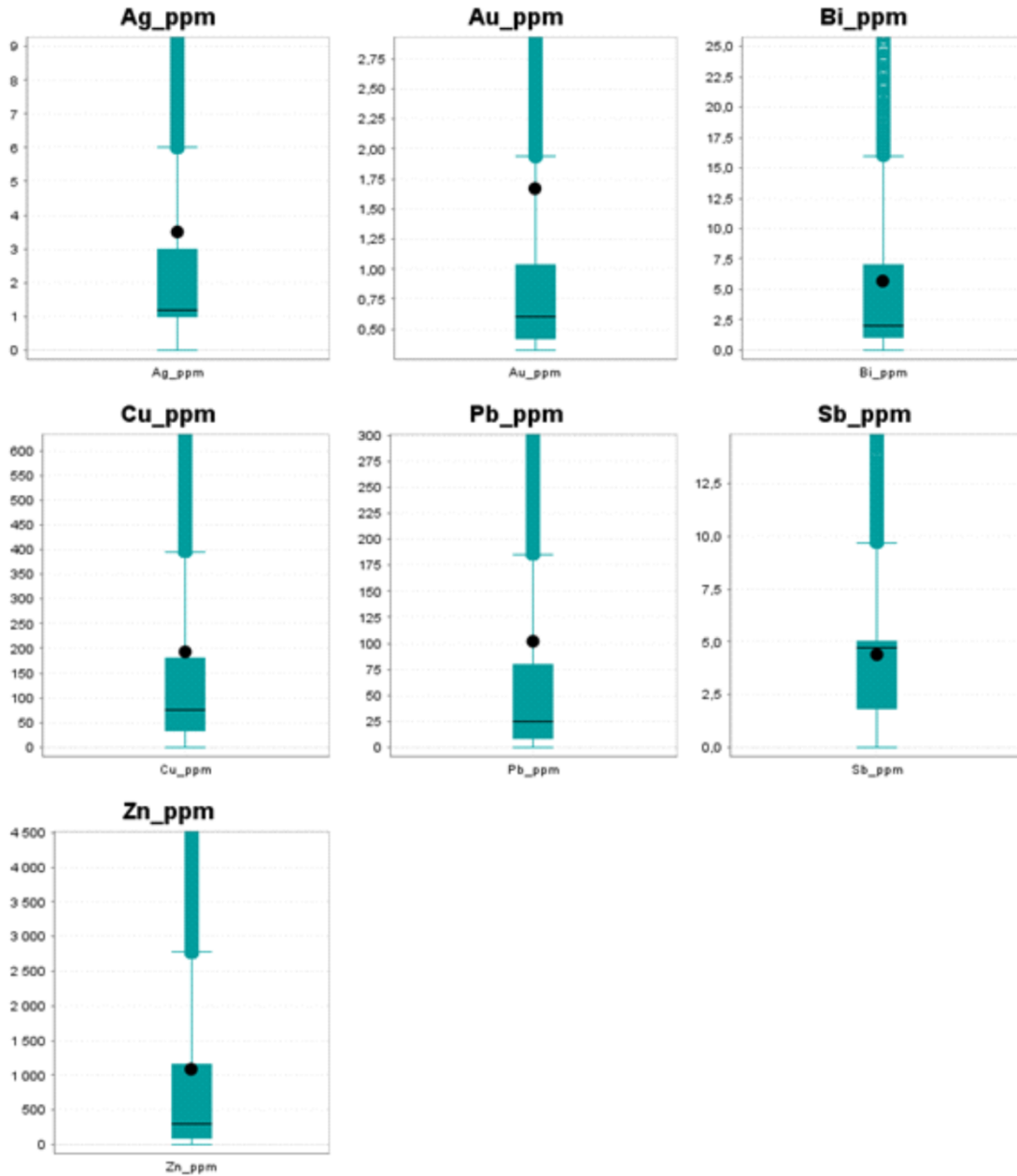
A correlation matrix of the samples taken within this study (n=327: table 6.5) demonstrates a relatively good correlation between gold and copper and gold and silver. Other relatively good positive correlations between elements are between silver, antimony, lead and zinc.

Table 6.5 : Correlation matrix using data from this study (n=327). Values above 0.5, indicating a good correlation, are highlighted in red. Calculations were generated using the REFLEX[®] ioGAS software version 6.0.1.

Correlation	Au	Ag	Sb	Cu	Pb	Zn	Bi
Au	1.0	0.5	0.33	0.59	0.24	0.26	0.11
Ag	0.5	1.0	0.86	0.41	0.56	0.41	-0.035
Sb	0.33	0.86	1.0	0.26	0.8	0.54	-0.061
Cu	0.59	0.41	0.26	1.0	0.24	0.39	0.24
Pb	0.24	0.56	0.8	0.24	1.0	0.52	-0.065

Zn	0.26	0.41	0.54	0.39	0.52	1.0	0.045
Bi	0.11	-0.035	-0.061	0.24	-0.065	0.045	1.0

Using the database provided by the company, the Q1 and Q3 quartile values for each metal (Fig. 6.15) indicate that samples with gold values above 0.325 ppm are systematically associated with one or several of the following metal in concentrations ranging between: 1 to 3 ppm for silver, 1 to 7 ppm for bismuth, 34 to 179 ppm for copper, 8 to 79 ppm for lead, 1.9 to 5 ppm for antimony and 87 to 1160.3 ppm for zinc.



	Au	Ag	Bi	Cu	Pb	Sb	Zn
Group size	42136	41282	41282	41282	41282	41282	41282
Min Regular (whisker)	0,326	0	0	0	0	0	0
Q1 (bottom of box)	0,425	1	1	34	8	1,86	87
Median (line)	0,603	1,175	2	75,3	25	4,735	290
Q3 (top of box)	1,032	3	7	179	79	5	1160,25
Max Regular (whisker)	1,941	6	16	396	185,5	9,7	2770
Upper Outlier Threshold	1,9425	6	16	396,5	185,5	9,71	2770,125
Upper Far Outlier Threshold	2,853	9	25	614	292	14,42	4380
Mean (black circle)	1,6706337	3,5018492	5,6864343	192,88315	101,89211	4,3938546	1085,174

Figure 6.15 : Whisker plots for a suite of metals correlated to gold values at Rainy River. Data consists in all sample within deposit that contain over 0.325 ppm Au, with summary statistics in table below. All concentration values are in parts per million (ppm).

6.3.2 Metal associations and zonation: section 425475E

As shown above, there is a relatively good correlation between gold and other trace metals when all the ore zones are considered, but a critical aspect is how these Au-metal associations are distributed in space with respect to the different mineralized zones. Are mineralized zones characterized by distinct metal associations? Also, are there any systematic variations in the metallic associations in space, and if so, what do those variations indicate about the hydrothermal system? To answer these questions, a preliminary evaluation using data along a composite drill hole located on section 425475E (Fig. 6.16) illustrates metal associations and their location in space with respect to the mineralized zones.

The composite drill hole profiles show three main auriferous zones that are characterized by distinct metal associations. The first gold-rich zone is located between 250 m and 500 m depth down hole and corresponds to the ODM body. In this gold-rich zone, gold is correlated with zinc, lead, antimony and arsenic. The second gold-rich interval, located between 625 m and 690 m represents a zone of Au-Ag-Zn-As-Cu-Bi±Sb metal association. The third auriferous zone, located between 700 m and 775 m down hole, represents the 433 zone. In this interval, gold rather correlates with copper, bismuth and somewhat arsenic. Two minor auriferous zones along the profile cannot be characterized by the main metal associations described above. They consist in a minor zone in the ODM hanging wall between 155 m and 180 m and has sub-economic (≤ 200 ppb Au) gold content associated with Zn-Cu-Sb±As. This auriferous zone is correlated with a high strain zone with a strong S_2 fabric between 153.5 and 155 m. Additionally, a part of the HS zone between approximately 525 m and 625 m depth (highlighted in light blue on Fig. 6.16) is characterized by gold grades steadily above 100 ppb, although no base metals are present. Although mineralized zones are globally preferentially developed in volcanoclastic dacitic rocks at deposit scale (see Chapter 3), the various metal associations that characterize the mineralized zones do not seem to be controlled by specific rock units or facies (Fig. 6.16).

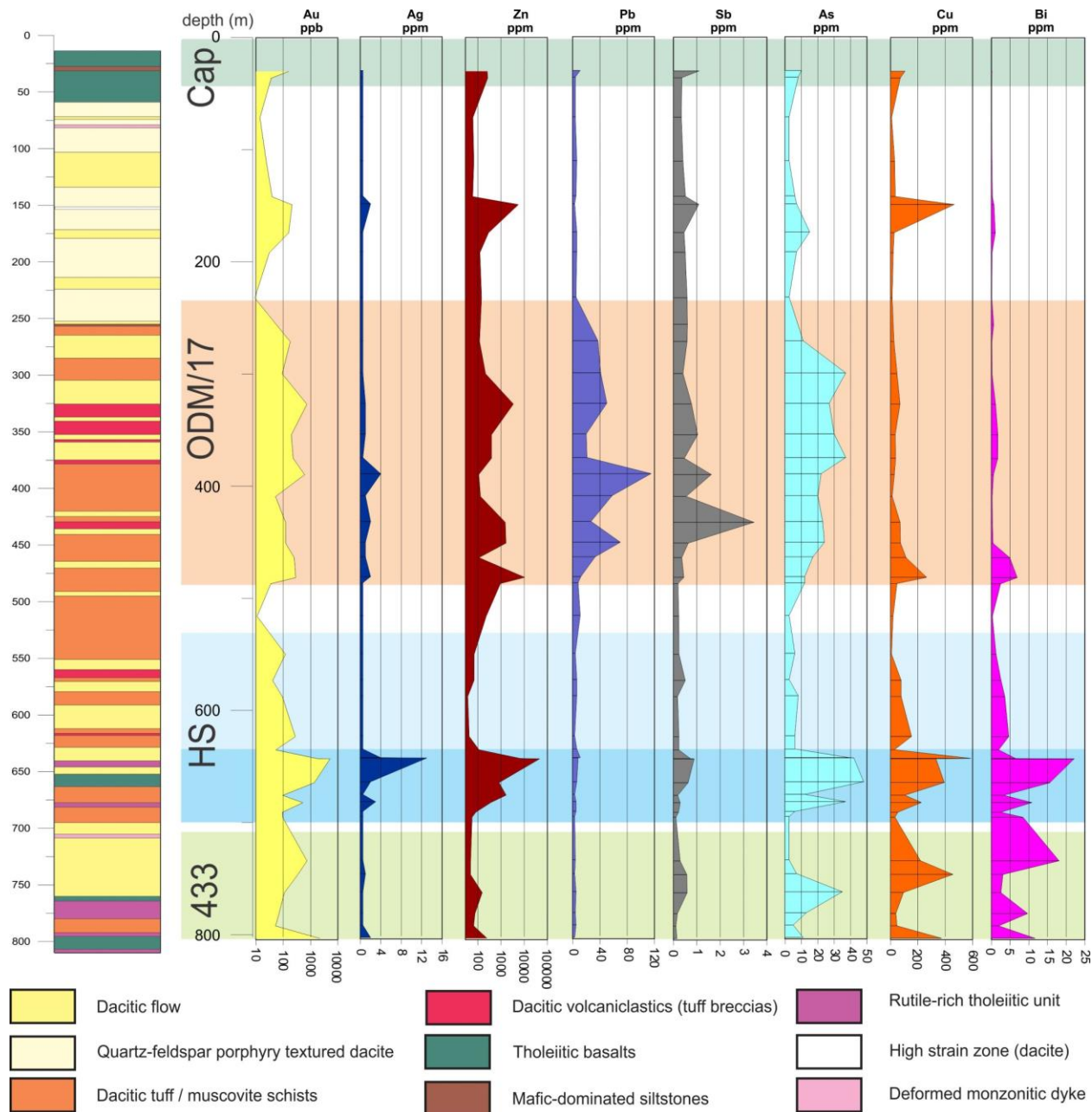


Figure 6.16 : Metal concentration values down composite drill hole going through all mineralized zones at 425475E. Logging data is located on the left, with legend at the bottom. Note that Au and Zn values are represented on the logarithmic scale, while the rest are represented on a linear scale.

6.3.3 Metal associations and metal zonation at deposit scale

Deposit-scale modelling was done using the Leapfrog[®] Mining software (version 2.5.3.61) to illustrate metal zonation and associations at deposit scale. The assay database was kindly provided by New Gold Inc.

6.3.3.1 Implicit modelling and grade interpolation of the Rainy River deposit

The dataset provided by the company contains over 450,000 assays, including Au. Analytical techniques as well as quality assurance-quality control (QA/QC) measures for this dataset can be found in the February 2014 NI 43-101 feasibility study prepared for New Gold Inc. available on SEDAR (www.sedar.com).

Prior to modelling grade shells, simple data transformation operations had to be applied to avoid error induced by outlier values as well as to reduce the database size, which made implicit modelling feasible with the computing resources available. Drill core sampling for Au assaying was done at a 1.5 metre interval within the deposit, although some sections have been sampled every metre, while other sections with low apparent mineralization potential were sampled sporadically. In terms of modelling, this variation in sampling interval length induces data clustering, which distorts the modelling. In order to reduce this effect, the entire assay database was composited to 3 m-long intervals, which also had the effect of "smoothing" the high grade data spikes and, consequently, the grade shells produced. Data compositing also significantly reduced the total number of assay points to 221,696, which is a more manageable dataset.

Subsequently, the composited data was cut using upper and lower bound values. These values correspond to the observed data breaks present in data distribution histograms (Fig. 6.17). Similar to data compositing, this data treatment operation reduces the impact of isolated, abnormally high (or low) outlier values that are common in highly skewed datasets such as gold assays (Reid, 2013). This again allows for the generation of smoother grade shells that would otherwise have been influenced by high values that are not representative of the overall deposit.

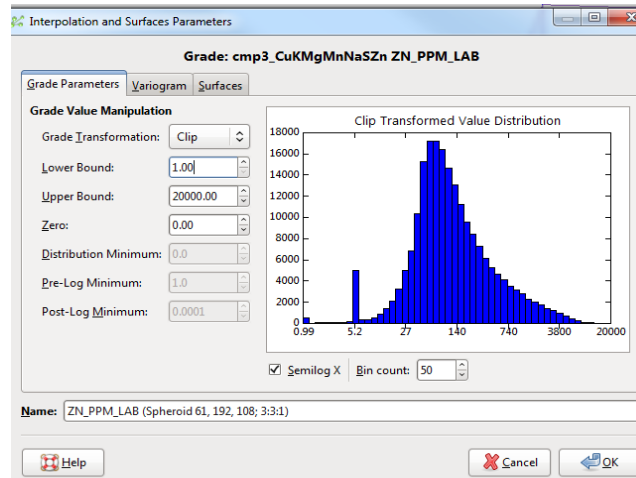


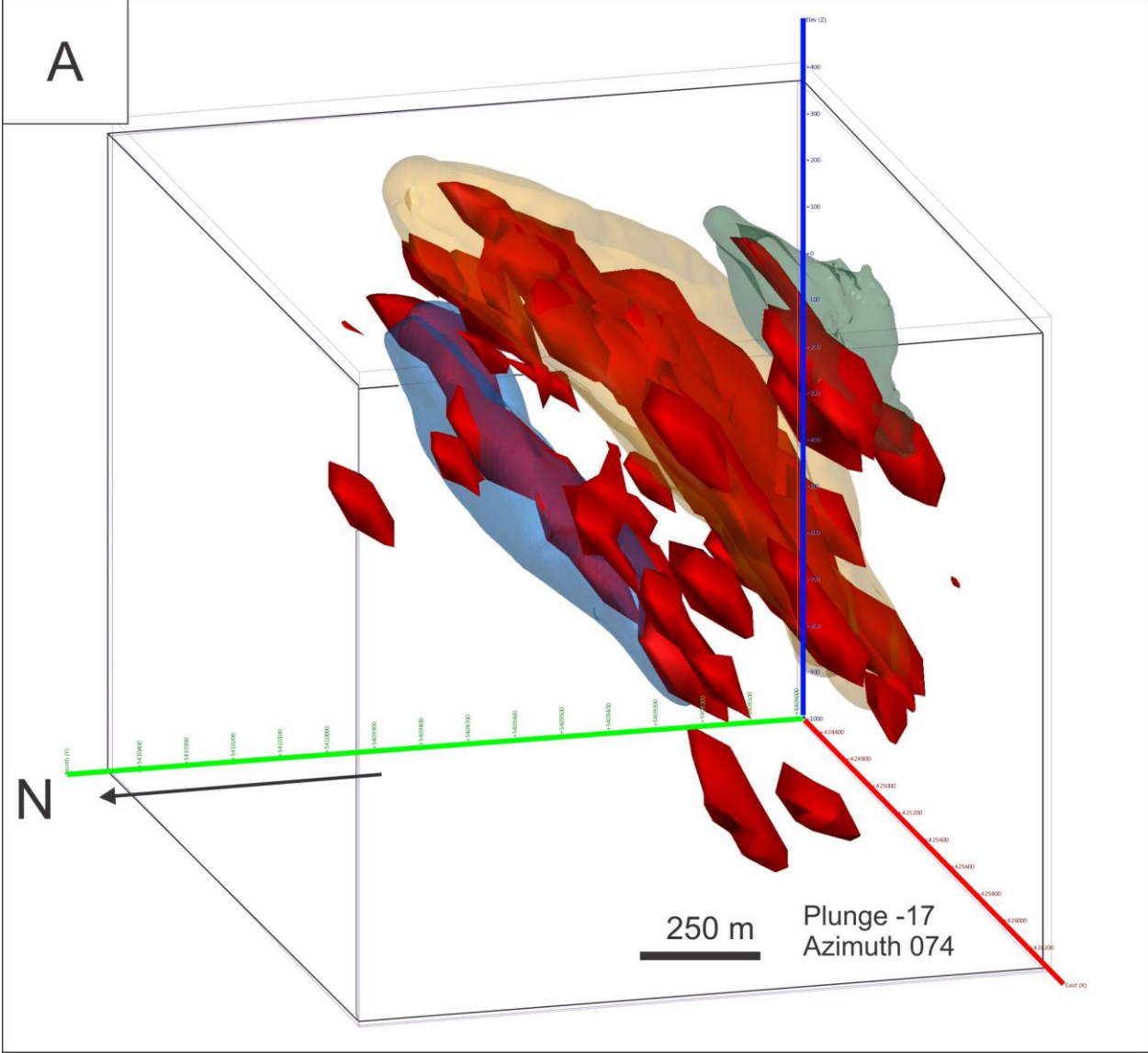
Figure 6.17 : Screen shot of Leapfrog[®] Mining showing histogram for Zn data to be modelled. The previously composited dataset has been assigned a lower bound value of 5 ppm and an upper bound value of 5000 ppm in this study to avoid distortion effects due to data outliers.

Following these data transformation operations, grade interpolation was done using spheroidal variogram transformations. At time of writing, a spheroidal variogram constitutes the norm in basic grade interpolation within a 3D environment such as Leapfrog[®] Mining (Reid, 2013). The variogram used consists in the one built in the Leapfrog[®] Mining software. Data range was set at 125 metres, the alpha value at 5, and the nugget at 25% of the sill value. Threshold values for shells were primarily determined using the first through third quartile values, and then modified in an iterative fashion until satisfactory (i.e. not too big or too spotty) shells were generated. In order to take into account the strong deformation that affects the mineralized zones (see Chapter 4), modelling was further constrained by forcing the global trend of the main S_2 foliation, including the L_2 lineation, into the interpolation parameters (range ellipsoid of 3:3:1 ratio). For the purpose of this study, interpolated grade shells were restrained to the proposed pit and underground mining area.

6.3.3.2 Testing the accuracy of the Leapfrog[®] Mining implicit modelling

Distribution of gold within the Rainy River deposit is well constrained in previous grade modelling work done through resource assessment and exhaustive modelling by wireframing (El-Rassi and Cole, 2008, 2010, 2014). Modelling done in this study was compared with the shells produced by the company to test the accuracy and relevance of the implicit modelling done with the parameters given above. There is a good fit between the Leapfrog[®] Mining-modelled grade shells generated in this study and the "ore bodies" defined by the company, as shown on figures 6.18A, B. Because of this, the grade shells modelled here using the Leapfrog[®]

Mining software with the parameters cited in section 6.3.3.1 are considered as a good approximation to the actual distribution of the metals at deposit scale and reliable and precise enough to illustrate metal zonation and global trends.



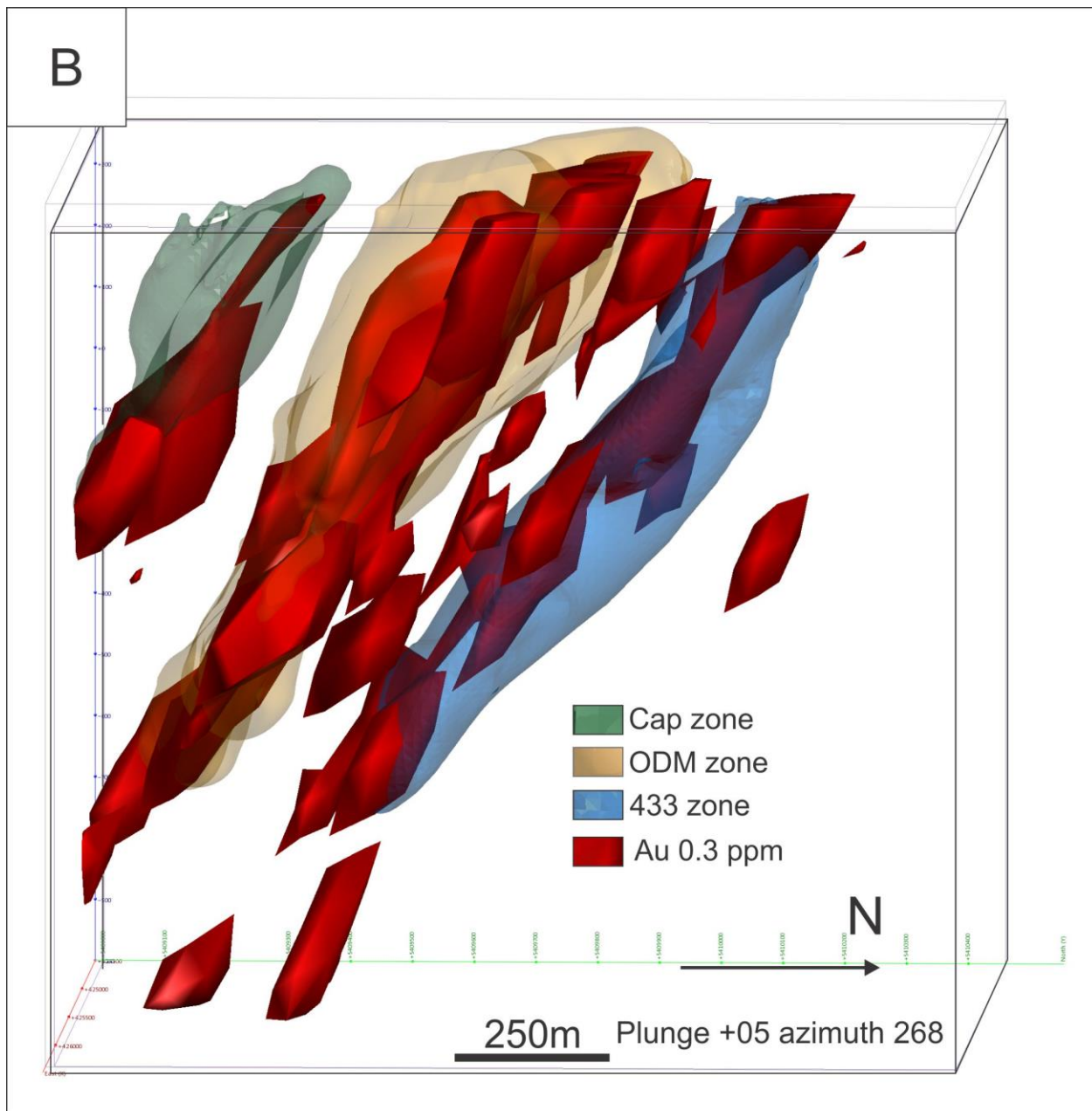


Figure 6.18 : A. NewGold inc. 0.3 g/t Au shells obtained from wireframing work of the Cap (in green), ODM (in yellow) and 433 (in blue) zones, onto which are superimposed the 0.3 g/t Au shells generated in this study using Leapfrog[®] Mining implicit modelling (in red). The bounding box represents the proposed mining extent. The cluster of Leapfrog[®] Mining-modelled Au shells between the ODM and 433 zones represent the HS zone, which has not yet been modelled by the company. B. Same as A, with view oriented at a different plunge and azimuth.

6.3.3.3 Results: distribution of silver

Silver is for the most part restricted to the ODM zone, and to some extent to the Cap zone (Fig. 6.19A, B). Furthermore, there is an increase in shell size, and presumably in total contained

metal as grades are generally relatively uniform along strike, in the eastern half of the ODM zone, compared with the western half where zones with over 2.2 ppm Ag are more sporadic. Silver also seem to be more abundant or concentrated in the lower and central part of the ODM (in what corresponds to the HS zone position just below the ODM), whereas it seems to form a discontinuous halo around the Cap zone. There is a clearly very minor amount of silver in the 433 zone.

6.3.3.4 Results: distribution of arsenic

Arsenic (≥ 31 ppm: Fig. 6.20A, B) has a somewhat similar distribution to silver; with a main body associated with the ODM zone and a discontinuous envelope around the Cap zone. The arsenic shell centered on the ODM zone is almost entirely constrained within it, in contrast to silver that was a bit more scattered in and around the ODM zone. As with silver, there is almost no As in and around the 433 zone.

6.3.3.5 Results: distribution of bismuth

Bismuth (≥ 2 ppm: Fig. 6.21A, B) is preferentially associated with the 433 zone, and to some extent to the lower part of the ODM zone and the HS zone (the area between the 433 and ODM zones). The modelled bismuth shells are strongly stretched parallel to L_2 . The modelled shells are in agreement with bismuth distribution on the composite drill hole profile of section 425475E (Fig. 6.16) where anomalous bismuth values are restricted to the 650 to 775 m interval that corresponds to the transition between the HS and 433 zones. Even though bismuth is spatially restricted structurally below the ODM zone, the ≥ 2 ppm shells do not correlate well with the extent of the HS or 433 zones, indicating a poor correlation between bismuth and gold and silver. This is also supported by a poor correlation value (0.11) between Au and Bi in the correlation matrix (see table 6.5).

6.3.3.6 Results: distribution of copper

Copper (≥ 150 ppm: Fig. 6.22A, B) is concentrated in two areas: firstly in the Cap zone and the ODM hanging wall, secondly within the 433 zone and deeper. When superimposed on modelled gold shells (Fig. 6.23), copper displays an overall poor association with gold, with a large volume at the base of the bounding box below the gold shells. The copper shells modelled are cigar-shaped, strongly influenced by L_2 and do not possess the characteristic lens shape of the S_2 -parallel gold and silver shells.

6.3.3.7 Results: distribution of lead

Lead (≥ 25 ppm: Fig. 6.24A, B) is distributed tightly around the ODM zone, along with minor shells dispersed around the Cap zone and above the 433 zone. This distribution of lead concentrations above the median value (25 ppm) almost exclusive to the ODM zone is in agreement with the distribution of lead on the composite drill hole profile of section 425475E (Fig. 6.16). The lead body concordant with the ODM zone follows the S_2 foliation, and the minor bodies outside the ODM zone do not seem to follow any preferential orientation.

6.3.3.8 Results: distribution of zinc

Sphalerite is, after pyrite, the second most abundant sulphide at Rainy River. As a result, modelling of zinc values ≥ 500 ppm (Fig. 6.25A, B) generates large zinc shells that encompass most of the Cap, ODM and HS zones. Modelling also generated a volume outside the Au-mineralized zones, more precisely to the west and along strike of the 433 zone. Similar to the arsenic halo around the Cap zone described in section 6.3.3.4., the modelled zinc shell that encompasses the Cap zone extends farther than the gold zone.

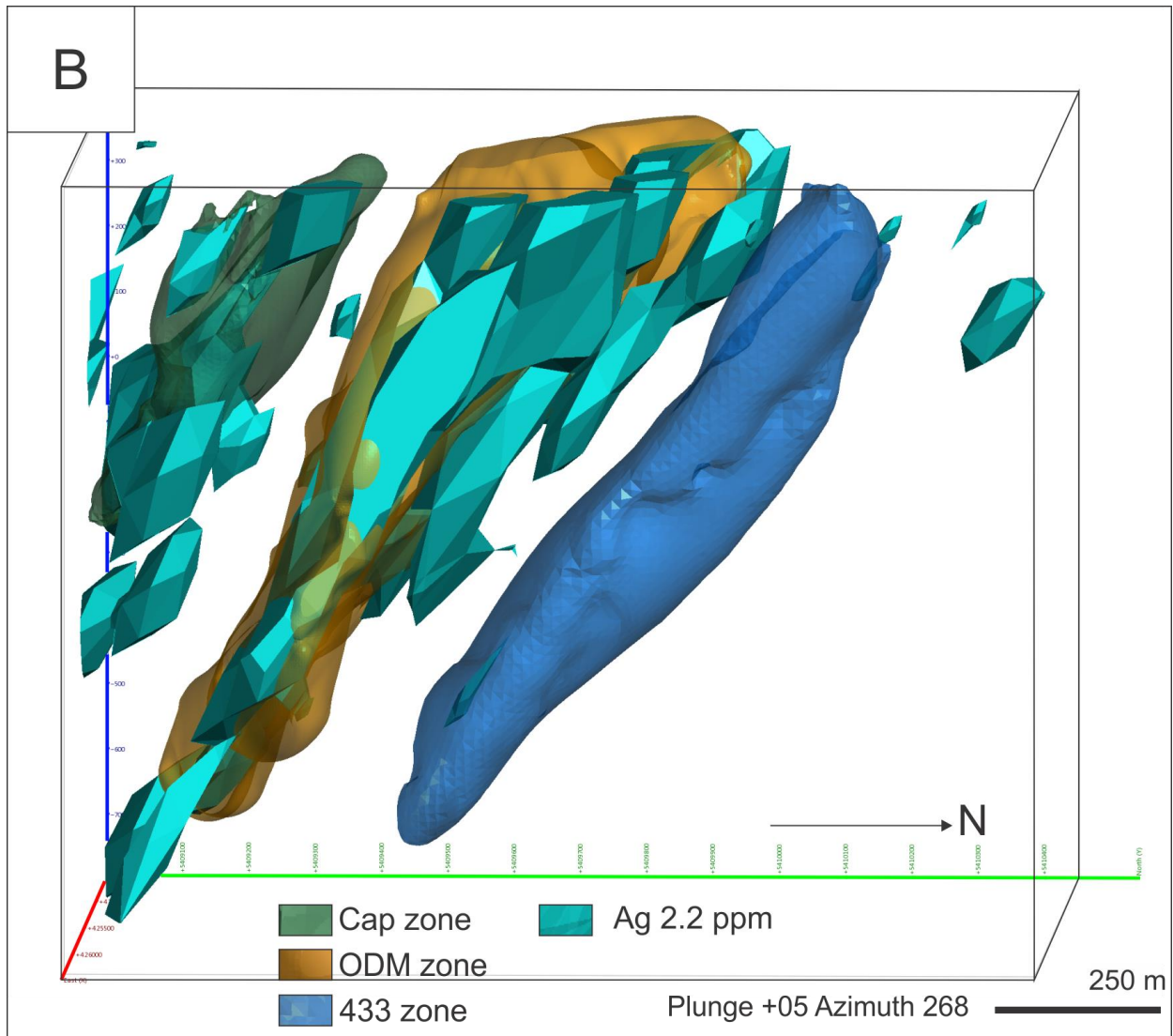
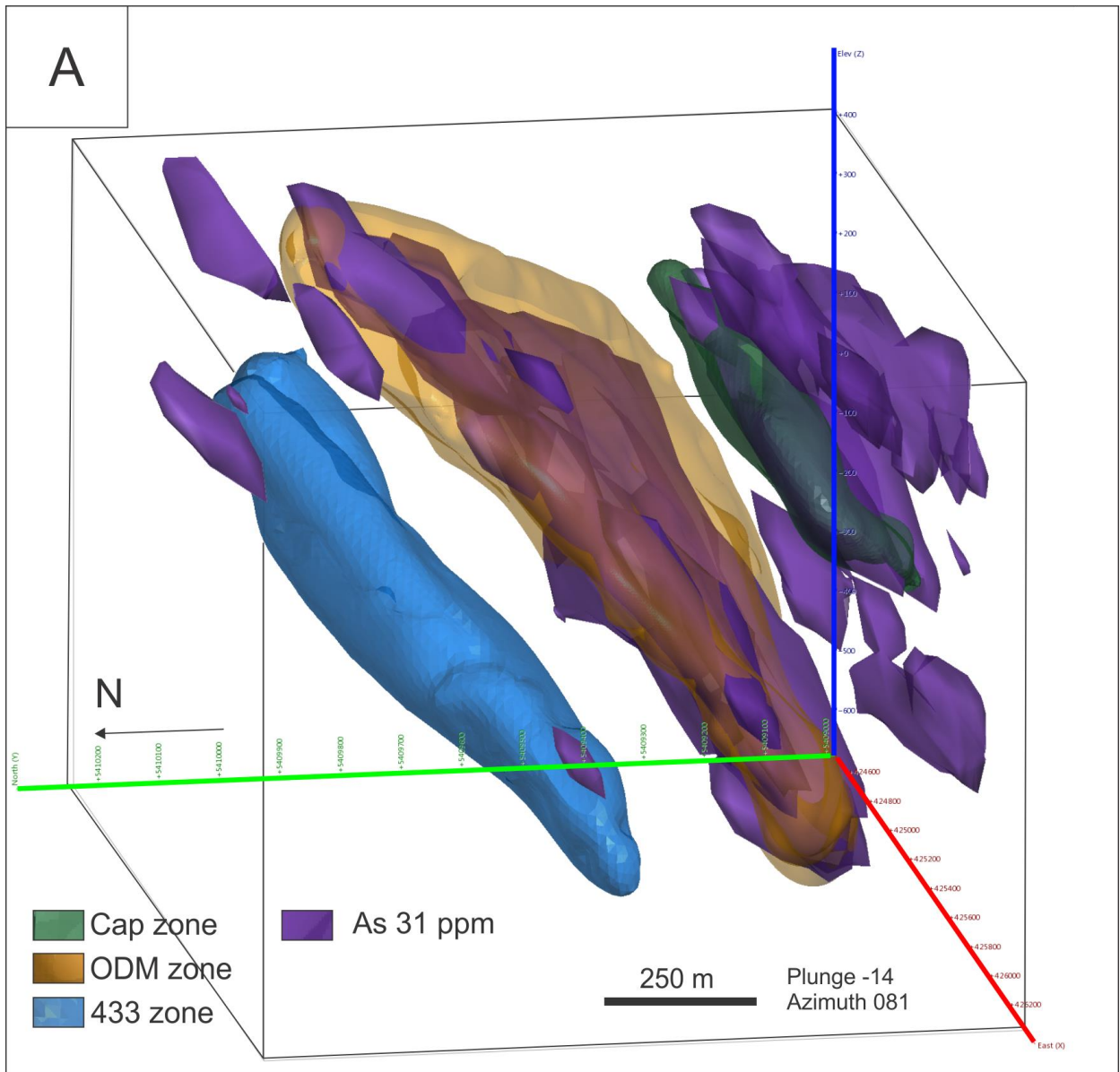


Figure 6.19 : Grade modelling of silver (≥ 2.2 ppm) using Leapfrog[®] Mining. Silver shells are shown in aquamarine and are superimposed on mineralized Cap, ODM and 433 zones.



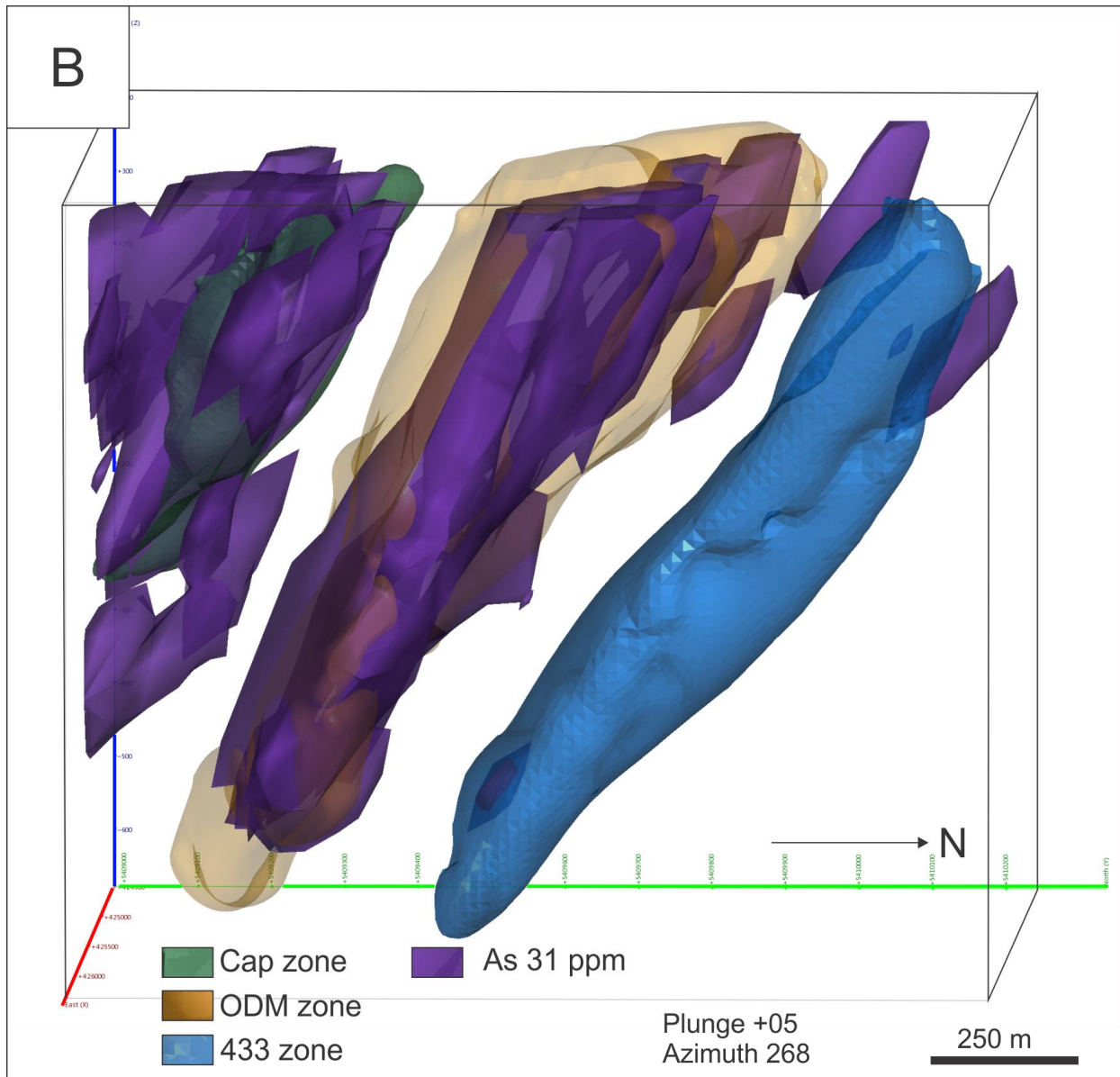
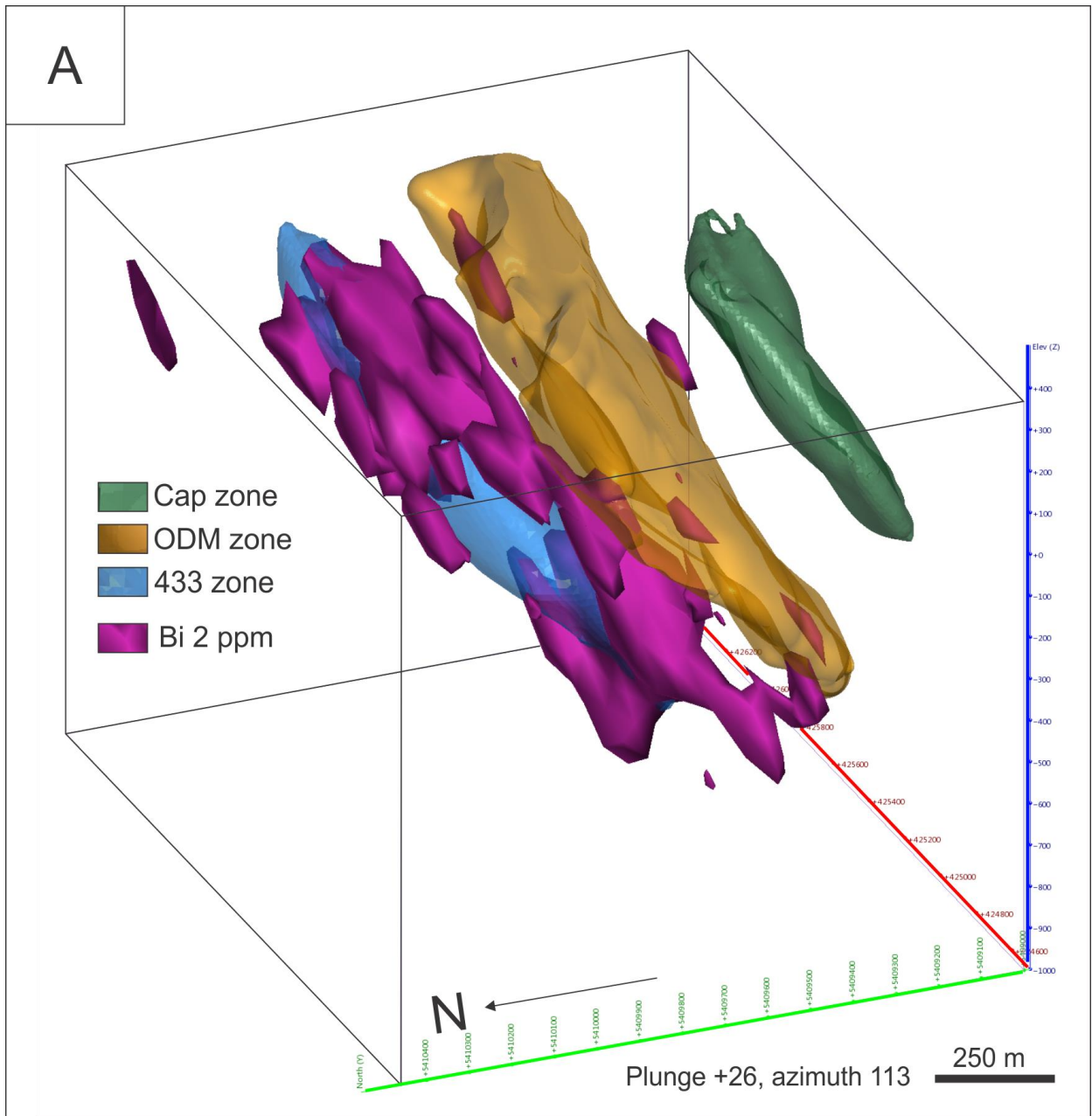


Figure 6.20 : A. Grade modelling of arsenic (≥ 31 ppm) using Leapfrog[®] Mining. Arsenic shells are shown in purple and are superimposed on mineralized Cap, ODM and 433 zones. B. Same as in A, with a different plunge and azimuth.



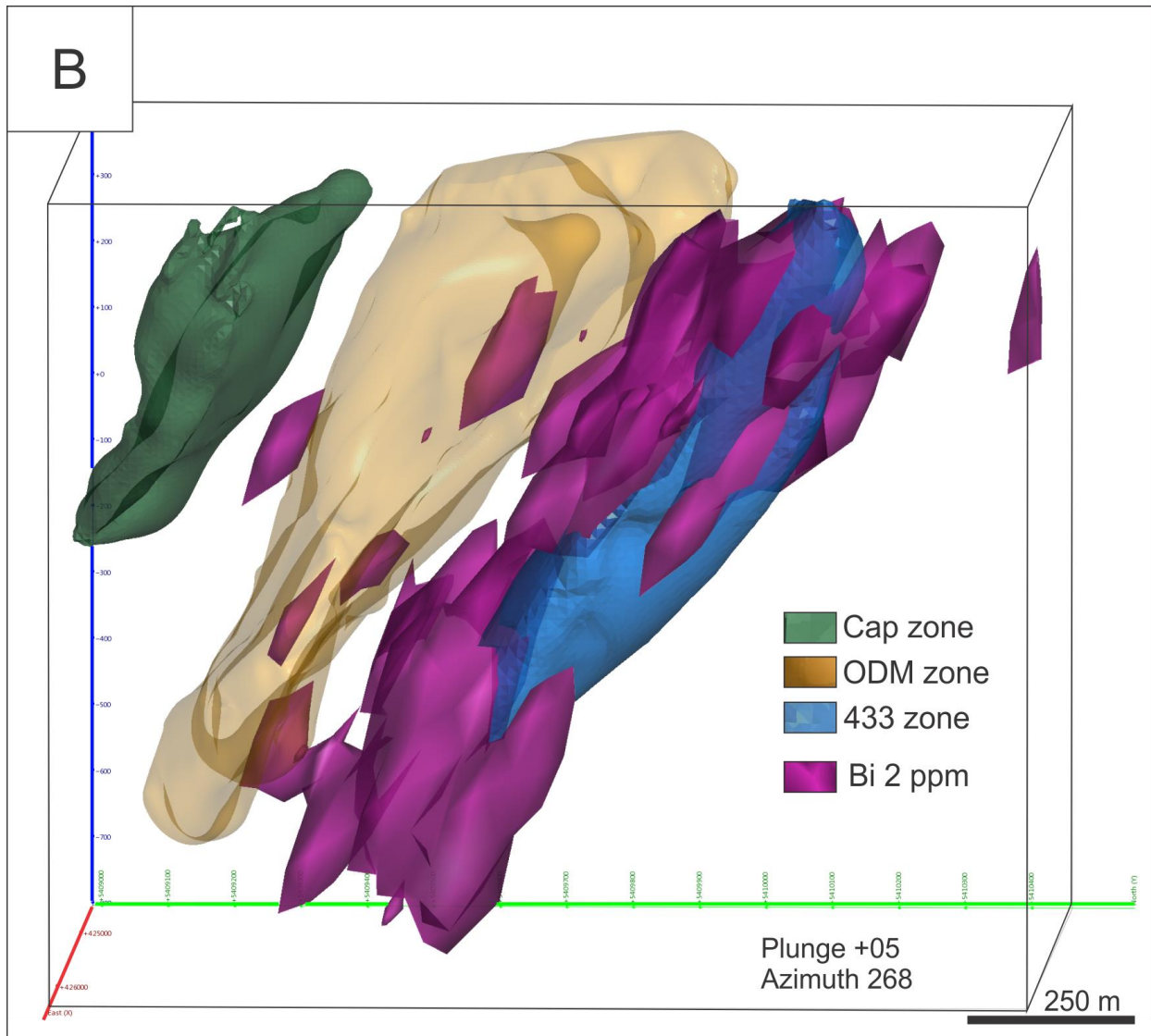
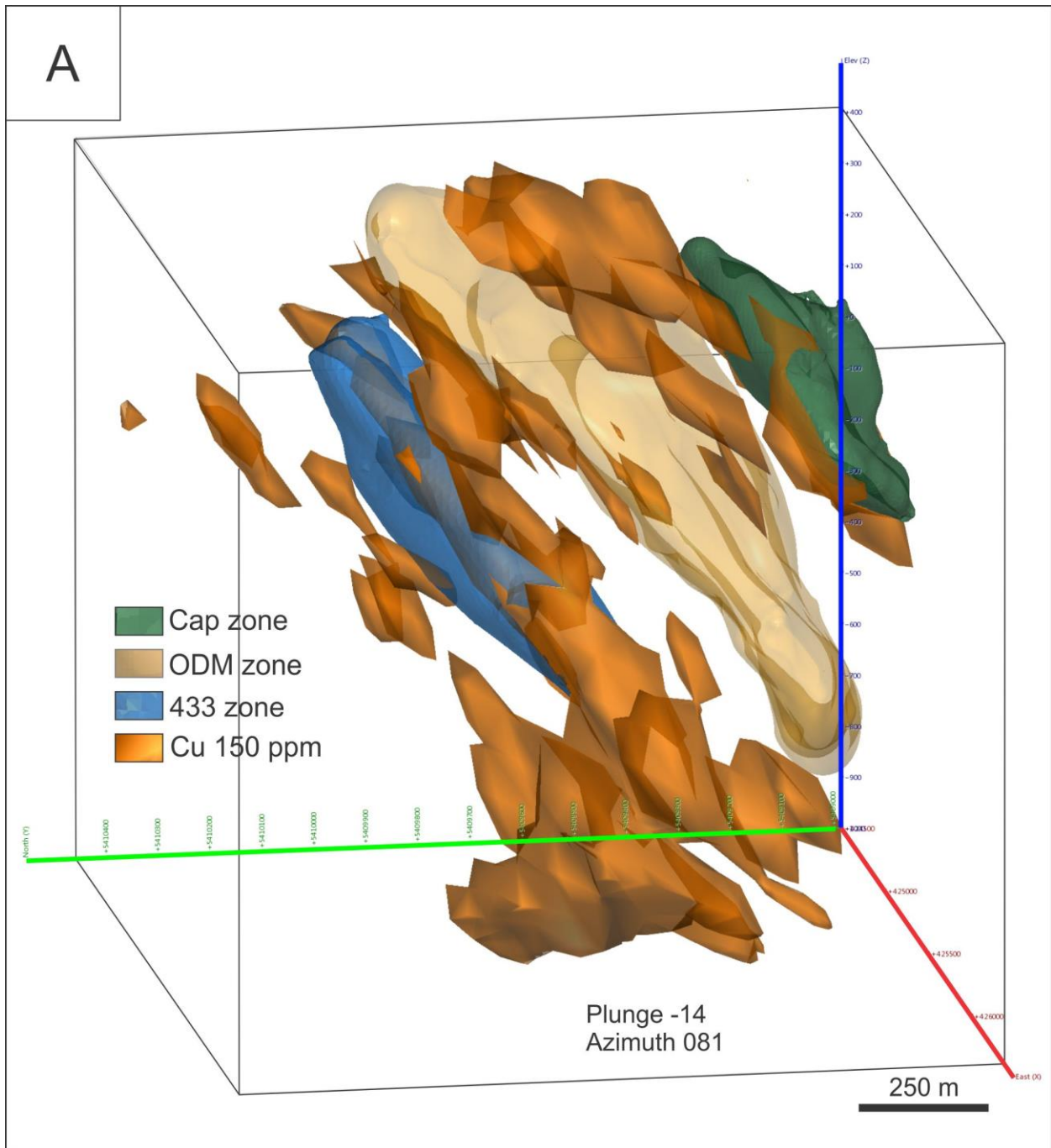


Figure 6.21 : A. Grade modelling of bismuth (≥ 2 ppm) using Leapfrog[®] Mining. Bismuth shells are shown in pink and are superimposed on mineralized Cap, ODM and 433 zones. B. Same as in A, but with a different azimuth and plunge view.



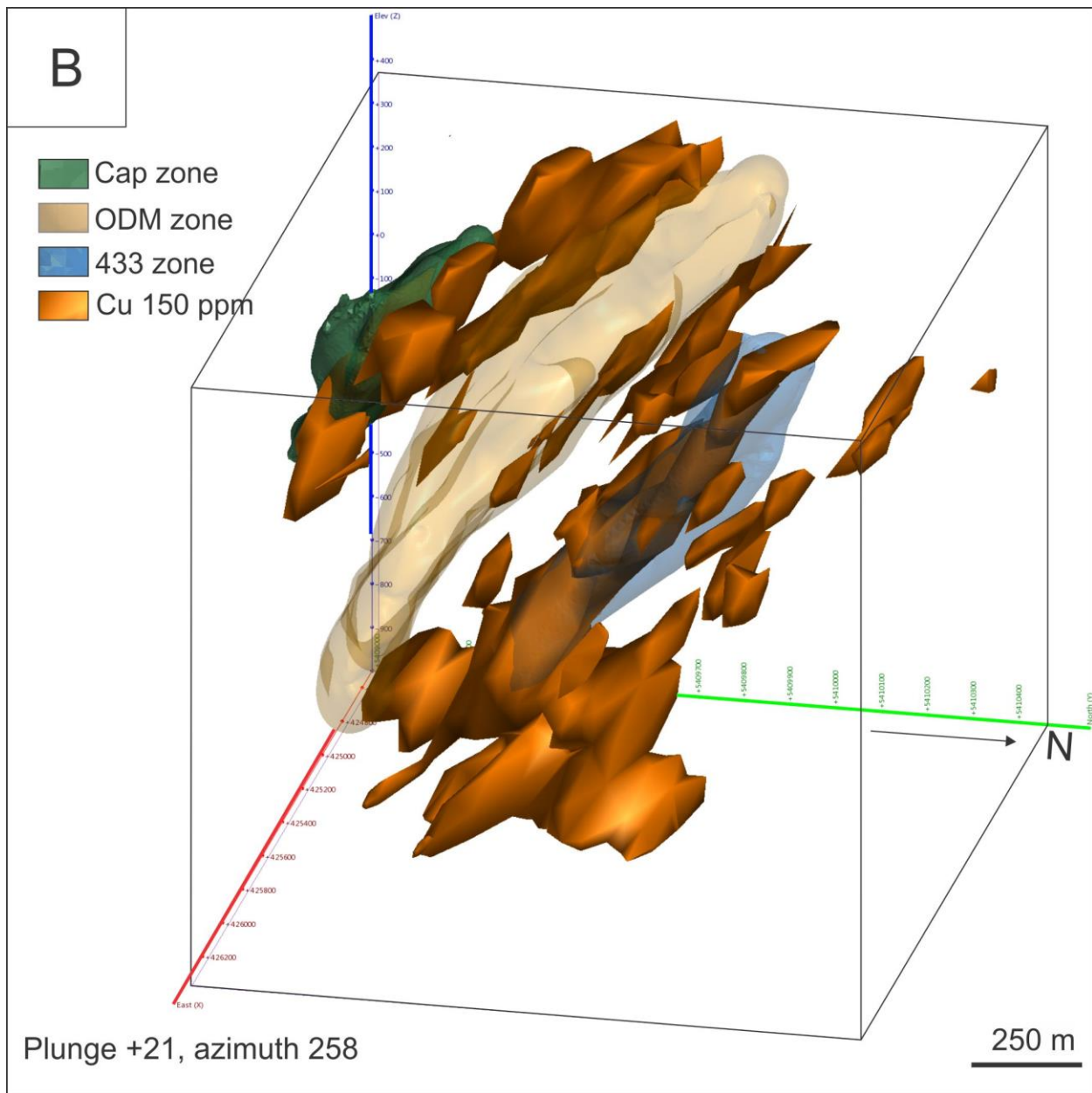


Figure 6.22 : A. Grade modelling of copper (≥ 150 ppm) using Leapfrog[®] Mining. Copper shells are shown in orange and are superimposed on mineralized Cap, ODM and 433 zones. B. Same as A, except with a different azimuth and plunge view.

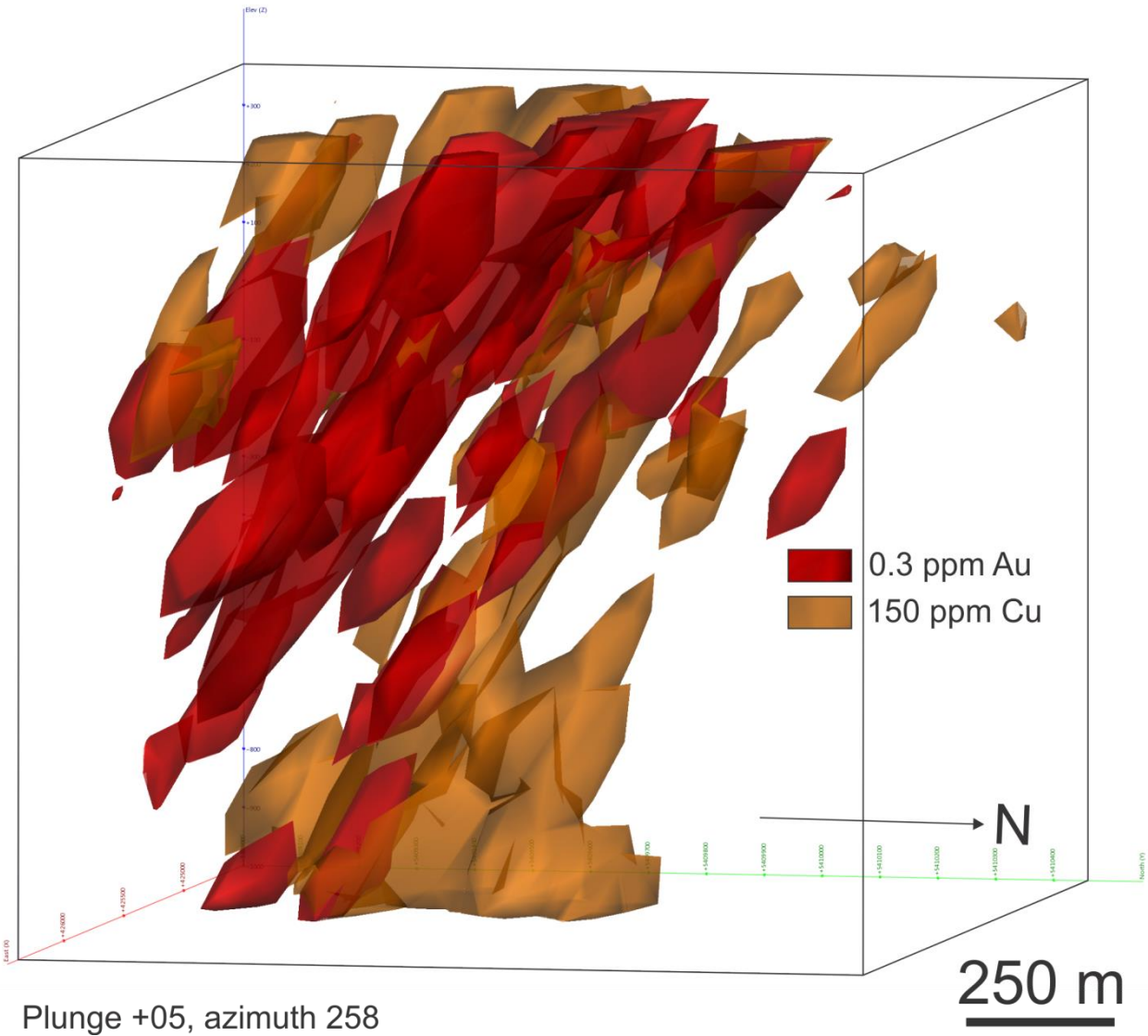
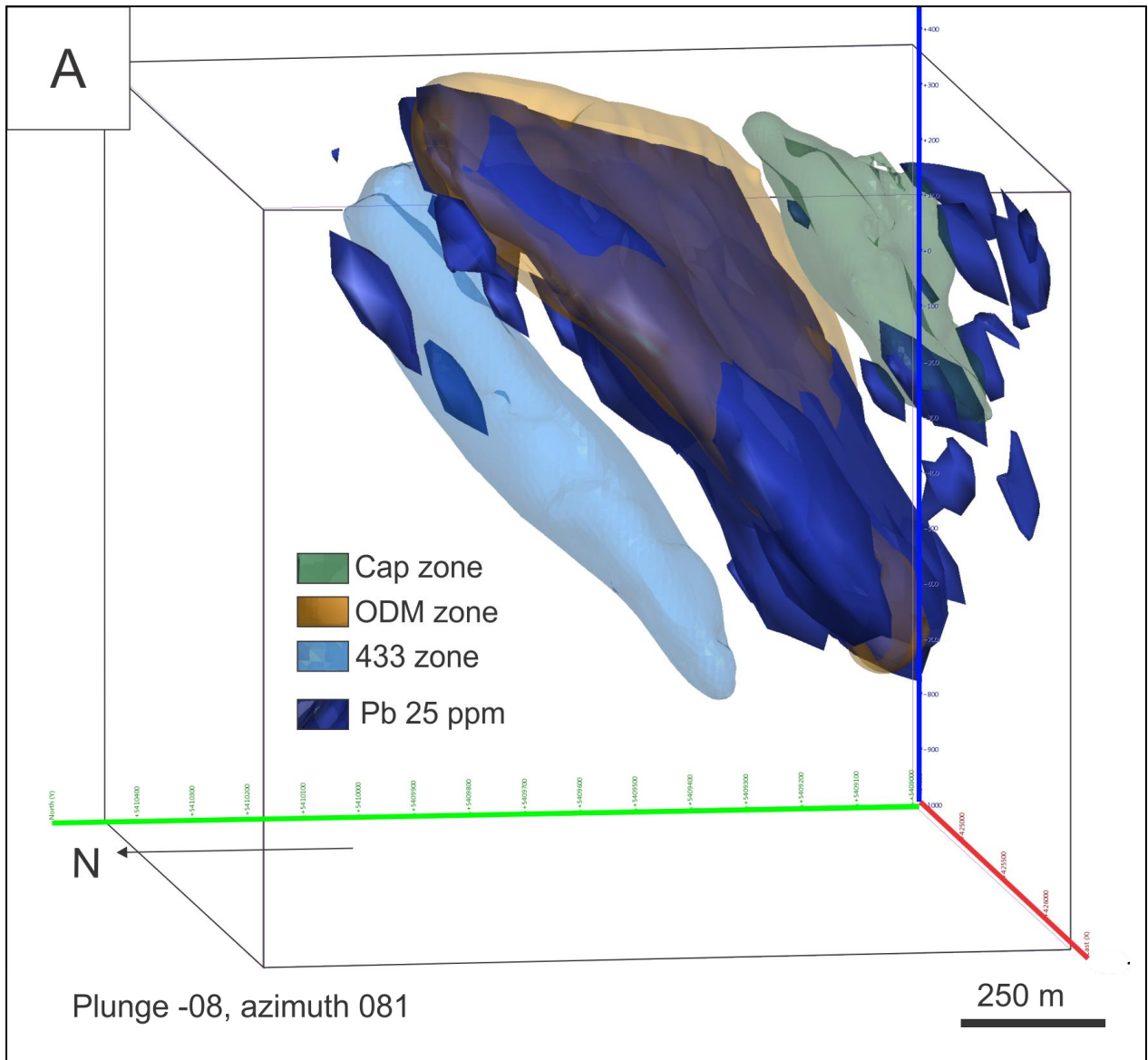


Figure 6.23 : Superimposed gold and copper grade modelling using Leapfrog[®] Mining showing a poor spatial correlation between copper and the main gold zone (ODM).



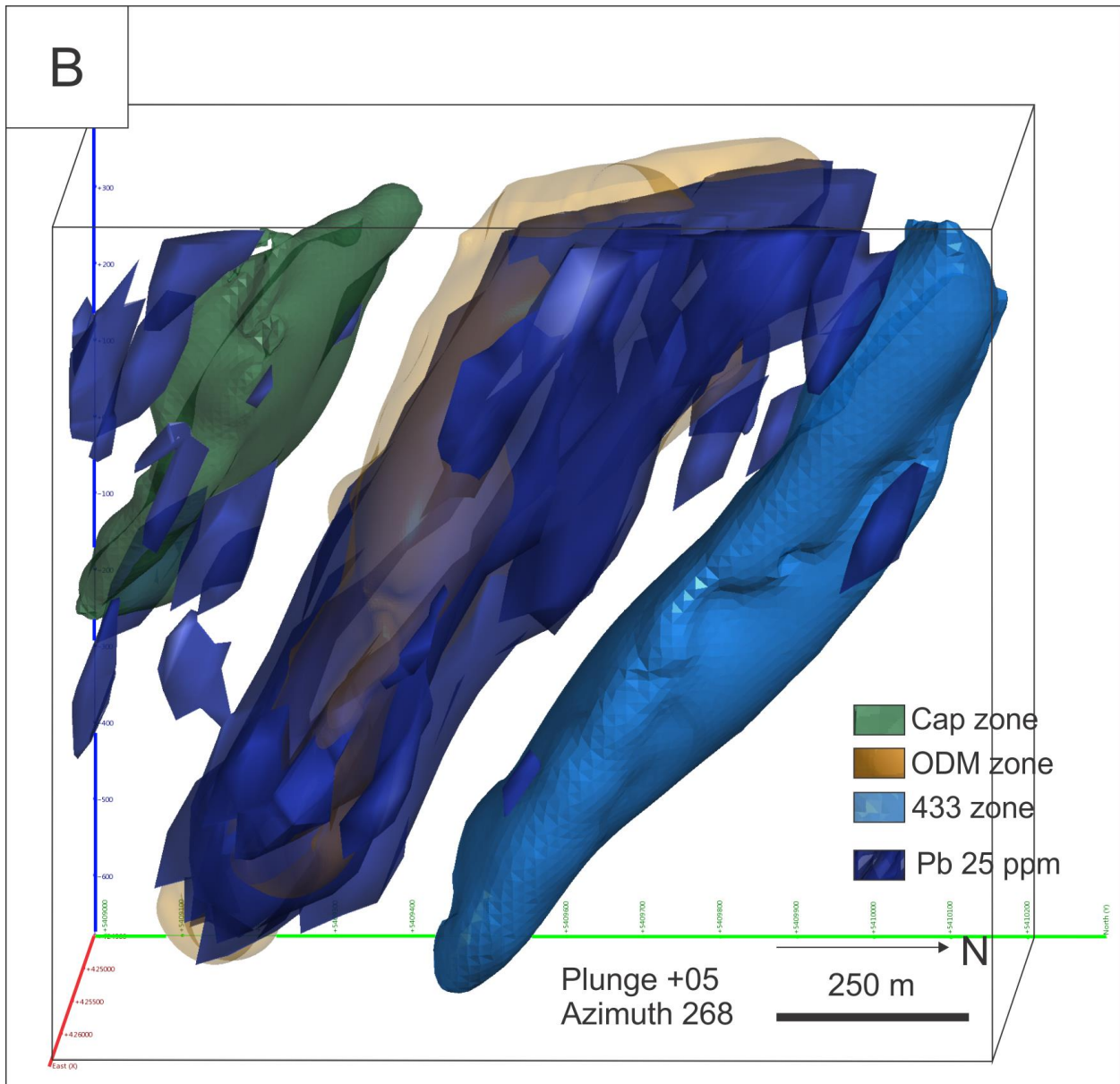
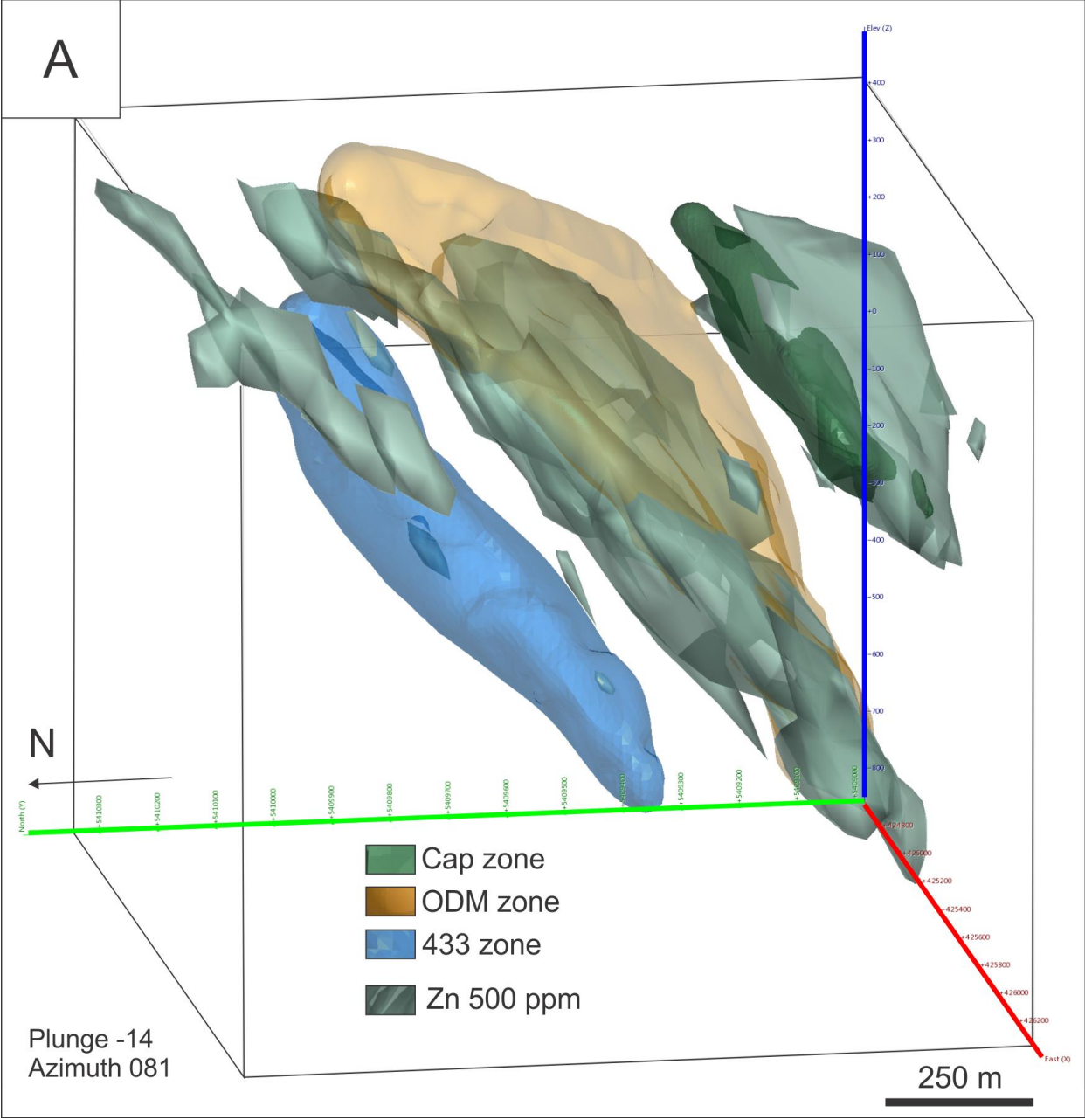


Figure 6.24 : A. Grade modelling of lead (≥ 25.0 ppm) using Leapfrog[®] Mining. Lead shells are shown in navy blue and are superimposed on mineralized Cap, ODM and 433 zones. B. Same as in A except from a different azimuth and plunge view.



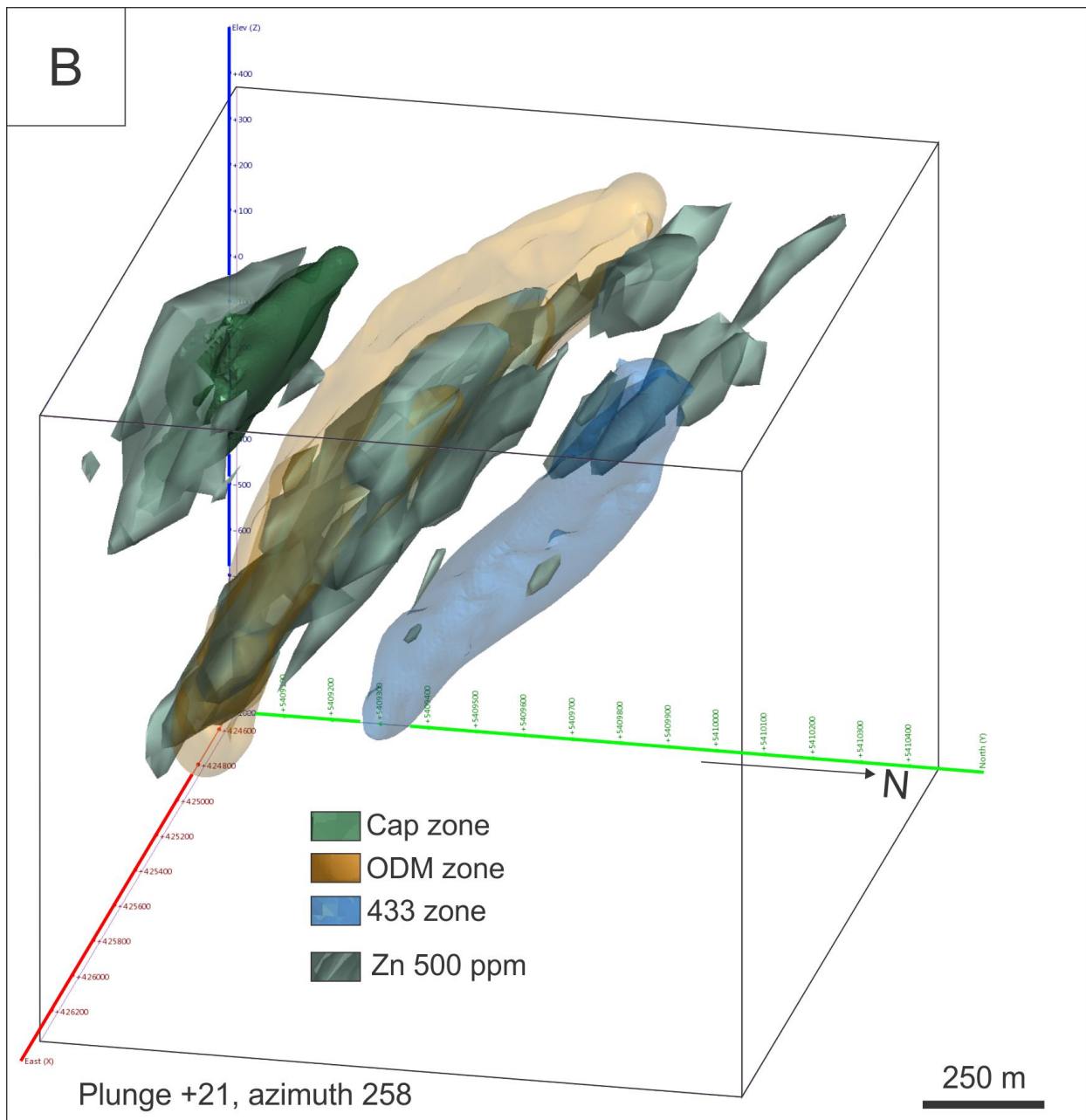


Figure 6.25 : A. Grade modelling of zinc (≥ 500 ppm) using Leapfrog[®] Mining. Zinc shells are shown in laurel green and are superimposed on mineralized Cap, ODM and 433 zones. B. Same as in A, with a different azimuth and plunge view.

6.3.3.9 Summary of Leapfrog[®] Mining implicit modelling on metal zonation

Most metals are characterized by a well-defined and distinct distribution, indicating significant zonation at zone and deposit scale. The modelled grade shells clearly indicate that there are two main gold-associated metal assemblages at Rainy River (Au-Ag-As \pm Zn-Pb-Sb and Au-Cu \pm Bi), in agreement with the associations present down hole (Fig. 6.16).

Spatially, these distinct associations define specific “domains”. The structurally uppermost domain includes the Cap, ODM and upper half of the HS zone and is characterized by Au-Ag-As±Zn-Pb-Sb association. In addition to that, the Cap zone displays an exclusive Au-Cu association (Fig. 6.22) and the ODM zone is characterized by a very good correlation with lead values above 25 ppm (Fig. 6.24). The second Au domain consists in the (approximate) lower half of the HS zone and the 433 zone. There, Au is associated with Cu±Bi (Figs. 6.21 and 6.22) with sparse zones of Ag and Zn in the HS zone (Figs. 6.19 and 6.25 respectively). Metals and metalloids that display the best fit with the Cap, ODM, HS and 433 zones are: lead with the ODM zone, copper with the 433 zone, arsenic with the Cap and ODM zones, and silver with the ODM, HS and Cap zones. Other metals (bismuth, zinc) have distributions that are discontinuous within the Au zones (Bi) or too widespread (Zn). Several pairs of metals and/or metalloids show an almost mutually exclusive distribution, for example arsenic and copper (Fig. 6.26), lead and copper (Fig. 6.27), zinc and copper (Fig. 6.28) and, to a certain extent, silver and copper (Fig. 6.29).

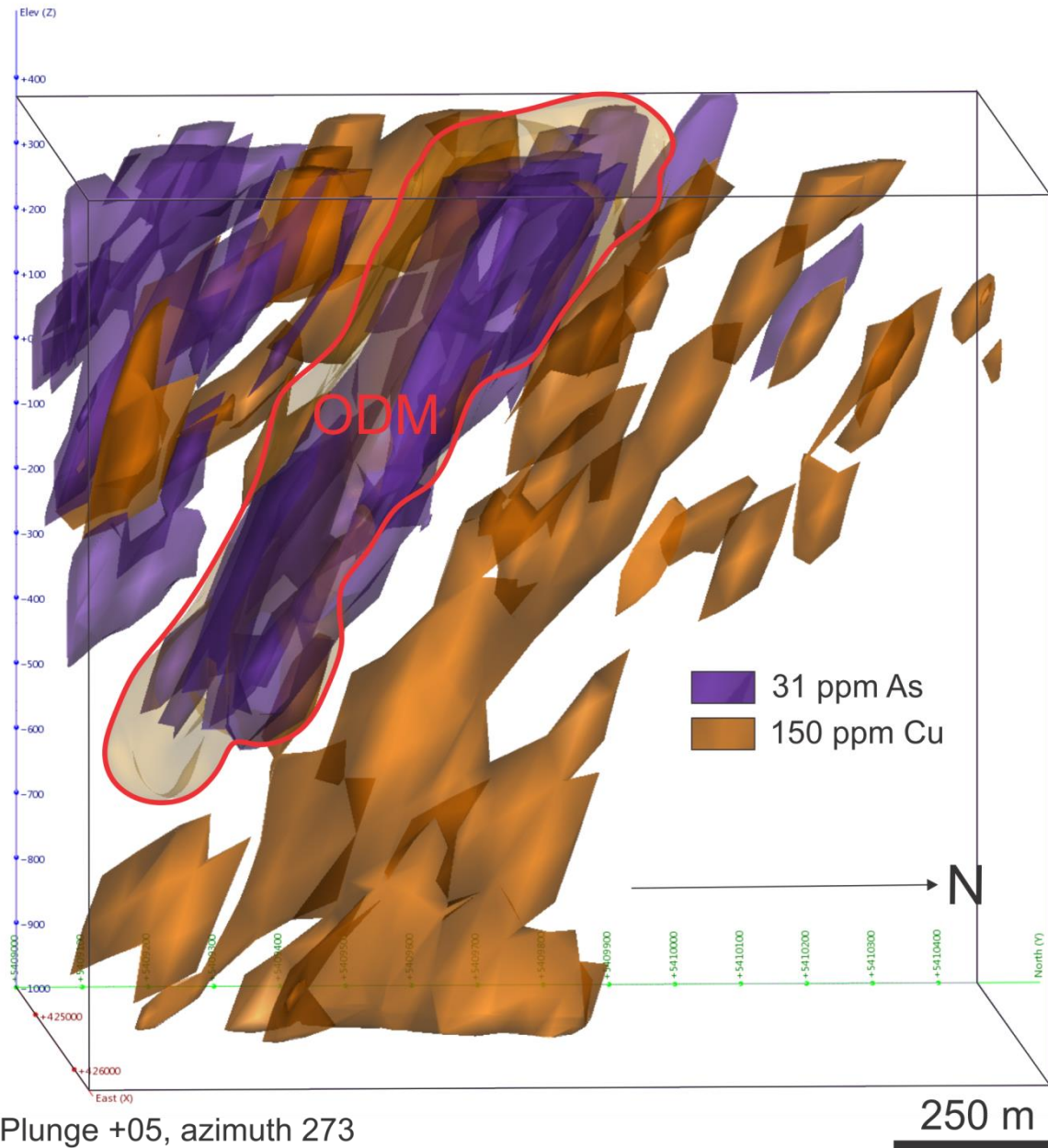


Figure 6.26 : Superimposed arsenic (≥ 31 ppm) and copper (≥ 150 ppm) grade shells constrained within proposed pit and underground mining area. Shells obtained through implicit modelling using the Leapfrog[®] Mining software. ODM mineralized zone is outlined in red.

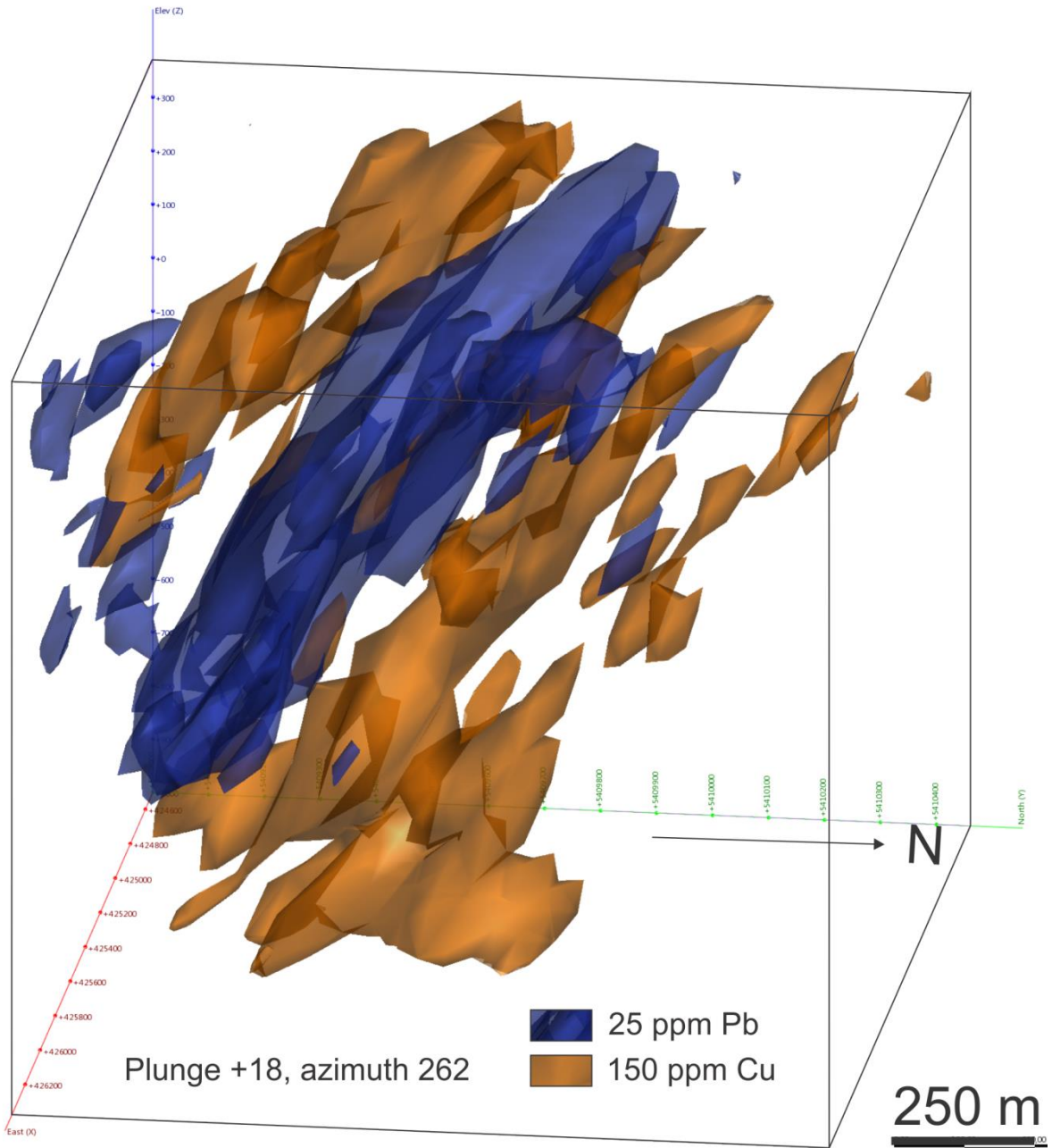


Figure 6.27 : Superimposed lead (≥ 25 ppm) and copper (≥ 150 ppm threshold) grade shells constrained within proposed pit and underground mining area. Shells obtained through implicit modelling using the Leapfrog[®] Mining software.

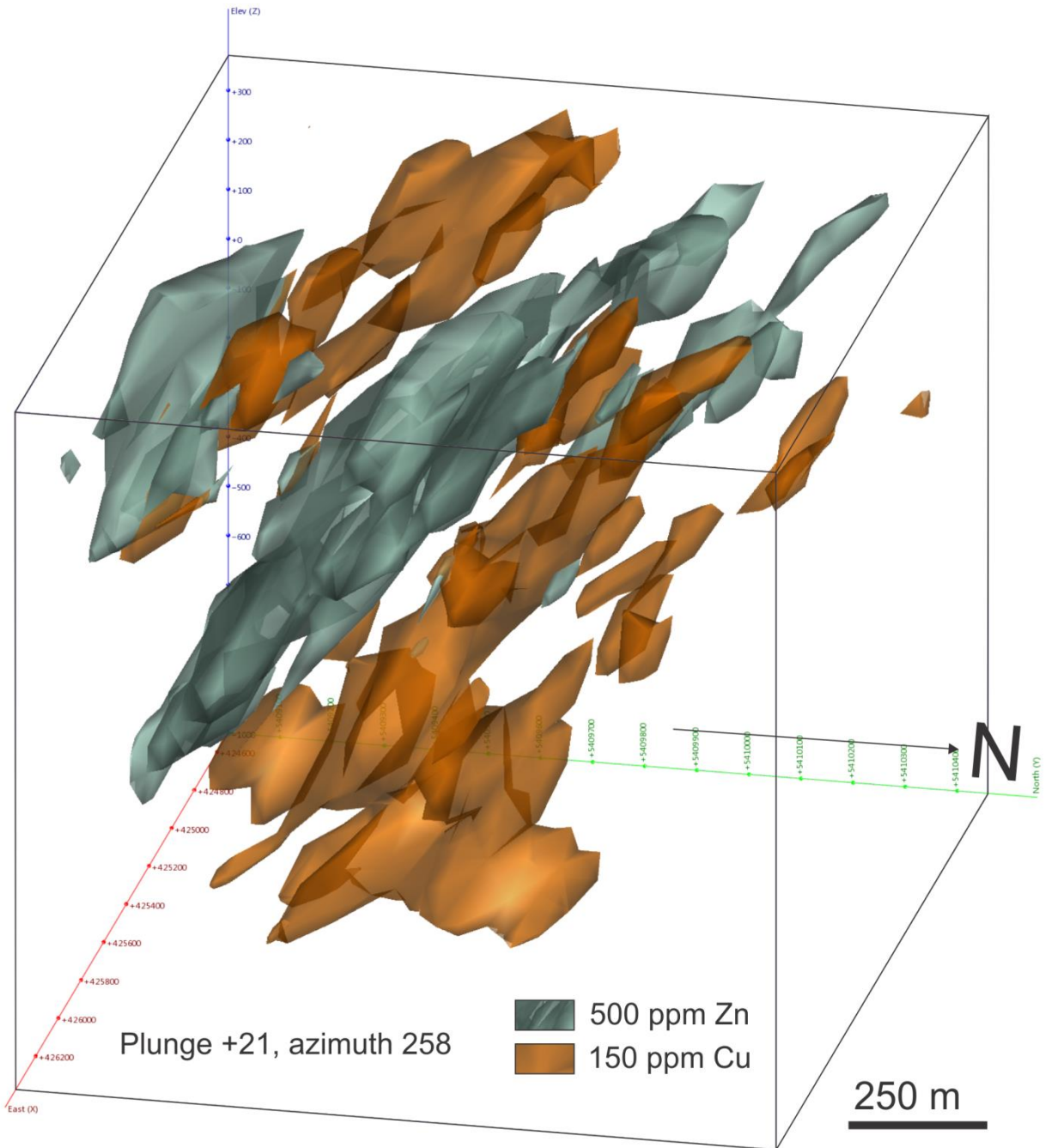


Figure 6.28 : Superimposed zinc (≥ 500 ppm) and copper (≥ 150 ppm) grade shells constrained within proposed pit and underground mining area. Shells obtained through implicit modelling using the Leapfrog[®] Mining software.

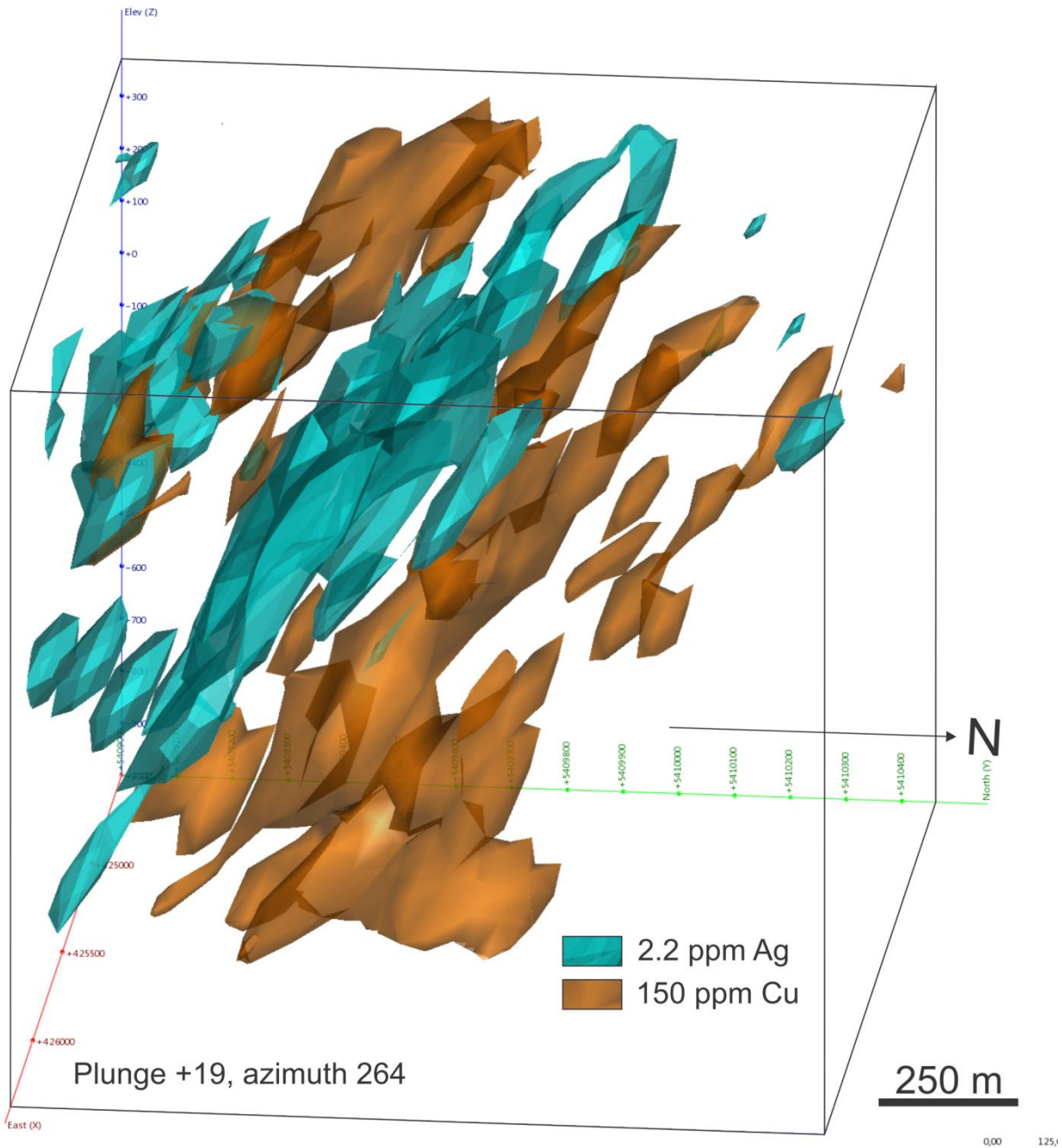


Figure 6.29 : Superimposed silver (≥ 2.2 ppm) and copper (≥ 150 ppm) grade shells constrained within proposed pit and underground mining area. Shells obtained through implicit modelling using the Leapfrog[®] Mining software.

The overall distribution and zonation of metals with respect to the different mineralized zones at Rainy River is summarized in figure 6.30.

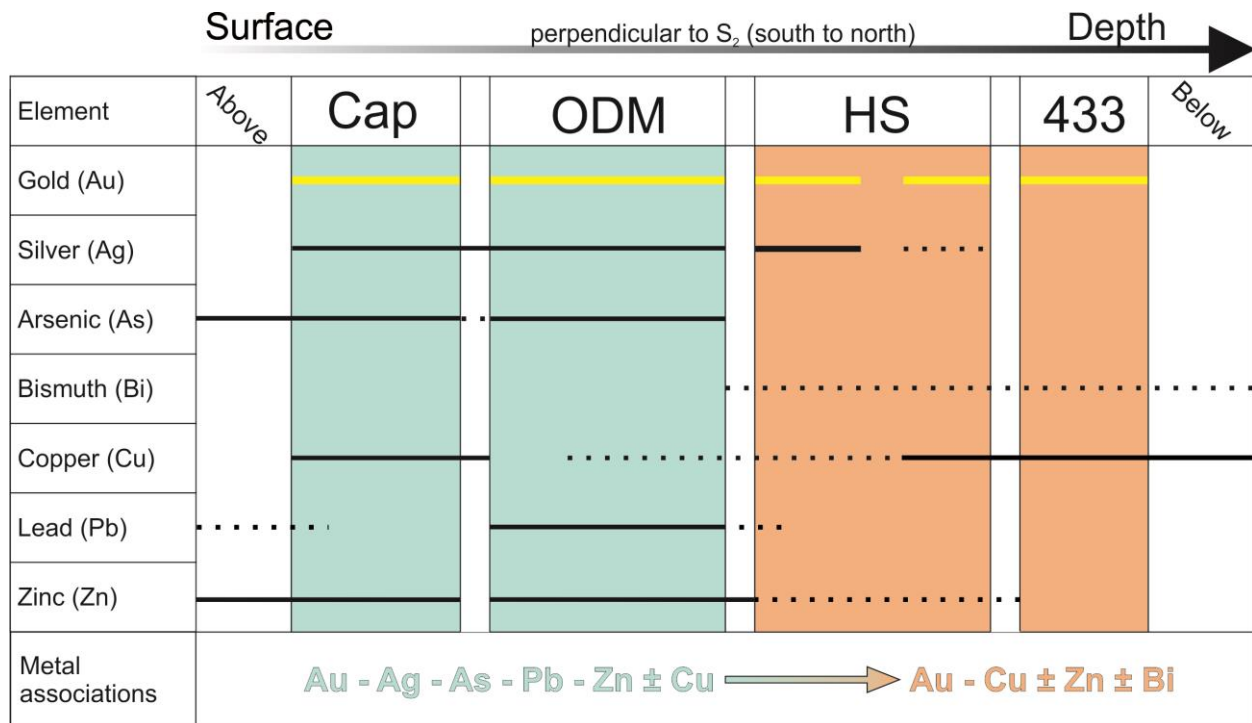


Figure 6.30 : Graphic summary of the distribution of base and precious metals with respect to the different mineralized zones using the assay database provided by New Gold Inc. Note: this illustration does not take variations down dip within a single mineralized zone into consideration. Dotted line corresponds to minor abundance, full line to a major sulphide phase.

6.4 Summary

6.4.1 Summary of the main sulphide phases and accessory phases

Gold and silver, which are the two metals to be recovered at Rainy River according to current development plans, are generally “invisible” to the naked eye, except for local concentrations of electrum (e.g. Fig. 6.4B) that are associated with exceptional grades. Anomalous gold and silver are typically associated with small amounts of sulphides (disseminated or as veinlets) as minute electrum inclusions in pyrite or in pyrite fractures along with other ductile sulphides. Geochemically, both precious metals correlate with a variety of base metals and metalloids. The main sulphide phases in the mineralized zones are pyrite, sphalerite of dominantly low iron content, chalcopyrite and rare galena. Most of the gold within the deposit is found within the ODM zone as part of a dominant pyritic sulphide assemblage located in an area characterized by anomalous to high zinc and lead values. Laser-ablation ICP-MS element mapping of a pyrite grain from the ODM zone showed that gold is distributed almost exclusively within the pyrite grain’s core (early phase?), whereas recrystallized coronas are almost devoid of gold. All

sulphide phases have undergone strong deformation, ductile and brittle, leaving granoblastic textures in disseminated pyrite grains and causing intense folding and transposition of pyrite veinlets and veins within the S_2 plane. As for sphalerite, chalcopyrite and galena, they have been remobilized during deformation due to their ductility although, since metal associations are preserved at the deposit scale, the remobilization is thought to have been minor.

Silver tellurides are one of the most common accessory phases documented within the deposit. They are present in the mafic tholeiitic rocks of the Cap zone as well as in the ODM and HS zones. Nickel telluride melonite is also documented in Ni-rich mafic tholeiitic volcanic rocks of the Cap zone. Tin-bearing sulphide phases are documented in the HS and Cap zones, along with appreciable silver concentrations within the former. Native bismuth is documented in the 433 zone. Electrum is found in dacitic tuffs and tuff breccias of the Cap, ODM and HS zones, at grain boundaries with pyrite and arsenopyrite. Electrum with the highest gold content is associated with the ODM zone.

6.4.2 Zonation in base and precious metals and implications for conditions of gold transport and deposition

Statistical analysis combined with grade modelling using the company's assay database revealed two main base and precious metals associations: Au-Ag-As-Pb-Zn \pm Cu and Au-Cu \pm Bi \pm Zn (Fig. 6.30). The Au-Ag-As-Pb-Zn \pm Cu assemblage extends from the Cap zone to the structurally upper half of the HS zone, with the distribution of lead closely delineating the ODM zone. This is followed deeper in the structural footwall by the zone of Au-Cu \pm Bi \pm Zn association that extends from the northern part of the HS zone through the bottom of the 433 zone. The Cu-rich modelled body extends at depth well below the 433 zone, but no gold and silver are associated with it.

Two notable areas within the deposit deviate from the two metal assemblages exposed above. The first one being a zone of Cu-Au association in the bottom (down dip) half of the Cap zone. The second zone consists in a transitional zone with no clear Au-base metal association located between the 433 and ODM zones, an area corresponding to the numerous HS zone mineralized bodies.

6.4.3 Paragenetic sequence

In terms of paragenetic sequence, pyrrhotite along with pyrite appear to be the earliest sulphide phases, which is supported by their pitted texture along with their presence as garnet inclusions not related to fractures (pre peak D₂-metamorphism). Pyrite has at least an early, Au-bearing crystallization event followed by recrystallization during regional metamorphism, as underlined by LA-ICP-MS element mapping of a pyrite grain from the ODM zone (Figs. 6.6, 6.7).

Precipitation of sphalerite, chalcopyrite and galena is probably synchronous to the precipitation of auriferous pyrite, since a classical zonation from high-temperature to low temperature metals (Ohmoto, 1996) is observed at the deposit scale. However, sphalerite, chalcopyrite and galena phases now observed show clear signs of remobilization associated with the main D₂ deformation event, suggesting an initial hydrothermal event responsible for the presence of these base metals within the deposit, followed by later structural deformation and limited remobilization. As for electrum, according to Huston *et al.* (1992), gold from hydrothermal-related auriferous pyrite is easily mobilized during structural deformation. Through pressure-solution mechanism, gold is liberated from the pyrite and migrates to cracks and grain boundaries. It then combines with silver, which is also released through pressure-solution, to form electrum that precipitates in grain fractures and boundaries. Electrum documented at Rainy River is present at grain boundaries and in fractures. In light of this, electrum would appear to have formed syn-D₂ and results from a local remobilization of Au rather than a second influx of Au within the system.

7 SUMMARY, DISCUSSION AND CONCLUSION

The documentation and characterization of volcanic products, hydrothermal alteration and deformation with respect to the auriferous mineralized zones at Rainy River presented in this study was done to identify the different controls on gold distribution at deposit scale. The data acquired in this project is briefly summarized here and subsequently discussed. A probable geological environment of formation of the deposit, mechanisms of transport and deposition of gold and a sequence of events responsible for the present geometry of the deposit are proposed.

7.1 Summary

The Rainy River gold deposit is located within the western part of the Neoproterozoic Wabigoon Subprovince, as part of the "Rainy River greenstone belt". The belt is dominated by pillowed to massive tholeiitic basalts, with felsic volcanics occurring as discontinuous tracts along the belt. Volcanic rocks are cross-cut by later stocks of zoned monzonitic to granodioritic compositions, with occasional porphyritic texture (Blackburn, 1976). Over 90% of the Rainy River deposit gold zones are hosted in calc-alkaline, coherent or volcanoclastic dacites (which also includes some rhyodacites and rhyolites). The remainder is hosted in tholeiitic basalts. The dacitic package forms an ESE-WNW oriented linear body, bounded to the north, west and south by tholeiitic basalts intercalated with minor mafic-dominated, fine-grained sedimentary rocks. Mineralization is present in both coherent and volcanoclastic dacites, but higher grade mineralization is predominantly hosted in the dacitic tuffs and tuff breccias. Preserved flow banding textures and abundant feldspar and quartz microphenocrysts and phenocrysts are present in coherent dacites, whether of extrusive lava flow or subvolcanic intrusive nature (sills, cryptodomes, etc.). An overall strong sericitization combined with pervasive foliation overprint introduced false volcanoclastic textures and/or destroyed primary features, locally generating muscovite schists. Multi-element, chondrite-normalized patterns of the calc-alkaline dacites show a strong coupled Nb-Ta negative anomaly and Th and LREE enrichment (with respect to HREE). All dacitic samples within the deposit have similar REE concentrations, plotting in a tight area on spider plots. Multi-element, chondrite-normalized patterns for tholeiitic basalts are slightly LREE enriched, mostly flat in HREE and display normalized concentrations 7 to 15 times the composition of the primitive mantle or zero to three times the idealized N-MORB composition of

Sun and McDonough (1989). Dacites that host the Rainy River deposit were dated at ca. 2717 Ma using U/Pb by ID-TIMS on zircon (V. McNicoll, unpublished data), in agreement with unpublished ages obtained by the company. A quartz monzonitic dyke has also been dated using the same technique. The dyke cross-cuts mineralized rocks and the associated alteration in the 433 zone, is unaltered but affected by the S_2 foliation, and is dated at ca. 2693 Ma (V. McNicoll, unpublished data), which constrains the age of the deposit between ca. 2717 and ca. 2693 Ma.

Deformation in the deposit area is dominated by strong N-S to NE-SW oriented shortening attributed to the Central Superior Orogeny (Melnik *et al.*, 2006). In the Western Wabigoon Subprovince, it is characterized by D_1 upright folding followed by D_2 isoclinal folding and associated S_2 foliation. The S_2 foliation, oriented 102N/61° on average at Rainy River, is the dominant structure into which lithological contacts as well as mineralized zones have been reoriented, flattened and/or transposed. This foliation is characterized by aligned phyllosilicates as well as flattening of quartz phenocrysts and lapilli. A weak C-S fabric is present on thin section from mica-rich samples. A stretching lineation (L_2) oriented 225°/55° on average plunges to the west on the S_2 plane. The high grade ore shoots within the mineralized bodies are transposed along the L_2 stretching lineation. The L_2 stretching lineation and kinematic indicators perpendicular to the S_2 plane indicate a south over north reverse component of motion, potentially associated with interpreted north-east directed thrusts resulting from the NE-SW shortening event (Poulsen, 2005). The terrane-bounding, dextral transpressive Quetico Fault runs to the south of the deposit, as highlighted on aeromagnetics maps. According to structural interpretation from geophysical data made by SRK (Figs. 4.3, 4.4; Siddorn, 2008), Rainy River sits immediately to the north of a second order structure or splay of the Quetico Fault. Structural interpretation based on aeromagnetic data from Poulsen (2005) interprets these S_2 -parallel discontinuities as part of a deformation corridor into which the Rainy River deposit is located. A high strain zone located in the footwall of the ODM zone is characterized by intense sericitization, steepening of S_2 and sub-horizontal kinking of S_2 . There is a poor correlation between mineralization and S_2 intensity, although higher grade ore shoots within the mineralized bodies are collinear and most probably controlled by L_2 . Brittle to brittle-ductile structures oriented 195N/75° on average crosscut the S_2 fabric and offset the mineralized zones at the metre scale, without generating any remobilization of the sulphides.

Metamorphic minerals documented in the immediate deposit area indicate a transitional environment between upper greenschist and amphibolite facies. Post-D₂ retrograde greenschist metamorphism is also recorded in the deposit.

Several minerals associated with hydrothermal alteration and subsequent metamorphism are present at the Rainy River deposit. Their composition as well as their relationship to mineralized zones and host rocks have been characterized. The dominant metamorphosed mineral associated with the gold zones is muscovite, with a distinct Mg-enriched composition in mineralized samples. It is pervasive and affected by D₂, occurring as disseminations, veinlets (<1 cm) and veins (<10 cm) in coherent as well as in volcanoclastic dacite. Intense sericitization of the host dacite combined with overprinting D₂ deformation have generated muscovite schists located structurally below the ODM zone as part of a high strain zone. Chlorite is the second most abundant alteration mineral in the study area and a higher Mg content in chlorite is also correlated with auriferous zones. Chlorite is fine grained and occurs as disseminations, folded veinlets transposed into S₂, and rimming disseminated pyrite grains. Chlorite is ubiquitous, although higher concentrations (≤15 vol. %) are restricted to mafic rocks. Secondary metamorphosed alteration minerals consist, in order of abundance, in ankerite to ferroan dolomite, calcite, epidote, biotite (almost completely retrograded to chlorite), spessartine garnet, kyanite, chloritoid, and rutile. Their distribution in space shows a zonation from epidote and biotite in least-altered parts of the deposit (ODM hanging wall) transitioning to muscovite-chlorite-carbonate assemblages within the ODM zone. Locally, S₂-parallel, ≤8 m-thick lenses of aluminosilicates (kyanite and chloritoid) and quartz are developed in the ODM zone. Spessartine garnets are restricted to the lower part of the ODM zone and the HS zone. Rutile dusting is present in the tholeiitic rocks of the 433 zone at depth. Changes in the alteration mineralogy and nature of mineralization occur along strike of the ODM body. To the west of the ODM zone is an increase in carbonate saturation, underlined by a higher density of S₂-transposed auriferous quartz-carbonate-pyrite±electrum veins.

Chronological development of alteration at Rainy River consists in early epidotization and albitization overprinted by sericitization (muscovite, through albite destruction) and combined Fe±Mn-carbonate and chlorite alteration (chlorite is favoured over epidote when CO₂ is present: Poulsen, pers. commun., 2015). Formation of spessartine garnets and kyanite and chloritoid are syn-prograde metamorphism. Muscovite generation through albite destruction dominates in the ODM zone, the intensity of which correlates with the gold concentration. Mass balance calculations as well as molar ratio diagrams underline a strong correlation between combined

potassium addition (≥ 1.5 wt.% K_2O ; associated with muscovite generation) and sodium depletion with the high grade part of the ODM zone. Zones of CO_2 , CaO and SiO_2 addition also show complementary zonation with respect to the zone of K_2O addition. Mass variation calculations also reveal a higher average mass variation value for volcanoclastic versus coherent dacite. All mineralized zones are characterized by isotopically heavy $\delta^{18}O$ values (whole-rock analyses) above 12.8‰, and values above 13.3‰ outline the ODM zone. These values are best correlated with the AAI index of Williams and Davidson (2004), hinting towards a common process responsible for both signatures. There is also lack of correlation between $\delta^{18}O$ values and silica addition, rejecting the hypothesis of silica dumping being responsible for such $\delta^{18}O$ values as invoked in other Archean deposits of the Superior (e.g. Kidd Creek, LaRonde Penna; Huston, 1999, Beaudoin *et al.*, 2014).

The deposit consists in a series of stacked lenses (perpendicular to S_2) that vary in strike length between <300 m to 1500 m. All lenses dip to the south, parallel to S_2 . From north to south, they are the 433, HS, ODM and Cap zones. The bulk of the Au (approximately 75%) is part of the ODM zone. The geometry of the higher grade zones is controlled by the L_2 lineation ($225^\circ/55^\circ$ on average) steeply plunging west within the S_2 plane. Gold occurs mainly as auriferous pyrite, $Au\pm Ag$ tellurides and minor electrum and native gold. It is associated with pyrite, which is granoblastic and occurs as disseminated or, on rare occasions, massive over <10 cm true width, and with pyrite-sphalerite \pm chalcopyrite \pm galena veinlets that are folded and transposed into S_2 . Segregation of the sulphide phases based on their ductility indicates local remobilization of the sulphide into S_2 during deformation. Microprobe analyses of sphalerite reveal low Fe (<1 mole % FeS) compositions, more particularly in the ODM zone, with an eastward gradient to higher mole % FeS values (≥ 8 mole % FeS) in the eastern parts of the deposit. Laser ablation ICP-MS trace element mapping of a pyrite grain from the ODM zone shows at least two pyrite crystallization events, with the majority of the contained gold located in the core of the pyrite grain and associated with Cu, Zn, As, Ag, In, Sn, Sb, and Pb. In contrast, the recrystallized pyrite rim is almost barren, suggesting an early gold-bearing hydrothermal event. Additional pyrite maps are however required to test reproducibility of results. Rare electrum and gold are present in S_2 -folded and transposed quartz-carbonate-pyrite \pm electrum veins as well as in late (post- D_2) brittle fractures. Three dimensional modelling of the metals distribution at the deposit scale shows two dominant metal associations: Au-Ag-As-Pb-Zn \pm Cu in the Cap, ODM and upper HS zones, transitioning to Au-Cu \pm Zn \pm Bi in the lower part of the HS and 433 zones.

7.2 Discussion

7.2.1 Timing of gold deposition and source of metals

Precious metal endowment at Rainy River can, in a similar way to known auriferous volcanogenic massive sulphide (VMS) systems, be hypothetically attributed to a primary (synvolcanic) source and/or to a secondary (e.g., syntectonic) mineralizing event (Mercier-Langevin *et al.*, 2015). As proposed in Wartman (2011) and shown in this study, a combination of elements suggest that at least part of the gold was introduced with the base metals as part of a pre-main deformation, and possibly synvolcanic hydrothermal system. These combined elements are: 1) a spatial correlation of gold with base metals at the deposit scale, 2) a close spatial association between gold and zoned hydrothermal alteration, 3) the stacking of auriferous bodies in a restrained volcanic pile, and 4) the preferential association of alteration and auriferous zones with volcanoclastic rocks (control on fluid circulation by primary permeability of the host rock). An early gold precipitation in the system is further supported by the presence of a gold-rich core and barren rim in pyrite (Figs. 6.6, 6.7). Hypothetically, peak hydrothermal activity and associated metal deposition occurred during a volcanic activity hiatus during which fine-grained, pyrite-rich sediments were deposited on top of the dacite volcanic rocks that host the ODM zone, and before the deposition of tholeiitic basalts in the uppermost part of the host succession. An early, pre-D₂ origin for the alteration and sulphide zones is further supported by the strong control of the combined S₂ and L₂ fabrics on the shape of the mineralized zones and lithological contacts. In VMS deposits, which represent the most common syngenetic Zn-Cu-Au-Ag deposit type during the Archean, the main source of metals can plausibly be the surrounding volcanic and/or sedimentary rocks, from which hydrothermal fluids scavenge metals and precipitate them in a massive sulphide body at or below seafloor (Franklin *et al.*, 2005 and references therein). At Rainy River, gold and silver are the dominant metals and the base metals (Cu-Pb-Zn) sulphides, although good indicators of the presence of gold, only represent <10 vol.% of the host rock. This contrasts with VMS systems that generally contain large amounts of base metals. However, there are exceptions, i.e. gold-rich VMS deposits that often contain modest amounts of base metals relative to gold (Mercier-Langevin *et al.*, 2015 and references therein). As with gold-rich VMS deposits, the difference in metal budget between Rainy River and typical VMS systems suggests a different source than the surrounding host rocks, for example a magmatic input, and/or efficient precipitation mechanisms for gold. In the scenario of a magmatic source of metals, specific petrogenetic processes related to specific

geodynamic environments can be inferred (e.g., Hannington *et al.*, 1999; Huston, 2000; Yang and Scott, 2003; Mercier-Langevin, 2005; Mercier-Langevin *et al.*, 2007b; 2011; 2015).

7.2.2 Potential geodynamic context and influence on gold endowment

Typically, preserved Archean VMS camps are associated with bimodal basalt-andesite and rhyolite magmatism (Franklin *et al.*, 2005), making the basalt-dacite (\pm rhyodacite-rhyolite) association found at Rainy River atypical. A series of tectonic discrimination diagrams (designed for Phanerozoic volcanic rocks) categorize the Rainy River volcanic rocks as being from a volcanic arc environment, with the tholeiitic basalts having more of a back-arc setting signature (section 3.6). Enrichment in LREE and Th in both the dacites and basalts also hints towards crustal contamination and/or contribution of a sedimentary component within the subduction zone. Tight clustering of REE profiles as well as Zr/TiO₂ ratios of dacite samples throughout the deposit indicate minimal crustal magmatic differentiation. In settings where a subvolcanic intrusion is the magma source, fractional crystallization generates a series of geochemically evolving volcanic products. The relative geochemical homogeneity of the Rainy River host dacites could be explained by crustal anatexis with limited AFC processes at the base of the Archean crust rather than resulting from fractional crystallization within a subvolcanic reservoir. Such processes have been documented to occur under the influence of magmatic volatiles (Litvinovsky and Podladchikov, 1993), which can supply a number of components and could have had implications on the gold endowment of the deposit.

According to Galley (1993), high level intrusive activity provides heat and potential magmatic components to generate a sustained fertile hydrothermal convection cell responsible for the formation of VMS deposits. A hypothetical scenario where the Rainy River deposit would have formed in an environment without the presence of a subvolcanic intrusion (*ie* by crustal anatexis) distinguishes it from typical VMS systems. It also implies a different heat source driving hydrothermal activity than high level intrusive activity. Although probable, this proposed volcanic environment for the Rainy River deposit remains highly speculative and would require further regional work to better constrain the stratigraphy and paleotectonic setting of the volcanic rocks found in the area.

7.2.3 Potential evolution of the volcanic environment and role in trapping/precipitation of metals

Wartman (2011) proposed a detailed volcanic evolution for the Rainy River deposit area. In his model, the dacites hosting the deposit are emplaced within basalts related to arc volcanism as shallow subvolcanic intrusions. This dacitic intrusive activity eventually reaches the surface, generating dacitic lobe-hyaloclastite flow(s). A subsequent quiescence in dacitic magmatism allows slumping and collapse (generating mass flows) of the surrounding arc basalts, which buries the dacite body.

Based on work from this study and the model proposed by Wartman (2011), we interpret a volcanic evolution of the Rainy River host volcanic succession where lower parts of the dacitic body would have been emplaced within the tholeiitic basalts as cryptodomes and associated breccias (Fig. 7.1A). Eventually, relatively viscous dacitic effusive activity forming domes and associated breccias would have reached the seafloor, forming a positive topography (Fig. 7.1B). The episode(s) of dacitic volcanism are interpreted as voluminous (high eruption rate?), since all REE profiles of dacite samples show a tight clustering, indicating minimal evolution of the source (magma chamber of significant size?). Although, alternatively, dacitic magmas produced from anatexis at the base of the Archean crust can produce geochemically homogeneous, relatively undifferentiated suites at any eruption rates. Following the subaqueous emplacement of the extensive dacitic body, a volcanic hiatus is underlined by the deposition of pyrite-rich, mafic-volcanic dominated siltstones of present ≤ 8 metre true thickness. A subaqueous depositional environment is proposed since minor siltstones strata conformably sit stratigraphically above and below the dacitic body hosting the deposit. In addition, peperitic contacts are developed in dacite from the deposit vicinity. A subaqueous environment is also in agreement with the pillowed nature of the mafic volcanic rocks documented on the property.

The volcanic hiatus may have allowed for the development and optimal circulation of metal-bearing hydrothermal fluids within the volcanic pile (Fig. 7.1C). Hydrothermal circulation (fluid pathways) was controlled by the primary porosity of the volcanic rocks, therefore metal-bearing fluids would have been channelled within the more porous volcanoclastic rocks, forming what are now the ODM, HS and 433 zones. This is supported by the distribution of high grade gold zones with respect to volcanic facies as well as higher mass variations of volcanoclastic dacites versus coherent dacite samples (Fig. 5.47). Synvolcanic faults could have been present and acted as fluid conduits, although the strong S_2 fabric most likely blurred these pathways. It can be hypothesized that zones of muscovite schists below the ODM zone are remnants of broad

zones of muscovite alteration and indicate the location of preferential hydrothermal fluid circulation.

In a scenario where boiling would have occurred, hydraulic conductivities at grain boundaries in porous volcanoclastics and within fracture systems in coherent volcanic rocks would have been lower pressure zones where boiling could have occurred. The porosity of volcanoclastics and fractures in coherent dacites would also have provided necessary void space to accommodate volume increase intrinsic to boiling. In its turn, boiling can generate hydro-fracturing, which further increases porosity and optimizes metal precipitation processes. The extensive dacitic lava flows with high phenocryst content of the ODM hanging wall could have been favourable to the precipitation of Au below, where the thick and dense lava flow would have acted as an impermeable barrier focusing metal deposition.

Mineralization at Rainy River is distributed in several mineralized zones hosted in dacite of various volcanic facies and stacked perpendicular to S_2 . Metal associations between these mineralized zones display strong metal zonation (see Chapter 6) perpendicular to the stacking, and the deposit is centered on a hydrothermal alteration system also showing clear mineralogical and mass variation zonation (Fig. 7.2A). For these reasons, stacking of ore zones is interpreted as resulting from a short-lived system, precipitating sulphide phases and alteration minerals with respect to the temperature gradient resulting from a single main event.

Subsequent resuming of back arc tholeiitic volcanism would have further insulated the dacitic volcanic pile and part of the mineralization within the system would be deposited within the basalts now part of the Cap zone (Fig. 7.1C). The fertile hydrothermal system would eventually wane and structural deformation would start, although it is uncertain if whether or not the two overlap in time.

7.2.4 Potential nature of fluids and discussion on gold transport and metal zonation

Globally, the Rainy River deposit is characterized by metal associations and a zonation of precious and base metals that resemble the Cu-Au versus Zn-Au classification of Huston and Large (1989) and Hannington *et al.* (1999) for Au-rich volcanogenic massive sulphide systems. In both contributions, the two metallic associations are interpreted as being the result of gold transport using potentially different ligands and operating at different temperatures in a seafloor environment. In the Zn-Au association, gold is transported as a bisulphide complex ($Au(HS)_2^-$),

at temperatures between 100 and 200°C. Gold tends to be concentrated in Zn-rich polymetallic sulphides along with other elements such as Ag, As, Sb, Hg, and Pb (Hannington *et al.*, 1999). According to Huston and Large (1989), zones of Cu-Au association are of higher temperature (200-300°C) and gold is transported as a chloride complex (AuCl_2^-) at high Ag/Au ratios in the fluid. Transport of gold as AuCl_2^- is favoured by acidic and oxidized fluids and/or by the presence of high-salinity brines (Huston and Large, 1989). Conversely, Hannington and Scott (1989) and Hannington *et al.* (1999) suggest that $\text{Au}(\text{HS})_2^-$ can be an important gold transporting agent at temperatures of up to 350°C, making the bisulphide complex the only gold transporting agent for both the Cu-Au and Zn-Au zones. In this scenario, gold is transported in a fairly oxidized fluid and undergoes combined precipitation with Cu at depth due to further oxidation of the gold-bearing fluid resulting from an interaction with seawater (Hannington and Scott, 1989; Huston, 2000). Since the Rainy River deposit is set in Neoproterozoic rocks, the premise stating oxidizing conditions of seawater is probably invalid; therefore making it unlikely that copper precipitation at depth was due to seawater interaction.

Although specific information about the nature of the mineralizing fluids would be necessary to get a precise idea of the transport and precipitation mechanisms for gold at Rainy River, it remains interesting to discuss in general terms some possible mechanisms for gold enrichment at Rainy River, taking into consideration the literature cited above. According to these works, gold from the Cu-Au association (in the lower HS and 433 zones) would have been transported as chloride or bisulphide complexes in the deeper parts of the system in a high temperature, low pH, oxidized fluid (Huston and Large, 1989; Huston, 2000) and would have precipitated mainly due to a decrease in temperature, coupled with a pH increase as fluids move upwards to cooler parts of the system (Fig. 7.2B; Huston and Large, 1989). The Zn-Au association, which is characteristic of the Cap, ODM and upper HS zones, would plausibly result from gold transport as $\text{Au}(\text{HS})_2^-$ complexes and precipitation due to cooling (below 150°C; Hannington and Scott, 1989) and/or as a result of oxidation by mixing with seawater (Fig. 7.2B; Huston and Large, 1989; Hannington and Scott, 1989). Once again, it is unlikely that oxidation from seawater played a major role in precipitating gold at Rainy River, as Archean seawater was reduced. Also, efficient fluid mixing may be less likely in a subsea-floor environment. For that reason, cooling is perhaps the most probable mechanism responsible for gold precipitation in the Zn-Au association zone.

Hannington and Scott (1989) establish a relationship between high gold solubilities (as bisulphide complexes), high sulphur activity ($a\text{S}_2$) and low iron sphalerite compositions.

Sphalerite grains analysed from the Rainy River deposit are consistently low in iron (less than 5 mole % FeS), especially in the Cap, western ODM and HS zones, suggesting an environment of optimal chemical conditions for high $\text{Au}(\text{HS})_2^-$ solubility. In light of this, it can be speculated that most of the gold present at Rainy River, which spatially correlates with Zn, was transported and precipitated within a pre-deformation hydrothermal system characterized by low temperature and high sulphur activity, where gold was transported as a bisulphide complex and precipitated in response to a decrease in temperature caused by cooling of fluids as they moved upwards within the system. At Rainy River, it can be hypothesized that boiling occurred locally, since sea water may have been sufficiently shallow near the top of the dacite dome complex to allow boiling of ascending fluids, resulting in much of the sulphides being deposited as stockwork mineralization beneath the sea floor. Boiling would have happened by degassing of ascending fluids in a shallow environment (Hannington et al., 1999). With the present data, it is not possible to determine if boiling occurred or not within the Rainy River deposit, although it is a possibility.

7.2.5 Deformation of the Rainy River deposit and impact on mineralization

As discussed above, the presence of auriferous zones at Rainy River is attributed, at least in part, to a pre-main deformation fertile subaqueous hydrothermal system. However, the current geometry of the mineralized zones is largely controlled by the main S_2 foliation and associated L_2 stretching lineation (Fig. 7.3A, B; Pelletier *et al.*, 2015; this study). Evidences for sulphide crystallization under stress are present at various scales, including remobilization of ductile sulphides in low strain sites. This small-scale remobilization occurs throughout the deposit, although the large-scale stacking of the different mineralized bodies and deposit-scale metal zoning within the volcanic pile are largely preserved.

In what is now the western ODM zone, the presence of auriferous quartz-carbonate-pyrite±electrum veins folded and transposed along S_2 suggests a pre- to early D_2 , deformation-related gold input, although the amount of gold brought or remobilized by the pre- to early D_2 event is unquantifiable with our present knowledge. Associated carbonate alteration is present in the western ODM zone and outlined by dacite samples with a high carbonate saturation index (>0.8). These deformed quartz-carbonate-pyrite±electrum veins represent the highest gold grades of the deposit, contain most of the visible electrum and native gold and are, to some extent, similar to Archean orogenic gold systems, which contrasts with the disseminated nature of the bulk of the mineralization. This carbonatisation is superimposed on an earlier carbonate

alteration recorded throughout the deposit, which is pre-deformation, of lower saturation values (between >0 and 0.7) and of ankerite to ferroan dolomite composition. In the ODM zone, the early carbonate alteration is characterized by a manganese-rich composition and is associated with higher grade mineralization.

Within the mafic rocks of the Cap zone, ≤ 0.5 m-thick auriferous extension quartz-ankerite-pyrite veins are developed locally in probable response to the elongation recorded by L_2 (Poulsen, 2006). These veins are either remobilizing gold already present within the system, or represent an external source tapped through deformation and associated metamorphism. Iron-carbonate alteration associated with these veins is restricted to the veins themselves, since the host rocks have similar carbonate saturation values as the rest of the deposit. Even if it is currently impossible to estimate the relative contributions of synvolcanic gold versus potentially syntectonic gold in the system, it must be highlighted that the pre- to early- D_2 auriferous quartz-carbonate-pyrite±electrum veins of the western ODM zone and the D_2 quartz-ankerite-pyrite veins of the Cap zone represent a minor amount of the total gold resources of the deposit, reinforcing the interpretation that a significant part of the contained gold in the deposit is pre-main deformation, and plausibly synvolcanic.

7.2.6 Potential analogues and comparison with other known synvolcanic gold deposits of the Superior Province and other localities

Other synvolcanic gold systems have been identified and thoroughly documented in the Superior Province, including those of the Doyon-Bousquet-LaRonde camp in the Blake River Group of the Abitibi greenstone belt. The synvolcanic timing for at least part of the gold has been demonstrated for the Bousquet, Bousquet 2-Dumagami, LaRonde Penna and Westwood deposits (Tourigny *et al.*, 1989; Tourigny *et al.*, 1993; Teasdale *et al.*, 1996; Dubé *et al.*, 2007; 2014; Mercier-Langevin *et al.*, 2007a; Yergeau *et al.*, 2015). Similar to the Rainy River deposit, the deposits of the Doyon-Bousquet-LaRonde mining camp are predominantly hosted in felsic calc-alkaline volcanic rocks. These deposits are also located in proximity to a major fault zone (Larder Lake-Cadillac fault zone). Additionally, spessartine garnets, kyanite and/or manganese-rich carbonates are associated with the mineralized zones at LaRonde Penna, Bousquet, Bousquet 2-Dumagami and Westwood, underlining potential similarities with the Rainy River deposit in terms of hydrothermal alteration conditions and nature of fluids. However, the Rainy River deposit differs from these syngenetic gold deposits by the style of its sulphide mineralization, which is disseminated and stockwork-dominated rather than massive. Within the

Doyon-Bousquet-LaRonde camp, the closest analogues to the Rainy River deposit would be the North Corridor ore zone of the Westwood deposit and the Bousquet deposit. In the North Corridor ore zone, gold mineralization consists in massive to semi-massive sulphide veins and disseminated sulphides, with major sulphide phases of pyrite-sphalerite-chalcopyrite (Yergeau *et al.*, 2015), which is also the case at Rainy River. An alteration dominated by sericite-quartz-pyrite along with higher grade mineralization associated with high permeability rocks (Yergeau *et al.*, 2015) adds to the similarities with the Rainy River deposit. The Bousquet deposit possesses disseminated auriferous sulphide and vein-type mineralization (Tourigny *et al.*, 1989) similar to Rainy River. Also, the presence of aluminosilicates at Bousquet is related to advanced argillic alteration linked to Au mineralization, which is similar to Rainy River, although less acidic, advanced argillic alteration conditions are interpreted to be the case here.

Closer to the Rainy River deposit, the Headway-Coulee prospect located east of the Rainy River area in the Wabigoon Subprovince, with its gold mineralization associated with sericite alteration (Osterberg *et al.*, 1987), is a potential analogue to Rainy River, although further investigation is necessary to compare their volcanic environment and the hydrothermal systems at Headway-Coulee.

Stepping out of the Superior Province, the Henty deposit hosted in the Cambrian Mount Read Volcanics of Tasmania (Australia) is a potential analogue to the Rainy River deposit. Similarities between the two deposits include a high gold to base metal ratio, low sulphide contents, a relatively shallow water environment (documented at Henty and proposed for Rainy River), and a correlation between volcanoclastic facies and mineralization (Halley and Roberts, 1997; Large *et al.*, 2001b).

7.3 Conclusion and implications for exploration

Study of the volcanology, hydrothermal alteration, deformation, metamorphism and metal endowment of the Rainy River deposit allowed the identification of key geological parameters that define this deposit. Building on previous work, it has been determined that the volcanic regime and products along with the nature of alteration minerals, ruled by specific hydrothermal conditions, control the presence of gold mineralization, hence the need to recognize these characteristics in a context of mineral exploration for similar deposits. When compared to pre-existing ore deposit models, the Rainy River deposit does not possess diagnostic features of high or low sulphidation epithermal deposits, such as clear evidence of a subaerial setting,

boiling, and mineralized veins with crustiform-colloform textures (Simmons *et al.*, 2005). The Rainy River deposit also differs from VMS deposits *sensu stricto* since mineralization does not occur as massive sulphide lenses and a typical conformable and semi-conformable VMS alteration zonation is absent. Hypothetically, the Rainy River deposit could represent a failed VMS system, where the formation of massive sulphide lenses was initiated but subsequently inhibited by a fluid temperature too low to transport base metals and/or due to the impossibility of fluids to reach the seafloor. Alternatively, the Rainy River deposit could represent a hybrid system between epithermal and VMS deposits, set in shallow water environment where metal precipitation, through cooling and/or boiling, forms at specific pressure-temperature conditions governed by both the interaction with seawater and pressure-temperature gradient. These scenarios remain hypothetical, since subsequent deformation and metamorphism partially destroyed primary features, but also because such deposit models might not apply in an Archean context.

Although the Rainy River deposit is characterized by stockwork and disseminated-style mineralization compatible with large-tonnage low-grade mining extraction method, it differs greatly in geological setting and mineralization style from other large tonnage gold systems of the Superior Province (e.g., Côté Gold, Hammond Reef and the Canadian Malartic Mine: Katz *et al.*, 2014; Backeberg, 2015; De Souza *et al.*, 2015). Thus, exploration for "Rainy River style" deposits would have to target similar deposit sizes, although with very different geological characteristics.

Similarly to exploration models for Archean gold-rich VMS systems (Hannington *et al.*, 1999; Dubé *et al.*, 2007; Mercier-Langevin *et al.*, 2011, 2015), exploration for "Rainy River style" deposits target areas of calc-alkaline intermediate to felsic volcanic rocks forming domes, lava flows and/or flow breccias. The FI (calc-alkaline) signature of the host dacite indicates a specific tectonic context and/or petrogenetic mechanisms (Leshner *et al.*, 1986; Hart *et al.*, 2004), which might be of importance to the genesis of synvolcanic gold deposits (see Mercier-Langevin *et al.*, 2015). Widespread sericite-dominated (\pm chlorite) alteration is also a good indicator to mineralization, along with the occurrence of Mn-rich carbonates, kyanite, chloritoid and spessartine garnets close to mineralization. A pervasive planar fabric combined with an oblique stretching lineation might be key as well, since it can locally remobilize disseminated bodies into better-constrained mineralized zones, which is of economic importance.

For the Rainy River deposit, absolute mineralization age constraints obtained through mapping and U-Pb geochronological work on post mineral dykes set mineralization at ≤ 2717 and ≥ 2693

Ma, and D₂ at ≤2693 Ma (McNicoll, unpublished data). In the context of the tectonic evolution of the Wabigoon Subprovince, this age is consistent with the period of terrane accretion and thrusting of the Neoproterozoic western Wabigoon Subprovince over the Winnipeg River continental terrane (Melnyk *et al.*, 2006). This timing of mineralization with respect to the tectonic evolution of the terrane is similar to the one observed in many deposits of the Superior (Robert *et al.*, 2005) and the Yilgarn cratons (Robert *et al.*, 2005; Vieilreicher *et al.*, 2015) and could represent a favourable setting and style of gold mineralization to be considered in designing future exploration models at large scale.

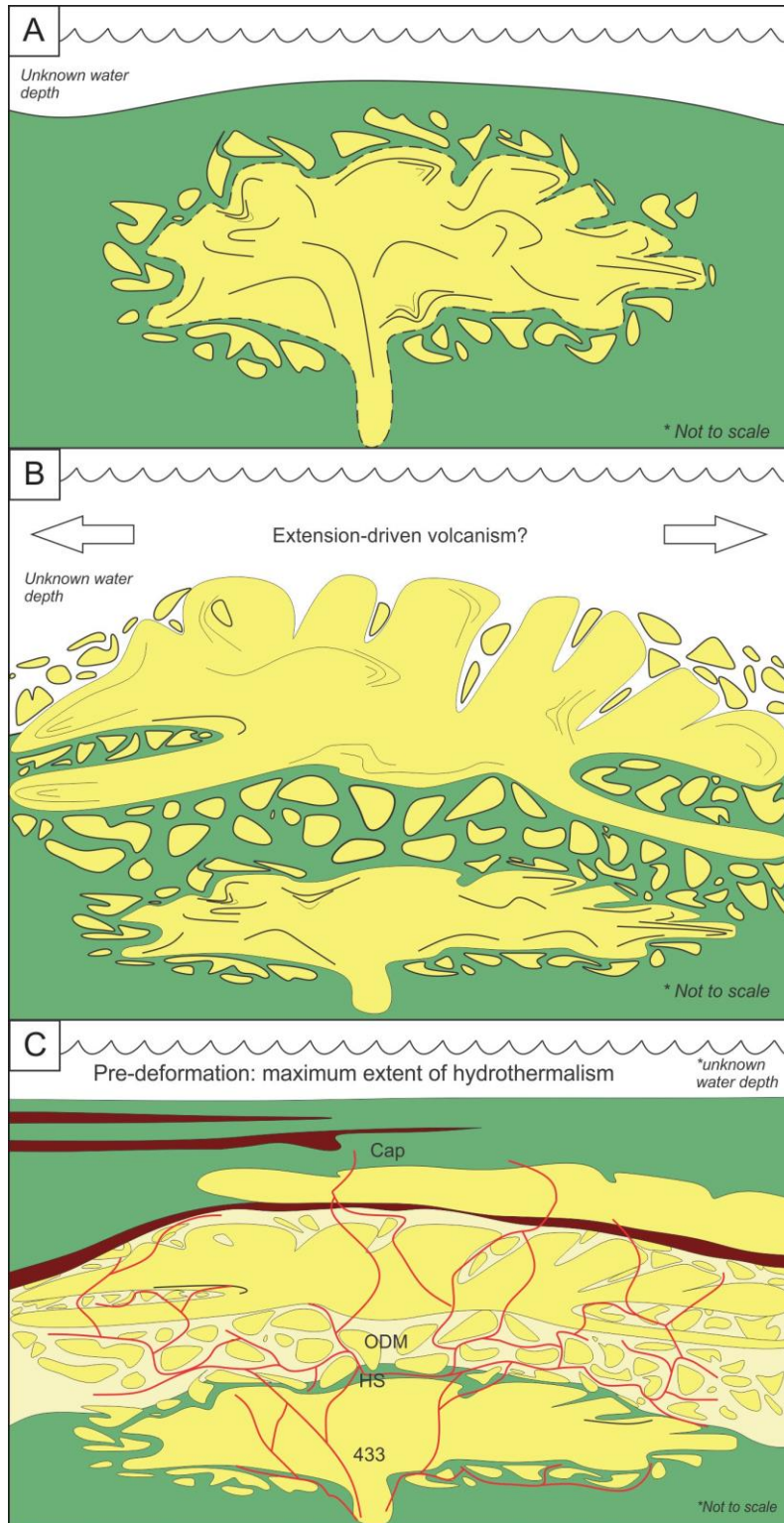


Figure 7.1 : Potential volcanic architecture and emplacement of the calc-alkaline dacitic body hosting the Rainy River deposit. A. Beginning of calc-alkaline volcanism by emplacement of dacite cryptodome in tholeiitic basalt. B. Prolonged and voluminous dacitic volcanism (extension-driven?) eventually reaching the seafloor, forming lava domes and flows and associated breccias. C. Final extent of volcanic activity and mineralization, here schematised in red, prior to deformation. NOTE: layers in dark brown correspond to sedimentary units.

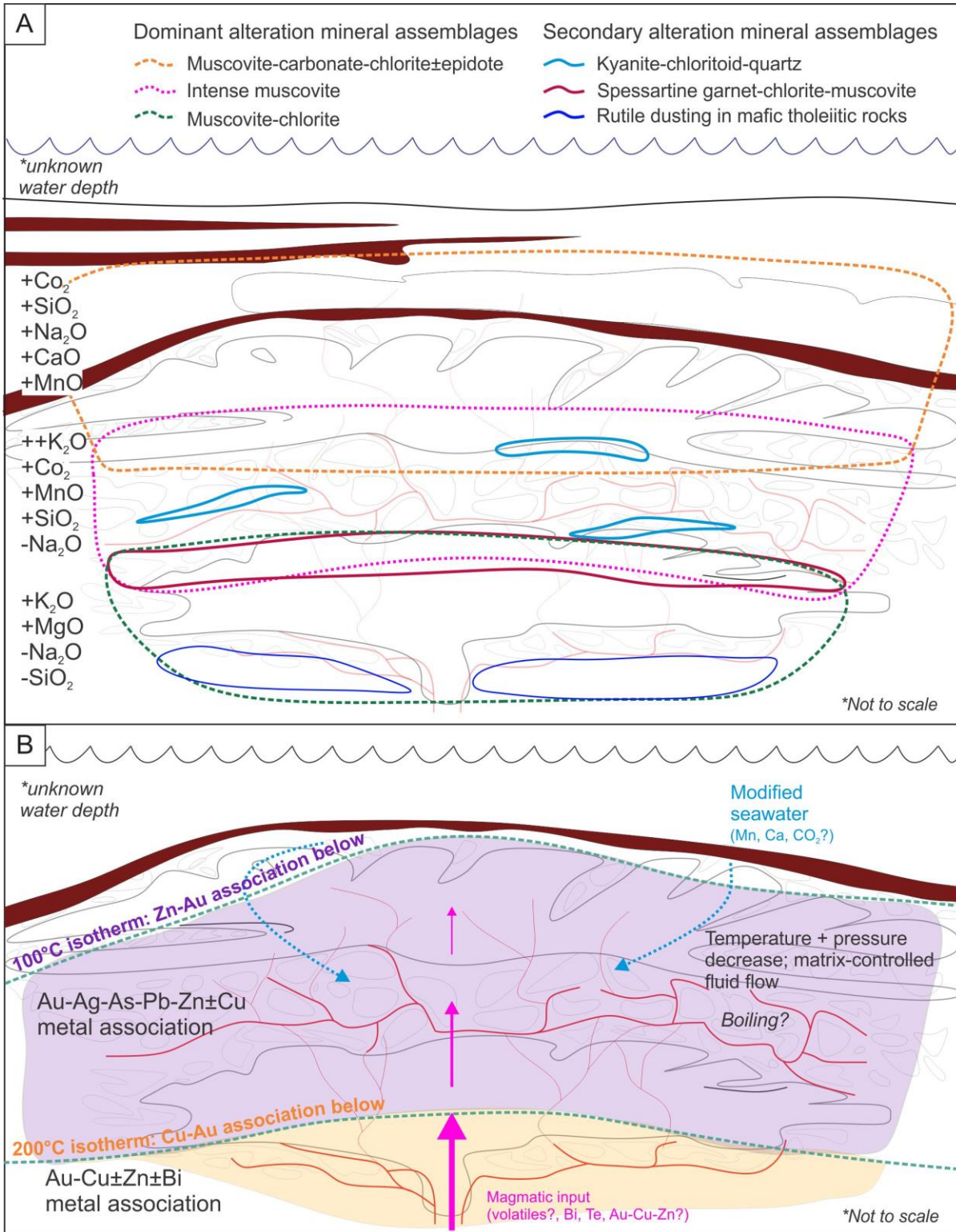


Figure 7.2 : A. Present zonation of alteration mineral assemblages and associated mass variations represented on the Rainy River deposit pre-deformation. B. Metal associations characterizing the Rainy River deposit with potential sources of metals and conditions of metal transport and precipitation at peak hydrothermalism (pre-deformation). NOTE: layers in dark brown correspond to sedimentary units.

8 REFERENCES

- Agnico-Eagle Mines Limited (2016) *Hammond Reef, overview, exploration update, geology and mineralization, reserves and resources*. Agnico-Eagle Mines Limited, Toronto, Ontario: <http://www.agnicoeagle.com/en/Exploration/Advanced-Projects/HammondReef/Pages/default.aspx> (visited on February 19, 2016)
- Allen, R.L. (1988) False pyroclastic textures in altered silicic lavas, with implications for volcanic-associated mineralization. *Economic Geology* 83 : 1424-1446.
- Aranz Geo Ltd. (2012) Fundamentals Training – Session notes, Leapfrog mining. Unpublished short course notes.
- Ayer, J. A., and Davis, D. W. (1997) Neoproterozoic evolution of differing convergent margin assemblages in the Wabigoon Subprovince: geochemical and geochronological evidence from the Lake of the Woods greenstone belt, Superior Province, northwestern Ontario. *Precambrian Research*. 81 : 155-178.
- Ayres, L.D. (2005) Relogging of diamond drill holes, Richardson township property, northwestern Ontario, formerly owned by Nuinsco Resources Ltd. 608457 BC Ltd. confidential report for Rainy River Resources Ltd. Unpublished internal report.
- Backeberg, N. R. (2015) Damaged goods: regional deformation history and structural controls on the Hammond Reef gold deposit, Atikokan, Ontario. Ph.D. thesis, McGill University, Montreal, Quebec, 194 p.
- Barrett, T.J. and MacLean, W.H. (1991) Chemical, mass, and oxygen isotopes changes during extreme hydrothermal alteration of an Archean rhyolite, Noranda, Quebec. *Economic Geology* 86 : 406-414.
- Barrett, T.J. and MacLean, W.H. (1999) Volcanic sequences, lithogeochemistry, and hydrothermal alteration in some bimodal volcanic-associated massive sulfide systems *in* Volcanic-associated massive sulfide deposits: processes and examples in modern and ancient settings, (ed.) Tucker Barrie, C. and Hannington, M.D. *Reviews in Economic Geology* v.8, p. 101–131.
- BBA (2012) *NI43-101 Preliminary economic assessment update of the Rainy River gold property, Ontario, Canada*. BBA Inc., Montréal, 353 p. : <http://www.sedar.com> (visited on December 20, 2015)
- BBA (2014) *NI43-101 Technical report feasibility study of the Rainy River deposit*. BBA Inc., Montréal, 566 p. : <http://www.sedar.com> (visited on December 20, 2015)
- Beaty, D.W., and Taylor, H.P., Jr. (1982) Some petrologic and oxygen isotope relationships in the Amulet mine, Noranda, Quebec, and their bearing on the origin of Archean massive sulfide deposits. *Economic Geology* 77 : 95-108.
- Beaudoin, G., Mercier-Langevin, P., Dubé, B., and Taylor, B.E. (2014) Low-temperature alteration at the world-class LaRonde Penna Archean Au-rich volcanogenic massive sulfide deposit, Abitibi Subprovince, Quebec, Canada: evidence from whole-rock oxygen isotopes. *Economic Geology* 109 : 167-182.

- Bédard, J., and Harris, L.B. (2014) Neoproterozoic disaggregation and reassembly of the Superior craton. *Geology* 42(11) : 951-954.
- Bigot, L. (2014) Typologie des altérations associées aux minéralisations aurifères en Abitibi. Public report CONSOREM 2013-07, 48 p. : http://consorem.ca/production_scienc/2013_07/2013-07_FINAL.pdf (visited on May 5, 2016).
- Blackburn, C.E. (1976) Geology of the Off Lake – Burditt Lake area, District of Rainy River; Ontario Geological Survey, Geological Report 140, 62 p. Accompanied by map 2352, 1 inch to 1 mile.
- Blackburn, C.E., Johns, G.W., Ayer, J., and Davis, D.W. (1991) Wabigoon Suprovince *In: Geology of Ontario*, Ontario Geological Survey, Special Volume 4, Part 1, p.303-382.
- Card, K.D., and Ciesielski, A. (1986) Subdivisions of the Superior Province of the Canadian Shield. *Geoscience Canada* 13: 5-13.
- Chang, Z. and Meinert, L.D. (2004) The magmatic-hydrothermal transition: evidence from quartz phenocrysts textures and endoskarn abundance in Cu-Zn skarns at the Empire Mine, Idaho, USA. *Chemical Geology* 210 : 149-171.
- Couture, J.-F. and Pilote, P. (1993) The geology and alteration patterns of a disseminated, shear zone-hosted mesothermal gold deposit: the Francoeur 3 deposit, Rouyn-Noranda, Quebec. *Economic Geology* 88 : 1664-1684.
- Davis, D.W and Edwards, G.R. (1986) Crustal evolution of Archean rocks in the Kakagi Lake area, Wabigoon Subprovince, Ontario as interpreted from high precision U-Pb zircon geochronology. *Can. J. Earth Sci.* 23 : 182-192.
- Davis, D.W., Sutcliffe, R.H., and Trowell, N.F. (1988) Geochronological constraints on the tectonic evolution of a late Archean greenstone belt, Wabigoon Subprovince, northwest Ontario, Canada. *Precambrian Research* 39 : 171-191.
- Davis, D.W., Poulsen, K.H., and Kamo, S.L. (1989) New insights into Archean crustal development from geochronology in the Rainy Lake area, Superior Province, Canada. *Journal of Geology* 97 : 379-398.
- Davies, J.F., and Whitehead, R.E. (2006) Alkali-Alumina and MgO-Alumina Molar Ratios of Altered and Unaltered Rhyolites. *Exploration and Mining Geology* 15 : 75-88.
- De Souza, S., Dubé, B., McNicoll, V.J., Dupuis, C., Mercier-Langevin, P., Creaser, R.A., and Kjarsgaard, I.M. (2015) Geology, hydrothermal alteration, and genesis of the world-class Canadian Malartic stockwork-disseminated Archean gold deposit, Abitibi, Quebec, *in Targeted Geoscience Initiative 4: Contributions to the understanding of precambrian lode gold deposits and Implications for exploration*, (ed.) B. Dubé and P. Mercier-Langevin; Geological Survey of Canada, Open File 7852, p. 113–126.
- Doyle, M. G. and Allen, R.L. (2003) Subsea-floor replacement in volcanic-hosted massive sulfide deposits. *Ore Geology Reviews* 23 : 183-222.
- Dubé, B., Mercier-Langevin, P., Hannington, M., Davis, D., and Lafrance, B. (2004) Le gisement de sulfures massifs aurifères volcanogènes LaRonde, Abitibi, Québec: Altérations, minéralisations et implications pour

l'exploration. Ministère des Ressources naturelles, de la Faune et des Parcs du Québec, report MB 2004-03, 112 p.

Dubé, B., Mercier-Langevin, P., Hannington, M.D., Lafrance, B., Gosselin, P., and Gosselin, G. (2007) The LaRonde Penna world-class Au-rich volcanogenic massive sulfide deposit, Abitibi, Quebec: Mineralogy and geochemistry of alteration and implications for genesis and exploration. *Economic Geology* 102 : 633–666.

Dubé, B., Mercier-Langevin, P., Castonguay, S., McNicoll, V.J., Pehrsson, S.J., Bleeker, W., Schetwelaar, E.M., and Jackson, S., (2011) 38. Targeted Geoscience Initiative 4. Lode gold deposits in ancient, deformed and metamorphosed terranes – footprints and exploration implications: a preliminary overview of themes, objectives and targeted areas: Ontario Geological Survey, Open File Report 6272, p.38-1 to 38-10.

Dubé, B., Mercier-Langevin, P., Kjarsgaard, I., Hannington, M., Bécu, V., Côté, J., Moorhead, J., Legault, and Bédard, N. (2014) The Bousquet 2-Dumagami world-class Archean Au-rich volcanogenic massive sulfide deposit, Abitibi, Quebec: metamorphosed submarine advanced argillic alteration footprint and genesis. *Economic Geology* 109 : 121-166.

Dubé, B., Mercier-Langevin, P., Castonguay, S., McNicoll, V.J., Bleeker, W., Lawley, C.J.M., De Souza, S., Jackson, S.E., Dupuis, C., Gao, J.-F., Bécu, V., Pilote, P., Goutier, J., Beakhouse, G.P., Yergeau, D., Oswald, W., Janvier, V., Fontaine, A., Pelletier, M., Beauchamp, A.-M., Katz, L.R., Kontak, D.J., Tóth, Z., Lafrance, B., Gourcerol, B., Thurston, P.C., Creaser, R.A., Enkin, R.J., El Goumi, N., Grunsky, E.C., Schneider, D.A., Kelly, C.J., and Lauzière, K., (2015) Precambrian lode gold deposits — a summary of TGI-4 contributions to the understanding of lode gold deposits, with an emphasis on implications for exploration, *In: Targeted Geoscience Initiative 4: Contributions to the understanding of Precambrian lode gold deposits and implications for exploration*, (ed.) B. Dubé and P. Mercier-Langevin; Geological Survey of Canada, Open File 7852, p. 1–24.

El-Rassi, D. and Cole, G. (2014) 14. Mineral resource estimation *in* BBA (2014) *NI43-101 technical report feasibility study of the Rainy River deposit*. BBA Inc., Montréal, p. 14-1 to 14-52. <http://www.sedar.com> (visited on December 20, 2015)

Fernandez, C. and Diaz-Azpiroz, M. (2009) Triclinic transpression with inclined extrusion. *Journal of Structural Geology* 31 : 1255-1269.

Fernandez, C., Czeck, D.M., and Diaz-Azpiroz, M. (2013) Testing the model of oblique transpression with oblique extrusion in two natural cases: steps and consequences. *Journal of Structural Geology* 54 : 85-102.

Fisher, R.V. (1961) Proposed classification of volcanoclastic sediments and rocks. *Geological Society of America Bulletin* 72 : 1409-1414.

Fletcher, G.L., and Irvine, T.N. (1954) Geology of the Emo area. Ontario Department of Mines, volume 63, Part 5, 36p. Accompanied by map 1954-2, 1 inch to 1 mile.

Franklin, J.M., Kasarda, J., and Poulsen, K.H. (1975) Petrology and chemistry of the alteration zone of the Matabi massive sulfide deposit. *Economic Geology* 70 : 63-79.

Franklin, J.M. (1993) Volcanic-associated massive sulphide deposits, *In: Mineral deposit modelling*, (ed) Thorpe, R.I. and Duke, J.M. Geological Association of Canada Special Paper 40, p. 315-334.

Franklin, J.M., Gibson, H.L., Jonasson, I.R., and Galley, A.G. (2005) Volcanogenic massive sulfide deposits in *Economic Geology* 100th Anniversary volume, (ed.) Hedenquist, J.W., Thompson, J.F.H., Goldfarb, R.J., and Richards, J.P., p. 523-560.

Galley, A.G. (1993) Characteristics of semi-conformable alteration zones associated with volcanogenic massive sulphide districts. *Journal of Geochemical Exploration* 48 : 175-200.

Gao, J.-F., Jackson, S.E., Dubé, B., Kontak, D.J., and De Souza, S., 2015. Genesis of the Canadian Malartic, Côte Gold, and Musselwhite gold deposits: Insights from LA-ICP-MS element mapping of pyrite, in Targeted Geoscience Initiative 4: Contributions to the understanding of Precambrian lode gold deposits and implications for exploration, (ed.) B. Dubé and P. Mercier-Langevin; Geological Survey of Canada, Open File 7852, p. 157–175.

Genna, D. and Gaboury, D. (2015) Deciphering the hydrothermal evolution of a VMS system by LA-ICP-MS using trace elements in pyrite: an example from the Bracemac-McLeod deposits, Abitibi, Canada, and implications for exploration. *Economic Geology* 110 : 2087-2108.

Gibson, H. L., Morton, R. L., and Hudak, G. J. (1999) Submarine volcanic processes, deposits, and environments favorable for the location of volcanic-associated massive sulfide deposits, in *Volcanic-associated massive sulfide deposits: processes and examples in modern and ancient settings*, (ed.) Tucker Barrie, C. and Hannington, M.D. *Reviews in Economic Geology* v.8, p. 13-51.

Gittins, J. and Harmer, R.E. (1997) What is ferrocarnatite? A revised classification. *Journal of African Earth Sciences* 25(1) : 159-168.

Gorton, M.P. and Schandl, E.S. (2000) From continents to island arcs: a geochemical index of tectonic setting for arc-related and within-plate felsic to intermediate volcanic rocks. *The Canadian Mineralogist* 38 : 1065-1073.

Grant, J.A. (1986) The isocon diagram; a simple solution to Gresens' equation for metasomatic alteration. *Economic Geology* 81(8) : 1976-1982.

Gresens, R.L. (1967) Composition-volume relationships of metasomatism. *Chemical Geology* 2 : 47-55.

Grew, E.S., Locock, A.J., Mills, S.J., Galuskina, I.O., Galuskin, E.V., and Halenius, U. (2013) Nomenclature of the garnet supergroup. *American Mineralogist* 98 : 785-811.

Hanmer, S. and Passchier, C. (1991) Shear-sense indicators: a review. Geological Survey of Canada paper 90-17. 72 p. Doi : 10.4095/132454

Hannington, M.D. and Scott, D. (1989) Sulfidation equilibria as guides to gold mineralization in volcanogenic massive sulfides: evidence from sulfide mineralogy and the composition of sphalerite. *Economic Geology* 84 : 1978-1995.

Hannington, M.D., Poulsen, K.H., Thompson, J.F.H., and Sillitoe, R.H. (1999) Volcanogenic gold in the massive sulfide environment, in: *Volcanic-associated massive sulfide deposits: processes and examples in modern and ancient settings*, (ed.) Tucker Barrie, C. and Hannington, M.D. *Reviews in Economic Geology* v.8, p. 325-356.

- Hannington, M.D., Kjarsgaard, I., and Galley, A.G. (2003) Mineral-chemical studies of metamorphosed hydrothermal alteration in the Kristineberg volcanogenic massive sulfide district, Sweden. *Mineralium Deposita* 38 : 423-442.
- Hannington, M.D., De Ronde, C.E.J., and Petersen, S. (2005) Sea-floor tectonics and submarine hydrothermal systems, *In: Economic Geology 100th Anniversary Volume*, (ed.) Hedenquist, J.W., Thompson, J.F.H., Goldfarb, R.J., and Richards, J.P., p. 111-141.
- Harker, A. (1909) *The natural history of igneous rocks*. Macmillan. New York.
- Harris, A. J. L., and Rowland, S. K. (2015) Chapter 17 - Lava flows and rheology, *In: The Encyclopedia of Volcanoes (Second Edition)*, (ed.) Sigurdsson, Amsterdam, Academic Press, p. 321-342. ISBN : 978-0-12-385938-9.
- Hart, T. R., Gibson, H. L., and Leshner, C. M. (2004) Trace element geochemistry and petrogenesis of felsic volcanic rocks associated with volcanogenic massive Cu-Zn-Pb sulfide deposits. *Economic Geology* 99 : 1003-1013.
- Hemley, J.J., Montoya, J.W., Marienko, J.W., and Luce, R.W. (1980) Equilibrium in the system Al₂O₃-SiO₂-H₂O and some general implications for alteration/mineralization processes. *Economic Geology* 75 : 210–238.
- Hey, M.H. (1954) A new reivew of the chlorites. *The Mineralogical Magazine* 224 : 277-292.
- Hrabi, B., and Vos, I. (2010) Rainy River structural study, interim results – northwestern Ontario; SRK consulting Inc. Confidential report to Rainy River Resources Ltd., unpublished report.
- Hudak, G.J. (2005) Field trip 10 – Mattabi/Sturgeon Lake historic VMS camp. *Proceedings of the 61st annual meeting of the Institute on Lake Superior Geology* (Dryden, Ontario, May 21-22, 2015), p. 116-151.
- Huston, D.L. and Large, R.R., (1989) A chemical model for the concentration of gold in volcanogenic massive sulfide deposits. *Ore Geology Reviews* 4 : 171–200.
- Huston, D.L., Bottrill, R.S., Creelman, R.A., Zaw, K., Ramsden, T.R., Rand, S.W., Gemmell, B.E., Jablonski, W. Sie, S.H., and Large, R.R. (1992) Geologic and geochemical controls on the mineralogy and grain size of gold-bearing phases, Eastern Australian volcanic-hosted massive sulfide deposits. *Economic Geology* 87 : 542-563.
- Huston, D.L. (1999) Stable isotopes and their significance for understanding the genesis of volcanic-hosted massive sulphide deposits: a review, *In: Volcanic-associated massive sulfide deposits: processes and examples in modern and ancient settings*, (ed.) Tucker Barrie, C. and Hannington, M.D. *Reviews in Economic Geology* v.8, p. 157–180.
- Huston, D.L. (2000) Gold in volcanic-hosted massive sulfide deposits: distribution, genesis, and exploration, *In: Gold in 2000* (ed.) Hagemann, S.G. and Brown, P.E., *Society of Economic Geologist Reviews* v.13, p.401-426.
- Irvine, T.N. and Baragar, W.R.A. (1971) A guide to the chemical classification of the common volcanic rocks. *Can. J. Earth Sci.* 8 : 523-548.

- Ishikawa, Y., Sawaguchi, T., Iwaya, S., and Horiuchi, M. (1976) Delineation of prospecting targets for Kuroko deposits based on modes of volcanism of underlying dacite and alteration haloes. *Mining Geology* 26 : 105-117.
- Johns, G. W. (1987) Geology of the Rainy River area, District of Rainy River, *In: Ontario Geological Survey Summary of Field Work 1987*, p. 45-48.
- Jones, R.R., Holdsworth, R.E., Clegg, P., McCaffrey, K., and Tavarnelli, E. (2004) Inclined transpression. *Journal of Structural Geology* 26 : 1531-1548.
- Katz, L.R., Kontak, D.J., Dubé, B., Rogers, J.R., McNicoll, V., and Creaser, R.A. (2014) The Archean Côté Gold intrusion-related Au-(Cu) deposit, Ontario, Canada: A large-tonnage, low-grade deposit centred on a magmatic-hydrothermal breccia, *In: Abstracts; Geological Association of Canada – Mineralogical Association of Canada Joint Annual Meeting, Fredericton, May 2014*, v. 37, p. 133–134.
- Kay, S. M. and Kay, R.W. (1994) Aleutian magmas in space and time. *In: The Geology of Alaska*. (ed.) Plafker, G and Berg, H.C. Geological Society of America *The Geology of North America*, v. G-1.: 687-722.
- Kerrick, R., and Polat, A. (2006) Archean greenstone-tonalite duality: Thermochemical mantle convection models or plate tectonics in the early Earth global dynamics? *Tectonophysics* 415: 141-165.
- Kishida, A., and Kerrich, R. (1987) Hydrothermal alteration zoning and gold concentration at the Kerr-Addison Archean lode gold deposit, Kirkland Lake, Ontario. *Economic Geology* 82 : 649-690.
- Kjarsgaard, I. (October 2013) Petrography of ten polished sections from Rainy River. Confidential report prepared for P. Mercier-Langevin (GSC-Quebec). Unpublished report.
- Krogh, T.E., and Davis, G. L. (1971) Zircon U-Pb ages of Archean metavolcanic rocks in the Canadian Shield. *Carnegie Inst. Wash. Yearb.* 70 : 241-242.
- Lafrance, B., Mueller, W. U., Daigneault, R., and Dupras, N. (2000) Evolution of a submerged composite arc volcano: volcanology and geochemistry of the Normétal volcanic complex, Abitibi greenstone belt, Québec, Canada. *Precambrian Research* 101 : 277-311.
- Langford, F.F., and Morin, J.A., (1976) The development of the Superior Province of northwestern Ontario by merging island arcs. *American Journal of Science* 276 : 1023-1034.
- Large, R. R., Gemmell, J. B., Paulick, H., and Huston, D. L. (2001a) The Alteration Box Plot: A Simple Approach to Understanding the Relationship between Alteration Mineralogy and Litho-geochemistry Associated with Volcanic-Hosted Massive Sulfide Deposits. *Economic Geology* 96 : 957-971.
- Large, R.R., McPhie, J., Gemmell, B. J., Herrmann, W., and Davidson, G.J. (2001b) The spectrum of ore deposit types, volcanic environments, alteration halos, and related exploration vectors in submarine volcanic successions: some examples from Australia. *Economic Geology* 96 : 913-938.
- Le Bas, M.J., Le Maître, R.W., Streckeisen, A., and Zanettin, B. (1986) A chemical classification of volcanic rocks based on the total alkali-silica diagram. *Journal of Petrology* 27 : 745-750.

- Leshner, C. M., Goodwin, A. M., Campbell, I. H., and Gorton, M. P. (1986) Trace-element geochemistry of ore-associated and barren, felsic metavolcanic rocks in the Superior Province, Canada. *Can. J. Earth Sci.* 23 : 222-237.
- Liou, J.G., Kuniyoshi, S., and Ito, K. (1974) Experimental studies of phase relations between greenschist and amphibolite boundary in a basaltic system. *American Journal of Science* 274 : 613-632.
- Litvinovsky, B. A. and Podladchikov, Y.Y. (1993) Crustal anatexis during the influx of magmatic volatiles. *Lithos* 30 (2) : 93-107.
- Lofgren, G. (1971) Experimentally produced devitrification textures in natural rhyolitic glass. *Geological Society of America Bulletin* 82 : 111-124.
- Mackie, B., Puritch, E., and Jones, J. (2003) Rainy River Project: Exploration Summary and Mineral Resource Estimate for the #17 Gold Zone. Confidential report for Nuinsco Resources Ltd. Unpublished company report.
- MacLean, W.H., and Barrett, T.J. (1993) Lithogeochemical techniques using immobile elements. *Journal of Geochemical Exploration* 48 : 109-133.
- Marquis, P. Hubert, C., Brown, A.C., and Rigg, D.M. (1990) Overprinting of early, redistributed Fe and Pb-Zn mineralization by late-stage Au-Ag-Cu deposition at the Dumagami mine, Bousquet district, Abitibi, Quebec. *Can. J. Earth Sci.* 27 : 1651-1671.
- Marquis, P., Hubert, C., Brown, A.C., Scherkus, E., Trudel, P., and Hoy, L.D. (1992) Géologie de la mine Donald J. LaRonde (Abitibi). Ministère de l'Énergie et Ressources du Québec Report ET 89-06, 106 p.
- Marquis, R. (octobre 2004) Pour une meilleure compréhension de la Province du Supérieur. Bulletin d'information minière, Ressources naturelles, faune et parcs, Gouvernement du Québec, Québec. <https://www.mern.gouv.qc.ca/mines/quebec-mines/2004-10/superieur.asp> (visited on February 11, 2016)
- Martin, H., Smithies, R.H., Rapp, R., Moyen, J.-F., and Champion, D (2005) An overview of adakite, tonalite-trondhjemitic-granodiorite (TTG), and sanukitoid: relationships and some implications for crustal evolution. *Lithos* 79 : 1-24.
- McDonough, W.F. and Sun, S.-s. (1995) The composition of the Earth. *Chemical Geology* 120 : 223-253.
- McNicoll, V., Goutier, J., Dubé, B., Mercier-Langevin, P., Ross, P.-S., Dion, C., Monecke, T., Legault, M., Percival, J., and Gibson, H. (2014) U-Pb geochronology of the Blake River group, Abitibi greenstone belt, Quebec, and implications for base metal exploration. *Economic Geology* 109 : 27-59.
- McPhie, J., Doyle, M., Allen, R. L., and Allen, R. (1993) Volcanic Textures: A Guide to the Interpretation of Textures in Volcanic Rocks. Centre for Ore Deposit and Exploration Studies, University of Tasmania. Hobart, Australia. 198 p.
- Melling, D.R. (1986) The occurrence of gold in the Cameron-Rowan lakes area: preliminary report on the Monte Cristo and Victor Island gold prospects. Ontario Geological Survey, Miscellaneous Paper 132, p. 252-260.

Melnyk, M., Davis, D.W., Cruden, A.R., and Stern, R.A. (2006) U-Pb ages constraining structural development of an Archean terrane boundary in the Lake of the Woods area, western Superior Province, Canada. *Can. J. Earth Sci.* 43 : 967-993.

Mercier-Langevin, P. (2005) Géologie du gisement de sulfures massifs volcanogènes aurifères LaRonde, Abitibi, Québec; Ph.D. thesis, Institut National de la Recherche Scientifique, centre eau, terre, environnement, Quebec, Quebec, 694 p.

Mercier-Langevin, P., Dubé, B., Hannington, M.D., Davis, D.W., Lafrance, B., and Gosselin, G. (2007a) The LaRonde Penna Au-rich volcanogenic massive sulfide deposit, Abitibi greenstone belt, Quebec: Part I. Geology and geochronology. *Economic Geology* 102 : 585–609.

Mercier-Langevin, P., Dubé, B., Hannington, M.D., Richer-Lafèche, M., and Gosselin, G. (2007b) The LaRonde Penna Au-rich volcanogenic massive sulfide deposit, Abitibi greenstone belt, Quebec : Part II. Litho geochemistry and paleotectonic setting. *Economic Geology* 102 : 611-631.

Mercier-Langevin, P., Hannington, M.D., Dubé, B., and Bécu, V. (2011) The gold content of volcanogenic massive sulfide deposits. *Mineralium Deposita* 46 : 509-539.

Mercier-Langevin, P., Lafrance, B., Bécu, V., Dubé, B., Kjarsgaard, I., and Guha, J. (2014) The Lemoine auriferous volcanogenic massive sulphide deposit, Chibougamau camp, Abitibi greenstone belt, Quebec, Canada : geology and genesis. *Economic Geology* 109 : 231-269.

Mercier-Langevin, P., Hannington, M.D., Dubé, B., Piercey, S.J., Peter, J.M., and Pehrsson, S.J., 2015. Precious metal enrichment processes in volcanogenic massive sulphide deposits - A summary of key features, with an emphasis on TGI-4 research contributions, *In: Targeted Geoscience Initiative 4: Contributions to the understanding of volcanogenic massive sulphide deposit genesis and exploration methods development*, (ed.) J.M. Peter and P. Mercier-Langevin. Geological Survey of Canada, Open File 7853, p. 117–130.

Monecke, T., Petersen, S., and Hannington, M. D. (2014) Constraints on water depth of massive sulphide formation: evidence from modern seafloor hydrothermal systems in arc-related settings. *Economic Geology* 109: : 2079-2101.

Morton, R.L., and Franklin, J.M. (1987) Two-fold classification of Archean volcanic-associated massive sulfide deposits. *Economic Geology* 82 : 1057-1063.

Nabil, H. and Lafrance, B. (2009) Outil de discrimination des carbonates et exemples d'applications pour l'exploration. CONSOREM workshop, Québec Exploration conference 2009, Ministère des Ressources Naturelles et Faune (Quebec City, November 23-26, 2009). <http://tinyurl.com/guldayq> (visited on February 12, 2016).

New Gold Inc. (February 4, 2015a) *Summary of Mineral Reserve and Mineral Resource Estimates*. New Gold Inc. news release. <http://www.newgold.com/investors/reserves-and-resources/default.aspx> (visited on February 10, 2016)

New Gold Inc. (July 28, 2015b) *New Gold Announces Second Quarter Results; Rainy River Construction on Schedule and on Budget*. New Gold Inc. news release, Toronto, Canada. <http://tinyurl.com/jsst337> (visited on February 10, 2016)

Osterberg, S.A., Morton, R.L., and Franklin, J.M. (1987) Hydrothermal alteration and physical volcanology of Archean rocks in the vicinity of the Headway-Coulee massive sulfide occurrence, Onaman area, northwestern Ontario. *Economic Geology* 82 : 1505-1520.

Paulick, H. and Franz, G. (2001) Greenschist facies regional and contact metamorphism of the Thalanga volcanic-hosted massive sulfide deposit (northern Queensland, Australia). *Mineralium Deposita* 36 : 786-793.

Pearce, J.A., Harris, N.B.W., and Tindle, A.G. (1984) Trace element discrimination diagrams for the tectonic interpretation of granitic rocks. *Journal of Petrology* 25 : 956–983.

Pearce, J. A. (2008) Geochemical fingerprinting of oceanic basalts with applications to ophiolite classification and the search for Archean oceanic crust. *Lithos* 100 : 14-48.

Pelletier, M., Mercier-Langevin, P., Crick, D., Tolman, J., Beakhouse, G.P., and Dubé, B. (2014) 41. Targeted Geoscience Initiative 4. Lode gold deposits in ancient and deformed terranes: Preliminary observations on the nature and distribution of the deformed and metamorphosed hydrothermal alteration associated with the Archean Rainy River gold deposit, northwestern Ontario. Ontario Geological Survey, Open File Report 6300, p.41- to 41-10.

Pelletier, M., Mercier-Langevin, P., Dubé, B., Crick, D., Tolman, J., McNicoll, V.J., Jackson, S.E., and Beakhouse, G.P. (2015) The Rainy River “atypical” Archean Au deposit, western Wabigoon Subprovince, Ontario, *In: Targeted Geoscience Initiative 4: Contributions to the Understanding of Precambrian Lode Gold Deposits and Implications for Exploration*, (ed.) B. Dubé and P. Mercier-Langevin, Geological Survey of Canada, Open File 7852, p. 193–207.

Pelletier, M., Mercier-Langevin, P., Dubé, B., Bécu, V., Lauzière, K., and Richer-Lafleche, M. (2016) Whole-rock litho-geochemistry of the Archean Rainy River gold deposit, western Wabigoon, Ontario. Geological Survey of Canada, Open File 8048, 1 .zip file.

Percival, J.A, McNicoll, V., and Bailes, A.H. (2006a) Strike-slip juxtaposition of ca. 2.72 Ga juvenile arc and >2.98 Ga continent margin sequences and its implications for Archean terrane accretion, western Superior Province, Canada. *Can. J. Earth Sci.* 43 : 895-927.

Percival, J.A., Sanborn-Barrie, M., Skulski, T., Stott, G.M., Helmstaedt, H., and White, D.J. (2006b) Tectonic evolution of the western Superior Province from NATMAP and Lithoprobe studies. *Can. J. Earth Sci.* 43 : 1085-1117.

Percival, J. A. (2007) Geology and metallogeny of the Superior Province, Canada, *In: Goodfellow, W.D., ed., Mineral Deposits of Canada: A Synthesis of Major Deposit-Types, District Metallogeny, the Evolution of Geological Provinces, and Exploration Methods: Geological Association of Canada, Mineral Deposits Division, Special Publication No. 5, p. 903-928.*

Peterman, Z.E., and Day, W.C. (1989) Early Proterozoic activity on Archean faults in the western Superior Province – Evidence from pseudotachylite. *Geology* 17 : 1089-1092.

Piercey, S.J. (2009) Lithogeochemistry of volcanic rocks associated with volcanogenic massive sulphide deposits and applications to exploration, *In: Submarine volcanism and mineralization: modern through ancient*, (eds.) Cousens, B. and Piercey, S.J. Geological Association of Canada, Short Course 29-30 May 2008, Quebec City, Canada, p. 15-40.

Poulsen, K.H., Borradaile, G.J., and Kehlenbeck, M.M. (1980) An inverted Archean succession at Rainy Lake, Ontario. *Can. J. Earth Sci.* 17 : 1358-1369.

Poulsen, H.K. (1983) Structural setting of vein-type gold mineralization in the Mine Centre-Fort Frances area: implications for the Wabigoon Subprovince (ed.) A.C. Colvine, Ontario Geological Survey, Miscellaneous Paper 110, 278p.

Poulsen, H.K. (2005) Memorandum regarding October, 2005 visit to the Richardson township property, Emo area, northwestern Ontario. Confidential memo prepared for Rainy River Resources Ltd., unpublished report.

Poulsen, H.K. (2006) Memorandum regarding July, 2006 visit to the Richardson township property, Emo area, northwestern Ontario. Confidential memo prepared for Rainy River Resources Ltd., unpublished report.

Rankin, L. R. (2013) Structural setting of the Rainy River Au mineralization – NW Ontario; Geointerp confidential report 2013/08 prepared for Rainy River Resources Ltd., unpublished report.

Rapp, R.P., Shimizu, N., Norman, M.D., and Applegate, G.S. (1999) Reaction between slab-derived melts and peridotite in the mantle wedge: experimental constraints at 3.8 Gpa. *Chemical Geology* 160 : 335-356.

Reid, R. (2013) Basic grade interpolation in Leapfrog. Orefind Pty Ltd. Blog, June 27, 2013 entry. http://www.orefind.com/blog/orefind_blog/2013/06/27/basic-grade-interpolation-in-leapfrog (visited on February 24, 2016).

Richer-Lafli che, M., Moorhead, J., Goutier, J., and Fallara, F. (2000) G ochimie des roches volcaniques et des formations de fer du groupe de Yasinki, sous-province de La Grande. Minist re des Ressources naturelles, de la Faune et des Parcs du Qu bec, report MB2000-13, 67p.

Robert, F. and Poulsen, K.H. (2001) Vein formation and deformation in greenstone gold deposits, *In: Reviews in Economic Geology*, v. 14, p. 111-155.

Robert, F., Poulsen, H.K., Cassidy, K.F., and Hodgson, C.J. (2005) Gold metallogeny of the Superior and Yilgarn cratons, *In: Economic Geology 100th Anniversary volume*, (ed.) Hedenquist, J.W., Thompson, J.F.H., Goldfarb, R.J., and Richards, J.P., p. 1001-1033.

Ross, P.-S. and B dard, J.H. (2009) Magmatic affinity of modern and ancient subalkaline volcanic rocks determined from trace-element discriminant diagrams. *Can. J. Earth Sci.* 46 : 823-839.

Sanborn-Barrie, M. (1991) Structural geology and tectonic history of the eastern Lake of the Woods greenstone belt, Kenora district, northwestern Ontario. Ontario Geological Survey Open File Report 5773, 137 p.

- Sanderson, D. and Marchini, R.D. (1984) Transpression. *Journal of Structural Geology* 6 : 449-458.
- Seedorff, E., Dilles, J.H., Proffett, J.M., Einaudi, M.T., Zurcher, L., Stavast, W.J.A., Johson, D.A., and Barton, M.D. (2005) Porphyry deposits: characteristics and origin of hypogene features *in* Economic Geology 100th Anniversary Volume, (ed.) Hedenquist, J.W., Thompson, J.F.H., Goldfarb, R.J., and Richards, J.P., p. 251-298.
- Setterfield, T., Watkinson, D.H., and Thurston, P.C. (1983) Quench-textured, pillowed metabasalts and copper mineralization, Maybrun mine, northwestern Ontario. *CIM Bulletin*, November 1983, p. 69-74.
- Siddorn, J. (2008) Regional geophysical interpretation, Rainy River Au project, Ontario, Canada; SRK Consulting Inc. confidential report for Rainy River Resources Ltd., unpublished report.
- Simmons, S.F., White, N.C., and John, D.A. (2005) Geological characteristics of epithermal precious and base metal deposits, *In*: Economic Geology 100th Anniversary volume, (ed.) Hedenquist, J.W., Thompson, J.F.H., Goldfarb, R.J., and Richards, J.P., p. 485-522.
- Spooner, E.T.C. and Fyfe, W.S. (1973) Sub-sea-floor metamorphism, heat and mass transfer. *Contributions to Mineralogy and Petrology* 42(4) : 287-304.
- Spooner, E.T. and Barrie, C. T. (1993) A special issue devoted to Abitibi ore deposits in a modern context: preface. *Economic Geology* 88 : 1307-1322.
- SRK (2009) *Mineral resource evaluation Rainy River gold project, western Ontario, Canada*. SRK Consulting (Canada) Inc., Toronto, 113 p. : <http://www.sedar.com> (visited on October 10, 2013)
- SRK (2011) *Mineral resource evaluation, Rainy River gold project, western Ontario, Canada*. SRK Consulting (Canada) Inc., Toronto, 145 p : <http://www.sedar.com> (visited on February 10, 2016)
- Sun, S.-s. and McDonough, W.F. (1989) Chemical and isotopic systematics of oceanic basalts: implications for mantle compositions and processes, *In*: Magmatism in the oceanic basins, (ed.) Saunders, A.D. and Norry, M.J. Geological Society of London, Special Publication No. 42, p. 313-345.
- Taylor, B.E. and Huston, D.L. (1999) Regional ¹⁸O zoning and hydrogen isotope studies in the Kidd Creek volcanic complex, Timmins, Ontario, *In*: The giant Kidd Creek volcanogenic massive sulfide deposit, western Abitibi Subprovince, Canada (ed. Hannington, M.D. and Tucker Barrie, C.). Economic Geology Monograph 10, p. 351-378.
- Teasdale, N., Brown, A.C., and Tourigny, G. (1996) Gîtologie de la mine Bousquet 2: Ministère des Ressources Naturelles, Québec, report MB 96–37, 43 p.
- Tomlinson, K.Y., Davis, D.W., Percival, J.A., Hughes, D.J., and Thurston, P.C. (2002) Mafic to felsic magmatism and crustal recycling in the Obonga Lake greenstone belt, western Superior Province: evidence from geochemistry, Nd isotopes and U-Pb geochronology. *Precambrian Research* 114 : 295-325.
- Tooth, B., Brugger, J., Ciobanu, C., and Liu, W. (2008) Modeling of gold scavenging by bismuth melts coexisting with hydrothermal fluids. *Geology* 36 : 815–818.
- Tourigny, G., Brown, A.C., Hubert, C., and Crépeau, R. (1989) Synvolcanic and syntectonic gold mineralization at the Bousquet mine, Abitibi greenstone belt, Quebec. *Economic Geology* 84 : 1875-1890.

- Tourigny, G., Doucet, D., and Bourget, A. (1993) Geology of the Bousquet 2 mine: An example of a deformed, gold-bearing, polymetallic sulfide deposit. *Economic Geology* 88 : 1578–1597.
- Trépanier, S. (2011) Guide pratique d'utilisation de différentes méthodes de traitement de l'altération et du métasomatisme. Public report CONSOREM 2008-07, 209p : <http://tinyurl.com/jyvrm2m> (visited on May 5, 2016).
- Valliant, R.I. and Barnett, R. L. (1982) Manganiferous garnet underlying the Bousquet gold orebody, Quebec: metamorphosed manganese sediment as a guide to gold ore. *Can. J. Earth Sci.* 19 : 993-1010.
- Vieilreicher, N., Groves, D., McNaughton, N., and Fletcher, I. (2015) The timing of gold mineralization across the eastern Yilgarn craton using U-Pb geochronology of hydrothermal phosphate minerals. *Mineralium Deposita* 50 : 391-428.
- Wartman, J.M. (2011) Physical volcanology and hydrothermal alteration of the Rainy River Gold Project, northwest Ontario; MSc thesis, University of Minnesota, Duluth, Minnesota, 163p.
- White, J. D. L., and Houghton, B. F. (2006) Primary volcanoclastic rocks. *Geology* 34(8): 677-680. Doi : 10.1130/G22346.1.
- White, J.D.L., McPhie, J., and Soule, A.S. (2015) Chapter 19 – Submarine lavas and hyaloclastite, *In: The Encyclopedia of Volcanoes (Second Edition)*: Amsterdam, Academic Press, p. 363-375. ISBN : 978-0-12-385938-9.
- Whitehead, R.E. and Davies, J.F. (1988) Discriminant analysis involving CO₂/CaO and arsenic in gold exploration. *Journal of Geochemical Exploration* 30 : 243-253.
- Williams, N.C. and Davidson, G.J. (2004) Possible submarine advanced argillic alteration at the Basin Lake prospect, western Tasmania, Australia. *Economic Geology* 99 : 987–1002.
- Winchester, J.A. and Floyd, P.A. (1977) Geochemical discrimination of different magma series and their differentiation products using immobile elements. *Chemical Geology* (20) : 325-343.
- Winter, J.D. (2001) *An introduction to igneous and metamorphic petrology*. Prentice-Hall Inc. New Jersey, USA. 697 p. ISBN 0-13-240342-0
- Wright-Holfeld, A., Mericet-Langevin, P., and Dubé, B. (2010) Contrasting alteration mineral assemblages associated with the Westwood deposit ore zones, Doyon-Bousquet-LaRonde mining camp, Abitibi, Quebec. Geological Survey of Canada current research no. 2010-9., 27 p.
- Yang, K. and Scott, S.D. (2003) Geochemical relationships of felsic magmas to ore metals in massive sulfide deposits of the Bathurst mining camp, Iberian pyrite belt, Holuroku district, and the Abitibi belt, *In: Massive sulphide deposits of the Bathurst mining camp, New Brunswick, and Northern Maine*, (ed.) Goodfellow, W.D., McCutcheon, S.R., and Peter, J.M. *Economic Geology Monograph* 11, p. 457-478.
- Yergeau, D. (2015) Géologie du gisement synvolcanique aurifère atypique Westwood, Abitibi, Québec; Ph.D. thesis, Institut National de la Recherche Scientifique, centre eau, terre, environnement, Quebec, Quebec, 641 p.

Yergeau, D., Mercier-Langevin, P., Dubé, B., Malo, M., McNicoll, V.J., Jackson, S.E., Savoie, A., and La Rochelle, F. (2015) The Archean Westwood Au deposit, southern Abitibi: Telescoped Au-rich VMS and intrusion-related Au systems, *In: Targeted Geoscience Initiative 4: Contributions to the Understanding of Precambrian Lode Gold Deposits and Implications for Exploration*, (ed.) B. Dubé and P. Mercier-Langevin; Geological Survey of Canada, Open File 7852, p. 177–191.

APPENDIX I : DETAILED MAPS AND CROSS SECTION

Here is a list of the cross section and maps that compose appendix I. They are inserted at the end of this .pdf document. Original size of all figures is A2 format. Note that these figures are also part of the main document, but in US letter size and lower resolution.

Map 3.1: Distribution of volcanic facies and lithologies on the oblique plane

Map 3.2: Distribution of volcanic facies on the 425475E cross section

Map 3.3: Detailed map (1:100) of McClain outcrop

Map 3.4: Detailed map (1:100) of Scott outcrop

APPENDIX II : MICROPROBE ANALYSES RESULTS

Microprobe analyses on silicates were done at Laval University under the supervision of Dr. Marc Choquette, using a CAMECA SX-100 wavelength dispersive X-ray spectrometer (WDS).

II.I Aluminosilicates

SAMPLE	MINERAL	SiO ₂ %	TiO ₂ %	Al ₂ O ₃ %	Cr ₂ O ₃ %
RRR435604	kyanite	31.112	0.045	49.261	0.000
RRR435660	kyanite	37.665	0.011	63.092	0.007
RRR435660	chloritoid	24.746	0.000	40.810	0.000
RRR435660	kyanite	37.239	0.077	63.122	0.007
RRR435660	chloritoid	25.031	0.000	40.544	0.003
RRR435660	kyanite	37.299	0.044	62.829	0.046
RRR435660	chloritoid	24.601	0.057	39.852	0.030
RRR435660	kyanite	37.479	0.000	60.766	0.016
RRR435752	chloritoid	24.844	0.000	37.216	0.000
RRR435752	chloritoid	24.055	0.036	38.684	0.038
RRR435752	chloritoid	24.163	0.000	38.530	0.000
RRR435798	kyanite	32.418	0.072	49.103	0.020
RRR435883	kyanite	38.689	0.017	27.245	0.000

SAMPLE	MINERAL	Y2O3 %	MgO %	CaO %	MnO %
RRR435604	kyanite	0.000	0.192	12.592	0.018
RRR435660	kyanite	0.000	0.024	0.000	0.001
RRR435660	chloritoid	0.000	3.329	0.003	0.637
RRR435660	kyanite	0.000	0.016	0.000	0.000
RRR435660	chloritoid	0.000	3.379	0.000	0.621
RRR435660	kyanite	0.000	0.014	0.001	0.000
RRR435660	chloritoid	0.000	3.607	0.000	0.537
RRR435660	kyanite	0.045	0.026	0.013	0.000
RRR435752	chloritoid	0.000	1.909	0.021	0.885
RRR435752	chloritoid	0.000	2.306	0.039	0.957
RRR435752	chloritoid	0.000	2.046	0.001	0.939
RRR435798	kyanite	0.000	0.090	11.607	0.010
RRR435883	kyanite	0.000	3.656	23.360	0.288

Appendix I : Microprobe analyses

Aluminosilicates

SAMPLE	MINERAL	FeO %	Na2O %	K2O %	Total
RRR435604	kyanite	0.205	0.738	0.291	94.454
RRR435660	kyanite	0.384	0.011	0.002	101.197
RRR435660	chloritoid	23.482	0.033	0.000	93.040
RRR435660	kyanite	0.274	0.012	0.002	100.749
RRR435660	chloritoid	23.351	0.005	0.000	92.934
RRR435660	kyanite	0.283	0.008	0.000	100.524
RRR435660	chloritoid	22.698	0.012	0.003	91.397
RRR435660	kyanite	0.401	0.034	0.004	98.784
RRR435752	chloritoid	23.894	0.021	0.023	88.813
RRR435752	chloritoid	24.511	0.005	0.000	90.631
RRR435752	chloritoid	25.149	0.021	0.000	90.849
RRR435798	kyanite	0.222	1.149	0.355	95.046
RRR435883	kyanite	1.117	0.011	0.004	94.387

II.II Biotite

SAMPLE	TARGET	SiO2 %	TiO2%	Al2O3 %	Cr2O3 %	MgO %
RRR435538	T016	34.462	1.231	18.247	0.021	12.852
RRR435538	T015	36.43	1.263	18.169	0.008	13.586
RRR435538	T014	35.547	1.345	17.971	0.071	13.743
RRR435538	T013	37.036	1.36	18.049	0.0	13.158
RRR435537	T009	34.828	1.42	18.379	0.0	10.899
RRR435537	T012	36.237	1.555	17.851	0.074	10.704
RRR435537	T010	35.5	1.712	18.719	0.025	10.182
RRR435548	T020	32.646	1.424	18.933	0.024	10.712
RRR435544	T054	36.454	1.318	18.535	0.038	13.696
RRR435544	T053	36.959	1.725	18.008	0.013	12.847
RRR435544	T052	33.456	1.049	18.373	0.025	12.955
RRR435612	T065	33.147	1.145	19.814	0.0	14.16
RRR435612	T063	34.779	1.166	18.84	0.0	14.765
RRR435680	T075	31.239	1.288	17.339	0.012	4.927
RRR435680	T074	29.48	0.923	17.526	0.0	5.507
RRR435680	T072	27.154	0.525	16.963	0.065	4.47
RRR435774	T095	34.719	1.49	17.97	0.086	8.881
RRR435777	T101	37.28	1.59	17.397	0.0	12.41
RRR435777	T100	36.623	1.388	18.086	0.0	10.801
RRR435777	T098	35.683	1.356	17.882	0.021	11.107
RRR435773	T094	35.557	1.563	18.162	0.016	8.515
RRR435773	T093	35.886	1.577	18.407	0.078	9.017
RRR435773	T092	36.283	1.616	17.834	0.098	8.737
RRR435773	T090	34.54	1.209	17.713	0.275	8.484
RRR435782	T102	35.685	1.75	17.411	0.025	11.517

Appendix I : Microprobe analyses

Biotite

SAMPLE	CaO %	MnO %	FeO %	NiO %	BaO %	Na2O %
RRR435538	0.032	0.059	18.908	0.0	0.0	0.066
RRR435538	0.005	0.079	16.921	0.0	0.0	0.082
RRR435538	0.013	0.062	16.438	0.0	0.0	0.088
RRR435538	0.006	0.055	16.012	0.053	0.0	0.141
RRR435537	0.379	0.051	20.01	0.0	0.0	0.111
RRR435537	0.023	0.058	19.413	0.026	0.0	0.112
RRR435537	0.031	0.062	19.338	0.0	0.014	0.127
RRR435548	0.029	0.369	23.155	0.0	0.0	0.041
RRR435544	0.074	0.199	15.538	0.0	0.0	0.158
RRR435544	0.169	0.169	14.997	0.041	0.0	0.158
RRR435544	0.068	0.22	18.667	0.0	0.0	0.097
RRR435612	0.04	0.573	18.574	0.002	0.0	0.033
RRR435612	0.048	0.528	16.484	0.005	0.0	0.068
RRR435680	0.095	0.413	32.95	0.0	0.0	0.01
RRR435680	0.067	0.443	33.72	0.0	0.0	0.01
RRR435680	0.068	0.644	37.985	0.0	0.0	0.106
RRR435774	0.055	0.12	22.783	0.002	0.0	0.109
RRR435777	0.02	0.127	17.183	0.0	0.0	0.103
RRR435777	0.025	0.146	17.963	0.014	0.0	0.112
RRR435777	0.003	0.132	18.844	0.0	0.0	0.079
RRR435773	0.155	0.11	21.252	0.053	0.0	0.166
RRR435773	0.074	0.066	21.008	0.038	0.0	0.099
RRR435773	0.031	0.118	21.527	0.0	0.0	0.087
RRR435773	0.188	0.091	21.674	0.017	0.0	0.088
RRR435782	0.059	0.203	18.68	0.016	0.0	0.105

Appendix I : Microprobe analyses

Biotite

SAMPLE	K2O %	Rb2O %	H2O %	F %	Cl %	Total
RRR435538	7.531	0.0	3.571	0.591	0.184	97.755
RRR435538	8.183	0.007	3.65	0.691	0.08	99.154
RRR435538	8.138	0.0	3.597	0.669	0.1	97.782
RRR435538	9.05	0.0	3.601	0.801	0.107	99.429
RRR435537	8.397	0.0	3.811	0.168	0.047	98.5
RRR435537	9.318	0.021	3.801	0.281	0.052	99.526
RRR435537	9.541	0.0	3.828	0.207	0.033	99.319
RRR435548	5.278	0.0	3.709	0.192	0.064	96.576
RRR435544	8.491	0.0	3.794	0.376	0.128	98.799
RRR435544	8.887	0.0	3.722	0.506	0.094	98.295
RRR435544	6.209	0.005	3.66	0.286	0.108	95.178
RRR435612	4.989	0.0	3.775	0.264	0.038	96.554
RRR435612	6.002	0.0	3.816	0.259	0.031	96.791
RRR435680	5.559	0.0	3.634	0.0	0.072	97.538
RRR435680	3.714	0.0	3.55	0.0	0.037	94.977
RRR435680	1.543	0.0	3.399	0.0	0.064	92.986
RRR435774	8.186	0.004	3.646	0.34	0.178	98.569
RRR435777	8.891	0.0	3.625	0.702	0.136	99.464
RRR435777	9.017	0.0	3.594	0.617	0.199	98.585
RRR435777	9.472	0.0	3.563	0.63	0.206	98.978
RRR435773	8.742	0.0	3.636	0.438	0.114	98.479
RRR435773	8.806	0.0	3.791	0.205	0.108	99.16
RRR435773	9.227	0.0	3.621	0.556	0.135	99.87
RRR435773	8.599	0.0	3.519	0.505	0.137	97.039
RRR435782	8.251	0.012	3.453	0.886	0.121	98.174

II.III Carbonate

SAMPLE	Mg(CO ₃) %	Ca(CO ₃) %	Mn(CO ₃)%	Fe(CO ₃) %	Total
RRR435524	28.437	50.156	3.208	15.935	97.736
RRR435524	28.447	51.06	2.684	15.973	98.164
RRR435524	28.178	50.646	1.906	18.224	98.954
RRR435524	30.993	51.948	3.299	12.239	98.479
RRR435524	28.344	50.436	3.353	16.773	98.906
RRR435524	16.232	51.622	0.872	17.518	86.244
RRR435530	0.118	99.022	1.577	0.015	100.732
RRR435537	26.64	49.999	1.934	19.93	98.503
RRR435537	27.116	50.844	1.939	19.04	98.939
RRR435537	22.892	52.442	1.357	22.446	99.137
RRR435537	23.585	50.868	1.305	23.101	98.859
RRR435537	2.058	92.615	0.997	3.577	99.247
RRR435537	23.74	52.819	1.458	20.405	98.422
RRR435538	25.921	51.682	1.261	20.245	99.109
RRR435538	35.576	51.733	0.924	10.889	99.122
RRR435538	27.97	50.82	1.906	18.233	98.929
RRR435538	29.919	51.503	4.56	12.45	98.432
RRR435538	29.436	48.412	2.279	12.796	92.923
RRR435544	1.715	92.155	2.542	1.855	98.267
RRR435544	0.436	91.907	0.781	0.085	93.209
RRR435548	1.61	92.379	1.624	2.561	98.174
RRR435548	0	89.66	0.407	0.11	90.177
RRR435548	1.25	86.487	1.47	2.268	91.475
RRR435548	0.962	88.064	1.257	0.606	90.889
RRR435548	0.162	87.945	1.225	0.293	89.625
RRR435548	1.346	93.999	1.414	2.086	98.845
RRR435548	0.369	97.653	0.68	0.318	99.02
RRR435558	1.925	94.105	1.233	2.96	100.223
RRR435558	0.261	92.001	0.933	0.494	93.689
RRR435580	0.445	95.162	0.847	0.479	96.933
RRR435593	0.087	97.695	1.762	0.209	99.753
RRR435593	0.079	99.314	0.324	0.353	100.07
RRR435593	0.064	99.583	0.439	0.214	100.3
RRR435604	31.085	48.935	5.048	8.589	93.657
RRR435604	31.537	51.733	6.989	7.639	97.898
RRR435612	0.069	96.915	0.856	0.67	98.51
RRR435612	0.376	93.852	1.995	0.075	96.298
RRR435612	0.17	94.503	0.988	0.145	95.806

Appendix I : Microprobe analyses

Carbonate

SAMPLE	Mg(CO3)%	Ca(CO3) %	Mn(CO3)%	Fe(CO3) %	Total
RRR435642	6.117	79.927	0.792	4.193	91.029
RRR435642	30.232	46.056	1.451	15.618	93.357
RRR435642	31.142	45.991	1.223	14.662	93.018
RRR435646	0.022	97.885	0.719	0.522	99.148
RRR435677	1.148	95.793	1.844	0.685	99.47
RRR435677	2.017	95.671	1.565	1.513	100.766
RRR435680	0	98.698	0.101	0.334	99.133
RRR435718	1.033	93.606	1.768	0.984	97.391
RRR435739	0.016	98.42	0.73	0.06	99.226
RRR435752	23.834	50.597	2.08	21.819	98.33
RRR435752	23.48	48.139	1.551	22.367	95.537
RRR435752	19.809	50.61	1.922	26.44	98.781
RRR435773	1.877	92.182	1.849	3.254	99.162
RRR435773	2.769	89.644	0.185	0.215	92.813
RRR435773	2.186	93.505	2.065	3.868	101.624
RRR435773	1.157	90.155	1.512	2.047	94.871
RRR435773	0.029	95.83	0.139	0.425	96.423
RRR435773	3.837	82.416	0.799	2.981	90.033
RRR435773	1.456	89.465	1.757	2.306	94.984
RRR435774	1.871	89.289	2.131	3.609	96.9
RRR435774	2.225	93.518	2.312	4.34	102.395
RRR435774	1.719	88.082	2.056	4.241	96.098
RRR435777	2.255	91.869	1.967	2.32	98.411
RRR435777	1.378	83.46	0.865	1.331	87.034
RRR435782	0.125	93.001	0.939	0.594	94.659
RRR435786	0.134	93.59	1.399	0.452	95.575
RRR435786	0.13	94.727	2.384	0.07	97.311
RRR435790	2.41	90.883	5.225	0.129	98.647
RRR435790	2.429	91.44	5.116	0.397	99.382
RRR435790	38.702	49.01	5.793	5.203	98.708
RRR435790	2.663	93.079	5.407	0.461	101.61
RRR435836	32.695	44.463	2.682	13.274	93.114
RRR435836	1.832	88.123	2.751	2.138	94.844
RRR435836	27.057	44.54	4.579	16.674	92.85
RRR435836	21.71	43.7	3.619	23.136	92.165
RRR435876	0.417	93.716	2.125	0.16	96.418
RRR435883	0.746	94.188	0.751	0.847	96.532
RRR435889	0.002	91.3	0.161	0.13	91.593
RRR435889	0.671	91.563	2.503	0.403	95.14

II.III Chlorite

SAMPLE	SiO2 %	TiO2 %	Al2O3 %	Cr2O3 %	MgO %
RRR435538	25.365	0.088	22.25	0.068	18.24
RRR435677	26.535	0.035	22.993	0.003	21.005
RRR435677	26.901	0.073	22.974	0.003	21.443
RRR435677	25.397	0.062	22.585	0	21.132
RRR435677	26.573	0.048	22.813	0.019	21.097
RRR435530	30.811	0.314	19.709	0.114	23.455
RRR435530	28.038	0.041	22.925	0	24.773
RRR435625	28.026	0.005	21.374	0.047	20.654
RRR435625	26.598	0.066	23.496	0	20.889
RRR435625	28.733	0.085	20.834	0.05	21.416
RRR435625	26.309	0.079	24.652	0.1	17.646
RRR435524	26.709	0.074	22.063	0.031	15.145
RRR435524	24.804	0.046	23.736	0.015	15.479
RRR435524	26.153	0.065	22.044	0.024	16.826
RRR435524	24.955	0.033	23.808	0.012	16.095
RRR435524	24.764	0.133	22.918	0.03	15.655
RRR435646	25.368	0.023	23.342	0.019	18.764
RRR435646	26.095	0.021	24.131	0	18.724
RRR435646	25.961	0	22.691	0	19.47
RRR435646	25.99	0.057	22.299	0	19.108
RRR435752	23.823	0.069	23.455	0.006	11.747
RRR435752	23.446	0.132	21.802	0.003	11.659
RRR435752	23.999	0.004	22.276	0	12.115
RRR435537	24.958	0.025	22.361	0	15.258
RRR435537	24.415	0.069	22.148	0	15.044
RRR435537	24.165	0.067	23.111	0	14.836
RRR435593	27.565	0.075	22.674	0	17.179
RRR435548	25.262	0.031	21.483	0	14.655
RRR435548	25.146	0.076	21.842	0.006	14.236
RRR435548	25.397	0.047	21.636	0.018	14.765
RRR435548	25.317	0.079	20.892	0	15.071
RRR435548	25.157	0.048	21.25	0.015	14.566
RRR435548	25.576	0.109	20.729	0.033	15.252
RRR435548	25.255	0.067	21.266	0	15.201
RRR435580	26.619	0.124	21.109	0.058	16.914
RRR435580	26.701	0.004	20.768	0.018	16.715
RRR435558	25.528	0.045	24.241	0	14.941
RRR435558	25.046	0.048	23.569	0	15.181

Appendix I : Microprobe analyses

Chlorite

SAMPLE	SiO2 %	TiO2 %	Al2O3 %	Cr2O3 %	MgO %
RRR435558	24.877	0.072	23.599	0.027	15.008
RRR435635	28.589	0.043	24.924	0.01	29.222
RRR435635	28.779	0.021	25.025	0	29.033
RRR435635	28.898	0.036	24.301	0	29.475
RRR435635	26.029	0.018	24.816	0	29.158
RRR435503	31.266	0.138	22.144	0.06	31.301
RRR435503	31.546	0.155	22.171	0.03	31.837
RRR435642	24.958	0.009	22.841	0.07	13.945
RRR435642	25.201	0.05	22.273	0.027	14.03
RRR435544	26.873	0.056	22.301	0	19.947
RRR435544	26.346	0.083	22.894	0.006	19.238
RRR435544	26.279	0.1	22.951	0	19.371
RRR435544	26.077	0.059	22.939	0.025	18.753
RRR435544	26.506	0.062	22.245	0.025	19.026
RRR435612	26.435	0.063	22.526	0.019	19.62
RRR435612	26.473	0.067	22.645	0.028	20.142
RRR435612	26.256	0.105	22.909	0.006	19.544
RRR435718	26.043	0.092	24.413	0.044	20.445
RRR435718	25.998	0.012	24.344	0.028	20.47
RRR435718	25.632	0.033	25.208	0	20.16
RRR435718	25.544	0.046	24.938	0.028	20.389
RRR435739	27.688	0.041	22.399	0	23.789
RRR435739	30.228	0.084	21.447	0.022	23.82
RRR435739	30.025	0.06	20.175	0.035	22.626
RRR435739	28.37	0.031	22.484	0.035	24.637
RRR435919	25.412	0.044	23.388	0.003	16.755
RRR435919	25.417	0.051	24.246	0	16.728
RRR435919	25.66	0.031	23.834	0	17.204
RRR435680	25.264	0.089	22.028	0.006	13.981
RRR435680	25.01	0.115	22.243	0.03	13.843
RRR435680	24.955	0.125	22.592	0	14.049
RRR435680	24.986	0.098	22.253	0	13.941
RRR435867	25.554	0.056	21.318	0	12.777
RRR435867	23.873	0.035	21.886	0.018	10.222
RRR435867	24.63	0.078	21.602	0.059	10.888
RRR435867	26.309	0.151	21.233	0.009	13.137
RRR435867	25.711	0.065	21.531	0.03	12.619
RRR435786	27.243	0.072	23.151	0	22.722
RRR435786	27.614	0.028	22.587	0.016	23.049

Appendix I : Microprobe analyses

Chlorite

SAMPLE	SiO2 %	TiO2 %	Al2O3 %	Cr2O3 %	MgO %
RRR435798	25.89	0.031	24.206	0.044	18.256
RRR435798	25.188	0.047	23.828	0	18.078
RRR435798	26.983	0.064	22.932	0.053	19
RRR435790	28.079	0.009	25.362	0	29.088
RRR435790	28.176	0.029	24.447	0.079	28.959
RRR435790	28.343	0.015	24.592	0.007	28.903
RRR435774	24.388	0.125	22.278	0	12.541
RRR435774	24.726	0.031	22.112	0.036	12.906
RRR435836	25.917	0.062	23.555	0	17.672
RRR435836	25.755	0.051	23.511	0.028	17.654
RRR435836	25.47	0.017	23.935	0.006	16.771
RRR435836	25.392	0.038	23.637	0.056	17.477
RRR435883	26.144	0.014	24.436	0	20.488
RRR435883	26.16	0.043	23.967	0	20.891
RRR435883	26.218	0.061	24.037	0	19.411
RRR435880	26.612	0.019	24.909	0.01	22.931
RRR435880	25.963	0.01	25.296	0.138	22.391
RRR435876	25.187	0.078	23.75	0.018	15.905
RRR435876	25.753	0.062	23.109	0.009	16.36
RRR435876	25.345	0.035	23.536	0.018	16.646
RRR435876	25.934	0.062	23.297	0.059	15.771
RRR435876	25.305	0.074	22.995	0.037	16.474
RRR435889	24.673	0.073	23.548	0.024	14.665
RRR435889	24.729	0.069	23.521	0	14.936
RRR435889	25.041	0.054	22.996	0.094	15.597
RRR435777	26.224	0.101	22.472	0.015	17.825
RRR435777	25.644	0.045	23.115	0.009	17.253
RRR435777	26.522	0.066	21.547	0	17.255
RRR435777	25.647	0.033	22.272	0.018	15.774
RRR435777	25.442	0.051	22.09	0.027	15.652
RRR435777	25.398	0.078	22.598	0	16.397
RRR435773	24.396	0.053	22.791	0	12.202
RRR435773	23.94	0.037	23.431	0.03	12.108
RRR435773	25.91	0.032	21.845	0.039	13.132
RRR435773	25.111	0.086	22.052	0.072	13.268
RRR435773	24.564	0.047	22.595	0.111	12.966
RRR435773	24.836	0.041	22.693	0.063	12.439
RRR435773	25.306	0.077	21.791	0.066	13.332

Appendix I : Microprobe analyses

Chlorite

SAMPLE	SiO2 %	TiO2 %	Al2O3 %	Cr2O3 %	MgO %
RRR435782	25.618	0.049	21.749	0	15.59
RRR435782	24.941	0.087	22.841	0.079	15.082
RRR435782	25.06	0.138	22.472	0.046	17.001
RRR435782	26.061	0.115	21.228	0.033	16.296

Chlorite

SAMPLE	CaO %	MnO %	FeO %	CoO %	NiO %
RRR435538	0.029	0.066	20.627	0	0.001
RRR435677	0.012	0.295	16.11	0	0
RRR435677	0.009	0.294	15.898	0	0.006
RRR435677	0.109	0.273	16.326	0.028	0.018
RRR435677	0.021	0.232	16.006	0.021	0.003
RRR435530	0.066	1.355	12.067	0.002	0
RRR435530	0.052	0.502	11.544	0	0.009
RRR435625	0.018	0.279	16.321	0	0.027
RRR435625	0	0.185	16.092	0	0.28
RRR435625	0.061	0.247	16.38	0	0.005
RRR435625	0.069	0.687	17.59	0	0.039
RRR435524	0.086	0.105	22.502	0	0.01
RRR435524	0.033	0.127	22.838	0	0.01
RRR435524	0.075	0.192	21.937	0.008	0
RRR435524	0.021	0.226	22.861	0	0.01
RRR435524	0.028	0.161	23.027	0	0.004
RRR435646	0.024	0.14	19.034	0.019	0.001
RRR435646	0.013	0.19	19.015	0	0
RRR435646	0.014	0.231	18.141	0.012	0
RRR435646	0.009	0.144	19.076	0	0
RRR435752	0.007	0.382	28.188	0	0
RRR435752	0.038	0.322	28.914	0	0
RRR435752	0.013	0.282	28.506	0	0
RRR435537	0.085	0.141	25.333	0	0.014
RRR435537	0.018	0.074	25.28	0.011	0.021
RRR435537	0.044	0.101	25.444	0.042	0.017
RRR435593	0.014	0.414	19.291	0.014	0
RRR435548	0.188	0.181	25.834	0	0
RRR435548	0.166	0.258	25.935	0	0.019
RRR435548	0.09	0.187	26.203	0.001	0

RRR435548	0.03	0.141	26.07	0	0
RRR435548	0.058	0.222	25.062	0	0.018
RRR435548	0.018	0.118	24.045	0	0.002
RRR435548	0.081	0.246	25.95	0	0
RRR435580	0.023	0.39	23.759	0	0
RRR435580	0.046	0.335	22.979	0	0.027
RRR435558	0.035	0.115	22.44	0	0.049
RRR435558	0.009	0.158	23.798	0.004	0

Appendix I : Microprobe analyses

Chlorite

SAMPLE	CaO %	MnO %	FeO %	CoO %	NiO %
RRR435558	0.081	0.037	23.967	0.014	0
RRR435635	0.011	1.042	4.265	0.001	0
RRR435635	0.021	1.002	3.939	0	0.011
RRR435635	0.003	1.055	4.17	0.003	0
RRR435635	0.179	1	3.787	0.008	0
RRR435503	0.022	0.646	2.399	0	0
RRR435503	0.017	0.555	2.081	0	0.009
RRR435642	0.015	0.161	25.654	0.009	0.02
RRR435642	0.044	0.133	25.813	0	0
RRR435544	0.084	0.276	18.564	0.008	0
RRR435544	0.111	0.292	18.405	0.006	0
RRR435544	0.006	0.353	19.051	0.014	0.019
RRR435544	0.061	0.313	18.992	0.006	0
RRR435544	0.005	0.27	19.009	0	0
RRR435612	0.025	0.653	19.152	0	0
RRR435612	0.022	0.656	17.666	0	0.017
RRR435612	0.003	0.621	18.362	0.021	0.036
RRR435718	0.007	0.331	16.214	0	0
RRR435718	0.012	0.34	16.271	0.008	0
RRR435718	0.009	0.302	16.499	0	0
RRR435718	0.014	0.35	16.282	0.023	0
RRR435739	0.044	0.823	13.045	0.032	0
RRR435739	0.078	0.682	12.452	0	0
RRR435739	0.095	1.037	14.875	0.003	0
RRR435739	0.031	0.763	12.726	0	0.001
RRR435919	0.009	0.558	21.812	0.002	0.009
RRR435919	0.016	0.497	22.229	0	0.001
RRR435919	0.015	0.477	21.35	0	0.011
RRR435680	0.013	0.457	26.378	0.008	0.011

RRR435680	0.066	0.389	26.815	0	0.048
RRR435680	0.086	0.489	25.37	0	0
RRR435680	0.028	0.491	26.342	0.014	0
RRR435867	0.055	0.126	28.25	0	0.106
RRR435867	0.031	0.181	30.819	0	0.186
RRR435867	0.007	0.147	31.008	0	0.112
RRR435867	0.013	0.235	26.173	0.005	0.034
RRR435867	0.059	0.08	27.335	0.007	0
RRR435786	0.022	0.521	14.732	0	0.015
RRR435786	0.062	0.621	14.707	0	0.005

Appendix I : Microprobe analyses

Chlorite

SAMPLE	CaO %	MnO %	FeO %	CoO %	NiO %
RRR435798	0.373	0.492	18.825	0	0.008
RRR435798	0.035	0.461	19.707	0.01	0
RRR435798	0.03	0.483	18.768	0	0.013
RRR435790	0.039	0.646	5.366	0	0.006
RRR435790	0.104	0.413	5.512	0.024	0.011
RRR435790	0.013	0.506	5.429	0	0.025
RRR435774	0.102	0.178	27.758	0	0.033
RRR435774	0.017	0.184	27.485	0	0.02
RRR435836	0	0.256	20.847	0.017	0.011
RRR435836	0.016	0.2	20.484	0.011	0
RRR435836	0.034	0.265	21.43	0	0
RRR435836	0.02	0.225	20.745	0	0
RRR435883	0.029	0.154	16.68	0.005	0.008
RRR435883	0.026	0.205	16.511	0	0
RRR435883	0.008	0.234	17.066	0.008	0
RRR435880	0.002	0.165	13.35	0	0.04
RRR435880	0.024	0.191	13.25	0	0
RRR435876	0.049	0.707	22.518	0	0
RRR435876	0.044	0.705	22.041	0.005	0
RRR435876	0	0.642	22.412	0	0.024
RRR435876	0.114	0.828	21.376	0	0
RRR435876	0.018	0.703	22.989	0.004	0
RRR435889	0.016	0.641	23.661	0.019	0.032
RRR435889	0.015	0.487	23.327	0.014	0.044
RRR435889	0.004	0.545	23.3	0	0.05
RRR435777	0.006	0.168	21.405	0	0.017
RRR435777	0.078	0.221	21.507	0	0
RRR435777	0.104	0.217	22.667	0	0.003

RRR435777	0.019	0.245	23.508	0	0
RRR435777	0	0.241	24.42	0.021	0.012
RRR435777	0.001	0.22	23.06	0	0
RRR435773	0.214	0.178	28.298	0	0
RRR435773	0.032	0.175	28.183	0	0.005
RRR435773	0.271	0.259	26.848	0	0.013
RRR435773	0.25	0.172	27.148	0	0.027
RRR435773	0.214	0.181	28.172	0	0
RRR435773	0.018	0.181	27.555	0	0
RRR435773	0.122	0.204	26.404	0	0

Appendix I : Microprobe analyses

Chlorite

SAMPLE	CaO %	MnO %	FeO %	CoO %	NiO %
RRR435782	0.25	0.337	24.064	0.002	0.01
RRR435782	0.031	0.342	25.054	0.01	0.013
RRR435782	0.03	0.195	23.842	0.026	0.038
RRR435782	0	0.362	23.859	0.001	0.034

Chlorite

SAMPLE	Na2O %	K2O %	H2O %	Total
RRR435538	0.011	0.024	11.551	98.32
RRR435677	0.021	0.022	11.896	98.927
RRR435677	0.028	0.005	12.001	99.635
RRR435677	0.042	0.006	11.685	97.663
RRR435677	0	0	11.877	98.71
RRR435530	0.019	0.267	12.296	100.475
RRR435530	0.025	0.147	12.324	100.38
RRR435625	0.076	0.029	11.883	98.739
RRR435625	0.017	0.006	11.979	99.608
RRR435625	0.006	0	12.027	99.844
RRR435625	0.058	0.043	11.841	99.113
RRR435524	0.008	0.038	11.496	98.267
RRR435524	0.036	0.029	11.483	98.636
RRR435524	0.024	0.06	11.577	98.985
RRR435524	0.006	0.006	11.6	99.633
RRR435524	0.141	0.093	11.414	98.368
RRR435646	0.054	0.022	11.666	98.476
RRR435646	0.009	0.108	11.903	100.209

RRR435646	0.045	0.025	11.695	98.285
RRR435646	0.051	0.038	11.662	98.434
RRR435752	0.05	0.019	11.197	98.943
RRR435752	0.009	0.002	10.925	97.252
RRR435752	0.035	0	11.1	98.33
RRR435537	0.004	0.006	11.449	99.634
RRR435537	0.021	0	11.289	98.39
RRR435537	0.014	0	11.383	99.224
RRR435593	0.067	0.735	11.82	99.848
RRR435548	0	0.006	11.339	98.979
RRR435548	0.017	0	11.34	99.041
RRR435548	0	0	11.421	99.765
RRR435548	0.012	0	11.318	98.93
RRR435548	0.033	0.004	11.218	97.651
RRR435548	0.057	0.042	11.227	97.208
RRR435548	0.01	0	11.383	99.459
RRR435580	0.007	0.021	11.674	100.698
RRR435580	0.042	0.034	11.539	99.208
RRR435558	0.002	0.012	11.582	98.99
RRR435558	0.006	0	11.524	99.343

Appendix I : Microprobe analyses

Chlorite

SAMPLE	Na2O %	K2O %	H2O %	Total
RRR435558	0.008	0	11.494	99.184
RRR435635	0.027	0	12.796	100.93
RRR435635	0.026	0.014	12.792	100.663
RRR435635	0	0.003	12.776	100.72
RRR435635	0.04	0.016	12.309	97.36
RRR435503	0.011	0.15	12.962	101.099
RRR435503	0.007	0.271	13.058	101.737
RRR435642	0.003	0.007	11.378	99.07
RRR435642	0.029	0.014	11.358	98.972
RRR435544	0.026	0.014	11.897	100.046
RRR435544	0.033	0.02	11.804	99.238
RRR435544	0.02	0.001	11.86	100.025
RRR435544	0.036	0.041	11.741	99.043
RRR435544	0.025	0.003	11.735	98.911
RRR435612	0.04	0.026	11.883	100.442
RRR435612	0.003	0.009	11.866	99.594
RRR435612	0.007	0.007	11.844	99.721

RRR435718	0.012	0	11.974	99.575
RRR435718	0	0	11.952	99.435
RRR435718	0.019	0.003	11.995	99.86
RRR435718	0.014	0.011	11.963	99.602
RRR435739	0.003	0	12.18	100.044
RRR435739	0.007	0.009	12.432	101.261
RRR435739	0.032	0.058	12.256	101.277
RRR435739	0	0.009	12.39	101.477
RRR435919	0.001	0	11.646	99.639
RRR435919	0.02	0.01	11.802	101.017
RRR435919	0.005	0	11.774	100.361
RRR435680	0	0.011	11.388	99.634
RRR435680	0.008	0	11.399	99.966
RRR435680	0	0.033	11.37	99.069
RRR435680	0.011	0.004	11.372	99.54
RRR435867	0.052	0.036	11.297	99.627
RRR435867	0.042	0.016	10.958	98.267
RRR435867	0.003	0	11.139	99.673
RRR435867	0.081	0.504	11.352	99.236
RRR435867	0.055	0.094	11.269	98.855
RRR435786	0	0.031	12.183	100.692
RRR435786	0.014	0.013	12.207	100.923

Appendix I : Microprobe analyses

Chlorite

SAMPLE	Na2O %	K2O %	H2O %	Total
RRR435798	0.051	0.035	11.867	100.078
RRR435798	0.048	0.024	11.694	99.12
RRR435798	0.06	0.019	11.926	100.331
RRR435790	0.007	0	12.804	101.406
RRR435790	0.007	0.004	12.677	100.442
RRR435790	0.002	0.001	12.703	100.539
RRR435774	0.043	0.014	11.188	98.648
RRR435774	0	0.005	11.227	98.749
RRR435836	0.006	0	11.787	100.13
RRR435836	0.01	0.002	11.723	99.445
RRR435836	0.024	0	11.693	99.645
RRR435836	0.035	0.006	11.681	99.312
RRR435883	0.024	0	12.01	99.992
RRR435883	0.018	0.012	11.988	99.821
RRR435883	0.015	0.002	11.862	98.922
RRR435880	0.017	0.037	12.239	100.331

RRR435880	0.007	0.033	12.122	99.425
RRR435876	0.087	0.04	11.634	99.973
RRR435876	0.047	0.061	11.652	99.848
RRR435876	0.017	0.002	11.695	100.372
RRR435876	0.089	0.033	11.611	99.174
RRR435876	0.025	0.007	11.638	100.269
RRR435889	0.022	0	11.427	98.801
RRR435889	0.034	0.022	11.432	98.63
RRR435889	0.049	0	11.498	99.228
RRR435777	0.015	0	11.736	99.984
RRR435777	0.069	0.014	11.675	99.63
RRR435777	0.003	0.011	11.67	100.065
RRR435777	0.038	0.025	11.496	99.075
RRR435777	0.051	0.034	11.488	99.529
RRR435777	0	0.005	11.547	99.304
RRR435773	0.046	0.012	11.261	99.451
RRR435773	0.011	0.006	11.241	99.199
RRR435773	0.003	0.001	11.401	99.754
RRR435773	0	0.011	11.338	99.535
RRR435773	0.02	0.006	11.357	100.233
RRR435773	0.021	0	11.283	99.13
RRR435773	0.012	0.014	11.275	98.603

Appendix I : Microprobe analyses

Chlorite

SAMPLE	Na2O %	K2O %	H2O %	Total
RRR435782	0.023	0.001	11.455	99.148
RRR435782	0.002	0.001	11.502	99.985
RRR435782	0.015	0.003	11.621	100.487
RRR435782	0.009	0	11.518	99.516

II.IV Epidote

SAMPLE	SiO2 %	TiO2 %	Al2O3 %	La2O3 %	Ce2O3 %
RRR435612	37.603	0.105	26.744	0	0.055
RRR435739	39.816	0.078	31.513	0	0
RRR435739	39.877	0	30.975	0	0.002
RRR435680	34.157	0.022	22.66	0	0
RRR435680	38.655	0.055	25.61	0.031	0.035
RRR435680	38.601	0.121	25.676	0	0
RRR435680	38.766	0.033	25.61	0.024	0.015
RRR435680	38.465	0.099	25.467	0.095	0.022
RRR435680	37.692	0.132	27.156	0.002	0.071
RRR435867	38.659	0.193	24.767	0.017	0
RRR435798	39.042	0.133	28.073	0.031	0.007
RRR435798	39.171	0	28.026	0	0.038
RRR435798	39.204	0.039	28.021	0.12	0.013
RRR435836	38.147	0.067	25.851	0	0
RRR435836	38.637	0.1	25.531	0	0
RRR435836	38.308	0.017	26.535	0	0
RRR435836	38.803	0.028	25.542	0	0
RRR435836	38.676	0.05	25.458	0.031	0.033
RRR435883	39.28	0.045	28.471	0.012	0
RRR435883	39.19	0.179	29.233	0	0
RRR435883	39.225	0.05	28.121	0	0
RRR435883	39.514	0.156	29.674	0	0
RRR435883	39.072	0.056	27.719	0	0.049
RRR435883	36.084	0.049	24.178	2.279	4.179
RRR435883	38.72	0.117	28.324	0.06	0.069
RRR435880	39.089	0	29.007	0	0
RRR435880	39.278	0	28.862	0.005	0.004
RRR435876	38.127	0.05	26.377	0.036	0
RRR435876	39.023	0	26.643	0	0
RRR435876	38.73	0.105	26.793	0.043	0.018
RRR435876	38.314	0	26.425	0.046	0
RRR435876	38.749	0.033	26.578	0.019	0.131
RRR435889	38.262	0	26.275	0.012	0.047
RRR435889	37.459	0.05	25.699	0.13	0.272
RRR435773	38.609	0.017	25.389	0	0.033
RRR435773	38.493	0	25.489	0	0
RRR435773	38.482	0.11	26.183	0.036	0
RRR435773	38.615	0.077	25.772	0.024	0

Appendix I : Microprobe analyses

Epidote

SAMPLE	SiO2 %	TiO2 %	Al2O3 %	La2O3 %	Ce2O3 %
RRR435773	38.54	0.039	25.82	0	0.02
RRR435773	38.656	0	26.012	0	0
RRR435773	38.49	0.331	25.749	0.022	0.027
RRR435782	38.475	0.11	26.022	0	0
RRR435782	38.309	0.044	25.831	0.038	0.011
RRR435782	38.983	0	26.049	0.05	0.053
RRR435782	38.412	0.116	25.74	0.055	0
RRR435782	33.782	0.048	21.649	3.074	6.655

Appendix I : Microprobe analyses

Epidote

SAMPLE	MgO %	CaO %	MnO %	FeO %	Na2O %
RRR435612	0.049	23.166	0.797	8.143	0.012
RRR435739	0.024	24.323	0.647	2.948	0.005
RRR435739	0.01	24.299	0.182	3.391	0.011
RRR435680	0.059	26.874	0.594	9.31	0.032
RRR435680	0.041	23.125	0.686	10.016	0
RRR435680	0.012	23.233	0.458	9.571	0
RRR435680	0.012	23.244	0.5	9.881	0.006
RRR435680	0.045	22.771	0.825	9.467	0.003
RRR435680	0.009	23.392	0.561	8.6	0.013
RRR435867	0.02	23.117	0.113	11.059	0.034
RRR435798	0.056	23.559	0.572	6.749	0
RRR435798	0.048	23.34	0.532	6.943	0.014
RRR435798	0.03	23.363	0.48	7.011	0
RRR435836	0.101	22.649	0.387	8.774	0.329
RRR435836	0.067	23.201	0.291	9.051	0.034
RRR435836	0.065	22.852	0.283	9.054	0.066
RRR435836	0.036	23.527	0.254	10.06	0.009
RRR435836	0.036	23.468	0.289	9.528	0.015
RRR435883	0.036	24.095	0.152	6.195	0.012
RRR435883	0.027	24.006	0.15	5.315	0.029
RRR435883	0.067	24.016	0.192	6.888	0
RRR435883	0.022	24.259	0.092	5.524	0.016
RRR435883	0.048	24.054	0.174	6.753	0.005
RRR435883	0.246	19.157	0.151	8.176	0.027
RRR435883	0.06	23.978	0.219	6.414	0.039
RRR435880	0.024	24.035	0.062	5.894	0.015

RRR435880	0.027	23.992	0.214	5.711	0.002
RRR435876	0.173	20.972	1.012	8.416	0.009
RRR435876	0.031	23.526	0.54	8.215	0
RRR435876	0.024	23.31	0.549	8.432	0.007
RRR435876	0.028	23.324	0.56	8.386	0.03
RRR435876	0.037	23.073	0.627	8.077	0
RRR435889	0.122	21.552	0.515	8.688	0.016
RRR435889	0.14	19.826	0.506	8.165	0.057
RRR435773	0.064	23.203	0.367	9.836	0.01
RRR435773	0.035	23.273	0.392	9.832	0.003
RRR435773	0.088	23.047	0.537	9.144	0.012
RRR435773	0.019	23.398	0.384	9.815	0.002

Appendix I : Microprobe analyses

Epidote

SAMPLE	MgO %	CaO %	MnO %	FeO %	Na2O %
RRR435773	0.025	23.673	0.279	8.955	0.023
RRR435773	0.032	23.593	0.232	9.268	0.027
RRR435773	0.065	23.06	0.534	9.208	0.006
RRR435782	0.01	23.423	0.184	9.186	0.039
RRR435782	0.014	23.714	0.259	9.044	0.022
RRR435782	0.009	23.469	0.278	8.844	0.024
RRR435782	0.08	22.795	0.728	9.543	0.017
RRR435782	0.145	15.611	0.173	9.953	0.047

Appendix I : Microprobe analyses

Epidote

SAMPLE	K2O %	H2O %	Cl %	Total
RRR435612	0	1.859	0.002	98.535
RRR435739	0.006	1.971	0.01	101.341
RRR435739	0.016	1.96	0.007	100.73
RRR435680	0.011	1.743	0.013	95.475
RRR435680	0.006	1.874	0.013	100.147
RRR435680	0.011	1.872	0	99.555
RRR435680	0	1.874	0.012	99.977
RRR435680	0	1.862	0.002	99.123
RRR435680	0.003	1.874	0.005	99.51
RRR435867	0.012	1.866	0.001	99.858
RRR435798	0.003	1.909	0.01	100.144
RRR435798	0	1.907	0.013	100.032
RRR435798	0.006	1.902	0.038	100.227
RRR435836	0.362	1.804	0.202	98.673
RRR435836	0.016	1.861	0.01	98.799
RRR435836	0	1.869	0.009	99.058
RRR435836	0.007	1.879	0	100.145
RRR435836	0.003	1.87	0	99.457
RRR435883	0.004	1.919	0.006	100.227
RRR435883	0	1.922	0.02	100.071
RRR435883	0	1.917	0.008	100.484
RRR435883	0.002	1.948	0	101.207
RRR435883	0.007	1.904	0.005	99.846
RRR435883	0.015	1.754	0.008	96.303
RRR435883	0.013	1.904	0.02	99.937
RRR435880	0.015	1.921	0.005	100.067
RRR435880	0.004	1.922	0.002	100.023
RRR435876	0.014	1.841	0.004	97.031
RRR435876	0	1.889	0.011	99.878
RRR435876	0	1.89	0	99.901
RRR435876	0.006	1.869	0.002	98.99
RRR435876	0.002	1.879	0	99.205
RRR435889	0.01	1.847	0	97.346
RRR435889	0.005	1.785	0.028	94.122
RRR435773	0.01	1.865	0.006	99.409
RRR435773	0	1.864	0.008	99.389
RRR435773	0	1.874	0.005	99.518
RRR435773	0	1.876	0.005	99.987

Appendix I : Microprobe analyses

Epidote

SAMPLE	K2O %	H2O %	Cl %	Total
RRR435773	0.013	1.869	0.007	99.263
RRR435773	0.009	1.876	0.009	99.714
RRR435773	0	1.87	0.005	99.367
RRR435782	0.008	1.87	0.01	99.337
RRR435782	0	1.862	0.015	99.163
RRR435782	0	1.882	0	99.641
RRR435782	0.007	1.865	0.009	99.367
RRR435782	0.002	1.639	0.002	92.78

II.V Feldspar

SAMPLE	SiO2 %	TiO2 %	Al2O3 %	MgO %	CaO %	MnO %
RRR435544	60.981	0	25.009	0	6.305	0.006
RRR435544	84.425	0	9.366	0.008	0.621	0
RRR435544	67.214	0.017	20.616	0.007	0.914	0
RRR435548	67.893	0	20.402	0.004	0.691	0
RRR435548	62.472	0.089	24.387	0.006	5.599	0.003
RRR435548	67.429	0	20.602	0.011	0.778	0.032
RRR435580	67.767	0.017	20.817	0.023	0.873	0.029
RRR435580	68.836	0.039	20.717	0	0.249	0
RRR435642	53.241	0.034	30.311	0.006	12.455	0.022
RRR435642	54.889	0	29.237	0.001	11.042	0
RRR435677	55.963	0	28.329	0.007	10.121	0
RRR435718	56.46	0.094	27.595	0	9.261	0.026
RRR435773	62.575	0.066	24.751	0.013	5.003	0
RRR435777	61.346	0.028	24.467	0.009	5.663	0.003
RRR435777	63.083	0.017	24.006	0.002	4.679	0
RRR435777	63.041	0.056	23.638	0.019	4.49	0.013
RRR435782	61.014	0	25.01	0.001	6.204	0
RRR435782	61.956	0	24.674	0.014	5.567	0
RRR435782	61.098	0.022	24.775	0.008	5.765	0.045
RRR435798	61.415	0	24.871	0.002	5.967	0
RRR435867	53.035	0.017	30.575	0.013	12.52	0
RRR435867	53.385	0	29.875	0.004	12.437	0
RRR435867	67.237	0	21.747	0.033	0.813	0.013
RRR435867	61.589	0.051	24.797	0.011	5.785	0
RRR435867	59.301	0.011	26.512	0.005	8.024	0
RRR435867	63.88	0.017	23.425	0.006	4.212	0
RRR435867	58.067	0.089	27.063	0.011	8.829	0
RRR435883	54.452	0	29.142	0.005	11.406	0
RRR435889	58.235	0.051	26.635	0.001	7.924	0
RRR435919	56.373	0	27.854	0	9.629	0.026

Appendix I : Microprobe analyses

Feldspar

SAMPLE	FeO %	SrO %	BaO %	Na2O %	K2O %	Total
RRR435544	0.005	0.235	0.043	8.27	0.033	100.887
RRR435544	0.031	0.096	0	5.311	0.023	99.881
RRR435544	0.08	0.098	0	10.917	0.103	99.966
RRR435548	0.021	0.069	0.004	10.983	0.05	100.117
RRR435548	0.004	0.165	0	8.617	0.07	101.412
RRR435548	0.15	0.2	0.005	10.94	0.243	100.39
RRR435580	0.031	0	0.009	11.419	0.025	101.01
RRR435580	0.032	0.095	0	11.502	0.03	101.5
RRR435642	0.007	0.168	0.025	4.722	0.033	101.024
RRR435642	0.05	0.187	0	5.357	0.032	100.795
RRR435677	0.059	0.23	0.013	5.992	0.04	100.754
RRR435718	0.02	0.19	0	6.419	0.026	100.091
RRR435773	0.242	0.146	0.032	8.58	0.078	101.486
RRR435777	0.016	0.311	0	8.486	0.03	100.359
RRR435777	0.018	0.248	0.02	8.82	0.036	100.929
RRR435777	0.006	0.348	0	9.262	0.02	100.893
RRR435782	0.01	0.311	0.027	8.275	0.033	100.885
RRR435782	0.013	0.394	0	8.386	0.039	101.043
RRR435782	0	0.305	0	8.271	0.04	100.329
RRR435798	0.023	0.279	0	8.407	0.035	100.999
RRR435867	0.023	0.108	0.011	4.601	0.019	100.922
RRR435867	0.01	0.117	0.011	4.546	0.039	100.424
RRR435867	0.094	0.095	0.023	10.492	0.231	100.778
RRR435867	0.097	0.106	0.009	8.22	0.043	100.708
RRR435867	0.056	0.189	0	7.178	0.052	101.328
RRR435867	0	0.178	0	8.856	0.026	100.6
RRR435867	0.31	0.11	0	6.71	0.061	101.25
RRR435883	0.069	0.197	0	5.268	0.028	100.567
RRR435889	0.096	0.12	0.07	7.176	0.056	100.364
RRR435919	0.156	0.197	0	6.287	0.022	100.544

II.VI Garnet

SAMPLE	SiO2 %	TiO2 %	ZrO2 %	Y2O3 %	Al2O3 %
RRR435530	36.565	0.071	0	0.012	21.891
RRR435530	37.324	0.275	0.022	0.007	20.962
RRR435530	37.097	0.26	0.01	0.028	20.952
RRR435530	37.522	0.071	0	0.002	21.069
RRR435530	36.99	0.294	0	0	20.611
RRR435752	34.297	0.092	0.026	0	19.233
RRR435752	36.769	0.132	0.024	0.005	20.78
RRR435593	36.082	0.156	0.01	0.066	21.032
RRR435593	36.568	0.091	0	0	20.939
RRR435593	36.774	0.076	0	0	20.649
RRR435593	36.717	0.066	0	0.023	20.599
RRR435739	37.215	0.421	0	0.01	20.683
RRR435739	37.396	0.218	0.001	0	20.831
RRR435680	37.598	0.268	0	0.051	20.756
RRR435786	37.396	0.181	0.007	0	20.755

SAMPLE	Cr2O3 %	FeO %	Fe2O3 %	MnO %	MgO %
RRR435530	0.003	5.609	0	28.485	1.612
RRR435530	0	6.287	0	28.042	1.634
RRR435530	0.046	7.933	0	25.399	1.799
RRR435530	0.018	6.397	0	26.335	1.608
RRR435530	0.021	5.572	0	29.338	1.7
RRR435752	0.032	24.839	1.456	8.916	0.969
RRR435752	0.047	28.558	0.139	8.592	1.528
RRR435593	0.042	14.898	0	21.553	1.429
RRR435593	0.024	20.349	0	15.836	1.98
RRR435593	0	14.763	0.152	20.841	1.505
RRR435593	0	14.544	0.231	20.935	1.536
RRR435739	0	8.93	0.541	26.39	1.657
RRR435739	0.003	9.31	0.542	26.285	1.578
RRR435680	0	24.085	0.932	8.745	1.223
RRR435786	0	11.076	0.69	25.982	1.709

Appendix I : Microprobe analyses

Garnet

SAMPLE	CaO %	Na2O %	Total
RRR435530	3.039	0.025	97.570
RRR435530	3.927	0.016	98.496
RRR435530	4.696	0.016	98.236
RRR435530	5.916	0.013	99.048
RRR435530	3.588	0.031	98.145
RRR435752	6.98	0	96.859
RRR435752	3.685	0.013	100.272
RRR435593	3.059	0.003	98.354
RRR435593	3.542	0.029	99.358
RRR435593	4.161	0.02	98.957
RRR435593	4.259	0.014	98.924
RRR435739	5.357	0.026	101.230
RRR435739	5.2	0	101.372
RRR435680	8.478	0.005	102.147
RRR435786	3.793	0.018	101.657

II.VII Muscovite

SAMPLE	SiO2 %	TiO2 %	Al2O3 %	FeO%	MnO %	MgO %
RRR435503	47.647	0.751	36.358	0.262	0	1.329
RRR435503	47.516	0.26	36.684	0.476	0.025	1.007
RRR435503	47.117	0.461	36.421	0.262	0.028	1.42
RRR435503	44.44	0	30.9	0.725	0.213	11.223
RRR435524	46.046	0.31	35.437	1.792	0	0.642
RRR435524	46.035	0.288	35.587	1.652	0	0.553
RRR435524	45.306	0.148	36.401	1.347	0	0.491
RRR435524	47.773	0.192	32.219	2.582	0.012	1.49
RRR435530	46.286	0.244	34.277	1.384	0.059	2.159
RRR435530	47.06	0.022	35.425	0.921	0.044	1.232
RRR435530	48.431	0.275	31.635	0.817	0.043	1.269
RRR435537	45.346	0.309	34.755	2.649	0	0.764
RRR435537	46.782	0.192	31.952	3.69	0.023	2.341
RRR435538	46.632	0.156	34.406	1.912	0	1.049
RRR435538	46.344	0	35.607	1.953	0	0.804
RRR435538	46.341	0.134	35.613	1.63	0.011	0.726
RRR435538	45.599	0.007	35.479	1.413	0.021	0.63
RRR435538	45.949	0.015	35.262	1.515	0.008	0.771
RRR435538	45.999	0.171	35.358	1.631	0.014	0.792
RRR435544	46.986	0.163	36.533	1.577	0.009	0.903
RRR435544	47.406	0.35	34.517	1.956	0	1.295
RRR435544	45.094	0.305	35.804	1.632	0.023	1.005
RRR435544	46.834	0.409	35.242	1.684	0	1.288
RRR435548	45.592	0.081	34.87	2.398	0.018	0.617
RRR435548	46.41	0.251	34.181	2.518	0.004	0.902
RRR435548	46.337	0.333	33.893	2.323	0	1.045
RRR435548	46.849	0.215	33.891	2.094	0.043	0.896
RRR435548	45.934	0.17	33.695	2.569	0.012	0.882
RRR435558	33.923	0	48.714	0.185	0	0.09
RRR435558	47.881	0.2	34.941	1.578	0.001	0.917
RRR435558	44.496	0.327	37.428	1.754	0.036	0.697
RRR435580	47.112	0.481	35.409	2.5	0.001	0.867
RRR435580	46.824	0.296	34.004	2.988	0.026	1.116
RRR435580	46.369	0.452	34.754	2.634	0	1.055
RRR435580	46.693	0.289	36.215	2.566	0.002	0.823
RRR435580	46.818	0.392	34.36	2.97	0	1.157
RRR435593	47.571	0.215	32.655	1.704	0.009	1.66
RRR435593	46.453	0.141	35.084	1.72	0.004	0.968

Appendix I : Microprobe analyses

Muscovite

SAMPLE	SiO2 %	TiO2 %	Al2O3 %	FeO%	MnO %	MgO %
RRR435593	46.493	0.133	33.458	2.476	0.042	1.755
RRR435593	46.908	0.207	33.896	1.658	0.009	1.334
RRR435593	43.937	0	33.921	0.709	0.031	0.944
RRR435604	46.204	0.289	35.962	0.885	0	0.727
RRR435604	45.984	0.193	35.649	0.809	0.003	0.73
RRR435604	46.723	0.385	36.191	0.819	0	0.825
RRR435604	46.907	0.252	35.903	0.885	0.021	0.792
RRR435604	46.262	0.356	34.953	0.841	0.009	1.082
RRR435612	46.86	0.045	38.166	1.106	0.004	0.419
RRR435612	47.484	0.022	37.501	0.681	0.021	0.406
RRR435612	46.979	0.439	35.067	1.67	0	1.235
RRR435612	47.073	0	35.504	1.539	0.013	1.22
RRR435612	47.782	0.394	35.901	1.447	0	1.157
RRR435625	46.067	0.059	35.339	2.073	0.005	1.912
RRR435625	46.269	0.296	36.225	1.21	0.016	0.651
RRR435625	47.985	0.23	35.127	0.702	0.001	0.944
RRR435625	46.466	0.215	36.05	0.743	0.002	0.727
RRR435625	46.738	0.473	35.126	1.109	0	1.109
RRR435635	46.47	0.127	37.647	0.189	0.028	0.642
RRR435635	47.577	0.179	36.039	0.369	0.022	1.078
RRR435635	47.552	0.127	36.979	0.365	0.009	0.872
RRR435642	46.782	0.112	36.963	1.223	0	0.491
RRR435642	47.317	0.334	34.817	2.058	0	1.116
RRR435642	47.181	0.283	36.43	1.346	0.009	0.694
RRR435646	46.96	0	36.367	1.347	0.009	0.72
RRR435646	47.865	0	35.443	0.889	0	0.715
RRR435646	47.497	0.289	33.15	1.436	0	1.375
RRR435646	46.167	0.111	35.949	0.923	0	0.607
RRR435646	46.391	0.333	34.943	1.609	0	0.985
RRR435646	46.919	0.126	36.285	1.24	0	0.66
RRR435660	46.268	0.015	34.796	1.552	0.026	1.036
RRR435677	46.895	0.384	34.478	1.664	0	1.169
RRR435677	47.309	0.14	35.125	1.254	0.002	1.03
RRR435677	47.225	0.318	33.654	1.776	0	1.438
RRR435677	46.503	0.236	35.639	1.344	0	0.714
RRR435680	46.879	0.081	35.78	2.77	0.003	0.59
RRR435680	46.04	0.199	34.4	3.426	0.002	0.827
RRR435718	46.587	0.253	36.31	1.19	0.011	0.805
RRR435718	46.966	0.283	37.399	0.837	0.01	0.839

Appendix I : Microprobe analyses

Muscovite

SAMPLE	SiO2 %	TiO2 %	Al2O3 %	FeO%	MnO %	MgO %
RRR435718	45.224	0.261	36.423	1.245	0	0.867
RRR435718	46.451	0.328	36.148	0.958	0	0.719
RRR435739	51.455	0.03	31.313	0.949	0.1	3.143
RRR435739	54.021	0	30.146	0.354	0.071	1.322
RRR435739	46.69	0.149	36.619	1.187	0	1.058
RRR435739	48.895	0.245	34.238	1.259	0.028	2.358
RRR435739	47.075	0.394	34.771	1.55	0.063	1.745
RRR435752	46.085	0.155	34.659	2.376	0.007	0.647
RRR435752	43.177	0.045	34.066	2.036	0.001	0.531
RRR435752	45.036	0.237	34.599	2.588	0.006	0.679
RRR435752	45.383	0.281	34.437	2.598	0	0.695
RRR435773	45.824	0.303	34.099	2.956	0.016	0.923
RRR435774	47.376	0.311	32.204	3.035	0	1.244
RRR435777	47.168	0.281	34.331	2.847	0	1.145
RRR435777	47.654	0.237	34.54	2.215	0	1.118
RRR435777	46.813	0.519	34.881	2.181	0.04	1.113
RRR435777	47.124	0.022	35.751	2.151	0	0.803
RRR435782	45.868	0.259	35.04	2.47	0.004	0.931
RRR435782	46.54	0.104	34.843	2.41	0	1.013
RRR435786	46.923	0.17	37.403	0.666	0.011	0.426
RRR435786	46.948	0.007	36.995	1.317	0.008	0.791
RRR435786	47.602	0.186	34.155	1.353	0.013	1.848
RRR435786	47.33	0.007	36.316	1.187	0.011	1.139
RRR435790	47.058	0.363	37.189	0.27	0.035	1.002
RRR435790	47.496	0.423	36.449	0.229	0.009	1.143
RRR435790	47.089	0.23	37.621	0.323	0.011	0.638
RRR435790	47.644	0.282	36.175	0.45	0.003	1.308
RRR435790	47.045	0.193	37.198	0.307	0.028	0.722
RRR435798	48.367	0.06	36.031	1.057	0	0.624
RRR435798	46.762	0.067	37.411	1.104	0.025	0.487
RRR435798	34.084	0.007	48.878	0.135	0	0.1
RRR435836	46.758	0.335	35.772	2.556	0.031	0.529
RRR435867	46.801	0.401	33.952	2.436	0.016	1.197
RRR435867	46.835	0.542	34.538	2.513	0.01	1.041
RRR435867	45.465	0.871	34.36	2.548	0.001	0.906
RRR435867	46.799	0.163	34.681	2.735	0	1.043
RRR435876	46.883	0.112	37.023	1.727	0	0.569
RRR435876	47.432	0.335	35.349	1.654	0.029	1.035
RRR435880	47.099	0.336	36.191	1.275	0	1.104

Appendix I : Microprobe analyses

Muscovite

SAMPLE	SiO2 %	TiO2 %	Al2O3 %	FeO%	MnO %	MgO %
RRR435880	47.178	0.537	35.99	0.867	0	0.848
RRR435880	47.021	0.298	37.216	0.765	0	0.693
RRR435883	46.998	0.223	37.054	1.098	0	0.757
RRR435883	49.078	0	35.18	1.044	0.021	1.419
RRR435883	47.855	0.454	35.932	1.463	0.009	1.015
RRR435889	45.955	0.305	35.647	1.38	0.041	0.561
RRR435889	45.858	0.216	37.163	1.28	0	0.895
RRR435889	47.165	0.178	36.798	1.7	0.002	0.571
RRR435919	46.654	0.201	36.939	1.291	0.005	0.579
RRR435919	46.619	0.208	37.265	1.388	0	0.605
RRR435919	47.518	0.141	36.252	1.244	0.019	0.741

Appendix I : Microprobe analyses

Muscovite

SAMPLE	CaO %	Na2O %	K2O %	BaO %	Rb2O %	F %
RRR435503	0.015	0.77	9.513	0	0	0.335
RRR435503	0.009	0.65	9.093	0.201	0	0.21
RRR435503	0.008	0.68	9.525	0	0	0.249
RRR435503	0.017	0.461	6.405	0.031	0	0.211
RRR435524	0.018	0.742	10.169	0.226	0	0.147
RRR435524	0.021	0.767	9.849	0.034	0	0.061
RRR435524	0.803	1.056	9.303	0.108	0	0
RRR435524	0.038	0.648	10.356	0.175	0	0.074
RRR435530	0.061	0.282	9.89	0	0	0.307
RRR435530	0.07	0.25	10.597	0.058	0	0.099
RRR435530	0.017	0.243	9.86	0.036	0	0.135
RRR435537	0.052	0.504	10.175	1.234	0	0.172
RRR435537	0.008	0.255	9.808	0.041	0	0.086
RRR435538	0.041	0.452	10.638	0.145	0	0.025
RRR435538	0.11	0.483	10.365	0.118	0	0.148
RRR435538	0.029	0.505	10.532	0.046	0	0
RRR435538	0.059	0.603	10.372	0.169	0	0
RRR435538	0	0.561	10.6	0.029	0	0.049
RRR435538	0.029	0.524	10.528	0.188	0	0.086
RRR435544	0.01	0.365	9.32	0.094	0	0.31
RRR435544	0.075	0.263	8.421	0.022	0	0.37
RRR435544	0.012	0.308	9.427	0.082	0	0.32
RRR435544	0.11	0.3	8.855	0.065	0	0.273

RRR435548	0.019	0.422	10.418	0.298	0	0.208
RRR435548	0.033	0.426	10.632	0.386	0	0.257
RRR435548	0.027	0.303	10.583	0.12	0	0.061
RRR435548	0	0.343	10.073	0.303	0	0.148
RRR435548	0.018	0.363	10.657	0.257	0	0.195
RRR435558	11.088	1.032	0.698	0.056	0	0.346
RRR435558	0.01	0.496	9.524	0.421	0	0
RRR435558	1.733	0.476	7.607	0.301	0	0.309
RRR435580	0.032	0.305	8.888	0.159	0	0.196
RRR435580	0.017	0.506	9.328	0.226	0	0.281
RRR435580	0.044	0.298	9.041	0.392	0	0.173
RRR435580	0.01	0.348	8.743	0.211	0	0.236
RRR435580	0.011	0.394	9.402	0.149	0	0.273
RRR435593	0.054	0.216	10.321	0.07	0	0.27
RRR435593	0.012	0.33	10.696	0.091	0	0.085

Appendix I : Microprobe analyses

Muscovite

SAMPLE	CaO %	Na2O %	K2O %	BaO %	Rb2O %	F %
RRR435593	0.026	0.286	10.269	0	0	0.11
RRR435593	0.017	0.268	10.548	0.07	0	0
RRR435593	3.75	0.17	9.476	0.106	0	0.232
RRR435604	0.019	0.339	10.538	0.176	0	0.06
RRR435604	0.047	0.29	10.453	0.157	0	0
RRR435604	0.076	0.325	10.335	0.048	0	0.048
RRR435604	0.015	0.343	10.352	0.022	0.007	0
RRR435604	0.331	0.316	10.36	0.002	0	0.037
RRR435612	0.041	0.319	9.29	0.106	0	0
RRR435612	0.053	0.32	9.206	0.179	0	0.209
RRR435612	0.025	0.237	8.724	0.046	0	0.124
RRR435612	0.212	0.384	9.2	0.075	0	0.332
RRR435612	0.015	0.271	9.442	0	0	0.135
RRR435625	0.014	0.702	9.215	0.094	0	0.098
RRR435625	0.081	0.782	9.864	0.166	0	0.185
RRR435625	0.039	0.694	9.364	0.159	0	0.049
RRR435625	0.089	0.862	9.867	0.077	0	0
RRR435625	0.01	0.69	10.014	0.072	0	0.209
RRR435635	1.849	1.752	6.559	0.191	0	0.434
RRR435635	0.032	1.017	9.156	0.165	0	0.222
RRR435635	0.044	0.972	9.24	0.082	0	0.199
RRR435642	0.034	0.566	8.932	0.135	0	0.347

RRR435642	0.064	0.393	8.726	0.125	0	0.062
RRR435642	0.044	0.517	8.5	0.085	0	0.282
RRR435646	0.093	0.737	9.855	0.295	0	0.049
RRR435646	0.014	0.733	9.967	0.149	0	0.26
RRR435646	0.052	0.403	9.703	0.147	0.007	0.159
RRR435646	0.193	0.823	9.884	0.219	0	0.256
RRR435646	0.018	0.673	9.817	0.12	0	0.231
RRR435646	0.022	0.743	9.879	0.221	0	0
RRR435660	0.017	0.924	9.464	0.772	0	0
RRR435677	0.024	0.954	9.789	0.379	0	0.321
RRR435677	0.002	1.061	9.607	0.185	0	0.391
RRR435677	0.008	0.874	9.926	0.101	0	0.359
RRR435677	0.094	1.285	9.455	0.259	0	0.327
RRR435680	0.02	0.329	9.015	0.235	0	0.2
RRR435680	0.045	0.528	8.52	0.237	0	0.285
RRR435718	0.205	0.95	9.134	0.075	0	0.396
RRR435718	0.813	0.67	7.98	0.087	0	0.074

Appendix I : Microprobe analyses

Muscovite

SAMPLE	CaO %	Na2O %	K2O %	BaO %	Rb2O %	F %
RRR435718	0.017	0.719	8.597	0.102	0	0.196
RRR435718	0.148	0.895	9.206	0.131	0	0.147
RRR435739	0.03	0.005	9.219	0.094	0	0.198
RRR435739	1.181	1.975	7.167	0.005	0	0.136
RRR435739	0.006	0.298	9.476	0.116	0	0.256
RRR435739	0	0.202	9.175	0.077	0	0.149
RRR435739	0.044	0.285	9.339	0.459	0	0.161
RRR435752	0.022	0.613	10.001	0.072	0	0.11
RRR435752	2.131	0.566	10.115	0	0	0.282
RRR435752	0.058	0.511	9.8	0.014	0	0.185
RRR435752	0.01	0.605	10.467	0.01	0	0.147
RRR435773	0.035	0.303	9.519	0.543	0	0.025
RRR435774	0.022	0.225	8.532	0.277	0	0.197
RRR435777	0.036	0.348	8.679	0.212	0	0.38
RRR435777	0.025	0.338	8.946	0.185	0	0.222
RRR435777	0.01	0.305	8.961	0.176	0	0.134
RRR435777	0.018	0.409	9.297	0.116	0	0.369
RRR435782	0.015	0.411	9.205	0.671	0	0.086
RRR435782	0.056	0.428	8.896	0.503	0	0.16
RRR435786	0.018	0.332	8.913	0.094	0	0.187
RRR435786	0.011	0.407	9.597	0.026	0	0.249

RRR435786	0.1	0.353	8.074	0.012	0	0.112
RRR435786	0.07	0.402	9.4	0.055	0	0.374
RRR435790	0.47	0.627	8.76	0.051	0	0.236
RRR435790	0.037	0.575	8.892	0	0	0.297
RRR435790	0.031	0.672	9.211	0.123	0	0.236
RRR435790	0.017	0.554	9.39	0	0	0.099
RRR435790	0.126	0.712	8.933	0	0	0.223
RRR435798	0.025	0.581	8.045	0.276	0	0.1
RRR435798	0.18	0.722	8.632	0.266	0	0.41
RRR435798	10.053	1.511	0.758	0.002	0	0.422
RRR435836	0.115	0.637	8.105	0.053	0	0.368
RRR435867	0.016	0.57	9.155	0.224	0	0.273
RRR435867	0.028	0.412	9.035	0.35	0	0.359
RRR435867	0.047	0.573	8.583	0.222	0	0.408
RRR435867	0.051	0.44	9.008	0.537	0.001	0.186
RRR435876	0.026	0.524	8.615	0.116	0	0.208
RRR435876	0.02	0.45	8.916	0.075	0	0.377
RRR435880	0.007	0.627	8.9	0	0	0.207

Appendix I : Microprobe analyses

Muscovite

SAMPLE	CaO %	Na2O %	K2O %	BaO %	Rb2O %	F %
RRR435880	0.008	0.666	10.054	0.024	0	0.343
RRR435880	0.055	0.599	8.847	0.216	0	0.244
RRR435883	0.062	0.546	7.931	0.643	0	0.257
RRR435883	0.054	0.545	8.438	0.44	0	0.254
RRR435883	0.013	0.511	8.063	0.406	0	0.28
RRR435889	0.028	0.686	8.602	0.164	0	0.16
RRR435889	0.993	0.754	7.497	0	0	0.149
RRR435889	0.018	0.734	7.958	0.058	0	0.123
RRR435919	0.013	1.419	8.306	0.017	0	0.087
RRR435919	0.004	1.343	8.434	0.089	0	0.161
RRR435919	0.078	1.277	8.578	0.099	0	0.137

Appendix I : Microprobe analyses

Muscovite

SAMPLE	Cl %	Cr2O3 %	NiO %
RRR435503	0.005	0.095	0.013
RRR435503	0.013	0.059	0.022
RRR435503	0	0	0
RRR435503	0.013	0.023	0.054
RRR435524	0.008	0.09	0.009
RRR435524	0.005	0	0
RRR435524	0.012	0.058	0
RRR435524	0.011	0	0
RRR435530	0.007	0	0
RRR435530	0.009	0	0.017
RRR435530	0.014	0.005	0.013
RRR435537	0.007	0	0.002
RRR435537	0.009	0	0
RRR435538	0.011	0.041	0
RRR435538	0.012	0.05	0
RRR435538	0	0.036	0.007
RRR435538	0	0.018	0.033
RRR435538	0	0	0.01
RRR435538	0.003	0.032	0
RRR435544	0.01	0.027	0
RRR435544	0.008	0	0.001
RRR435544	0.006	0.041	0.02
RRR435544	0.007	0	0
RRR435548	0.006	0	0.019
RRR435548	0.004	0.063	0
RRR435548	0.016	0.063	0.006
RRR435548	0.01	0.027	0
RRR435548	0.016	0	0.039
RRR435558	0.001	0.045	0.031
RRR435558	0.007	0.046	0.045
RRR435558	0.006	0	0
RRR435580	0.004	0.14	0.007
RRR435580	0.006	0	0
RRR435580	0.009	0.005	0.002
RRR435580	0.018	0.023	0
RRR435580	0.003	0.027	0
RRR435593	0.011	0	0
RRR435593	0	0.13	0

Appendix I : Microprobe analyses

Muscovite

SAMPLE	Cl %	Cr2O3 %	NiO %
RRR435593	0	0.086	0
RRR435593	0.022	0.059	0
RRR435593	0.021	0.036	0
RRR435604	0.012	0.018	0.004
RRR435604	0.047	0.044	0
RRR435604	0.011	0.031	0.016
RRR435604	0.001	0	0.014
RRR435604	0.007	0.094	0
RRR435612	0.003	0	0
RRR435612	0.006	0	0.003
RRR435612	0.026	0.032	0
RRR435612	0.003	0.068	0
RRR435612	0.015	0.077	0.003
RRR435625	0.008	0.023	0
RRR435625	0.004	0.018	0
RRR435625	0.006	0.05	0.01
RRR435625	0.003	0	0
RRR435625	0	0.045	0
RRR435635	0	0	0.011
RRR435635	0.003	0.091	0
RRR435635	0.006	0.027	0
RRR435642	0.003	0.095	0
RRR435642	0.015	0.005	0
RRR435642	0.03	0	0.029
RRR435646	0	0	0
RRR435646	0.007	0	0
RRR435646	0.004	0	0.037
RRR435646	0.001	0	0.031
RRR435646	0.003	0	0
RRR435646	0.001	0	0.008
RRR435660	0.001	0	0
RRR435677	0	0	0.01
RRR435677	0.005	0.009	0
RRR435677	0.017	0.036	0.018
RRR435677	0.017	0.027	0.037
RRR435680	0	0.1	0.011
RRR435680	0.009	0.073	0
RRR435718	0	0.027	0
RRR435718	0.023	0	0

Appendix I : Microprobe analyses

Muscovite

SAMPLE	Cl %	Cr2O3 %	NiO %
RRR435718	0.012	0	0.013
RRR435718	0.003	0.099	0.034
RRR435739	0.004	0.054	0
RRR435739	0.013	0.041	0
RRR435739	0.011	0.093	0
RRR435739	0.006	0.041	0.002
RRR435739	0.009	0	0
RRR435752	0	0.045	0.005
RRR435752	0	0.769	0.019
RRR435752	0.006	0.397	0
RRR435752	0	0	0
RRR435773	0.004	0	0
RRR435774	0.002	0.027	0.048
RRR435777	0	0.009	0.016
RRR435777	0	0.032	0.033
RRR435777	0.004	0.135	0
RRR435777	0	0.027	0
RRR435782	0.005	0.041	0.002
RRR435782	0.002	0.023	0.005
RRR435786	0.006	0.064	0
RRR435786	0.011	0.091	0.045
RRR435786	0.004	0.136	0
RRR435786	0.01	0.068	0
RRR435790	0.009	0.114	0
RRR435790	0.008	0.05	0.03
RRR435790	0.005	0.113	0.013
RRR435790	0.013	0.082	0
RRR435790	0.006	0	0.027
RRR435798	0.015	0.023	0.002
RRR435798	0.009	0.05	0
RRR435798	0.005	0.005	0.012
RRR435836	0.006	0.09	0.012
RRR435867	0.009	0.027	0.044
RRR435867	0	0.018	0
RRR435867	0.007	0.041	0
RRR435867	0.015	0.032	0.005
RRR435876	0.012	0	0
RRR435876	0.003	0.023	0.01
RRR435880	0	0	0.031

Appendix I : Microprobe analyses

Muscovite

SAMPLE	Cl %	Cr2O3 %	NiO %
RRR435880	0.003	0	0
RRR435880	0.004	0	0
RRR435883	0.009	0.018	0
RRR435883	0.017	0.031	0.022
RRR435883	0.007	0	0.006
RRR435889	0.014	0.005	0
RRR435889	0.025	0.227	0.034
RRR435889	0.02	0.054	0.015
RRR435919	0	0.023	0
RRR435919	0.01	0.036	0
RRR435919	0.002	0.095	0.025

Muscovite

SAMPLE	H2O*	Subtotal	O=F,Cl	Total
RRR435503	4.470	101.563	0.142	101.420
RRR435503	4.498	100.723	0.091	100.632
RRR435503	4.473	100.644	0.105	100.539
RRR435503	4.412	99.128	0.092	99.036
RRR435524	4.428	100.064	0.064	100.000
RRR435524	4.459	99.311	0.027	99.284
RRR435524	4.494	99.527	0.003	99.524
RRR435524	4.447	100.017	0.034	99.983
RRR435530	4.339	99.295	0.131	99.165
RRR435530	4.490	100.294	0.044	100.250
RRR435530	4.359	97.152	0.060	97.092
RRR435537	4.372	100.341	0.074	100.267
RRR435537	4.412	99.599	0.038	99.561
RRR435538	4.479	99.987	0.013	99.974
RRR435538	4.445	100.439	0.065	100.374
RRR435538	4.514	100.124	0.000	100.124
RRR435538	4.455	98.858	0.000	98.858
RRR435538	4.447	99.216	0.021	99.195
RRR435538	4.447	99.802	0.037	99.765
RRR435544	4.426	100.733	0.133	100.600
RRR435544	4.337	99.021	0.158	98.864
RRR435544	4.296	98.375	0.136	98.239
RRR435544	4.393	99.460	0.117	99.344
RRR435548	4.345	99.311	0.089	99.223
RRR435548	4.362	100.429	0.109	100.320

RRR435548	4.432	99.542	0.029	99.512
RRR435548	4.397	99.289	0.065	99.224
RRR435548	4.332	99.139	0.086	99.053
RRR435558	4.406	100.615	0.146	100.469
RRR435558	4.559	100.626	0.002	100.625
RRR435558	4.362	99.532	0.131	99.401
RRR435580	4.462	100.563	0.083	100.480
RRR435580	4.361	99.979	0.120	99.859
RRR435580	4.410	99.638	0.075	99.563
RRR435580	4.442	100.619	0.103	100.516
RRR435580	4.385	100.341	0.116	100.226
RRR435593	4.339	99.095	0.116	98.979
RRR435593	4.467	100.181	0.036	100.145

Appendix I : Microprobe analyses

Muscovite

SAMPLE	H2O*	Subtotal	O=F,Cl	Total
RRR435593	4.418	99.552	0.046	99.506
RRR435593	4.479	99.475	0.005	99.470
RRR435593	4.251	97.584	0.102	97.481
RRR435604	4.477	99.710	0.028	99.682
RRR435604	4.463	98.869	0.011	98.858
RRR435604	4.526	100.359	0.023	100.336
RRR435604	4.540	100.054	0.000	100.054
RRR435604	4.466	99.116	0.017	99.099
RRR435612	4.609	100.968	0.001	100.968
RRR435612	4.500	100.591	0.089	100.502
RRR435612	4.452	99.056	0.058	98.998
RRR435612	4.383	100.006	0.140	99.866
RRR435612	4.537	101.176	0.060	101.116
RRR435625	4.474	100.083	0.043	100.040
RRR435625	4.443	100.210	0.079	100.131
RRR435625	4.533	99.893	0.022	99.871
RRR435625	4.523	99.624	0.001	99.623
RRR435625	4.426	100.021	0.088	99.933
RRR435635	4.394	100.293	0.183	100.111
RRR435635	4.476	100.426	0.094	100.332
RRR435635	4.517	100.991	0.085	100.906
RRR435642	4.394	100.077	0.147	99.931
RRR435642	4.495	99.527	0.029	99.498
RRR435642	4.421	99.851	0.125	99.726

RRR435646	4.546	100.978	0.021	100.957
RRR435646	4.436	100.478	0.111	100.367
RRR435646	4.394	98.653	0.068	98.585
RRR435646	4.380	99.544	0.108	99.436
RRR435646	4.383	99.506	0.098	99.408
RRR435646	4.561	100.665	0.000	100.665
RRR435660	4.475	99.346	0.000	99.346
RRR435677	4.367	100.434	0.135	100.299
RRR435677	4.359	100.479	0.166	100.313
RRR435677	4.332	100.082	0.155	99.927
RRR435677	4.368	100.305	0.142	100.163
RRR435680	4.447	100.460	0.084	100.376
RRR435680	4.318	98.909	0.122	98.787
RRR435718	4.364	100.307	0.167	100.140
RRR435718	4.568	100.549	0.036	100.512

Appendix I : Microprobe analyses

Muscovite

SAMPLE	H2O*	Subtotal	O=F,Cl	Total
RRR435718	4.369	98.045	0.085	97.960
RRR435718	4.462	99.729	0.063	99.666
RRR435739	4.536	101.130	0.084	101.046
RRR435739	4.606	101.038	0.060	100.978
RRR435739	4.439	100.398	0.110	100.288
RRR435739	4.545	101.220	0.064	101.156
RRR435739	4.463	100.358	0.070	100.288
RRR435752	4.410	99.207	0.046	99.161
RRR435752	4.210	97.948	0.119	97.829
RRR435752	4.328	98.444	0.079	98.365
RRR435752	4.361	98.994	0.062	98.932
RRR435773	4.426	98.976	0.011	98.965
RRR435774	4.333	97.833	0.083	97.749
RRR435777	4.332	99.784	0.160	99.624
RRR435777	4.431	99.976	0.093	99.883
RRR435777	4.456	99.728	0.057	99.670
RRR435777	4.374	100.461	0.155	100.306
RRR435782	4.432	99.440	0.037	99.402
RRR435782	4.414	99.397	0.068	99.329
RRR435786	4.477	99.690	0.080	99.610
RRR435786	4.466	100.969	0.107	100.862
RRR435786	4.458	98.406	0.048	98.358
RRR435786	4.403	100.772	0.160	100.612

RRR435790	4.493	100.677	0.101	100.575
RRR435790	4.445	100.083	0.127	99.956
RRR435790	4.494	100.810	0.100	100.709
RRR435790	4.546	100.563	0.045	100.519
RRR435790	4.473	99.993	0.095	99.898
RRR435798	4.533	99.739	0.045	99.694
RRR435798	4.382	100.507	0.175	100.333
RRR435798	4.367	100.339	0.179	100.160
RRR435836	4.356	99.723	0.156	99.566
RRR435867	4.356	99.477	0.117	99.360
RRR435867	4.342	100.023	0.151	99.872
RRR435867	4.239	98.271	0.173	98.098
RRR435867	4.418	100.114	0.082	100.033
RRR435876	4.471	100.286	0.090	100.196
RRR435876	4.373	100.081	0.159	99.922
RRR435880	4.473	100.250	0.087	100.163

Appendix I : Microprobe analyses

Muscovite

SAMPLE	H2O*	Subtotal	O=F,Cl	Total
RRR435880	4.412	100.930	0.145	100.785
RRR435880	4.471	100.429	0.104	100.326
RRR435883	4.450	100.046	0.110	99.936
RRR435883	4.497	101.040	0.111	100.929
RRR435883	4.458	100.472	0.119	100.352
RRR435889	4.382	97.930	0.071	97.859
RRR435889	4.475	99.566	0.068	99.498
RRR435889	4.511	99.905	0.056	99.849
RRR435919	4.527	100.061	0.037	100.024
RRR435919	4.507	100.669	0.070	100.599
RRR435919	4.526	100.732	0.058	100.674

APPENDIX III : SEM AND EDS SPECTROMETRY ANALYSES

The scanning electron microscope (SEM) used for this study is a JEOL 840-A, coupled to a Siemens D5000 energy dispersive X-ray spectrometer (EDS). Analyses were done at the Laval University under the supervision of André Ferland. Below is a list of all sulphide phases tested with the EDS.

Sample	Mineral phase	Formula	Ag at%	Au at%	As at%	Bi at%	Fe at%	Ni at%
RRR435502	sphalerite	ZnS					0.81	
RRR435502	rutile	TiO ₂						
RRR435502	pyrite	FeS ₂						
RRR435502	rutile	TiO ₂						
RRR435502	pyrite	FeS ₂						
RRR435502	galena	PbS						
RRR435502	pyrite	FeS ₂						
RRR435502	galena	PbS						
RRR435506	rutile	TiO ₂						
RRR435506	pyrite	FeS ₂						
RRR435506	Melonite	NiTe ₂						
RRR435506	Petzite	AuAg ₃ Te ₂	49.18	9.36			2.45	
RRR435506	Chalcopyrite	CuFeS ₂						
RRR435506	Pyrite	FeS ₂						
RRR435506	Stibnite-Ullmanite Melonite	NiSbS +						
RRR435506	Antimony	NiTe ₂						29.2
RRR435506	pyrite	FeS ₂						
RRR435506	sphalerite	ZnS					3.08	
RRR435506	Hessite	Ag ₂ Te	64.85	1.2				
RRR435506	Pyrite	FeS ₂						
RRR435506	Sphalerite	ZnS						
RRR435506	Hessite	Ag ₂ Te	66.6					
RRR435572	Pyrrhotite	FeS						
RRR435572	Pyrite	FeS ₂						
RRR435572	Pyrrhotite	FeS						
RRR435572	Pyrite	FeS ₂						
RRR435572	Galena	PbS						
RRR435572	Sphalerite	ZnS						
RRR435732	Stützite-sphalerite	Ag ₅ Te ₃ -ZnS	41.7				3.98	
Sample	Mineral phase	Formula	Ag at%	Au at%	As at%	Bi at%	Fe at%	Ni at%

RRR435732	pyrite	FeS2					
RRR435732	chalcopyrite	CuFeS2					
RRR435732	Pyrite	FeS2					
RRR435732	Sphalerite	ZnS				1.64	
RRR435732	Hessite	Ag2Te	61.34			2.41	
RRR435732	Galena	PbS					
RRR435732	Pyrite	FeS2					
RRR435732	Arsenopyrite	FeAsS					
RRR435732	Pyrite	FeS2					
RRR435732	Chalcopyrite	CuFeS2					
RRR435732	Electrum	(Au,Ag)	22.43	35.6			
RRR435732	pyrite	FeS2					
RRR435732	monazite	(Ce,La)PO4					
RRR435737	Pyrite	FeS2					
RRR435737	Galena	PbS					
RRR435737	silver telluride	AgxTex					
RRR435737	Pyrite	FeS2					
RRR435737	Sphalerite	ZnS					
RRR435737	Galena	PbS					
RRR435737	Pyrite	FeS2					
RRR435737	Electrum	(Au,Ag)	23.64	18.08		5.16	
RRR435737	Pyrite	FeS2					
RRR435737	Sphalerite	ZnS					
RRR435737	Petzite	AuAg3Te2	45.52	11.39		3.8	
RRR435749	Bismuth telluride	Bi3Te2				56	
RRR435795	Sphalerite	ZnS					
RRR435795	Chalcopyrite	CuFeS2					
RRR435795	Electrum	(Au,Ag)	78.04	21.96			
RRR435795	Sphalerite	ZnS				2.34	
RRR435795	Pyrite	FeS2					
RRR435795	Pyrargyrite	Ag3SbS3					
RRR435795	Chalcopyrite	CuFeS2					
RRR435795	Pyrargyrite	Ag3SbS3	47.52			3.09	
RRR435806	Galena	PbS				27.03	
RRR435806	Pyrite	FeS2					
RRR435806	Chalcopyrite	CuFeS2					
RRR435806	Galena	PbS					
RRR435806	Pyrite	FeS2					
RRR435806	Arsenopyrite	FeAsS					

Sample	Mineral phase	Formula	Ag at%	Au at%	As at%	Bi at%	Fe at%	Ni at%
--------	---------------	---------	--------	--------	--------	--------	--------	--------

RRR435806	Galena	PbS					
RRR435806	Sphalerite	ZnS				2.51	
RRR435806	Pyrite	FeS2					
RRR435806	Chalcopyrite	CuFeS2					
RRR435806	Galena	PbS					
RRR435830	Arsenopyrite	FeAsS			35	33.3	
RRR435830	Pyrite	FeS2					
RRR435830	Electrum	(Au,Ag)	53.88	29.15	6.15	10.82	
RRR435830	Pyrite	FeS2					
RRR435830	sphalerite	ZnS				3.48	
RRR435830	Ullmanite	NiSbS			0.72		29.89
RRR435830	Ti2O	Ti2O					
RRR435830	Arsenopyrite	FeAsS					
RRR435830	Pyrite	FeS2					
RRR435830	Electrum	(Au,Ag)	52.9	26.59		20.51	
RRR435830	Sphalerite	ZnS				3.02	
RRR435875	Pyrite	FeS2					
RRR435875	sphalerite	ZnS				1.79	
RRR435875	sphalerite-incl	ZnS				6.89	
RRR435875	sphalerite-rim	Zns				1.4	
RRR435875	Stützite-altaite	Ag5Te3- PbTe	48.56			1.13	
RRR435875	Sphalerite	ZnS				1.29	
RRR435875	Galena-Stützite	PbS-Ag5Te3	19.64				
RRR435883	Pyrite	FeS2					
RRR435883	Chalcopyrite	CuFeS2					
RRR435883	Bismuth	Bi					
RRR435883	Pyrite	FeS2					
RRR435883	Bismuth	Bi					

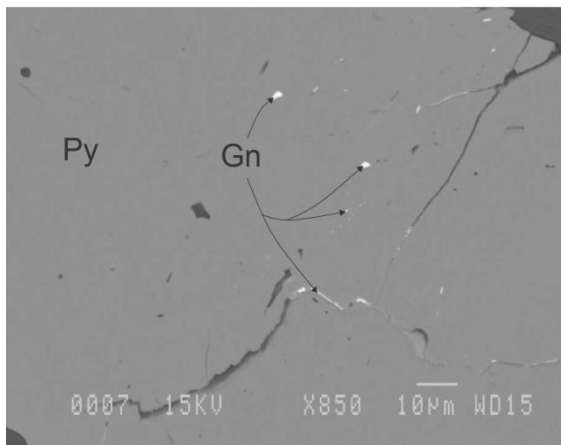
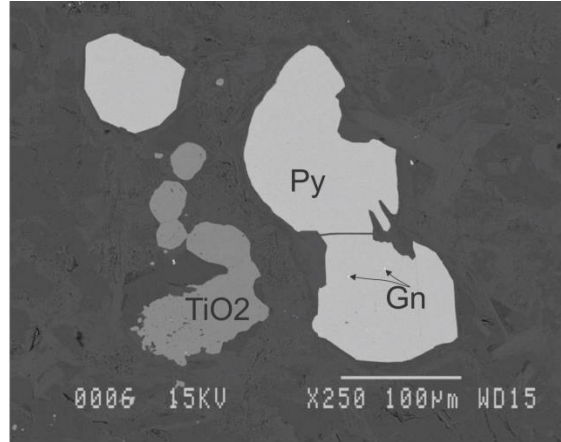
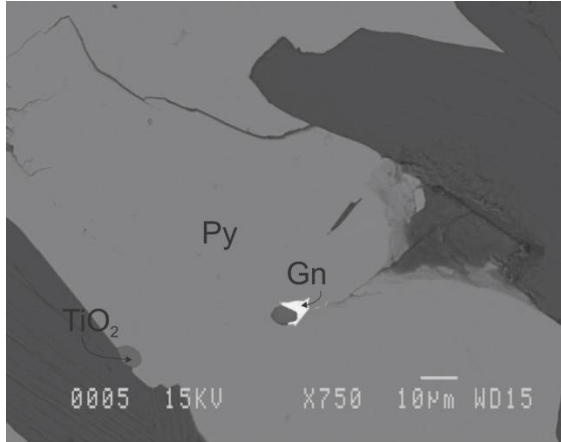
Sample	Mineral phase	Formula	Pb at%	S at%	Sb at%	Te at%	Ti at%	Zn at%	total
RRR435502	sphalerite	ZnS		40.17				59.02	100
RRR435502	rutile	TiO2							0
RRR435502	pyrite	FeS2							0
RRR435502	rutile	TiO2							0
RRR435502	pyrite	FeS2							0
RRR435502	galena	PbS							0
RRR435502	pyrite	FeS2							0
RRR435502	galena	PbS							0
RRR435506	rutile	TiO2							0
RRR435506	pyrite	FeS2							0
RRR435506	Melonite	NiTe2							0
RRR435506	Petzite	AuAg3Te2				39			99.99
RRR435506	Chalcopyrite	CuFeS2							0
RRR435506	Pyrite	FeS2							0
RRR435506	Stibnite-Ullmanite + Melonite	NiSbS							0
RRR435506	Antimony	NiTe2			7.69	63.11			100
RRR435506	pyrite	FeS2							0
RRR435506	sphalerite	ZnS		38.31				58.61	100
RRR435506	Hessite	Ag2Te				33.94			99.99
RRR435506	Pyrite	FeS2							0
RRR435506	Sphalerite	ZnS							0
RRR435506	Hessite	Ag2Te				33.4			100
RRR435572	Pyrrhotite	FeS							0
RRR435572	Pyrite	FeS2							0
RRR435572	Pyrrhotite	FeS							0
RRR435572	Pyrite	FeS2							0
RRR435572	Galena	PbS							0
RRR435572	Sphalerite	ZnS							0
RRR435732	Stützite-sphalerite	Ag5Te3-ZnS		14.28		32.86		7.17	99.99

Sample	Mineral phase	Formula	Pb at%	S at%	Sb at%	Te at%	Ti at%	Zn at%	total
RRR435732	pyrite	FeS2							0
RRR435732	chalcopyrite	CuFeS2							0
RRR435732	Pyrite	FeS2							0
RRR435732	Sphalerite	ZnS		40.48				57.88	100
RRR435732	Hessite	Ag2Te		2.58		33.67			100
RRR435732	Galena	PbS							0
RRR435732	Pyrite	FeS2							0
RRR435732	Arsenopyrite	FeAsS							0
RRR435732	Pyrite	FeS2							0
RRR435732	Chalcopyrite	CuFeS2							0
RRR435732	Electrum	(Au,Ag)							58.03
RRR435732	pyrite	FeS2							0
RRR435732	monazite	(Ce,La)PO4							0
RRR435737	Pyrite	FeS2							0
RRR435737	Galena	PbS							0
RRR435737	silver telluride	AgxTex							0
RRR435737	Pyrite	FeS2							0
RRR435737	Sphalerite	ZnS							0
RRR435737	Galena	PbS							0
RRR435737	Pyrite	FeS2							0
RRR435737	Electrum	(Au,Ag)							46.88
RRR435737	Pyrite	FeS2							0
RRR435737	Sphalerite	ZnS							0
RRR435737	Petzite	AuAg3Te2				39.29			100
RRR435749	Bismuth telluride	Bi3Te2				44			100
RRR435795	Sphalerite	ZnS							0
RRR435795	Chalcopyrite	CuFeS2							0
RRR435795	Electrum	(Au,Ag)							100
RRR435795	Sphalerite	ZnS		32.53				65.13	100
RRR435795	Pyrite	FeS2							0
RRR435795	Pyrargyrite	Ag3SbS3							0
RRR435795	Chalcopyrite	CuFeS2							0
RRR435795	Pyrargyrite	Ag3SbS3		30.87	18.51				99.99
RRR435806	Galena	PbS	25.52	47.45					100
RRR435806	Pyrite	FeS2							0
RRR435806	Chalcopyrite	CuFeS2							0
RRR435806	Galena	PbS							0
RRR435806	Pyrite	FeS2							0
RRR435806	Arsenopyrite	FeAsS							0

Sample	Mineral phase	Formula	Pb at%	S at%	Sb at%	Te at%	Ti at%	Zn at%	total
RRR435806	Galena	PbS							0
RRR435806	Sphalerite	ZnS		46.33				51.16	100
RRR435806	Pyrite	FeS2							0
RRR435806	Chalcopyrite	CuFeS2							0
RRR435806	Galena	PbS							0
RRR435830	Arsenopyrite	FeAsS		31.71					100.01
RRR435830	Pyrite	FeS2							0
RRR435830	Electrum	(Au,Ag)							100
RRR435830	Pyrite	FeS2							0
RRR435830	sphalerite	ZnS		48.67				47.84	99.99
RRR435830	Ullmanite	NiSbS		24.19	45.2				100
RRR435830	Ti2O	Ti2O					66.9		66.9
RRR435830	Arsenopyrite	FeAsS							0
RRR435830	Pyrite	FeS2							0
RRR435830	Electrum	(Au,Ag)							100
RRR435830	Sphalerite	ZnS		47.27				49.7	99.99
RRR435875	Pyrite	FeS2							0
RRR435875	sphalerite	ZnS		36.35				61.86	100
RRR435875	sphalerite-incl	ZnS		36.47				56.64	100
RRR435875	sphalerite-rim	Zns		34.79				63.82	100.01
RRR435875	Stützite-altaite	PbTe	7.17			34.25		8.89	100
RRR435875	Sphalerite	ZnS		50.17				48.54	100
RRR435875	Galena-Stützite	PbS-Ag5Te3	29.3	19.35		9.91		21.8	100
RRR435883	Pyrite	FeS2							0
RRR435883	Chalcopyrite	CuFeS2							0
RRR435883	Bismuth	Bi							0
RRR435883	Pyrite	FeS2							0
RRR435883	Bismuth	Bi							0

III.I Sample RRR435502

SEM photos, sample RRR435502



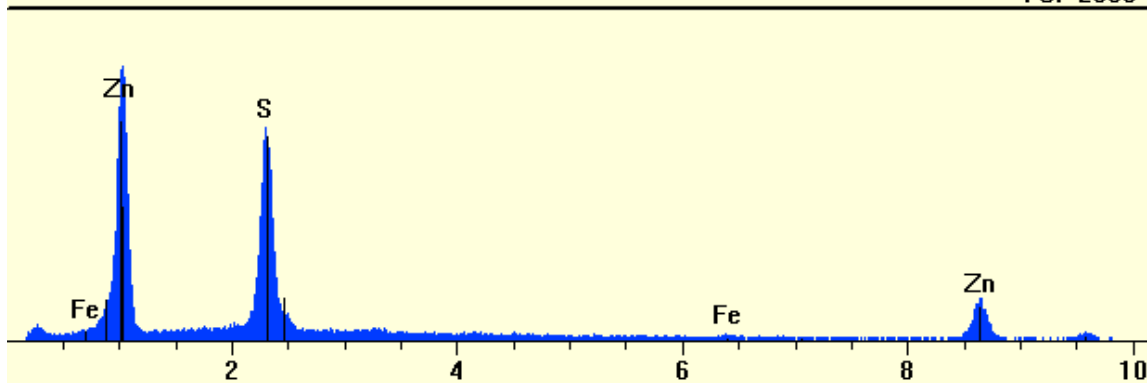
RRR435502: From the intrepid zone, contains light colored sphalerite, very altered garnets (low MnO values) and good crenulation cleavage marked by sericite. 74% SiO₂. Sphalerite composition is to be tested, and also try to obtain shots of replacement textures of fds-gt-ser-chl-py. Also, potential weird phases rimming rare py grains and v rare Po-cpy.

Spectrum report, sample RRR435502

Live Time: 60,00 Count Rate: 3704 Dead Time: 30,88 %
 Beam Voltage: 15,00 Beam Current: 1,00 Takeoff Angle: 30,00

■ EDS_502b-nopic_sph.pgt

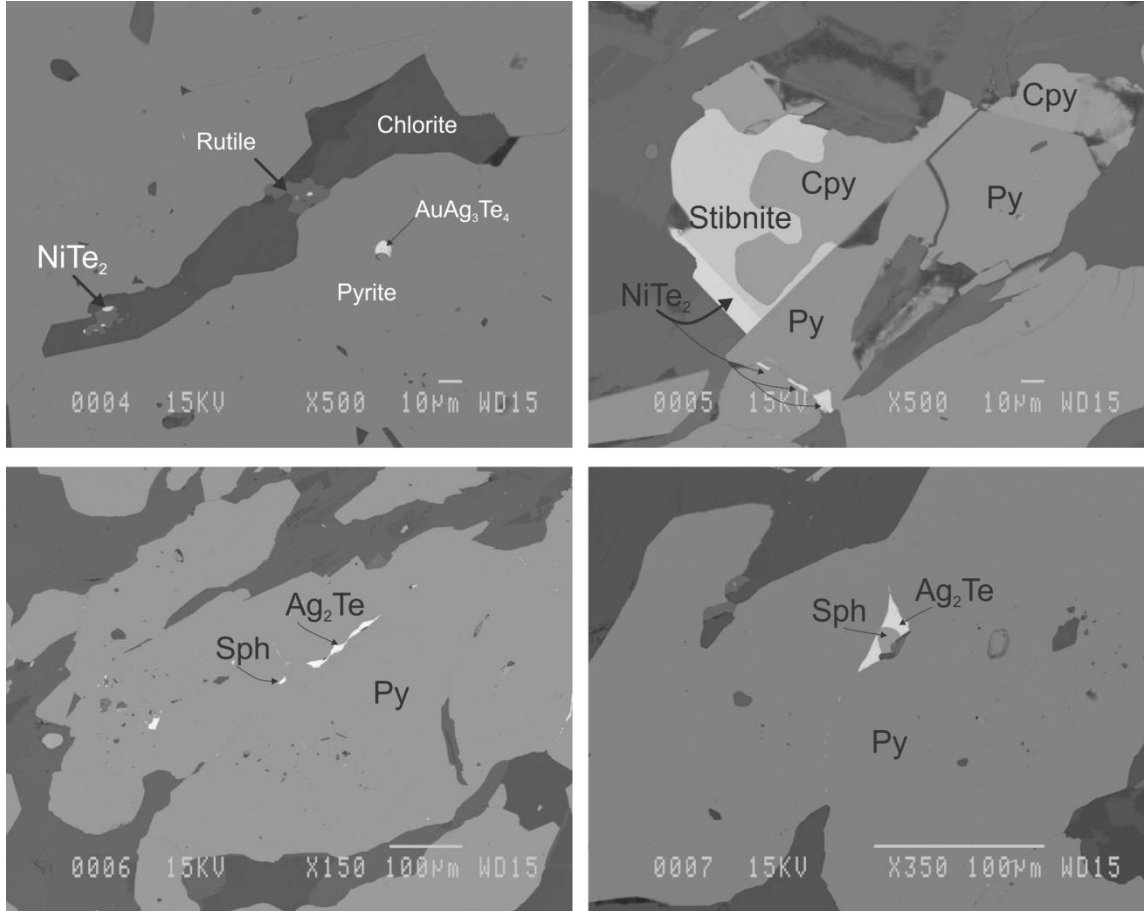
FS: 2800



Element	Gross (cps)	BKG (cps)	Net (cps)	P:B Ratio	Z Corr	A Corr	F Corr
S	532,3	104,9	427,4	4,1	0,900	1,422	1,000
Fe	17,6	13,0	4,6	0,4	1,002	1,017	0,926
Zn	148,0	25,1	122,9	4,9	1,035	1,002	1,000

III.II Sample RRR435506

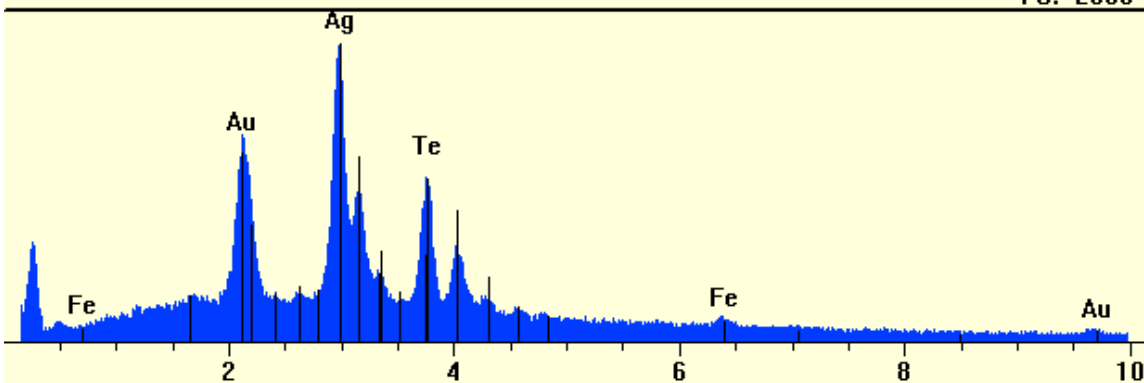
SEM photos, sample RRR435506



RRR435506: Located in the Cap zone, intense deformation and abundant disseminated pyrite in tholeiitic-affinity felsic dominant lapilli tuff. Abundant carbonate-chlorite alteration. Diss pyrite in ser-dominated domains, abundant pyrite-cpy +/- sph in carbonate-chlorite domain. 8,7 g/t Au, with Te and 1,308% TiO₂

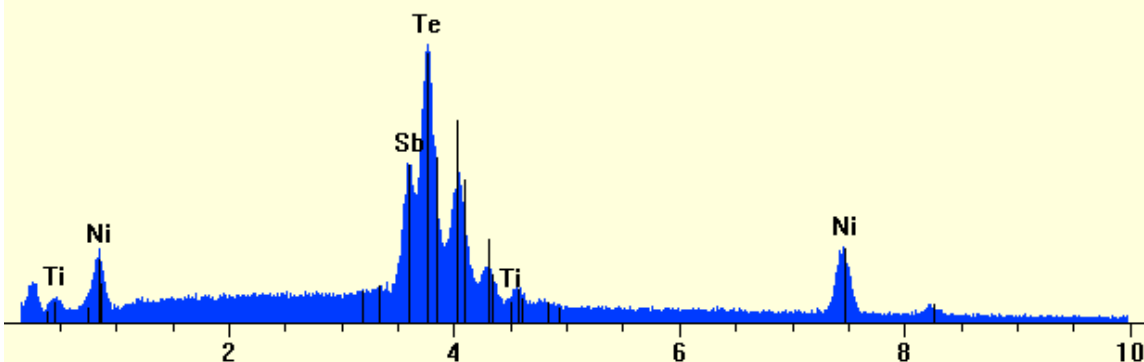
Spectrum reports, sample RRR435506

Live Time:	60,00	Count Rate:	7230	Dead Time:	49,00 %
Beam Voltage:	15,00	Beam Current:	1,00	Takeoff Angle:	30,00



Element	Gross (cps)	BKG (cps)	Net (cps)	P:B Ratio	Z Corr	A Corr	F Corr
Fe	64,7	43,9	20,8	0,5	0,832	1,103	0,998
Au	372,8	89,5	283,3	3,2	1,152	1,098	0,997
Ag	595,7	200,0	395,7	2,0	0,966	1,102	0,990
Te	351,7	211,8	139,9	0,7	0,996	1,181	1,000

Live Time: 60,00 Count Rate: 6144 Dead Time: 45,51 %
 Beam Voltage: 15,00 Beam Current: 1,00 Takeoff Angle: 30,00

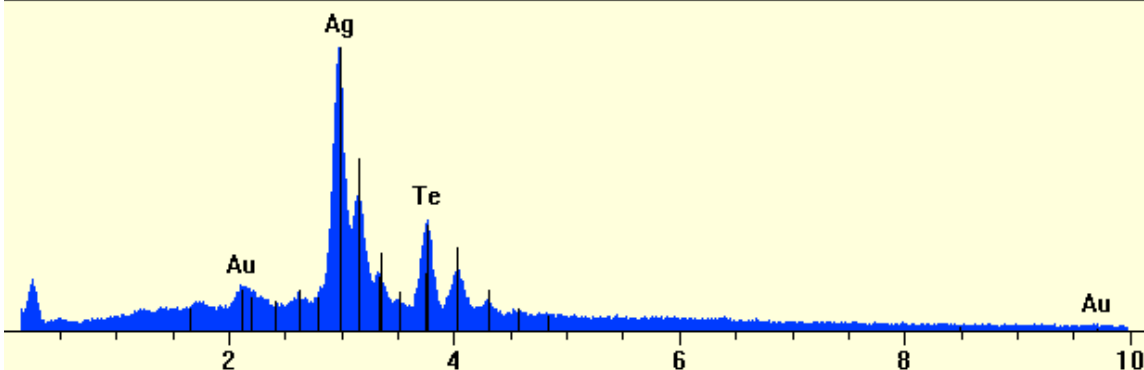


Element	Gross (cps)	BKG (cps)	Net (cps)	P:B Ratio	Z Corr	A Corr	F Corr
Ni	214,6	34,7	179,9	5,2	0,876	1,057	1,000
Sb	370,2	367,8	2,4	0,0	1,024	1,007	0,999
Ti	74,8	86,4	-11,6	-0,1	0,823	1,198	0,998
Te	667,8	411,9	255,9	0,6	1,030	1,001	0,998

Live Time: 60,00 Count Rate: 7300 Dead Time: 49,34 %
 Beam Voltage: 15,00 Beam Current: 1,00 Takeoff Angle: 30,00

■ EDS_pic6_white.pgt

FS: 3200

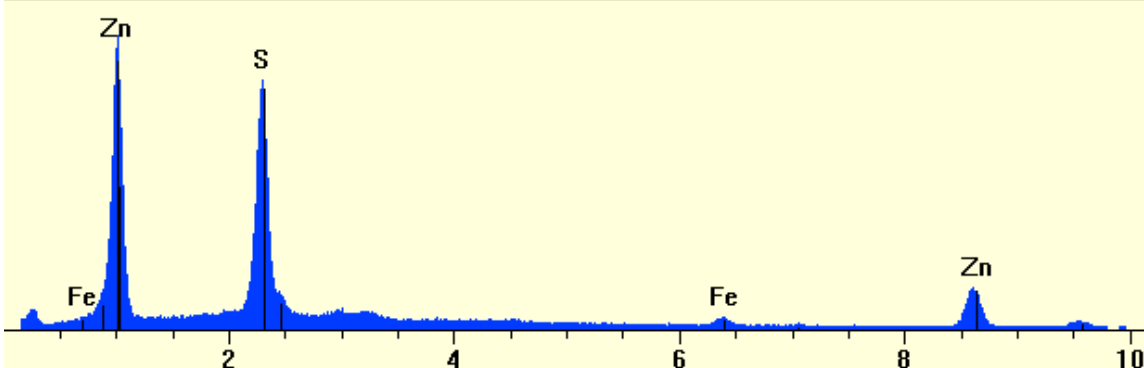


Element	Gross (cps)	BKG (cps)	Net (cps)	P:B Ratio	Z Corr	A Corr	F Corr
Te	370,9	223,4	147,5	0,7	1,016	1,192	1,000
Ag	878,4	260,6	617,8	2,4	0,985	1,033	0,990
Au	138,0	91,5	46,5	0,5	1,176	1,100	0,996

Live Time: 59,99 Count Rate: 8534 Dead Time: 51,17 %
 Beam Voltage: 15,00 Beam Current: 1,00 Takeoff Angle: 30,00

■ EDS_pic6_sph.pgt

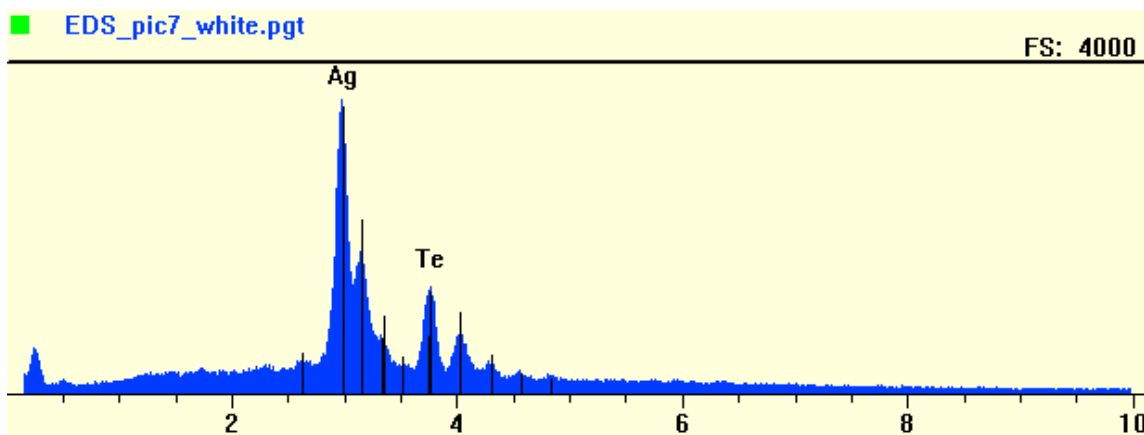
FS: 5400



Element	Gross (cps)	BKG (cps)	Net (cps)	P:B Ratio	Z Corr	A Corr	F Corr
S	1217,6	85,1	1132,5	13,3	0,899	1,424	1,000
Zn	303,0	23,6	279,5	11,9	1,034	1,003	1,000

Fe	79,4	33,8	45,6	1,3	1,001	1,016	0,929
----	------	------	------	-----	-------	-------	-------

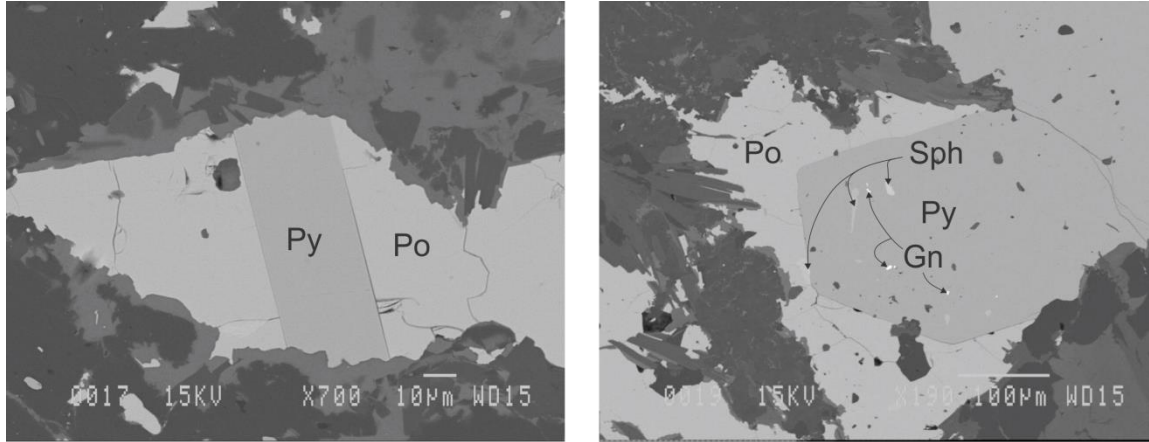
Live Time: 60,00 Count Rate: 8957 Dead Time: 56,07 %
 Beam Voltage: 15,00 Beam Current: 1,00 Takeoff Angle: 30,00



Element	Gross (cps)	BKG (cps)	Net (cps)	P:B Ratio	Z Corr	A Corr	F Corr
Ag	1147,2	351,5	795,7	2,3	0,989	1,022	0,990
Te	469,9	280,0	189,9	0,7	1,019	1,192	1,000

III.III Sample RRR435572

SEM photos, sample RRR435572



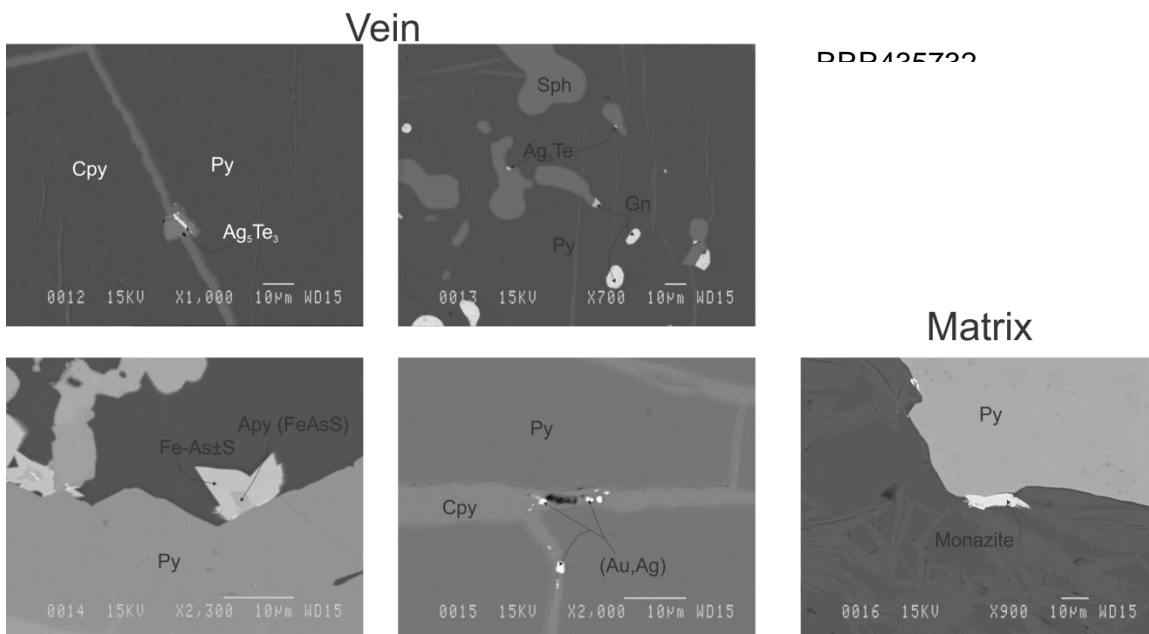
Sample RRR435572: Sedimentary unit 'capping' the ODM zone with interesting Py-Po relationship.

Spectrum reports, sample RRR435572

No spectrum reports measured for sample RRR435572.

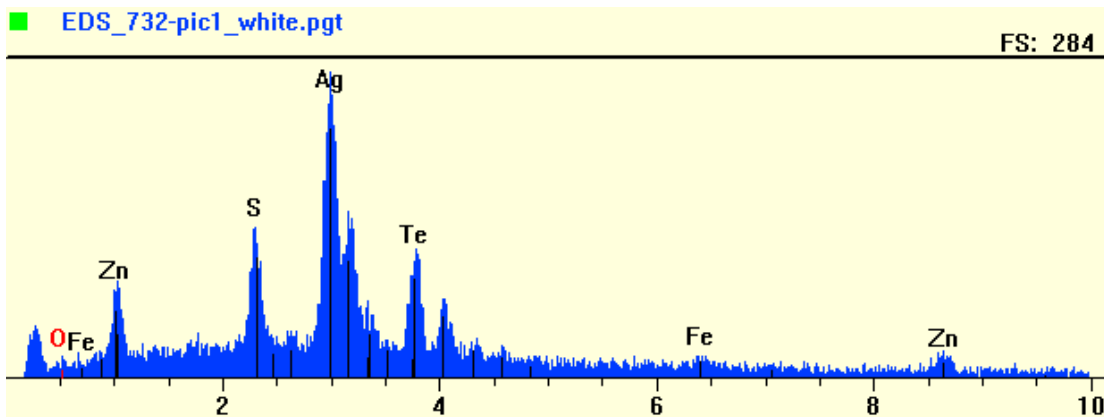
III.IV Sample RRR435732

SEM photos, sample RRR435732



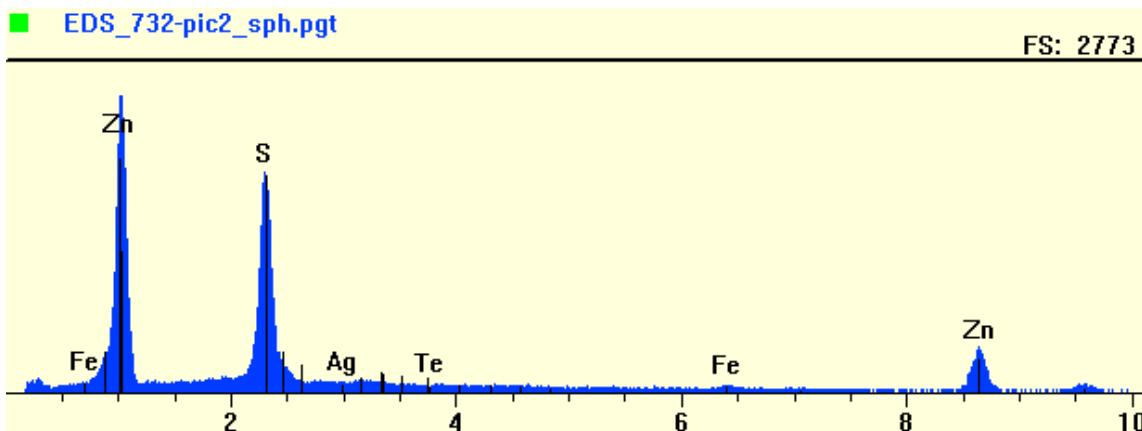
Spectrum reports, sample RRR435732

Live Time: 11,41 Count Rate: 4322 Dead Time: 34,82 %
 Beam Voltage: 15,00 Beam Current: 1,00 Takeoff Angle: 30,00



Element	Gross (cps)	BKG (cps)	Net (cps)	P:B Ratio	Z Corr	A Corr	F Corr
Ag	428,6	33,9	394,7	11,7	1,011	1,046	0,988
Fe	41,2	18,2	23,0	1,3	0,869	1,097	0,998
Te	193,8	32,2	161,6	5,0	1,042	1,148	1,000
S	188,7	33,3	155,4	4,7	0,773	1,318	0,980
Zn	46,0	12,9	33,1	2,6	0,901	1,030	1,000

Live Time: 53,78 Count Rate: 4286 Dead Time: 33,33 %
 Beam Voltage: 15,00 Beam Current: 1,00 Takeoff Angle: 30,00



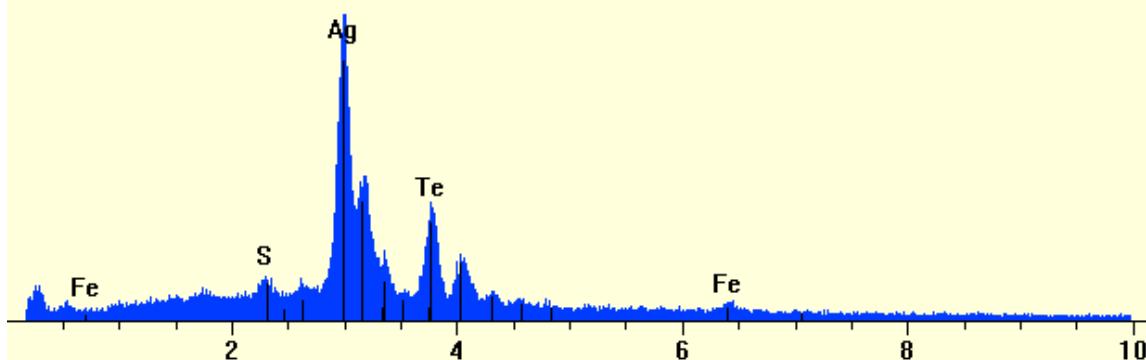
Element	Gross (cps)	BKG (cps)	Net (cps)	P:B Ratio	Z Corr	A Corr	F Corr
Ag	35,5	93,1	-57,6	-0,6	1,176	1,174	1,000

Fe	29,6	13,5	16,1	1,2	1,002	1,017	0,928
Te	27,0	66,9	-39,8	-0,6	1,209	1,058	0,999
S	603,2	111,4	491,9	4,4	0,901	1,419	1,000
Zn	171,2	28,3	142,9	5,1	1,036	1,002	1,000

Live Time: 43,22 Count Rate: 4595 Dead Time: 35,80 %
 Beam Voltage: 15,00 Beam Current: 1,00 Takeoff Angle: 30,00

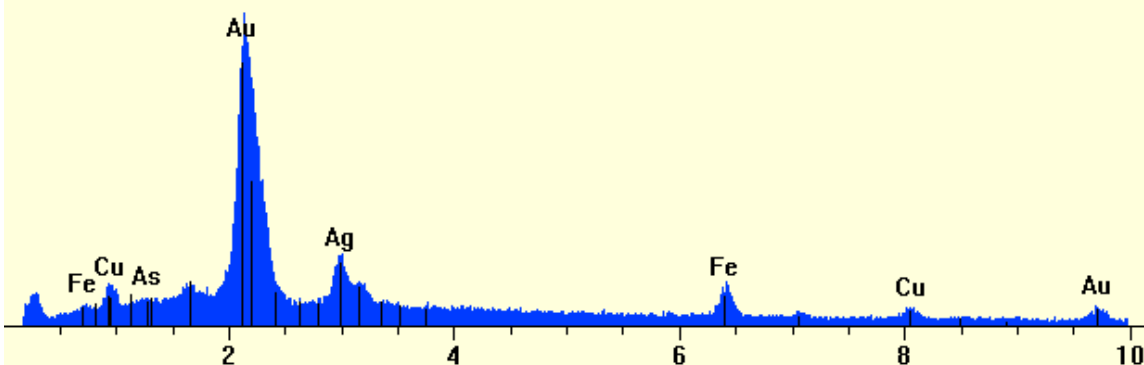
■ EDS_732-pic2_white.pgt

FS: 1429



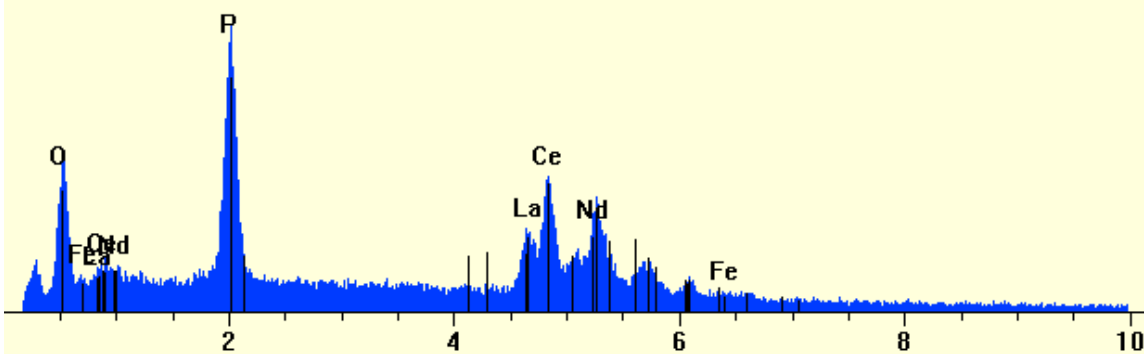
Element	Gross (cps)	BKG (cps)	Net (cps)	P:B Ratio	Z Corr	A Corr	F Corr
Ag	548,3	26,3	522,0	19,8	0,993	1,026	0,990
Fe	44,8	28,8	16,0	0,6	0,854	1,103	1,000
Te	228,9	27,8	201,1	7,2	1,023	1,183	1,000
S	81,2	24,4	56,7	2,3	0,759	1,307	0,975

Live Time: 54,60 Count Rate: 4653 Dead Time: 36,72 %
 Beam Voltage: 15,00 Beam Current: 1,00 Takeoff Angle: 30,00



Element	Gross (cps)	BKG (cps)	Net (cps)	P:B Ratio	Z Corr	A Corr	F Corr
Fe	91,6	27,8	63,8	2,3	0,809	1,072	0,986
Ag	139,2	52,6	86,6	1,6	0,938	1,316	1,000
Au	512,9	58,2	454,7	7,8	1,118	1,058	0,999
Cu	48,3	36,4	11,8	0,3	0,834	1,033	0,975
As	46,4	60,8	-14,4	-0,2	0,843	1,792	1,000

Live Time: 60,00 Count Rate: 3056 Dead Time: 28,58 %
 Beam Voltage: 15,00 Beam Current: 1,00 Takeoff Angle: 30,00

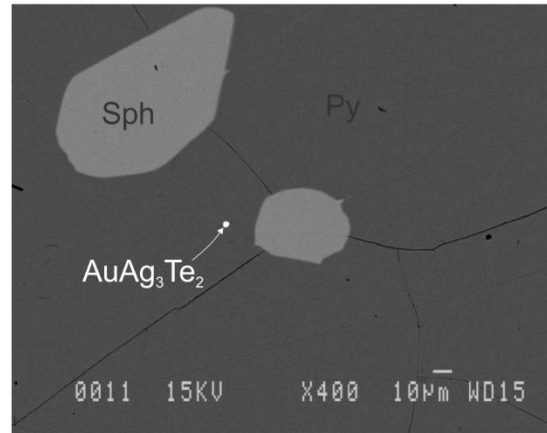
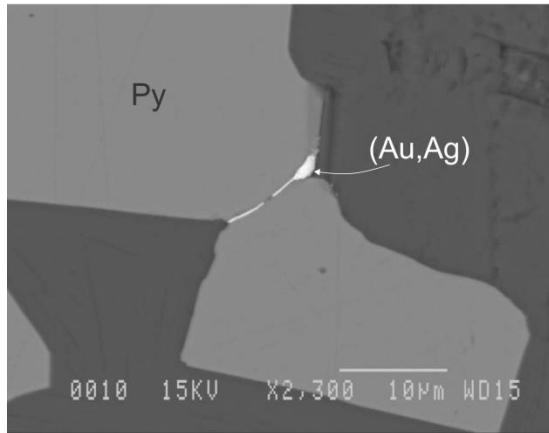
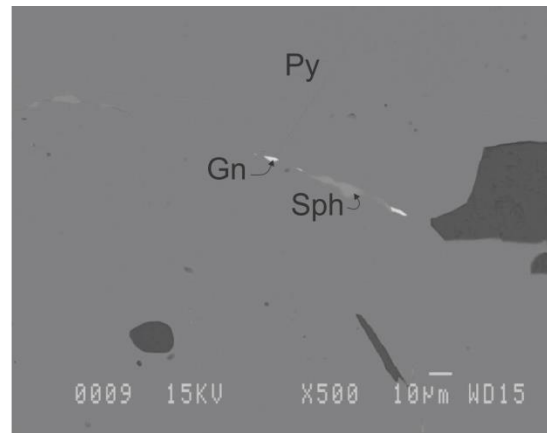
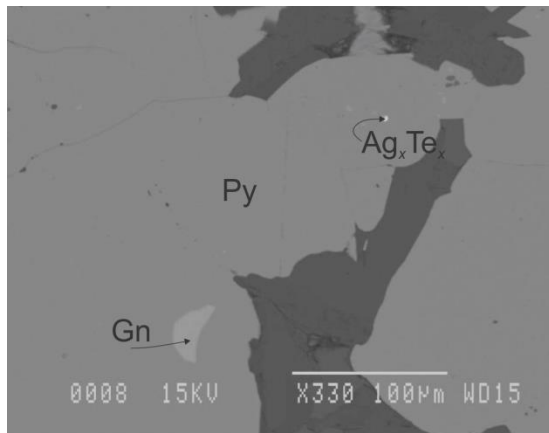


Element	Gross (cps)	BKG (cps)	Net (cps)	P:B Ratio	Z Corr	A Corr	F Corr
Fe	26,3	33,2	-6,9	-0,2	0,915	1,112	1,000
P	233,8	49,8	184,0	3,7	0,807	1,689	0,997
O	103,1	18,4	84,7	4,6	0,722	2,266	1,000
Nd	108,1	89,2	18,8	0,2	1,147	0,983	1,000

La	91,6	77,6	14,0	0,2	1,130	0,997	1,000
Ce	145,2	77,0	68,2	0,9	1,136	0,991	1,000

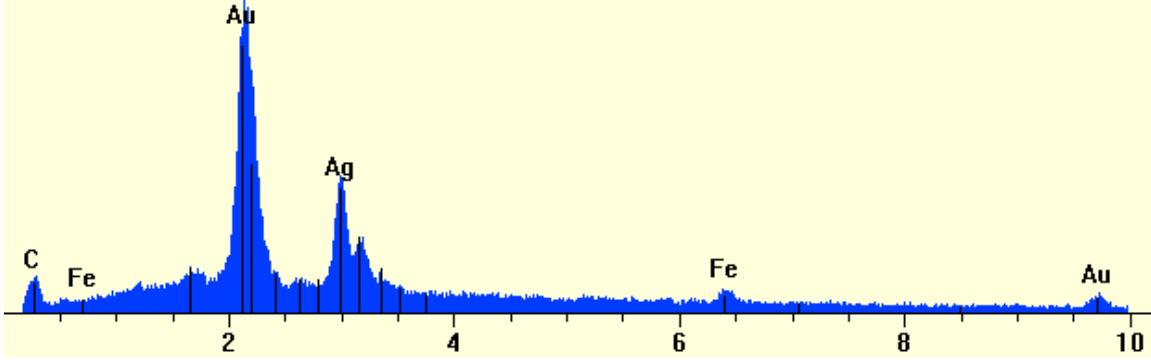
III.V Sample RRR435737

SEM photos, sample RRR435737



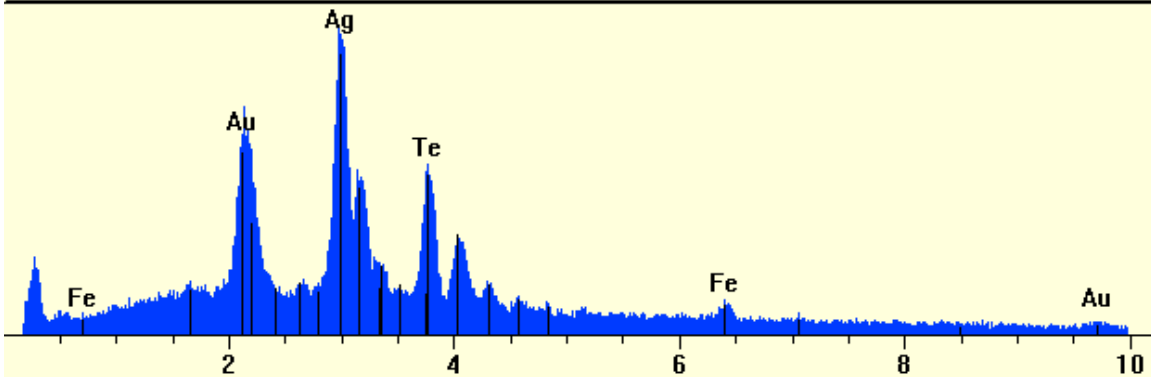
Spectrum reports, sample RRR435737

Live Time:	48,31	Count Rate:	4660	Dead Time:	37,23 %
Beam Voltage:	15,00	Beam Current:	1,00	Takeoff Angle:	30,00



Element	Gross (cps)	BKG (cps)	Net (cps)	P:B Ratio	Z Corr	A Corr	F Corr
Ag	245,6	103,0	142,5	1,4	0,973	1,265	1,000
C	47,9	6,9	41,0	6,0	0,629	3,152	1,000
Fe	54,7	30,1	24,6	0,8	0,838	1,079	0,994
Au	502,7	64,2	438,4	6,8	1,161	1,015	0,998

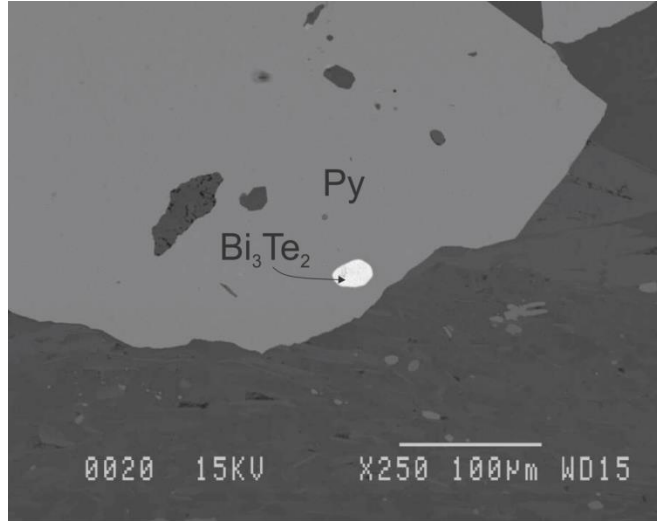
Live Time: 60,00 Count Rate: 4129 Dead Time: 34,22 %
 Beam Voltage: 15,00 Beam Current: 1,00 Takeoff Angle: 30,00



Element	Gross (cps)	BKG (cps)	Net (cps)	P:B Ratio	Z Corr	A Corr	F Corr
Ag	317,5	55,4	262,1	4,7	0,962	1,118	0,990
Fe	42,6	26,9	15,7	0,6	0,829	1,102	0,998
Au	204,5	46,9	157,6	3,4	1,148	1,096	0,997
Te	190,3	53,0	137,2	2,6	0,992	1,180	1,000

III.VI Sample RRR435749

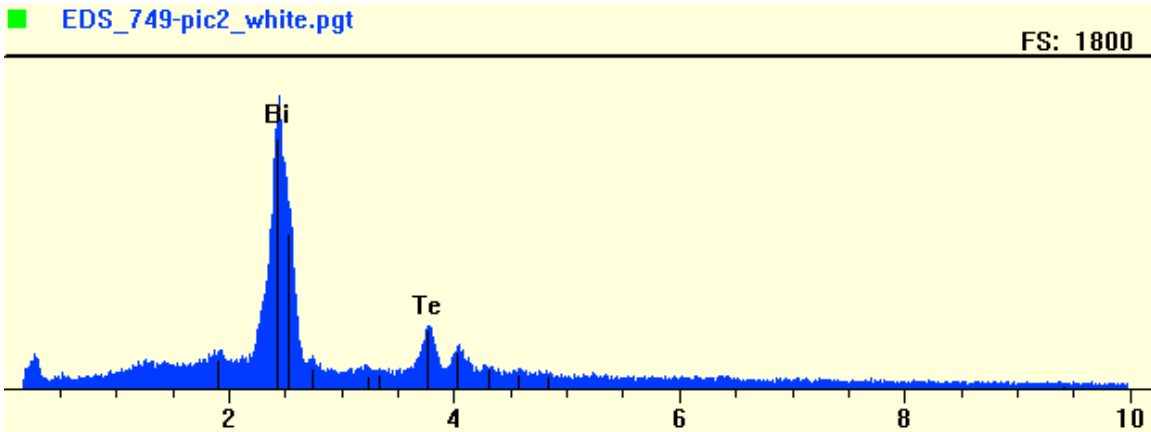
SEM photos, sample RRR435749



RRR435749: Mafic tholeiitic sample North of the ODM body (footwall), with bismuth telluride (Au scavenger?)

Spectrum reports, sample RRR435749

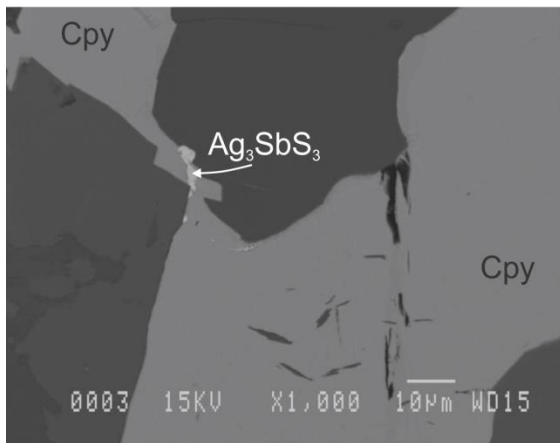
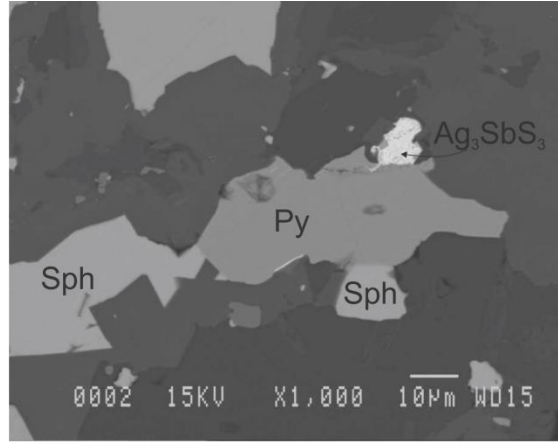
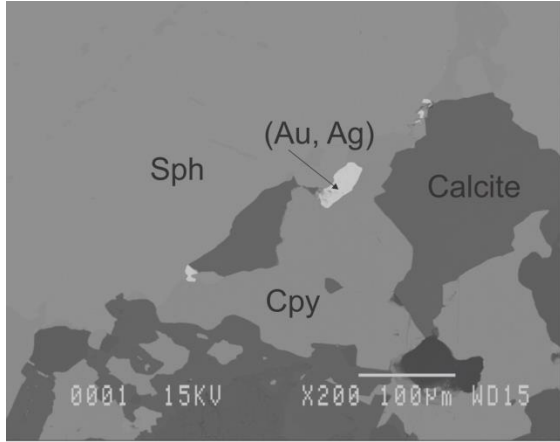
Live Time:	56,35	Count Rate:	3948	Dead Time:	33,08 %
Beam Voltage:	15,00	Beam Current:	1,00	Takeoff Angle:	30,00



Element	Gross (cps)	BKG (cps)	Net (cps)	P:B Ratio	Z Corr	A Corr	F Corr
Bi	473,7	26,8	446,9	16,6	1,058	1,024	0,999
Te	127,6	29,5	98,2	3,3	0,901	1,244	1,000

III.VII Sample RRR435795

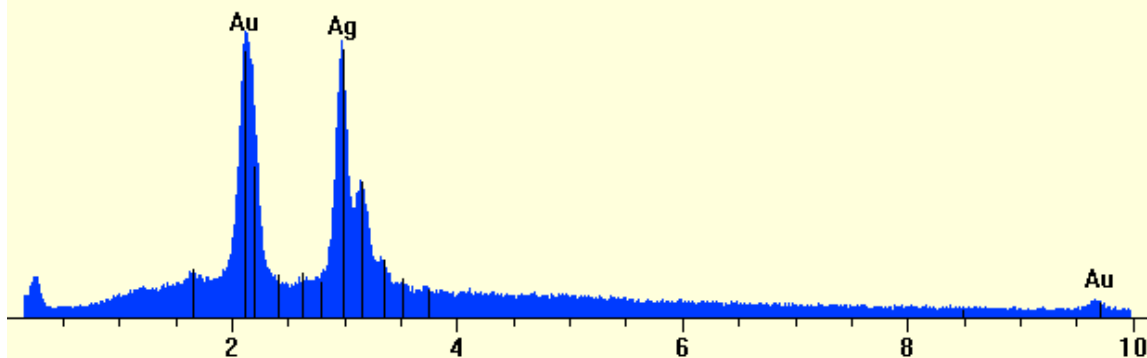
SEM photos, sample RRR435795



RRR435795: Felsic tuff from the HS zone, has abundant sphalerite and cpy associated with pyrite, with a spatial distribution prob. Caused by ductility contrasts between sulphides. VVFG sericite grains have almost totally replaced the feldspars. Net-like anastomosing sericite distribution around more competent qtz. Sphalerite also observed in what seems to be highly folded and dismembered veinlets. Cpy present too. Similar deformation seems to have affected vf rutile vlets (see photo 435795-9)

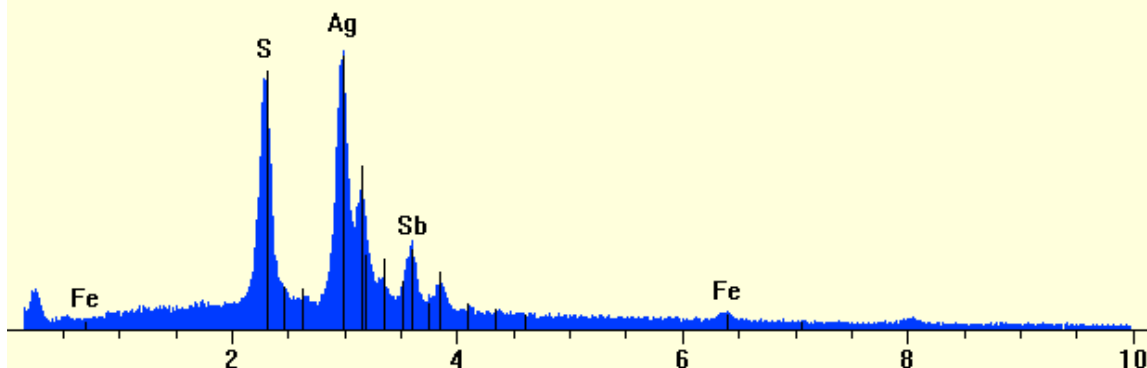
Spectrum reports, sample RRR435795

Live Time:	60,00	Count Rate:	8400	Dead Time:	53,41 %
Beam Voltage:	15,00	Beam Current:	1,00	Takeoff Angle:	30,00



Element	Gross (cps)	BKG (cps)	Net (cps)	P:B Ratio	Z Corr	A Corr	F Corr
Ag	734,2	113,2	621,1	5,5	0,946	1,175	1,000
Au	719,0	103,4	615,7	6,0	1,128	1,036	0,997

Live Time: 60,00 Count Rate: 4390 Dead Time: 34,49 %
 Beam Voltage: 15,00 Beam Current: 1,00 Takeoff Angle: 30,00



Element	Gross (cps)	BKG (cps)	Net (cps)	P:B Ratio	Z Corr	A Corr	F Corr
S	428,6	55,8	372,8	6,7	0,789	1,262	0,976
Fe	40,8	21,8	19,0	0,9	0,886	1,092	1,000
Ag	484,1	143,7	340,4	2,4	1,032	1,048	0,992
Sb	153,4	83,6	69,8	0,8	1,057	1,229	1,000

Live Time: 60,00 Count Rate: 4597 Dead Time: 34,12 %

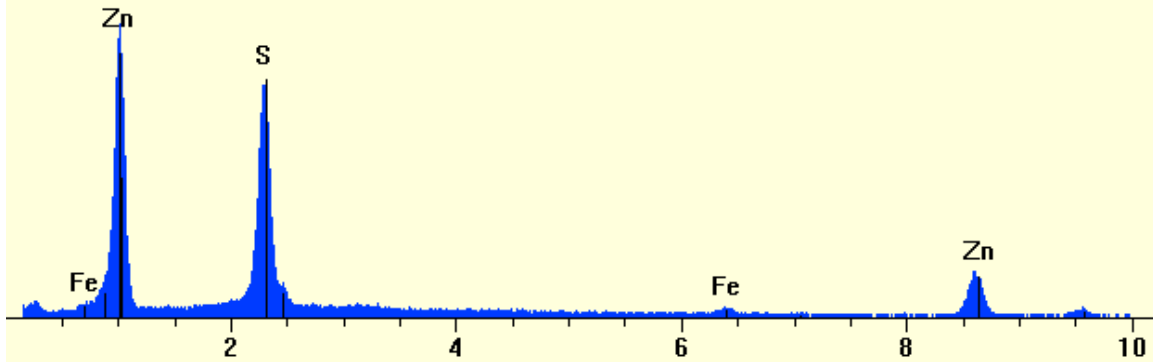
Beam Voltage: 15,00

Beam Current: 1,00

Takeoff Angle: 30,00

EDS_pic2_Lgray.pgt

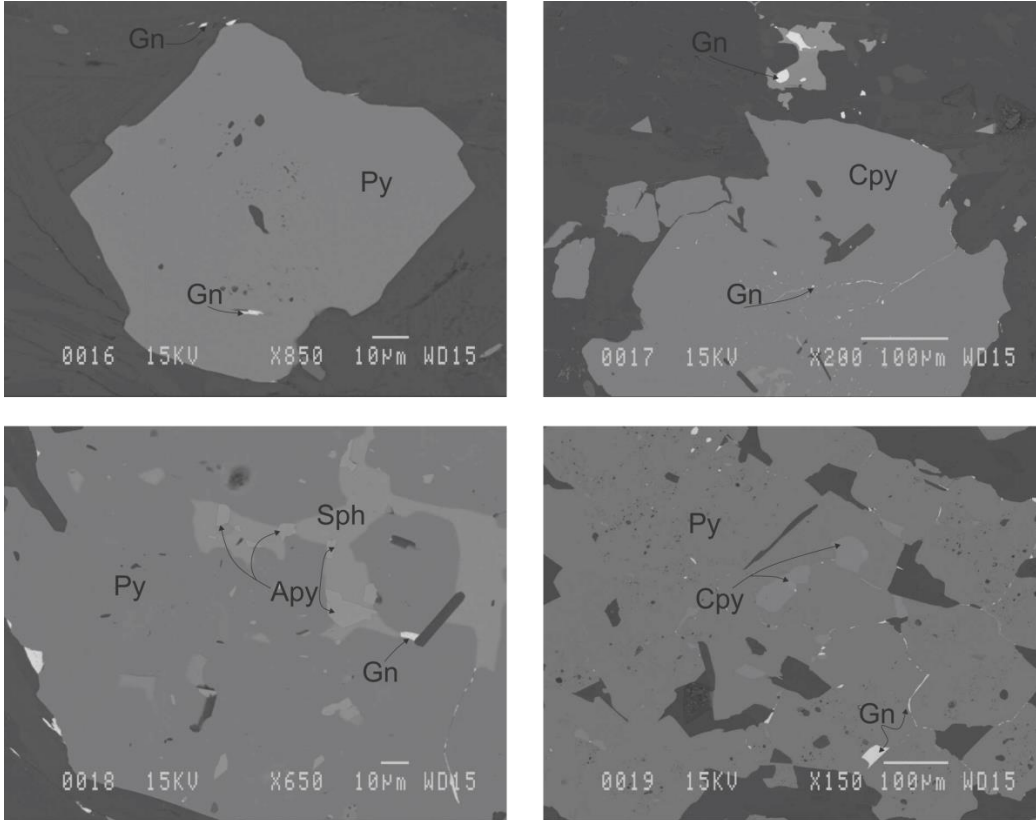
FS: 3200



Element	Gross (cps)	BKG (cps)	Net (cps)	P:B Ratio	Z Corr	A Corr	F Corr
S	699,2	40,5	658,7	16,3	0,893	1,450	1,000
Fe	39,0	16,2	22,8	1,4	0,994	1,015	0,922
Zn	185,3	12,7	172,6	13,6	1,028	1,002	1,000

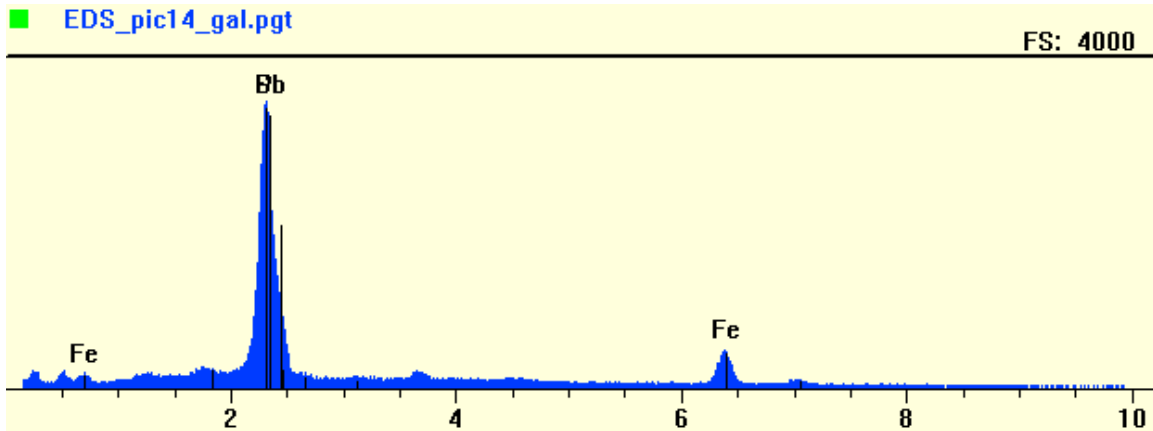
III.VIII Sample RRR435806

SEM photos, sample RRR435806



Spectrum reports, sample RRR435806

Live Time:	60,00	Count Rate:	5225	Dead Time:	38,88 %
Beam Voltage:	15,00	Beam Current:	1,00	Takeoff Angle:	30,00

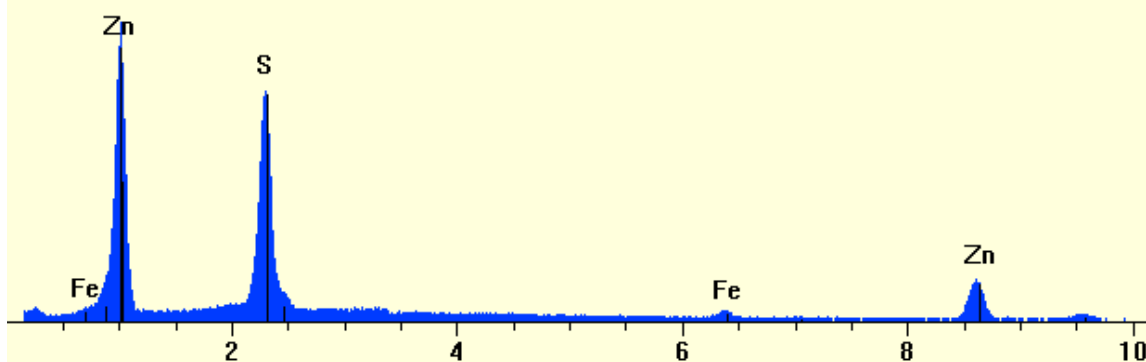


Element	Gross (cps)	BKG (cps)	Net (cps)	P:B Ratio	Z Corr	A Corr	F Corr
Fe	182,4	25,5	156,9	6,2	0,842	1,069	0,997
Pb	1062,7	12,8	1050,0	82,3	1,183	0,978	1,000
S	1055,9	12,5	1043,4	83,5	0,747	1,230	1,000

Live Time: 59,99 Count Rate: 5729 Dead Time: 39,99 %
 Beam Voltage: 15,00 Beam Current: 1,00 Takeoff Angle: 30,00

■ EDS_pic16_sph.pgt

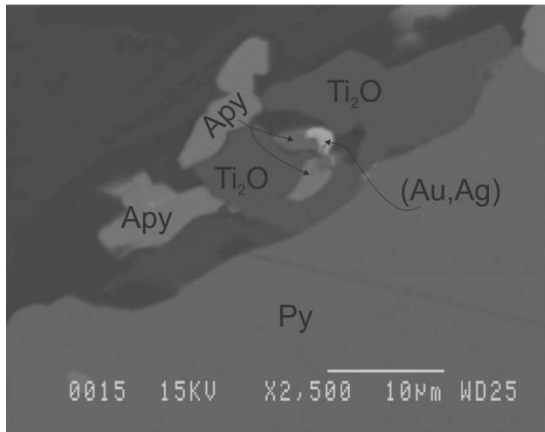
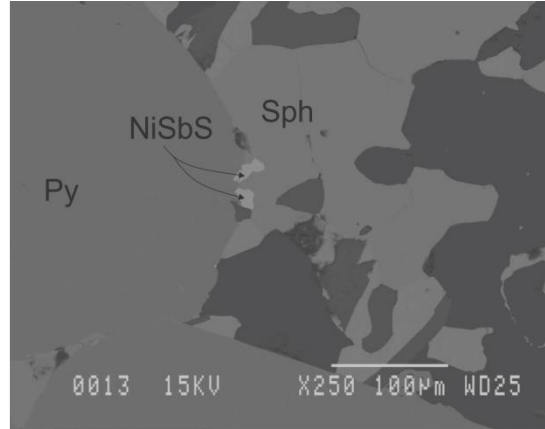
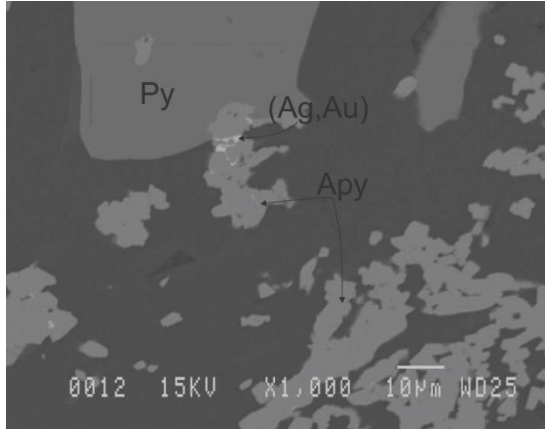
FS: 4000



Element	Gross (cps)	BKG (cps)	Net (cps)	P:B Ratio	Z Corr	A Corr	F Corr
S	849,8	9,2	840,6	91,1	0,908	1,390	1,000
Fe	50,1	20,7	29,4	1,4	1,009	1,018	0,936
Zn	221,8	15,3	206,5	13,5	1,043	1,003	1,000

III.IX Sample RRR435830

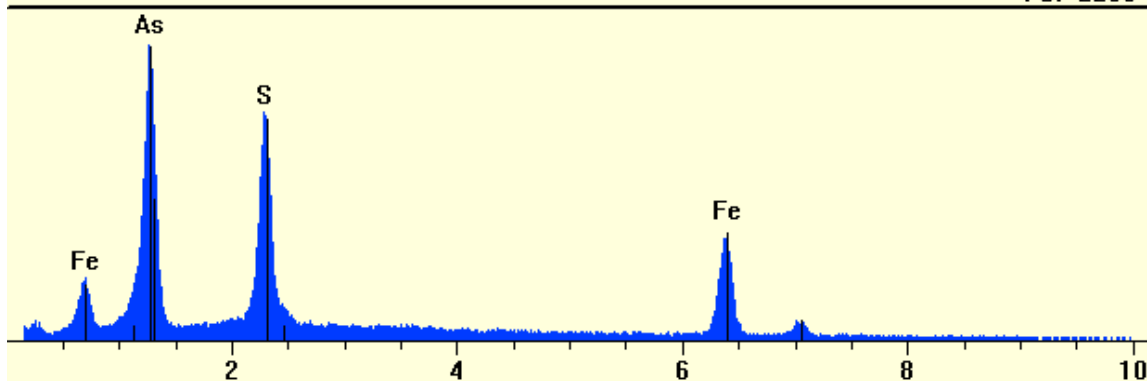
SEM photos, sample RRR435830



RRR435830: Calc-alkaline felsic tuff within a deformation zone in the CAP zone, possess unidentified, light yellow-colored pyrite-like vfg sulphide (apy?). Also, pyrrhotite inclusions within the pyrite, and two different sphalerite generations with different mol FeS concentrations. High arsenic content as well. Arseno-like+ sphalerite replacement in altered relic fds has been observed as well.

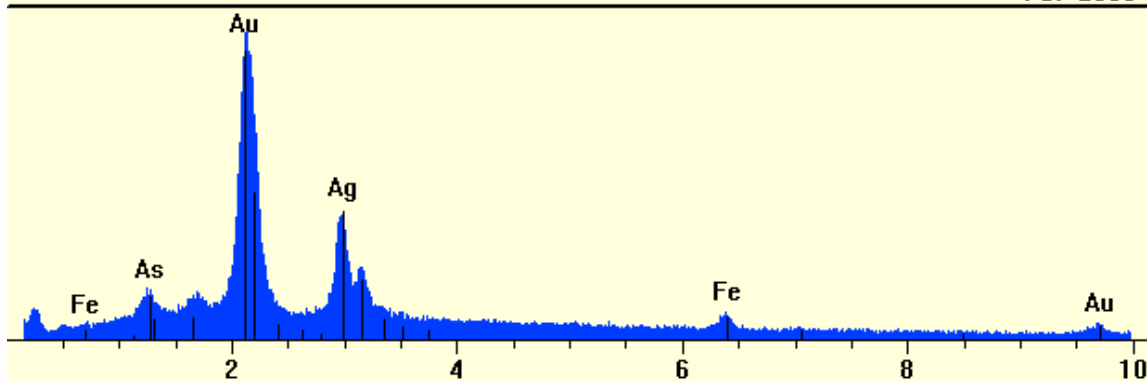
Spectrum reports, sample RRR435830

Live Time:	60,00	Count Rate:	4223	Dead Time:	33,03 %
Beam Voltage:	15,00	Beam Current:	1,00	Takeoff Angle:	30,00



Element	Gross (cps)	BKG (cps)	Net (cps)	P:B Ratio	Z Corr	A Corr	F Corr
S	470,4	7,6	462,7	60,5	0,892	1,463	0,999
Fe	282,9	17,7	265,2	15,0	0,993	1,016	0,992
As	531,3	3,5	527,7	149,7	1,056	1,436	0,999

Live Time: 60,00 Count Rate: 6223 Dead Time: 44,17 %
 Beam Voltage: 15,00 Beam Current: 1,00 Takeoff Angle: 30,00

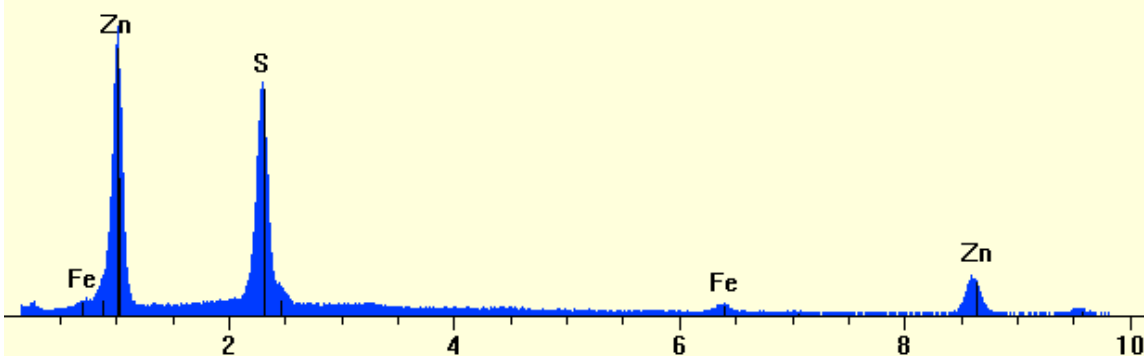


Element	Gross (cps)	BKG (cps)	Net (cps)	P:B Ratio	Z Corr	A Corr	F Corr
Fe	76,2	40,9	35,3	0,9	0,811	1,083	0,995
As	106,4	7,4	98,9	13,3	0,845	1,686	0,999
Au	695,5	14,2	681,3	47,9	1,121	1,049	0,998
Ag	320,7	22,5	298,3	13,3	0,940	1,244	1,000

Live Time: 60,00 Count Rate: 5568 Dead Time: 39,11 %
 Beam Voltage: 15,00 Beam Current: 1,00 Takeoff Angle: 30,00

EDS_pic12_sph.pgt

FS: 4000

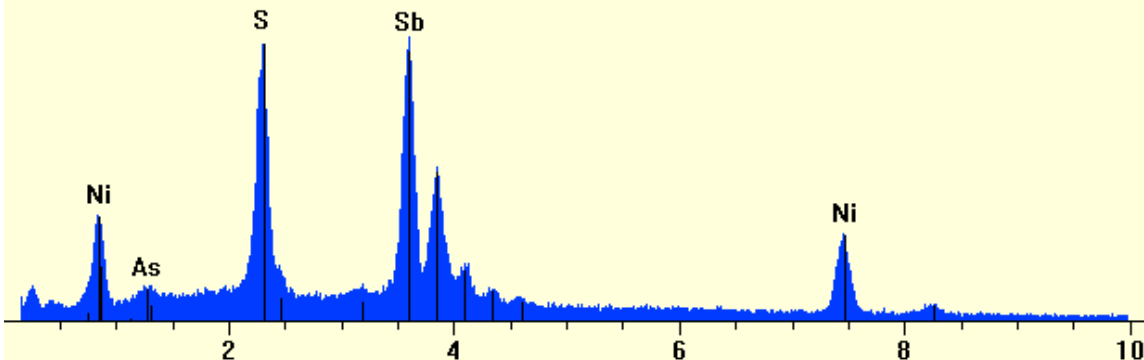


Element	Gross (cps)	BKG (cps)	Net (cps)	P:B Ratio	Z Corr	A Corr	F Corr
S	839,2	9,5	829,7	87,5	0,911	1,376	1,000
Zn	203,0	13,6	189,4	14,0	1,046	1,004	1,000
Fe	61,9	20,1	41,8	2,1	1,013	1,018	0,940

Live Time: 60,00 Count Rate: 5180 Dead Time: 39,64 %
 Beam Voltage: 15,00 Beam Current: 1,00 Takeoff Angle: 30,00

EDS_pic12_white.pgt

FS: 1800



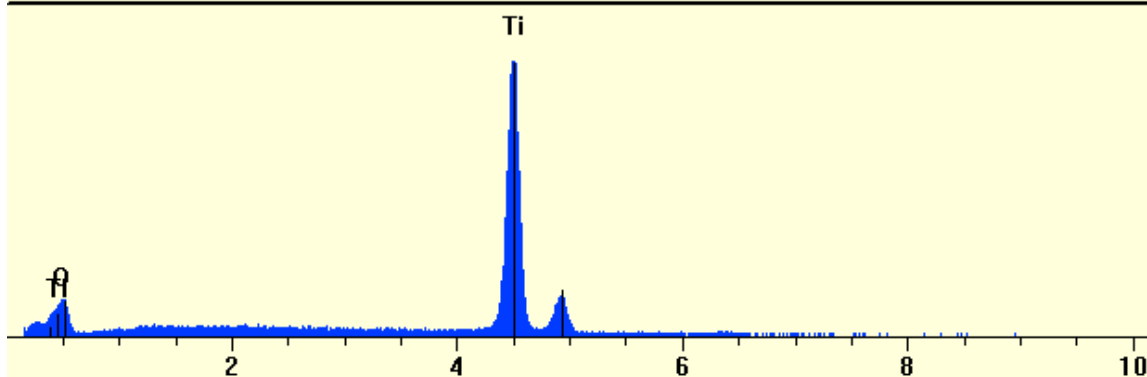
Element	Gross (cps)	BKG (cps)	Net (cps)	P:B Ratio	Z Corr	A Corr	F Corr
S	458,3	11,7	446,6	38,3	0,800	1,356	0,987
As	52,8	5,5	47,4	8,7	0,945	2,184	0,998

Sb	513,0	21,1	491,9	23,3	1,071	1,019	0,998
Ni	188,5	41,1	147,4	3,6	0,914	1,047	1,000

Live Time: 60,00 Count Rate: 2703 Dead Time: 24,83 %
 Beam Voltage: 15,00 Beam Current: 1,00 Takeoff Angle: 30,00

EDS_pic13_TiO2.pgt

FS: 2750

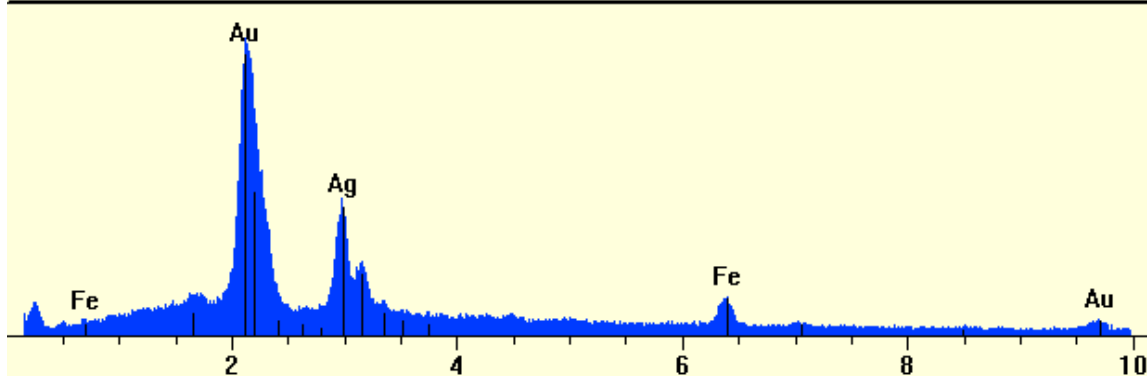


Element	Gross (cps)	BKG (cps)	Net (cps)	P:B Ratio	Z Corr	A Corr	F Corr
Ti	837,1	78,9	758,2	9,6	1,027	0,998	1,000
O	77,3	8,5	68,8	8,1	0,853	10,439	1,000

Live Time: 60,00 Count Rate: 5672 Dead Time: 41,57 %
 Beam Voltage: 15,00 Beam Current: 1,00 Takeoff Angle: 30,00

EDS_pic13_white.pgt

FS: 2250



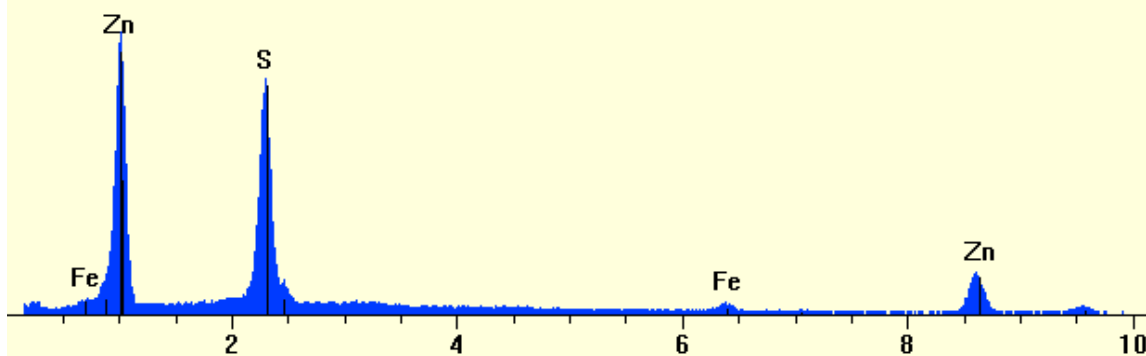
Element	Gross (cps)	BKG (cps)	Net (cps)	P:B Ratio	Z Corr	A Corr	F Corr
---------	-------------	-----------	-----------	-----------	--------	--------	--------

Fe	106,9	33,1	73,8	2,2	0,817	1,082	0,995
Au	596,6	14,4	582,1	40,3	1,130	1,039	0,998
Ag	292,9	22,6	270,3	12,0	0,947	1,227	0,999

Live Time: 60,00 Count Rate: 5624 Dead Time: 39,26 %
 Beam Voltage: 15,00 Beam Current: 1,00 Takeoff Angle: 30,00

■ EDS_830-sph.pgt

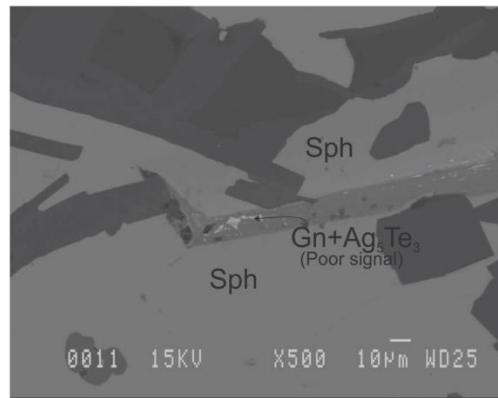
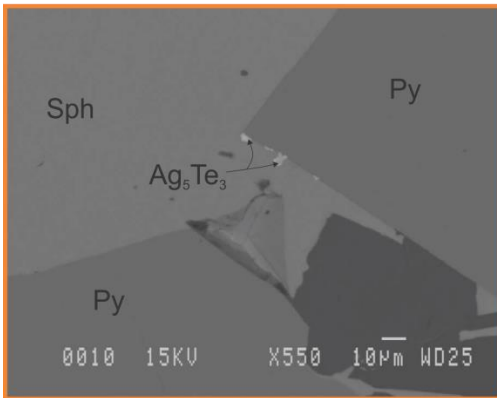
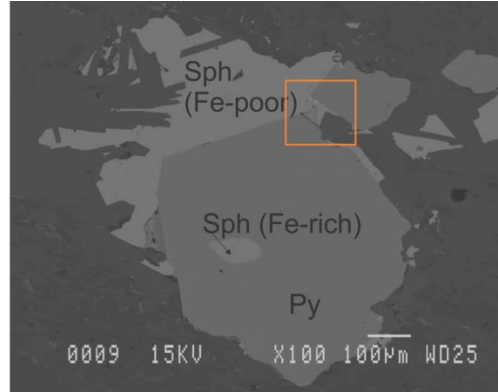
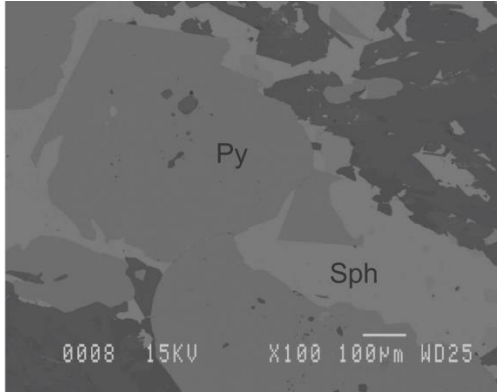
FS: 4000



Element	Gross (cps)	BKG (cps)	Net (cps)	P:B Ratio	Z Corr	A Corr	F Corr
Fe	52,5	20,7	31,8	1,5	1,011	1,018	0,938
Zn	211,9	12,7	199,1	15,6	1,044	1,004	1,000
S	856,8	9,9	846,9	85,8	0,909	1,384	1,000

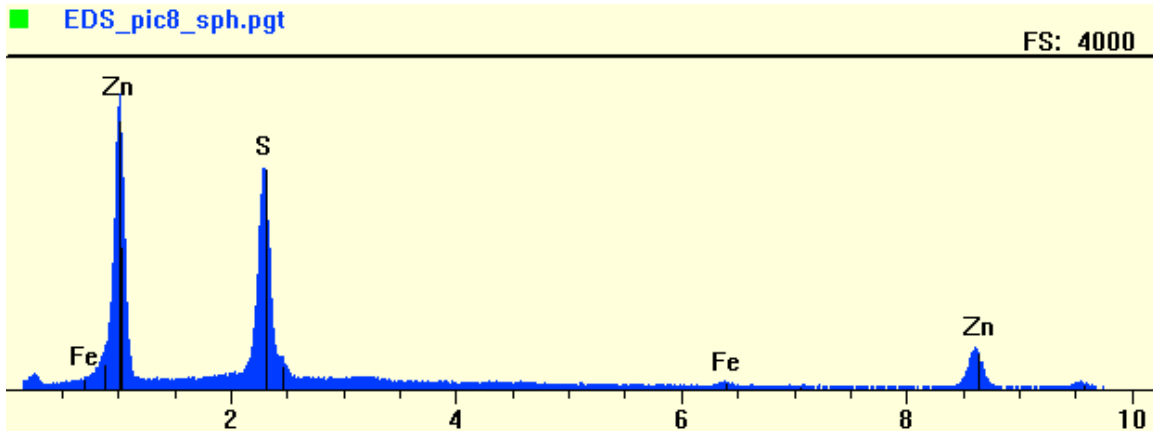
III.X Sample RRR435875

SEM photos, sample RRR435875



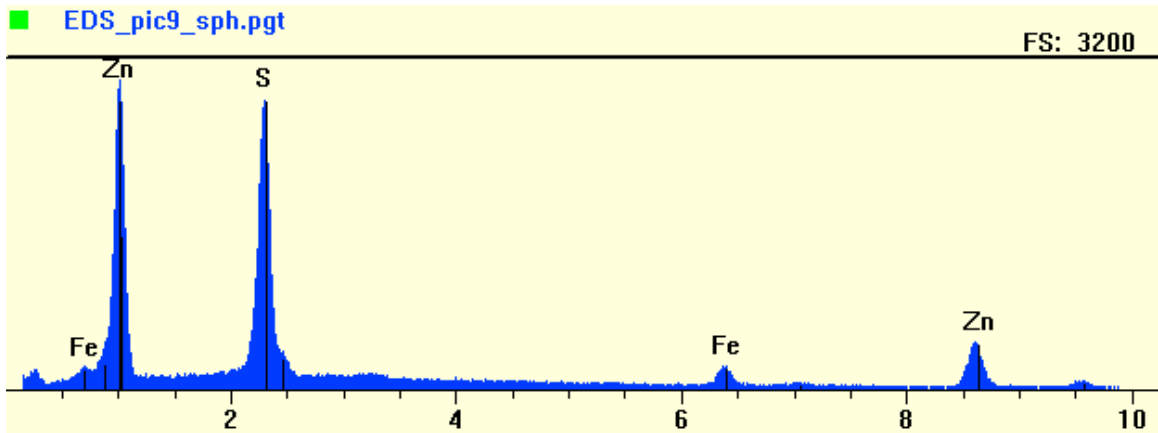
Spectrum reports, sample RRR435875

Live Time:	60,00	Count Rate:	5533	Dead Time:	38,62 %
Beam Voltage:	15,00	Beam Current:	1,00	Takeoff Angle:	30,00



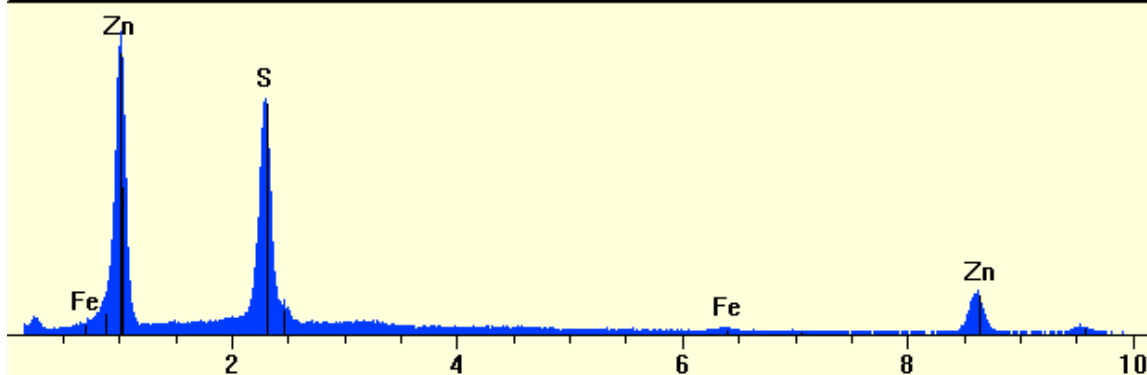
Element	Gross (cps)	BKG (cps)	Net (cps)	P:B Ratio	Z Corr	A Corr	F Corr
Zn	212,8	13,9	198,9	14,3	1,031	1,002	1,000
S	815,9	45,5	770,4	16,9	0,897	1,436	1,000
Fe	34,4	21,0	13,4	0,6	0,998	1,016	0,925

Live Time: 60,00 Count Rate: 5486 Dead Time: 38,73 %
 Beam Voltage: 15,00 Beam Current: 1,00 Takeoff Angle: 30,00



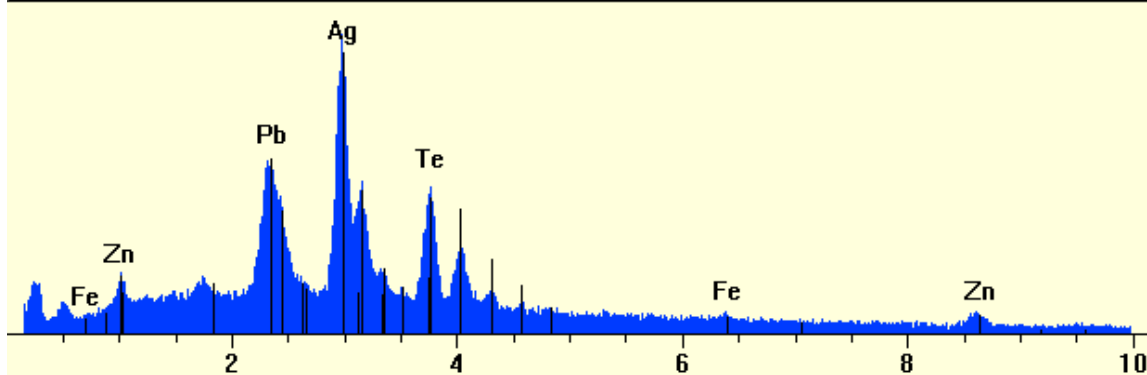
Element	Gross (cps)	BKG (cps)	Net (cps)	P:B Ratio	Z Corr	A Corr	F Corr
Zn	196,5	11,5	185,0	16,1	1,033	1,005	1,000
S	859,9	48,8	811,1	16,6	0,899	1,422	1,000
Fe	91,1	21,1	70,0	3,3	1,000	1,015	0,935

Live Time: 60,00 Count Rate: 5804 Dead Time: 39,95 %
 Beam Voltage: 15,00 Beam Current: 1,00 Takeoff Angle: 30,00



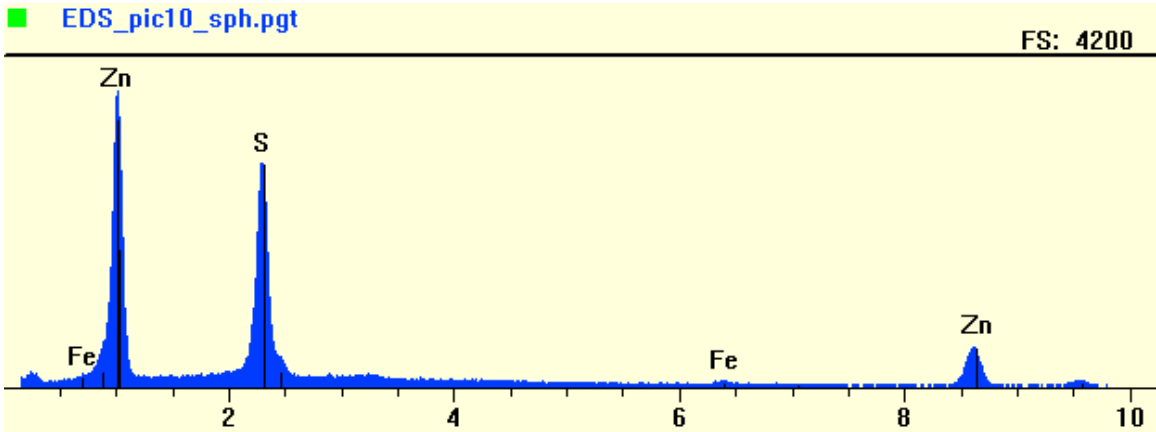
Element	Gross (cps)	BKG (cps)	Net (cps)	P:B Ratio	Z Corr	A Corr	F Corr
Zn	222,5	13,3	209,3	15,8	1,029	1,002	1,000
S	859,7	59,9	799,8	13,4	0,895	1,443	1,000
Fe	36,1	20,1	16,0	0,8	0,996	1,016	0,922

Live Time: 60,00 Count Rate: 6139 Dead Time: 44,19 %
 Beam Voltage: 15,00 Beam Current: 1,00 Takeoff Angle: 30,00



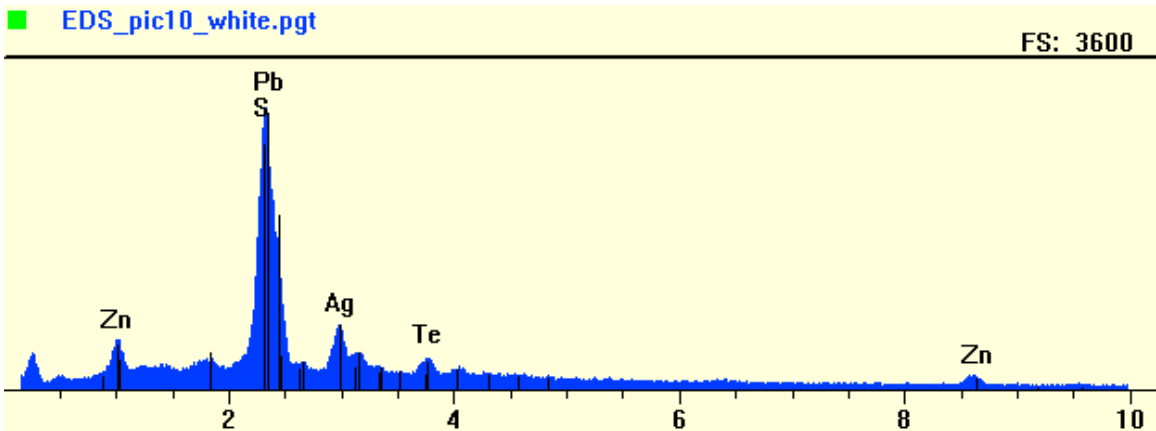
Element	Gross (cps)	BKG (cps)	Net (cps)	P:B Ratio	Z Corr	A Corr	F Corr
Zn	51,8	25,1	26,7	1,1	0,871	1,030	0,997
Fe	44,5	39,0	5,6	0,1	0,839	1,100	0,998
Ag	504,0	82,3	421,7	5,1	0,974	1,087	0,990
Te	274,3	126,8	147,5	1,2	1,005	1,181	1,000
Pb	318,1	79,7	238,5	3,0	1,179	1,047	0,996

Live Time: 60,00 Count Rate: 5836 Dead Time: 40,27 %
 Beam Voltage: 15,00 Beam Current: 1,00 Takeoff Angle: 30,00



Element	Gross (cps)	BKG (cps)	Net (cps)	P:B Ratio	Z Corr	A Corr	F Corr
Zn	225,4	13,3	212,2	16,0	1,047	1,003	1,000
S	861,4	9,2	852,2	92,2	0,912	1,375	1,000
Fe	34,4	20,2	14,2	0,7	1,013	1,018	0,937

Live Time: 60,00 Count Rate: 6925 Dead Time: 46,73 %
 Beam Voltage: 15,00 Beam Current: 1,00 Takeoff Angle: 30,00

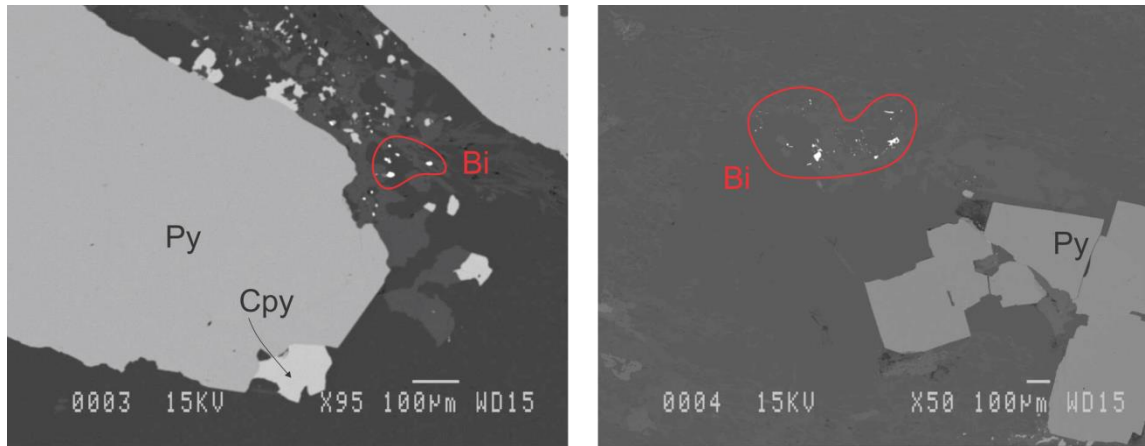


Element	Gross (cps)	BKG (cps)	Net (cps)	P:B Ratio	Z Corr	A Corr	F Corr
Zn	70,2	24,1	46,1	1,9	0,843	1,025	0,986
Ag	230,0	81,6	148,4	1,8	0,939	1,282	0,998

Te	124,3	74,0	50,3	0,7	0,969	1,248	1,000
Pb	980,9	85,8	895,1	10,4	1,135	1,028	0,999
S	875,4	85,6	789,8	9,2	0,717	1,295	0,995

III.XI Sample RRR435883

SEM photos, sample RRR435883



Spectrum photos, sample RRR435883

There are no spectrum reports for sample RRR435883.

APPENDIX IV: SELECTED MICROPROBE RESULTS FROM KJARSGAARD (2013) STUDY

Selected microprobe results from a study of ten thin sections from the Rainy River deposit, undergone by I. Kjarsgaard for the Geological Survey of Canada at the request of P. Mercier-Langevin.

Mineral	S %	Mn%	Fe %	Co %	Ni %	Cu %	Zn %	Ga %
?PbBiAgS	15.736	0.000	13.269	0.006	0.000	0.058	0.015	0.000
Ag-pentlandite	31.245	0.024	37.296	0.026	17.771	0.327	0.011	0.000
bismuthinite	18.624	0.010	1.189	0.000	0.000	2.653	0.038	0.000
bismuthinite	18.767	0.026	1.182	0.051	0.000	0.641	0.010	0.007
electrum	0.837	0.016	0.497	0.000	0.010	0.057	0.000	0.000
electrum	0.411	0.000	0.833	0.000	0.000	0.055	0.000	0.000
electrum	0.232	0.032	0.084	0.041	0.012	0.071	0.000	0.000
electrum	0.217	0.003	0.132	0.012	0.023	0.114	0.000	0.000
electrum	2.061	0.000	4.331	0.004	0.009	0.494	0.000	0.137
electrum	0.192	0.003	0.277	0.016	0.000	0.184	0.000	0.194
electrum	0.193	0.000	0.482	0.020	0.000	0.183	0.000	0.287
gold	0.255	0.015	0.154	0.000	0.032	0.052	0.000	0.142
gold	0.134	0.000	0.100	0.014	0.000	0.052	0.000	0.178
gold	0.088	0.023	0.069	0.006	0.038	0.018	0.000	0.200
gold	0.010	0.000	0.013	0.056	0.014	0.061	0.000	0.154
gold	0.038	0.000	0.006	0.023	0.000	0.017	0.000	0.183
gold	0.057	0.013	0.010	0.000	0.021	0.000	0.000	0.172
sphalerite	32.274	0.027	2.765	0.000	0.009	0.205	61.892	0.098
sphalerite	32.357	0.038	2.914	0.000	0.023	0.095	64.515	0.169
sphalerite	32.550	0.003	2.888	0.000	0.036	0.068	65.073	0.224
sphalerite	31.733	0.004	0.143	0.000	0.015	0.019	65.194	0.116
sphalerite	32.057	0.002	0.110	0.015	0.016	0.000	66.767	0.108
sphalerite	31.871	0.008	0.144	0.005	0.000	0.000	65.878	0.138
sphalerite	32.809	0.001	1.561	0.004	0.021	1.009	63.771	0.000
sphalerite	32.378	0.047	0.516	0.017	0.005	0.032	65.856	0.107
sphalerite	32.236	0.020	0.601	0.000	0.000	0.052	66.669	0.118
sphalerite	32.096	0.151	6.707	0.008	0.000	0.001	60.564	0.063
sphalerite	32.363	0.104	6.645	0.010	0.005	0.019	60.538	0.042
sphalerite	32.506	0.106	6.501	0.000	0.000	0.000	60.696	0.068
sphalerite	32.688	0.123	5.536	0.021	0.000	0.026	60.248	0.051
tellurobismuthite	0.980	0.010	2.440	0.008	0.019	0.027	0.080	0.008
troilite	36.633	0.016	62.721	0.026	0.000	0.025	0.000	0.000

troilite	35.823	0.004	62.710	0.019	0.000	0.000	0.024	0.000
troilite	35.771	0.007	62.594	0.009	0.000	0.046	0.084	0.002
troilite	36.064	0.002	62.128	0.028	0.047	0.000	0.009	0.048
troilite	36.334	0.000	62.690	0.034	0.000	0.000	0.000	0.000
troilite	36.316	0.002	62.931	0.049	0.000	0.054	0.036	0.022
ullmannite	15.339	0.000	0.333	0.020	27.715	0.006	0.000	0.000

Mineral	As %	Se %	Ag %	Cd %	Sn %	Sb %	Te %	Au %
?PbBiAgS	8.755	0.044	1.964	0.042	0.033	0.013	0.234	0.076
Ag-pentlandite	0.021	0.010	12.983	0.107	0.000	0.000	0.039	0.000
bismuthinite	0.000	0.346	0.575	0.033	0.000	0.086	0.104	0.176
bismuthinite	0.000	0.253	0.038	0.000	0.013	0.126	0.000	0.054
electrum	0.001	0.008	53.634	0.000	0.000	0.000	0.127	44.860
electrum	0.000	0.013	37.537	0.000	0.000	0.000	0.027	60.753
electrum	0.000	0.008	47.159	0.000	0.000	0.000	0.042	51.754
electrum	0.015	0.000	62.009	0.000	0.000	0.000	0.139	36.556
electrum	0.019	0.000	41.768	0.000	0.000	0.000	0.162	52.985
electrum	0.000	0.009	32.352	0.000	0.000	0.000	0.107	67.394
electrum	0.000	0.019	37.513	0.000	0.000	0.000	0.115	61.075
gold	0.000	0.000	20.079	0.000	0.000	0.000	0.048	78.587
gold	0.000	0.003	16.832	0.000	0.000	0.000	0.080	85.098
gold	0.008	0.000	17.090	0.000	0.000	0.002	0.022	82.699
gold	0.008	0.000	13.580	0.000	0.000	0.000	0.034	84.937
gold	0.000	0.000	13.433	0.015	0.000	0.000	0.039	85.644
gold	0.001	0.000	13.158	0.005	0.000	0.000	0.036	85.172
sphalerite	0.007	0.005	0.000	0.328	0.000	0.000	0.006	0.000
sphalerite	0.000	0.000	0.000	0.337	0.000	0.000	0.000	0.072
sphalerite	0.034	0.009	0.000	0.299	0.023	0.000	0.000	0.005
sphalerite	0.000	0.038	0.000	0.381	0.000	0.000	0.000	0.000
sphalerite	0.032	0.012	0.000	0.310	0.010	0.012	0.000	0.039
sphalerite	0.016	0.000	0.000	0.253	0.023	0.006	0.000	0.000
sphalerite	0.000	0.000	0.000	0.297	0.028	0.000	0.000	0.000
sphalerite	0.000	0.000	0.000	0.279	0.000	0.000	0.000	0.063
sphalerite	0.000	0.000	0.016	0.290	0.000	0.006	0.041	0.024
sphalerite	0.000	0.007	0.009	0.243	0.000	0.000	0.005	0.130
sphalerite	0.010	0.023	0.060	0.232	0.002	0.025	0.000	0.000
sphalerite	0.000	0.014	0.014	0.259	0.000	0.000	0.000	0.038
sphalerite	0.000	0.025	0.028	0.156	0.000	0.005	0.000	0.000
tellurobismuthite	0.000	0.128	0.000	0.068	0.000	0.269	44.707	0.051
troilite	0.012	0.000	0.000	0.000	0.004	0.000	0.000	0.000

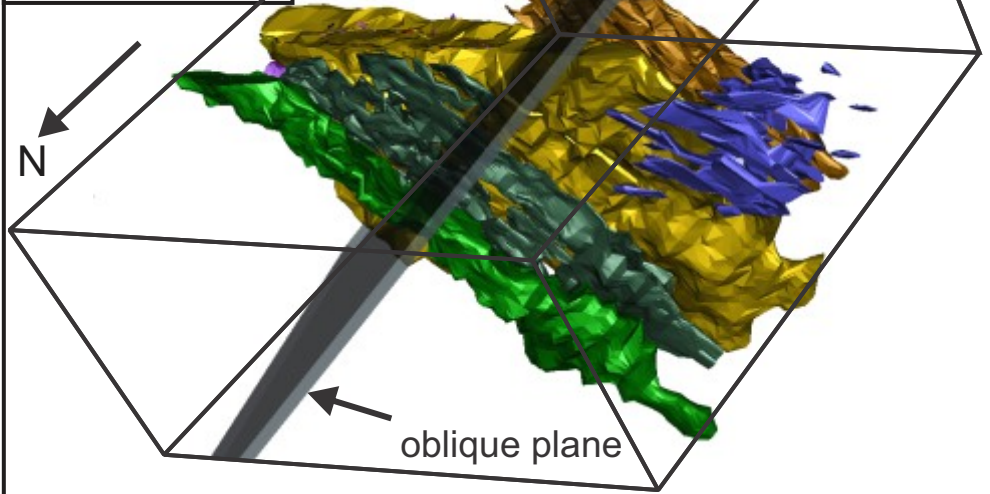
troilite	0.000	0.004	0.000	0.009	0.006	0.000	0.000	0.000
troilite	0.000	0.000	0.000	0.000	0.009	0.000	0.000	0.000
troilite	0.011	0.006	0.000	0.007	0.005	0.000	0.004	0.000
troilite	0.000	0.000	0.041	0.002	0.026	0.000	0.018	0.000
troilite	0.000	0.006	0.009	0.000	0.000	0.000	0.000	0.000
ullmannite	1.439	0.007	0.010	0.000	0.263	55.977	0.000	0.000

Mineral	Hg %	Pb %	Bi %	Total
?PbBiAgS	0.000	53.149	4.273	97.666
Ag-pentlandite	0.000	0.000	0.152	100.013
bismuthinite	0.000	1.033	74.689	99.557
bismuthinite	0.041	0.731	78.110	100.050
electrum	1.087	0.000	0.007	101.141
electrum	0.488	0.000	0.022	100.139
electrum	0.371	0.000	0.000	99.806
electrum	1.280	0.000	0.000	100.500
electrum	0.000	0.000	0.128	102.099
electrum	0.260	0.000	0.000	100.989
electrum	0.655	0.000	0.007	100.550
gold	0.000	0.000	0.000	99.364
gold	0.000	0.000	0.000	102.491
gold	0.000	0.000	0.000	100.263
gold	1.357	0.000	0.000	100.224
gold	1.181	0.000	0.000	100.579
gold	1.276	0.000	0.041	99.962
sphalerite	0.009	0.000	0.142	97.767
sphalerite	0.000	0.000	0.178	100.698
sphalerite	0.127	0.000	0.174	101.513
sphalerite	0.018	0.000	0.000	97.661
sphalerite	0.070	0.000	0.168	99.728
sphalerite	0.123	0.000	0.084	98.549
sphalerite	0.000	0.000	0.074	99.575
sphalerite	0.000	0.000	0.048	99.348
sphalerite	0.039	0.000	0.057	100.169
sphalerite	0.000	0.000	0.015	99.999
sphalerite	0.000	0.000	0.038	100.116
sphalerite	0.000	0.000	0.083	100.285
sphalerite	0.043	0.000	0.177	99.127
tellurobismuthite	0.125	0.000	49.355	98.275
troilite	0.061	0.021	0.102	99.621

troilite	0.027	0.000	0.164	98.790
troilite	0.000	0.000	0.102	98.624
troilite	0.000	0.000	0.161	98.520
troilite	0.000	0.000	0.008	99.153
troilite	0.072	0.023	0.005	99.525
ullmannite	0.000	0.000	0.124	101.233

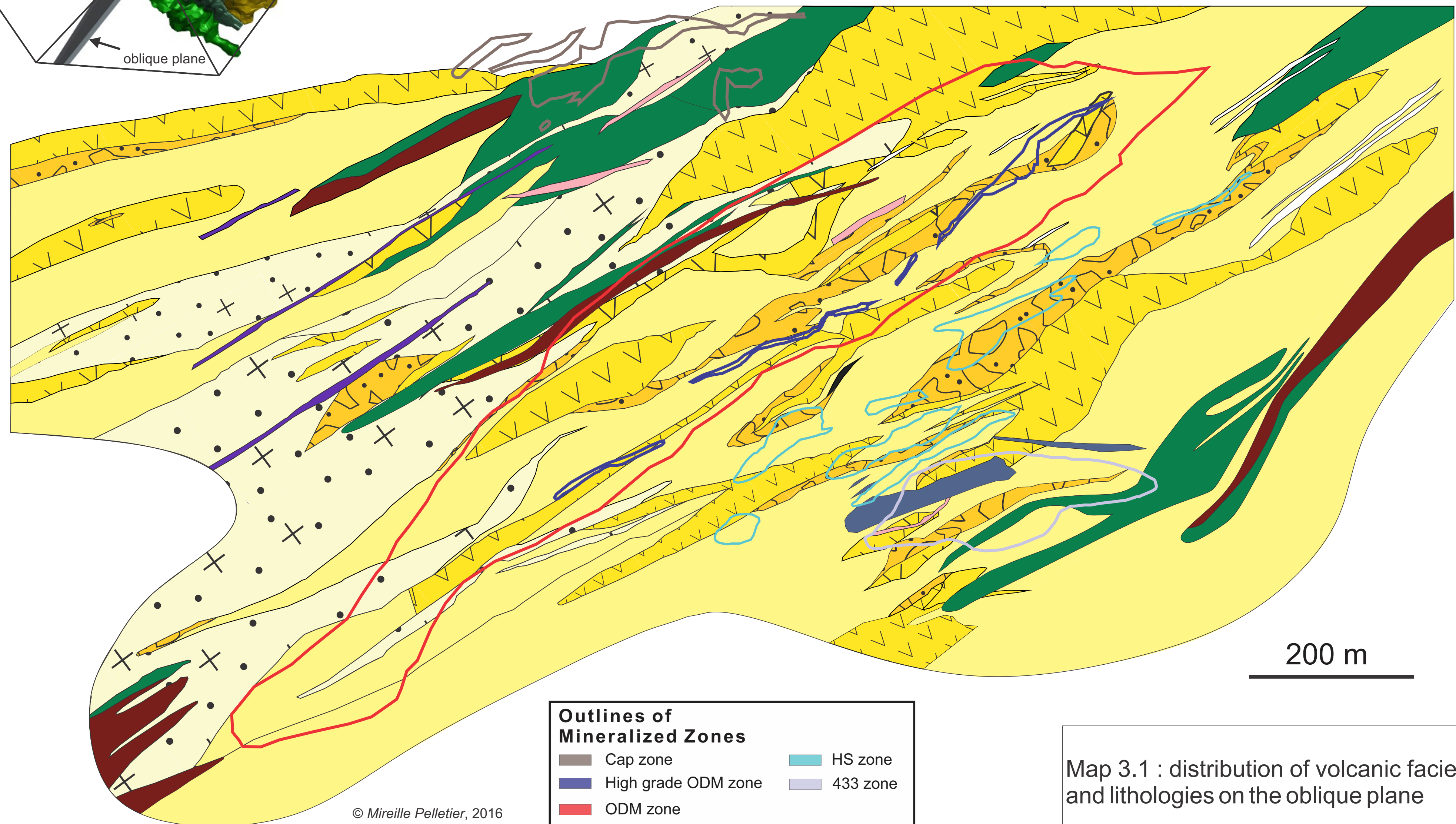
Mineralized zones

- 433 zone
- HS zone
- ODM/17 zone
- High-grade ODM/17 zone
- CAP zone
- Beaver Pond zone



Legend

- | | | |
|--|----------------------------|------------------|
| Coherent dacite (lava flow or subvolcanic intrusion) | Tholeiitic basalt | Diabase dyke |
| Quartz feldspar porphyry-textured (QFP) dacite | Mafic-dominated siltstones | High strain zone |
| Dacitic tuff / muscovite schists | Deformed granitic dyke | |
| Dacitic volcanoclastics (tuff breccia) | Deformed gabbroic dyke | |



Outlines of Mineralized Zones

Cap zone	HS zone
High grade ODM zone	433 zone
ODM zone	

© Mireille Pelletier, 2016

Map 3.1 : distribution of volcanic facies and lithologies on the oblique plane

Map 3.2 : Distribution of volcanic facies on 425475E cross section

+300 m

Ore zones outlines

-  Cap zone
-  ODM zone
-  ODM high grade zone
-  HS zone
-  433 zone

Legend

-  Coherent dacite (lava flow or subvolcanic intrusion)
-  Quartz feldspar porphyry-textured (QFP) dacite
-  Dacitic tuff / muscovite schists
-  Dacitic volcanoclastics (tuff breccia)
-  Tholeiitic basalt
-  High Nb-Ta tholeiitic basalt
-  Rutile-rich tholeiitic basalt
-  Mafic-dominated siltstones
-  Diabase dyke
-  High strain zone
-  Deformed gabbroic dyke
-  Deformed granitic dyke

-300m

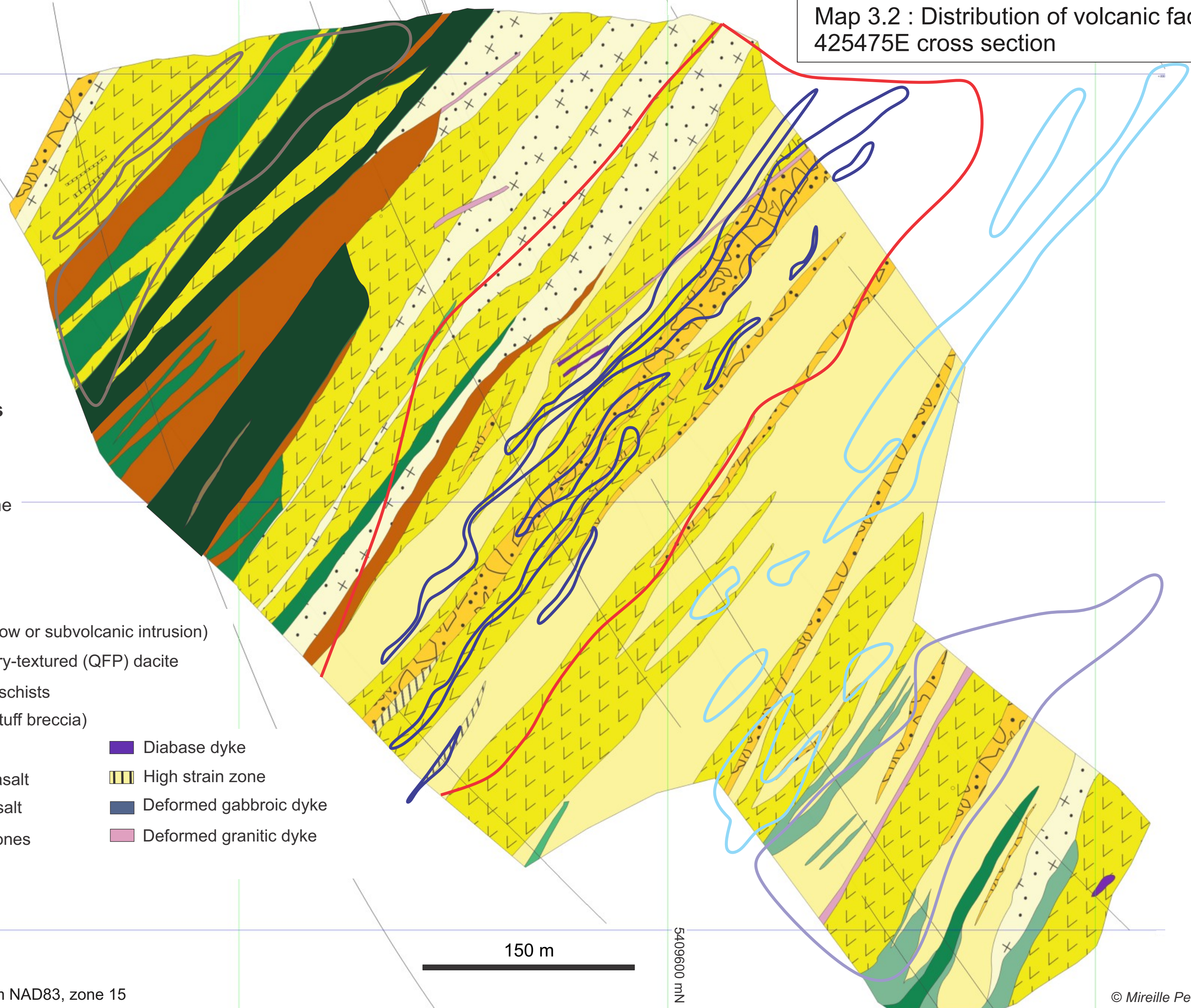
150 m

5409000 mN

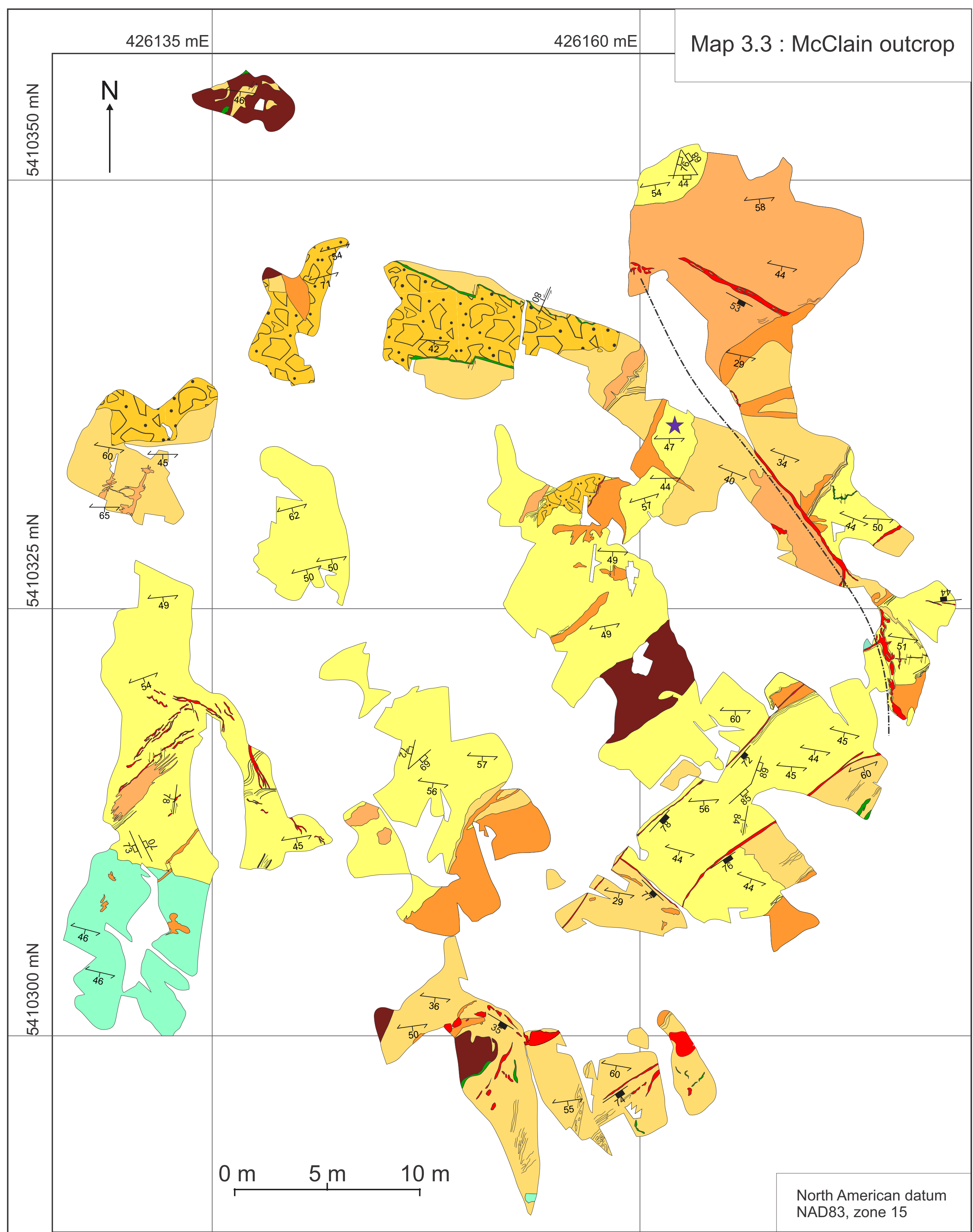
North American Datum NAD83, zone 15

5409600 mN

© Mireille Pelletier, 2016



Map 3.3 : McClain outcrop



North American datum
NAD83, zone 15

Lithology legend

- Coherent dacite
- Feldspar-phyric dacite
- Sulphide-poor (<0.5% sulphide) dacitic tuff
- Sulphide-bearing (0.5-1% sulphide) dacitic tuff
- Sulphide-rich (>1% sulphide) dacitic tuff
- Dacitic breccia and tuff breccia
- Pyrite-rich mafic tuff

- Flow bands
- Sample site for U-Pb geochronology
- Veins legend
- Quartz vein (150N/59°)
- Massive to semi-massive chlorite bands
- Sulphide-bearing veins

Structural legend

- Sulphide-bearing veins
- Main foliation
- Senestral fault plane
- Joints

427075 mE

427100 mE

427125 mE

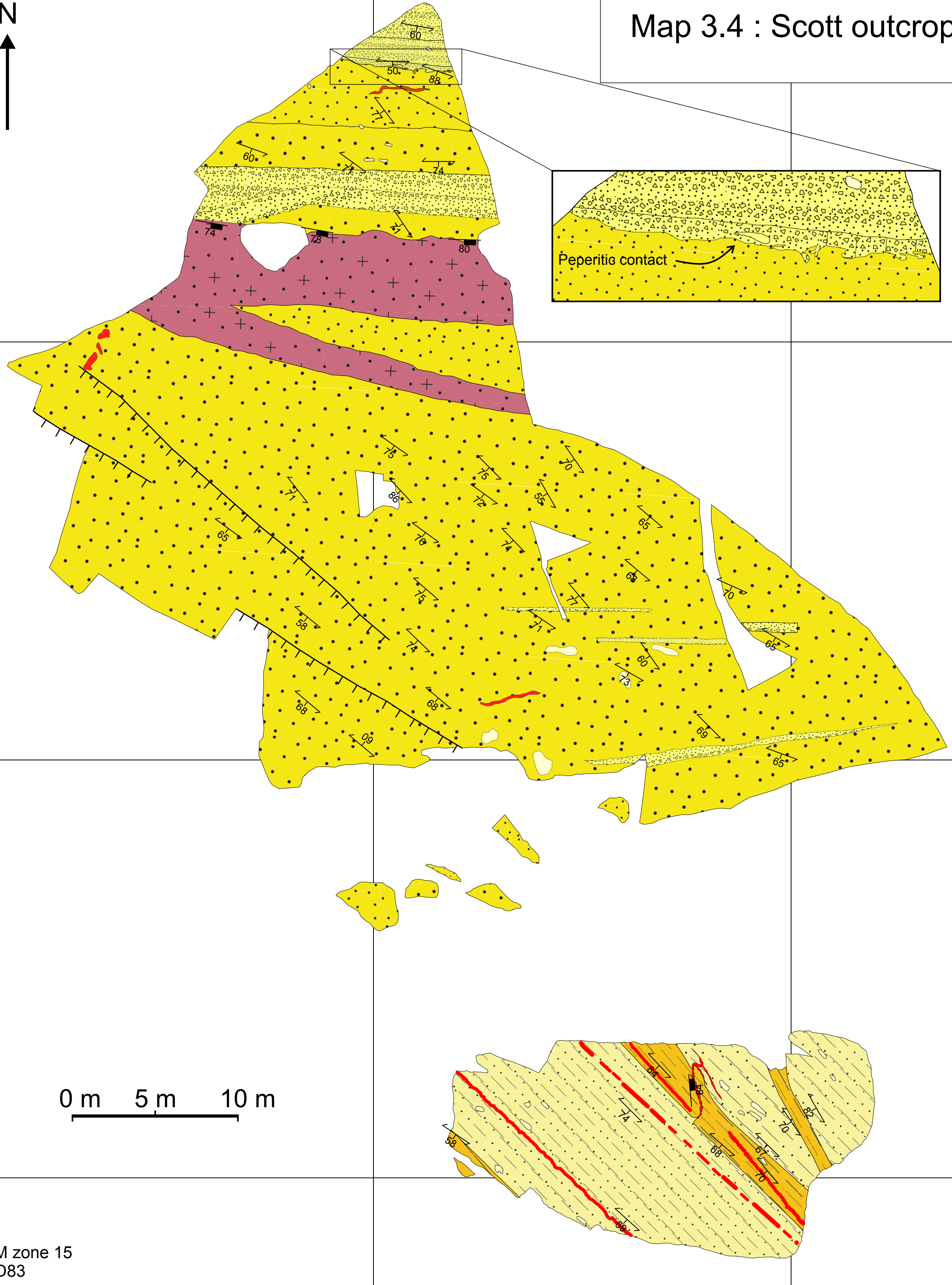


Map 3.4 : Scott outcrop

5408440 mN

5408415 mN

5408390 mN



0 m 5 m 10 m

UTM zone 15
NAD83

Scott outcrop legend

- Brecciated porphyritic dacite
- Laminated fine grained dacite
- Massive dacite
- Graded dacite tuff beds
- Synvolcanic dacitic porphyritic sill
- Blocks
- Deformed quartz veins
- Topography break
- Sulphide-bearing vein and porphyritic dyke
- Main foliation

